ORNL-4911

GAS-COOLED REACTOR PROGRAMS

ANNUAL PROGRESS REPORT

Period Ending December 31, 1972

OAK RIDGE NATIONAL LABORATORY
OPERATED BY UNION CARBIDE CORPORATION • FOR THE U.S. ATOMIC ENERGY COMMISSION

Printed in the United States of America. Available from
National Technical Information Service
U.S. Department of Commerce
5285 Port Royal Road, Springfield, Virginia 22151
Price: Printed Copy $7.60; Microfiche $0.95

ORNL-4911
UC-77 — Gas-Cooled Reactor Technology

Contract No. W-7405-eng-26

GAS-COOLED REACTOR PROGRAMS ANNUAL PROGRESS REPORT

For Period Ending December 31, 1972

P. R. Kasten, Program Director
J. H. Coobs, Associate Director
A. L. Lotts, Associate Director

MARCH 1974

OAK RIDGE NATIONAL LABORATORY
Oak Ridge, Tennessee 37830
operated by
UNION CARBIDE CORPORATION
for the
U.S. ATOMIC ENERGY COMMISSION

Contents

Foreword

The Gas-Cooled Reactor Programs being carried out at the Oak Ridge National Laboratory contribute to the development and evaluation of high-temperature gas-cooled reactors (HTGRs) and of gas-cooled fast reactors (GCFRs). These programs are sponsored by the U.S. Atomic Energy Commission and include the Thorium Utilization Program (HTGR Fuel Recycle Development Program), the HTGR Base Program, the HTGR Safety Program, and the GCFR Program. The major effort is in HTGR technology with emphasis on fuel and fuel recycle development and includes fuel fabrication and irradiation testing, head-end processing, fission product behavior, and fuel performance studies. Work is also carried out on the performance of prestressed concrete reactor vessels (PCRVs) under possible reactor conditions. Work in GCFR development emphasizes fission product behavior in vented fuel elements and involves irradiation testing of a vented fuel element concept under various venting conditions. Close coordination is maintained with Gulf General Atomic (GGA) relative to their efforts in the design and development of gas-cooled reactors and in HTGR fuel-recycle development.

Major incentives for developing HTGRs are the prospects for economically attractive power production, the conservation of low-cost uranium ore reserves, the potential for obtaining low environmental impact at a diversity of plant sites, and the potential for high-temperature direct cycle and process heat applications. The good neutron economy and fuel performance permit high burnup and associated low fuel-cycle costs. The high-temperature capability of the graphite core structure facilitates reactor plant operation at high thermodynamic efficiency, and thus requirements for heat dissipation to the environment are relatively low. Excellent fission product retention by the coated fuel particles leads to coolant circuits with low radioactivity levels. Further, the high exposures attainable with HTGR fuels permit the development of economic fuel recycling. At the same time, the development of fuel-recycle technology is important to the commercial acceptance of HTGRs as economic power producers.

The fuel-recycle effort is part of the national HTGR fuel-recycle development program being carried out by the USAEC at ORNL, GGA, and the Idaho Chemical Processing Plant. The objective of the fuel-recycle program is to develop the pertinent technology so that commercial plants for reprocessing and refabrication of HTGR fuels can be built and operated economically. The operations to be considered take place between the discharge of spent fuel elements from the reactor and the return of refabricated fuel elements to the reactor; these include fuel shipping, storage, fuel recovery and purification, refabrication, and waste management. The work involves fuel reprocessing development, fuel refabrication development, irradiation testing of refabricated fuels, and fuel-recycle systems analyses involving the economics associated with various processes and equipment. The program at ORNL includes development of head-end processing methods for irradiated fuels and associated off-gas cleanup technology, production of microspheres containing recycle-type fuel, microsphere coating technology, recycle-fuel-element fabrication technology, associated equipment and process development, recycle-fuel irradiations, and fuel-recycle evaluation analyses.

HTGR fuel development work at ORNL is largely concerned with evaluating, understanding, and improving fuel performance and with studying the behavior of certain fission products, including their effect

on fuel performance. Coated-particle fuel studies involve irradiation testing, with emphasis on demonstration of satisfactory fuel and materials performance at the required fuel burnup and fast-neutron fluences. In these tests, the High-Flux Isotope Reactor (HFIR) has proved highly useful as an irradiation facility; an in-core facility at the ORR is also being utilized, which provides relatively large volumes for testing fuel bodies. A small effort has been placed on development of fuels having higher temperature capabilities; successful development would have important implications relative to helium-turbine and/or process-heat HTGRs.

In work on PCRVs, a thermal cylinder experiment has been conducted to study the time-dependent stress-strain behavior of a simulated segment of a PCRV vessel. The prestressing, pressure, and thermal-gradient conditions were those expected under HTGR design conditions; prior to disassembly a built-in heater was activated to simulate a hot-spot condition. Disassembly of the experiment and analysis of the results are now being carried out.

Relative to HTGR safety studies, a fission product technology program has been carried out for a number of years involving the behavior of fission products and of fuel under various circumstances, including abnormal conditions. Included in these efforts is a fission product surveillance program being carried out in the Peach Bottom HTGR, which provides information on fission product behavior in an HTGR environment. These studies are continuing, and, in addition, an expanded HTGR safety program is being planned; this expanded effort will include analysis of accident sequences and of postulated consequences, and study and evaluation of fission product and coolant technology, of core and component technology, and of materials, instrumentation, and containment behavior as they relate to HTGR safety.

The helium-cooled GCFR offers a high breeding ratio, a doubling time of about ten years, a core conversion ratio of approximately 1.0, and a small reactivity change from loss of coolant. The high core conversion ratio makes possible extended operating periods without refueling and results in low reactivity swings during fuel exposure. The fuel performance requirements for this reactor are basically similar to those for the liquid-metal-cooled fast breeder reactor (LMFBR), and thus the GCFR program draws heavily on the fuel development of the LMFBR program. ORNL fuel work for the GCFR now principally involves irradiation testing of fuel pins. Irradiation test results for a vented fuel element were obtained during this report period, with encouraging results. A second test of a vented fuel pin was initiated. Other work being carried out in the GCFR program includes mathematical modeling of the steam generator to simulate response under transient conditions and planning for a Core Flow Test Facility which would be utilized to perform heat transfer and fluid flow testing of simulated GCFR fuel assemblies.

Work on gas-cooled reactors is also being performed in Europe, with significant efforts being carried out on the HTGR concept by the Dragon Project and by Germany. Associated information pertaining to HTGR research and development work is obtained through the USAEC/Dragon HTGR Agreement and the USAEC/KFA Exchange Arrangement. These exchange programs include information on fuel development, performance and testing, fission product behavior, and fuel reprocessing.

The organization of this report is based on an orderly presentation of technical information which largely follows program lines but not completely. Chapter 8, for example, covers work supported by both the HTGR Base Program and HTGR Safety Program; the overall results, such as those on fission product behavior, can be presented more clearly when done in an integrated manner. Similarly, Chapter 7 covers work supported by the HTGR Base Program and the Thorium Utilization Program, since HTGR fuel irradiations and results from postirradiation examinations of various fuels are better understood when presented in an overall manner. In general, however, this report presents information associated with specific programs as follows: Thorium Utilization Program, chapters 1 to 5, 7; HTGR Base Program, chapters 6 to 8, 12, 13; HTGR Safety Program, chapters 8 to 11; and GCFR Program, chapters 14 and 15.

Although this report is called an annual progress report, the material covers the 15-month period from Oct. 1, 1971, to Dec. 31, 1972. Henceforth, progress reports will be prepared on a calendar-year basis.

Summary

1. HTGR HEAD-END FUEL REPROCESSING DEVELOPMENT

1.1 Reprocessing Studies of Irradiated Fuels

Head-end fuel reprocessing studies are directed primarily toward determining the nature of the radioactive contaminants in the off-gas from fuel burning and developing a process using absorption of gaseous fission products in liquid CO_2 as a means of decontaminating the burner off-gas.

Hot-cell experiments involving burning a variety of fuel types are being conducted. Laboratory equipment duplicating much of that in the hot cell has been set up and operated to provide information on the gas flow and heat transfer and temperature behavior to be expected from the hot-cell equipment. This work provides a necessary guide to operating and interpreting results from the hot-cell burner. In addition, the laboratory experiments are providing guidance in selecting equipment to be used in the hot cell to characterize the burner off-gas. This equipment includes cascade impactors, electrostatic precipitators, and several other particulate and gas analyzers.

1.2 Laboratory Studies of Burner Off-Gas Decontamination

Accurate measurements of the distribution of krypton between liquid and gaseous CO_2 have been made, and work with xenon has started. These data and information from published papers have been used in a computer code developed for use in predicting and correlating the behavior of Kr, CO, O_2, and N_2 in the KALC process and in guiding the engineering development work.

1.3 Engineering Development of Burner Off-Gas Decontamination

The development work for the KALC process has two facets: (1) the work being carried out at the Oak Ridge Gaseous Diffusion Plant, where large equipment will be used to demonstrate operation of an integrated off-gas decontamination system, and (2) the experimental engineering work being carried out at ORNL to provide such information as basic design data on mass transfer, process control procedures, and component performance. A computer model of the KALC system has been developed and used to calculate KALC process behavior. Variations in temperatures and flow rates and enthalpy data have been used in the calculations to date. It has been found that close control of the operating variables (e.g., boilup rate from the fractionator reboiler) is required if both high decontamination factor and high concentration factor for krypton are to be attained.

1.4 Whole-Block Burner Studies

The reference reprocessing flowsheet specifies fluidized-bed burning of crushed fuel elements as the method for removing the bulk graphite from the fissile and fertile fuel particles. An alternate approach to the reference flowsheet is to simply burn the whole fuel element intact. Gulf General Atomic (GGA) has been developing the reference approach, and at ORNL we have sustained a small effort on burning the whole fuel element (block).

By use of a small burner that accommodates a one-sixth segment of a block, we have achieved carbon burning rates of 130 g/min, which is an acceptably high burning rate. The burner is air-cooled, and fuel particles fall out the bottom of the burner as the graphite matrix burns away from them. Ranges of burner temperatures, burning rates, fuel types, and reagent gases (oxygen plus diluents) have been studied. Particle breakage in the burner has been shown to be acceptably low using Triso-coated ThC_2 particles. Techniques for starting the burner and controlling burner temperature have been developed.

1.5 Particle Separation Studies

Separation of particles containing ^{235}U from those containing ^{233}U will be necessary for economical operation of HTGRs. Screening to separate the particles on the basis of size difference is the reference process. However, some proposed combinations of particle types would make this impractical. Thus, we have studied alternative chemical and physical methods to effect the separation. Reaction of the SiC layer on Triso-coated particles with Na_2CO_3 has been shown to satisfactorily remove it from ThO_2 particles, making possible a subsequent separation based on size. It has also been shown that two types of particles of closely similar size but different densities can be separated by elutriation with water or carbon tetrachloride.

2. HTGR FUEL MICROSPHERE PREPARATION DEVELOPMENT

2.1 Engineering Demonstration of UO_2 Sphere Preparation

The feasibility of the CUSP process for UO_2 sol preparation and use of a nonfluidized-bed microsphere-forming column were demonstrated in engineering equipment. A total of about 22 kg of nominal 200-μ-diam UO_2 spheres was prepared at a rate of 3 kg/day. Ion exchange was used to remove nitrate and formate ions from the alcohol used to extract water from the sol droplets to form gel spheres.

2.2 Sol-Gel Preparation of ThO_2 Spheres

The upper sphere size limit attainable with the ORNL sol-gel process was determined using ThO_2 sols. With 2.6 *M* ThO_2 sol, droplets which produce 600-μ-diam product tend to break up. The effect worsens with increasing size, reaching several percent at ~650-μ-diam product and up to 50% for ~700-μ-diam product. Increasing the sol concentration to 3 *M* ThO_2 raises the product diameter size limit to ~670 μ before excessive droplet breakup occurs.

A new sol droplet forming technique has been developed that greatly increases the uniformity of droplet size. In this method a piston is immersed in the sol at the entrance to the orifice or capillary where the sol enters the drying alcohol. Vibration of the piston at a rate approximately matching the natural frequency of droplet formation produces extraordinarily uniform sol droplets. Batches of from 1 to 13 kg of fired ThO_2 spheres of 370 to 500 μ diameter formed with the two-fluid nozzle had average diameters within 1% of the predicted diameters, with standard deviations of 2.5 to 5.0 μ. A shear nozzle with vibration had a much higher throughput rate and produced ThO_2 spherical product of 303 μ mean diameter with a standard deviation of 5.9 μ.

2.3 Sol-Gel Preparation of ThO_2-UO_2 Spheres

ThO_2-UO_2 spheres (Th/U = 3.0) containing natural uranium were prepared for use in fuel fabrication studies. Smaller amounts of ThO_2-UO_2 spheres containing ^{235}U and ^{233}U were prepared for use in fuel irradiation tests.

2.4 Resin-Based Microsphere Development

Loading ion exchange resin with uranium as a step in preparing HTGR fuel kernels was demonstrated in a Higgins-type countercurrent contactor. Strong-acid resin was loaded using uranyl nitrate solution. Work is in progress on using this type of contactor for loading weak-acid resin.

When weak-acid resin is loaded, it is necessary to equilibrate solid UO_3 with the uranyl nitrate that is circulated to the resin. The UO_3 serves the function of reacting with the H^+ released from the resin by exchange with UO_2^{2+}, thus shifting the equilibrium to favor further resin loading. The rates of dissolution of UO_3 prepared in various ways were studied to determine if $^{235}UO_3$ and $^{233}UO_3$ could be mixed in a specified ratio to yield resin loaded with that same ratio. The dissolution rates were found to differ, depending on the source of the UO_3; therefore no simple mixing procedure will work.

Resin was also loaded from UO_2F_2 solutions (such as might result from UF_6 hydrolysis). Strong-acid resin loaded fully, but weak-acid resin did not, presumably

because of inhibition by initially formed hydrofluoric acid.

It was shown that strong-acid resins may be partially, uniformly loaded to any prescribed degree and, further, that weak-acid resin loading may be carried out nonuniformly when the resin is in the ammonia or sodium form. In the case of the weak-acid resin, the loading is in a more or less uniform outer spherical shell.

3. FUEL FABRICATION PROCESS DEVELOPMENT

The objective of the fuel fabrication process development is to provide a basis for the design and operation of the remote refabrication line to be installed in the Thorium-Uranium Recycle Facility (TURF) to demonstrate the recycle of HTGR fuel. This fabrication line will accept bare fissile microspheres and perform the necessary fabrication and inspection operations for production of graphite-based fuel elements on a pilot scale. The principal activities of the process development during this period have been particle coating and inspection and fuel stick fabrication.

3.1 Microsphere Coating

Operation of two 5-in.-diam coating systems continued during this report period, and numerous equipment modifications were made to these systems. These modifications include redesign of the lower portion of the 5-in.-diam prototype coating furnace, design and demonstration of fritted-plate-type gas distributors with and without water cooling, lengthening of the prototype furnace, and modification of gas handling equipment to allow improved control and calibration.

Encouraging preliminary results were obtained on reclamation of SiC-coated graphite coating chambers by oxidation of the undesirable carbon deposits. Significant improvements were made in the application of buffer coatings in 5-in.-diam coating systems. Using statistically designed experiments, we vastly improved our understanding of the buffer coating process and found a new set of operating parameters that reduced the within-batch coating thickness standard deviation from about 25% of the mean coating thickness to about 14%. Charges as large as 3200 g of ThO_2 kernels were successfully buffer coated in the 5-in.-diam coater, and excellent quality SiC coatings were produced in the 5-in.-diam remote prototype coater.

Work in particle inspection has been directed toward the development of rapid inspection techniques. A light blockage-type particle size analyzer which uses a 1000-channel analyzer linked to a small computer was constructed, and the factors which affect its accuracy and precision were investigated. Recent developments in particle handling have been in the area of pneumatic particle transferring and particle valving.

3.2 Fuel Rod Fabrication

The major steps involved in the fabrication of fuel rods are particle dispensing and blending, rod molding, rod inspection, and carbonization and annealing. The major accomplishment in fuel rod fabrication was the design, fabrication, installation, and operation of an automatic fuel rod machine. This machine, which uses the slug injection process for molding fuel rods, is presently capable of manufacturing fuel rods at a rate of 4000 rods per 20-hr day. Startup problems were minimal, and several thousand fuel rods have been fabricated on this machine.

A pinch valve system was developed and evaluated as a means of volumetrically dispensing particles. Pneumatic batch blending and individual rod blending were evaluated. For individual rod blending, a system which splits the particles required for a single fuel rod into ten approximately equal increments and loads these increments into the mold sequentially looks promising.

In rod molding, the effects of the process variables of temperature, pressure, matrix composition, and fuel particle size on the injection rate of fuel rods were determined. The major factors affecting matrix intrusion are matrix composition and the particle size distribution. Carbonization studies have been limited to preliminary in-block carbonization tests to minimize the tendency of the fuel rods to bond to the graphite element. Assessment of techniques for heavy-metal assay of ^{233}U-containing HTGR fuels was begun.

4. HTGR FUEL RECYCLE PILOT PLANT STUDIES

4.1 Reprocessing Pilot Plant Demonstration

A decision was made by the AEC to perform the hot reprocessing demonstration at the Idaho Chemical Processing Plant. In support of AEC's evaluation of sites for the Reprocessing Pilot Plant, ORNL is working with the Allied Chemical Corporation in preparing equipment layouts, equipment descriptions, and cost estimates. The selected head-end flowsheet consists of a burn-crush-leach process followed by solvent extraction using 5% TBP. The uranium will be purified by hexone.

The reprocessing operation will be unique in that the first step consists in burning the graphite fuel elements, which results in the formation of large quantities of carbon dioxide. This gas will be highly contaminated with both particulate and gaseous impurities. The particulate matter will be removed by HEPA filters, the vapors by the KALC process, and combination contaminants by a combination of filters, solid absorbers, and liquid scrubbers.

4.2 Refabrication Pilot Plant Demonstration

The hot Refabrication Pilot Plant will be built and demonstrated in the TURF at ORNL. The design studies for this pilot plant have focused upon the overall plant layout and capabilities and on establishing criticality parameters for the equipment. Conceptual plant layouts have been completed for pilot plants with capacities of both 25 and 100 kg of heavy metal per day. Comparison cost estimates of the plants were completed for design, procurement, installation, unit testing, and plant operation.

Process flowsheets were prepared for the major processing systems, including sol preparation, microsphere preparation, microsphere coating, fuel stick fabrication, and fuel element assembly. Scoping studies were made of the individual items of equipment to be required for the microsphere coating and fuel stick fabrication systems.

A study was initiated to determine the critical dimensions of equipment used for refabrication of HTGR fuels. The criticality of homogeneous mixtures of ^{235}U, ^{232}Th, C, and H was explored by calculation. The critical dimensions of bare and water-reflected infinite cylinders were determined by the ANISN code using the Hansen-Roach neutron cross sections set. The k_{eff} for 5-, 9-, and 11-in.-diam coating furnaces containing mixtures of ^{233}U, ^{232}Th, C, and H were calculated using the KENO computer code.

5. STUDIES AND EVALUATION OF COMMERCIAL HTGR FUEL RECYCLE PLANTS

5.1 Evaluation of Commercial HTGR Fuel Recycle Processes

To assist in the development program and as an aid in establishing priorities, technical and economic studies are being made of the various processes and parameters of interest to commercial-size recycle technology. Four basic functions of a commercial recycle plant have been identified: spent fuel handling, processing of the various fuels, disposal of wastes, and the handling and shipment of fresh fuel. The various processes which may be used in such a plant have been identified, their feasibility established, their costs calculated, and the most economically promising set of processes selected. Processes have been studied for fuels based on ^{233}U, ^{235}U, and ThO_2. The economic studies included factors for the different kind of processing areas required, such as the type and amount of shielding.

The studies of fuel kernel preparation have concentrated on the recycle of ^{233}U. It has been shown that in preparing ^{233}U fuel kernels, the CUSP process equipment costs about two-thirds as much as that for the Solex process. Further, the CUSP process makes more efficient use of space.

Technical data were developed for both the Biso and Triso particle coating processes. Six processes, plus options of in-block or out-of-block carbonization and thermosetting or thermoplastic binders, were included. The slug injection process with thermoplastic binders and in-block carbonization was selected for additional study.

Studies identifying the major waste streams and their compositions have been completed. A major problem was encountered with the reprocessing of the ^{235}U. The weight ratio of fission products to uranium in this stream is greater than 3. This stream represents only about 6% of the heavy metal entering the reactor but accommodates 40% of the fission events. It was recommended that the ^{235}U be irradiated for two cycles and then retired since it will contain too much ^{236}U.

5.2 Economics Associated with Timing of HTGR Fuel Recycle

This work was initiated to show the influence on fuel cycle costs of delaying the introduction of fuel reprocessing capability. The first schedule studied calls for 124 HTGRs to be built, with the first reactor producing power in 1979; modifications to this schedule include three cases of extending it in increments of 125 reactors. Using best current estimates of fuel cycle costs, the optimum year to initiate recycle is 1983. The added costs of beginning reprocessing before this date are insignificant, while those associated with delays are two to three times as large but are only significant where a lengthy delay has occurred. The calculated fuel cycle costs were shown to be very sensitive to changes in assumed costs of uranium ore and toll enrichment.

6. HTGR FUEL ELEMENT DEVELOPMENT

6.1 Coating Development

Emphasis was placed on optimizing the geometrical design of Biso coatings for fertile particles. A series of particles with widely varying buffer- and outer-coating thicknesses were fabricated and irradiation tests initiated. The principal problem in coating technology is the characterization of coatings, particularly the measurement of anisotropy. Standards were prepared for BAF and OPTAF measurements, and the OPTAF equipment was continually upgraded. The scanning electron microscope was found to be a useful tool for determining the effects of irradiation on the structure of pyrolytic carbon coatings.

6.2 Bonded Fuel Development

Continuous-matrix fuel rods 0.5 in. in diameter and 30 in. long were extruded on a semiproduction scale at the rate of 10 fpm. The particle volume loading was 31.5%, and the matrix density was 1.75 g/cm^3. Dimensional control and fuel distribution were good, warpage was not excessive, and there was no indication of broken particles due to extrusion. Experimental work on a small scale showed that the matrix density decreased with increase in volume loadings up to 45% unless the extrusion reduction ratio was increased accordingly. Unirradiated extrusions with low volume loadings had a thermal conductivity value at low temperature about seven times that for a close-packed-particle bonded rod.

Preliminary results of carbonizing close-packed bonded rods containing a pitch binder indicate that in-block carbonization is feasible, but further work should be directed toward in-block carbonization on a large scale.

6.3 Resin Particle Development

Fuel kernels derived from weak-acid resins were emphasized because they contain no sulfur. Processes for loading, carbonizing, and heat treating were studied and developed. Particles carbonized to 1000°C were mildly reactive with moist air; however, sealing of the surface with acetylene or simple heat treatment reduced the extent of the problem. Coating of resin-derived kernels was found to be no different from that of other types of fissile particles except that buffer coatings may be much thinner. Since the bed volume increase is much smaller when such kernels are coated, the coating operation is thereby simplified.

7. HTGR FUEL IRRADIATIONS AND POSTIRRADIATION EVALUATIONS

7.1 Irradiation Tests in the HFIR Removable Beryllium Facility

The third instrumented experiment in the HFIR, capsule HRB-3, was built, installed, and irradiated to a maximum fast fluence of 10^{22} neutrons/cm^2. Preliminary results from visual and dimensional examinations indicated good performance of slug-injected fuel rods and slurry-blended and molded specimens. These rods contained Biso-coated ThO_2 fertile and strong-acid-resin-derived fissile particles. Detailed examinations are in progress. Companion capsules HRB-4 and -5 were built and installed, and irradiation was begun. These capsules, with similar loadings, are designed to test slug-injected and extruded fuel rods to a range of exposures. The slug-injected rods vary in matrix composition and carbonization technique. All specimens contain weak-acid-resin-derived fissile and ThO_2 fertile particles. These capsules were operated successfully through the fourth cycle (about 80 days). Specimen preparation and construction are in progress for the sixth capsule, which is designed to test slug-injected and extruded fuel rods containing "reference recycle" $(Th,U)O_2$ fissile particles. Two fuel rods are fueled with $(Th,U)O_2$ containing ^{233}U, and other loose samples of resin-derived fissile particles containing ^{233}U will be included for testing.

7.2 Irradiation Tests in the HFIR Target Facility

Examination of specimens and evaluation of results from target capsules HT-7 to HT-10 were completed and reports prepared. Another series of capsules, HT-12 to HT-15, were intended to investigate the minimal requirements for Biso coatings on fertile particles. Various Biso-coated samples with different thickness and thickness ratios were designed, and their performance was predicted by using the STRETCH code. The series of 16 batches, including 7 from GGA, were prepared and characterized, and 8 samples were selected from each for testing in the four capsules. The capsules were designed to test samples at two temperatures, 900 and 1250°C nominal particle holder temperature, and a range of fluences. The four capsules were loaded, assembled, and inserted in the target facility, and the irradiation of the first, HT-12, to a maximum fast-neutron fluence of 4.1×10^{21} neutrons/cm^2 was completed. All samples that had dense isotropic coatings survived except one that had a thin outer coating

unprotected by a buffer coating. Other samples that had anisotropic structures or property gradients within the outer coating exhibited some failures. This demonstrated again that anisotropy is the most significant property affecting the performance of the outer coating.

7.3 Irradiations in ORR Core Facilities

We designed and are preparing two facilities for irradiation of large instrumented capsules in the C-3 and E-3 core positions of the ORR. The core loading of ORR was adjusted so that these positions were surrounded by fuel elements; measurements of flux and gamma heating under this condition enabled thermal analysis and detailed design of the capsule to be completed. The capsule will test fuel rod samples within several channels of a graphite fuel body and is designed to test fuel rod fabrication variables. Preparation of fuel specimens is in progress.

7.4 Irradiation Tests in the ETR Capsule Facilities

The irradiation of a set of two capsules, H-1 and H-2, containing specimens of candidate recycle fuels was completed in the ETR. Accidental inversion of both capsules during the last quarter of the irradiation period produced extremely high heat ratings and high temperatures in some fuel rod samples. This resulted in some fuel migration and extensive coating failures in the affected specimens, but other fuel rods that were relatively unaffected performed well. Detailed examination of specimens by metallography and other means is in progress, and flux measurements will enable detailed thermal analysis of the capsule and evaluation of fuel performance.

7.5 Recycle Test Elements in the Peach Bottom Reactor

Test element RTE-7 was dismantled and examined after about 250 days operation in the Peach Bottom reactor. At the low fast-neutron fluence ($\sim 10^{21}$ neutrons/cm^2), all fuel rods performed well and could be unloaded from the graphite fuel blocks without difficulty. Dimensional change data were generally consistent with data predicted by the coating densification model. Test element RTE-4 was removed after 384 days operation and is awaiting examination; irradiation of the other 5 is continuing.

7.6 Nuclear Analysis in Support of Irradiation Experiments

Documentation of all recent flux measurements in HFIR facilities was prepared. Data from several flux profile measurements in the ORR were collected and analyzed to provide design parameters for new in-core experiments by GGA and ORNL. Neutron spectra and flux profiles for the ETR core facilities were used to resolve operating conditions for the two recycle fuel capsules H-1 and H-2. Many specimens in these capsules operated at very high heat ratings during the last cycle when the capsules were accidentally inverted.

7.7 Characterization of Irradiated Particle Coatings

Microhardness measurements on irradiated coatings from capsules HT-7, -9, and -10 indicated that densification of the coatings is accompanied by increased hardness and that hardness decreases as swelling commences at high fluences.

7.8 Summary of Fuel Rod Dimensional Changes under Irradiation

All data on dimensional changes in fuel rods containing Biso- or Triso-coated particles or combinations thereof were observed to be consistent with shrinkage predicted by coating densification models.

8. HTGR FUEL CHEMISTRY, FUEL INTEGRITY, AND FISSION PRODUCT BEHAVIOR

8.1 Mass Transport in HTGR Particles in a Temperature Gradient

A theoretical description of gas-phase carbon transport in oxide particles is being attempted in an effort to provide a general method for the chemical design of oxide particles. An analysis of the failure of Biso particles during irradiation was inconclusive, in contrast to an earlier, apparently adequate description of the failure of the SiC-coated Dragon reference particle. An experimental program is now operational for the out-of-reactor measurement of carbon and fuel migration in coated particles that are placed in a temperature gradient.

A thermodynamic study of the UO_2-U_2N_3 solid solution at 1250 to 1850°C indicates that the activity coefficient ratio of these two components is $\leq 10^{-4}$. This system can be synthesized to give an (O + N)/U ratio that is substantially less than 2 and may provide a

means for the maintenance of a low carbon monoxide pressure in a particle during nuclear fission; such behavior may substantially reduce the probability of coating failure via gas-phase transport of carbon.

8.2 Chemical Characteristics of Fuel and Fission Products

The possibility of using additions of refractory oxides to Biso UO_2 particles to retain cesium, barium, and strontium has been reviewed. The literature indicates that Al_2O_3 would be effective for strontium and barium, but retention of cesium by oxide addition appears questionable.

Observed expansion of pyrocarbon coatings on UO_2 particles at $T \geq 2200°C$ is apparently caused by pressures of carbon monoxide established by the UO_{2-x}-C-CO equilibrium instead of an equilibrium involving UC_2, as previously postulated.

8.3 Postirradiation Evaluation of Irradiated Fuels

The C1-28 experiment, which was to have provided 21 different types of coated particles irradiated to 35% FIMA, released excessive amounts of fission products during irradiation and only achieved 11% FIMA at the time of removal. An extensive postirradiation examination showed that the possible causes of failure were mechanical damage in the bonded rods and differential expansion between the coated particles and the fuel tubes. Cesium diffused throughout the graphite capsule and fuel tubes at temperatures less than 800°C. Zirconium contamination in the fuel tubes was directly related to the number of visible coated particle failures.

Additional experiments were performed on pyrocarbon-coated fuel particles. The more recent cesium diffusion coefficients for high-temperature isotropic (HTI) pyrocarbon deposited from methane were higher than previous determinations but were still lower than those for low-temperature isotopic (LTI) pyrocarbon deposited from propylene in the temperature range from 1400 to 1600°C. Cesium diffusion coefficients for LTI pyrocarbon deposited from propane were in between values for the methane- and propylene-deposited coatings. No correlation of cesium diffusion with preirradiation density, isotropy, and crystallite size was found. Postirradiation measurements are needed and are being planned to narrow the range of these variables, since it is known that fast-neutron damage induces changes in these properties.

Eight methods were tried for disintegration of bonded coated-particle fuel rods in order to determine numbers of broken fuel particles and fuel and fission product distribution in the fuel rods. Only two of these methods seemed practical: the electrolytic method using nitric acid, which has been used previously, and a high-pressure water jet.

9. REACTIONS OF HTGR CORE MATERIALS WITH STEAM

9.1 Out-of-Pile Laboratory Experiments

The reactions of steam with various graphites are being studied to develop methods for calculating the effects of steam on the core of an HTGR and the rates of hydrogen and carbon monoxide production. Investigations are centered upon the determination of rate constants and the understanding of the reasons why the observed rate of reaction varies with the extent of reaction. The results will be used in the analysis of accidents involving steam ingress.

Reaction rate data for H-327 graphite with steam at 0.0950 atm partial pressure are reported over the temperature range 800 to 1000°C. The percentage of carbon oxidized in these experiments varied from 0 to 5%. Changes in specific surface area and gas diffusion characteristics were measured as functions of extent of reaction at each temperature.

A series of experiments to compare the rates of reaction of bonded rod matrices and H-327 graphite were performed. Inhibition of corrosion by the reaction products was observed.

9.2 In-Pile Experiments

A series of in-pile experiments was performed to confirm that the radial temperature gradient in a real fuel element may influence the relative rates of oxidation of fuel and structural graphite and to determine whether radiolytic effects were important.

The fraction of the fuel matrix oxidized was found to be less in the higher temperature experiment, as predicted, indicating that reaction of water with the porous graphite sleeve was protecting the fuel. It was not found necessary to invoke radiolytic reaction mechanisms to explain the observed carbon removal. However, this conclusion must be qualified by the degree of precision with which the reaction rate could be predicted.

Fission products, with the exception of the noble gases and iodine, were retained by the oxidized fuel element. Exposure of UC_2 kernels to steam caused rapid evolution of krypton and xenon. However,

further irradiation following removal of steam led to a reduction in the rate of noble gas release.

10. FISSION PRODUCT BEHAVIOR IN HTGR COOLANT CIRCUITS

10.1 Iodine Adsorption and Desorption

Measurements of iodine adsorption and desorption on Fe_3O_4 were continued in the temperature range 250 to 450°C. At the lower temperatures both adsorption and desorption were slow. Thermochemical calculations relating to compositions of phases in the Fe-I system were repeated for the Cr-I and Ni-I systems.

10.2 Fission Product Behavior in the Coolant Circuit of the Peach Bottom HTGR

Measurements of radionuclides circulating and deposited in the accessible parts of the coolant circuit of the Peach Bottom HTGR were made. No evidence that cesium and strontium were being released from core II at a significant rate other than as gaseous precursors was found. Activities in the primary circuit remained below 2 $\mu Ci/cm^2$ for measured gamma emitters downstream of the steam generator. Indications were that some deposits of cesium are being slowly transferred from the circuit to the purification plant or some inaccessible part of the primary circuit.

No gas-borne molecular species were measured by the first coolant sampler to be installed downstream of the steam generator above the "background" created by radioactive dust. This indicates that cesium in the coolant is being attenuated about tenfold by passage through the steam generator.

11. HTGR SAFETY PROGRAM PLAN AND SAFETY ANALYSIS

11.1 HTGR Safety Program Plan

A draft plan for a National HTGR Safety Program is being prepared for submission to the AEC.

11.2 Systems and Safety Analysis

The aims of future safety analyses are discussed. A pilot study of the emergency diesel engine generator arrangement used at Fort St. Vrain indicated that this system is equivalent in reliability to more conventional arrangements.

12. PRESTRESSED CONCRETE PRESSURE VESSEL DEVELOPMENT

12.1 PCRV Thermal Cylinder Test

The thermal cylinder experiment was designed to provide test data for evaluating the capability of analytical methods to predict stress-strain behavior of a simulated cylindrical barrel of a PCRV and to demonstrate structural behavior under design and off-design thermal conditions. The experimental phase of the program is essentially complete. The model was cast in February 1971, and since then it has been prestressed and subjected to a planned series of loadings without structural failure or schedule slippage. An overtemperature test was performed with no apparent distress to the system. Initial predictions of the structural behavior are satisfactory, and further analyses will be performed.

12.2 Concrete Triaxial Creep Studies

Completion reports were issued on creep recovery and the effect of curing on the creep behavior of concrete.

13. EXCHANGE PROGRAMS

The USAEC/Dragon HTGR Agreement and the USAEC/KFA Exchange Arrangement involve routine exchange of reports on HTGR research and development, exchange and discussion of current test results during visits of personnel, exchange of test samples, and assignment of personnel. Under the Dragon agreement, crushing tests and metallographic examination of irradiated fuel compacts confirmed the excellent performance of coated ORNL fuel irradiated in Dragon fuel elements. As part of the KFA arrangement, an exchange of personnel was initiated to work in the fuel reprocessing development programs at the respective laboratories.

14. GCFR IRRADIATION EXPERIMENTS

In the joint ORNL-GGA irradiation testing program for the evaluation of $(U,Pu)O_2$-fueled metal-clad fuel rods for the gas-cooled fast reactor (GCFR), current emphasis is on the testing of fuel rods of the vented-and-pressure-equalized concept. The vented fuel rod is the present reference GCFR fuel rod design because of its better performance potential and because information being developed in LMFBR fuel-rod testing programs is more applicable to this design. The better performance potential results from the elimination of

large pressure differentials across the cladding by venting the fuel rod interior to a pressure-equalization system.

The current irradiation tests, capsules GB-9 and GB-10, were designed to permit an initial evaluation of the overall performance of the vented-and-pressure-equalized fuel rod. Various aspects of the GCFR pressure-equalization system are also being studied in these tests. Capsules GB-9 and GB-10 are unique experiments in that they are providing direct measurements of the release and transport of fission products from an operating fast breeder reactor fuel rod.

14.1 Irradiation of GCFR-ORR Capsule GB-9

The thermal-flux irradiation of capsule GB-9 in the ORR poolside facility was terminated in November 1971, after the fuel rod had operated for 471 days to an estimated fuel burnup of 54,000 MWd per metric ton of heavy metal. The test was terminated when a gas line to the secondary containment vessel was broken. The burnup goal had been extended from the original 55,000 to 75,000 MWd/metric ton; however, most of the test objectives had already been realized when the experiment was terminated.

The fuel rod in capsule GB-9 was a shortened prototype of the GCFR vented rod with a 10-in. fuel column, a 1.9-in. upper blanket region, and a 3-in.-long charcoal trap. The release of fission products to and through the charcoal trap was measured with the rod operating under the design conditions of 14.8 kW/ft peak heat-generation rate, 685°C peak cladding outer surface temperature, and 300°C charcoal trap temperature.

The experiment provided substantial information on the fission product release behavior to be expected from the GCFR vented fuel rod, and the results have already been used in many aspects of the GCFR pressure-equalization system design.

14.2 Postirradiation Examination of GCFR-ORR Capsule GB-9

Postirradiation examination of the vented fuel rod from capsule GB-9 is nearing completion at ANL. The fuel rod appearance was excellent. Dimensional measurements indicated less than 0.001 in. diametral change.

The gamma spectrometry studies at ANL showed that the volatile fission product species migrated from the hot regions of the fuel to some extent and plated out at the fuel-blanket interfaces, where the temperatures drop sharply. No measurable activity was found in the charcoal trap, indicating that the fuel and blanket were quite effective in retaining volatile fission products under the conditions of the GB-9 test.

One segment of the GB-9 fuel rod from a position having nearly the peak heat rating was returned to ORNL for metallographic and microprobe analyses. Examination of this sample revealed cladding attack varying in depth from about 1 to 4 mils, the more severe attack being on the cooler side of the fuel rod.

14.3 Design and Operation of GCFR-ORR Capsule GB-10

Capsule GB-10 was designed with increased capability for measuring fission product release and transport, including examination of the direct release from the oxide fuel. The GB-10 fuel rod is similar to the GB-9 rod, but it has a roughened outer surface and contains solid instead of hollow $(U,Pu)O_2$ fuel pellets. The fuel stack height is slightly less than in the GB-9 rod, the upper blanket is one pellet longer, and the charcoal trap length is 1 in. instead of 3 in. The charcoal trap was shortened to 1 in. in GB-10 to provide the same potential fission product loading per unit mass of charcoal as will be the case for the trap in the reference GCFR rod. The thermal design of the GB-10 capsule and the full-power design operating conditions are essentially the same as for GB-9.

The high-pressure helium sweep system for GB-10 permits fission product release measurements under ten different sweep flow modes, including passage of the sweep through each main region of the rod (fuel, blanket, and charcoal trap) separately.

To date, capsule GB-10 has operated successfully in the thermal flux of the ORR poolside facility to a burnup of 10,000 MWd per metric ton of heavy metal at a power level of 12 kW/ft and 565°C peak cladding temperature.

Steady-state fission-gas release rates have been measured as a function of time at the 12-kW/ft power level under all the planned sweep flow modes. Relatively high initial fission-gas release rates decreased by a factor of about 10 during the first month of irradiation

(burnup of ~2500 MWd/metric ton) and then began an increasing trend. Monitoring the activity release from the fuel during two rapid cooloffs (reactor scrams) and two heatup periods indicates that release bursts triggered by the power transients are insignificant compared with the total release during steady-state operation at 12 kW/ft.

In the operation of the GB-10 fuel rod to date, there has been no evidence suggesting the rod trap is needed either for reducing the volatile-fission-product decay heat loads on the GCFR trapping system or for protecting the manifold passages against plate-out constriction or plugging. Should this continue to be the case throughout operation at the higher power levels, consideration may be given to eliminating the rod traps from the GCFR design. The data obtained from the GB-9 and GB-10 capsules to date indicate the vented fuel rod concept to be a feasible and practicable fuel rod design for the GCFR.

15. GCFR STEAM GENERATOR MODELING STUDIES

Development of a hybrid computer model of a steam generator for a gas-cooled fast reactor (GCFR) is being carried out in order to simulate the thermal transients in the system and evaluate the design of the proposed control system. An existing model of a once-through supercritical steam generator can be modified and used to simulate the subcritical steam generator of a GCFR by adding two-phase relationships for the appropriate sections. Improvements to the existing model were completed, and alterations to the computer program to represent the water-steam two-phase system were begun.

1. HTGR Head-End Fuel Reprocessing Development

R. W. Glass K. J. Notz
R. S. Lowrie M. E. Whatley

Head-end fuel reprocessing studies at ORNL have been largely confined to work on irradiated fuel specimens in the hot cell and to studies of the use of liquid CO_2 as an absorbent for gaseous radioactive contaminants. In both cases the primary emphasis is on developing a process for decontaminating HTGR fuel burner off-gas.

A limited amount of work has been expended on a study of the practicability of burning whole HTGR fuel elements as a backup to the reference process of crushing and grinding the fuel elements and then burning the resultant material in one or more fluidized-bed burners.

1.1 REPROCESSING STUDIES OF IRRADIATED FUELS

R. S. Lowrie

1.1.1 Laboratory Support Studies

K. J. Notz R. S. Lowrie

A miniature HTGR fuel burner with its associated off-gas equipment which duplicates the equipment installed in the hot cell has been assembled in a laboratory hood. This equipment is being used to evaluate flow and thermal properties of the burner and to test various particulate removal and sampling devices, such as cascade impactors and an electrostatic precipitator, before they are installed in the hot cell.

The body of the miniburner is a tapered tube that is 0.625 in. ID at the bottom, 1.275 in. ID at the top, and 6.0625 in. long. Thus the gas velocity is highest at the bottom of the burner. A number of experiments (Table 1.1) were run to determine the gas velocity at which incipient fluidization occurred in a bed of particles representative of those in the hot-cell experiments. Sand approximates Triso-coated particles in both size and density; Al_2O_3 is the same as is added to the fluidizing medium; and the carbon was derived from pulverized H-327 graphite fuel block material. For sand and alumina, the tabulated argon velocities just barely caused fluidization; no elutriation of particles was observed. For carbon, the tabulated velocity fluidized the largest particles and was sufficient to carry the smaller particles to the top of the tapered burner. Since most of the hot-cell tests will be run at gas flows of 500 cc/min (STP) or less, only very fine carbon particles will be entrained in the gas stream and subsequently collect on the roughing filter.

Experiments were run to determine the relationship among the internal temperatures, outer burner shell temperatures, and oxygen (or argon) flow rates when burning was carried out while the outside of the burner was being heated in a furnace. With the furnace control set at 800°C, the following temperature differentials were observed:

1. with argon flowing, internal temperature was 5°C lower;
2. with O_2 at 50 cc/min, internal temperature was 15°C higher;
3. with O_2 at 100 cc/min, internal temperature was 45°C higher;
4. with O_2 at 200 cc/min, internal temperature was 70°C higher;
5. with O_2 at 400 cc/min, internal temperature was 100 to 130°C higher.

Table 1.1. Incipient fluidization velocities in miniburner

Material	Mesh size	Burner temperature (°C)	Argon flow (std cc/min)	Superficial gas velocity[a] (fps)
Sand	−35 +40	25	975	0.27
Sand	−35 +40	600	400	0.35
Al_2O_3	−80 +100	25	700	0.19
Al_2O_3	−80 +100	600	360	0.32
Carbon	−325	625	225	0.16

[a]Calculated superficial gas velocities at bottom of the burner and at the burner temperature indicated.

The outer burner shell temperature rose about one-fifth as much as the internal temperature. For the usual size fuel stick (0.5 in. OD, 2 in. long) and at flow rates of 50 cc/min, oxygen consumption is nearly 100%, but at higher flows it is much less. If desired, the oxygen can be diluted with CO_2 to limit the burning rate, and thus the internal temperature rise, while maintaining the total gas flow at a high rate.

Various types of particulate samplers are being tested in conjunction with the miniature burner to provide data on particles formed during combustion of unirradiated fuel sticks, with the expectation that some of these samplers will subsequently be useful in hot-cell work with irradiated samples. The samplers are: (1) an electrostatic sampler (Thermosystems model 3100); (2) a thermal sampler (Aminco model 5-3900); (3) silver membrane filters (Selas Corp.); and (4) two multistage impactors (Enviro-Chem. Div. of Monsanto). The electrostatic sampler is designed to deposit samples on a variety of plates [e.g., microscope slides, SEM (scanning electron microscopy) and EM (electron microprobe) plates, or TEM (transmission electron microscopy) grids]. Preliminary tests of this sampler are being run, using a cadmium dispersion generated by an electric discharge as a stand-in aerosol. The thermal sampler will also be tested using the above aerosol, but the samples will be more difficult to examine because collection is done differently.

The silver membrane filters are already being used in hot-cell work. They have two major advantages over conventional fiber filters: (1) they can be used at higher temperatures, and (2) they are electrically conductive and can therefore be used directly for SEM and EM. Also, they will not adsorb moisture. However, they would be expected to react with iodine. Presently, in hot-cell work, they are being used at 500°C and at room temperature. We are using the finest porosity available, 0.2 μm; the room-temperature filter is backed up with a Gelman absolute filter.

Our multistage impactors have five stages, each of which is of single-jet design and therefore useful with the relatively low gas flow rates we must employ. The bodies are all stainless steel with asbestos gaskets, so that these samplers can be operated at elevated temperatures. The supplier used our operating conditions (CO_2 at 500°C, flow at 500 STP cc/min, and particles with an estimated density of 6 g/cc) and calculated by means of his computer program that our particulate size cut points are 4.6, 2.8, 1.9, 1.1, and 0.7 μm equivalent diameter. One impactor is being used for cold testing, and the other will be installed in the hot cell. The collection plates are designed for easy removal and can readily be replaced after each hot run.

1.1.2 Hot-Cell Studies

R. S. Lowrie C. L. Fitzgerald

As part of a cooperative program between ORNL and Gulf General Atomic (GGA), several recycle test elements (RTEs) are being irradiated in the Peach Bottom Reactor. Most of the types of fuel particle combinations proposed for HTGR fuel are included in these elements.[1,2]

During the past year the hot-cell effort was interrupted to permit decontamination and renovation of the hot cell and the installation of a shielded cave on the top of the cell. This cave is equipped with a 6-in.-thick lead glass viewing window, a pair of model G compact manipulators, and standard glove ports inside

1. *Chem. Technol. Div. Annu. Progr. Rep. Mar. 31, 1971*, ORNL-4682, pp. 92–94.
2. R. P. Morissette and K. P. Steward, *Recycle Test Element Design, Fabrication and Assembly*, GGA-10109 (September 1971).

the shielding. The cave was designed to accommodate a periscope-camera facility and to serve as a sample and waste removal area and as an equipment addition, assembly, disassembly, and removal station.

Recycle test element 7 (RTE-7) was removed from the Peach Bottom Reactor in April 1971 and became available for hot-cell studies. Irradiation of this element started July 14, 1970, and was completed April 22, 1971, after 252 effective full-power days in the Peach Bottom Reactor. The average element burnup was estimated by GGA to be 2.38% FIMA. A peak fast-neutron fluence of $\sim 1 \times 10^{21}$ neutrons/cm^2 was accumulated.[3] The fuel had cooled 265 days when we started hot-cell experiments.

Although RTE-7 contained several types of fuel, we chose to study type *i*, which contained large Triso-coated ThC_2 particles and small Triso-coated UC_2 particles. It is thus quite similar to the Triso ThC_2–Triso (4Th-U)C_2 fuel combination used in the Fort St. Vrain Reactor.

Procedure. The fuel stick was weighed and placed on a bed of −80 mesh alumina in the bottom of the burner (Fig. 1.1) and slowly burned using an oxygen flow rate of 50 cc/min (quiescent burn). The off-gas generated during the burning step was filtered through a 20-μ-porosity sintered metal filter, passed through CO, CO_2, and ^{85}Kr detectors followed by a wet test meter, and finally collected in a bag. The burner residue was separated into a +42 mesh (>400 μ) fertile fraction, a +80 mesh (>177 μ) fissile fraction, and a −80 mesh (<177 μ) fraction consisting mostly of the alumina. The −80 mesh fraction was leached twice with Acid Thorex reagent; the fertile and fissile fractions were ground and burned, and the burner residue was leached twice with Acid Thorex reagent. The +80 mesh fissile fraction was heated at 750°C for 12 hr after the initial burn period to determine if additional fission products were evolved. A schematic diagram of the off-gas train used for the fertile and fissile fraction burns is shown in Fig. 1.2. The ground fissile or fertile material was burned in the miniburner shown in Fig. 1.1 at 750 ± 25°C. The off-gas passed first through two sintered nickel (porosity, 20 μ) primary filters held at 500°C and then, after cooling, through a series of fiber filters with decreasing porosities. The filtered off-gas was scrubbed successively with boiling 6 *M* HCl and cold 4 *M* NaOH. It was subsequently dried, analyzed (for CO, CO_2, and ^{85}Kr), and collected. This rather elaborate off-gas train was devised to study the carry-over of particulates in the off-gas during the burning step.

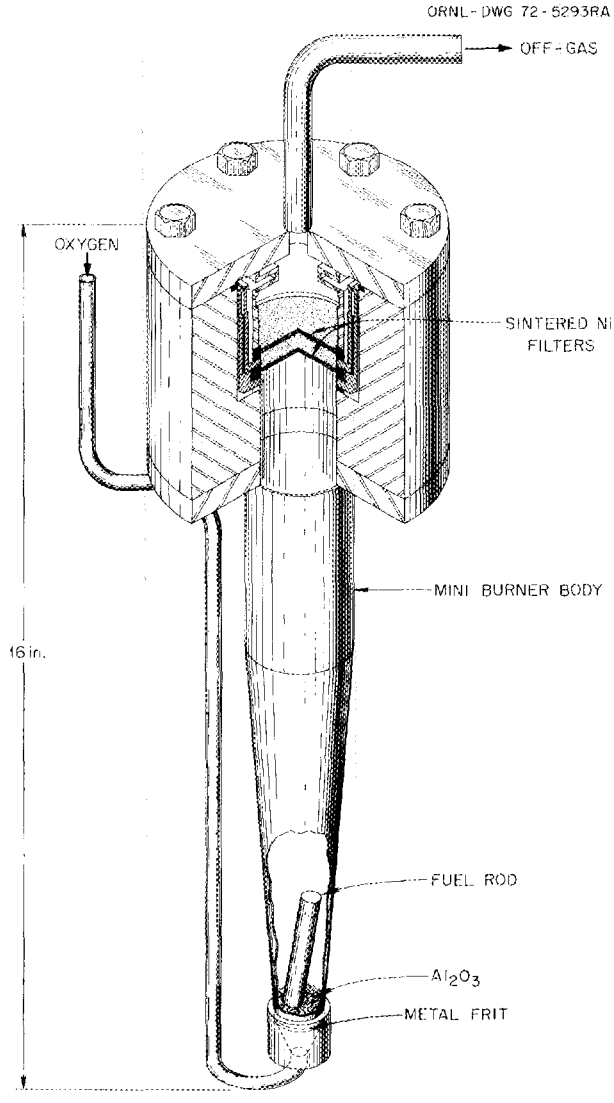

Fig. 1.1. Miniburner and filter assembly.

Results. Figure 1.3 shows the flowsheet used with RTE-7 along with the material balance results obtained. The fuel stick weighed 10.8 g and was 0.478 in. in diameter and 1.94 in. long. Using the average coated particle parameters reported by GGA and the weights of the fissile (+80 mesh) and fertile (+42 mesh) fractions shown in Fig. 1.3, we calculated that the fuel stick contained 0.543 g of uranium and 2.159 g of thorium and that the amount of graphite oxidized in

3. *GCR-TU Programs Annu. Progr. Rep. Sept. 30, 1971*, ORNL-4760, pp. 65–66.

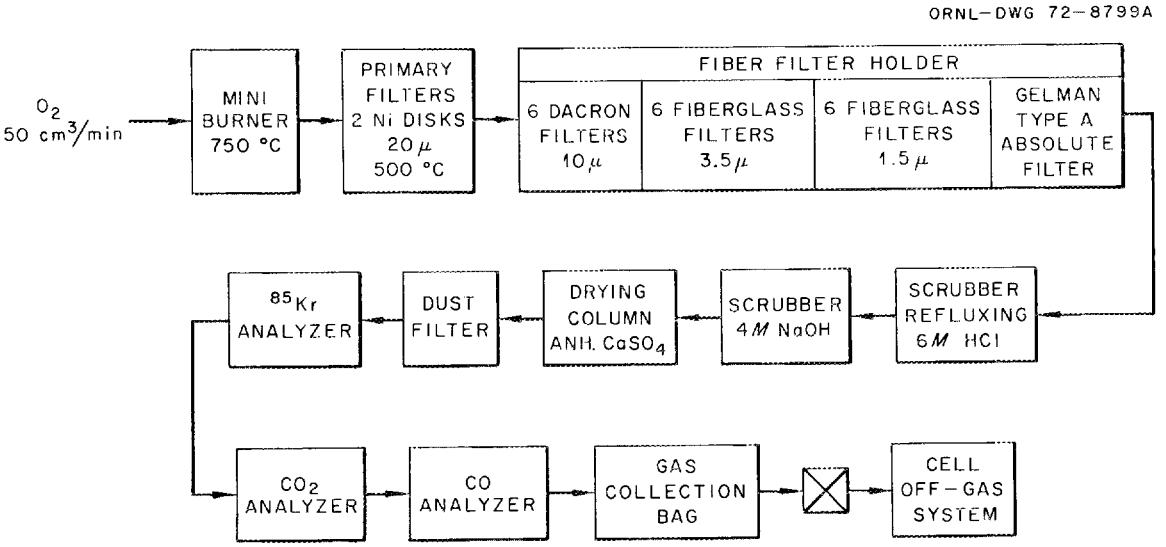

Fig. 1.2. Off-gas train used for RTE hot-cell tests.

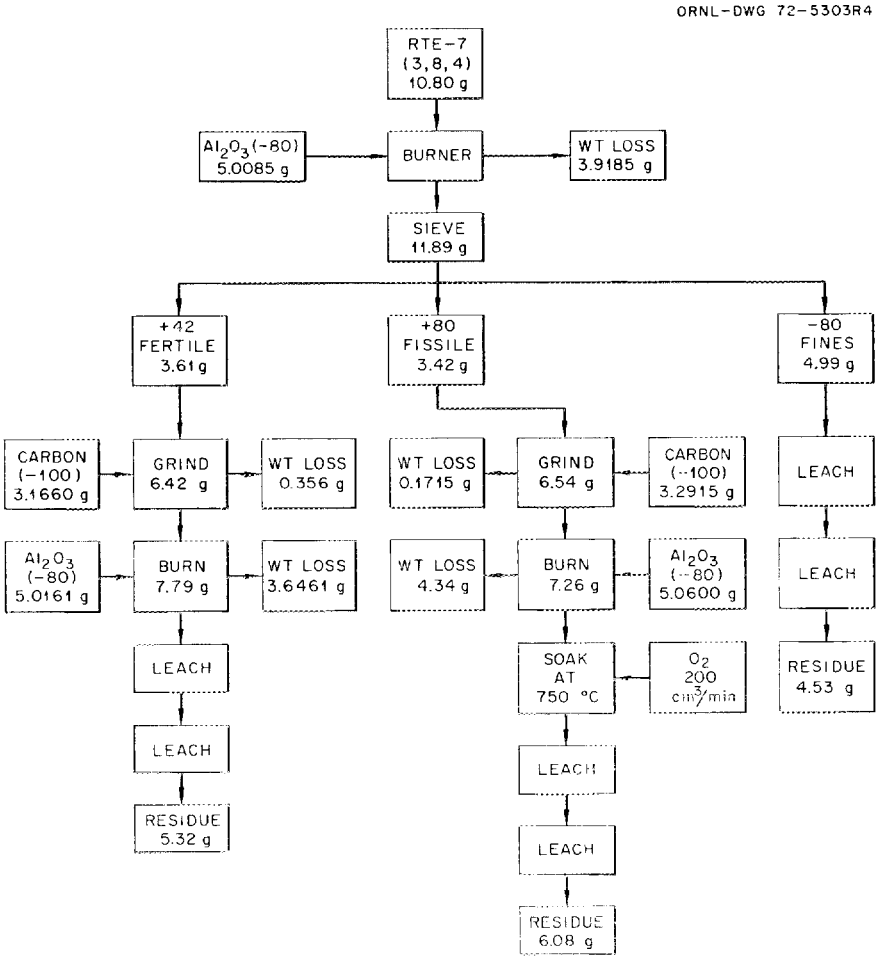

Fig. 1.3. Flowsheet used for fuel stick RTE hot-cell tests.

the initial burn was 3.84 g. This is an excellent check with the 3.78 g actually lost in the burning step.

Tables 1.2 and 1.3 give the distribution and the amounts of uranium and thorium recovered and the uranium isotopic distribution for the +42 mesh fertile and +80 mesh fissile fractions respectively. Based on the total amounts recovered, 0.24% of the uranium and 0.06% of the thorium remained in the insoluble residues after leaching. We calculated burnup by assuming that the ^{137}Cs activity associated with the +80 mesh fissile and −80 mesh fines fraction was due to ^{235}U fission and that the ^{137}Cs activity in the +42 mesh fertile fraction was due to ^{233}U fission. Using the appropriate ^{137}Cs yields, we calculated that ~2.3% of the thorium was converted to ^{233}U and that ~11.9% of the original ^{235}U had fissioned. Crossover of the fertile fraction to the fissile fraction was ~3.3%, and crossover of the fissile to the fertile fraction was 2.1% using ^{235}U as a basis of calculations and 5.2% using ^{238}U.

Table 1.2. Uranium-thorium distribution for RTE-7 tests

	Uranium (g)	Found (%)	Thorium (g)	Found (%)
+42 fraction				
L-1	0.05292	10.66	1.8424	94.92
L-2	0.00004	0.008	0.0046	0.24
Residue	0.00005	0.010	<0.0011	0.006
+80 fraction				
L-1	0.43600	87.82	0.0850	4.38
L-2	0.00380	0.77	0.002	0.10
Residue	0.00024	0.05	<0.0002	0.01
−80 fraction				
L-1	0.00240	0.48	0.0067	0.35
L-2	0.00004	0.0008	<0.0001	0.005
Residue	0.00091	0.18	0.0001	0.005
Total	0.49649		1.94102	

Table 1.3. Uranium isotopic distribution in RTE-7 fractions

Isotope	As charged (%)	+42 fraction (%)	+80 fraction (%)
^{233}U		71.90	0.30
^{234}U	0.76	3.70	0.87
^{235}U	93.13	15.59	85.16
^{236}U	0.28	5.54	6.66
^{238}U	5.83	3.25	7.02

Fission gas release. The amounts of released tritium and ^{85}Kr found during the various processing steps are shown in Table 1.4. As expected, most of the ^{85}Kr found (97.42%) was released during the crushing and burning steps of the fissile (+80 mesh) fraction. Note that 1.6% of the krypton found was released during the 12-hr soak period, and there was still detectable ^{85}Kr released during the leach step. The tritium release pattern was somewhat different: a large amount of the tritium found was released during the fissile (+80 mesh) fraction soak period. However, the tritium material balance was very poor, and more reliable tritium release values await results of a duplicate experiment with the second RTE-7 fuel stick.

Table 1.4. Fission gas release for RTE 7-3 hot-cell tests[a]

Operation	^{3}H	^{85}Kr
Total dis/min	2.961×10^{8}	1.35×10^{11}
Percent of total in:		
Initial burn	70.562	0.135
+42 fraction		
Grind	33.771	1.263
Burn	2.685	0.989
Leach	0.008	0.106
Total	36.464	2.358
+80 fraction		
Grind	1.431	70.072
Burn[b]	4.594	25.696
Soak[c]	35.803	1.565
Leach	0.042	0.091
Total	41.870	97.424
−80 fraction		
leach	1.104	0.083

[a] RTE 7-3 indicates recycle test element 7, fuel block 3.

[b] Three-hour active burning period.

[c] Held for 12 hr at 750°C after completion of burning.

Fission product distribution. The fission product distribution in the leached burner products is shown in Table 1.5. As expected, the bulk of the fission product activity is associated with the fissile fraction. The distribution of the fission products along the off-gas train for the initial, fertile fraction, and fissile fraction burns is shown in Table 1.6. About 3.5% of the gross gamma activity was carried over by the off-gas stream.

Table 1.5. Fission product distribution in the leached burner products, RTE 7-3

	Gross gamma (counts/min)	Disintegrations per minute					
		^{95}Zr	^{95}Nb	^{106}Ru	^{134}Cs	^{137}Cs	^{144}Ce
+42 fraction							
L-1	9.29	11.68	7.26	9.02	16.62	15.47	6.30
L-2	0.75	0.06	2.83	0.27	0.53	0.48	0.02
Residue	1.27	0.03	1.10	20.66	0.56	0.50	0.03
Total	11.31	11.78	11.20	29.97	17.71	16.46	6.36
+80 fraction							
L-1	65.66	77.51	48.56	20.98	57.43	60.21	91.48
L-2	4.54	8.08	5.10	1.40	4.18	4.48	1.24
Residue	14.34	2.23	33.94	30.56	13.05	14.21	0.41
Total	84.57	87.78	87.60	52.94	74.70	78.95	93.13
−80 fraction							
L-1	2.19	0.10	0.12	1.42	5.66	3.16	0.26
L-2	0.08	0.002	0.01	0.19	0.20	0.15	0.005
Residue	1.82	0.36	1.04	15.59	1.65	1.33	0.24
Total	4.08	0.47	1.17	17.20	7.51	4.63	0.505

Table 1.6. Distribution of fission products in the off-gas trains from RTE-7 tests

Operation	Percent of total carry-over						
	Gross gamma	^{95}Zr	^{95}Nb	^{106}Ru	^{134}Cs	^{137}Cs	^{144}Ce
Initial burn	7.91	0.052	0.019	0.534	19.82	14.34	0.081
Fertile fraction burn							
Metal filter 1	0.0261	0.006	0.007	0.107	0.029	0.019	0.008
Metal filter 2	0.0007	0.0001	0.0001	0.003	0.001	0.0006	0.0006
Fiber filters				0.010	0.0003	0.0002	0.0001
Acid scrub	0.720				0.519	0.989	0.010
Base scrub	0.100	0.004	0.0009	0.011	0.243	0.188	0.007
Subtotal	0.850	0.01	0.008	0.131	0.794	0.196	0.026
Fissile fraction burn							
Metal filter 1	85.11	82.81	88.40	75.20	73.09	77.90	82.79
Metal filter 2	5.96	17.03	11.32	23.98	6.07	6.24	16.98
Fiber filters		0.001		0.182	0.0005	0.0002	0.0006
Acid scrub	0.05	0.024	0.087	0.039	0.042	0.033	0.060
Base scrub	0.10	0.007	0.005	0.010	0.240	0.178	0.007
Subtotal	91.23	99.872	99.812	99.339	79.410	84.454	99.888

Six isotopes, ^{95}Zr, ^{95}Nb, ^{106}Ru, ^{134}Cs, ^{137}Cs, and ^{144}Ce, accounted for ~90% of that activity. Fission product activity was found on the metallic filter, on the fiber filters, and in the scrub solutions.

1.2 LABORATORY STUDIES OF BURNER OFF-GAS DECONTAMINATION

K. J. Notz

1.2.1 Krypton-CO_2 System

A. B. Meservey K. J. Notz

Detailed engineering design of a KALC-type system to separate krypton from CO_2 requires knowledge of the Kr-CO_2 separation factors at the operating temperatures. Since the limited amount of information available on this system was not in good agreement,[4] a careful study was made to determine experimentally precise values of Kr-CO_2 separation factors over the entire liquid range of CO_2. The method used was based on in situ counting of ^{85}Kr radioactive tracer. The equipment assembled to do this work was described in the previous report in this series.[4] Partial results were reported at two meetings held last year,[5,6] and a final report is in preparation. The final results are summarized below.

Table 1.7 gives the data obtained. The results are expressed as separation factors, Y/X, where Y and X are the mole fractions of krypton in the gas phase and the liquid phase respectively. These data are presented graphically in Fig. 1.4. Over the temperature range −53 to 22°C, the data fit the equation

$$\log (Y/X) = 0.709 - 0.1395T(^{\circ}C),$$

with a correlation coefficient of 0.9992. Above 22°C, as the critical temperature of CO_2 is approached, the curve falls off rapidly toward a value of unity, as it must.

Other constants can be calculated from the separation factors. The Henry's law constant is approximately 6×10^{-3} atm^{-1} over the range −53 to 22°C. The Bunsen and Ostwald coefficients are given at various temperatures in Table 1.8. The Ostwald coefficient remains more or less constant, as it should, while the Bunsen coefficient varies systematically. From the temperature dependence of the Bunsen coefficient, the heat of solution of krypton in CO_2 can be determined using a modified form of the Clausius-Clapyron equation. The values obtained are −900 cal/mole at −50°C and −130 cal/mole at 20°C (at the critical temperature the heat of solution must, of course, be zero).

We have now started work on the Xe-CO_2 system, using the same equipment and ^{133}Xe as the tracer. After that, we will examine the solubility of krypton in various electrolytes. We have already measured the solubility of krypton in pure water by this technique and obtained excellent agreement with published data.

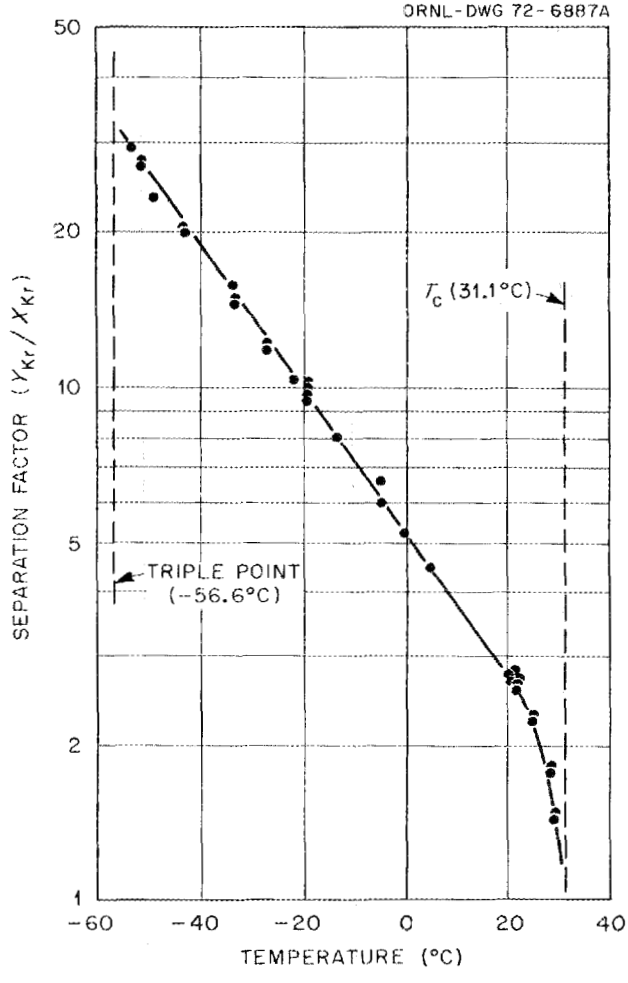

Fig. 1.4. Krypton distribution between gaseous and liquid CO_2.

4. Ibid., p. 22.

5. R. W. Glass et al., "Removal of Krypton from the HTGR Fuel Reprocessing Off-Gases," *ANS Trans.* 15(1), 95 (1972).

6. M. E. Whatley et al., "Decontamination of HTGR Reprocessing Off-Gases," *Proceedings of 12th USAEC Air Cleaning Conference, August 1972*, CONF-720823, vol. I, pp. 86–99 (January 1973).

Table 1.7. Separation Factors (Y/X) for krypton in CO_2

Temperature (°C)	Y/X		Comments
	>400 keV[a]	>40 keV[a]	
20.9	2.73		20 mCi, 2-in. cylinder[b]
-21.2	10.35		20 mCi, 2-in. cylinder[b]
-33.2	15.72		20 mCi, 2-in. cylinder[b]
-50.8	26.92	27.10	100 mCi, 1-in. cylinder
-42.6	20.09	19.86	100 mCi, 1-in. cylinder
20.3	2.70	2.68	100 mCi, 1-in. cylinder
21.6	2.56	2.53	100 mCi, 1-in. cylinder
-33.0	14.51[c]	14.40[d]	100 mCi, 1-in. cylinder
-4.6	6.57	5.91	120 mCi, 2-in. cylinder[b]
-43.0	20.15	20.16	100 mCi, 1-in. cylinder[e]
-26.9	11.83	11.88	Equilibrium reached from below
-26.9	11.81	11.85	Equilibrium reached from above
-48.6	24.84	24.82	
21.0	2.67	2.62	
5.30	4.40	4.39	
-13.55	7.94	7.98	
-52.8	29.34	29.53	
25.1	2.19	2.21	*f*
29.1	1.43	1.44	With other counting equipment[f]
28.2	1.76	1.80	With other counting equipment[f]
0.0	5.19	5.12	With other counting equipment
-19.03	9.29	9.38	
-19.03	9.32	9.51	With 100 psi krypton
-19.03	9.47	9.54	With 100 psi oxygen
-19.03	9.86	9.65	With 450 psi oxygen[b]
-19.03	9.85	9.62	With 450 psi oxygen[b]
-19.03	9.90	9.92	With 450 psi oxygen, for recalculated attenuation[b]

[a]Gamma energy range counted.

[b]Not used in computing the least-squares line because a nonstandard cylinder was used.

[c]Average of four determinations: 14.54, 14.49, 14.49, and 14.53.

[d]Average of four determinations: 14.38, 14.42, 14.43, and 14.38.

[e]Second loading of ^{85}Kr in 1-in. cylinder. This was used for the remaining determinations.

[f]These temperatures are above the range where a linear relationship exists between temperature and log (Y/X).

Table 1.8. Coefficients for the Kr-CO_2 system

Temperature (°C)	Bunsen coefficient[a]	Ostwald coefficient[b]
-50	3.37	2.75
-20	2.77	2.57
0	2.68	2.68
20	2.58	2.77

[a]STP liters of gas dissolved in 1 liter of solvent at the specified temperature and under a partial pressure of 1 atm of the gas.

[b]The volume of gas, at the temperature and pressure of the experiment, dissolved in one volume of solvent at the temperature and pressure of the experiment.

1.2.2 Separation Factors for H_2O and I_2 in CO_2

K. J. Notz

Present plans for the decontamination of off-gas from HTGR fuel reprocessing call for the removal of iodine and water (tritiated) prior to krypton removal via the KALC process, which involves liquefaction of the CO_2. The behavior of I_2 and H_2O in liquid CO_2 is thus of interest for two reasons: (1) to predict the fate of any I_2 or H_2O which may get by their respective traps and (2) to consider the possibility of using the liquid CO_2 system itself as a trap for either I_2 or H_2O or for both.

The solubilities of I_2 and H_2O in liquid CO_2 have been reported[7,8] and are shown in Fig. 1.5. The solid phase in the case of water is a CO_2 hydrate, $CO_2 \cdot 5.75H_2O$.[9] Using these values in conjunction with the vapor pressures of the pure components and assuming Dalton's law for the gas phase and that the liquid CO_2 is saturated with solute, the separation factors shown in Table 1.9 were calculated. These results indicate that I_2 and H_2O will concentrate in the liquid CO_2 phase and that carry-over to the vapor phase can be limited. Multiple stages will give any desired degree of decontamination.

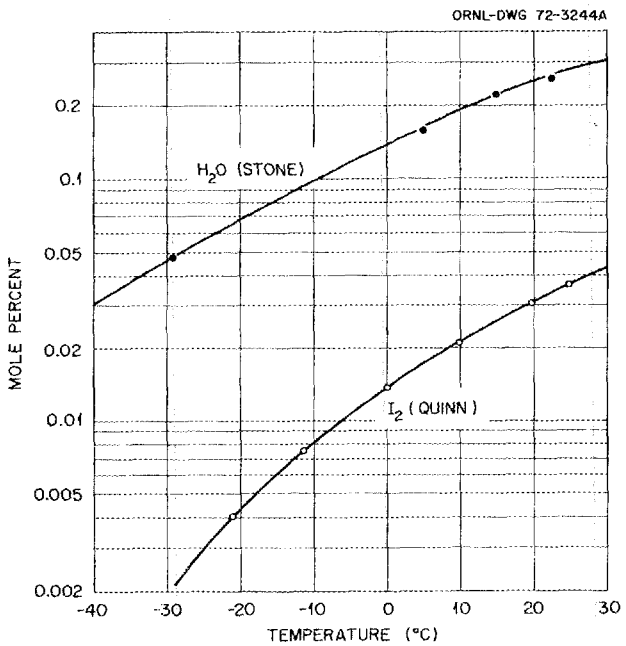

Fig. 1.5. Solubilities in liquid CO_2.

Table 1.9. Separation factors (X/Y) for I_2 and H_2O in liquid CO_2[a]

	Temperature (°C)		
	0	−20	−40
H_2O	10.3	15	29
I_2	157	270	390

[a] X is mole fraction of solute in the liquid phase and Y is its mole fraction in the gaseous phase.

The above calculations presuppose that there are no chemical reactions involved. This is not necessarily true (see Sect. 1.2.3). The effect of any chemical reactions on the overall separation factors depends on the relative volatility of the reaction products and their concentrations. The major reaction product is probably HI, which must also be considered as a potential source of corrosion.

1.2.3 The CO_2-H_2O-I_2 System

J. T. Bell K. J. Notz

The CO_2-H_2O-I_2 system is of interest because of the presence of ^3H and I in the irradiated fuel. Their volatility makes their presence in the off-gas a virtual certainty (^3H will of course be converted to H_2O in the burner). A spectrophotometric study of this system has been started.[10] The spectrum of I_2 in liquid CO_2 is very similar to that of I_2 in CCl_4 and in *n*-hexane. In CO_2 a very slight shift is noted (maximum at 5130 vs 5150 Å in CCl_4). Preliminary results indicate that I_2 disappears when the CO_2 is "wet" at a rate which is first order with respect to I_2 concentration. It is believed that this is due to reaction with water. Numerous reactions occur between I_2 and H_2O,[11–14] including:

$$I_2 + H_2O \rightarrow H^+ + I^- + HOI ,$$

$$I_2 + H_2O \rightarrow H_2OI^+ + I^- ,$$

$$3I_2 + 3H_2O \rightarrow 6H^+ + 5I^- + IO_3^- ,$$

$$I_2 + H_2O \rightarrow 2H^+ + 2I^- + 1/2O_2 .$$

7. H. W. Stone, "Solubility of Water in Liquid CO_2," *Ind. Eng. Chem.* (Ind. Ed.) **35**, 1284–86 (1943).
8. E. L. Quinn, "The Internal Pressure of Liquid Carbon Dioxide from Solubility Measurements," *J. Amer. Chem. Soc.* **50**, 672–81 (1928).
9. S. Takenouchi and G. C. Kennedy, "Dissociation Pressures of the Phase $CO_2 \cdot 5.75\ H_2O$," *J. Geol.* 72(2), 383–90 (1965).
10. This work is being done in collaboration with Clifford Thompson of Memphis State University.
11. T. Moeller, *Inorganic Chemistry*, p. 421, Wiley, New York, 1952.
12. A. E. J. Eggleton, *A Theoretical Examination of Iodine-Water Partition Coefficients*, AERE-R-4887 (February 1967).
13. Y. Nishizawa et al., "Vapor-Water Partition Coefficients of Iodine and Organic Iodides," *Nippon Genshiryoku Gakkaishi* 11, 205–10 (1969); English translation ORNL-tr-2255.
14. L. F. Parsly, *Design Considerations of Reactor Containment Spray Systems — Part IV. Calculation of Iodine-Water Partition Coefficients*, ORNL-TM-2412 (January 1970).

This work will be continued, with emphasis on identification of the I_2-H_2O reaction products in liquid CO_2 and determination of the reaction kinetics.

1.2.4 Radiolysis of CO_2

K. J. Notz

Since off-gas treatment involves mixtures of CO_2 and radiokrypton, the question of how much ozone might be produced by radiolysis of CO_2 arises.

The presence of gram quantities of ozone would present an explosion hazard. The literature was surveyed in order to answer this question. In the gaseous phase, ozone production can be neglected. Although there is, in fact, a significant initial production of radiolysis products in the gas phase,

$$\left.\begin{array}{l} CO_2 \rightsquigarrow CO + O \\ CO_2 \rightsquigarrow C + O + O \end{array}\right\} G_{calc} = 12\,,\ G_{obs} = 8.5 \text{ to } 11\,,$$

these products rapidly recombine, giving a very low net yield. Even in the presence of inhibitors which block recombination (e.g., the graphite surfaces in HTGR fuel), the main effect of radiation is to enhance the rate of the chemical reaction between carbon and CO_2.

In liquid CO_2, as is present in the KALC process and may also be present in the cylinders planned for final storage of separated radioactive gases, significant quantities of radiolytic products may accumulate. Baulch[15] gives the following yields (data were obtained at −48°C with gamma radiation estimated to be 90% <3 MeV):

$$CO_2 \rightsquigarrow CO \ (G = 3.5 \pm 0.2)\,,$$

$$CO_2 \rightsquigarrow O_2 \ (G = 0.6 \pm 0.2)\,,$$

$$CO_2 \rightsquigarrow O_3 \ (G \leq 0.7)\,.$$

It was concluded that ionic reactions are absent in the liquid phase and that the primary species are CO_2* (excited state), CO, and O, the last being the source of O_2 and O_3.

Using the above value for $G(O_3)$, it was calculated that only 1.4 mg of O_3 would accumulate in the stripper section of the KALC process. This calculation is based on a CO_2 exposure time of 10 min in the stripper and a krypton concentration in the stripper equivalent to 2 hr input of ^{85}Kr (1.7×10^{13} dis/sec for 6-year-irradiated, 150-day-cooled Fort St. Vrain fuel, processing 9.7 fuel blocks per 24-hr day). Ozone accumulation should not continue beyond the above steady-state value in the stripper, because the ozone (b.p. = −112°C) will be carried out along with the krypton.

Applying the same type of calculation to the storage cylinder gives 27 kg of ozone, assuming one-year storage of a cylinder containing a one-month output of ^{85}Kr. Although this quantity of ozone would probably never accumulate, the calculation does indicate that this matter must be considered. There appear to be two ways to minimize ozone buildup in the presence of CO_2, both based on promoting decomposition to O_2. One way is to add a decomposition catalyst such as MnO_2 or other heavy-metal oxide. The other way is to allow the temperature to rise to about 300°C; O_3 reportedly reverts to O_2 spontaneously at that temperature. This temperature can be attained easily from the radioactive decay heat, which will be in the neighborhood of several hundred watts per cylinder. Alternatively, ozone formation could be precluded by removing all the CO_2 from the rare gases prior to storage.

Formation of carbon suboxide, C_3O_2 (which, like ozone, is thermodynamically unstable), does not occur by radiolysis of CO_2. The suboxide is formed during radiolysis of CO, but the presence of CO_2 inhibits CO radiolysis, primarily by deactivating CO^+ by charge transfer; in addition, CO_2 back reacts with C_3O_2 and C to regenerate CO.

1.3 ENGINEERING DEVELOPMENT OF BURNER OFF-GAS DECONTAMINATION

M. E. Whatley R. W. Glass

Burner off-gas produced during the reprocessing of spent HTGR fuel blocks is primarily CO_2, with varying amounts of light gases such as O_2, N_2, and CO. Contaminants which may be present in the off-gas include radioactive particulates, iodine, and tritium, in addition to the noble-gas contaminants krypton and xenon. The removal of krypton in a concentrated form is an important part of the overall burner off-gas decontamination and presently forms a focal point for our studies. A solution to the krypton problem may well provide a foundation for the total burner gas decontamination effort.

15. D. L. Baulch, F. S. Dainton, and R. L. S. Willix, "Radiolysis of Liquid Carbon Dioxide with Gamma Rays," *Trans. Far. Soc.* 61, 1146–55 (1965).

Several processes commonly employed or suggested for noble-gas retrieval have been reviewed[16] for possible application in the burner gas cleanup, and the use of liquid CO_2 as a separation medium appears to be the most expedient method. A method based on complete liquefaction at high pressure and rectification is being developed at Jülich.[17]

Our process for krypton absorption in liquid CO_2 (KALC) consists of two parts: the first includes absorption of krypton from the burner off-gas by liquid CO_2 and the closely coupled fractionation and return of gases co-absorbed with the krypton, and the second includes the stripping of the absorbed krypton from the liquid CO_2 and its associated rectification for yielding a concentrated krypton product. The stripper thus provides decontaminated liquid CO_2 for use as scrub in the absorption operation.

Efforts to develop the KALC process for use in HTGR fuel reprocessing plants are being directed along several lines.

1.3.1 ORGDP Demonstration of Feasibility (Joint Program)

The Rare-Gas-Removal Pilot Plant[18] at the Oak Ridge Gaseous Diffusion Plant was used to explore the operability of a KALC system. The initial campaign was designed to provide experience necessary for subsequent KALC system development. Although not built for KALC-type operation, the ORGDP system provided a means of qualitatively evaluating some important operations required in the KALC process such as CO_2 liquefaction, vapor-liquid contacting, and partial condensation. Areas that required careful study for KALC system development were noted. In addition to demonstrating the tractability of the necessary process steps, the initial pilot campaign suggested that the KALC process will serve as an attractive means of removing krypton from the burner off-gas.

Following the feasibility demonstration of KALC at the ORGDP pilot facilities, a joint ORNL-ORGDP program was organized for a study of both HTGR and LMFBR off-gas decontamination. The joint program includes modification of the existing ORGDP pilot facility for development of a complete krypton removal train for an LMFBR fuel reprocessing plant. Moreover, the unified HTGR-LMFBR Fuel Reprocessing Plant Off-Gas Decontamination Program provides for experimental engineering and laboratory studies to be carried out at ORNL for both the HTGR and the LMFBR programs. The plan allows for the use of both facilities for both HTGR and LMFBR fuel reprocessing off-gas decontamination work in a mutually beneficial way. The ORGDP pilot operation will be used primarily for demonstrating integrated operation of the complete off-gas decontamination systems. Limited scale-up information will also be obtained.

1.3.2 Experimental Engineering

Experimental engineering work at ORNL will provide basic design data. Since the KALC system is unusual and the domain of its operating variables essentially unexplored, there is a lack of essential design data. Mass transfer data will be obtained as the primary objective, but secondary objectives will include studies of component performance, control procedures, and general operational techniques. Although the ORNL facility will be smaller than the ORGDP pilot plant, and therefore more useful in the experimental work, the unit will be large enough to provide meaningful engineering data. Absorption studies will use a $1\frac{1}{2}$-in.-diam packed column; a 3-in. packed column will be used for the stripping studies. Both columns will be operated simultaneously to allow complete recycle operation.

1.3.3 Process Analysis

The principal basis for confidence that the KALC process will effect both acceptable decontamination of krypton from the HTGR burner off-gas and yield the separated krypton in a form sufficiently concentrated for simple disposal lies in our understanding of the relative behaviors of krypton and the light gases (O_2, N_2, and CO) in a CO_2 system. Since our last reporting period this information has been compiled, correlated, and incorporated into a computer model of the KALC system.[19] The model considers either the absorber-fractionator part of the flowsheet or the stripper-rectifier part, but does not couple them. The weak

16. R. W. Glass et al., *HTGR Head-End Processing: A Preliminary Evaluation of Processes for Decontaminating Burner Off-Gas*, ORNL-TM-3527 (July 1972).

17. M. Laser et al., "Off-Gas Treatment and Krypton Disposal in HTGR Fuel Element Reprocessing," paper presented at Symposium on the Management of Radioactive Wastes from Fuel Reprocessing, Paris, France, Nov. 27–Dec. 1, 1972.

18. M. J. Stephenson et al., *Experimental Investigation of the Removal of Krypton and Xenon from Contaminated Gas Streams by Selective Absorption in Fluorocarbon Solvents: Phase I Completion Report*, K-1780 (August 1970).

19. M. E. Whatley, *Calculations on the Performance of the KALC Process*, ORNL-4859 (May 1973).

dependence of each part on the other was shown to justify this decoupling. The algorithm consists of sequentially and repetitively imposing conditions of equilibrium while satisfying enthalpy and mass balances around each theoretical stage. The efficiency of this technique is perhaps not as good as that of some matrix inversion techniques, but the method used is inherently free from instabilities and offers the advantage of simulating in a practical sense the performance of a real unit. Also, it does not require excessive amounts of computer time. By using the best literature data available for the distribution of O_2, N_2, and CO between the vapor and liquid CO_2 phases, along with the krypton distribution data developed by Notz and Meservey (see Sect. 1.2.1), and by allowing for temperature and flow variations through the incorporation of enthalpy data, it is felt that the system will yield useful calculated results.

The purpose of the absorber-fractionator system is to remove the krypton from the gas stream [measured by the decontamination factor (DF) = Kr_{in}/Kr_{out}] and to reject the other light gases from the solvent [measured by the concentration factor (CF) = other light gases per unit Kr into the system/other light gases per unit Kr in solvent to stripper]. It was found that close control of the operating variables at a "best" operating point was required to attain both high DF and high CF values. When displaced from a "best" operating point by a change in one of the variables, the system could be brought to another "best" point by adjustment of another variable. The system was studied by treating most operating variables parametrically and using the boilup rate from the fractionator reboiler as the adjusting variable to compare operation at "best" performance. When all other variables were fixed, the domain of satisfactory operation was confined to ±0.2% change in this variable. Figure 1.6 shows plots of CF and DF against the boilup rate for two typical cases. Decontamination factors and concentration factors greater than 100 and 1000, respectively, appear attainable in a properly designed and operated unit.

The system should operate at about 20 atm pressure, but no sharp optimum was found. There should be at least 22 theoretical stages in the absorber and 16 in the fractionator. Provision should be made for controlled condensation between the fractionator and the absorber. When the feed gas contains as much as 10% light gases, the scrub rate should be at least 20 times the feed rate. The boilup rate from the fractionator reboiler at "best" operation will usually be between 2.5 and 4.0 times the feed rate. The loss of CO_2 from the exit gas

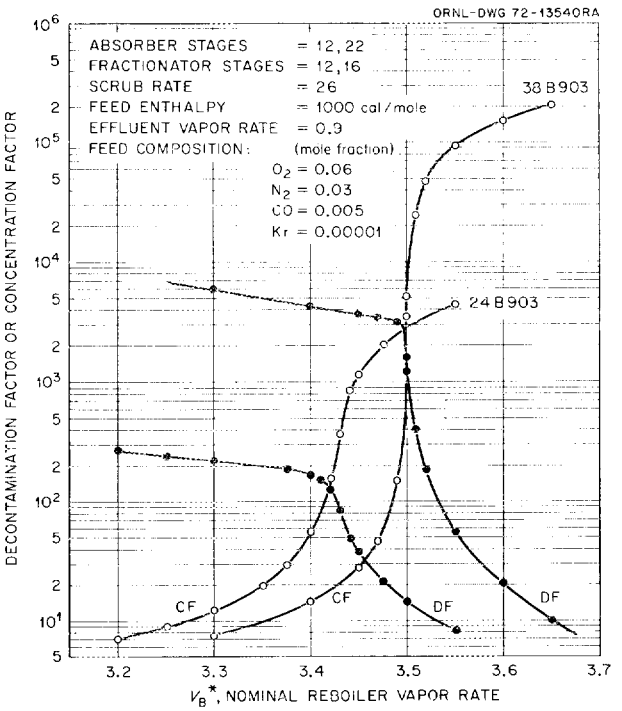

Fig. 1.6. Concentration factors (CF) and decontamination factors (DF) as functions of boilup rate.

can be controlled by a condenser above the absorber and has little effect on the unit performance. The temperature at the feed point will normally be about 7 or 8°C colder than the temperature of the top of the absorber, which in turn may be 5°C colder than the temperature of the reboiler. The temperature profile, which is sensitive to system performance, can probably be used as an index to system control. The light-gas content of the feed gas is an important variable that determines both the scrub and reboil rate for "best" operation. Comparable performance is observed when both the light gases in the feed and the scrub rate are cut in half.

The stripper-rectifier system is much simpler than the absorber-fractionator system in that there are no conflicting objectives. Krypton and all the light gases can be stripped from the CO_2 to any desired degree by increasing the boilup rate in the stripper reboiler and increasing the number of stages. The concentration of krypton and light gases in the gas stream leaving the rectifier final condenser is limited primarily by its temperature and has little effect on system performance. Flow rates in the rectifier are determined by the amount of condensation in the condenser between the

stripper and the rectifier. For economy, this condenser should take the bulk of the heat load. A rectifier section of up to seven or eight stages was found to be important to good system performance.

It was found that the performance of the stripper-rectifier system is greatly improved by operating at pressures lower than 20 atm. However, at 20 atm, 14 stripper stages with a boilup rate 0.3 times the stripper feed will reduce the krypton concentration in the purified CO_2 recycle stream to 10^{-6} of the feed concentration.

These calculations indicate the feasibility of the KALC process and provide insight into the areas of development requiring attention; however, only when our experimental program is under way will the full utility of the computer model be realized.

1.4 WHOLE-BLOCK BURNER STUDIES

H. Barnert-Wiemer R. S. Lowrie

Recovery of bred ^{233}U and unburned ^{235}U from spent HTGR fuel elements entails separation of the fissile and fertile particles from the much larger amount of graphite. In the reference reprocessing flowsheet this is accomplished by crushing the fuel element in several crushing operations and then burning the crushed material in a fluidized-bed burner. Since both the crushing and burning steps release fission products in both gaseous and particulate form, complete containment and decontamination of the cover gas of the crushers and of the burner off-gas are necessary. Further, crushing and fluidized-bed burning promise to be challenging operations to carry out in hot cells. For these reasons a low level of development effort has been continued on the concept of burning the whole fuel block as a backup to crushing and fluidized-bed burning. The primary aim of this effort has been to show that practical burning rates are attainable in a whole-block burner. A secondary objective is to develop preliminary concepts for full-scale whole-block burners and determine those areas where further development effort is needed.

The proposed reprocessing pilot plant at the Idaho Chemical Processing Plant (capacity 12 Fort St. Vrain Reactor fuel elements per day) requires an average burning rate of 0.83 kg of graphite per minute. A full-scale plant handling 1 ton of heavy metals per day will require about ten times that burning rate. A full-scale plant will use multiple burners; the minimum capacity of a single unit should be at least the 0.83 kg required for the pilot plant.

We have demonstrated a burning rate of 130 g of carbon per minute in the one-sixth-block burner. Depending on the method used to calculate burning rate for a full-scale whole-block burner, values ranging from 780 to 1020 g/min may be calculated from the demonstrated rate, which means 31 to 41 kg hr^{-1} ft^{-2} for a 17-in.-diam burner. The expected rate for the fluidized-bed burner is 30 kg min^{-1} ft^{-2}.

1.4.1 Description of Test Equipment

The HTGR fuel elements are hexagonal graphite blocks about 30 in. high and ~14 in. across the flats containing both coolant and fuel stick holes. The layout of the fuel holes permits cutting (in an axial direction) the fuel element into six pieces without cutting into the fuel sticks. The test burner was sized to use one-sixth of a fuel element. The burner was fabricated from a 4-ft length of 10-in. sched-40 type 347 stainless steel pipe flanged on each end (see Figs. 1.7 and 1.8). Cooling air is passed through the annulus between the liner and the outer shell. Provision was also made to cool the vessel heads. Thermocouples are provided for measuring internal temperatures, liner temperatures, and outer shell temperatures. Initially the fuel block sat on a grate which sat on a pan to collect the particles. Later, the pan was replaced with a funnel. The combustion feed gas enters the top of the vessel so the direction of burning is downward with the fuel block remaining stationary. Particles released from the fuel stick matrix drop into the funnel and are swept out with the off-gas into the combined cyclone-filter collection vessel.

1.4.2 Experimental Results

The results of the 20 one-sixth-block burner runs are discussed below.

Burning conditions. A burning rate of 0.83 kg of carbon per minute or higher can result in high temperatures in the burning zone. The temperature of the burning graphite affects the CO-CO_2 ratio in the off-gas and the release of fission products that are expected to be volatile (e.g., Ru, I, Tc, ^3H, and Cs). Further, some of the fuel elements to be reprocessed contain Triso-coated particles which, according to present plans, must be kept mostly intact; thus the maximum temperature of the graphite should be held at least several hundred degrees below the ~1800°C temperature, at which highly irradiated Triso-coated particles start "popping."[20] This puts the maximum graphite block temperature in the 1300 to 1400°C range, which is the

20. J. Scott, personal communication, Metals and Ceramics Division, Oak Ridge National Laboratory.

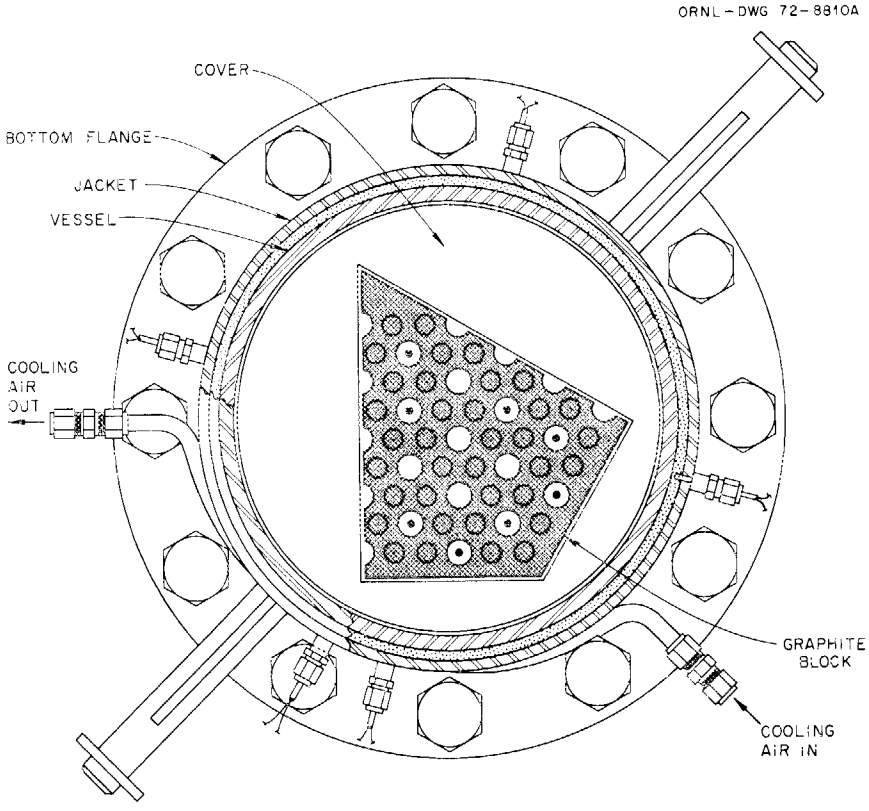

Fig. 1.7. Sectional view of whole-block burner.

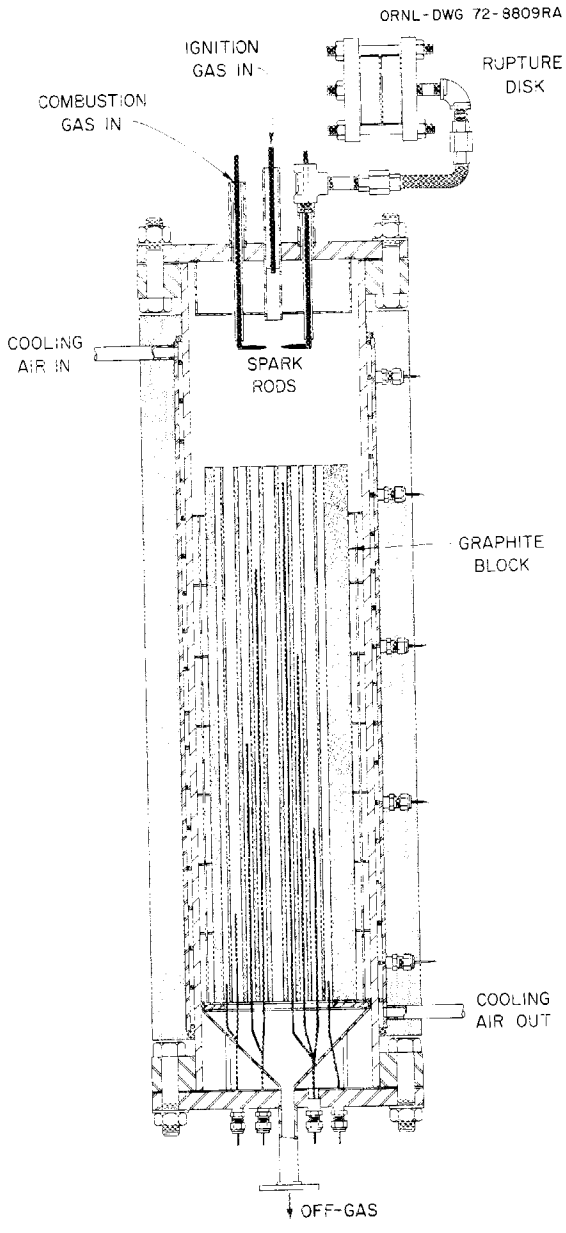

Fig. 1.8. Whole-block burner.

maximum temperature range the particles will encounter in the reactor, and reduces the possibility of particle coating breakage due to thermal stress. The criteria for burning were to keep the maximum block temperature below 1400°C and the wall temperatures below the 900°C design temperature.

Carbon monoxide and carbon dioxide are formed in the combustion of carbon, the former in the presence of excess carbon and the latter in an excess of oxygen. Our burner operates with a nominal excess of graphite, but much of this graphite is not kinetically available. Experiments show that there is no CO in the off-gas until the block temperatures reach 1200°C. With block temperatures between 1300 and 1400°C, the CO concentration ranges from 15 to 25%, and it is assumed that at the low flow rates used for the experiments the CO is partially oxidized in the gas phase before leaving the burner. This assumption has not been verified, because the gas flow capacity of the burner used in our studies is limited. In all runs the flow was laminar, with Reynolds numbers below 1500.

Considering the oxidation of graphite, we can discriminate among three temperature ranges characterized by different mechanisms. Below 800°C the oxidation is determined by the velocity of the chemical reactions on the surface of the graphite and by the diffusion of O_2, CO, and CO_2 into and out of the pores of the graphite. Above 1200°C the reaction is controlled by the diffusion of O_2, CO, and CO_2 through the boundary layer. Between 800 and 1200°C a continuous transition region exists. That means that at temperatures higher than 800°C, there is an increasing influence of the turbulence of the gas on the oxidation rate, because the turbulence helps to transport the O_2 to the surface of the block and the combustion products away. Since the burner is operated with the fuel block at temperatures higher than 1000°C, the burning rate is predominantly influenced by the flow rate rather than by the reaction kinetics.

At gas velocities below 1 m/sec in the coolant holes, the burning rate was so low that the oxygen was not used up and there was considerable O_2 in the off-gas (up to 20%). We assume that at very low flow rates, not only the main stream but also the boundary layers are laminar. If the gas velocity is higher than 1 m/sec the boundary layer becomes turbulent, although the main stream is still laminar. One would expect an even higher burning rate when the main stream becomes turbulent also. However, due to the limited flow capacities of the burner, no turbulent flow could be reached.

As mentioned above, the O_2 utilization is not complete at very low flows or at times when some of it goes around the block instead of through the coolant holes. In the initial tests, only one baffle around the block was provided, and the O_2 consumption was 94% at steady state for runs with velocities higher than 1 m/sec. Once the block was burned down to this baffle, the amount of O_2 in the off-gas steadily rose. After we inserted five close-fitting baffles that forced the O_2 through the coolant holes, the O_2 consumption rose to 99%, and about two-thirds of the block could be burned before the O_2 in the off-gas started increasing.

The off-gas system for the one-sixth-scale burner consisted of a 7-in.-diam cyclone (located 20 ft below the outlet of the burner) with two internally mounted 20-μ-pore sintered metal filters followed by a packed fiber-glass filter (6 by 13 in. long). The maximum amount of graphite removed from the cyclone for any run was about 2 wt % of the burned graphite. It appears that the amount of graphite transferred out of the burner is primarily a function of the diluent gas flow rate (see Table 1.10).

Note that the amount of graphite removed from the burner varied from a negligible amount at no diluent flow up to 2% at very high diluent flows. The packed fiber-glass filter only contained a very small amount of graphite at the point where the inlet gas impinged directly onto the packed fiber-glass bed.

We found no noticeable influence of the pressure on the burning rate at the pressure range of 1 to 20 psig; the pressure at which the rupture disk would break was 25 psig.

Heat removal and temperature control. Some of the heat from the oxidation reaction is removed from the burner as sensible heat in the off-gas stream. The remaining heat is radiated to the walls, where part of it is transferred to the wall cooling air and the rest is radiated to the cell atmosphere. Heat removal data are shown in Table 1.11 for several runs in which steady-state operation was maintained for 30 min or longer. A cocurrent flow of combustion feed gas and burner wall cooling air was used in these tests, and maximum wall temperature was held to 900 ± 25°C. The area of the wall below the burning zone was about the same during these four runs, so the amount of heat lost to the cell atmosphere was also about the same for each run.

One run was made with countercurrent cooling air flow, which proved less efficient than the cocurrent flow. About the same amount of heat is removed in both cases, but in countercurrent flow the cooling air is heated up at the hot lower part of the burner and reaches the burning zone with a higher temperature than is the case with cocurrent flow that passes the colder upper part of the burner. Thus the temperature

1.10. Unburned graphite dust

Run	Time (min)	Feed gas		Dust in cyclone (% of weight loss of block)
		Average gas flow (std liters/min)	CO_2 in flow (%)	
WBB-12	333	110	0	0
WBB-23	268	170	19	0.23
WBB-24 / WBB-25	350	216	43	0.42
WBB-26	180	211	65	1.71
WBB-27	207	176	28	0.26

Table 1.11. Heat removal data

Maximum wall temperature inside insulation: 900 ± 25°C

	WBB-22	WBB-23	WBB-24	WBB-25
Feed gas, std liters/min				
O_2	140	140	112	220
CO_2	72	50	220	90
Off-gas				
CO_2, %	88	92.5	80	90
CO_2, %	12	7.5	20	10
Temp, °C	750	750	650	850
Heat generated, kcal/min	564	575	410	885
Heat removed, kcal/min				
Off-gas	84	75	104	141
Cooling air	254	270	58	411
Radiation and cell air	226	230	248	333[a]
Cooling air				
Flow, std liters/min	965	1052	270	1443
Exit temp, °C	785	775	650	850

[a]Includes an unknown amount of heat removed by air passing through the cooling coil on the bottom flange.

difference between air and furnace wall in the burning zone is smaller with countercurrent flow, and consequently less heat is removed provided that the amount of gas is the same in both cases (see Figs. 1.9 and 1.10). Therefore about 20% more cooling air was required with countercurrent flow to keep the wall temperatures in the burning zone below the upper limit of 950°C. As to be expected, the off-gas temperature was lower with the countercurrent flow. In general, the heat transfer coefficients from the wall to the cooling air are very high, due to high velocity and high temperature.

The introduction of CO_2 into the combustion feed gas may be used to control heat generation and removal. Table 1.12 shows the effect of a CO_2 diluent in the feed gas on the block temperature reached. Thus it is apparent that some control of block temperature may be achieved by using CO_2 as a diluent gas. Tests with nitrogen as the diluent show the same effect but, since N_2 has a lower heat capacity, about 60% more gas is required.

Since there is always an excess of graphite present in the burner and the oxygen flow rate is fixed by the desired burning rate, control of the burner temperature

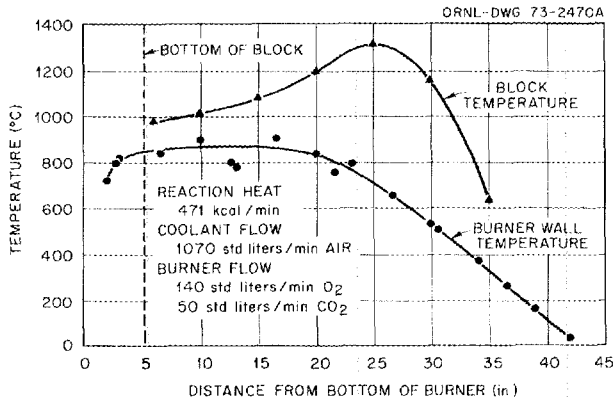

Fig. 1.9. Cocurrent coolant air flow.

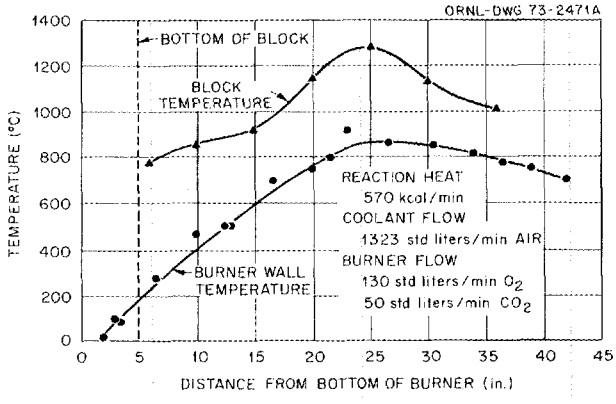

Fig. 1.10. Countercurrent coolant air flow.

Table 1.12. Effect of CO_2 diluent in the feed gas on block temperature

Run No.	Feed gas[a] (std liters/min)		Maximum block temperature (°C)
	O_2	CO_2	
17	90	0	1200
	90	60	1140
21	140	0	1324
	140	41	1278
22	140	36	1326
	140	72	1272

[a]In all cases the oxygen measured in the off-gas was less than 1%.

is restricted to two heat removal mechanisms: (1) removal of heat from the burner wall by cooling air, radiation, convection, etc., and (2) the use of a diluent gas, preferably CO_2, to remove sufficient heat to maintain the desired block temperature.

Product recovery and particle breakage. Particles released from the fuel stick matrix during runs 1 to 15 were collected in a pan positioned directly below the grate which supported the fuel block. Consequently, the particles were exposed to a hot, oxidizing atmosphere for the entire burning period, a time sufficient to ensure that any graphite associated with the collected particles, whether in the form of unburned coatings or of dust, would be burned away. Thus, in the three runs using fuel blocks containing fuel sticks made by extruding a mixture of graphite, binder, and Triso-coated ThC_2 particles, visual examination of the collected particles showed that the outer PyC coating was burned off. The overall particle breakage was about 5%.[21]

One run was made using a fuel block containing fuel sticks made by the injection molding technique at ORNL with Triso UO_2 and Biso ThO_2 particles. The graphite burning rate was 55 g of carbon per minute, and the block temperatures were between 1200 and 1400°C. Examination of the collected particles showed that the Biso coating on the ThO_2 particles was burned off, as was the outer PyC coating on the Triso UO_2 particles. In a subsequent leaching of the collected particles with Acid Thorex reagent, 0.55% of the uranium and 99.8% of the thorium reported to the leach solution. This means that 0.55% of the Triso UO_2 particle coatings were broken and confirms that the Biso coatings were burned off, exposing the ThO_2 kernel to the Acid Thorex leachant.

After run 16 the collection pan was replaced by a funnel, so that the released particles dropped into the funnel and were swept out with the off-gas into the combined cyclone-filter collection vessel (see Fig. 1.7). This system was first used in burning a fuel block containing fuel sticks made at ORNL with Biso-coated $(4Th/U)O_2$ particles. The graphite burning rate was 125 g of carbon per minute, and block temperatures were 1200 to 1300°C. Visual observation of the recovered particles indicated that the Biso coatings were not completely burned away from the oxide kernel when the particles fell from the fuel stick matrix. Analyses

21. These particles were reject Triso ThC_2 particles obtained from GGA. The breakage during fabrication is unknown, so the breakage caused by burning could be anywhere from 0 to 5%.

showed ~70% of the Biso coating was unburned. This indicates the need for a secondary burner to complete burning of the Biso coatings and any graphite dust. After the remaining Biso coating was burned off at 750°C in air, the particles were leached, first in 2 *M* HNO_3 and then with Acid Thorex reagent. About 1% of the uranium and 0.2% of the thorium reported to the 2 *M* HNO_3 leachant; the remaining thorium and uranium were found in the Acid Thorex leachant. Apparently, there was some preferential leaching of the uranium with dilute nitric acid.

Burner capacity. The maximum burning rate obtained with the one-sixth-block burner was 130 g of carbon per minute, which was sustained for 30 min. During this period ~4 kg of graphite was burned, operation of the burner was stable, and the burning zone moved downward ~6 in. Baffles were used to force most of the combustion feed gas through the 13 open coolant holes.

The rate at which a whole block might burn may be estimated in two ways:

1. Assume that a burning rate of 130 g/min will hold for each one-sixth section of the fuel block. This gives a burning rate for a whole block of 780 g/min (31 kg hr^{-1} ft^{-2}, based on a 17-in.-diam burner).
2. Assume that all the burning occurred on the surface of the 13 coolant holes. Since there are 102 coolant holes in a Fort St. Vrain fuel block, the whole-block burning rate calculated in this way would be 1020 g/min (41 kg hr^{-1} ft^{-2}, based on a 17-in.-diam burner).

It is important to note that the maximum burning rate test was limited by the flow capacity of the off-gas system (originally designed to handle flow from a 2-in.-diam fluidized-bed burner) rather than by the heat removal capacity of the burner, so even higher burning rates are probably possible. In any case, burning rates for a whole-block burner equal to or greater than the minimum 830 g/min mentioned before appear feasible.

Burner startup and shutdown. We chose to heat the block to ignition temperature using a CO-O_2 torch which was built as an integral part of the burner and was ignited by a high-voltage arc. To ensure safe operation, certain safety interlocks were provided. Loss of the arc (which is on as long as the torch is lit), loss of the flame, or a drop in the temperature of the torch tip would immediately shut off the CO flow. The torch would not be lit again unless the CO concentration in the off-gas was less than 5%.

At least half of the block should be at a temperature of 800°C or higher before the combustion feed gas is turned on. The best startup procedure is to gradually decrease the torch flows while increasing the combustion gas feed flow over a 5- to 10-min period. There is a slight oxygen concentration peak in the off-gas when the torch is shut off, but it disappears in 15 min or less. Simply shutting off the torch and turning on the combustion feed gas results in a large oxygen concentration peak, and 1 to 2 hr are required to reach steady state. Pure oxygen should be used as the combustion feed gas for the startup period.

The shutdown procedure is quite simple. The oxygen flow is turned off, a flow of inert purge gas, preferably CO_2, is started, and the fire goes out.

1.4.3 Laboratory-Scale Burner

There are a number of points that need to be examined further. In particular, more information is needed about the interrelationships among burning rates and feed gas flow rate, oxygen/diluent ratio, block temperature, and off-gas composition. Much of this information can be obtained from laboratory-scale experiments. Some of it can only be obtained from an engineering-scale test of the full-scale burner concept because of the important geometry efforts.

A small laboratory-scale burner has been designed for use with fuel specimens made of round pieces of graphite, each with a single central axial hole. The burner will have r-f heating so that the graphite can be heated without disturbing the gas flow. Temperatures will be measured both by thermocouples and by an optical pyrometer. This equipment will be used to study the influence of flow parameter, feed gas composition, and block temperature on the length of the burning zone and to study the off-gas composition as a function of the temperature profile of the block and the feed gas composition. A movable probe will allow sampling the off-gas over the length of the block. One way to reduce considerably the reaction heat in the burner is to form more CO during burning and to use an afterburner for the CO.

1.4.4 Full-Scale Whole-Block Burner Concept

More detailed studies must be made of the full-scale burner concepts. These studies would ultimately generate sufficient information with regard to equipment complexity, layout, capital costs, and operating cost for comparison with the head-end flowsheet using the fluidized-bed burner. Several features will probably be common to any full-scale whole-block burner; some of these are listed below.

1. The normal operating charge will be several blocks aligned axially, with the principal burning zone

concentrated where the combustion feed gas first flows through the coolant holes in the block.

2. The block temperature must be controlled by heat removal through the wall and by way of the off-gas stream. Some additional control will be achieved by control of combustion feed gas composition.
3. The burner wall will be provided with positive protection from "burnout," probably by using a ceramic liner and controlling of wall temperatures.
4. Diluent gas will probably be CO_2 (it could be recycled burner off-gas).

The choice between a horizontal or a vertical burner will probably be determined by the transfer problems (i.e., loading in blocks and removing the solid products). Since it will be desirable to keep the location of the burning zone in the burner relatively constant, it will be necessary to provide for a nearly continuous slow feed (~1.5 ft/hr at 1 kg of carbon per minute). A horizontal or sloped furnace is favored at present because it appears to eliminate many problems associated with supporting the fuel blocks in a vertical furnace.

A concept for a horizontal whole-block burner is shown in Figs. 1.11 and 1.12. A fuel block is picked up

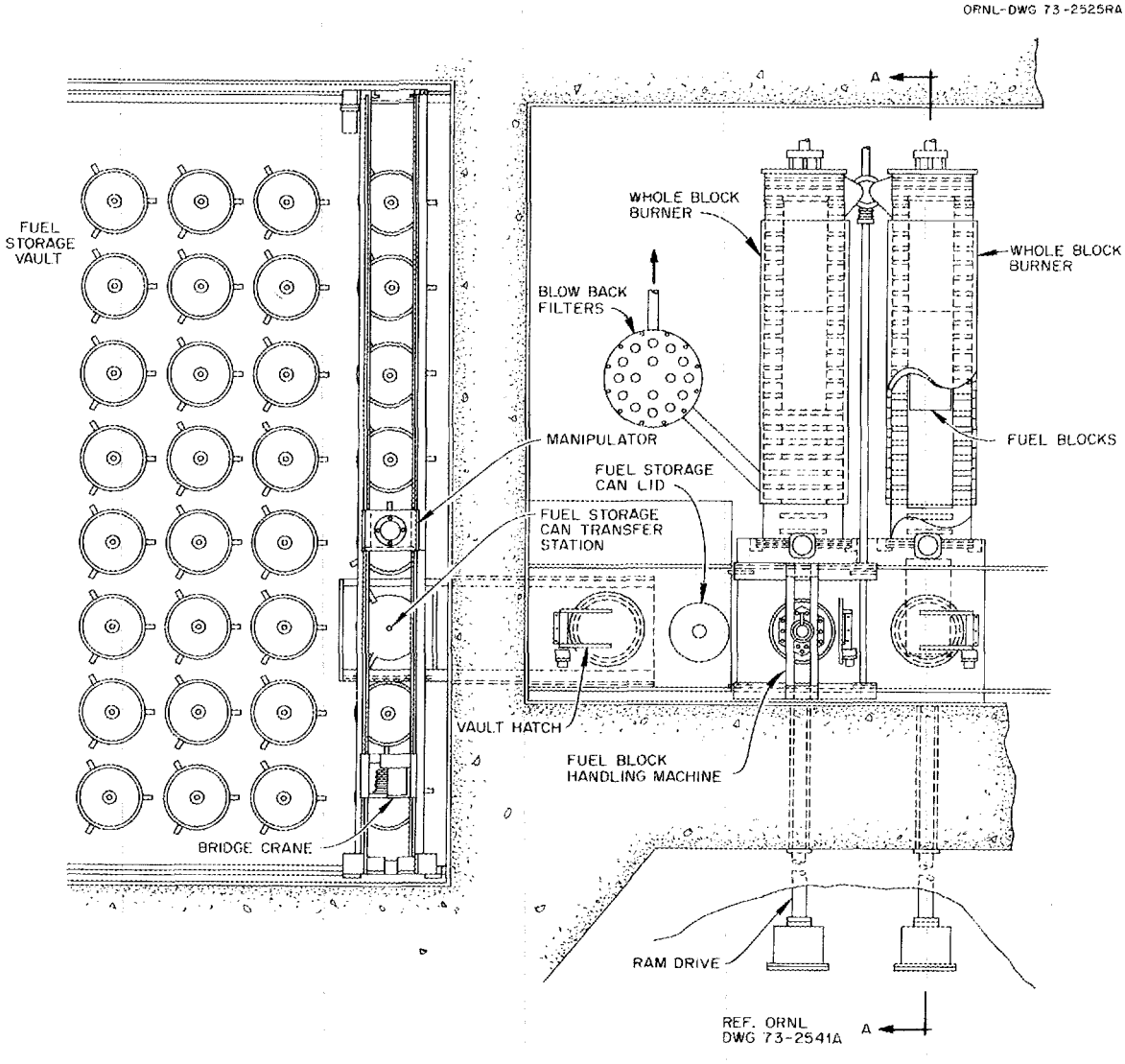

Fig. 1.11. Plan view of a whole-block burner concept for handling one reload segment per month [1160 MW(e), four years irradiation].

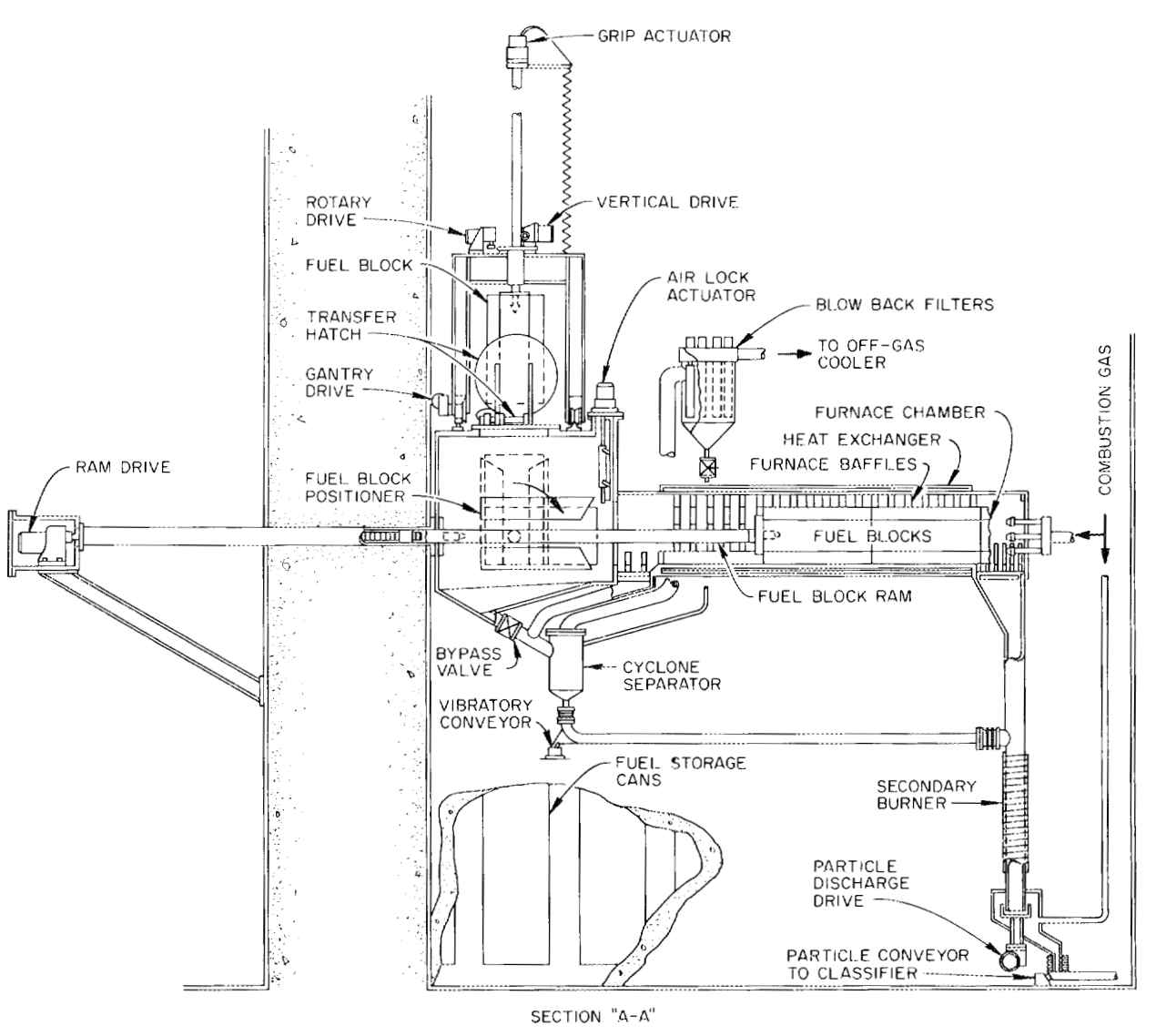

Fig. 1.12. Sectional view of the conceptual whole-block burner showing the block handling mechanisms and the conceptual secondary burner.

from the storage can and loaded into the fuel block positioner. The transfer hatch is closed, the positioner tilted downward, and the air lock door to the furnace opened. The ram drive pushes the block into the burner and also feeds the blocks into the furnace chamber. When it is necessary to load another block, the ram is retracted, the air lock door closed, the fuel block positioner tilted into the upright position, the hatch door opened, and the loading process repeated. Particles fall into a secondary burner where any carbon coating left is burned off. Solids swept out by the off-gas are recovered in the cyclone and filter and also fed to the secondary burner. The purpose of the secondary burner is to complete the burning of the Biso coatings and the outer PyC coating of the Triso control particles so that efficient particle separation can be accomplished in the next step of the head-end flowsheet.

1.5 PARTICLE SEPARATION STUDIES

K. J. Notz

1.5.1 Removal of SiC

Chemical methods of removing SiC coatings from Triso particles were tested. This was primarily for possible application to scrap recycle, but is also of potential interest for head-end reprocessing. A number of methods were tried, including high-temperature oxidation, dissolution in iron or silicon, and alkali fusion. The following alkaline melts were tested on Triso-coated ThO_2 kernels: Na_2CO_3, NaOH, Na_2O_2, $K_2Cr_2O_7 + Pb(NO_3)_2$, and $Na_2B_4O_7$. The carbonate fusion was the best overall. It effectively dissolved SiC without excessive attack on the ThO_2 kernels. However, some attack did occur, and trace amounts of a silicate-type residue remained after water washing to remove reaction products and unreacted carbonate. Subsequent air oxidation burned off the remaining carbon, leaving the thoria kernels. Test results using Na_2CO_3 under various conditions are given in Table 1.13. Based on these results, 2 hr contact at 950°C in air or 1100°C in argon is adequate for SiC dissolution. This would be suitable for reprocessing, but probably not for recycling, since the thoria kernels are slightly damaged. The action of the carbonate on the SiC is to form silicates. With excess SiC, free carbon was observed:

$$SiC + Na_2CO_3 \rightarrow Na_2SiO_3 + 2C .$$

With excess carbonate, CO was liberated:

$$SiC + 3Na_2CO_3 \rightarrow Na_4SiO_4 + Na_2O + 4CO .$$

In the latter case, some CO_2 was also observed; the presence of Na_2O is indicated by its sublimation and by attack on the quartz reaction tube.

1.5.2 Particle Separation by Density Difference

The most recent reference fuel description specifies fissile and fertile particles that will not be separable on the basis of size. After combustion, the Triso-coated fissile particles will have a diameter of 480 μm, while the Biso-coated fertile particles will be 500 μm. However, the densities will be far apart: about 10 g/cc for the fertile ThO_2 kernel and about 2.5 g/cc for the UO_2 kernel plus buffer carbon, dense carbon, and silicon carbide coatings. This density difference should permit separation by any one of several schemes. We have demonstrated excellent separation by fluidization with water. For test particles we used 500-μm, theoretically dense ThO_2 and 600- to 800-μm ThO_2 + C spheres of density 3.1 g/cc. Since the latter were both larger and denser than the actual particles would be, the test separation was a bit more difficult than the actual separation would be. Virtually 100% separation was achieved by elutriation with water in a column having a center feed and product takeoff at both top and bottom. The system was operated successfully in both laminar and turbulent modes. By suitable adjustment of operating conditions the crossover, which is nearly zero anyway, can be constrained to go only in one direction or the other. Substitution of a denser fluid for water (carbon tetrachloride, 1.6 g/cc, viscosity approximately equal to that of water) gave no obvious change in operating characteristics.

Table 1.13. Results of Na_2CO_3 fusions with SiC-coated ThO_2 microspheres

Atmosphere	Temp (°C)	Time (hr)	Percent recovered[a]	Comments
Air	950	1	60	
Air	950	2	100	Some kernels were etched
Argon	950	5	5	
Argon	1000	1	5	
Argon	1050	1.3	10	
Argon	1100	2	100	Some silicate-type residue
Argon	1100	4.7	100	Some kernels were etched

[a]As clean ThO_2 kernels.

2. Fuel Microsphere Preparation Development

P. A. Haas K. J. Notz

With completion of the engineering demonstration of the CUSP process for preparing UO_2 sol and forming it into microspheres in a nonfluidized-bed column, sol-gel work has settled into the fairly routine preparation of large amounts of spheres for use in fuel fabrication development studies and smaller amounts of spheres containing ^{235}U or ^{233}U for use in fuel irradiation tests. An important exception is the development and use of a new sol disperser for preparing sol droplets of a very uniform size and restricted size spread. This development significantly reduces the amount of off-specification and recycle fuel particles and simplifies subsequent fuel fabrication studies, especially as relates to the carbon-coating steps.

Work on loading uranium onto strong- and weak-acid resins has proceeded to the point that it is also more or less routine, although some work is still needed to demonstrate the continuous loading of weak-acid resin. These particles have potential as HTGR fuels in the case of certain compositions and densities.

2.1 ENGINEERING DEMONSTRATION OF UO_2 SPHERE PREPARATION

B. C. Finney P. A. Haas

A sol-gel process for the preparation of high-density UO_2 microspheres in the size range 125 to 210 μ was demonstrated on an engineering scale and reported.[1] The purpose of the work was to demonstrate the engineering feasibility of the process. Because of manpower limitations, sol preparation and microsphere forming could not be carried out simultaneously; consequently, the sol was prepared the week prior to each microsphere-forming run. The objective of each run was to operate the microsphere-forming column at a UO_2 production rate of about 3 kg/day and produce acceptable calcined microspheres in the size range 125 to 210 μ.

The process consists in preparing a 1 M UO_2 sol by the CUSP process, forming the sol into gelled spheres in a nonfluidized-bed microsphere-forming column using hot 2-ethyl-1-hexanol as the dehydrating agent, and calcining the gelled spheres to dense UO_2. Eight batches of sol containing approximately 4 kg of UO_2 each were prepared, and microspheres were produced in a microsphere-forming column that was operated continuously for two one-week periods. Drying was carried out in glass product catchers, and firing was done in alumina crucibles in a muffle furnace.

Four batches of sol were prepared the week prior to each microsphere-forming run. Sols with NO_3^-/U mole ratios of 0.09 to 0.14, $HCOO^-/U$ mole ratios of 0.38 to 0.47, and U(IV) contents of 85 to 87% were prepared following the standard CUSP operating path. Overall uranium material balances for the two demonstration runs were 102.2 and 104%, and the sol yields were 98 and 96.5% respectively. No differences were noted in the microsphere-forming properties of the various batches of sol.

The performance of the nonfluidized-bed microsphere-forming column was satisfactory. Minor difficulty was encountered with plugging of the two-fluid nozzle capillaries; however, this was minimized by installing glass frit filters in the sol feed line. An

1. B. C. Finney and P. A. Haas, *Sol-Gel Process: Engineering-Scale Demonstration of the Preparation of High-Density UO_2 Microspheres*, ORNL-4802 (November 1972).

on-stream factor of 96% was attained for each run. Operating conditions were established during the first run, and the desired production capacity of approximately 3 kg of UO_2 per day was attained during the second run. Ion exchange using Amberlyst A-21 resin was used to remove nitrate and formate ions from the alcohol used to extract water from the sol droplets to form gel spheres. Water was removed from the alcohol by distillation.

Results of the second run (Table 2.1) indicated an 87% yield of calcined microspheres in the size range 125 to 210 μ. The mean size varied from approximately 158 to 167 μ, with a standard deviation of approximately 10%. The O/U atom ratio was 2.005, and the carbon and iron contents were 24 to 60 and 12 to 33 ppm respectively.

Table 2.1. Summary of physical and chemical properties of calcined UO_2 microspheres produced during nonfluidized column demonstration run 2

	Batch 3	Batch 7
Weight of calcined product, g	1132.5	727.2
125- to 210-μ-diam fraction, g	965.0	649.9
125- to 210-μ-diam fraction, wt %	85.2	89.4
Mean size, μ	158.0	167.0
Standard deviation, μ	15.0	16.0
Roundness ratio, D_{max}/D_{min}	1.02	1.02
Density, % of theoretical	98.6	100.0
BET surface area, m^2/g	0.009	0.008
O/U atom ratio	2.005	2.005
Carbon content, ppm	60	24
Iron content, ppm	33	12
Gas release to 1200°C, cc/g	0.004	0.004
Average crushing strength, g	1435	1444

2.2 SOL-GEL PREPARATION OF ThO_2 SPHERES

P. A. Haas C. C. Haws

2.2.1 ThO_2 Microsphere Preparation

Although most of the information for the ORNL sol-gel preparation of ThO_2 spheres has been published previously, it is scattered throughout a number of reports and some significant requirements are only vaguely indicated. A new report was published to describe the important process requirements; the abstract is as follows.[2]

Process requirements are given for the preparation of ThO_2 spheres by the use of ORNL sol-gel processes. The hydrothermal denitration of thorium nitrate to yield a dispersible ThO_2 powder has three critical requirements that can be satisfied by batch operation in a rotating stainless steel drum reactor. Stable 2.5 M ThO_2 sols are prepared by agitation of the ThO_2 powder with the optimum amount of dilute, hot nitric acid. Conditions have been improved for recycle of the 2-ethyl-1-hexanol medium for forming ThO_2 gel spheres. The optimum drying-firing conditions require argon to a temperature of 110°C and then argon-steam to at least 220°C, followed by firing in air to 1150°C.

This report, along with a previous report on the design and operation of fluidized-bed columns,[3] and an improvement on sol dispersers (see Sect. 2.2.2) provide a complete description of our processes for preparing ThO_2 spheres.

Results from HTGR fuel development and evaluation studies have indicated that the optimum diameter for the fertile ThO_2 kernels is larger than the initially proposed 400 μ. Therefore, we rechecked the upper limit of ThO_2 sphere diameter for the ORNL sol-gel process. For our routine operating conditions of 2.6 M ThO_2 sol and the 2-ethyl-1-hexanol (2EH) inventory after six months of operation, the limiting effects are as follows:

1. Breakup of the drops to give two smaller spheres is not noticeable for 580-μ-diam product, is several percent for 650-μ product, and is 30 to 50% for 690- to 720-μ product.
2. A slight, but acceptable, nonsphericity with D_{max}/D_{min} of less than 1.05 is detectable in 650- and 720-μ product.
3. Our standard drying and firing procedures did not result in significant cracking for any diameters tested (up to 720 μ).
4. The two-fluid nozzle with vibration gives good uniformity of drop size for all sizes tested (up to 1800-μ sol drop diameter).

We can make about 670-μ-diam product without excessive drop breakup by using sol feed of about 3 M ThO_2.

2.2.2 Nozzle Development to Improve Sphere Size Uniformity

P. A. Haas

In the ORNL processes for formation of gel spheres by extraction of water into an alcohol, formation of the

2. P. A. Haas, *Process Requirements for Preparing ThO_2 Spheres by the ORNL Sol-Gel Process*, ORNL-TM-3978 (December 1972).

3. P. A. Haas, *Sol-Gel Preparation of Spheres: Design and Operation of Fluidized Bed Columns*, ORNL-4398 (September 1969).

sol drops is a critical operation. The uniformity of the drops is important to the yield, since oversized and undersized spheres constitute the principal off-specification material. Uniformity of the drops is also essential to continuous operation of fluidized-bed sphere-forming columns.[3] Scale-up to large capacities is difficult for many of the techniques that have been used to form drops. The average drop diameter must be predictable and controllable so that the specified fired sphere size can be produced from sols with different properties. The sphere preparation processes require formation of 10^4 to 10^6 drops of aqueous sol per minute in the 2EH water extraction medium. A positive flow of the 2EH is required to separate and prevent coalescence of the freshly formed drops. After a few seconds aging, surfactants in the 2EH form a surface film which minimizes coalescence.[3]

A recently developed technique has met the dispersion requirements for our ORNL sol-gel processes better than any of the sol dispersers previously tested. With the new technique, the breakup of sol streams from orifices or capillaries is made more uniform and regular by imposing a vibration at the natural frequency of drop formation on the sol at the entrance to the orifices or capillaries.[4] Two of the disperser types previously tested appeared particularly suitable to the concept of promoting the natural frequency of breakup by imposing a vibration. In both, the sol drop size depends on the sol flow rate and the flow rate of a 2EH drive fluid. The natural frequency of breakup can be estimated, thus allowing selection of a suitable matching vibration frequency. The drive fluid flow removes and spaces the drops after formation. Other dispersion devices, with much smaller rates of drop formation from a larger number of orifices or capillaries, generally show flow variations between orifices and do not have a single natural frequency of drop formation.

The procedure selected for applying the vibration was to vibrate a piston immersed in the sol at the entrance to the orifice or capillary from which the drops were formed. A typical arrangement was a piston of 0.110 in. diameter in a sol feed channel of 0.13 in. ID (Fig. 2.1). The piston was coupled by a rod to a standard small electronic vibrator driven by a 0- to 25-V-A, 50- to 10,000-Hz sine wave power supply. The coupling rod was sealed to the sol feed channel by a short section of thin-walled, $^3/_{16}$- or $^1/_4$-in.-ID, rubber tubing. The difference between the piston diameter and the sol feed

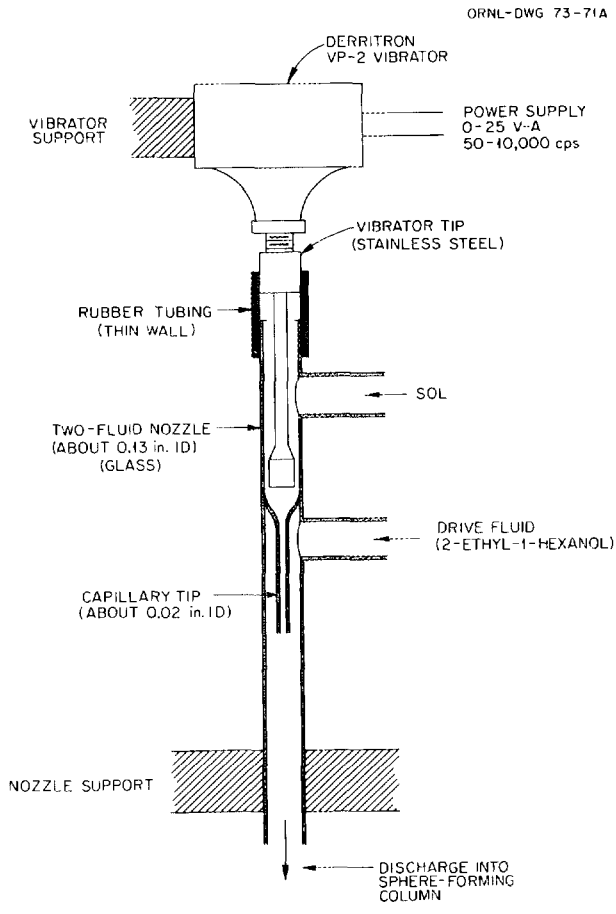

Fig. 2.1. Two-fluid nozzle with vibration.

channel was kept small to reduce the loss of vibration input as a result of backflow by the piston.

Detailed size analyses were performed on each of ten batches of ThO_2 microspheres. Kernel diameters were determined by screen analysis and by radiographic measurements. The more precise measure of the quality of this material was obtained from the radiographic measurements. Histograms constructed from the radiographic data are shown in Fig. 2.2, from which it is apparent that the spheres made with the technique employing vibration were extremely uniform in size.

This dispersion technique constitutes an important improvement in our sol-gel preparation of spheres. By adding a vibration to promote the natural frequency of drop formation, the vibration is effective over a wide range of conditions without careful tuning. By imposing the vibration through a stiff rod immersed in the sol, the vibration is effective for a wide range of frequencies without effects from structural resonances. The mechanical arrangement is simple and has operated

4. P. A. Haas and W. J. Lackey, *Improved Size Uniformity of Sol-Gel Spheres by Imposing a Vibration on the Sol in Dispersion Nozzles*, ORNL-TM-4094 (in reproduction).

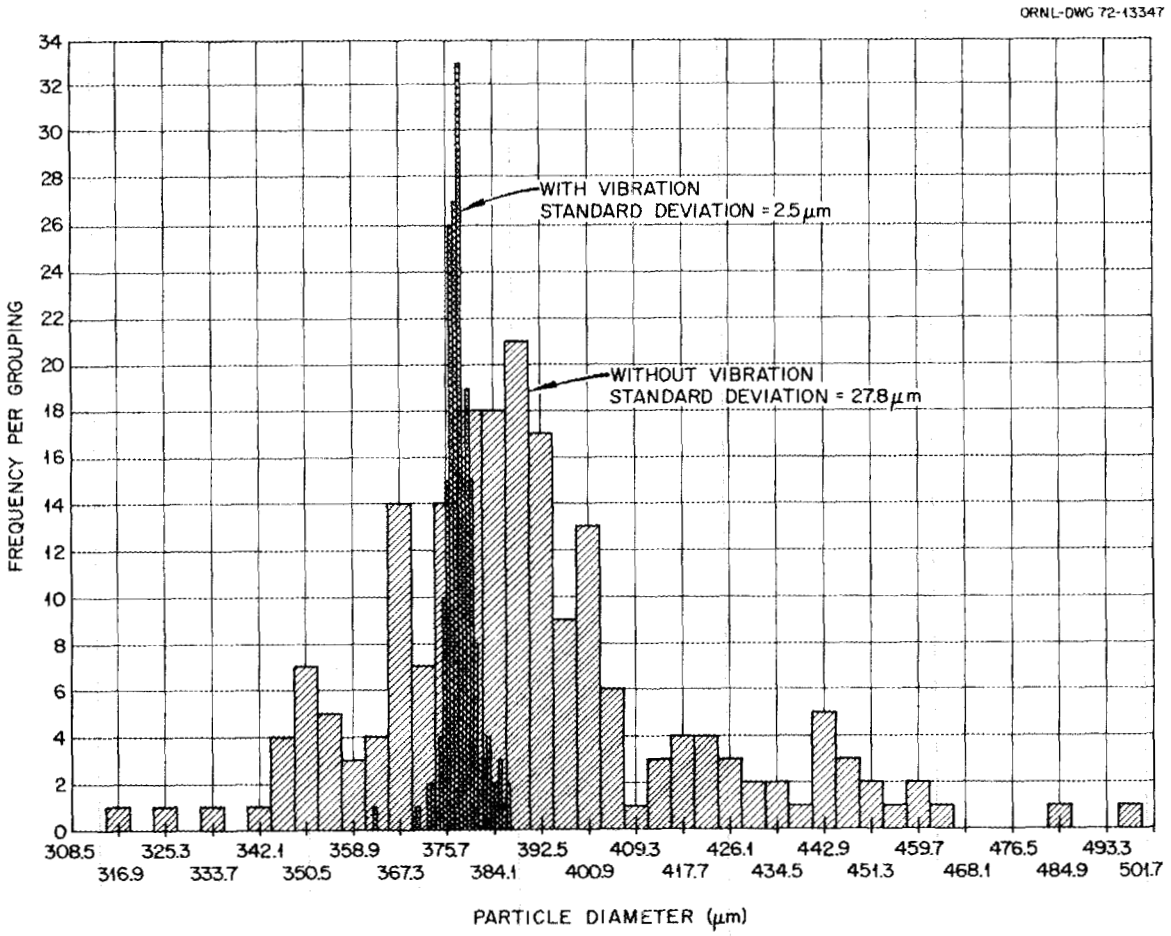

Fig. 2.2. Comparison of size distribution of ThO_2 microspheres made with and without vibration.

trouble free for over 400 hr and over 100 startups and shutdowns. The allowable rate of drop formation is limited by the ability to remove freshly formed drops so they do not contact each other and coalesce.

Most of the vibration-promoted drop formation was with single two-fluid nozzles with formation of 10^3 to 88×10^3 drops/min. The vibration gives a controlled rate of drop formation for multiple two-fluid nozzles, but equal divisions of sol flow between parallel capillaries result in poorer uniformity of sol drops. Shear nozzles[5] were also used with vibration and appear more satisfactory for multiple sol feed channels, since the orifices suffer less from unequal divisions of flow. Shear nozzles were operated to prepare 3×10^3 to 192×10^3 sol drops/min, and they could be easily scaled up to larger capacities.

Detailed size analyses on ten batches of ThO_2 spheres show excellent uniformity and control of average diameter by use of two-fluid nozzles with vibration.[4] Data determined by radiographic measurements and screen analyses were treated by standard statistical methods. Batches of from 1 to 13 kg of fired ThO_2 spheres of 370- to 500-μ diameters had average diameters within 1% of the predicted diameters, with standard deviations of 2.5 to 5.0 μ (Table 2.2). Comparable samples prepared at rates greater than 10^4 drops/min without vibration show standard deviations of 28 μ for ThO_2, 16 to 19 μ for 160-μ UO_2,[1] or 19 to 38 μ for 360-μ ThO_2-UO_2. The shear nozzle with vibration can give almost as good uniformity, as shown

5. A shear nozzle differs essentially from a two-fluid nozzle in that sol enters the alcohol at right angles to the alcohol flow in the shear nozzle and parallel to it in the two-fluid nozzle.

Table 2.2. Summary of size distribution results for sol-gel ThO_2 spheres made with vibration

Batch No.	Batch weight (kg)	Average diameter[a] (μm)	Diameter standard deviation[a] (μm)	Conservative estimate of diameter standard deviation (μm)	Tolerance intervals (μm)		Rejected by shape plate (wt %)
					95%, 95%[b]	99%, 99%[c]	
J-146	2.2	378.0 ± 0.3	$2.5^{+0.4}_{-0.3}$	3.7	378.0 ± 8.0	378.0 ± 10.9	1.1
J-147	4.2	379.2 ± 0.5	$3.7^{+0.6}_{-0.5}$	4.6	379.2 ± 9.9	379.2 ± 13.5	1.4
J-148	2.6	489.4 ± 0.6	$4.2^{+0.7}_{-0.5}$	4.2	489.4 ± 9.1	489.4 ± 12.4	1.1
J-149	2.6	282.7 ± 0.7	$5.0^{+0.8}_{-0.6}$	7.7	282.7 ± 16.6	N.D.[d]	0.4
J-154	3.0	374.1 ± 0.3	$2.4^{+0.4}_{-0.3}$	4.7	374.1 ± 10.2	374.1 ± 13.8	0.9
J-157[e]	22.4	390.0 ± 3.9	$27.8^{+4.5}_{-3.4}$	N.D.	N.D.	N.D.	0.9
J-172	13.2	499.8 ± 0.5	$3.6^{+0.6}_{-0.4}$	7.5	499.8 ± 16.2	499.8 ± 22.0	1.4
J-189	2.2	302.5 ± 0.8	$5.9^{+0.9}_{-0.7}$	5.9	302.5 ± 12.7	302.5 ± 17.3	0.15
J-190	0.9	207.2 ± 5.4	$38.9^{+6.3}_{-4.7}$	N.D.	N.D.	N.D.	0.7
J-192	12.8	495.0 ± 0.3	$2.1^{+0.3}_{-0.3}$	N.D.	N.D.	N.D.	0.6

[a]The uncertainty values give the 95% confidence interval assuming that the distribution is normal.
[b]The probability is 0.95 that the reported range would include at least 95% of the kernels made by such a process.
[c]The probability is 0.99 that the reported range would include at least 99% of the kernels made by such a process.
[d]Not determined because departure from normal distribution was large.
[e]Made without vibration.

by a standard deviation of 5.9 μ for a batch of spheres 303 μ in average diameter.

The improved uniformity possible with these dispersers with vibration virtually eliminates kernel size variations as a source of variability in coated-particle fabrication and in consequent irradiation behavior. The improved kernel size uniformity will result in much improved precision in the determination of coating thickness uniformity. For buffer-coated HTGR fuel particles, uniformity of kernel diameter is expected to minimize undesirable variations in coating thickness.

2.2.3 Material Preparation

P. A. Haas

More than 360 kg of ThO_2 spheres were delivered during 1972 for HTGR programs, including coating development studies, irradiation tests, and reprocessing development test elements. Over 100 kg of ThO_2 spheres were on hand or in process for delivery during January 1973. About 50 kg of sol-gel thoria in several forms (hydrothermally denitrated powder, sol, gel spheres, and fired spheres) were prepared for a variety of uses.

Most of the thoria spheres were prepared in process development equipment which has a maximum capacity of 20 kg/week. One trained operator can easily handle all operations from sol to fired spheres at a 15-kg/week rate.

The thoria spheres initially prepared during this report period showed excessive impurities (typical values were 100 ppm B and 200 ppm Fe) as compared with the specification for irradiation samples. Only a small fraction of the ThO_2 spheres are needed for irradiation tests, and we supplied these by using an old stock of thorium nitrate which contained 10 ppm boron and 100 ppm iron. Our thorium nitrate feed shows drum-to-drum variations, even though it is all from one batch production run (FMPC-142). Of the approximately 60 drums of thorium nitrate (200 lb/drum), 20 were sampled for spectrographic analyses. Analyses of these samples and samples from previous

drums show 1 very bad drum, 4 poor drums, 12 intermediate drums, and 7 drums of fair purity. Purified $Th(NO_3)_4$ solution containing 780 kg of thorium was procured from the National Lead Company at Fernald, Ohio, and samples were taken and submitted for spectrographic analyses. The analyses reported by Fernald indicated a better purity than the $Th(NO_3)_4$ crystals we currently use as sol-gel feed, but the ORNL analyses did not show a significant improvement. Hydrothermal denitration runs were made with this solution as feed, using about 1 hr extra run time to evaporate the additional water as compared with that for $Th(NO_3)_4$ crystals.

2.3 SOL-GEL PREPARATION OF ThO_2-UO_2 SPHERES

P. A. Haas F. L. Daley
B. C. Finney C. C. Haws
W. T. McDuffee

ThO_2-UO_2 spheres containing natural uranium were formed from the ThO_2-UO_3 sol prepared in the previous report period.[6] This sol (Th/U = 3.0) was formed into gel spheres using approximately equal amounts of Span 80 and Ethomeen S/15 with periodic additions of surfactants and distillation to remove H_2O for 2EH recycle. Small amounts of ThO_2-UO_2 spheres containing enriched uranium (93% ^{235}U) were prepared by mixing ThO_2 sols with UO_2 sols prepared by the precipitation-peptization process. Small amounts of ThO_2-UO_2 spheres containing ^{233}U were formed from ThO_2-UO_3 sol prepared by solvent extraction.

2.4 RESIN-BASED MICROSPHERE DEVELOPMENT

K. J. Notz P. A. Haas

Uranium-loaded resin beads, which are subsequently carbonized and coated, are being developed for possible use as fissile particles in HTGRs. The uranium loading operation is described here, while carbonization and coating are discussed in Sect. 6.4. Our loading work during this reporting period covered the following areas: loading from UO_3; loading continuously in a countercurrent column; special studies involving loading from UO_2F_2, loading to partial capacity of the resin, loading in a shell configuration, and loading with thorium or thorium-uranium mixtures; preparation of about 17 kg of test material, including some loaded with ^{233}U; and tests on a wet-screening device to achieve a narrow size distribution.

2.4.1 Resin Loading from UO_3

The previous report in this series[7] described our early results on the loading of ion exchange resins, particularly weak-acid resins, by using UO_3 and a nitrate intermediate. Since then a topical report on this process has been issued[8] and a patent applied for. The abstract from the report is reproduced below.

Coated particles made from ion exchange resins offer an attractive alternative to "fissile" particles specified for advanced HTGR's. The concept of reacting cation exchange resins in the hydrogen form with UO_3, using dilute uranyl salt solutions as a transfer medium, has important advantages for preparation of HTGR fuel particles from ion exchange resins. Dowex 50W-X8 (with exchange groups attached to a styrene-divinylbenzene polymer lattice) satisfies the product requirements better than do other strong acid resins, but the exchange group leaves sulfur in the carbonized particle. Weakly acidic cation exchange resins with carboxylic acid exchange groups leave only carbon and oxygen after carbonization and thus give particles more comparable with the UC_2 or UO_2 commonly used for HTGR fuels. Amberlite IRC-72 was identified as having a better combination of properties than any other weak acid resin tested. The procedure of reacting UO_3 with cation exchange resins in the hydrogen form using uranyl nitrate as the transfer solution allows efficient and well controlled loading of either strong or weak acid resins without formation of dilute uranium solution. The final solution concentration can be selected and controlled by mixing the desired amounts of UO_3, resin, and solution without any need to monitor flow rates or concentrations. Mixing of UO_3 with the resin is the only procedure which has demonstrated practical, stoichiometric loadings of a weak acid resin with uranium. Satisfactory mixing of resins, UO_3, and uranyl nitrate solution was demonstrated in agitated baffled vessels, in a screen-bottom basket of the resin-in-pulp type of contactor, and in a fluidized resin bed with a separate mixer for the addition of UO_3.

A study of the dissolution kinetics of UO_3 powders in dilute (0.3 *M*) HNO_3 was carried out in cooperation with the MIT practice school at ORNL. Representative normal and enriched (93% ^{235}U) uranium oxides were used. The purpose of the study was to provide a basis for evaluating the soundness of a procedure to load resins at intermediate levels of enrichment by using a mixture of normal and highly enriched UO_3 powders. The normal UO_3 produced by thermal denitration of UNH, had a lower specific surface area but smaller gross

6. P. R. Kasten et al., *GCR-TU Programs Annu. Progr. Rep. Sept. 30, 1971*, ORNL-4760, p. 40.

7. Ibid., p. 42.

8. P. A. Haas, *HTGR Fuel Development. Use of UO_3 to Load Cation Exchange Resin for Microsphere Preparation*, ORNL-TM-3817 (September 1972).

particle size than the enriched UO_3, which was prepared from an ammonium diuranate intermediate. The enriched UO_3 consisted of smaller elementary crystallites, but these were agglomerated into large aggregates. The actual values of BET surface areas and gross particle sizes are:

	BET area (m^2/g)	Gross size (μm)
Natural UO_3	0.62	150
Enriched UO_3	1.28	500

It was found that the dissolution rate was controlled by the gross particle size; at 25°C, natural UO_3 dissolved 1.5 times as fast as enriched UO_3, and at 70°C, 2.5 times as fast. Since agitation rate had no effect on dissolution rate at 25°C, it was concluded that at this temperature the reaction rate was not controlled by diffusion of reactant through the surface film to the UO_3 to yield uranyl ion ultimately. At 70°C, dissolution rate did depend on agitation rate, from which it is deduced that the chemical reaction rate was fast relative to film diffusion. From these results it is obvious that simple mixing of natural and enriched UO_3 will not give the desired isotopic mixture on the loaded resin.

2.4.2 Resin Loading Using a Continuous Column Method

The last annual report[9] described an effective resin loading method for strong-acid resins in sequential columns, and the suggestion was made that a modified Higgins-type countercurrent contactor would be an elegant way to optimize this method. This has now been done, and the results have proved this method to be very well suited for this purpose.

Figure 2.3 shows the essential features of such a system, and Fig. 2.4 is a photograph of an assembled column. The column is made of 1-in.-ID Pyrex pipe and is 7 ft tall. The active loading length of the column, 6 ft, determines the maximum throughput, since the exposure time of the resin must be at least 2 hr (at ambient temperature) to allow sufficient time for diffusion to the centers of 600-μm resin beads. The air-operated ball valves are solenoid controlled, as are the cutoff valves on the four aqueous streams. Variable-flow pumps provide the desired flow rates on the three input streams. The entire operating cycle is controlled by a pair of adjustable timers. A typical time cycle is a 10-sec pulse (to move the resin) every 5 min. During the remaining time the wash water and feed solution flow

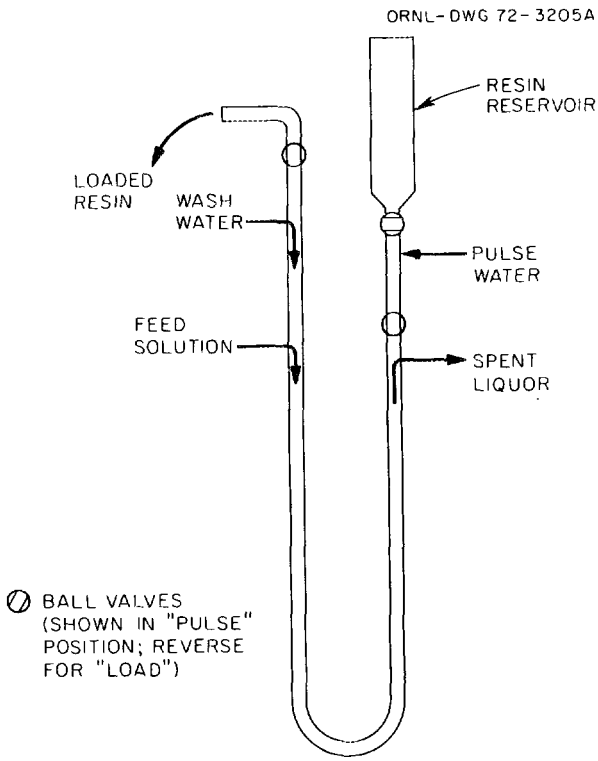

Fig. 2.3. Schematic drawing of continuous resin loading column.

in, while the spent liquor is discharged. With strong-acid resin the feed is uranyl nitrate solution (~0.1 *M*) and the effluent is dilute HNO_3. The progress of the loading reaction and the condition of the column are monitored by means of conductivity probes inserted at appropriate locations (marked by white tabs in Fig. 2.4). Figure 2.5 shows a typical startup profile and the attainment of steady-state conditions.

The column described above has a demonstrated loading capacity of 3000 ml of resin per 8-hr day, or 640 g of uranium. This can be scaled up by a factor of 150 and still meet criticality limitations by using a 5-in.-ID column, doubling the active column length, and going to a 24-hr day. The corresponding output, 100 kg of uranium, would be adequate to produce fissile particles from uranium (^{235}U or ^{233}U) from a reprocessing plant handling 2 tons of heavy metal per day.

The above information has been reported in part.[10] Work in progress is directed toward extending the

9. *GCR-TU Programs Annu. Progr. Rep. Sept. 30, 1971*, ORNL-4760, p. 42.

10. K. J. Notz and P. A. Haas, "Resin-Based Fuels for HTGRs, Part II – Uranium Loading of Resins," *Bull. Amer. Ceram. Soc.* 51(8), 655 (1972).

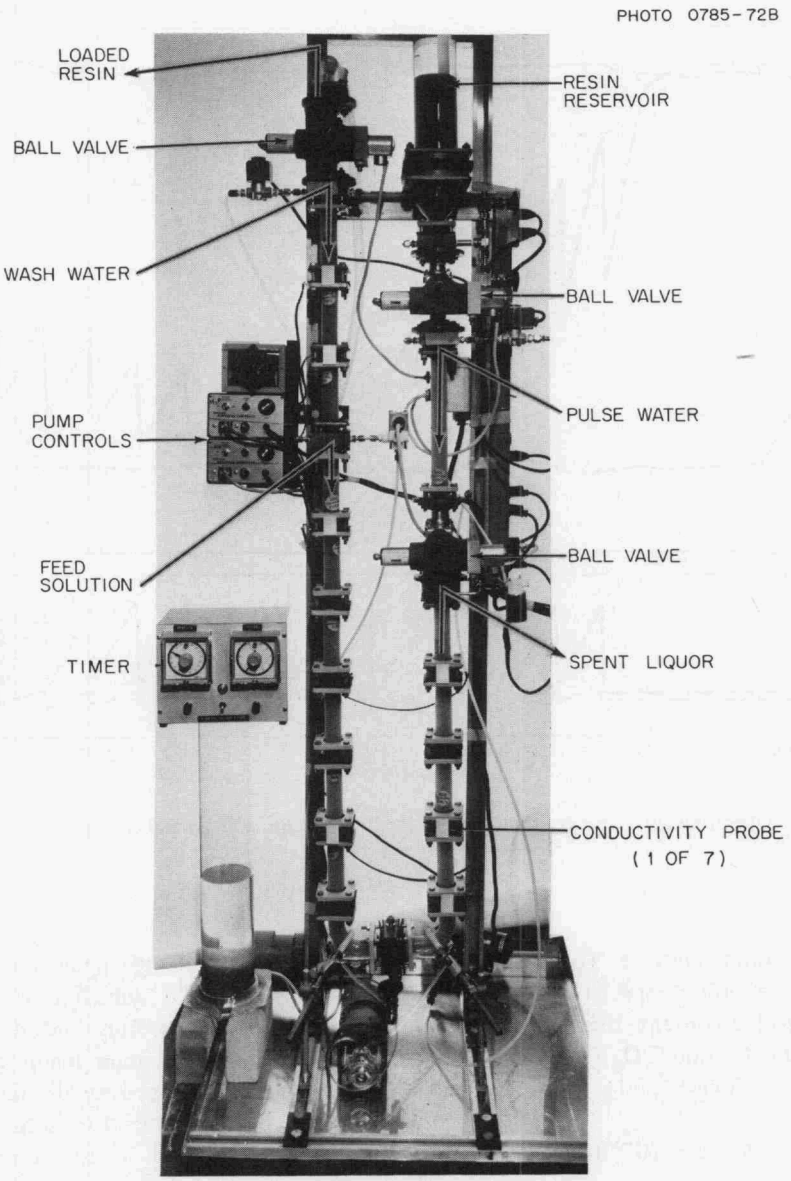

Fig. 2.4. Continuous resin loading columns.

continuous-column technique to the loading of weak-acid resins.

2.4.3 Other Resin Loading Experiments

In other resin loading experiments we have dealt with four aspects of loading: (1) loading from UO_2F_2, (2) partial loading of the resin beads, (3) loading the uranium in a shell configuration, and (4) loading thorium on resin beads.

Uranium loading from UO_2F_2 is of interest for new or makeup fissile particles, which use ^{235}U, since enriched uranium must come from $^{235}UF_6$, and UO_2F_2, resulting from hydrolysis of UF_6, is more nearly a primary source of ^{235}U than is uranyl nitrate. Strong-acid resin (Dowex 50W-X8) was loaded successfully from 0.1 *M* UO_2F_2 solution in a static column. This resin was loaded to 92% of capacity using a 67% excess of uranium, which is comparable to the loading

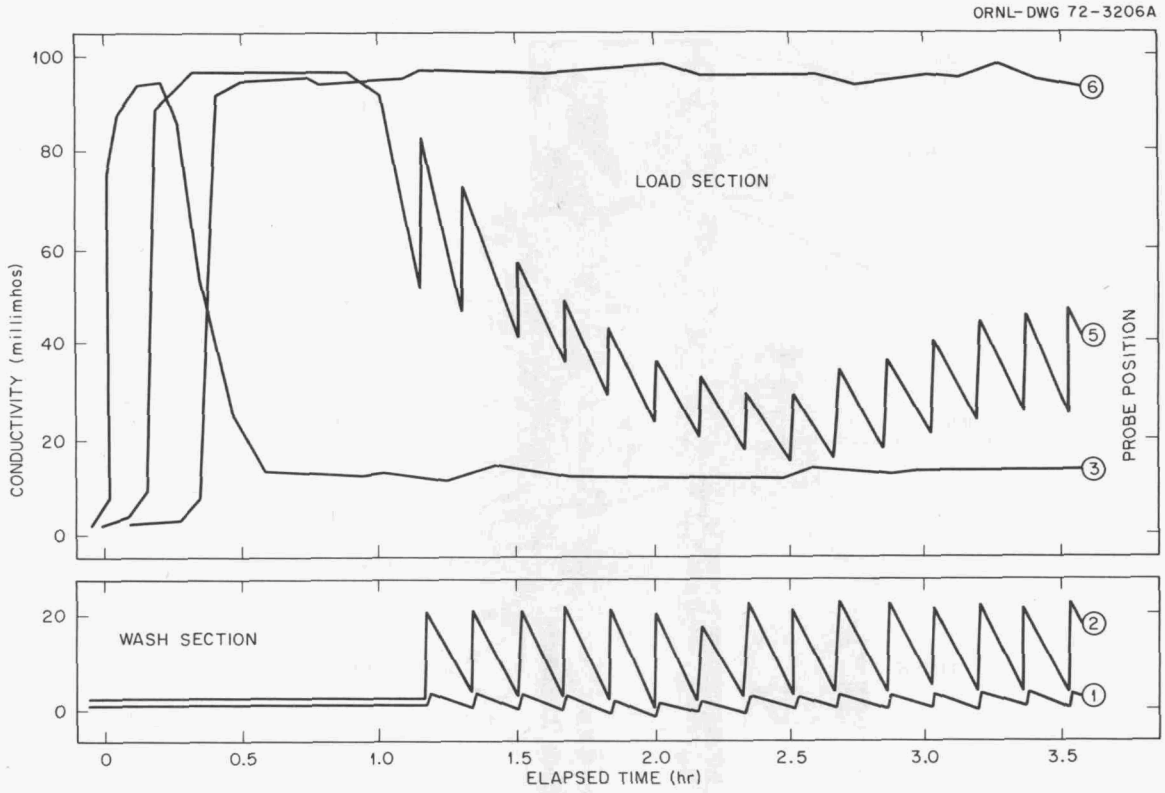

Fig. 2.5. Operating curves for continuous resin loading column: startup and steady state.

efficiency obtained using uranyl nitrate. The product contained 540 ppm fluorine, and no special effort was made to minimize the fluoride content. Because of the strong complexing between F^- and UO_2^{2+}, UO_2F_2 is usually considered to be a weak electrolyte:

$$UO_2F_2 \rightleftharpoons UO_2F^+ + F^-, \; K = 5 \times 10^{-5} \; (25°C).$$

However, in the presence of a strong-acid resin the complex is evidently split, causing the exchange to proceed as

$$UO_2F^+ + 2HR \rightarrow UO_2R_2 + HF + H^+ .$$

For a net reaction,

$$UO_2F_2 + 2HR \rightarrow UO_2R_2 + 2HF .$$

The very weak dissociation of HF ($K = 7.2 \times 10^{-10}$) provides the driving force for this reaction. With weak-acid resin (Amberlite IRC-72), loading from UO_2F_2 did not occur to a useful degree. After an initial reaction, further exchange appeared to be inhibited, perhaps by the liberated hydrofluoric acid.

For some applications, fully loaded resin may not be desirable. At lower uranium loadings, the final C/U ratio is greater.[11] The porosity also tends to be greater, which may be desirable for some situations, for example, when the fuel is to experience very high burnups. In the batch loading of weak-acid resins from UO_3, partial loading is easily achieved by simply limiting the quantity of UO_3. Uniformity of loading from bead to bead is achieved by using vigorous agitation. Loadings of kilogram amounts of Amberlite IRC-72 beads at 50 and 75% of their total capacity have been prepared this way. X radiographs of the products indicate that the uranium distributes itself more or less uniformly across the diameter of the beads by the time the beads are dried and ready for carbonization.

11. The loaded resin beads are carbonized in a nonoxidizing atmosphere to yield a product containing uranium compounds and carbon in intimate mixture.

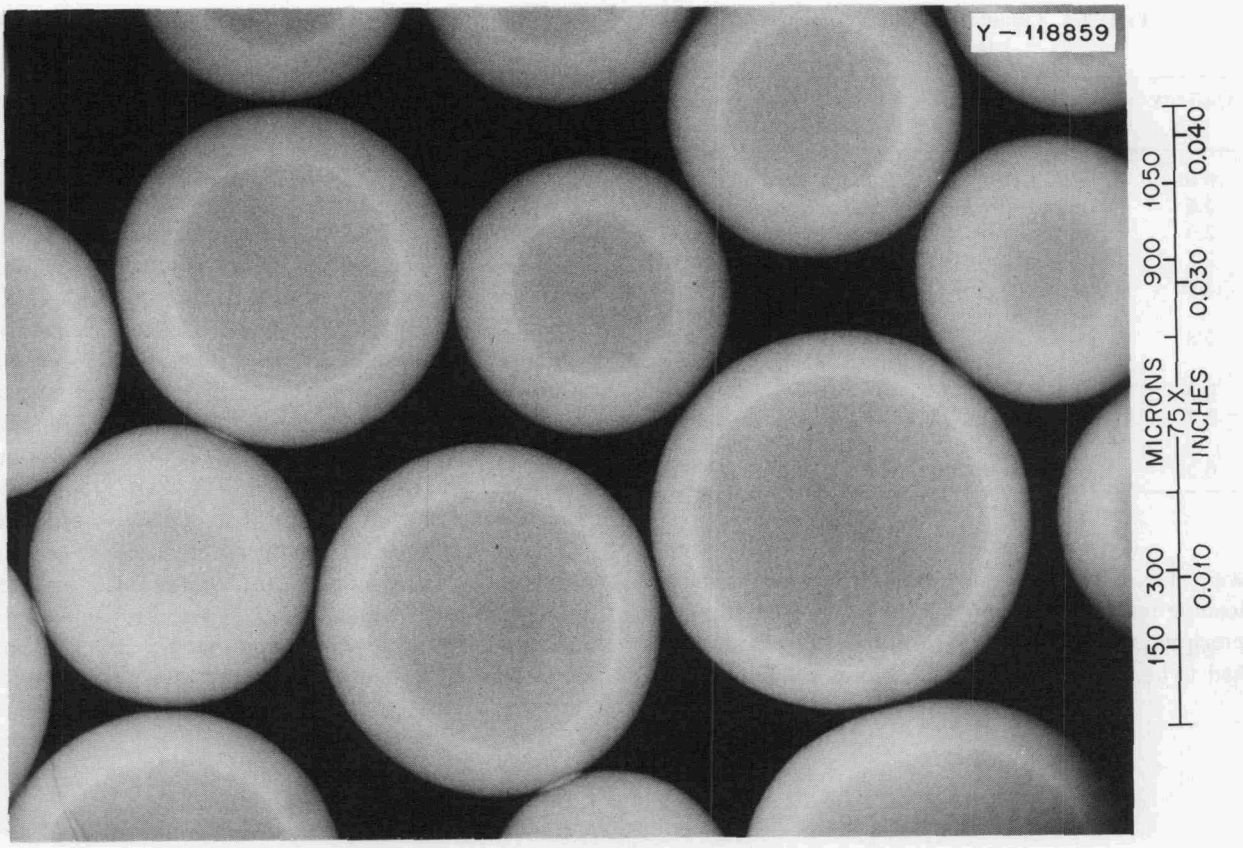

Fig. 2.6. X radiograph of "shell-loaded" Amberlite IRC-72.

In contrast to the uniform partial loading described above, a procedure for nonuniform, or "shell-type," loading of weak-acid resin has been developed. This would have application where uranium-free centers are desired in carbonized resin beads. This procedure (for Amberlite IRC-72 weak-acid resin) is based on exchanging uranium with the NH_4^+ form of the resin. The same effect can be achieved by exchange with the Na^+ form, but this is not desirable, since sodium, unlike ammonia, would then remain in the carbonized resin. Ammonia is removed during firing, leaving only uranium, carbon, and oxygen (at lower firing temperatures). Figure 2.6 is an x radiograph of a shell-loaded resin after drying at 110°C.

Resin beads were also loaded with thorium and with mixed uranium-thorium. Only a limited number of exploratory runs was made. The thorium loadings were made on both strong- and weak-acid resins, using a once-through column and thorium nitrate solution as the thorium source. The flow of thorium nitrate was continued until equilibrium was obtained. Under these conditions, Dowex 50W-X8 loaded to 114% of theoretical capacity for Th^{4+}; Amberlite IRC-72 loaded to 72%. Mixed uranium-thorium loadings were done on a batch basis, using thorium nitrate solution and UO_3 with Amberlite IRC-72. Products were prepared which had Th/(Th + U) mole ratios of 0.21 and 0.58.

2.4.4 Preparation of Test Materials

Kilogram quantities of uranium-loaded resins were prepared for subsequent firing and carbonization tests or for eventual use in irradiation experiments. Table 2.3 lists these materials in the order they were prepared. In addition, small quantities of resin for special tests were loaded with thorium or strontium.

The two batches loaded with ^{233}U were made in a glove box, using the UO_3 batch method. The starting material was freshly purified uranyl nitrate solution which contained 7 ppm ^{232}U. The maximum working time with this material in the unshielded alpha box is about 30 days. Two methods were used to obtain UO_3: calcination of ammonium diuranate and precipitation of $UO_4 \cdot H_2O$ followed by calcination. Both methods

Table 2.3. Uranium-loaded resins prepared for test purposes

Quantity (kg)	Resin	Comments
0.8	Weak acid	Batch loading, from UO_3
2.6	Dowex 50W-X8	Batch loading, from UO_3
2.0	Amberlite IRC-72	Batch loading, from UO_3
2.5	Dowex 50W-X8	Batch loading, from UO_3
3.4	Dowex 50W-X8	Continuous column, from uranyl nitrate solution
3.8	Dowex 50W-X8	Continuous column, from uranyl nitrate solution
0.33	Amberlite IRC-72	^{233}U
2.7	Amberlite IRC-72	Partial (50, 75, 100%) uranium loadings
0.32	Amberlite IRC-72	^{233}U

were successful. However, in both cases the batch-loading reaction was complicated by the formation of a precipitate, apparently a hydrous U(IV) oxide, which had to be filtered off, oxidized, and recycled. It appears that in the presence of the (organic) resin the high alpha activity level of the ^{233}U and its daughters promotes reduction of U(VI).

2.4.5 Resin Pretreatment

Commercially supplied ion exchange resins, the raw material for this method of microsphere formation, must meet certain requirements regarding size, sphericity, purity, and integrity. The two resins now being used almost exclusively (Dowex 50W-X8 and Amberlite IRC-72) appear to satisfy specifications on sphericity, purity, and integrity. However, the range of as-produced size (20–50 mesh) is far too broad for our purposes. We have purchased a KASON 18-in. wet-screen classifier with a range of screen sizes from 18 to 72 mesh (1185- to 260-μm openings). These screens are made of "tensile boating cloth," which is less prone to blind than other weaves. Nonetheless, throughput must be kept relatively low to obtain the very clean size cuts desired for our product.

3. Fuel Fabrication Process Development

J. D. Sease

The objective of fuel fabrication process development is to provide equipment and processes necessary for the design and operation of the remote refabrication line to be installed in the Thorium-Uranium Recycle Facility (TURF) to demonstrate the recycle of HTGR fuel. The line will accept bare fissile microspheres, coat them with the proper pyrolytic-carbon coatings, blend them with the fertile particles, and form them into rods which will be carbonized, annealed, and assembled into the graphite fuel elements. The inspection and quality assurance procedures that will be required for each step are an integral part of the process development.

3.1 MICROSPHERE COATING

W. J. Lackey W. H. Pechin C. F. Sanders
F. C. Davis D. D. Cannon

The particle coating task includes particle inspection and particle handling in addition to the coating operation. The particles must be sampled and inspected, they must be classified to the proper size range and shape separated, and provisions must be made for particle transfer, storage, and blending. The preliminary coating process equipment flowsheet shown in Fig. 3.1 illustrates the complexity of the remote coating operation. The entire coating equipment and process development effort is focused on obtaining adequate engineering information to allow design and operation of such a remote system. Only in the case of particle inspection can the operations be performed in glove boxes; the remaining operations involve larger quantities of fuel and thus require shielding by a hot cell.

3.1.1 Particle Coating

Fluidized-bed-type particle coating equipment and processes are being developed for remote coating of recycled HTGR fuel. Porous carbon coatings which provide void space for accommodation of fission products and dense, strong, isotropic carbon coatings (and perhaps SiC coatings) will be required for fission product containment. The reference recycle fissile particle[1] is of the Biso type and consists of a 350-μm-diam sol-gel (Th–20% U)O_2 kernel coated with buffer and isotropic carbon coatings each about 100 μm thick. For particles of this type, about 10 kg of heavy metal will be coated daily in the TURF pilot plant. Such particles have been produced numerous times in 1- to 2-kg batches in the 5-in.-diam prototype remotely operated coating furnace previously described.[2,3] Although extensive additional equipment modification will be required for fully remote operation, the coater is currently a highly automated, versatile, and reliable system. Areas most deserving of future efforts are (1) furnace maintenance, which includes remote and economical methods of keeping the coating chamber sufficiently free of both hard and sootlike carbon deposits; (2) coupling of the coating furnace with other parts of the refabrication system in a manner such that

1. *National HTGR Fuel Recycle Development Program Plan*, ORNL-4702, Rev. 1 (in preparation).
2. R. B. Pratt and S. E. Bolt, *Status and Progress Report for Thorium Fuel Cycle Development for Period Ending December 31, 1966*, ORNL-4275, pp. 61–78.
3. W. J. Lackey et al., *GCR-TU Programs Annu. Progr. Rep. Sept. 30, 1971*, ORNL-4760, pp. 45–50.

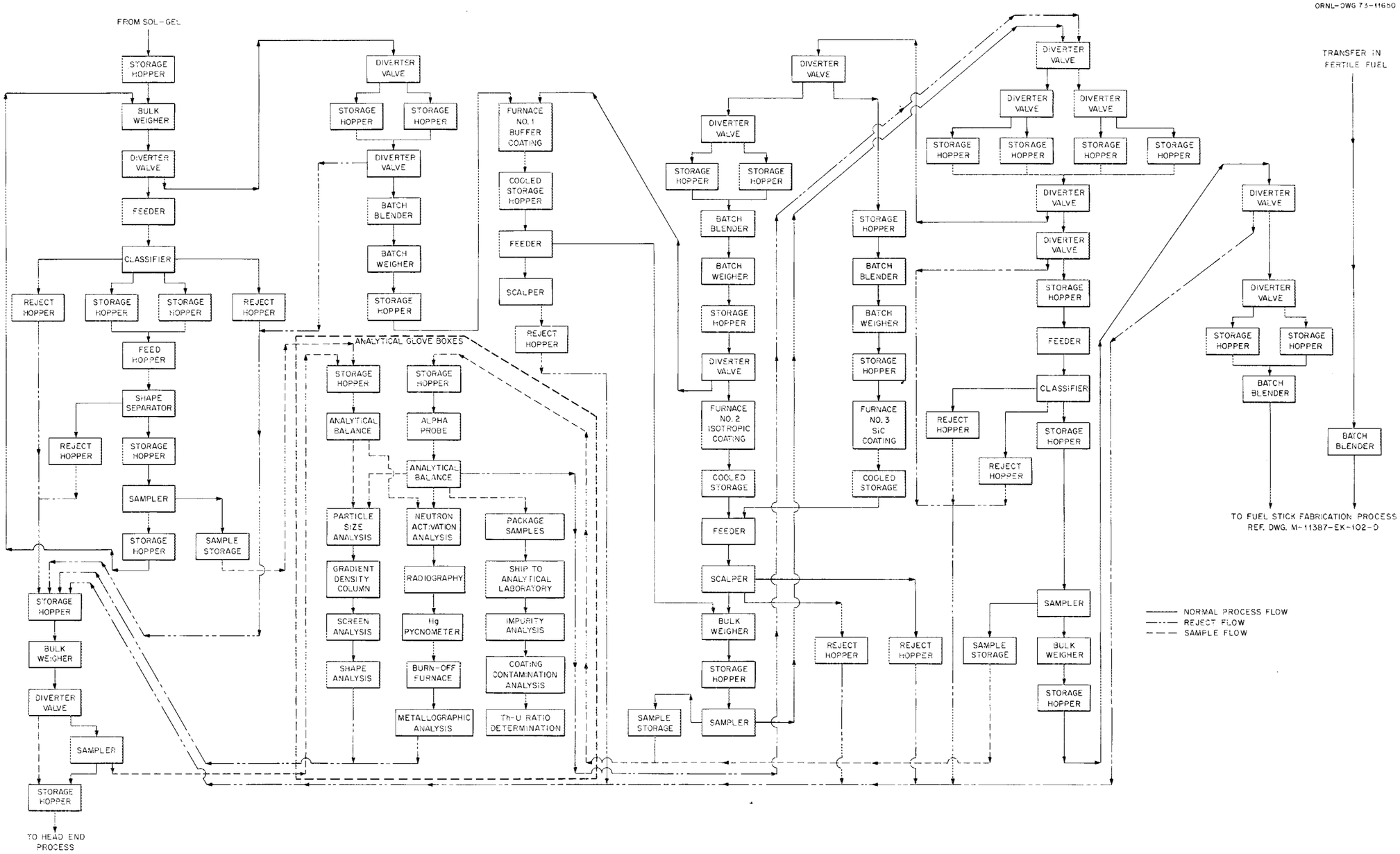

Fig. 3.1. Remote coating process equipment flowsheet.

particles can be reliably transferred to and from the coating furnace (in particular, the exact scheme for furnace unloading remains to be decided); and (3) an understanding of the process used for deposition of the isotropic coating sufficient to allow routine production of suitable coatings.

Equipment modifications. The numerous items of equipment investigated during the year are briefly described below.

About six man-months of engineering design was devoted to redesign of the lower portion of the 5-in.-diam prototype coating furnace. One objective was to adapt the furnace for use with either a conical or a fritted plate-type gas distributor. Of equal importance was redesign of the furnace support structure, electrodes, and water and gas services to provide more open space under the furnace. This additional space will allow greater flexibility in design of gas injectors and equipment for removing coated particles from the furnace. The new design, which is nearly completed, will also facilitate remote replacement of the furnace heating element and provide increased water cooling of the heating element electrodes.

A second 5-in.-diam furnace was modified to permit use of a water-cooled fritted plate-type gas distributor. Previous tests with a non-water-cooled frit showed that without water cooling almost immediate plugging of the frit occurred at normal operating temperatures. The maximum temperature at which a run could be completed without water cooling was about 900°C, and the resulting coatings were much too dense for buffer coatings. Our first water-cooled frit holder was mushroom shaped, and only the stem was water cooled. Plugging of frits was extensive, since the large-diameter portion of the frit holder operated at about 700°C when the furnace temperature was 1200°C. After adding water cooling to the large-diameter portion of the holder, which is located only $1/32$ in. from the lower surface of the fritted plate, coating runs could be completed. Some plugging of the frits occurred, but acetylene-derived buffer coatings were deposited at 1375°C. Gas velocity measurements showed that the frits plugged preferentially near the periphery, apparently because it is hotter in this region.

The prototype coating furnace was lengthened $9\frac{1}{2}$ in. by adding a cylindrical steel segment to the top of the furnace shell, and the graphite coating chamber was lengthened a similar amount. This new system can be used with either the original $18\frac{1}{4}$-in.-long heating element or with a newly designed $27\frac{3}{4}$-in. element. The longer furnace was desired in order to reduce the quantity of fuel thrown by the spouting bed out of the furnace and into the soot filter. The longer hot zone may also result in coatings with fewer soot inclusions, but this has not yet been evaluated.

In addition to the above source of particle loss, it was determined that particles were being lost from the unloading reservoir into the vacuum system used to assist pneumatic transfer of particles from the coating furnace to the unloading reservoir. Baffling of the pipe leading from the reservoir to the vacuum pump was not effective. However, the particle loss problem was solved by installing, within the reservoir, a screen between the particles and the vacuum line. A screen with openings small enough to prevent passage of particles and large enough not to be plugged by soot was found by trial and error.

We investigated the feasibility of using nongraphite coating chambers that could be reclaimed by removing deposited carbon by oxidation. A survey revealed two candidate materials (graphite coated with SiC and TZM or molybdenum coated with one of the $MoSi_2$-type coatings) that might withstand cyclic oxidizing and reducing atmospheres and cyclic heating to about 1350°C. Commercially available[4] SiC-coated graphite was selected for testing, and initial results were promising. A radiograph of a coated cone is shown in Fig. 3.2. Cones of this type experienced no damage when used as the coating chamber in the prototype furnace, but when carbon deposits were removed by oxidation in flowing air at 800°C, the underlying graphite cone was partially oxidized over the region of the cone where the SiC coating was only about 0.006 in. thick (Fig. 3.2). All other regions were unharmed. The vendor was able to obtain a uniformly thick SiC coating by modification of the coating process, but the only test to date with such a cone resulted in spalling of a piece of SiC from the cone because of an excessively thick (0.080 in.) coating. Further testing of uniformly coated cones with coating thicknesses of 0.015 and 0.030 in. is planned.

Several changes were made to the gas handling equipment of the prototype coating furnace. Some of the changes were made to eliminate the possibility of a temporary loss of gas flow during the switch from carrier gas to coating gas. Such a loss of flow could allow a portion of the particles to become unfluidized and fall into the unloading reservoir without having been coated. These modifications consisted in replacing three valves with quick-acting Bellows-Valvair spool-type valves and placing the solenoid for each within several inches of the valve to minimize the time delay

4. Ultra Carbon Corporation, Bay City, Mich.

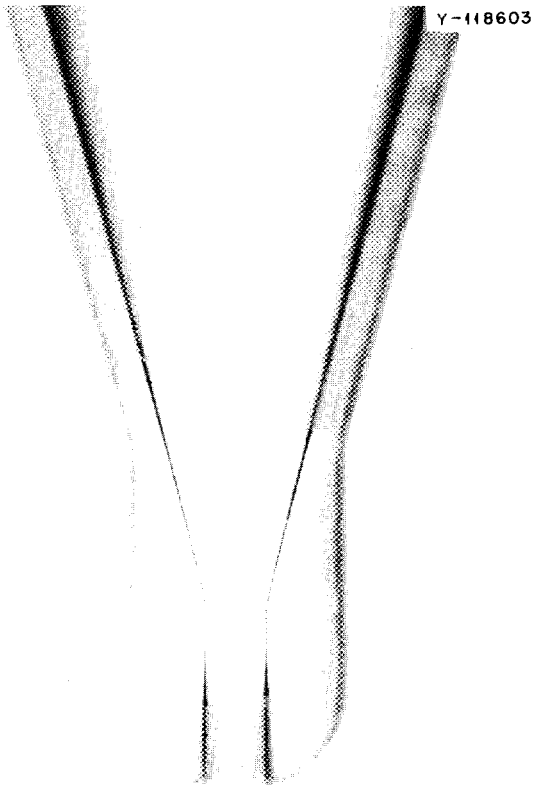

Fig. 3.2. Radiograph of graphite coating chamber coated with SiC. Note the thin coating near the apex of the cone.

associated with the pneumatic signal. Other changes to the gas supply system included resizing and calibrating all differential-pressure cells and regulating valves. These changes were made so that the valves would operate in the midrange for currently employed gas flow rates and thus yield more accurate flow rate control. A wet test meter was purchased for use in periodically checking the calibration of gas handling equipment.

An automatic-recording optical pyrometer was purchased and will be evaluated to determine its usefulness as a temperature sensor and as a secondary calibration instrument for radiomatic-type temperature sensors. Experience with these sensors indicates that they might be adequate for the TURF, but their calibration must be checked frequently. This is easily done now with a manually operated optical pyrometer, but an automatic pyrometer or some other device will be required for remote operation.

Because of an indication of a high oxygen level in the prototype furnace effluent, the entire furnace and exhaust system was systematically leak checked. The tightness of the system was improved considerably by installing newly designed furnace electrode insulation and by eliminating a number of leaks associated with fittings and O-rings. After this maintenance, the combined furnace and effluent system was pressurized to 1 psig and the leak rate was 0.008 psi/min. The oxygen level in the effluent when the system was being purged at room temperature with 2 scfm of argon was less than the detection limit of the analyzer, which is about 0.1%. This leak rate and the oxygen level will be valuable reference points during future design and maintenance.

Carbon felt heat shields were investigated as a potential substitute for the comparatively expensive molybdenum heat shields currently used in the prototype coating furnace. Even though the felt used was slightly more rigid than normal carbon felts, it was not sufficiently rigid and the heat shield slumped during a short period of use. Additional supports would be required for use of this material. A vendor[5] who supplies seamless carbon felt cylinders that are sufficiently rigid to be self-supporting was located, but current technology does not allow the manufacture of cylinders that are large enough for our purpose. However, the vendor is continually increasing the size of cylinder that can be made, and the progress will be followed.

Filtering and disposing of the rather large quantity of soot present in the effluent gas during deposition of carbon coatings are significant problems. The soot is efficiently separated from the effluent gas by a fiberglass cloth filter several square feet in area, but the layer of soot that builds up on the filter at the rate of about $\frac{1}{8}$ in. per coating run causes a pressure drop across the filter of 1 to 2 psi. This pressure drop complicates flow of the effluent, and thus it is necessary to periodically clean the filter. The problem is complicated by the fact that a small filter is desired because of the cost penalty associated with a large piece of equipment in a hot cell and because a critically safe filter geometry is desired. Several soot filter designs were evaluated. We attempted to remove the soot from the filter media by vibration and by back purging the filter with argon, but had no success. We then tried a filter equipped with mechanical scrapers which removed the soot by rubbing across a flat slablike filter media. The removed soot fell to the bottom of the filter housing where a ram compacted it into a 4-in.-diam cylinder. This design was not completely satisfactory, because poor guidance of the

5. Fiber Material Inc., Granitville, Mass.

scraper caused a compacted layer of soot about $1/32$ in. thick to be left on the filter which resulted in a pressure drop of about 1 psi. Moreover, poor alignment of the compacting ram occasionally led to difficulties in compacting the soot. However, a filter of this type, with improved guidance of the scrapers and compacting ram, might be suitable for remote operation. This type of filter and commercially available multiple sock-type filters where the soot would be removed pneumatically by back purging with a blast of gas or mechanically by moving rings will be considered in the future.

To deposit SiC coatings, one of the silanes, CH_3Cl_3Si, is decomposed at high temperatures in the presence of hydrogen to form SiC and HCl. The acid vapor must be removed from the effluent before venting to the atmosphere. The scrubbing system used for this purpose was improved considerably this year. The updated system is shown schematically in Fig. 3.3, which also shows the coating furnace and the silane injection system. About 95% of the acid leaving the furnace is absorbed by contact with a spray of NaOH solution in a Venturi-type scrubber. The remaining HCl vapor is removed by NaOH solution flowing at the rate of 1 to 2 gpm countercurrent to the effluent through a 6-in.-ID, $3\frac{1}{2}$-ft-long column packed with polypropylene cylinders. The upper 6 in. of the packed column is kept dry and acts as a demister; the demister is needed to prevent the downstream absolute filters from becoming saturated with water. These two scrubbers operating in series were successful in removing the HCl, but a white smoke, thought to be some silicon polymer formed as a result of incomplete silane decomposition, was always present at the gas inlet end of the packed column and, to a small extent, downstream of the column. It is important that this material be removed, since it slowly reacts with water vapor to form acid. The efficiency with which the white smoke was removed was improved significantly by increasing the NaOH concentration from 10 lb to 45 lb of NaOH per 25 gal of water. Complete cleanup of the effluent will probably require an additional length of packed column to allow a longer contact time with the caustic solution.

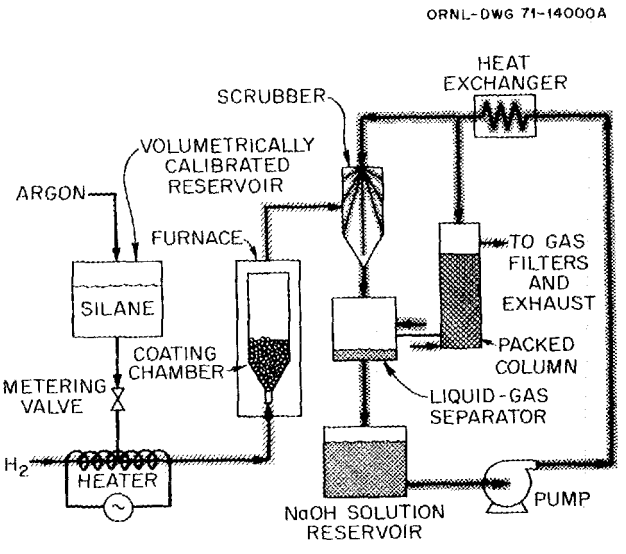

Fig. 3.3. Schematic of equipment for depositing SiC in the 5-in.-diam prototype remote coater and the effluent handling system.

Process development. Most of our effort in the area of process development was devoted to the buffer coating process using a single-inlet, 30° included angle, conical-type gas distributor. Several statistically designed experiments were conducted and analyzed. The variables of interest were acetylene flow rate, type of diluent gas, diluent gas flow rate, temperature, time, kernel size, standard deviation of kernel size, and charge weight. Responses of interest were coating thickness, particle-to-particle variation in coating thickness, coating density, coating efficiency, and various system responses such as the extent of soot formation and the influence of soot on the behavior of the soot filter. In addition to achieving a vastly improved understanding of the buffer coating process that will allow us in the future to confidently deposit buffer coatings having the required properties, we found a new set of operating parameters that reduced the within-batch coating thickness standard deviation from about 25% of the mean coating thickness to about 14%. For the reference buffer thickness of 100 μm, this improvement in coating thickness uniformity means that instead of 1% of the particles in a batch having coatings thinner than 40 μm, only 1% of the coatings will be thinner than 66 μm. Since particles with thin buffer coatings are more likely to fail during irradiation, this process improvement should yield fuel significantly superior in irradiation performance. Not only did the new set of operating conditions yield coatings more uniform in thickness from particle to particle, but the coatings were of the desired density (1.1 ± 0.2 g/cm^3) and the process was rather insensitive to the quantity of material being coated (Fig. 3.4). Charges as large as 3200 g of ThO_2 kernels were successfully coated.

The improved buffer coating process was accomplished by increasing the diluent flow rate, the acetylene flow rate, and the temperature. The most important factor was the increased diluent flow rate. Higher diluent flow rates decreased the particle-to-particle

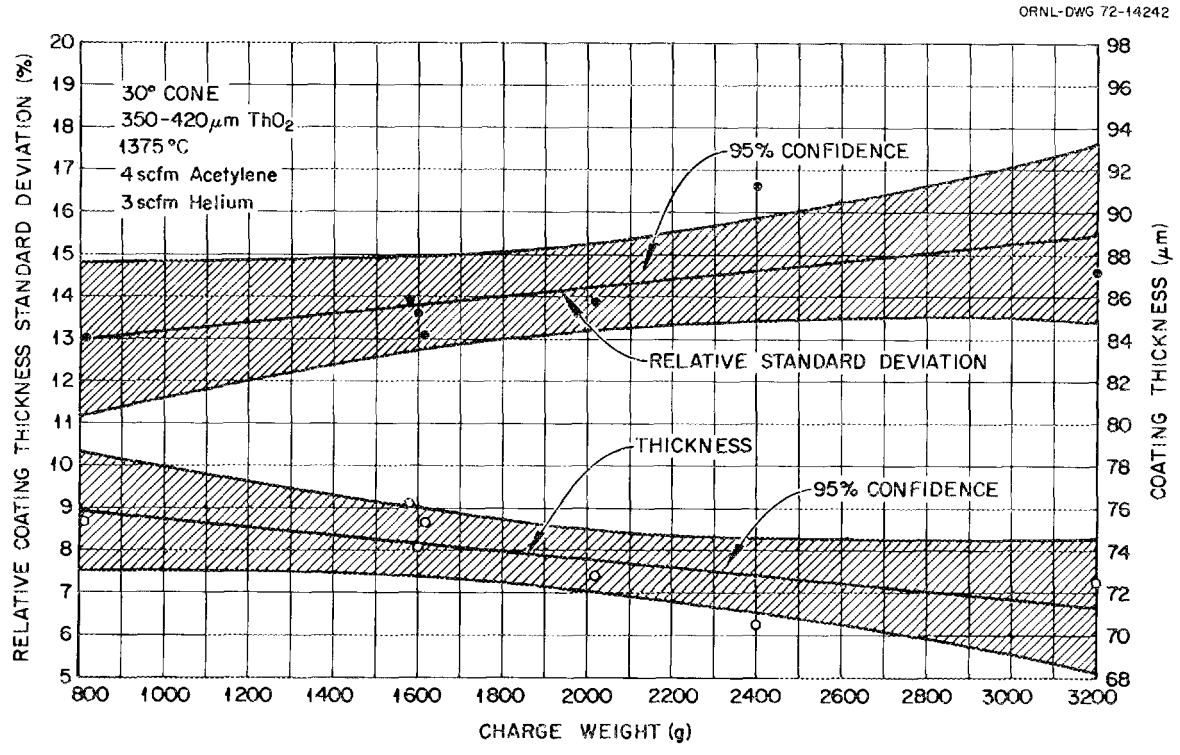

Fig. 3.4. Effect of charge weight on the average buffer coating thickness and particle-to-particle thickness variation. The coating time was increased proportionately to the charge weight and was 3 min for the 800-g charge and 12 min for the 3200-g charge.

variation in coating thickness; however, unless the acetylene flow rate and/or temperature are also increased, coating densities are unacceptably high. Higher gas flow rates apparently led to better mixing of the spouting particle bed and, therefore, more uniform coating thicknesses. Helium is preferable to argon as a diluent, since coating densities are lower and thus higher diluent flows can be used without producing coatings that are too dense.

These experiments gave us a better qualitative understanding of the buffer process and considerable success in a quantitative understanding. Phenomenological equations were developed for predicting the mass of carbon deposited, the coated-particle volume and density, and the standard deviation of coating thickness. The independent variables in these expressions were charge weight L (g), time t (min), acetylene flow rate F (g/min), ratio of diluent flow to acetylene flow R (g of diluent/g of acetylene), standard deviation of kernel diameter σ_k, and kernel diameter D_k (μm). The equation for predicting coating weight and a comparison of the observed and predicted values are given in Fig. 3.5. The agreement is considered excellent.

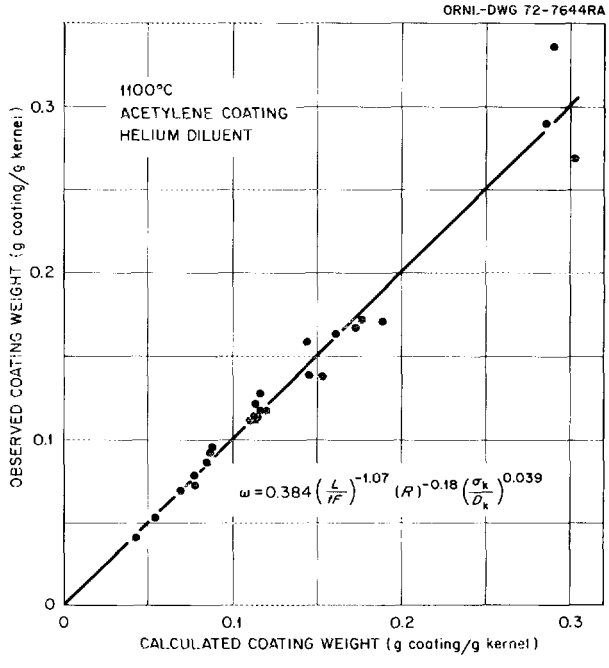

Fig. 3.5. Comparison of observed coating weights with calculated values.

The effect of varying the included angle of the single inlet conical-type gas distributor was investigated. For angles of 30, 90, and 135° the performance, as measured by uniformity of coating thickness and coating efficiency, improved considerably as the cone angle was decreased.

We discovered that for a given buffer coating run, the coating density was greater for the thin coatings. The observed relationship between coating thickness and density is shown in Fig. 3.6. The fact that the thinner coatings are more dense means that the average buffer coating thickness will have to be about 5% larger than would be required if there were no relationship between thickness and density.

A limited number of coating runs were made using the water-cooled fritted plate holder. Buffer coating runs were made using flat frits and various modified porous gas distributors. In each case the temperature was 1375°C, and the acetylene and helium flow rates were each 2.65 scfm. Coating thickness standard deviations have ranged from 13.2 to 18.5%, with no apparent correlation with frit geometry. Coating densities were in the range 1.0 to 1.2 g/cm^3, and the efficiency varied from 56 to 69%. However, we still experience partial plugging of the frit, requiring that a given frit be used for only one coating run.

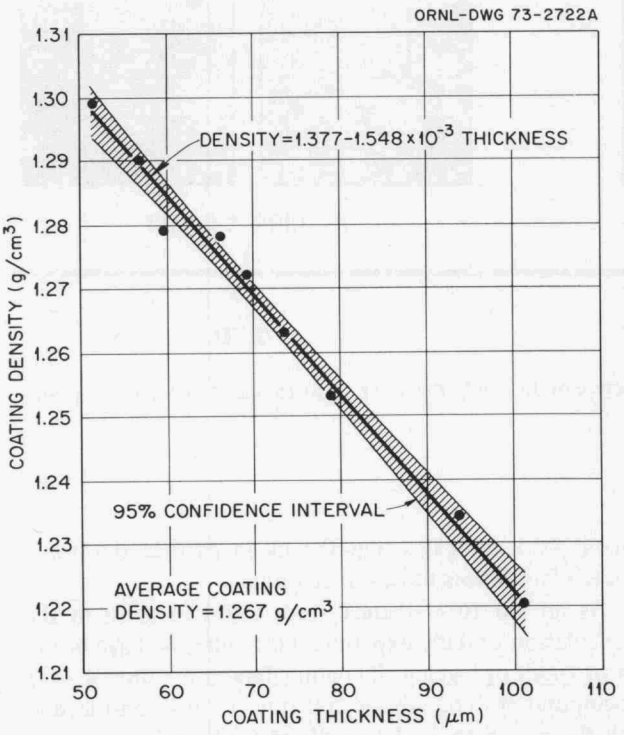

Fig. 3.6. Variation of coating density with coating thickness for a single buffer coating run.

A limited effort was directed toward investigating the effect of temperature and deposition rate on the properties and structure of SiC coatings. Figures 3.7 and 3.8 show that as the deposition rate is increased, there is a decrease in density and an increase in surface roughness. Both of these effects are expected to result in weaker coatings.[6] Figure 3.9 shows coatings deposited at a rate of 0.18 μm/min; the coatings are dense and fine grained and appear to be of excellent quality.

In addition to the above equipment and process development, we coated fissile, fertile, and inert carbon kernels for use in the OF-1 and HRB-7 irradiation tests. Also, more than 100 kg of Biso- and Triso-coated particles was prepared for use in fuel stick fabrication, blending, and head-end reprocessing studies.

3.1.2 Particle Inspection

We have nearly completed the construction of a new electronic particle size analyzer based on the same light blockage principle as one previously described.[7,8] The new instrument has 1000 channels of memory as opposed to 10 channels in the old one. The instrument is also capable of direct interfacing with the PDP-8/E computer for the statistical analysis and printout of the data.

One of the important components of the particle size analyzer is the particle singularizer shown in Fig. 3.10. The flow of compressed gas through the power jet tube propels particles individually through the delivery tube, which has an inside diameter about 1.5 times the particle diameter. The rate of the singularizer can be varied from about 20,000 particles/min to several hundred thousand per minute, depending on the air pressure, the particle size, and the diameter of the singularizer outlet tube.

The particle size analyzer is illustrated in Fig. 3.11. As the particles pass through the sensor they partially block the flow of light falling on a photocell. The light

---

6. A. G. Evans, C. Padgett, and R. W. Davidge, "Strength of Pyrolytic SiC Coatings of Fuel Particles for High-Temperature Gas-Cooled Reactors," *J. Am. Ceram. Soc.* **56**(1), 36–41 (1973).

7. F. J. Furman and R. A. Bowman, *Status and Progress Report for Thorium Fuel Cycle Development January 1, 1969, through March 31, 1970,* ORNL-4629, p. 80.

8. W. J. Lackey et al., *GCR-TU Programs Annu. Progr. Rep. Sept. 30, 1971,* ORNL-4760, p. 50.

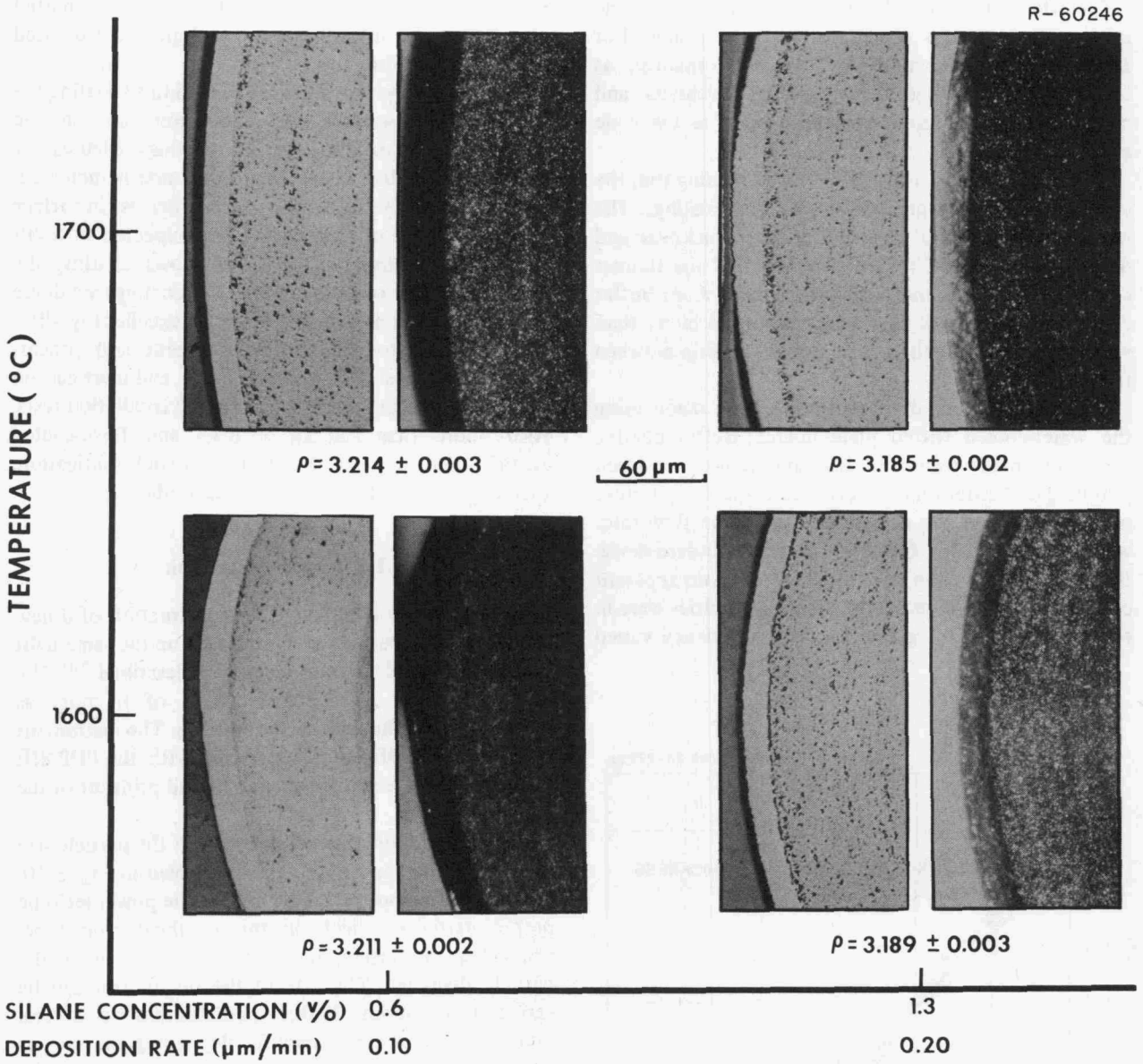

Fig. 3.7. Effect of deposition conditions on the density and structure of SiC. Only the outer 10 to 15 μm of each particle is SiC. Bright field, polarized light.

blockage creates a pulse which is amplified and sent to the multichannel analyzer, where the pulse height is converted to digital information and assigned as a count to the appropriate channel. The number of counts in each channel is then transferred electronically to the computer, which applies the calibration factor and prints the particle size distribution. The machine is complete except for the data link with the computer, which is awaiting delivery of a circuit board. Preliminary work indicates that the mean particle size for a batch reproduces to less than 1 μm.

As an aid to statistical studies and to assist in the calculation of daily experimental results, we have begun a program of logging all coating data in the time-sharing computer system. About 200 runs are now on file, and all the new runs are being added for both 5-in. coaters.

An investigation is under way of the crush strength of particles. The crush strength is an important property,

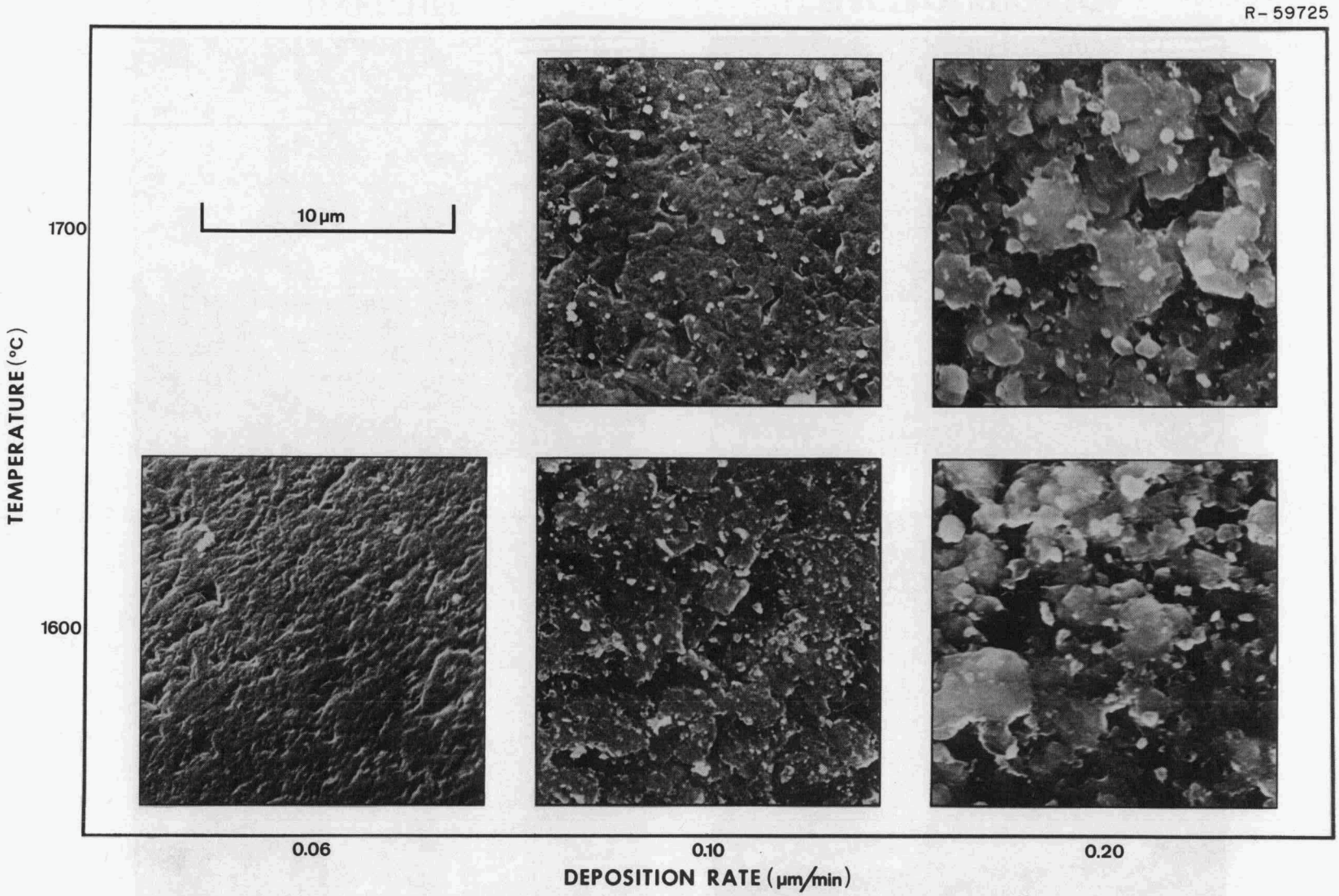

Fig. 3.8. Effect of deposition conditions on the surface roughness of SiC coatings as revealed by scanning electron microscopy.

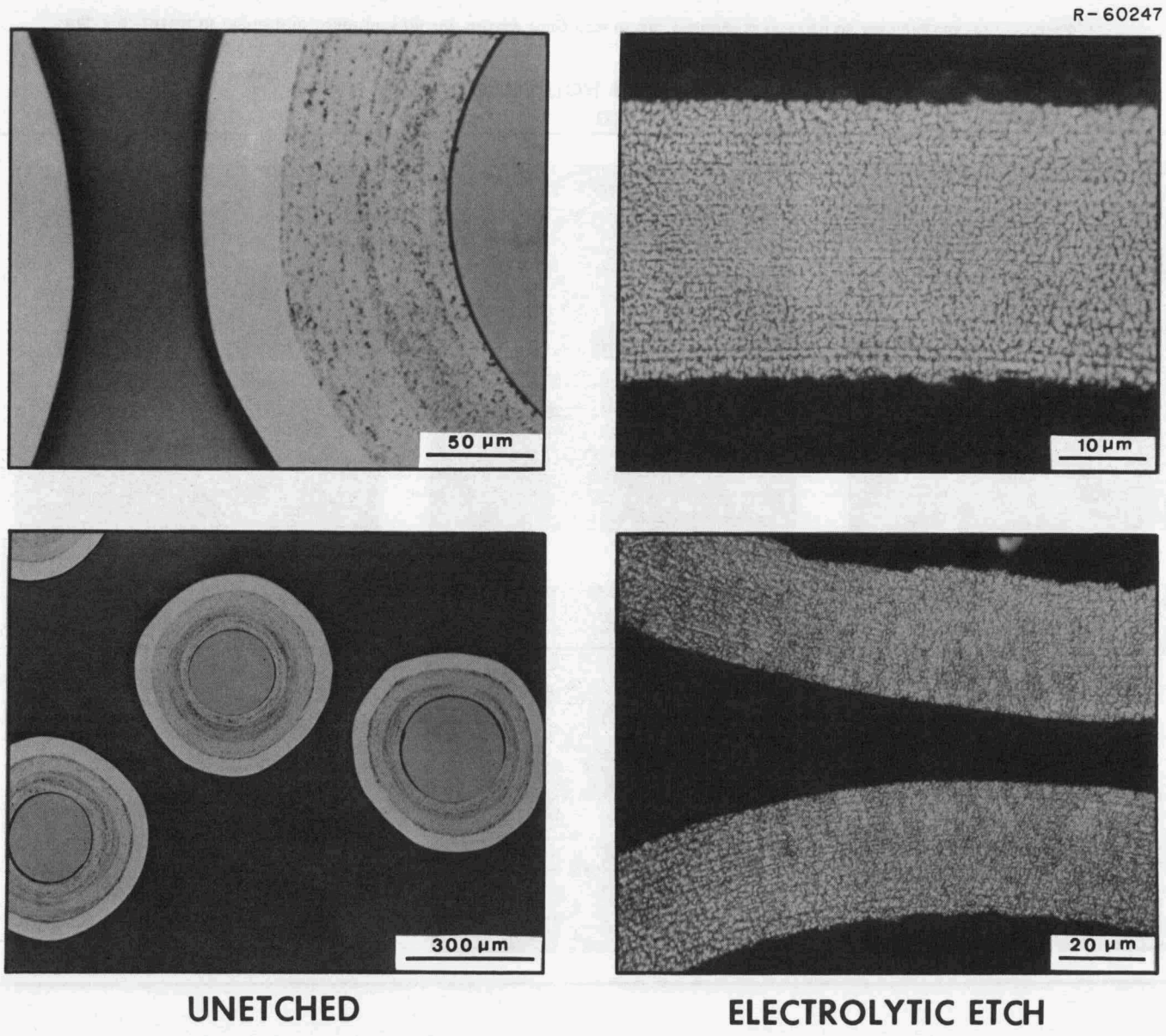

Fig. 3.9. High-density small-grained silicon carbide deposited at 0.18 μm/min at 1600°C.

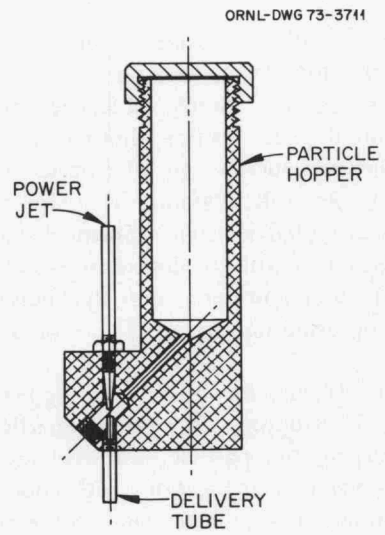

Fig. 3.10. Jet pump particle singularizer.

because the particles must withstand the loads involved in the stick-forming operation. As an indicator of coating tensile strength, the crush strength may also provide useful information about the expected in-service performance of fuel.

We made strength measurements for two different batches of particles, using a simple load frame designed only to measure load at failure. In the process of analyzing these data, we developed criteria for further work: (1) the diameter of each particle should be measured before crushing, (2) the deflection at failure should be measured in addition to load, (3) a sufficient number of particles must be tested to ensure a good determination of the standard deviation of strength, and (4) there should be some measurement of particle shape.

We have had about one year's experience with the system for reading microradiographs in which the

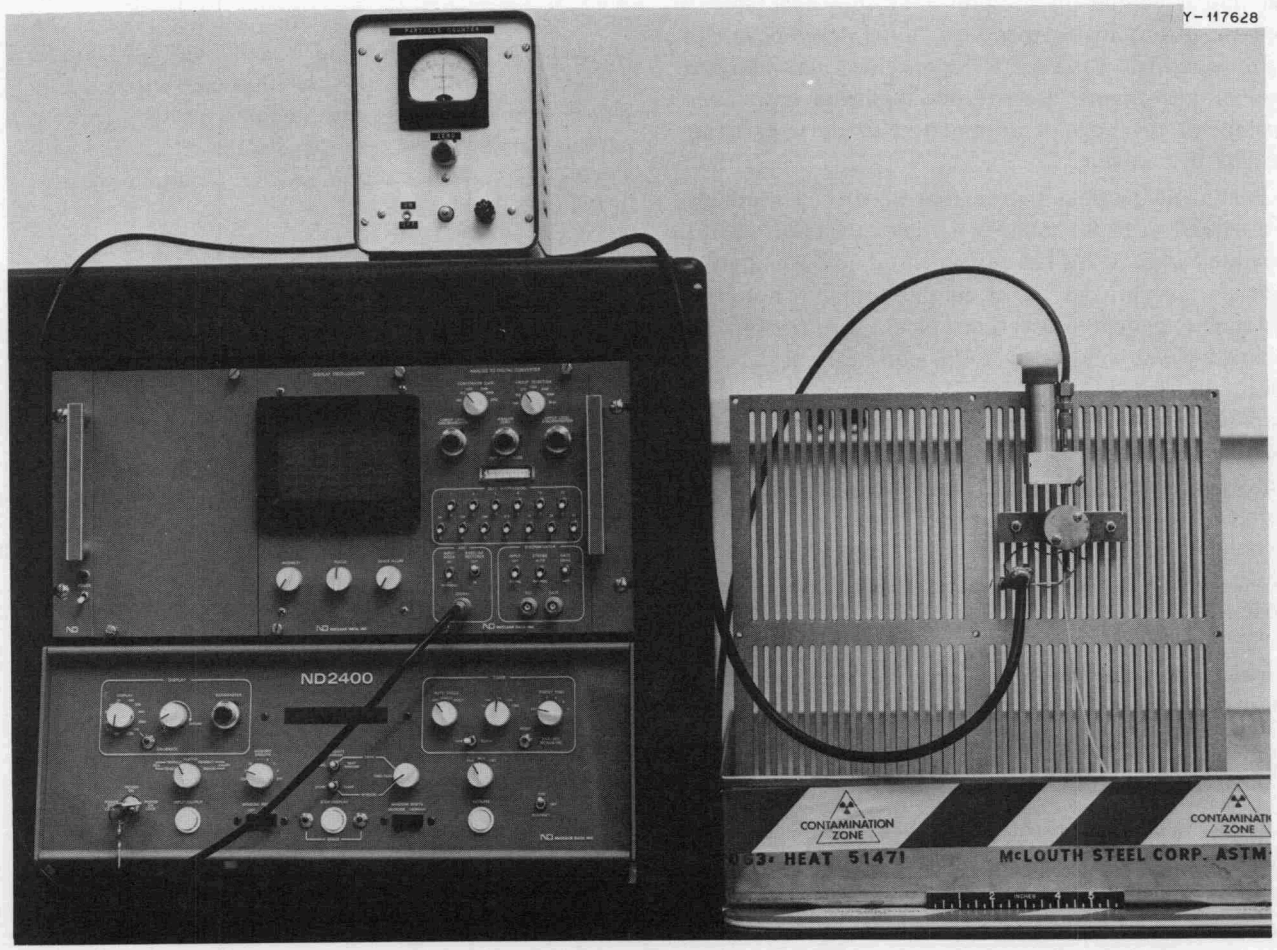

Fig. 3.11. Electronic particle size analyzer.

digital output from a split-image eyepiece is immediately processed and printed by a small computer. With this equipment the diameters and coating thicknesses of 50 particles can be determined in 10 to 15 min instead of the 2 to 3 hr previously required. We have recently acquired a filar eyepiece for this system which will allow us to measure the low-temperature isotropic (LTI) coating thickness independently. By measuring two LTI coating thicknesses for each particle, we will be able to determine a shape factor, since the nonsphericity of the particles is almost entirely due to variations in LTI coating thickness.

3.1.3 Particle Handling

Particle handling involves the development of devices to remotely store, classify, blend, and sample kilogram amounts of ^{233}U-bearing particles. Most commercial materials handling equipment is not suitable, since either it is designed to handle ton quantities or it is laboratory equipment and thus not readily adaptable to remote or automatic operation. Initial development of remote particle handling techniques was accomplished several years ago.[9] Recent developments have been mainly in the area of pneumatic particle transferring and particle valving.

Pneumatic particle transfer has been used routinely for several years to transfer particles to and from the coating furnaces. We have experienced no difficulties in transferring particles to the coating furnaces; however, we have experienced occasional blockage of the furnace unloading line caused by extraneous carbon deposits with the coated particles. The extraneous carbon deposits come from carbon which deposits on the coating chamber walls and flakes off during coating or unloading and from soot balls which are sometimes formed during coating. A system to eliminate these extraneous carbon deposits after coating has been designed for installation on the prototype remote coater.

We performed an abrasion test of buffer-coated particles to determine if coatings might be damaged during particle transfer, screening, and blending operations. The test consisted in fluidizing 1100 g of buffer-coated ThO_2 with 2.5 scfm He. The particles were contained in a single-inlet, 30° included angle cone that was heated to 1200°C. The particles were fluidized for 15, 60, and 120 min, and the coating thickness of a riffled sample was compared with the initial thickness. In each case coating thicknesses were determined radiographically for 100 to 200 particles. The results are plotted in Fig. 3.12. Statistical analysis of a linear plot of coating thickness vs time showed that the 95% confidence interval for the rate of abrasion was 0 to 0.13 μm/min. In other words, if there was any abrasion it was negligible from a practical standpoint. This is in agreement with previous results that showed negligible reduction in buffer coating thickness during 2 hr of screening using micromesh screens on a Syntron test shaker.

For particle valving, the pinch valve appears to be suitable for interrupting or stopping particle flow without damaging the particle. We have used pinch valves in a number of applications with good success. The major disadvantage of the pinch valve is that it requires the use of an elastomer member, which limits its radiation life and operating temperature. Close-tolerance slide valves have been found satisfactory for holding and dumping particles. We have used slide valves on the incremental blender (see Sect. 3.2.1) and on a large batch blending system without particle damage. A plunger-type valve has also been found satisfactory for holding and dumping particles without particle damage. We experienced some difficulties with a swing-type valve because of particle holdup in the area of the swing actuator.

3.2 FUEL ROD FABRICATION

R. A. Bradley D. D. Cannon F. C. Davis
C. R. Reese[10] J. D. Sease C. F. Sanders

The purpose of this work is to develop processes and equipment suitable for fabricating about 8000 fuel rods per day at the TURF. The fuel rods are about ½ in. in diameter by 2 in. long and contain mixtures of fissile and fertile coated particles bonded by a matrix of pitch binder and graphite filler.

The principal activities in fuel rod fabrication are dispensing, blending, and loading particles into molds, injecting the matrix into a bed of particles to form a rod, carbonizing and annealing the rod, and inspecting and assaying the fuel stick.

3.2.1 Particle Dispensing, Blending, and Loading

The particle dispensing, blending, and loading system must be capable of rapidly dispensing precisely controlled quantities of fissile and fertile particles and blending and loading them into the mold in such a

9. F. J. Furman, J. T. Meador, and J. D. Sease, *Microsphere Handling Techniques,* ORNL-TM-2782 (March 1970).

10. Presently at Harvard University.

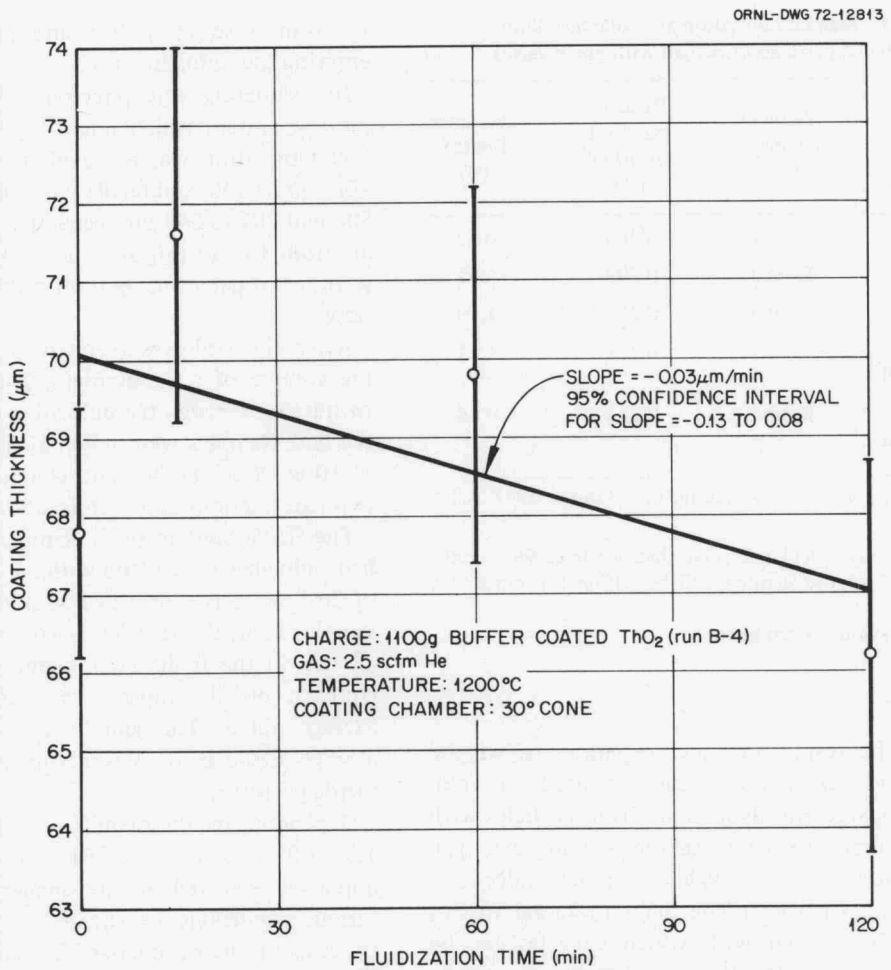

Fig. 3.12. Abrasion of buffer coating during fluidization.

manner that they are distributed uniformly throughout the fuel rod. The system should also be capable of blending graphite shim particles with the fissile and fertile particles, since some of the fuel rods may require shim particles to reduce the fuel loading. Our target specification is that the variation in heavy-metal content per inch of fuel rod be less than 5%.

We are investigating the use of pinch valves to volumetrically dispense the particles. A pinch valve consists of a section of latex tubing enclosed in a double-walled container such that pneumatic pressure can be applied to the outside of the latex tubing. When pressure is applied, the tubing collapses, thus closing the valve. Venting the air pressure opens the valve and allows the particles to flow from a hopper through the pinch valve into a collector tube with a measured volume. After the collector tube is filled, the pinch valve is closed and the particles are emptied from the collector tube through a valve at its base.

Pinch valves made with latex tubing with uniform wall thickness and with tubing containing thinned wall sections were evaluated by dispensing at least 100 approximately 1.5-g samples of 420- to 500-μm particles and then weighing them. Collector tubes with circular and square cross sections were also evaluated. The standard deviation for 100 samples of about 1.5 g ranged from 0.003 to 0.005 g. The standard deviation of each set of samples, expressed as a percentage of the mean sample weight, is given in Table 3.1. For the pinch valve with a curved thin section in the latex tubing wall, the tolerance limits are such that we can say with 99% confidence that 99% of the samples dispensed will be within ±0.66% of the mean sample weight. The mean can be adjusted by changing the volume of the collector tube.

Table 3.1. Standard deviation and tolerance limits of samples of particles dispensed with pinch valves

Type of pinch valve	Shape of collector tube	Relative standard deviation[a] (%)	Tolerance limits[b] (%)
Uniform wall	Square	0.264	0.82
Uniform wall	Round	0.293	0.91
Uniform wall[c]	Round	0.350	1.09
V-shaped thin section in wall	Round	0.357	1.11
Curved thin section in wall	Round	0.212	0.66

[a]Expressed as percent of sample mean – sample mean is 1.5 to 1.8 g.

[b]Tolerance limits calculated such that we have 99% confidence that 99% of the samples will be within the range $\bar{x}$ ± tolerance limit.

[c]Repeat of previous experiment.

Based on the results of these experiments, we are confident that pinch valves can be used to volumetrically dispense the fissile and fertile particles with sufficient accuracy to meet the fuel loading specifications. (We have not yet evaluated pinch valves for dispensing shim particles.) The main advantage of this technique is the speed with which particles can be dispensed. The total cycle time for dispensing a sample is 2 to 4 sec. Volumetric dispensing with pinch valves can be used with either of the two blending techniques described below.

Two approaches to blending the fissile and fertile particle have been investigated, batch blending and individual rod blending. The pneumatic blender used for batch blending consists of a 5-in.-diam, 5-ft-tall cylindrical mixing chamber with a conical bottom for ease of unloading. Low-pressure air (1 to 11 psig) introduced through the cone at the bottom of the chamber fluidizes the particle bed, and blending is accomplished by the relative motion between particles in the fluidized bed. Two systems for introducing and dispersing the air at the bottom of the chamber were evaluated. One consisted of an inverted metal cone with eight gas nozzles covered by screens to retain the particles and a central unloading hole which was closed with a plug during blending. The other was an inverted cone made of a porous graphite frit through which the air passed to fluidize the bed. With this arrangement, air was also introduced through the central unloading hole to form a spouting bed and prevent particles from entering the unloading tube.

In evaluating this pneumatic blender, the extreme particle system which might be encountered in HTGR fuel fabrication was assumed, that is, a Th/U ratio of 10/1 and fissile and fertile particle size ranges of 420 to 500 and 707 to 841 μm respectively. Gas pressures ranging from 1 to 11 psig and charge sizes from 0.18 to 5 kg were investigated, using both pulsed and continuous air flow.

After the bed was blended, samples approximating the volume of a 0.5-in.-diam, 2-in.-long fuel rod were withdrawn through the unloading port at the bottom of the bed. Samples were taken at intervals representing 5 to 10 wt % of the bed and were then screened into the two size fractions and each fraction was weighed.

The fissile content of the sample vs the percent of the bed unloaded for a blend with an average fissile content of 26.5 wt % is shown in Fig. 3.13. It can be seen that samples from the first 3 wt % of the bed unloaded were all rich in the fissile component. After that the fissile contents of all samples were within ±5 wt % of the average value. The sine wave oscillation about the average fissile content was apparent in all the experiments performed.

Depending on the blending conditions used, the first 1.5 to 8 wt % and the last 1 to 16 wt % of the bed unloaded were rich in the smaller fissile particles. The various conditions investigated and the results of these experiments are summarized in Table 3.2.

In the experiments to determine the effect of charge size, it was found that 0.18- and 2.3-kg batches were blended adequately except for the end effects previously described. Gross segregation of the fissile particles could be seen through the Plexiglas walls of the blender with the 5-kg batch. It is believed that the pneumatic blender is most efficient when charged such that the bed height is approximately equal to the bed diameter. When the blender was operated at various air inlet pressures, we found that the initial end effect remained unchanged at approximately 2.5 wt % of the unloaded bed but that the final end effect was reduced from 16 wt % of the unloaded bed at inlet pressure of 1 psig to 3 wt % at 2.8 psig. Pressures above 2.8 psig are not considered desirable, because some particles are blown 2 to 3 ft high and could be broken. No appreciable difference was seen between pulse blending and continuous blending.

Several experiments were performed to determine why the initial samples were rich in fissile particles. The order in which the constituents were loaded into the blender was reversed, but the initial end effect remained

Table 3.2. Summary of conditions used and results of experiments with pneumatic blenders

Fissile size of blender charge, 420–500 μm

Blender charge				Blending conditions			Results
Total weight (kg)	Fissile weight fraction (kg)	Fertile size (μm)	Fertile weight fraction (kg)	Gas pressure (psig)	Type of gas flow	Total blending time (sec)	
Type of gas disperser: inverted metal cone with 8 gas nozzles and central unloading hole plugged							
3.4	0.265	707–841	0.735	11	Pulse[a]	100	First 3% of bed unloaded rich in fissile; after that bed leveled to ±5% of nominal
3	0.14	707–841	0.86	11	Pulse[a]	100	First 8% of bed rich in fissile; after that bed leveled to ±10% of nominal; order of loading constituents had no effect; blending, unloading entire bed into container and emptying container into blender to invert bed, and reblending had no effect (nonuniform first 8% and last 3%)
Type of gas disperser: inverted fritted cone with central unloading hole used as spouting bed nozzle							
2.3	0.18	595–841	0.82		Continuous	240	First 1.5% of bed rich in fissile; after that bed within ±5% of nominal until last 1% of bed
0.180	0.15	707–841	0.85	2.1	Continuous	100	First 2.5 wt % and last 10% of bed unloaded rich in fissile
2.3	0.15	707–841	0.85	2.1	Continuous	100	First 2.5 wt % and last 10% of bed unloaded rich in fissile
5	0.15	707–841	0.85	2.1	Continuous	100	Gross segregation of fissile particles could be seen through Plexiglas walls of blender; conclusions: pneumatic blender not suitable for beds where $L/D \gg 1$
2.3	0.15	707–841	0.85	1	Continuous	100	First 2.5 wt % and last 16 wt % of bed unloaded rich in fissile
2.3	0.15	707–841	0.85	2	Continuous	100	First 2.5 wt % of bed unloaded rich in fissile
2.3	0.15	707–841	0.85	2.8	Continuous	100	First 2.5 wt % and last 3 wt % of bed unloaded rich in fissile; pressures greater than 2.8 psig not desirable because particles blown 2–3 ft high and may become broken
2.3	0.15	707–841	0.85		Pulse[a]	100	No effect seen from pulse blending; results about the same as continuous blending under comparable conditions

[a] *100 pulses of 1-sec duration.*

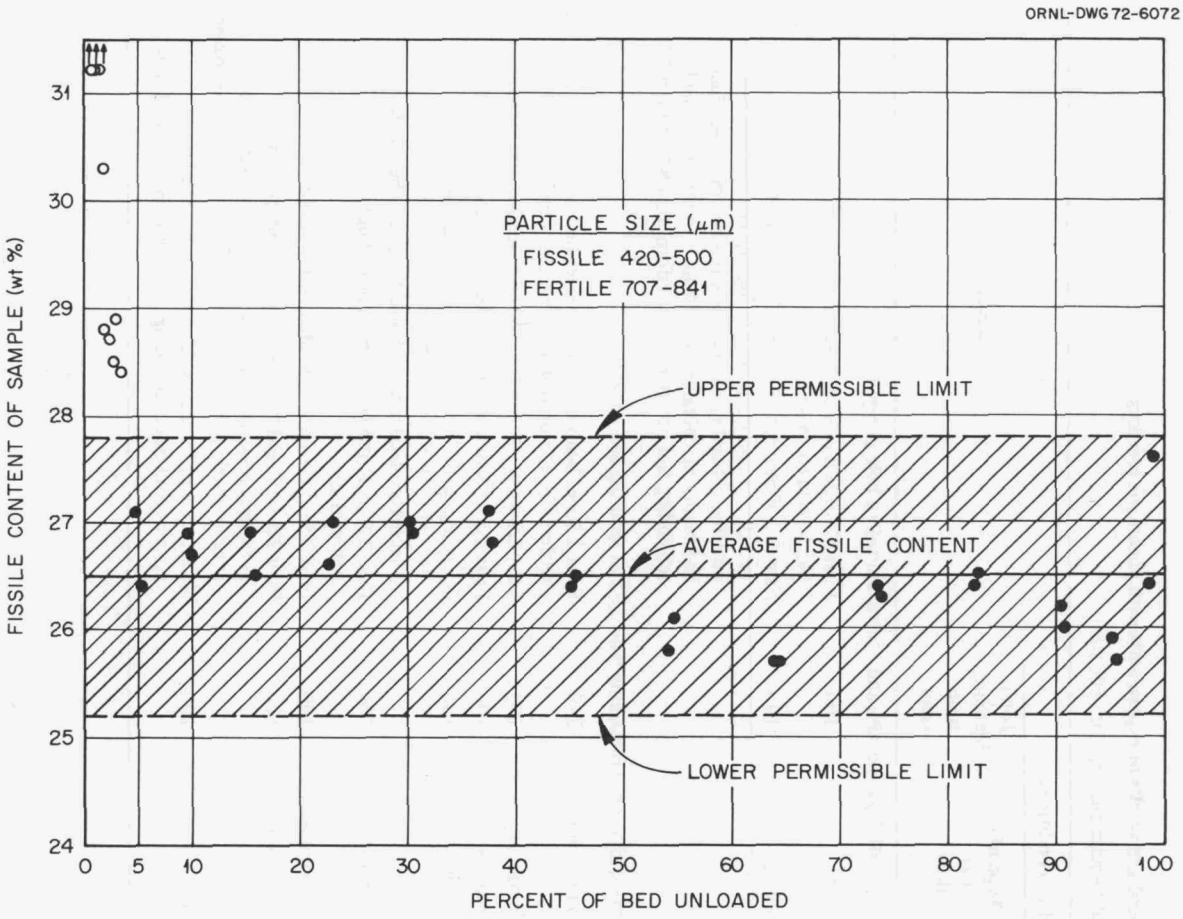

Fig. 3.13. Fissile-fertile particle distribution of pneumatically blended bed.

the same. The bed was blended, unloaded into a container, and then emptied back into the blender, giving a rough approximation of inverting the bed. The bed was blended again, but the initial end effect persisted. We were never able to determine the cause of this initial end effect.

An experiment was performed to determine if the final end effect was due to the top of the bed not being uniformly blended or to the relative particle motion seen during unloading. Samples taken from the top of the bed immediately after blending were found to contain the correct fraction of each type of particle. After 33 wt % of the bed had been unloaded, the center of the partially unloaded bed tended to be lean in the fissile content, while samples taken from the circumference were slightly rich. It is believed that this is an unloading phenomenon and is partially responsible for the final samples being rich in the fissile constituent.

It should be pointed out that all these experiments with the pneumatic blender were performed with very small fissile particles (420–500 μm) and large fertile particles (707–833 μm). The tendency for these particles to segregate was exaggerated due to their size difference. The reference fissile and fertile particles for the recycle element containing ^{233}U are 940 and 740 μm respectively; for the recycle element containing ^{235}U they are 540 and 740 μm respectively.[11] Since the size differences are less than on those used in pneumatic blender experiments, the tendency to segregate will be less and the end effect might be acceptably small.

Another requirement for particle blending is that of cross blending particles of nominally the same size and density but from different coating runs. The pneumatic blender looks particularly promising for this application.

---

11. R. A. Bradley, C. F. Sanders, and D. D. Cannon, "Fuel Stick Fabrication," *GCR-TU Programs Annu. Progr. Rep. Sept. 30, 1971,* ORNL-4760, pp. 52–55.

The other approach to blending which we have investigated, individual rod blending, involves splitting the charge required for one fuel rod into ten approximately equal increments and sequentially loading each increment into the fuel rod mold. For a 2-in. fuel rod, each increment would be 0.2 in. high. Although the fissile and fertile particles within any one increment may not be perfectly blended, the ratio of fissile to fertile in any increment will be about the same as any other increment. This splitting technique was selected because it is the most positive way of assuring that the fissile and fertile particles are distributed along the entire length of the fuel rod.

The laboratory device, termed a decade splitter, used to evaluate this technique consists of a splitting cone fitted into the bottom of a cylindrical sleeve containing an orifice which is centered over the apex of the cone. Around the base of the cone are ten knife edges forming ten gates leading to separate cups. A slide valve serves as the bottom of the cups and provides a means of emptying each cup sequentially into the funnel leading to the mold.

Our evaluation of the decade splitter and slide valve showed that a uniform distribution of fissile, fertile, and shim particles along the length of the fuel rod can be achieved. We found that selection of the proper cone angle for the funnel leading to the mold was critical to prevent segregation of the particles as they were loaded into the mold. In a funnel with a large cone angle (90°), there is appreciable rebound of particles from the walls of the funnel, and the particles tend to segregate. On the other hand, there is almost no rebound from the walls of a funnel with a small cone angle (20°), and the particles can be loaded into the mold without segregating.

3.2.2 Fuel Rod Molding

The process we are developing for molding fuel rods, called slug injection, is illustrated in Fig. 3.14. A preformed slug of matrix is inserted into the mold containing particles, the mold is heated to melt the matrix, and then the matrix is injected into the bed of particles by applying pressure to the top punch. Entrapped air and excess matrix are forced through a circumferential gap around the bottom end plug. The cutaway portion of the bottom end plug serves as a reservoir for the excess matrix.

The feasibility of the slug injection process for making acceptable fuel rods was demonstrated previously and the concept for an automatic fuel rod machine was described.[11] We completed the design, fabrication, and installation of this laboratory automatic rod machine and have operated it at a production rate of 4000 fuel rods per 20-hr day.

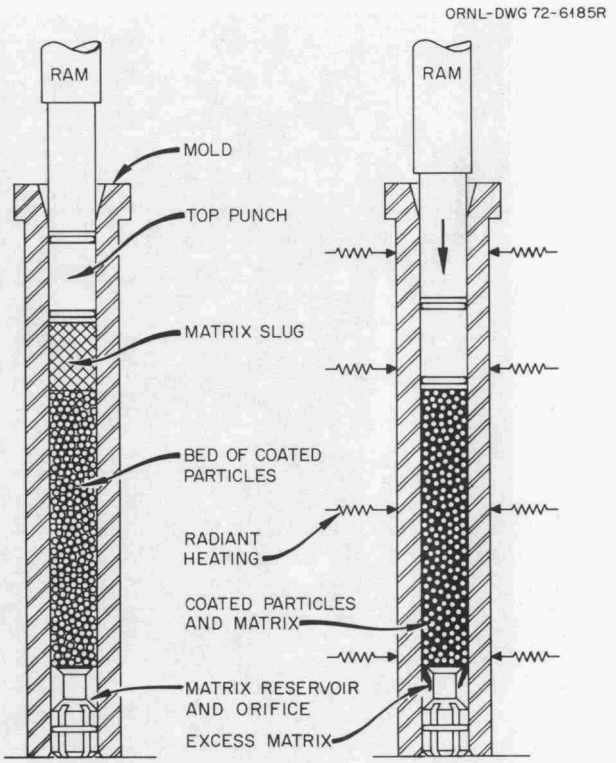

Fig. 3.14. The slug injection technique for molding HTGR fuel rods.

The automatic fuel rod machine, shown in Fig. 3.15 and illustrated graphically in Fig. 3.16, employs a 24-station index table which indexes the fuel rod molds through the various operational steps required to produce a green fuel rod. The molds are simple hardened steel cylinders having polished bores sized to produce the green fuel rod in the desired diameter.

A mold is first cleaned and lubricated with a thin film of release agent to prevent sticking when a completed fuel rod is to be ejected. This operation is accomplished by a rotating nylon bristle brush traversing vertically within the mold while lubricant is sprayed into the top of the mold. No cleaning solvent is required.

The next operations, in order, as the molds progress around the table are insertion of the bottom punch, blending and dispensing of the fuel particles into the mold, insertion of a matrix slug, and insertion of the top punch. The three insertion operations are performed by conventional vibratory parts feeders commonly used in commercial automatic assembly equipment. Each parts feeder is equipped with a gravity feed

Fig. 3.15. Photograph of the laboratory automatic fuel rod machine.

ORNL-DWG 71-9836R1

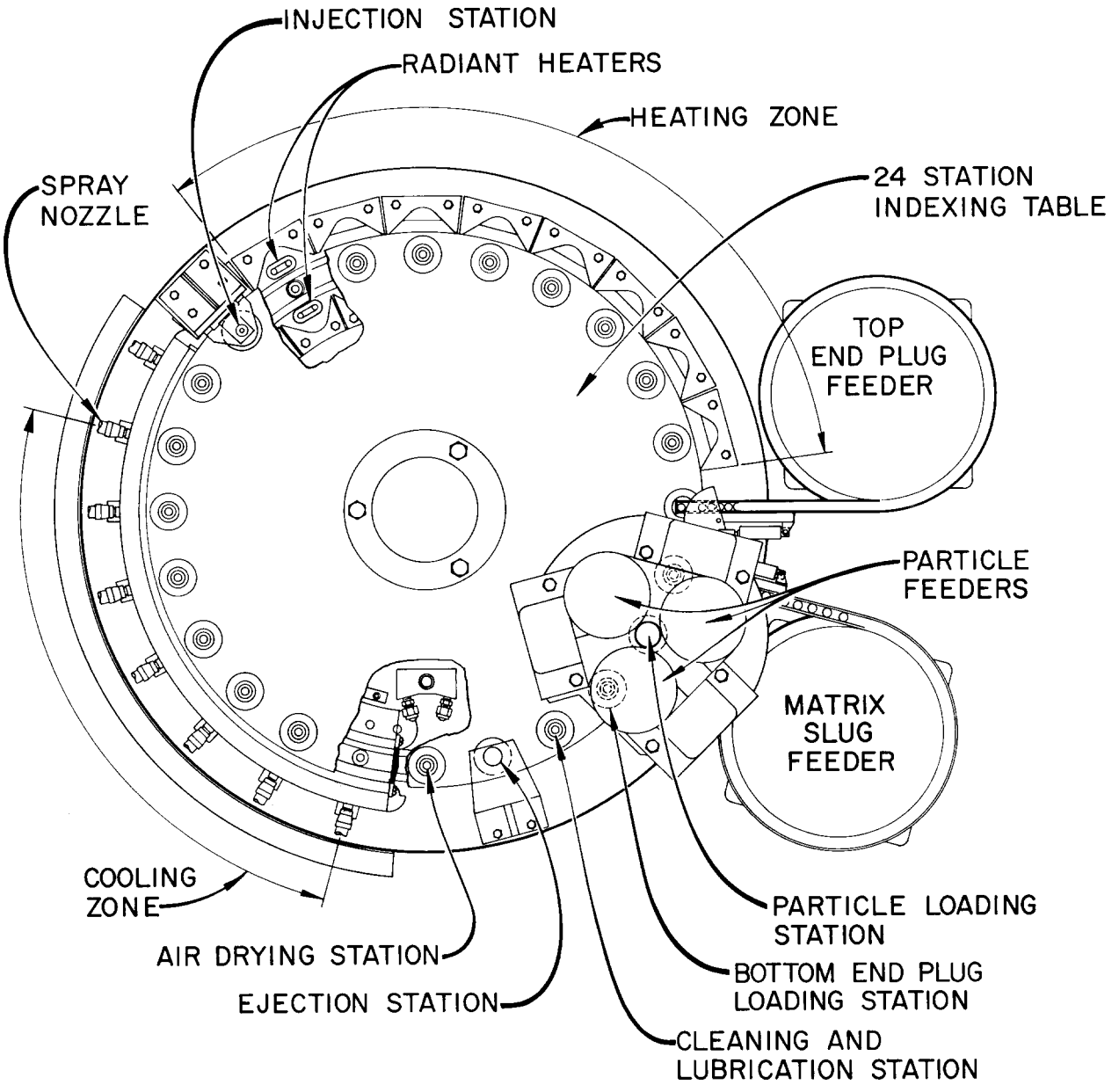

Fig. 3.16. Schematic of the laboratory automatic fuel rod machine.

tube leading from a vibratorily energized bowl that delivers parts to a shuttle device. This shuttle device positions the part over the mold where a placement ram forces the part into the mold. Each placement ram is equipped with a linear displacement indicator to indicate the low position of the ram stroke. This serves as a check to ensure the correct total quantity of parts and that fuel particles have been placed in the mold.

At present, there is no fuel particle blender on the machine, but equipment to perform this function is being designed for future evaluation and installation. To automatically dispense particles, there is a single hopper provided with two pinch valves in the line below. Volumetric measurements are made by closing the bottom pinch valve and opening the top pinch valve, allowing fuel particles to fill the measured volume

between the valves. Once a fuel rod mold is positioned and the filling tube engaged, the bottom pinch valve is opened, allowing the particles that were trapped between the two pinch valves to flow into the mold. The top pinch valve is closed during this operation to prevent additional particles from flowing from the hopper. The fill tube is disengaged from the mold, and the table is ready to be indexed.

Molds which have indexed through the four loading stations progress into a heating zone that consists of six stations equipped with infrared radiant heaters which heat the molds to approximately 180°C. The heating stations are equipped with thermocouples that contact the molds to indicate their temperature at each station and provide appropriate information to the heater control system.

The properly heated mold is indexed to the injection station. A pneumatic ram is energized which forces the molten matrix through the particle bed. The top punch continues downward until it contacts the top of the particle bed. Excess matrix accumulates in the annular groove in the bottom punch. The pressure, which is limited to 1000 to 1500 psi to prevent the breaking of particles, is maintained for a preset time controlled by an adjustable timer in the control system. This operation normally controls the cycle time of the entire machine.

The mold is indexed through four cooling stations to reduce the temperature of the mold and solidify the matrix. Each cooling station has a water spray nozzle directed at the mold at that station. After cooling, the mold is indexed to a station with air jets directed at the mold to remove excess water.

Finally, at the ejection station a ram forces the top and bottom punches and the fuel rod from the mold into a separator located beneath the base ring of the machine. The function of the separator is to separate the top and bottom punches from the fuel rod and deliver each part to an appropriate container. The separator also removes the excess matrix from the bottom punch. After the ejection cycle is complete, the mold is indexed to the cleaning and lubrication station for the start of another cycle to produce a fuel rod. The top and bottom punches are reusable and need only minimal cleaning and lubrication before being placed back in their respective parts feeders.

The entire machine is controlled by a series circuit and an adjustable timer. The series circuit prevents the table from indexing until the operations at each station have been completed and the rams have returned to their home positions. The adjustable timer is set so that the cycle time is slightly longer than is required for the longest operation, which is normally the injection of matrix into the particle bed. Although the injection time varies for different particle systems, filler types, and filler contents, it is typically about 20 sec.

We have made several thousand fuel rods on this machine, although many of them were made in small batches while we were checking out and modifying individual components of the machine. The machine is now completely operational, and we will soon perform sustained operating runs to obtain data on component failure rate and product acceptance level.

Concurrently with the design of the laboratory fuel rod machine, several investigations were conducted to obtain data required in its design. For example, it was necessary to know how many heater stations would be required to heat the mold to about 180°C and allow the particle bed to equilibrate before the mold reached the injection station.

We evaluated several techniques for heating the mold, including infrared radiant heaters, clamp-on heated platens, and induction. Heating curves for these techniques are shown in Fig. 3.17. These curves show the bed temperature as a function of elapsed time. The bed temperature was measured by a thermocouple located in the center of a 0.490-in.-diam, 2-in.-long bed of particles. The first two curves illustrate the time required to heat the mold with infrared radiant strip heaters. With a 1-kW infrared heater and with a heated platen operating at 165°C, about 110 sec is required to reach 160°C.

By operating the heated platen at 185°C, the time required to reach 160°C is reduced to about 60 sec. The fastest heating rate we obtained was with a 10-kc, 5-kW induction unit. With a power application of 4 sec duration, the particle bed was heated to 160°C in about 30 sec.

Infrared radiant heaters were selected for use on the laboratory fuel rod machine because their use simplified its design. Our tests indicated that with a cycle time of 15 to 20 sec, six preheat stations would be sufficient to heat the mold to the injection temperature. It turned out that the laboratory fuel rod machine can be operated with cycle times of about 10 sec before mold heating becomes the rate-limiting step.

We also conducted a series of experiments to determine the effect of temperature, pressure, particle size, pitch type, and filler type and amount on the intrusion rate of matrix into a bed of particles. In the first set of experiments we determined the effect of temperature and pressure on the intrusion rate of matrix containing 28.5 wt % Asbury 6353 natural flake graphite in

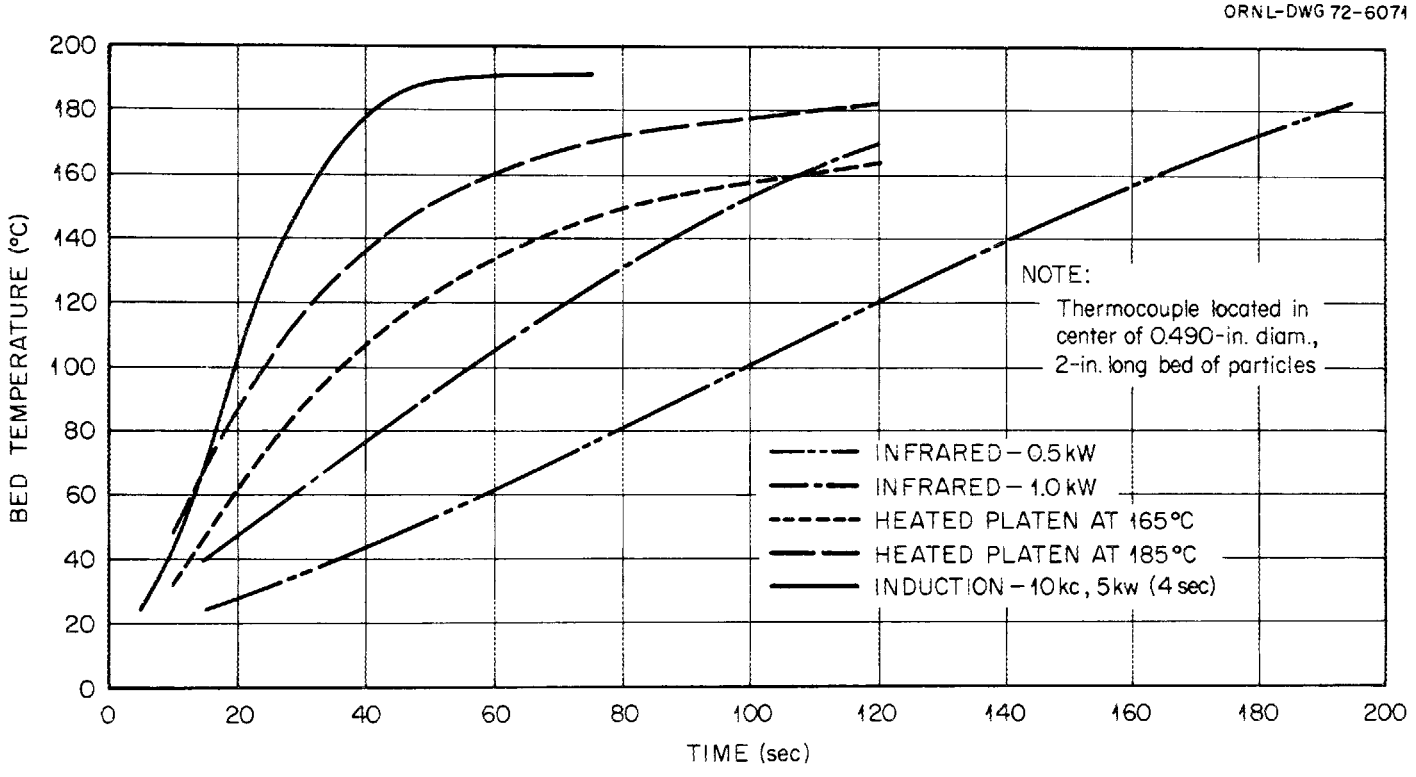

Fig. 3.17. Mold heating rates for various methods of heating.

Ashland A240 petroleum pitch into a bed of 595- to 707-μm particles. A statistically designed experiment was used to investigate three levels of temperature (160, 175, and 190°C) and five levels of pressure ranging from 1000 to 2000 psi. A multiple linear regression performed on the data from these experiments yielded the following empirical relationship between length L (in.) of particle bed intruded, time t (sec), pressure P (psi), and temperature T (°C):

$$L = -8.8758 + 0.0005114P + 0.048359T + 0.8147 \log t \ .$$

This equation had a correlation coefficient R^2 of 0.92.

The effect of temperature and pressure on the intrusion rate of this matrix is shown in Fig. 3.18. It should be noted that the intrusion rate, which is the slope of the curves, decreases as the rod length increases. Thus it will be necessary in selecting the optimum rod length to make a tradeoff between the number of rods required and the unit production rate.

In another set of experiments the effect of particle size on the intrusion rate was determined. The matrix described above was injected at 165°C and 1000 psi into particle beds containing particles of 595 to 707 and 420 to 500 μm. As shown in Fig. 3.19, much longer intrusion times are required for the smaller particles.

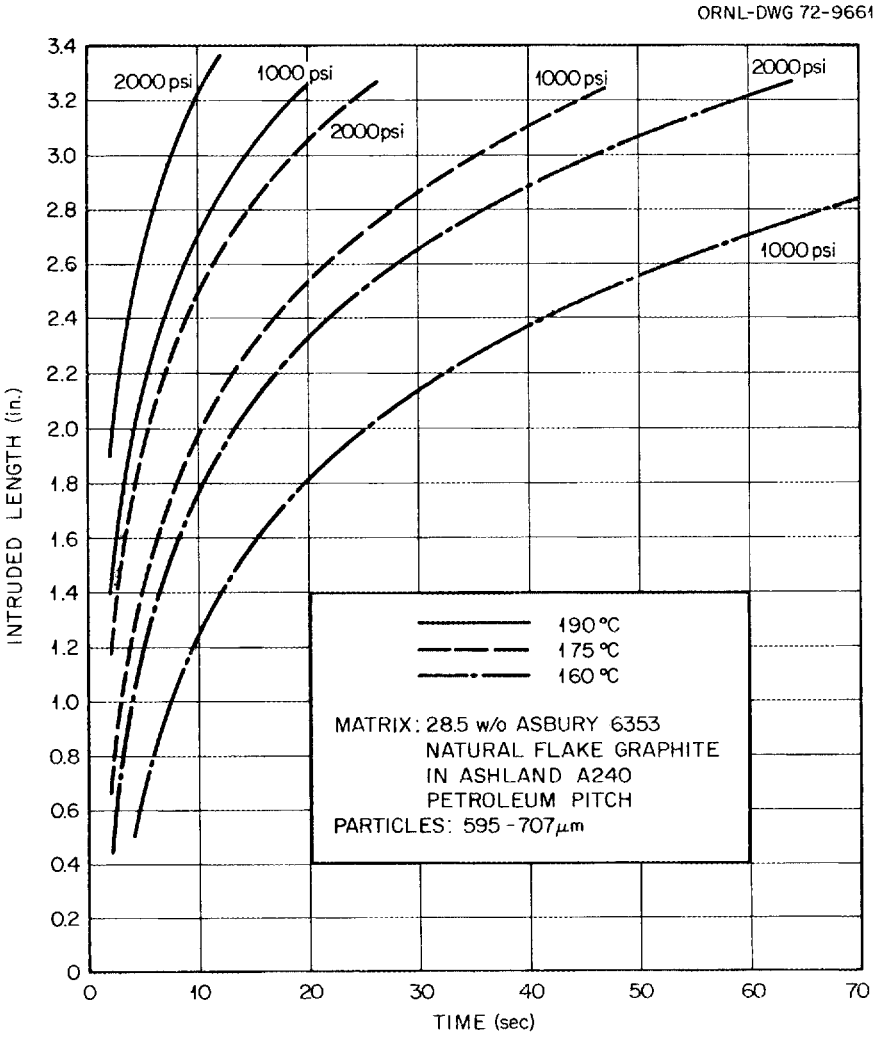

Fig. 3.18. Effect of temperature and pressure on the matrix intrusion rate.

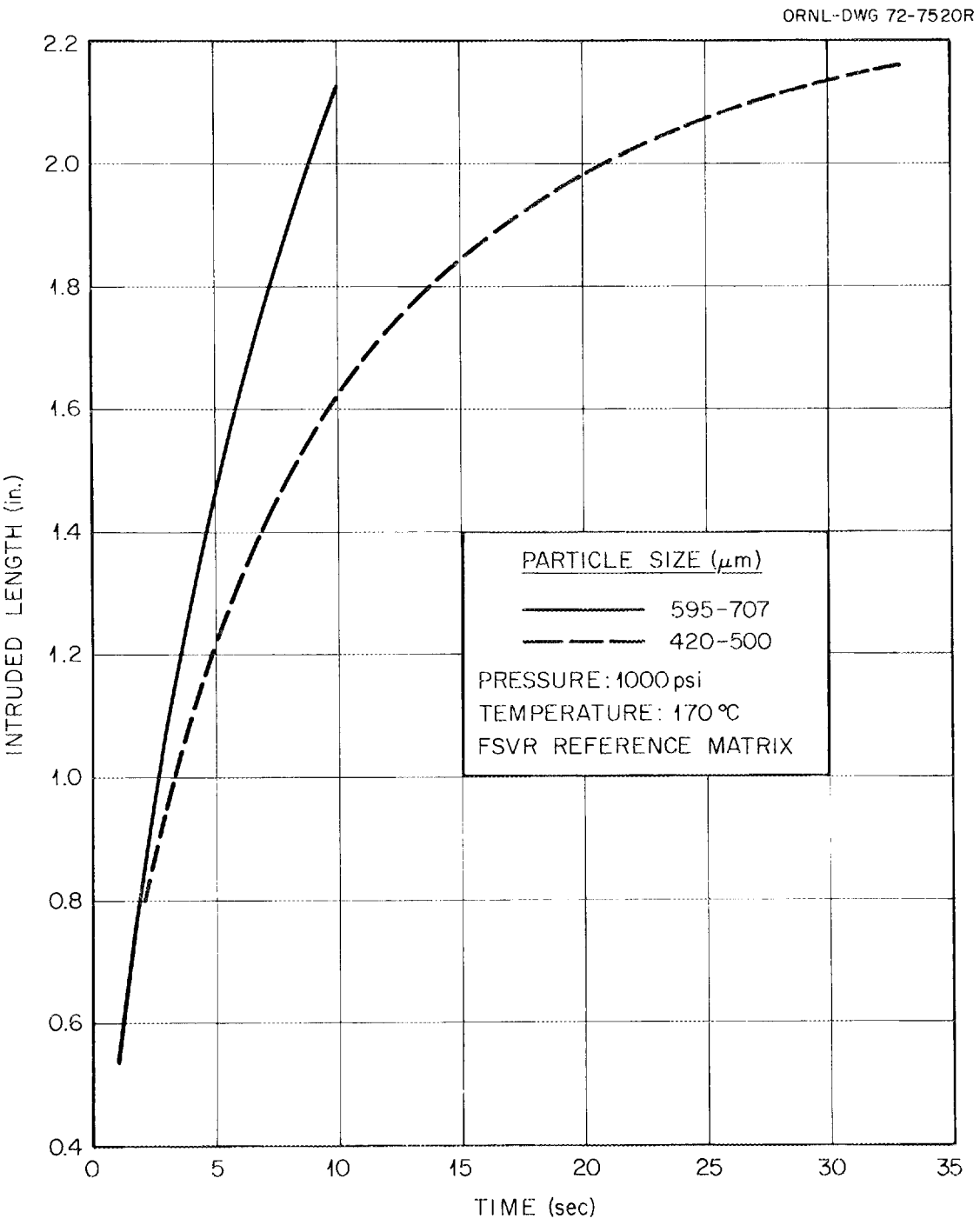

Fig. 3.19. Effect of particle size on matrix intrusion rate.

We found no significant difference between the intrusion rate of matrices made with Allied 15 V coal tar pitch and Ashland A240 petroleum pitch. Similar intrusion rate experiments were performed with matrix made with the filler materials currently considered to be the leading candidates for use in the 1100-MW(e) HTGRs. One of these is an isotropic graphite (GLC-1089) and the other a gilsonite material (RC4). These experiments indicated that with filler contents of 38 to 40 wt %, a 2-in.-long rod can be intruded in 10 to 30 sec, depending on the particle system ultimately selected.

3.2.3 Carbonization and Annealing

After the fuel rod is molded, it must be heated to 700 to 1000°C to carbonize the pitch and then to 1800°C to remove residual volatiles and stabilize the dimensions of the rod. The rod must be supported during carbonization to prevent dimensional distortion, since the pitch melts then decomposes. In the past, rods have been supported during carbonization by packing them in graphite or Al_2O_3 powder.

We installed a carbonization furnace which provides a capacity of about 1000 rods per week. Using the established technique of packing the rods vertically in Al_2O_3 powder, we carbonized several thousand fuel rods for use in the whole-block burner tests described in Sect. 1.4 of this report. After annealing at 1800°C the rods were within dimensional tolerances.

Packing the rods in Al_2O_3 powder would be very difficult to accomplish remotely; therefore, we intend to load the green fuel rods directly into the graphite fuel element and carbonize and anneal them in the graphite block. Laboratory-scale experiments have been performed to establish the feasibility of in-block carbonization, and a few rods carbonized in graphite tubes to simulate in-block carbonization were included in the HRB-4 and HRB-5 irradiation tests described in Sect. 6.1. The main problem with in-block carbonization appears to be the tendency of the rods to bond to the graphite block. Experiments are under way to determine carbonization conditions which will minimize this bonding.

3.2.4 Fuel Stick Inspection and Assay

The fuel stick characterization will consist in inspection to determine the filler distribution, the fission gas release, the fuel distribution, the variation in fuel content from stick to stick, and the amount of fuel in a given stick or a batch of sticks.

For the characterization of fuel sticks, we have techniques for determining the filler distribution and the particle distribution. The axial distribution of graphite filler in slug-injected fuel sticks is determined by breaking the green fuel sticks into three approximately equal sections, dissolving the matrix in pyridine, and separating the insoluble graphite. The axial distribution of the fissile and fertile particles is determined by gamma scanning the fuel stick. The sticks are rotated at 4 rpm during counting to minimize the effect of the radial distribution. The data are collected on magnetic tapes, and a computer program is used to separate the gamma peaks. The equipment being used has the capability of looking at a very thin section (~0.020 in.) of the fuel stick. This equipment is being used to evaluate the blending.

The combined stick contamination and fuel particle breakage is determined by fission gas released. The fission gas release is determined by irradiating the sticks in a thermal-neutron flux in the ORR to approximately 10^{14} fissions, heating the sample to 1100°C and collecting the gases, and determining the amount of ^{85m}Kr in the gas sample by gamma spectrometry. The production of ^{85m}Kr is calculated using the fission yield for ^{85m}Kr and the burnup as determined by certain fission products (^{132}Te, ^{131}I, and ^{140}Ba). This technique has been used on several plutonium-bearing samples,[12] and we plan to use it on samples for irradiation tests.

The major problem in characterizing fuel sticks is determining the amount of fissionable material in each stick to the precision needed for this program. We have a cooperative program with the A-1 Safeguard Group at Los Alamos Scientific Laboratory, which is performing scoping experiments on HTGR fuel sticks. This work will be completed in the spring of 1973. After results from these experiments are evaluated, we will procure one or two assaying systems which will be used for development work. A number of variables are to be investigated in order to determine their influence on the responses; among these are particle size, particle composition, hydrogen content of sticks, dimensions of stick, etc. We hope to have a development system operating by the end of 1973 or spring of 1974. The most promising technique at this time is a multispectra neutron irradiation. With this technique we will induce fission in the material using different energy neutrons and count the prompt or delayed fission neutrons.

12. J. D. Sease et al., "Fabrication of Plutonium Fuels for HTGR," paper presented at ANS meeting in Las Vegas, Nev., June 19–22, 1972.

4. HTGR Fuel Recycle Pilot-Plant Studies

J. W. Anderson J. D. Sease
J. W. Snider

Engineering-scale development of processes and equipment in the HTGR Fuel Recycle Development Program will culminate in the demonstration of recycle technology in pilot-plant operations. These operations will be carried out in two pilot plants: the Reprocessing Pilot Plant, a combination of the Head-End and Acid Thorex plants discussed last year, and the Refabrication Pilot Plant. This chapter reports the activities associated with the planning and design of these pilot plants with regard to both facilities and equipment. During the past year, ORNL has been involved in the planning of these pilot plants and with some conceptual design studies for equipment and systems for pilot-plant application.

4.1 REPROCESSING PILOT-PLANT DEMONSTRATION

J. W. Anderson

Early in this reporting period, a decision was made to perform the hot reprocessing demonstration task of the program at the Idaho Chemical Processing Plant (ICPP). In support of the AEC's evaluation of sites for the Reprocessing Pilot Plant, ORNL was asked to work with Allied Chemical Corp. (ACC) and Gulf General Atomic in assessing the capabilities of existing ICPP facilities for this work. During December, January, and February, extensive cooperative studies were carried out by ORNL and ACC in preparing equipment layouts, equipment descriptions, and cost estimates for the pilot-plant installation.

4.1.1 Evaluation of Idaho Facilities

J. W. Snider

The HTGR fuel processing demonstration at the ICPP is currently being planned to demonstrate a processing rate of 12 spent Fort St. Vrain Reactor (FSVR) fuel elements per day. The spent FSVR fuel elements will be stored in the Irradiated Fuel Storage Facility until the HTGR Fuel Processing Demonstration Pilot Plant is operable. The Irradiated Fuel Storage Facility, which will have storage capacity for more than 2500 spent FSVR fuel elements (four elements per storage can), is under construction and is scheduled to be ready to receive spent FSVR fuel elements by April 1974.

The current best estimate of the schedule for the demonstration is 1979. The estimate assumes a three-year time interval between initial funding and operation.[1]

The head-end flowsheet for the demonstration is the burn-crush-leach process. The solvent extraction process for the demonstration will be a 5% TBP flowsheet to separate uranium from the fission products and the thorium. Since the fertile particles will be processed, it is not anticipated that thorium recovery will be demonstrated. The uranium from the fertile particles

1. A. P. Roeh, personal communication, Allied Chemical Corp., Idaho Falls, Idaho.

will be further purified by a hexone flowsheet prior to conversion to UO_3 for shipment. The fissile particles will be stored in the Irradiated Fuel Storage Facility for processing after the demonstration has been completed.

4.1.2 Off-Gas Treatment and Decontamination System Design Criteria

J. W. Snider

The first step in the proposed method for reprocessing HTGR spent fuel elements consists, in part, in burning the graphite fuel elements in oxygen. This step is unprecedented in nuclear fuel reprocessing in that the fuel elements are prepared for dissolution by combustion. The large quantity of carbon present in the fuel elements is converted into carbon dioxide during this combustion step. This carbon dioxide, which is formed in intimate contact with the spent fuel, will be contaminated with fission products and actinide elements.

The objective of the off-gas treatment process for the HTGR fuel processing demonstration is to demonstrate a method of removing the fission products and actinides from the combustion off-gas stream to a level as low as practicable.

The contaminants of the combustion off-gas streams can be classified as (1) contaminants in particulate form, (2) contaminants which exist in the vapor phase at the high temperatures of combustion but exist in the solid phase at ambient temperatures, and (3) contaminants which exist in the gaseous phase at both the combustion and ambient temperatures.

The current flowsheet utilizes high-efficiency particulate aerosol (HEPA) filters to remove particulates from the off-gas stream; a combination of HEPA filters, solid absorbers, and liquid scrubbers to remove the contaminants of the second category [i.e., ^{3}H (as HTO), I, Ru (as RuO_4), etc.]; and the KALC process to remove the contaminants of the third category (e.g., Kr). An attempt will be made to define the technical limits on the achievement of "as low as practicable" for the various radioactive nuclides which might be in the combustion off-gas stream.

The radioactive nuclides which will require the largest overall process decontamination factors in particulate form are ^{238}Pu, ^{244}Cm, and ^{144}Ce. Of the radioactive nuclides in the second category, the ones requiring the largest overall process decontamination factors are ^{106}Ru, ^{103}Ru, ^{131}I, and ^{129}I. Technology which has been developed for other reprocessing fuel cycles, but appears to be suitable for the HTGR reprocessing, indicates that decontamination factors greater than 10^4 for iodine and greater than 50 for tritium can be obtained. Calculations indicate that decontamination factors greater than 100 for krypton removal by the KALC process are feasible.

4.2 REFABRICATION PILOT-PLANT DEMONSTRATION

J. W. Anderson

The hot refabrication demonstration task of the program will be performed in facilities at ORNL. Conceptual design studies for the Refabrication Pilot Plant to be installed in the TURF, Building 7930, were continued at a low level through the year. These studies focused primarily on overall plant layout and capability studies, with a fair amount of work directed toward establishing criticality parameters as criteria for equipment design.

4.2.1 Feasibility Study for Increasing Capacity in the Refabrication Pilot Plant

J. W. Anderson

One approach that has been considered for providing fuel recycle capability to the developing HTGR economy is to increase the capacity of the TURF pilot plant to provide production capability. This, of course, would require some cooperative arrangement between the AEC and private industry. This option would allow some flexibility in meeting the recycle needs of the economy if the growth rate is not sufficient to support a large-scale commercial recycle plant when it becomes economically advantageous to recycle fuel.

During this report period, a study was completed to determine the maximum production capacity of the TURF Refabrication Pilot Plant in terms of heavy-metal product per day. The current planned pilot plant is rated at 25 kg/day, or about 2.5 product elements per day. Due to space limitations, for process support materials, element storage and loading, and space requirements for analytical and inspection facilities, the 25-kg/day rate cannot be sustained on a continuous basis.

The study indicated that the production capacity of the TURF could be increased to about 100 kg of heavy metal per day (10 elements/day) for sustained operation (on-line efficiency of 80%). This would support an HTGR economy in excess of 9000 MW(e).

Conceptual plant layouts were completed for both the 25- and 100-kg/day plants. Cost estimates for

design, procurement, installation, unit testing, systems testing, and plant operation were prepared for the 25-kg/day pilot plant and for the incremental cost increases for design, procurement, installation, unit testing, system testing, and plant operation for the proposed 100-kg/day production plant. A schedule was also prepared for both proposals.

4.2.2 Design of Processing Equipment

W. W. Davis J. D. Sease

Process flowsheets were prepared for five of the six major processing systems to be located in the pilot plant: (1) sol preparation, (2) microsphere preparation, (3) microsphere coating, (4) fuel stick fabrication, and (5) fuel element assembly. Each system was divided into subsystems of related operations, and equipment and system diagrams were prepared for each system. These diagrams outline the equipment components required to perform the functions presented in the process flowsheets.

Scoping studies of each item of equipment required in the microsphere coating system and part of the equipment required in the fuel stick fabrication system were performed to assist in preparing conceptual designs of the components and to outline the need for development efforts. These items include storage hoppers, valves, bulk weighers, batch weighers, feeders, classifiers, shape separators, samplers, batch blenders, fuel particle dispensers, parts feeders, a fuel stick molding machine, coating furnace, coating furnace exhaust system, and fuel stick carbonization and annealing furnace.

4.2.3 Design Criteria to Assure Critically Safe Equipment

C. F. Sanders

A study was initiated to determine the critical dimensions of equipment used for refabrication of HTGR fuels. The criticality of homogeneous mixtures of $^{233}UO_2$ and C and of $(^{232}Th,^{233}U)O_2$ and C was explored by calculation. The critical dimensions of bare and water-reflected infinite cylinders were determined by the ANISN code using the Hansen-Roach neutron cross-sections set. The basic calculated data were used to establish the characteristics of the mixtures and the influence on criticality of the C/U and H/U ratios and the density of the ^{233}U in the region of interest to the program. The specific geometries of furnaces were examined by the KENO Monte Carlo code to estimate changes in the neutron multiplication factor attributable to container materials, poisons, and finite geometry.

In the investigation of mixtures, we examined three particles, $^{233}UO_2$, $(^{232}Th,^{233}U)O_2$, and $(4^{232}Th,^{233}U)O_2$. We assumed that the uranium was 100% ^{233}U and that the mixed oxide particles were Biso coated and the pure uranium particles were Triso coated. The particle designs are shown in Table 4.1, and the results of the investigations are summarized in Tables 4.2 and 4.3.

The maximum H/U ratios in Table 4.3 were calculated assuming that the particle beds were flooded with water at 0°C and that a 60 vol % packing occurred in the bed. These results can be used to determine the maximum size of hoppers, etc., and also to indicate areas which should be investigated in more detail.

The second part of this study consisted in calculating the k_{eff} for specific pieces of equipment (e.g., furnaces, hoppers) using the KENO Monte Carlo code.

One of the major problems in determining a safe design in reference to criticality is determining the accident which will represent the worst case. We have considered several accidents, including a broken coating chamber, flooding of the interior of the furnace with water, and a water leak directly into the inlet of the coating chamber. The general calculations indicated that the critical mass decreases sharply with increasing H/U ratio and at an H/U ratio of a few hundred the critical mass is minimum.[2] Therefore, the worst case is when an H/U ratio of a few hundred is present. Since a high H/U ratio could only exist under accident conditions, we evaluated the criticality under a number of accident conditions. In initial studies of coating accidents, the worst case seems to be one where the coating chamber is broken, all particles are dumped into the lower furnace section, and this section is flooded with water up to a height 6 in. above the particles.

The results of these calculations for bare $^{233}UO_2$ particles are given in Table 4.4. These data show that the 5-, 9-, and 11-in.-diam furnaces are safe with bare particles of $^{233}UO_2$. The other accident cases gave us less severe conditions. The case of a water leak directly into the inlet of the coating chamber was investigated. If the water remains as a liquid, it will require greater than 20 gpm of water to fluidize the bed, and the water inlet to the gas distribution could be easily limited to

2. J. T. Thomas, *Calculated Criticality of Water Modulated Oxides of ^{233}U, ^{232}Th, and Carbon Mixtures*, Y-DR-107.

Table 4.1. Particle designs for criticality calculations

Composition	Kernel		Buffer		Inner LTI		SiC		Outer LTI	
	Diam (μm)	Density (g/cm^3)	Thickness (μm)	Density (g/cm^3)	Thickness (μm)	Density (g/cm^3)	Thickness (μm)	Density (g/cm^3)	Thickness (μm)	Density (g/cm^3)
$(4^{232}Th,^{233}U)O_2$	350	10	75	1.0					100	1.8
$(^{232}Th,^{233}U)O_2$	275	10	75	1.0					100	1.8
$^{233}UO_2$	200	10	50	1.0	20	1.8	20	3.2	30	1.8

Table 4.2. Critical dimensions of reflected spheres and infinite cylinders

H/U atom ratio	Geometry	R_{crit} (cm)	
		(1 Th, 1 $^{233}U)O_2$, 20.32-cm H_2O reflector, C/U = 11.9	(4 Th, 1 $^{233}U)O_2$, 20.32-cm reflector C/U = 21.16
0	Sphere	18.0668	29.23
0	Cylinder	11.4926	19.65
1	Sphere	17.4345	28.54
1	Cylinder	11.0550	19.12
2	Sphere	16.9069	24.47
2	Cylinder	10.6965	18.34
3	Sphere	16.3408	26.26
3	Cylinder	10.3113	17.48
10	Sphere	13.8371	19.92
10	Cylinder	8.6427	12.99
30	Sphere	11.7104	14.99
30	Cylinder	7.2869	9.62
100	Sphere	11.0595	12.76
100	Cylinder	6.9934	8.21
300	Sphere	12.4893	13.73
300	Cylinder	8.1952	9.10
500	Sphere	14.3659	15.52
500	Cylinder	9.6596	10.51
600	Sphere	15.3920	16.56
600	Cylinder	10.4515	11.32

approximately 1.5 to 2 gpm by an orifice in the line. If the water is evaporated, the steam could fluidize the bed, but even with a 20 vol % packing of the particles the H/U will be lower than in a 60 vol % packed bed with liquid water.

The KENO code was used to refine the calculation for the 5-, 9-, and 11-in.-diam coating furnaces under accident conditions. The results of these calculations are listed in Table 4.5. In these calculations we used two modes for terminating the run: when $k_{eff} \simeq 1$ and when the volume of material exceeded the volume of the coating chamber. For the 5-in.-diam furnace, we went to the maximum volume in each case; the maximum k_{eff} was calculated to be 0.85. The 5-in.-diam furnace design is critically safe for coating any of the reference particles. For the 9-in.-diam furnace, we went to the maximum volume for the 4/1 and 1/1 particles, and the critical masses for the UO_2 were

Table 4.3. Critical radius of infinite cylinder and critical masses of sphere

Water-moderated 60 vol % particle packing

Kernel composition	Particle condition	C/U ratio	Maximum H/U ratio	Critical radius of infinite cylinder (cm)	Critical mass in spherical geometry (kg ^{233}U)
(4Th,^{233}U)O_2	Bare	0	9.8	10	15
(4Th,^{233}U)O_2	Coated	122	78.5	12	3.5
(Th,^{233}U)O_2	Bare	0	3.9	6.8	16
(Th,^{233}U)O_2	Coated	76	46.1	9.5	4
$^{233}UO_2$	Bare	0	2.0	4.8	12
$^{233}UO_2$	Coated	100	40.8	10	4

Table 4.4. Results of criticality calculations for the accident case of 5-, 9-, and 11-in.-diam coating furnaces which have $^{233}UO_2$ particles

Diameter (in.)	Th/U ratio	H/U ratio	^{233}U density (g/cm^3)	^{233}U mass (kg)	k_{eff}[a]	Batch weight[b] (kg)
5	0/1	1.84	5.61	19.07	0.830	21.67
5	1/1	3.68	2.808	9.55	0.480	21.70
5	4/1	9.22	1.123	3.82	0.315	21.70
9	0/1	1.84	5.61	38.82	0.995	44.11
9	1/1	3.68	2.808	30.74	0.965	69.89
9	4/1	9.22	1.123	12.30	0.746	69.89
11	0/1	1.84	5.61	49.76	0.998	56.54
11	1/1	3.68	2.808	34.54	0.917	78.5
11	4/1	9.22	1.123	18.36	0.841	104.3

[a]For the TURF we will work with a maximum k_{eff} of 0.90.
[b]Based on all the uranium being ^{233}U and heavy metal = 88% of oxides.

Table 4.5. Results of criticality calculation for coating furnaces using the KENO code[a]

Furnace diam (in.)	Th/U ratio	Bare				Buffer coated				Fully coated			
		Weight (kg)		Volume (liters)	k_{eff}	Weight (kg)		Volume (liters)	k_{eff}	Weight (kg)		Volume (liters)	k_{eff}
		^{233}U	Particle[b]			^{233}U	Particle[b]			^{233}U	Particle[b]		
5	4/1	3.82	21.72	3.4	0.315								
	1/1	9.55	21.72	3.4	0.480								
	0/1	19.07	21.69	3.4	0.830					2.86	8.17	3.4	0.724
9	4/1	12.30	69.95	10.95	0.746	4.78	32.38	13.18	0.680	1.74	20.83	13.18	0.610
	1/1	30.75	69.95	10.95	0.965	21.42	61.84	13.18	0.747	6.74	41.68	13.18	0.717
	0/1	38.82	44.15	6.92	0.995					4.61	13.16	5.48	0.911
11	4/1	18.36	104.41	16.35	0.841	6.45	43.69	17.8	0.728	2.35	28.13	17.8	0.677
	1/1	40.78	92.76	14.52	0.999	28.93	83.52	17.8	0.813	9.10	56.27	17.8	0.764
	0/1	49.76	56.59	8.87	0.998					6.89	19.68	8.19	1.019

[a]Accident conditions: broken coating chamber and flooded with water, assuming 60 vol % packing for particles.
[b]Uranium 100% ^{233}U.

calculated to be 44.15 kg for bare particles and 13.16 kg for fully coated particles. Therefore, the 9-in.-diam furnace is critically safe for the $(4Th,U)O_2$ and $(Th,U)O_2$ reference particles. If the 9-in.-diam furnace is used for coating UO_2 particles, the batch size must be less than 13.16 kg. The calculation for the 11-in.-diam furnace showed that it is critically safe for the 4/1 reference particles and is mass limited for the 1/1 and 0/1 reference particles. In an 11-in.-diam furnace with $(Th,U)O_2$ particles, the critical masses are 92.76 kg for bare particles and 56.27 kg for fully coated particles. With the (0 $Th,U)O_2$ particles, the critical masses are 56.59 kg for bare particles and 19.68 kg for fully coated particles. Again we are critically safe with the 4/1 and the 1/1 particles if the mass is below 56.67 kg in the 11-in.-diam furnace. With the UO_2 particles the k_{eff} is greater than 1 at a mass of 19.7 kg; therefore, to use an 11-in.-diam furnace for coating UO_2, the present furnace design will have to be modified.

Since the hydrogen in the water is causing the small critical mass, one way of solving this problem is to remove the water from the system. This could be done by replacing the cooling water with another coolant such as one of the freons.

5. Studies and Evaluation of Commercial HTGR Fuel Recycle Plants

J. W. Anderson A. L. Lotts

To adequately direct the fuel recycle development program, it is necessary to understand the economic and technical problems and considerations of a commercial fuel recycle plant. The objective of this project is to make design and economic studies of commercial-size plants so as to provide input to the development efforts. Present emphasis is on the technical and economic evaluation of various fuel recycle processing options. For each of the major operations in such a plant, the advantages, disadvantages, and economics of the various combinations of processes and materials have been studied and the most promising combinations selected.

5.1 EVALUATION OF COMMERCIAL HTGR FUEL RECYCLE PROCESSES

J. W. Anderson

These studies are concerned with the developments in fuel design, performance, reprocessing, and refabrication and their impact on the timing, operability, maintainability, and economics of a commercial recycle plant.

The objective of these evaluations is to help guide development work and to provide the basis for assigning priority for the development effort required to establish the base technology for commercial recycle operations. The project is also intended to yield methods of analysis that can be used by others for assessing the effect of alternative or modified processes on fuel cycle cost. The goals to be achieved in pursuit of these objectives are as follows:

1. to identify the various processes for performing fuel recycle operations that are judged to be technically feasible and that have some potential for application to commercial fuel recycle operations,
2. to assess the technical feasibility of each process and to verify that it is, in fact, feasible and of interest to commercial recycle operations,
3. to define the unit cost ($/kg of heavy-metal product) that may realistically be attributed to each process,
4. to define the integrated unit cost ($/kg of heavy-metal product) that may realistically be attributed to major areas of fuel recycle operations, such as head-end reprocessing, fuel fabrication, etc.,
5. to identify the most promising (economically) set of processes, methods, or practices for commercial application,
6. to be able to assess changes in fuel cycle cost as a result of changes in processes, methods, or practices or due to selection of alternative processes, methods, or practices.

To carry out this study, several basic ground rules were set up for recycle operations. It was assumed that four basic functions would take place in an HTGR fuel recycle plant in the commercial industry: (1) spent fuel handling at the processing site (2) processing of ^{233}U and ^{235}U recycle fuels, type IM fuel (^{235}U for either

initial or makeup fueling), and thoria preparations, (3) the disposal of waste as well as the recovery of by-products, and (4) the handling and shipment of fresh fuel from the processing plant. These functions are all illustrated in Fig. 5.1.

The different processing operations envisioned for a commercial recycle plant are shown schematically in Fig. 5.2. This figure shows the major steps in reprocessing and refabricating ^{233}U recycle fuel elements, reprocessing and refabricating ^{235}U recycle fuel elements, preparation of thoria microspheres that would be used in either of the three kinds of fuel elements that would be fabricated in the plant, and the fabrication of IM fuel elements.

In general, the recycle process lines are expected to require heavy shielding and to be conducted remotely or semiremotely, while the thoria preparation and the IM fuel lines are expected to be handled unshielded and in glove-box-type facilities.

To evaluate the processing options of interest to commercial recycle operations, the following series of work tasks were planned:

1. itemize process options to be studied;
2. develop reference fuel specifications;
3. determine heavy-metal material balance for the overall plant;
4. establish the technical basis for evaluation of each process option, including process flow diagram, equipment and systems design, equipment sizing based upon throughput and criticality considerations, and equipment operation and maintenance philosophy – type of facilities required;
5. develop equipment capital cost and processing space estimate for each process option;
6. develop process operating cost for each process option;
7. determine estimate of total and unit ($/kg of heavy-metal product) costs for increments of a processing plant associated with each process (unit cost should include both capital and operating costs);
8. determine estimates of total and unit costs for various combinations of fuel and processing alternatives applied to each processing area.

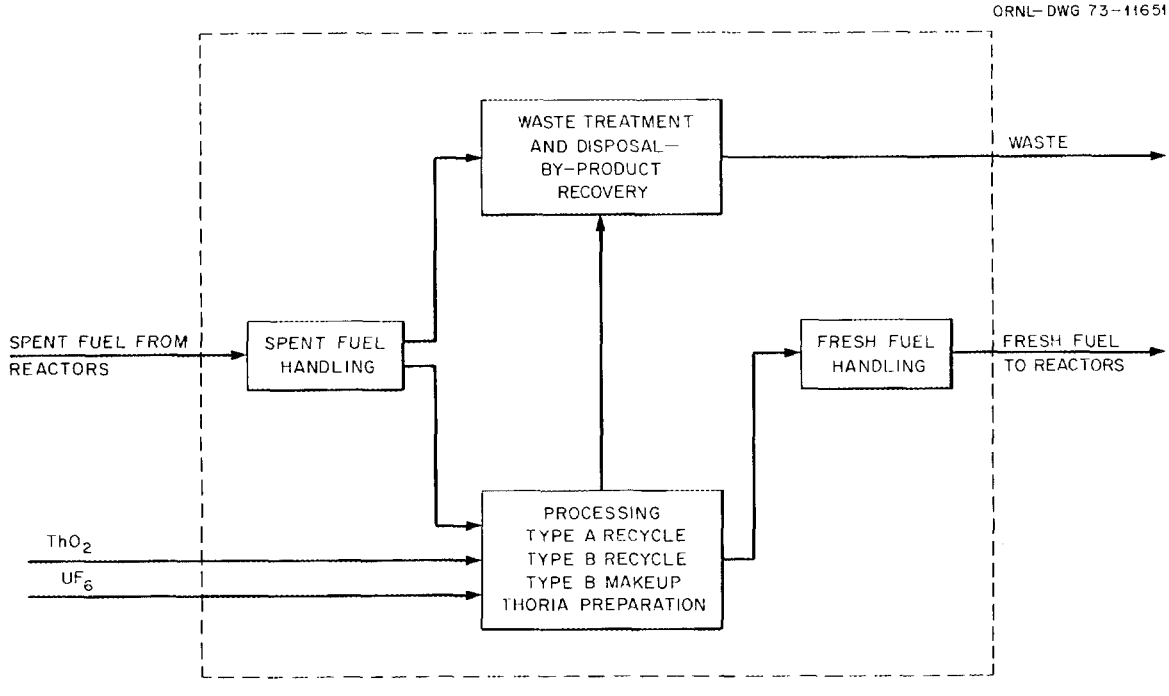

Fig. 5.1. HTGR fuel recycle plant.

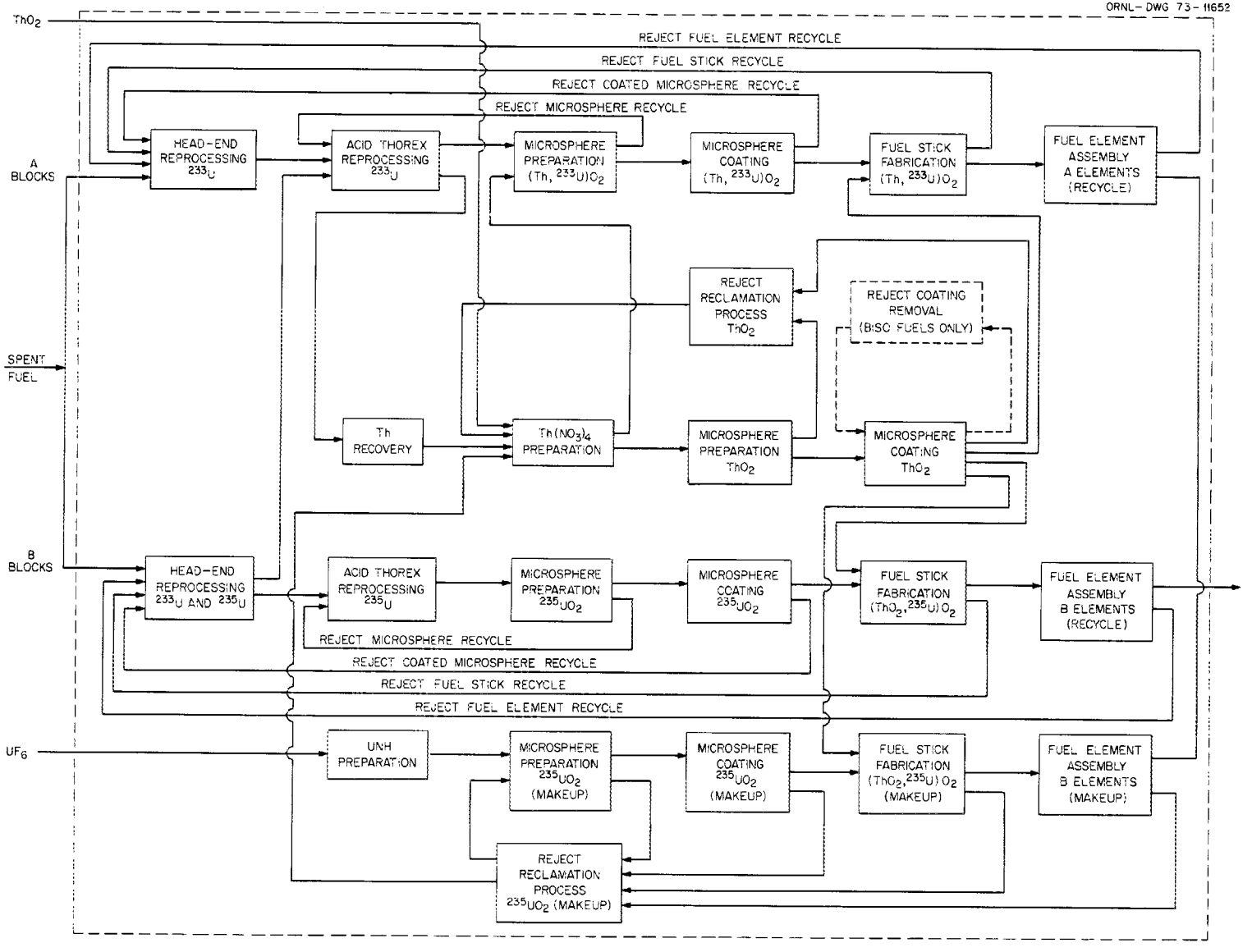

Fig. 5.2. HTGR fuel processing.

5.1.1 Processing Analysis Methods

T. W. Pickel J. W. Anderson

To perform process trade-off studies, a computer program was written to yield overall material balance data for the processing plant shown schematically in Fig. 5.2. With one of the project goals to determine relative economics between process alternatives, another program has been prepared to determine capital and operating costs. To date, only the capital cost portion of the program is in operation. The program estimates the capital cost associated with any given process as an incremental cost of the total commercial plant, as illustrated in Fig. 5.3.

Plans are to develop a third program to use the material balance data and the cost data and summarize processing costs, given a set of fuel specifications, a set of processes, and a plant production rate.

5.1.2 Conceptual Design of Plant

J. W. Snider J. W. Anderson

To economically assess the advantages and disadvantages of various combinations of processes and material or waste handling practices, it is necessary to consider the effects of process operations on plant design and space requirements as well as on plant operations. Previous conceptual plant studies by Aerojet Nuclear Corporation, Bechtel, Gulf General Atomic, and ORNL have been reviewed and the basic plant requirements identified. A design basis for commercial plant concepts was developed and is shown in Table 5.1.

A set of general criteria for a commercial recycle plant was prepared. These criteria generally describe the base-line requirements for the commercial plant design, based on a set of reference processes chosen from process alternatives previously identified. To assist in economic evaluation of process options, basic cost factors have been developed for the different kinds of direct processing areas that would be required to meet the plant criteria. In general, these included hot-cell areas, with heavy shielding (6-ft normal concrete), medium shielding (4-ft normal concrete), and light shielding (2-ft normal concrete), and alpha-contained cells (no shielding). These cost factors also reflect the operating and maintenance philosophy that would be used in the various processing areas of the plant, that is, remote maintenance, contact maintenance, or direct maintenance.

A very rough layout for the concept of a 1.5-metric ton/day plant was prepared to verify the estimating

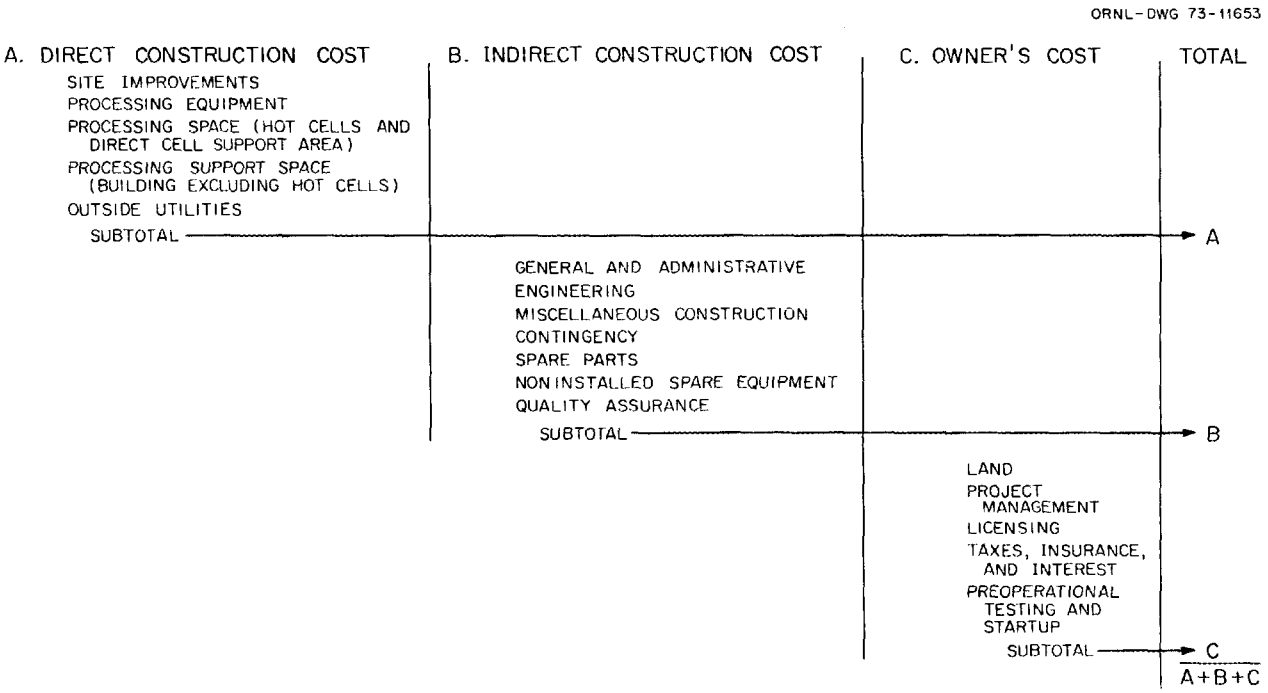

Fig. 5.3. Capital cost elements.

Table 5.1. Plant and process design basis

Item description	Value or condition
Rated capacity of plant, case I	0.5 metric ton/day (heavy metal)
Rated capacity of plant, case II	1.5 metric tons/day (heavy metal)
Rated capacity of plant, case III	3 metric tons/day (heavy metal)
Minimum cool time for spent fuel before processing	150 days
Composition of fuel for reprocessing and fabrication	Equilibrium cycle conditions
Useful life of plant	15 years
Plant operating basis	
Hours per day	24
Days per year	365
On-stream efficiency	80%
Plant design capacity, case I: rated capacity × design factor is 500 kg/day (heavy metal) × 1.25	625 kg/day
or	
23 recycle elements	25/day
25 recycle elements	3/day
IM elements	39/day
Total	67/day
Plant design capacity, case II: rated capacity × design factor is 1500 kg/day (heavy metal) × 1.25	1875 kg/day
or	
23 recycle elements	75/day
25 recycle elements	9/day
IM elements	117/day
Total	201/day
Plant design capacity, case III: rated capacity × design factor is 3000 kg/day (heavy metal) × 1.25	3750 kg/day
or	
23 recycle elements	149/day
25 recycle elements	18/day
IM elements	235/day
Total	402/day
Reactor economy serviced by case I: $\frac{\text{rated capacity/day} \times \text{operating days/year} \times \text{on-stream efficiency} \times \text{power/reactor}}{\text{heavy metal/element} \times \text{elements/reactor}}$	
$= \frac{500 \times 365 \times 0.80 \times 1100}{9.35 \times 986} =$	17,400 MW(e)
Reactor economy serviced by case II:	
$\frac{1500 \times 365 \times 0.80 \times 1100}{9.35 \times 986} =$	53,400 MW(e)
Reactor economy serviced by case III:	
$\frac{3000 \times 365 \times 0.80 \times 1100}{9.35 \times 986} =$	104,500 MW(e)
Internal recycle of material	
Reject microspheres	10%
Reject coated particles	5%
Reject fuel sticks	5%
Reject fuel elements	1%
Disposition of plant following useful life	Decommissioning, removal, land reclamation

procedures and cost factors for different kinds of space required. Early in this conceptual study of possible layouts for a commercial plant, it became apparent that a set of reference processes should be identified around which to design this plant. These were selected as follows:

Head-end reprocessing

Primary and secondary crushing for burner feed preparation
Exo followed by endo fluidized-bed burning process – all graphite
Size separation for ash handling
Alumina recycle for ash handling
Crushing and burning of Triso particles – classified ash treatment
Leaching, centrifuging, washing and drying, and solvent extraction feed preparation

Solvent extraction reprocessing

Acid Thorex solvent extraction processes

Microsphere preparation processes

Steam denitration process for ThO_2 microsphere preparation
CUSP process for UO_2 microsphere preparation, $^{235}UO_2$ IM fuel
CUSP process for UO_2 microsphere preparation, $^{235}UO_2$ 25 recycle fuel
Solex process for $(Th,U)O_2$ microsphere preparation, $(Th,^{233}U)O_2$ 4.25:1 recycle

Fuel fabrication

Biso microsphere coating process $(Th,U)O_2$ 4.25:1 ratio, 23 recycle particles, 425 μm
Triso microsphere coating process, $^{235}UO_2$ 25 recycle particles
Triso microsphere coating process, $^{235}UO_2$ IM fuel
Biso microsphere coating process, ThO_2
Fuel stick fabrication process, slug injection – thermoplastic
Fuel element assembly process, out-of-block carbonization

5.1.3 Fuel Preparation

J. W. Snider J. W. Anderson

A comparative economic assessment is being made of methods for preparing HTGR fuel kernels. The study includes several types of HTGR fuel kernels, including fresh uranium and thorium plus recycled ^{233}U, thorium, and ^{235}U. The study to date has been limited to processes for ^{233}U.

The Solex process for oxide fuel kernels with a thorium-to-uranium ratio of 4.25 and the CUSP process for urania fuel kernels have been evaluated. The evaluation included process equipment and total increment of plant capital cost. The costs associated with waste handling and with operating will be evaluated later.

The method used to arrive at the cost is as follows:

1. A flowsheet which includes all the significant steps (process and equipment) was prepared and a volumetric material balance made to determine the volume of each equipment item.
2. Costs were estimated for process equipment items for a conventional-type chemical plant. Where parallel units were required because of criticality considerations, a learning factor for their fabrication was applied. This factor reduced the estimated cost of additional units by 15% for each multiple of 2 (i.e., units 2, 4, 8, 16, etc., cost 15% less than the previously listed unit, and units 3, 5, 6, 7, 9, 10, 11, 12, 13, 14, 15, etc., were reduced a proportionate amount).
3. The type of hot cell required for each equipment item was identified (five types), and its area and height were estimated. The five cell types identified were (1) medium shielded – remote maintenance, (2) medium shielded – contact maintenance, (3) unshielded alpha – contact maintenance, (4) chemical makeup, and (5) dry chemical storage.
4. Scale factors were applied to the process equipment component costs to estimate installation, piping, and instrumentation costs.

For plants which could process ^{233}U at rates of from 30 to 180 kg/day, the equipment cost for the CUSP process is about two-thirds of that for the Solex process. Further, the CUSP process apparently makes more efficient use of the processing spaces than does the Solex process as the processing rate increases. At 30 kg of ^{233}U per day, the process equipment cost is 10% of its total increment of plant cost for the CUSP process and 9.25% for the Solex process; at 180 kg/day, the process equipment cost is 11% of its total increment of plant cost for the CUSP process and 8% for the Solex process.

5.1.4 Fuel Specifications

J. L. Scott J. W. Anderson

For the fuel cycle of primary interest to the HTGR system, there are several possible fuels and fuel combinations that have potential for application in a large commercial economy. To serve as a basis for process evaluation, those receiving the greatest interest at this time were identified and some very general specifications prepared for them.

Fuel elements. The element being considered is the GGA reference fuel element for the 1160-MW(e) HTGR having 72 coolant holes and 132 fuel holes. The fuel

block is H-327 graphite with dimensions as shown in ref. 1. The types of fuel elements being considered are:

1. IM element: ThO_2 Biso + $^{235}UO_2$ Triso
2. IM element: ThO_2 Biso + $^{235}UC_2$ Triso
3. IM element: ThO_2 Triso + $^{235}UO_2$ Triso
4. IM element: ThO_2 Triso + $^{235}UC_2$ Triso
5. IM element: ThO_2 Biso + $^{235}UO_2$ Biso
6. IM element: ThO_2 Biso + $^{235}UC_2$ Biso
7. 23 recycle element: ThO_2 Biso + $^{233}UO_2$ Triso
8. 23 recycle element: ThO_2 Biso + $^{233}UC_2$ Triso
9. 23 recycle element: ThO_2 Triso + $^{233}UO_2$ Triso
10. 23 recycle element: ThO_2 Triso + $^{233}UC_2$ Triso
11. 23 recycle element: ThO_2 Biso + $^{233}UO_2$ Biso
12. 23 recycle element: ThO_2 Biso + $^{233}UC_2$ Biso
13. 23 recycle element: ThO_2 Biso + (Th,^{233}U)O_2 Triso (0:1 to 4:1)
14. 23 recycle element: ThO_2 Triso + (Th,^{233}U)O_2 Triso (0:1 to 4:1)
15. 23 recycle element: ThO_2 Biso + (Th,^{233}U)O_2 Biso (0:1 to 4:1)
16. 23 recycle element: ThO_2 Biso + (Th,^{233}U)C_2 Triso (0:1 to 4:1)
17. 23 recycle element: ThO_2 Triso + (Th,^{233}U)C_2 Triso (0:1 to 4:1)
18. 23 recycle element: ThO_2 Biso + (Th,^{233}U)C_2 Biso (0:1 to 4:1)
19. 25 recycle element: ThO_2 Biso + $^{235}UO_2$ Triso
20. 25 recycle element: ThO_2 Biso + $^{235}UC_2$ Triso
21. 25 recycle element: ThO_2 Triso + $^{235}UO_2$ Triso
22. 25 recycle element: ThO_2 Triso + $^{235}UC_2$ Triso
23. 25 recycle element: ThO_2 Biso + $^{235}UO_2$ Biso
24. 25 recycle element: ThO_2 Biso + $^{235}UC_2$ Biso
25. 25 recycle element: ThO_2 Biso + (Th,^{235}U)O_2 Triso (0:1 to 4:1)
26. 25 recycle element: ThO_2 Triso + (Th,^{235}U)O_2 Triso (0:1 to 4:1)
27. 25 recycle element: ThO_2 Biso + (Th,^{235}U)O_2 Biso (0:1 to 4:1)
28. 25 recycle element: ThO_2 Biso + (Th,^{235}U)C_2 Triso (0:1 to 4:1)
29. 25 recycle element: ThO_2 Triso + (Th,^{235}U)C_2 Triso (0:1 to 4:1)
30. 25 recycle element: ThO_2 Biso + (Th,^{235}U)C_2 Biso (0:1 to 4:1)
31. IM element: ThO_2 Biso + (Th,^{235}U)O_2 Triso (0:1 to 4:1)
32. IM element: ThO_2 Triso + (Th,^{235}U)O_2 Triso (0:1 to 4:1)
33. IM element: ThO_2 Biso + (Th,^{235}U)O_2 Biso (0:1 to 4:1)
34. IM element: ThO_2 Biso + (Th,^{235}U)C_2 Triso (0:1 to 4:1)
35. IM element: ThO_2 Triso + (Th,^{235}U)C_2 Triso (0:1 to 4:1)
36. IM element: ThO_2 Biso + (Th,^{235}U)C_2 Biso (0:1 to 4:1)

Fuel rods. The fuel rods are 3 in. long and $\frac{5}{8}$ in. in diameter. The fuel rod matrix material is 28.5 wt % Asbury 6253 natural flake graphite, and the binder material is 15V coal-tar pitch.

Fuel particles. Sixteen different fuel particles are under consideration, as defined in Table 5.2.

Table 5.2. Reference particle specifications for economic analyses

Composition	Sieve sizes	Approximate mean diameter (μm)	Type of coating
ThO_2	35, 45	425	Biso
ThO_2	35, 45	425	Triso
ThO_2	25, 35	600	Biso
ThO_2	25, 35	600	Triso
UO_2	60, 80	210	Biso
UO_2	60, 80	210	Triso
(1:1 Th/U)O_2	50, 70	250	Biso
(1:1 Th/U)O_2	50, 70	250	Triso
(2:1 Th/U)O_2	45, 60	300	Biso
(2:1 Th/U)O_2	45, 60	300	Triso
(4.25:1 Th/U)O_2	35, 45	425	Biso
(4.25:1 Th/U)O_2	35, 45	425	Triso
Resin UO_2	35, 45	425	Biso
Resin UO_2	35, 45	425	Triso
Resin UO_2	25, 35	600	Biso
Resin UO_2	25, 35	600	Triso

1. *National HTGR Fuel Recycle Development Program Plan*, ORNL-4702 (Rev. 1) (in preparation).

5.1.5 Fuel Fabrication

J. D. Sease J. W. Anderson

Fuel fabrication steps include microsphere coating, fuel rod fabrication, and fuel element assembly. In the microsphere coating area, two basic processes are being considered: Biso and Triso. Of course, these vary slightly depending upon the particular fuel kernel being coated, but basically the same flowsheet is followed. Technical data for both these processes were developed which included flowsheets, equipment and system diagrams, and equipment size and space requirement estimates. Equipment cost estimates and the total increment of total plant cost were calculated for both processes. Operating cost and cost comparisons have not been completed at this time.

In the area of fuel rod fabrication, six basic processes have been considered: intrusion (thermosetting), admix, slug injection, slurry blending, extrusion, and hot intrusion.

Options of in-block and out-of-block carbonization were considered along with both thermosetting and thermoplastic binders. For each process considered, flowsheets were prepared and preliminary evaluations made. The slug injection thermoplastic process was chosen for additional study. Technical and cost data were prepared for the process considering both in-block and out-of-block carbonization options. A conceptual design study of commercial-scale equipment necessary for process application was also performed.

Operating cost and detail economic trade-off studies for the carbonization processes have not been completed yet; however, preliminary results show significant economic incentives for development of the in-block carbonization process.

5.1.6 Fuel Reprocessing

J. W. Snider J. W. Anderson

The disposal methods developed for handling high-level radioactive wastes in the United States have been tailored to the requirements of LWRs. A study has been initiated to determine the adequacy of these methods for handling the high-level radioactive wastes from the HTGR fuel cycle. The first phase of the study, identifying the major waste streams and estimating the composition of each, has been completed.

The HTGR fuel cycle chosen for the study was the recycle of the residual HTGR fuel. In this fuel cycle the ^{235}U passes through the reactor twice and is disposed of following the second irradiation cycle (see Fig. 5.4), while the ^{233}U is repeatedly recycled. The study assumes that processes and fuel element loading schemes will be developed which will make possible the separation of the various fuel kernels.

The reprocessing of the ^{235}U after one irradiation cycle presents problems that are not encountered in reprocessing any other fuel. This is caused by the high concentration of fission products in this uranium stream. The weight ratio of fission products to uranium in this stream is greater than 3. While this stream represents only about 6% of the total heavy metal entering the reactor, it accommodates about 40% of the total number of fission events occurring during the irradiation cycle. Stated differently, the uranium in this stream undergoes a burnup greater than 800,000 MWd/ton.

The flowsheet which was studied for reprocessing this ^{235}U stream was based upon the following assumptions:

1. The fuel was processed after one year of cooling.
2. The concentration of uranium in the feed to solvent extraction was determined by heat generation limitations. It was assumed that 5 W/liter was the maximum volumetric heat generation tolerable. This yields a feed stream with a uranium concentration of 10 g/liter.
3. The extractant was 15% TBP in *n*-dodecane.

The ^{235}U which had been irradiated for two cycles contained too much ^{236}U to be of further value. Therefore, this stream was retired and disposed of as a solid without reprocessing.

The Th-^{233}U stream undergoes a burnup of about 65,000 MWd/ton of heavy metal. It was assumed that the Acid Thorex process would be used to process this stream. It has been reported[2] that at burnups greater than about 15,000 MWd/ton, a precipitate (mainly rare earths) forms in the Acid Thorex process during the feed adjustment step. It was assumed that a fission product partition cycle prior to the feed adjustment step would remove sufficient fission products to prevent precipitation during feed adjustment.

There are several high-level waste streams generated by the solvent extraction processes used to purify the ^{233}U and ^{235}U. These streams and their estimated compositions are shown in Fig. 5.5. The total volume of all high-level and alpha waste streams amounts to 15,000 liters per ton of heavy metal.

---

2. L. Küchler, L. Schäfer, and B. Wajtech, "The Thorex Two-Stage Process for Reprocessing Thorium Reactor Fuel with High Burnup," *Kerntechnik* 13(7/8), 319–22 (1971).

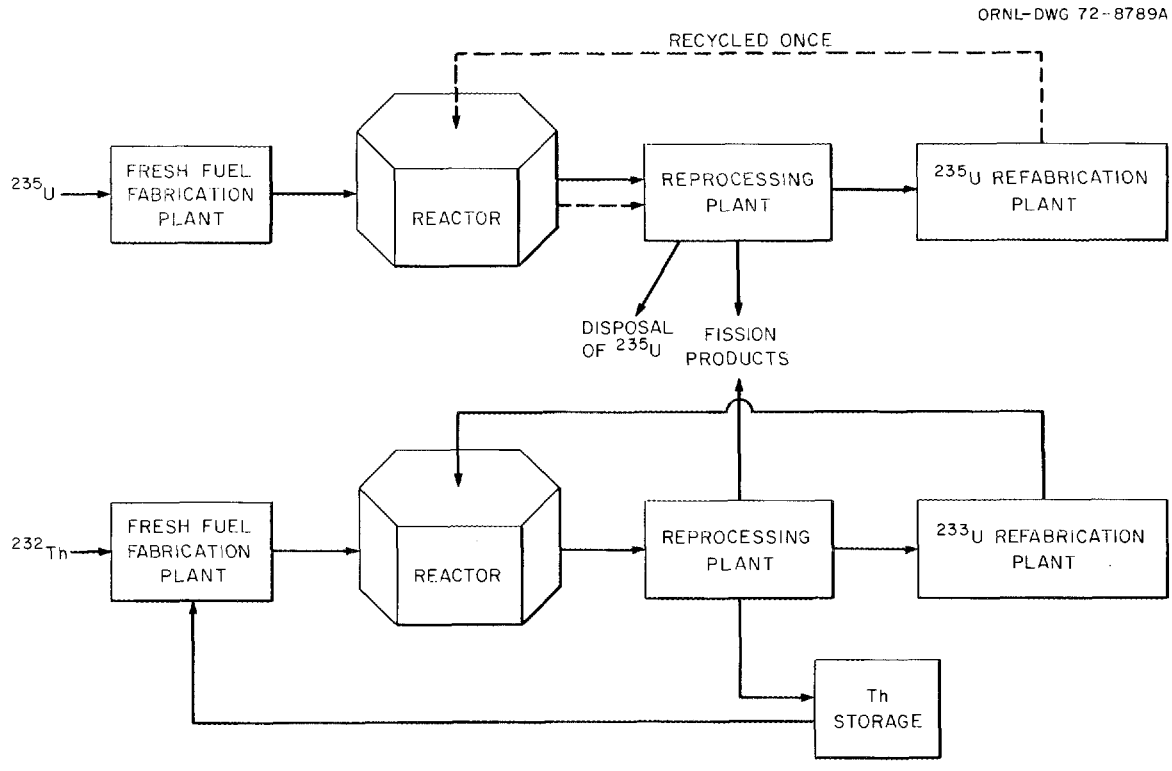

Fig. 5.4. ^{235}U and ^{232}Th HTGR fuel cycles for the twice-through ^{235}U case.

Tritium is shown as a gaseous waste in Fig. 5.5. If 0.01% of the tritium contained in these ^{235}U particles is transferred into any liquid waste stream, the amount of low-level waste formed during evaporation of all combined liquid waste systems would be insufficient to dilute the tritium concentration below that which can be discharged under existing federal regulations.[3]

5.2 ECONOMICS ASSOCIATED WITH TIMING OF HTGR FUEL RECYCLE

F. J. Homan

This work was initiated to study the influence on component fuel cycle costs of delaying the introduction of reprocessing for HTGR fuels. Delaying reprocessing increases the amount of uranium and separative work which must be purchased and increases the storage cost for spent fuel blocks, but it decreases reprocessing and refabrication expenses. It is intuitive that there is a strategy whereby a balance is achieved between savings and increased costs producing a minimum fuel cycle cost. The objective of this work was to find this strategy.

The initial work by Furman et al.[4] was extended to permit use of actual mass balances for commercial HTGRs. In addition, recent estimates of fuel cycle plant capital and operating costs were utilized. A report describing the updated analysis has been prepared.[5]

The computer program DELAY was used to make the computations required by the analysis. Inputs to DELAY include (1) build schedules for HTGRs; (2) estimates of capital and operating costs for fabrication, reprocessing, refabrication, and block storage facilities; (3) cost estimates for uranium, thorium, and credits for spent fuel; (4) shipping cost estimates; and (5) mass balances for HTGR commercial generating stations. Using these inputs, DELAY "constructs" a fuel cycle industry to support the reactor build schedule input.

3. *Code of Federal Regulations*, Title 10, Part 20.

4. F. J. Furman, R. B. Pratt, and A. L. Lotts, *Prediction of the Economically Optimum Time to Initiate Recycle for the High-Temperature Gas-Cooled Reactor Industry Using Computer Program DELAY*, ORNL-TM-2704 (December 1969).

5. F. J. Homan, "Timing the Development of Recycle Fuels for the HTGR," to be submitted to *Nuclear Technology*.

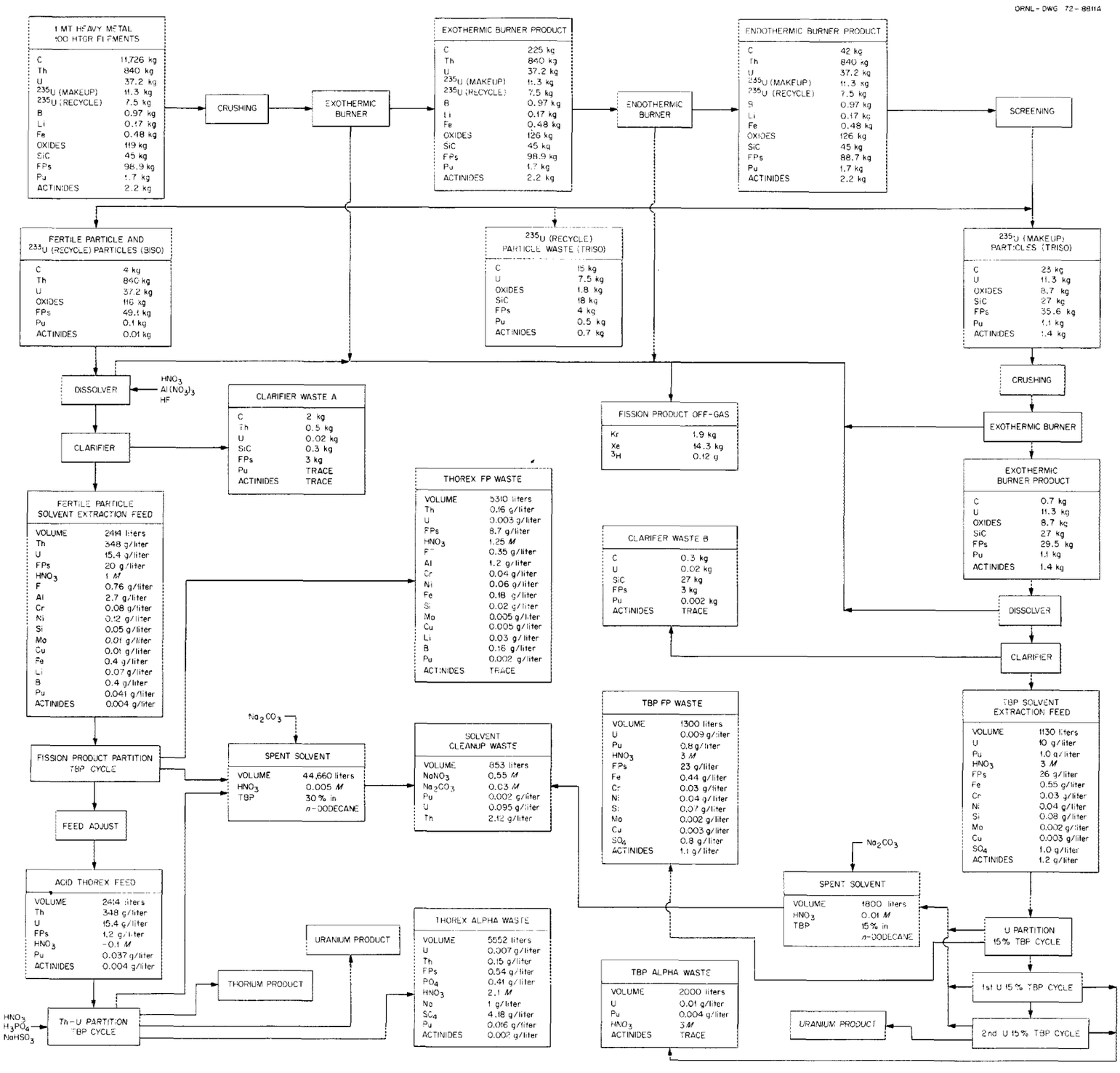

Fig. 5.5. Solvent extraction process flowsheet.

Prior to the time reprocessing is allowed, all reactors operate in the nonrecycle mode, and spent fuel blocks are stored. When recycle is permitted, spent fuel blocks are shipped directly to reprocessing facilities. Blocks previously stored are also reprocessed when capacity permits. The quantity of reprocessed and refabricated fuel available determines how many of the reactors can be operated in the recycle mode. Processing plants are sized to minimize their levelized cost of operation over a 15-year lifetime. Year-by-year costs are computed, and present worth at the beginning of the study is calculated. This process can be repeated for different assumed dates for initial reprocessing and the results compared to determine the best time to begin reprocessing.

Several build schedules described in the program plan[6] are shown in Table 5.3. These schedules, calling for 20, 41, and 124 reactors respectively, are similar in that they all call for the first commercial reactor to go on line in 1979, and all have a uniform progression ending abruptly in the late 1980's. It is assumed that this abrupt termination of HTGR sales is due to utility interest in the LMFBR, which should be commercially available about that time. These three build schedules could be considered to span a range of market penetrations ranging from pessimistic (20 reactors) to optimistic (124 reactors). For a build schedule calling for the first reactor to begin producing power in January 1979, the fuel must be fabricated in 1978, and reprocessing cannot occur before 1980. Table 5.4 shows the calculated total fuel cycle expenditure and levelized fuel cycle costs for each of the build schedules shown in Table 5.3. In each case the minimum costs are associated with initial reprocessing in year 1983. The cost penalties associated with initial commercial reprocessing in years other than 1983 are shown in Fig. 5.6. The economic assumptions which went into this result are as follows:

1. Fuel is charged into a reactor on January 1 and discharged on December 31.
2. All processing of fuel is accomplished in the calendar year preceding charge into the reactor.
3. Ore and separative work requirements for 93%-enriched uranium are \$12.61 per gram of the ^{235}U isotope.
4. Thorium cost assumed to be \$10 per kilogram.
5. Discharged ^{235}U worth \$8.84 per gram.

6. *National HTGR Fuel Recycle Development Program Plan*, ORNL-4702 (Rev. 1) (in preparation).

Table 5.3. Year-by-year tabulation of reactor startups for three build schedules

Calendar year	Number of reactors going on line		
	20	41	124
1979	1	1	1
1980	1	0	3
1981	2	4	5
1982	2	4	7
1983	3	4	10
1984	3	6	13
1985	4	6	17
1986	4	8	20
1987		8	23
1988			25

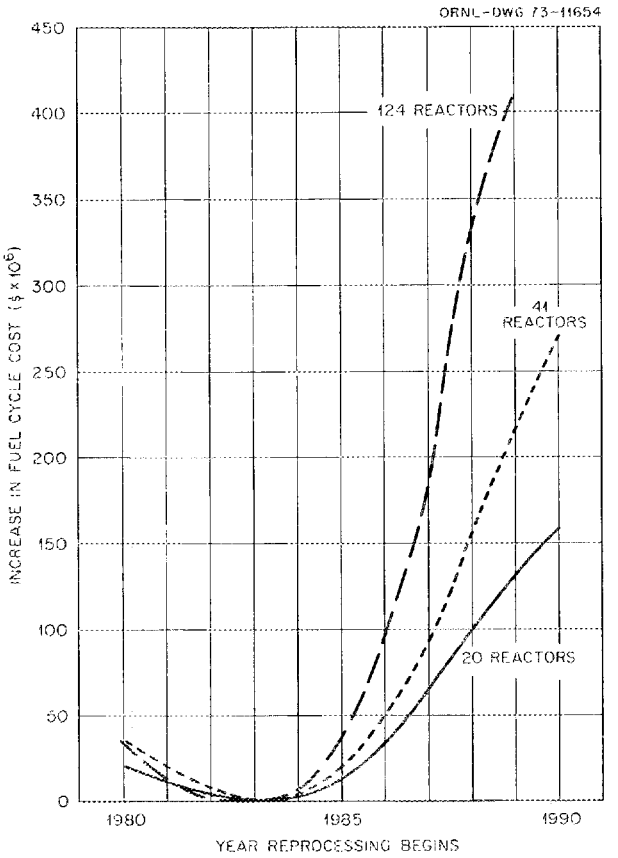

Fig. 5.6. Increased fuel cycle costs (discounted to 1978) as a function of time of initial reprocessing.

Table 5.4. Variation in total fuel cycle costs with year reprocessing is introduced and build schedule assumed

Year reprocessing begins[a]	20 Reactors			41 Reactors			124 Reactors		
	Billions of dollars[b]	Billions of dollars[c]	Mills per kilowatt-hr[d]	Billions of dollars[b]	Billions of dollars[c]	Mills per kilowatt-hr[d]	Billions of dollars[b]	Billions of dollars[c]	Mills per kilowatt-hr[d]
1980	6.030	1.361	1.1690	11.198	2.394	1.0931	30.251	6.142	1.0127
1981	5.981	1.349	1.1586	11.132	2.378	1.0857	30.137	6.121	1.0092
1982	6.013	1.342	1.1526	11.175	2.365	1.0800	30.149	6.109	1.0073
1983	6.028	1.339	1.1503	10.991	2.358	1.0766	30.021	6.109	1.0072
1984	6.084	1.343	1.1532	11.101	2.364	1.0794	30.084	6.116	1.0084
1985	5.974	1.350	1.1595	11.037	2.376	1.0848	30.561	6.150	1.0141
1986	6.053	1.373	1.1795	11.112	2.405	1.0983	30.533	6.205	1.0232
1987	6.289	1.406	1.2076	11.285	2.452	1.1197	30.574	6.283	1.0359
1988	6.413	1.437	1.234	11.661	2.509	1.1458	30.962	6.411	1.0571
1989	6.580	1.469	1.2618	11.890	2.571	1.1739	31.891	6.568	1.0829
1990	6.755	1.496	1.2848	12.184	2.628	1.2001	32.557	6.735	1.1106

[a]First reactor goes on line in 1979; so 1980 is the earliest reprocessing could begin.
[b]Undiscounted.
[c]Present worth calculated to beginning of 1978 using 10% discount factor.
[d]Levelized values assume 100% plant factor for 1160-MW(e) reactors.

6. Discharged fissile plutonium worth $10 per gram.
7. Fresh-fuel shipping cost is $1.75 per kilogram; spent-fuel shipping cost is $45 per kilogram.
8. A 30%/year fixed charge rate and 15-year lifetime assumed for all fuel processing facilities.
9. Discount factor used was 10%.
10. Mass balances were provided by Gulf General Atomic.

At present it is assumed that commercial reprocessing will begin in 1987. From Fig. 5.6 it can be seen that the cost penalty associated with this planning ranges from $67 million to $174 million, present worth calculated to 1978 using a 10% discount factor. The undiscounted penalty is $261 to $553 million, but increased cost of uranium ore and toll enrichment will increase this penalty sharply.

The following conclusions are drawn from this analysis:

1. Using best current estimates of fuel cycle costs, the optimum year to initiate recycle of HTGR spent fuel is 1983.

2. The added cost associated with beginning reprocessing before this date is insignificant.

3. The added costs associated with late introduction of reprocessing do not become significant until a lengthy delay has occurred. For example, for the 124-reactor build schedule it has been calculated that a delay of five years past 1983 increases costs by about 5%; a ten-year delay increases costs by about 18%.

4. Calculated fuel cycle costs are very sensitive to changes in the assumed costs of uranium ore and toll enrichment.

6. HTGR Fuel Element Development

J. H. Coobs J. L. Scott
W. P. Eatherly

The objectives of the fuel element development program continue to be (1) to demonstrate HTGR reference design coated particles and fuel rods to the full fluence and burnup of the reactor; (2) to develop alternative fabrication processes with better economics, performance, and recycle capability than reference fuel fabrication methods; and (3) to develop advanced fuels with higher temperature capability than reference materials. To meet these objectives, we continued the three-phase program described last year.[1]

Presently, several fuels appear to be very attractive for the HTGR application, and their performance has been good in the limited irradiation tests which have been performed. Since we know of no better way than more extensive irradiation testing to determine which fuel design will perform best, first priority on the HTGR Base Program has been given to irradiation testing. Each irradiation capsule requires extensive fuel preparation, characterization, and quality assurance work; this work is reported as a part of the individual capsules in Chap. 7 of this report. The development work leading to process improvements or better characterization methods is reported here.

6.1 COATING DEVELOPMENT

C. B. Pollock W. H. Cook
D. M. Hewette II

In general, past approaches to coated particle experiments have been primarily aimed toward producing successful fuel rather than toward determining the limits in particle design and coating properties which lead to failure. To perform such experiments requires not only a high confidence in the techniques of characterizing the coatings but also high reproducibility and predictability in the coating operation. Moreover, since the fertile particles predominate in the core, we elected to concentrate on Biso-coated ThO_2. In support of improved characterization, we have prepared samples to serve as standards for optical anisotropy measurements (OPTAF) and Bacon anisotropy factor (BAF) techniques and have examined the structure of pyrolytic carbon coatings with scanning electron microscopy (SEM) and transmission electron microscopy (TEM) techniques. In the second area, we chose a set of coating properties with respect to density, anisotropy, and crystallite size that had been demonstrated to be stable under HTGR conditions of fluence and temperature and then modeled the particles with the aid of the STRETCH code[2] for a variety of coating designs using the most reasonable values for carbon properties and constants that were available. Particles were then fabricated to the desired designs and became the subject for irradiation experiments HT-12 to HT-15.

We have continued the fundamental studies of pyrolytic carbon and the processes that are important in understanding and controlling this material. During the past year the SEM and TEM techniques have been

1. "HTGR Fuel Element Development," *GCR-TU Programs Annu. Progr. Rep. Sept. 30, 1971,* ORNL-4760, pp. 96–125.

2. J. W. Prados and T. G. Godfrey, *STRETCH, a Computer Program for Predicting Coated-Particle Irradiation Behavior; Modification IV, December 1967,* ORNL-TM-2127 (April 1968).

employed in conjunction with conventional reflected-light microscopy to study these materials. The objective, of course, was to characterize the microstructure and to follow the changes in that microstructure after heat treatment and after prolonged exposure to fast neutrons at elevated temperature.

6.1.1 Coating Characterization

Pyrolytic carbon (PyC) coatings used as a cladding of HTGR fuel particles are turbostratic layers of dense isotropic carbon formed by the pyrolysis of a gaseous hydrocarbon in a fluidized-bed furnace. The principal properties which are used to characterize coatings are density, thickness, and degree of preferred orientation. Coating densities for both PyC and silicon carbide (SiC) may be determined, in principle, by use of a sink-float technique using benzene-tetrabromoethane mixtures for carbon and methylene chloride–tetrabromoethane mixtures for SiC. For convenience, the procedure is normally carried out in a density gradient column using standards calibrated by the sink-float technique. The major uncertainty with PyC coatings is the unknown degree of penetration of the liquids into open-surface porosity.

The currently favored technique for determining the degree of preferred orientation is the OPTAF system; the developments in this area are reported in Sect. 6.1.5. We prepared a series of pyrolytic carbon plates that were designed to serve as standards for the ORNL OPTAF setup. The plates were formed by coating graphite disks in a bed of particles. The bed conditions varied so as to provide a range of coating rates, which influence the preferred orientation. The preferred orientation will be determined by the conventional x-ray method, and selected samples will then be used as OPTAF standards.

To determine coating thicknesses, we measure 30 particles as contact radiographs. The measurements are then treated statistically to determine compliance with specifications. We routinely qualify each batch of material on a statistical basis, and our data accumulation forms have been rewritten in a manner that better displays this information.

6.1.2 Coating in Glove Box Facilities

We continued the development of equipment and characterization techniques for coating plutonium and ^{233}U. We now have the capability of depositing both SiC and PyC on these materials and have coated several batches for irradiation experiments. We found that the surfaces of the coatings can be maintained free of contamination if proper precautions are taken. These materials are more difficult to characterize than conventional particles, but the same rigid specifications were met, except for the OPTAF value. Equipment for measuring the optical anisotropy of coatings on plutonium-bearing particles is not yet available.

6.1.3 Scanning Electron Microscope (SEM) Characterization of Pyrolytic Carbon Coatings as Deposited and Irradiated

We have begun to use the SEM[3] to examine PyC coatings consisting of (1) free-standing strips from which the substrate graphite was removed prior to their characterization and testing and (2) restrained coatings on isotropic graphite substrates. The SEM has been useful in characterizing these coatings in the as-deposited and heat-treated plus as-irradiated conditions.

The work with pyrolytic strips involved specimens derived from methane (CH_4) and propene (C_3H_6); both sets of strips had apparent densities of 2.0 g/cm^3. However, the strips derived from methane were highly anisotropic with a BAF estimated to be 1.4, and those derived from propene were isotropic with a BAF of 1.0.

The results of the SEM examinations of these materials graphically show the changes created by the fast-neutron damage and the differences in the resistance to the damage by the different materials[4] (see Figs. 6.1 and 6.2). In the unirradiated condition, the polished strip shown in Fig. 6.1*a* is only 0.0032 in. thick in the direction parallel to the *c* axis of the crystallites of the pyrolytic carbon. This thickness increased[5] by 500% under the fluence of 3.2×10^{22} neutrons/cm^2 ($E > 50$ keV) accumulated at 715°C, as shown in Fig. 6.1*b*. This also clearly illustrates the ability of graphite to make these large dimensional changes with plastic flow without fracturing.

In contrast, the 0.0043-in.-thick isotropic pyrolytic carbon derived from the propene decreased slightly, approximately 5%, under the same neutron irradiation. In Fig. 6.2 a high magnification is used to show that the

3. The scanning electron microscope (SEM) work was done by R. S. Crouse, D. R. Cuneo, and T. J. Henson of the Metals and Ceramics Division. The SEM is a recently acquired new one with improved resolution. It is a model JSM-U3, manufactured by the Japan Electron Optical Laboratory.

4. Additional irradiation details on the propene-derived pyrolytic graphite were reported previously by D. M. Hewette II, *Metals and Ceramics Div. Annu. Progr. Rep. June 30, 1970,* ORNL-4570, pp. 162–63.

5. The width and length decreased by 50 and 53%, respectively (personal communication from C. R. Kennedy and H. Keating of the Metals and Ceramics Division).

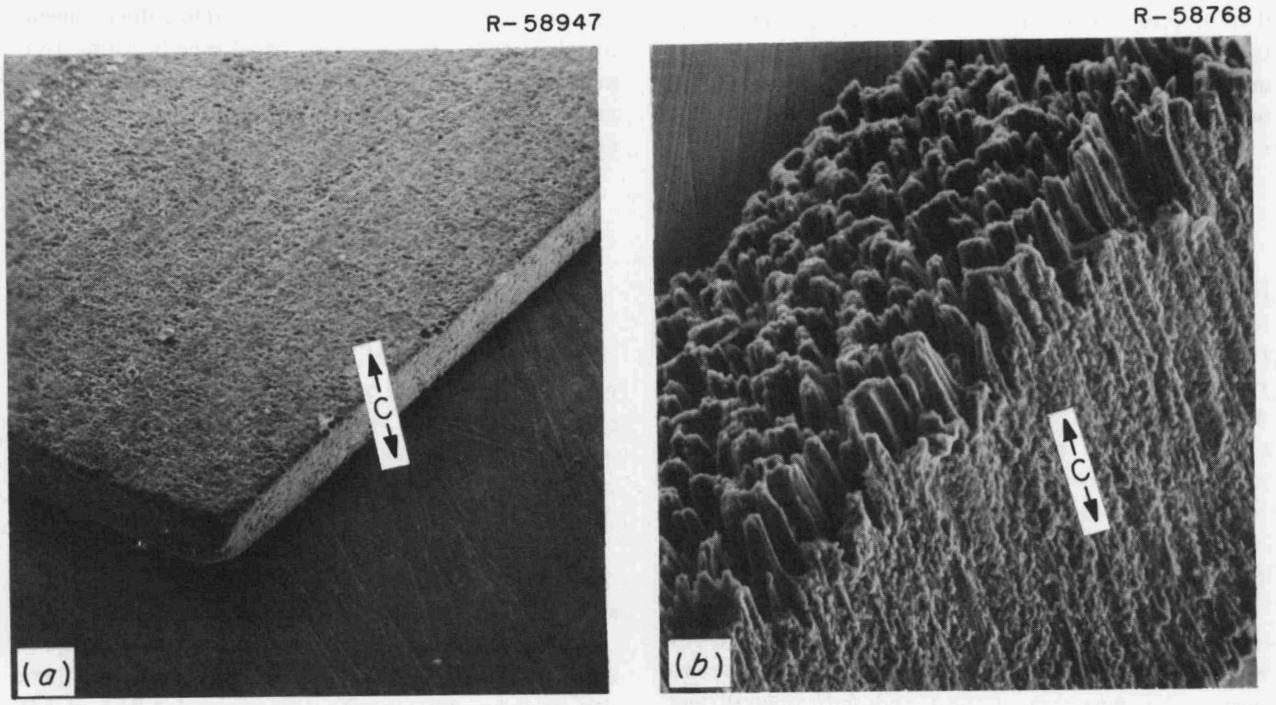

Fig. 6.1. Pyrocarbon strip derived from methane at 2000°C. (*a*) Unirradiated control; (*b*) irradiated to 3.2×10^{22} neutrons/cm^2 ($E > 50$ keV) at 715°C. 100×.

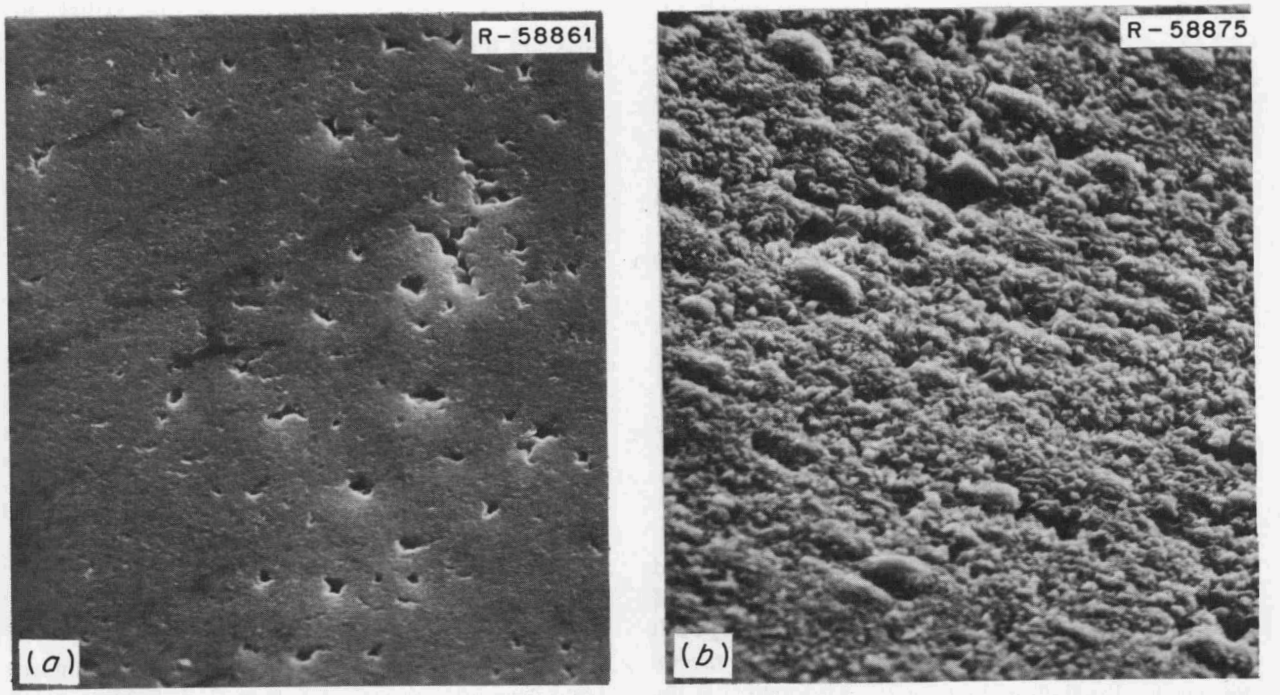

Fig. 6.2. Pyrocarbon strip derived from propene at 1250°C. (*a*) Unirradiated control; (*b*) irradiated to 3.2×10^{22} neutrons/cm^2 ($E > 50$ keV) at 715°C. 1000×.

original polished surface of the control had some porosity and the surface was slightly roughened by the exposure to the fast neutrons.

Since the propene-derived pyrolytic carbon coatings have demonstrated the greatest dimensional stability under fast-neutron irradiation at 715°C, the major portion of our work has been concentrated on parametric studies of these deposited on isotropic graphite substrates. These were deposited from propene at low temperatures of 1100, 1150, 1200, 1250, and 1300°C and heat treated at 1800°C. We selectively examined 25% of the specimens produced for this series prior to irradiation to characterize the unirradiated coatings relative to the deposition parameters and to establish reference data to assist in their evaluation as a function of their exposure to fast-neutron damage at 715°C. A summary of the SEM observations on these series of coated specimens is given below.

1. Rounding the sharp edges of these HFIR-type specimens appeared to eliminate cracking and spalling of the pyrocarbon coatings that sometimes occurred on the sharp edges of previous specimens.

2. The quality of the pyrolytic carbon coating appeared to be directly related to the quality, lack of roughness, in the machined surfaces of the substrate graphite, grade AXF-5Q.

3. The pyrolytic carbons deposited at the lower temperatures appeared to be more continuous and have less bridging of pyrocarbon particles than those deposited at higher temperatures. The bridging of pyrocarbon particles produces porosity in the coating.

4. The basic pyrolytic deposition particles start as oblate spheroids at 1100°C, become almost flat platelets at 1200°C, and finally become more spheroidal at 1300°C.

5. At 1100 and 1150°C, the longer coating period appeared to improve the overall physical appearances of the coatings. Lack of time and specimens prevented such evaluation for the other deposition temperatures.

6. The physical nature of a coating at a particular deposition temperature is sensitive to the geometry and/or orientation of the specimen in the coating furnace. For example, the coating on the cylindrical surface of a specimen may not be the same as that on the rounded edges of the specimen.

Figure 6.3 illustrates the typical range of the structures observed in this series. The pyrocarbon deposited at 1100°C, as shown in Fig. 6.3*a*, appeared to be composed of agglomerates of poorly formed crystallites heavily impregnated with amorphous-appearing carbon. The structure varies among specimens coated for different periods at 1100°C. At 1200°C (Fig. 6.3*b*), the agglomerates, believed to be nucleated in the gas phase, are more perfectly formed but have a platelike appearance. At 1300°C the agglomerates are larger and more spherical (Fig. 6.3*c*). At the same time, the individual crystallites which make up the agglomerates appear to be smaller at the higher temperatures. At 1250 and 1300°C, there was a tendency for a fine network composed of individual crystallites less than 1 μm in diameter to deposit in a debris-like manner between the larger agglomerates.

Under fast-neutron irradiation at 715°C in the High Flux Isotope Reactor (HFIR) to fluences ranging from 0.54×10^{22} to 0.95×10^{22} neutrons/cm^2 ($E > 50$ keV), all coatings deposited at 1200°C and below failed the test and exhibited extensive cracking and fragmentation. Most of the coatings deposited at 1250 and 1300°C survived the irradiation with no apparent ill effects.

We examined samples that survived the irradiation reasonably well. This limited our examinations to those pyrocarbon coatings that had been deposited at 1200, 1250, and 1300°C. We found that the fine, open network of less than 1-μm crystallites mentioned above was uniformly absent from these irradiated samples. The agglomerates forming the basic structure of the pyrocarbon coating appeared to have become slightly more spheroidal. All the irradiated specimens had a clear, uncluttered appearance, as shown in Fig. 6.4. At this time, we do not know if the changes in structure were due to irradiation alone or to irradiation plus limited oxidation. There were no measurable weight changes, but they are not sensitive enough to resolve the question. When cracks occurred in the irradiated coatings, they appeared to be across agglomerates and between agglomerates in the pyrocarbon coatings deposited at 1200 and 1250°C respectively.

We have prepared an array of samples as a second generation of coated graphite samples for the next irradiation experiment. These have two separate pyrolytic carbon coatings; the first is a low-density layer designed to alleviate stresses between the outer coating and the substrate, and the outer coating again serves to seal the sample. The inner coatings were deposited at 1000°C from acetylene (C_2H_2) and have a thickness and a density of 25 μm and 1.0 g/cm^3 respectively. The outer coating is again derived from propene (C_3H_6) at 1300°C and, in this case, heat treated at 1500°C. The coating thickness ranges from 40 to 80 μm, and the density is near 2.0 g/cm^3.

The outstanding features of the external surfaces of the pyrocarbon coatings are: (1) there is a complete absence of the fine, open network of $\leq$1-μm crystallites

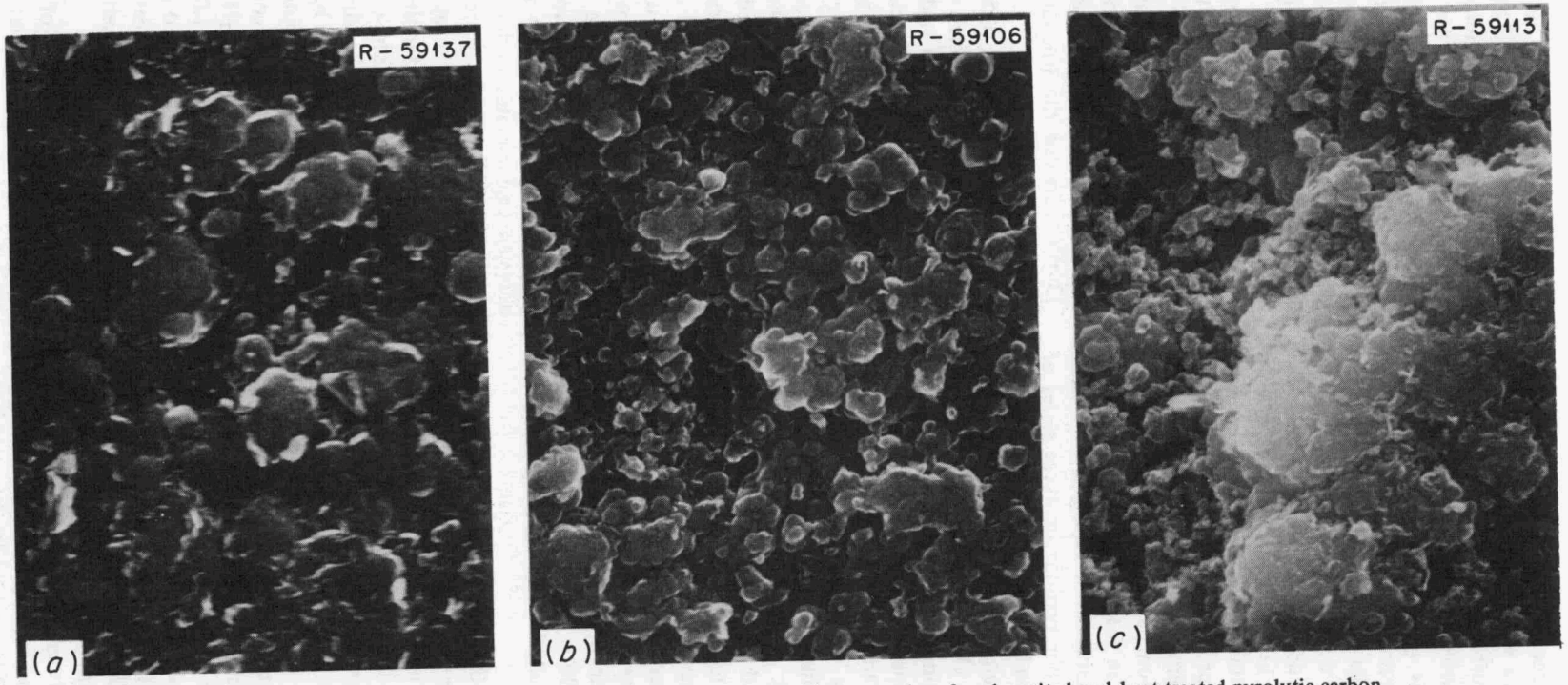

Fig. 6.3. SEM photomicrographs showing typical microstructural topography of as-deposited and heat-treated pyrolytic-carbon coatings derived from propene and deposited on grade AXF-5Q graphite at (*a*) 1100°C, (*b*) 1200°C, and (*c*) 1300°C and heat treated at 1800°C. 5000×.

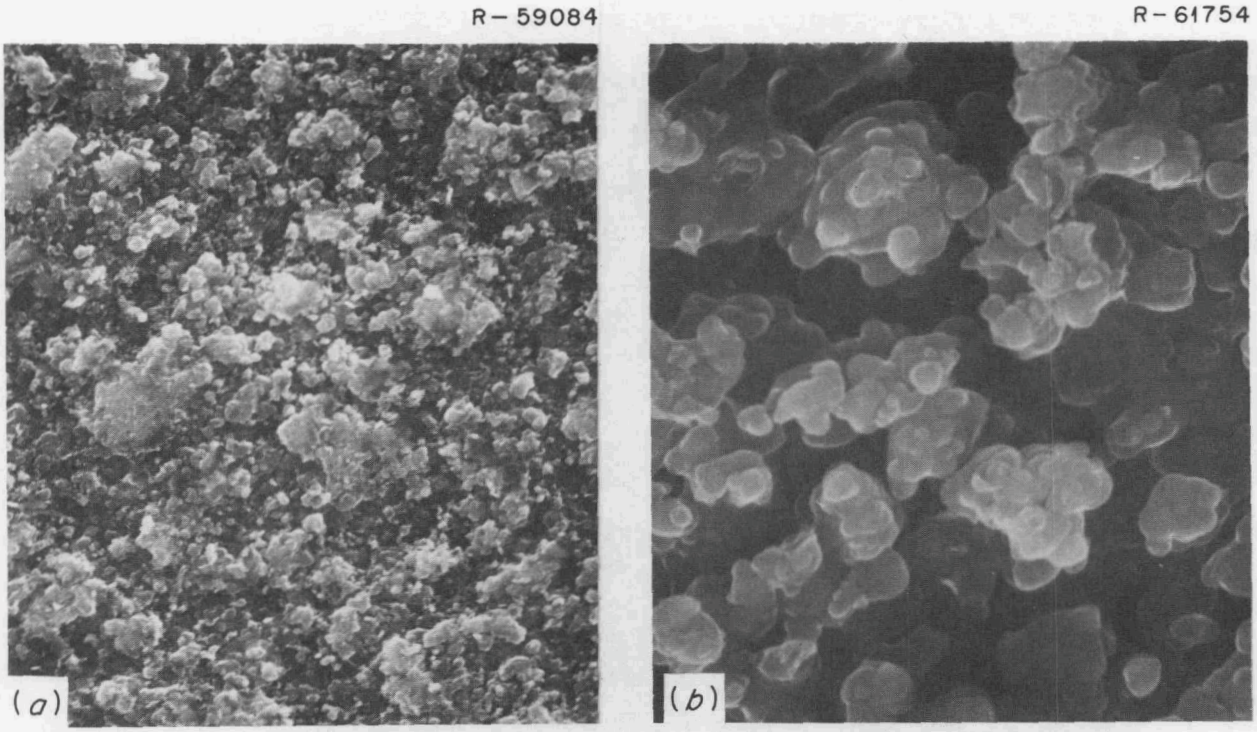

Fig. 6.4. SEM photomicrographs showing the microstructural topography of a pyrolytic-carbon coating deposited on grade AXF-5Q graphite at 1250°C. (*a*) As deposited; (*b*) irradiated to 5.8×10^{22} neutrons/cm^2 ($E > 50$ keV) at 715°C. 2000×.

that were observed as a debris-like portion between agglomerates of the 1250 and 1300°C as-deposited coatings prepared for the earlier irradiation experiment; and (2) they are uniformly alike except for subtle stacking differences by the basic spheres making up the agglomerates. In the previous single-layer coatings that were deposited from propene at 1300°C, the basic, spherelike crystallites were 1 to 3 μm in diameter and the agglomerates were nominally 10 μm maximum diameter. In this new series of samples, the unit building crystallite diameters in the outer layer are essentially 1 μm. The agglomerates are less predominant, and, when they do occur, their maximum diameters are 6 to 8 μm. We shall continue to monitor these recent specimens and the previous surviving specimens as they accumulate increments of fluence.

6.1.4 Transmission Electron Microscopy (TEM) of Unirradiated Pyrolytic Carbons

In the irradiation studies reported previously,[4] pyrolytic carbons deposited from propene and annealed at 1900°C apparently exhibited better dimensional stability than as-deposited materials. In an effort to understand the difference in irradiation behavior between the as-deposited and annealed pyrolytic carbons, structural evaluations were made by TEM using ion milling.[6] These results, shown in Fig. 6.5, indicate that the as-deposited structure (Fig. 6.5*a*) consists of closely packed spheroidal particles with little evidence of crystallinity or porosity. On the other hand, the structure annealed at 1900°C (Fig. 6.5*b*) indicates that some crystallinity has developed, since some diffraction contrast is now apparent. This is in the form of small dark striations oriented radially within the spheroidal particles. Also, some porosity has been developed by annealing. This takes the form of concentric delaminations within the spheroidal areas. Thus, at first glance, the better irradiation stability of the annealed materials can be attributed to their being more crystalline.

6. The transmission electron microscopy (TEM) work was done by C. K. H. DuBose and J. O. Stiegler of the Metals and Ceramics Division.

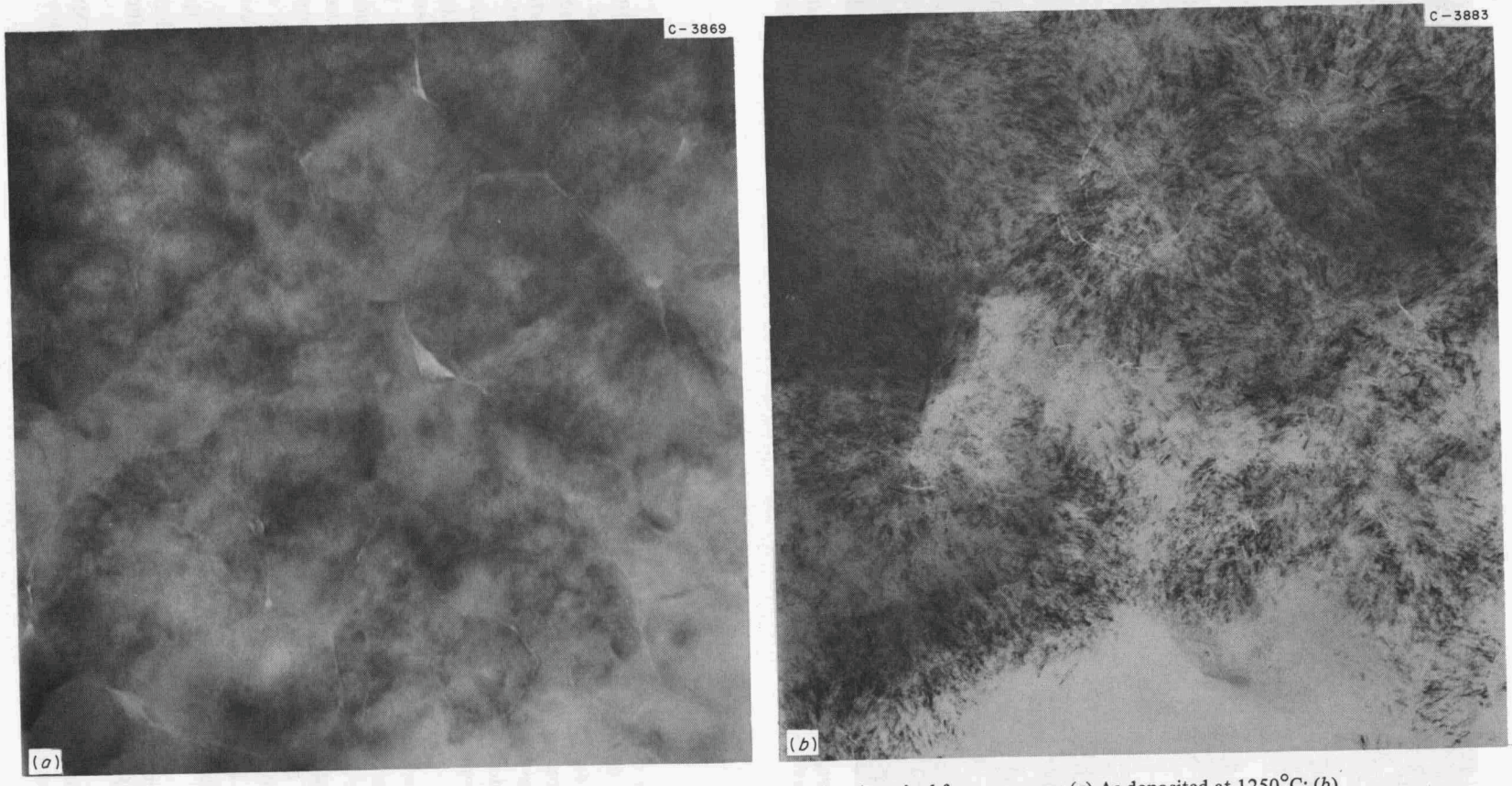

Fig. 6.5. Transmission electron micrograph of pyrolytic-carbon coating deposited from propene. (*a*) As deposited at 1250°C; (*b*) annealed 1 hr at 1900°C. 100,000×. Reduced 40%.

6.1.5 Optical Anisotropy (OPTAF) Measurements

E. S. Bomar W. P. Eatherly

We have continued to be plagued with difficulties in measuring the anisotropy of pyrolytic coatings on particles, namely, the lack of fourfold symmetry in the reflectivity as a function of crystal orientation in the crossed-polarized position. At the same time, the preliminary results from HFIR capsule HT-12 further emphasize the sensitivity of coating survival under irradiation to anisotropy.[7]

The equipment utilized has been described previously.[8] Because of their relative inflexibility, the Reichert microphotometer and Bausch and Lomb metallograph have been temporarily abandoned in favor of the Leitz microscope and photometer. Effort has further concentrated on single-crystal graphite (Ticonderoga flake) until the equipment problems are solved.

Two internal surfaces in the light path through the photometer body were either bypassed or removed to avoid introducing spurious reflections into the true ray beam. The triple mirror was bypassed by removing a fully surfaced mirror normally used for examining dim objects, and a multifaceted diffuser plate immediately preceding the photomultiplier tube was removed. The lenses were tested for strain fields in the glass, which could introduce depolarization, but no significant effect was found. No further deficiencies in the optical equipment could be detected.

The current output of the photomultiplier tube for anode voltages ranging from 440 to 1120 V was observed for light reflected from a graphite single crystal in its orientation for maximum and minimum reflections. The OPTAF of the crystal was then calculated. OPTAF values calculated from currents read directly on the picoammeter varied widely for anode voltages from 440 to 630 V; the spread was much smaller in the range of 630 to 1120 V. Since an implied dependence of OPTAF on anode voltage is false, we looked for a fault in the equipment and found that OPTAF values calculated from photometer currents read on a calibrated recorder chart were independent of anode voltage. Readings obtained directly from the picoammeter were, therefore, in error.

We determined the period necessary to reach stable operation of the light source and photometer by simultaneously monitoring the current drawn by the xenon light and the current output of the photomultiplier tube. The current drawn by the xenon light slowly dropped 2.5% during the 3-hr period following startup, and there was a proportionate reduction in output of the photomultiplier current. By comparison, however, if the xenon light was stabilized before the photomultiplier was turned on, the operating time necessary to stabilize the photomultiplier and its high-voltage supply was less than 15 min. We found that we could avoid both an unnecessary delay in making reflectivity measurements each day and undue shortening of the working life of the xenon light by substituting a dummy load for the xenon light and thus keep its power supply in a continuous ready state.

Attention was next fixed on the sample mounting apparatus. Obviously any lack of perpendicularity between the sample surface and the optical axis of the microscope would superimpose a spurious twofold symmetry over the true fourfold symmetry. The mounted and polished sample had been held by its rear face on a metal slide by putty.[9] It was quickly found that the putty crept, introducing to the sample a nonperpendicularity with time. This difficulty was eliminated by mounting the sample against its front (polished) face in a holder with a spring clip with three setscrews providing leveling of the face.

With these corrections, excellent fourfold symmetry with crossed polarizers and twofold symmetry with no analyzer present have been obtained on the single crystals. Secondary standards of polished nickel plates have been employed to determine absolute reflectivities. Scanning over various portions of the single crystal yields about a 10% variation in the maximum (*c*-axis) reflectivities. Since the single crystals are known to be twinned, to possess ribbon dislocations, and to have lenticular voids, these variations in reflectivity may be attributed to such defects. Assuming the maximum anisotropy areas of the crystal face to be representative of the true single crystal, principal reflectivities of 0.299 and 0.085 were obtained, compared with values of 0.280 and 0.083 reported by Ergun et al.[10] Work on single crystals is continuing along the lines of the approach used by Woodrow et al.[11] to determine phase angles and indices of refraction and attenuation.

---

7. See Chap. 7, this report.
8. *GCR-TU Programs Annu. Progr. Rep. Sept. 30, 1971,* ORNL-4760, pp. 102–8.
9. Plastalena, Stewart Clay Company, New York.
10. S. Ergun, J. B. Yasinsky, and J. R. Townsend, "Transverse and Longitudinal Optical Properties of Graphite," *Carbon* **5**, 403–8 (1967).
11. J. Woodrow, B. W. Mott, and H. R. Haines, "Analysis of Polarized Light Reflected from Absorbing Materials at Normal Incidence," *Proc. Phys. Soc. B* **65**, 603–16 (1952).

We are satisfied at this point that the Leitz equipment is operating correctly and that further difficulties must be attributed to the sample.

Such further difficulties have indeed occurred. Examinations of particle coatings have yielded reasonably good twofold symmetries with no analyzer present; with a crossed analyzer, no good fourfold symmetries can generally be obtained. Any possible tilting of the sample can be determined by observing displacement of the aperture diaphragm image at the back focal plane of the objective lens using the Bertrand lens system built into the Leitz microscope. For coated particles, it is extremely difficult, if not impossible, to eliminate this image wobble. The contour of the polished coating surface can be determined by using an interference microscope. A nonflatness due to rounding of the coating edges is immediately evident. This rounding is due to differences in hardness between the buffer, low-temperature isotropic (LTI), and SIC layers as well as the epoxy mounting material. The effects of both polishing time and the use of harder mounting materials are being investigated. In a few cases, polished surfaces of coatings have been obtained with regions larger than the 15-μm measuring spot which had elevation variations of only a small fraction of a 5500-Å light wave. A lack of fourfold symmetry still emerges. It is, perhaps, too much to assume the small crystallite pyrolytics with their void structures can be treated mathematically as a collection of single crystals. The theoretical bases for optical reactivity of a polycrystal are being reexamined.

In summary, the studies of optical anisotropy have been both tedious and frustrating. This is not to say such measurements cannot be utilized in a practical sense, but their physical significance remains in doubt at the present time.

6.1.6 Coating Dimensional Statistics

In order to facilitate the collection and statistical interpretation of coated-particle dimensions, a simple computer program has been written to calculate the mean, standard deviation, central confidence limits, skewness, and kurtosis. We have now collected statistical data on a wide variety of coated particles with several types of kernels, including sol-gel microspheres, resin-derived fuel kernels, and inert carbon kernels. Coatings include low-density buffer, high-density carbon, and SiC layers, all produced in several different furnaces in several different sizes of reaction tubes. The statistics also cover quite a range of deposition conditions whose significant variables are time, temperature, hydrocarbons, and total gas flux.

Buffer coatings. The buffer coating of low-density carbon is normally deposited from C_2H_2 at 1100 to 1300°C at deposition rates of 10 to 100 μm/min. The low efficiency of this operation allows the accumulation of significant quantities of soot in the reaction chamber. The efficiency is defined as the percentage of the carbon supplied which ends up as coatings on particles. Process control is more difficult in the buffer coating operation than in the others; however, the mean thickness can normally be predicted within the range of ±15 μm. It is more difficult to predict the mean of thick buffers on small-diameter particles (≈100 μm) or low-density kernels (<2.0 g/cm^3), but most of the buffers made in this laboratory are deposited on kernels with diameters from 200 to 600 μm and densities of 3 to 10 g/cm^3.

The relative standard deviation of the distribution for buffer coatings decreases with increasing coating thickness, because the magnitude remains relatively constant. The average standard deviation for runs performed in this reporting period was 9.8 μm, with a maximum of less than 14 μm. The distribution is largely normal within a run and from run to run. The average skewness number was 0.2, but all were in the range 1.0 to −1.1. The kurtosis had an average value of −0.35 for all runs, but again the range was small (−1.2 to 1.7).

LTI coatings. Dense isotropic (LTI) coatings are deposited from propene in the temperature range 1200 to 1400°C. Deposition rates are in the range of 5 to 20 μm/min, with carbon densities ranging from 1.7 to 2.1 g/cm^3. The process is characterized by good coating control, and the mean of the coating thickness can be predicted in the normal coating range to within ±7 μm.

The standard deviation of the distribution falls within a narrow range (4 ± 1.2 μm), but again the relative standard deviation is strongly dependent on coating thickness. The average relative standard deviation for all runs was 8.8%, with a range between 5.2 and 13.3%. Coatings of 50 μm or less had a relative standard deviation of approximately 10.5%, while those of 50 to 100 μm had a relative standard deviation of 6.0%. Again these coatings were deposited under a wide range of conditions of cone size, batch size, temperature, and hydrocarbon supply rate, but the statistics appeared to be sensitive only to coating thickness.

Again the distribution of size within a batch and from batch to batch appeared to be nearly normal. The average skewness of all batches was 0.25, while the range was 1.4 to −0.6. The average kurtosis for all batches was −0.28 with a range of 2.1 to −1.3.

SiC coatings. Silicon carbide coatings are deposited from methyltrichlorosilane in the presence of hydrogen

at about 1550°C. The process is characterized by a slow deposition rate and relatively thin coatings. The mean of the distribution of such a coating can be predicted to within ±5 μm, and the standard deviation of the distribution averages 2.5 μm in a large number of runs. The relative standard deviation is 7.5%, largely because some of the coatings are so thin. Typically, coatings range in thickness from 20 to 30 μm with standard deviations from 1 to 4 μm. Again the distribution can be described as normal. The average skewness number for a larger number of runs was −0.06, or a very slightly larger tail to the left. The range in skewness was −1.1 to 0.6, and the average kurtosis was −0.6.

6.2 BONDED FUEL DEVELOPMENT

R. L. Hamner J M Robbins

6.2.1 Extrusion of Fuel Elements

At the present state of the art, fuel rods such as those for the Fort St. Vrain Reactor are restricted to short (2-in.) lengths, and the high volume loadings lead to low matrix densities which in turn result in poor thermal conductivity.

We generated curves (Fig. 6.6) that indicated that the particle volume loading might be reduced and still maintain the required fuel loadings by increasing the kernel size of the fissile and fertile particles. This led us to explore the possibilities of a continuous-matrix-type element which could be made by extrusion at high production rates and in long lengths.

The flowsheet for the extrusion process is relatively simple, as shown in Fig. 6.7. Extrusions were made on a semiproduction scale (approx 520 ft) for whole-block burning studies connected with head-end reprocessing. The materials used were an acicular graphite powder containing 13 wt % Thermax as filler, 28 pph by weight Varcum (prepolymerized furfuryl alcohol) as binder, and pyrolytic-carbon-coated ThC_2 particles as fuel. The mixture was extruded with a piston-type press in 6-ft lengths at a rate of 10 fpm. The reduction ratio (materials chamber cross-sectional area/die cross-sectional area) was 45. The pressure was too low to register on the pressure gage. The extrusions were cured in air on a 24-hr cycle to 250°C, carbonized on a 48-hr cycle to 1000°C, and then heat treated at 1800°C and cut in 30-in. lengths, as shown in Fig. 6.8. Diametral control was good – 0.491 ± 0.002 in. The matrix density was 1.75 g/cm^3, and the particle volume loading was 31%. Some warpage occurred but was not sufficiently severe to prevent insertion into a reference fuel block. Radiography of sections of extrusions

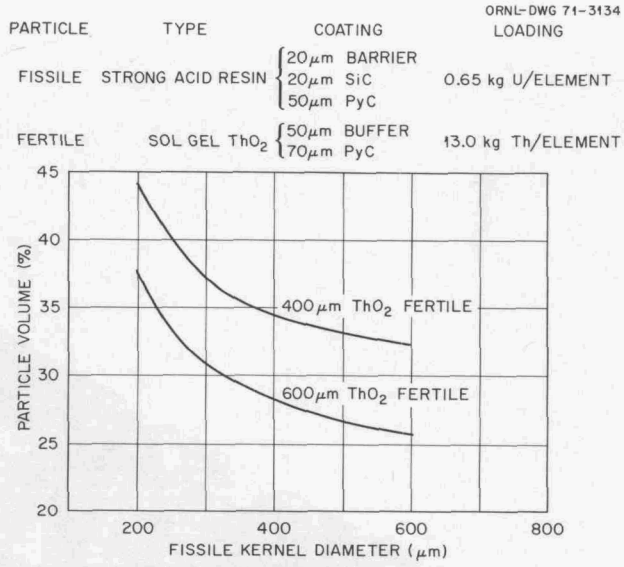

Fig. 6.6. Effect of fissile kernel size on particle volume loading in average HTGR fuel element.

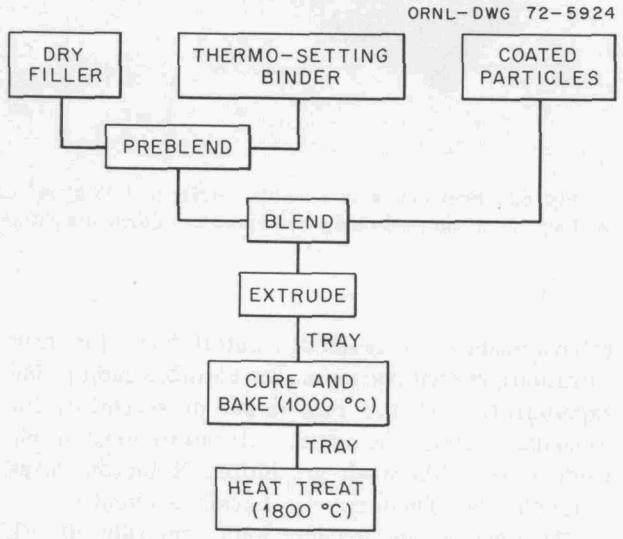

Fig. 6.7. Process schematic for extruding fuel sticks.

indicated good fuel distribution. About one-third of the extrusions were weighed, and the weight of 95% of the rods was within 2% of the mean value, which is also an indication of uniform fuel content from rod to rod. Microstructures of conventional intrusion-bonded rods and extruded elements are compared in Fig. 6.9.

Since this semiproduction project, our efforts have been directed primarily toward increase in particle

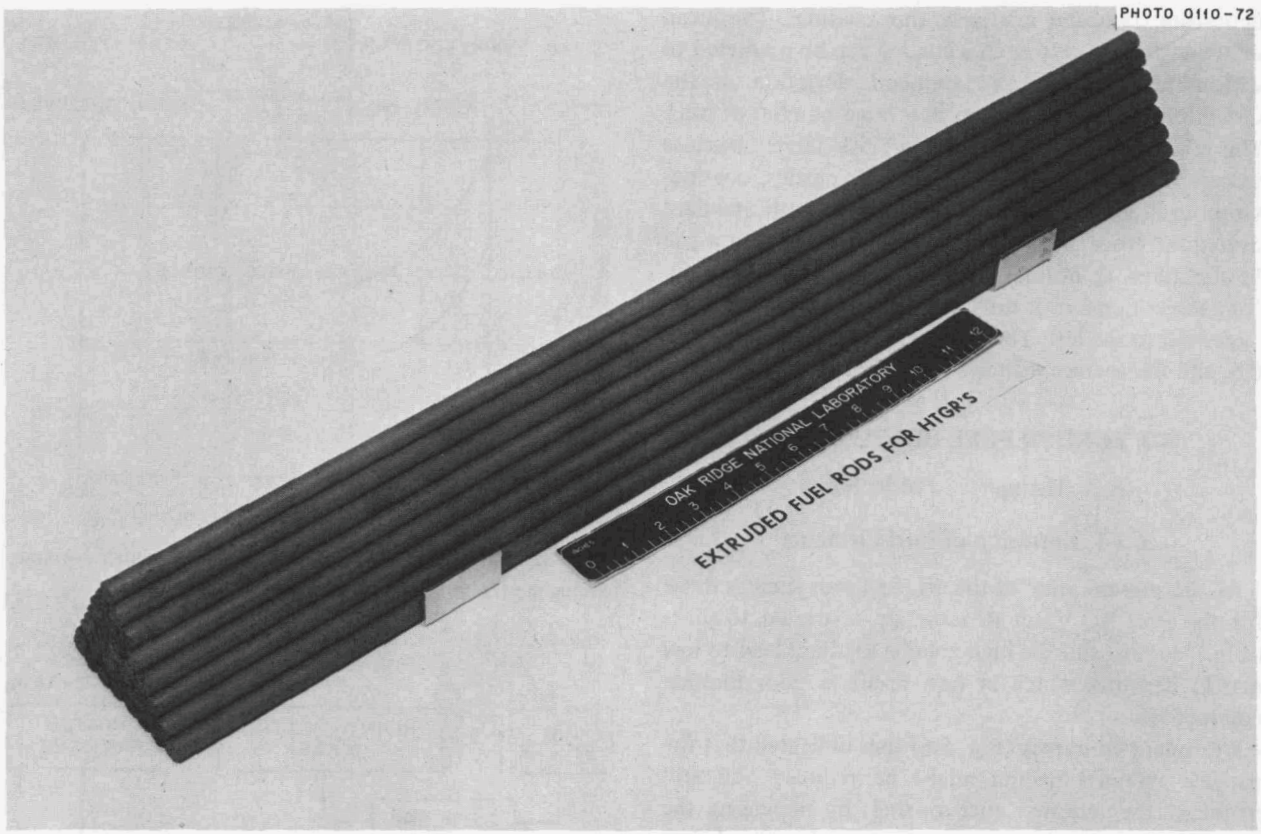

Fig. 6.8. Fuel rods with a matrix density of 1.75 g/cm^3 and particle volume loading of 31% prepared by extrusion. The neat stacking of randomly selected rods demonstrates their straightness and uniformity.

volume loading, the design of a cutoff device for green extrusions, evaluations for broken particles, carbonizing experiments, and the preparation of specimens for irradiation testing. The matrix materials for most of this work were −200 mesh graphitized Robinson cokes containing 24% Thermax with Varcum as a binder.

Attempted volume loadings were nominally 30, 40, 45, and 50%, and the extrusion mixes were deliberately kept slightly "wetter" than unfueled graphite mixes to minimize particle breakage. Preliminary attempts at 50% volume loadings were unsuccessful (i.e., the extrusions were of very poor quality, and the matrix did not compact well). In order to maintain a reasonably constant matrix density, it was necessary to increase the extrusion reduction ratio as the volume loading was increased, as indicated in Table 6.1. At the same time, it was necessary to control the consistency of the extrusion mix (i.e., if the mix was too wet the matrix density was lowered even with an increase in reduction ratio).

Table 6.1. Effect of extrusion reduction ratio on matrix density with increasing volume loadings

Nominal volume loading (%)	Reduction ratio	Matrix density (g/cm^3)
30	45	1.75
30	20	1.63
30	30	1.7
40	30	1.56
40	42	1.7
45	42	1.65

We conducted curing and carbonizing experiments to determine whether the heating schedule could be reduced without detriment to the specimens. Heretofore it has been standard practice to cure at 90°C in air for 16 hr and carbonize to 1000°C on a 24-hr cycle.

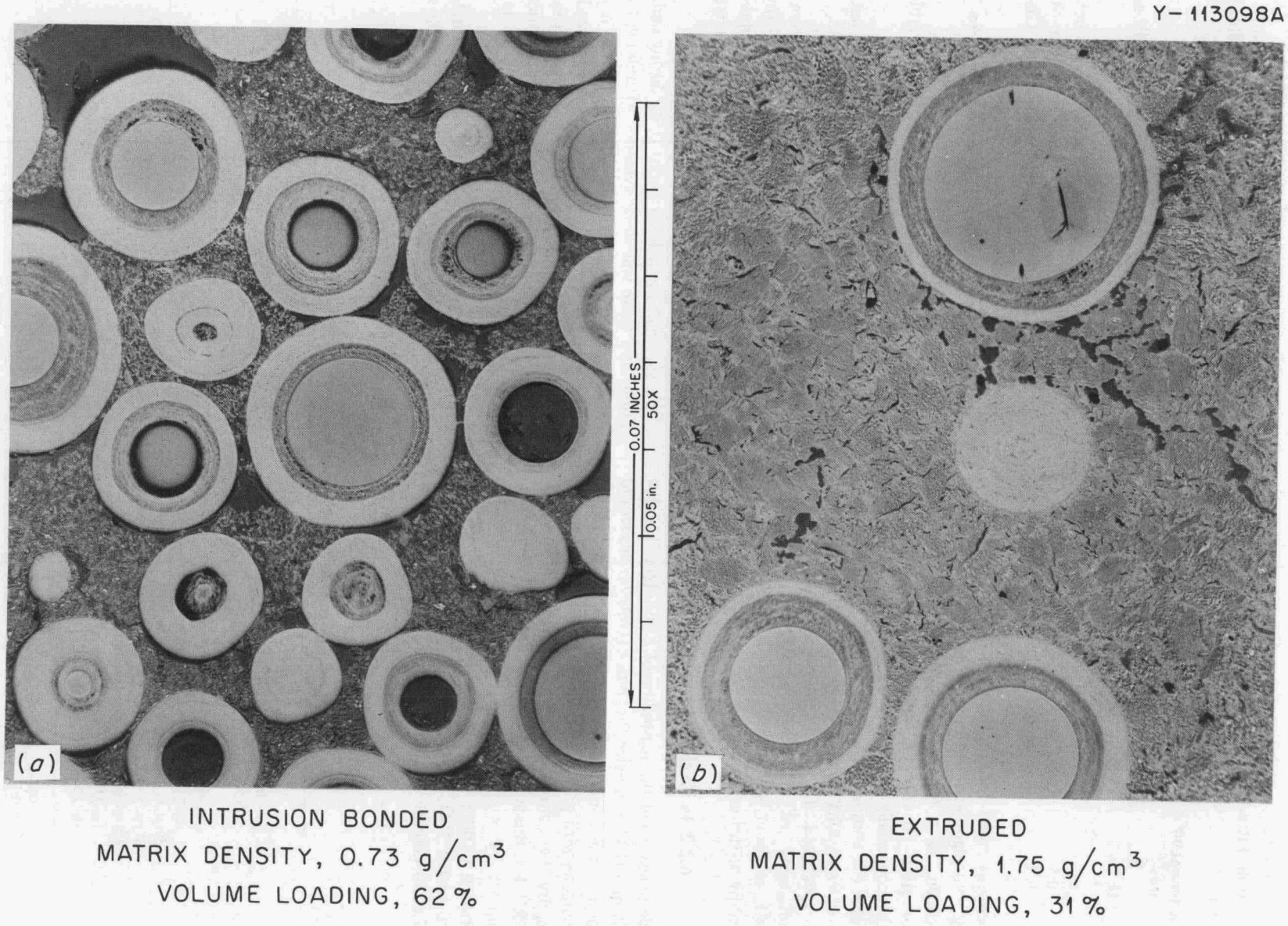

Fig. 6.9. **Bonded fuel rod microstructures.** Reduced 50%.

These rates are prohibitive from the standpoint of production rates. Our experiments included the following:

Curing time at 90°C (hr)	Carbonizing time to 1000°C (hr)
16	3
2	3
1	3
0.5	3
0.0	3

Specimens cured for less than 2 hr were surface cured only. No significant differences were noted between specimens as a function of curing time except that those given no cure and then carbonized on the fast cycle occasionally exhibited axial cracking.

Table 6.2 compares the thermal and electrical properties of extrusions with those of other types of bonded rod specimens. It will be noted that the thermal conductivity of unirradiated extruded material at 400°K is about seven times that for specimens fabricated by intrusion bonding.

6.2.2 In-Block Carbonization Studies

We investigated the feasibility of carbonizing bonded rods in a GGA reference fuel block (H-327); this would eliminate the cumbersome practice of surrounding the specimens with graphite or alumina powder and greatly simplify the carbonizing operation, particularly for the TURF. For this study, specimens nominally 0.490 in. in diameter by 2 in. long were prepared by the slug-injection technique. They contained about 62 vol % of Biso-coated ThO_2 particles in a matrix of 29.7 wt % of NF 6353 graphite powder in 15V pitch. In preliminary experiments the number of specimens per bore (fuel hole) ranged from 1 to 4 but later was increased to 14 per bore. Carbonization was carried out in the following modes:

1. vertical and horizontal bores;
2. specimens restrained by graphite plugs at both ends of the block;
3. specimens unrestrained (i.e., graphite plug touching one end of the stack and a space left at the other end between stack and plug according to GGA's present concept for loading fuel rods);
4. specimens carbonized on a 24-hr cycle and on a 3-hr "fast" cycle to 800°C;
5. specimens carbonized and heat treated in the block to 1800°C;
6. specimens carbonized in bores coated with natural flake graphite powder and in uncoated bores.

Evaluations were based on ease of removal from the bore, appearance of specimens and bores with particular regard for sticking to the block, out of roundness, dimensional changes, and fraction of broken coatings (by metallographic inspection).

The specimens expanded about 0.5% during carbonization, and there was some evidence of sticking to the block at this stage so that they were difficult to remove from the block. However, the specimens carbonized and heat treated to 1800°C in the block had a net shrinkage of about 0.5% and were removed without difficulty. Specimens carbonized in bores coated with natural flake graphite were very easily removed. Figure 6.10 shows a full-length stack of fuel rods after in-block carbonization and heat treatment. In this case the stack

Table 6.2. Thermal and electrical properties of bonded fuel rod specimens

Specimen No.	Method of fabrication	Matrix density (g/cm^3)	Particle volume loading (%)	Electrical resistivity at 295°K ($\mu\Omega$-cm)	Thermal conductivity at 400°K ($W\ cm^{-1}\ deg^{-1}$)
JG-25-1	Intrusion bonding	0.85	62	8178	0.0478
JH-112-1	Warm molding	1.40	44	5875	0.1274
JH-203-1	Warm molding	1.44	37	4714	*a*
JH-105-1	Warm molding	1.45	30	4591	0.1598
JH-212	Extrusion	1.74	29	1780	0.340
JH-296-3	Extrusion	1.81	*b*	1472	0.508

[a]Not measured.
[b]No particles.

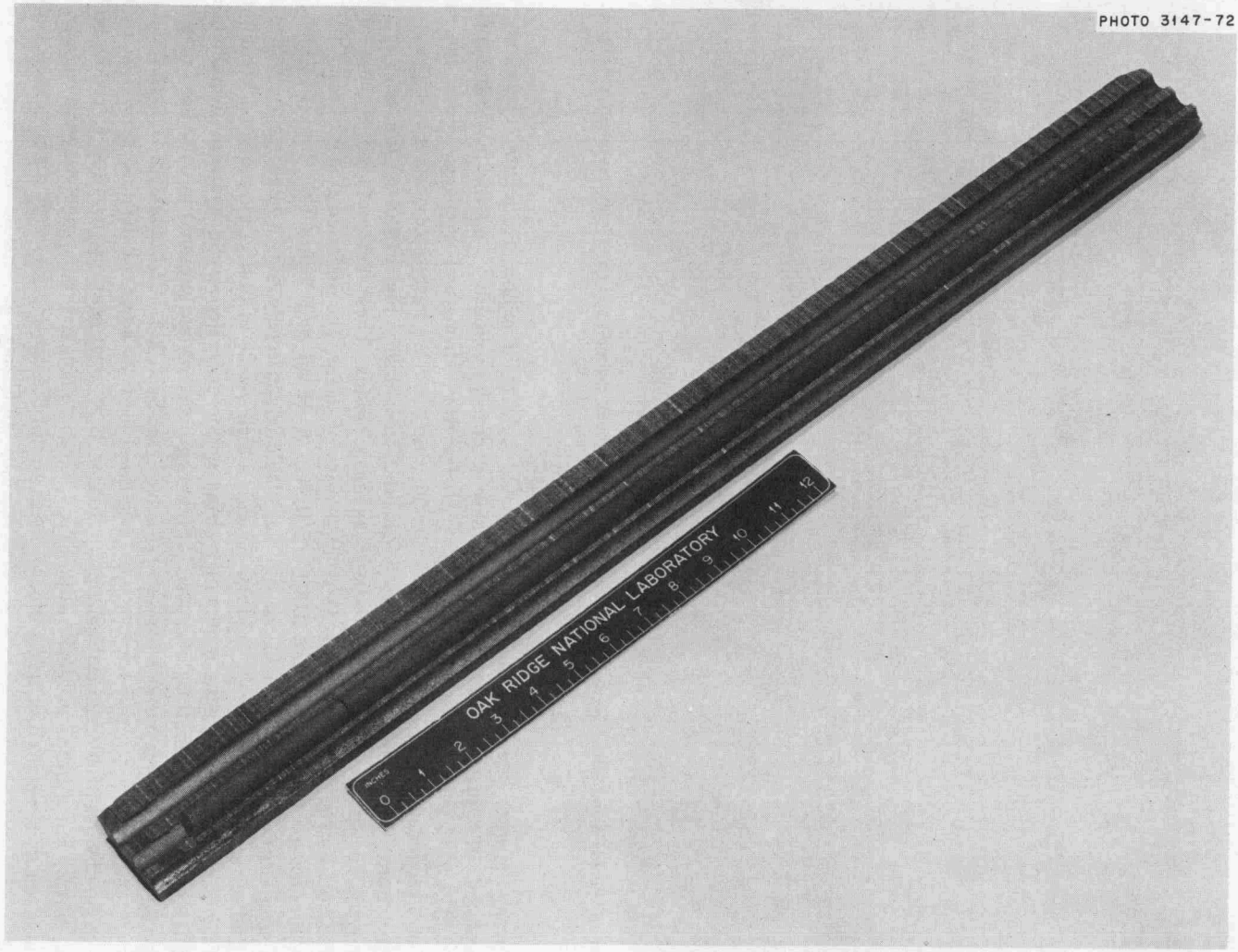

Fig. 6.10. Slug-injected fuel rods carbonized and heat treated in the block.

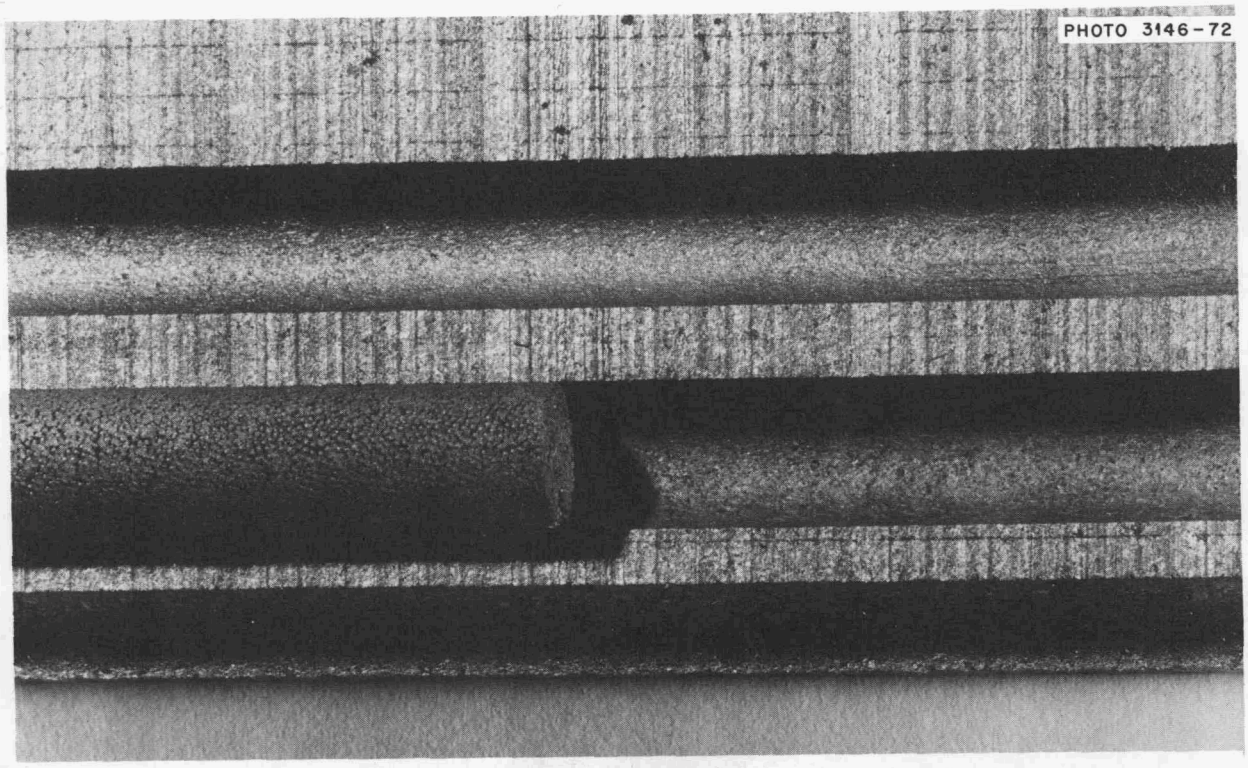

Fig. 6.11. Closeup of specimen and bore (one specimen removed) after in-block carbonization and heat treatment at 1800°C.

was first pushed from the bore, the block sectioned, and the stack replaced. It will be noted that the specimens (2 in. long) tend to stick end to end. Figure 6.11 is a closeup of a sectioned block showing part of the stack and the bore from which an adjacent specimen was removed. The specimens appeared to be undamaged, and the bore looked relatively clean. Most out-of-roundness values for specimens were about 0.001 in. There was no significant difference in behavior of specimens carbonized vertically or horizontally, and the heating cycle had no apparent effects on the results of carbonization. Metallographic examination of specimens showed no broken coatings after in-block carbonization.

There seems to be no obvious problem in carbonizing fuel rods in the block, but further in-block work directed toward in-block carbonization of larger block sections is planned.

6.3 RESIN PARTICLE DEVELOPMENT

C. B. Pollock M. D. Silverman

Fuel particles formed from cation exchange resins are attractive because of simplicity of fabrication and easier quality control in remote fabrication operations. We have reported previously[12] on the fabrication of fuel particles from strong-acid exchange resins and early irradiation tests. We have since developed a process for making high-quality fuel particles from weak-acid ion exchange resins. These are preferred because of the absence of sulfur. The preferred grades of resin, IRC-72 (Rohm & Haas) and Relite CC (Ionac), which are available commercially over a large range of sizes and with a high degree of purity, are prepared by polymerizing acrylic or methylacrylic acid with divinylbenzene. Loading problems encountered initially have now been solved (see Sect. 2.4). Carbonization is carried out in a fluidized bed in argon by heating slowly to 600°C; further heat treatment up to 1800°C produces fuel kernels containing uranium oxide, uranium carbide, or a mixture of the two species in a matrix of excess carbon. Various fluidizing gas media have been tested to determine their effect on surface area, to seal the particle surfaces and thereby prevent pyrophoricity,

12. C. B. Pollock, "Resin Particle Development," *GCR-TU Programs Annu. Progr. Rep. Sept. 30, 1971*, ORNL-4760, pp. 96–100.

and to examine possible production of other fuel species.

6.3.1 Kernel Fabrication

Detailed descriptions of the processes used to load ion exchange beads with uranium are given in Sect. 2.4, along with a detailed breakdown of the various loadings. In summary, two kinds of resin (Dowex 50W-X8 and Amberlite IRC-72) were loaded, mostly with normal uranium, but some with ^{233}U. (During the previous reporting period, ^{235}U was also loaded.) A total of 18.4 kg (110°C dried weight) of loaded resin was prepared for further carbonization experiments and for the preparation of irradiation test elements. This included 12.3 kg of Dowex, 5.5 kg of Amberlite, and 650 g of Amberlite loaded with ^{233}U. Most of this material was loaded to 100% capacity, but some Amberlite was loaded to 50 and 75%. Small quantities of special test materials loaded with thorium, mixed thorium-uranium, and strontium were prepared.

6.3.2 Carbonization Studies

Preliminary scouting experiments were undertaken to ascertain the temperature range in which the loaded resins decomposed, lost weight, and emitted various gaseous species. For investigative purposes, three types of instruments were employed: the differential thermal analyzer (DTA), the thermogravimetric analyzer (TGA), and the gas chromatograph. In the DTA apparatus, a known weight of uranium-loaded resin was heated in an inert atmosphere (argon) from room temperature to some higher temperature at a controlled heating rate, usually 3 to 5°C/min. A standard of plain carbon spheres was heated similarly at the same time.

In the TGA apparatus, a known weight of uranium-loaded resin was heated at a controlled rate in an inert atmosphere and the loss in weight continuously monitored.

Separate samples of loaded resin were heated and the gaseous products passed through the gas chromatograph. Water, CO, and CO_2 were definitely noted, along with mixtures of light unsaturated hydrocarbons.

The DTA and TGA curves were obtained by heating samples of the uranium-loaded resins (IRC-72 and Relite CC) at a controlled rate (3 to 5°C/min) in an inert atmosphere. A typical DTA curve for uranium-loaded IRC-72 is shown in Fig. 6.12. The following distinctive features may be noted: a broad endothermic region between 100 and 200°C with a minimum at about 150°C; a small endotherm between 300 and 400°C with a rather sharp minimum at about 340°C; a broad exotherm from 350 to 450°C with a distinctive peaking at about 420°C; and finally, another endothermic region from 450 to 440°C with a minimum near 500°C.

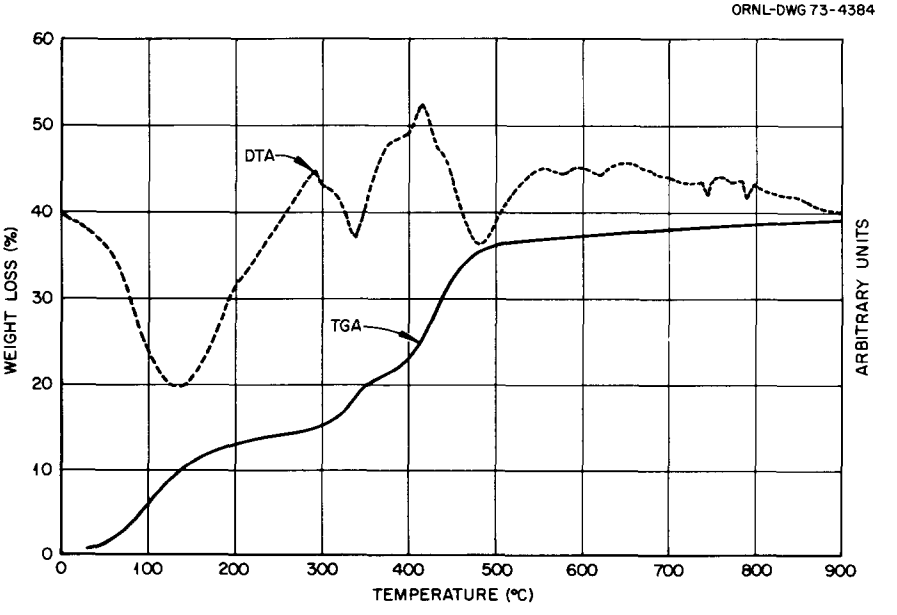

Fig. 6.12. Carbonization of uranium-loaded weak-acid resin (IRC-72).

A typical TGA curve is also shown in Fig. 6.12. The resin loses approximately 10% by weight in the 100 to 200°C range, coinciding with the first broad endotherm noted on the DTA curve. An approximately 8% weight loss between 300 and 400°C coincides with the second, or smaller, DTA endotherm. An additional 15% loss in weight occurs in the 400 to 500°C range, which includes the exotherm peak at 420°C and the broad endothermic region at 480°C on the DTA curve. Finally, a small weight loss takes place very gradually on further heating from 500 to 900°C, a region in which the DTA curve shows very little character.

Data from the TGA and DTA experiments were used as guides to plan a series of low-temperature (600 to 1000°C) carbonization experiments to determine the temperature range for satisfactory carbonization, confirm the reproducibility of the carbonization cycle, and better define the precision obtained from chemical analyses of these materials, which are mildly pyrophoric and must be handled under a cover gas. The data and results from these experiments are listed in Table 6.3. The tap densities and the uranium analyses both confirm the different uranium loadings of the two batches. The overall composition of the carbonized microspheres, after heating to 1000°C, is approximately UO_{2+x} + 5C.

Heretofore, chemical analyses have not always shown good reproducibility, especially with respect to oxygen, and material balances have not been satisfactory. Analyses for uranium and carbon are of the gravimetric type. Uranium, on ignition, is converted to and weighed as U_3O_8; the precision of this analysis is estimated to

Table 6.3. Carbonization of weak-acid (IRC-72) uranium-loaded resins

Furnace run No.	Final temperature[a] (°C)	Time at temperature[b] (hr)	Tap density[c] (g/cm³)	Analysis (wt %)		
				U	O	C
		Batch 38-IR[d]				
A6541-49	600		2.8	66.2	13.6	19.6
A6541-49A	1000		2.9	68.4	11.5	19.6
A6541-28	1000		3.0	68.4	9.5	19.4
A6541-29	1000		3.1	68.0	9.3	
A6541-33	1000		3.0	67.8	8.9	
A6541-35	1000			70.2	10.2	
A6541-38	1000		3.2	69.6	10.7	
A6541-41	1000		3.1	68.6	11.8	
A6541-47	1000			67.9	8.6	
A6541-56	1000	3	3.2	69.7	10.2	18.8
		Batch 51-IR[d]				
IE-25	750	0.5	3.8	73.2	11.1	15.8
IE-26	750	0.5	3.6	72.2	10.8	16.6
IE-27	750	0.5	3.9	74.8	8.9	16.1
IE-28	1100	0.08	4.0	73.8	9.9	15.2
IE-29	750	0.5	3.7	72.3	10.1	17.4
IE-30	750	0.5	3.8	73.3	10.4	16.0
IE-44	938	0.5	3.9	72.0	11.2	16.0
IE-45	650	0.5	3.5	72.3	10.6	16.4
IE-46	1100	0.5	3.9	73.8	10.6	15.4
IE-47	715	0.5	3.5	70.3	13.0	16.8
IE-48	750	0.5	3.7	72.2	12.6	15.7

[a]Temperature was raised at rate of about 200°C/hr in all experiments, with helium as the fluidizing gas at 3 liters/min.

[b]Where no time is given, the experiment ended when the listed temperature was reached.

[c]BET surface area values ranged from 63 to 87 m^2/g.

[d]Starting materials were from two different batches: 38-IR was loaded to 42.8% U; 51-IR was loaded to 44.4% U.

be equal to or better than 1%. Also, upon ignition, carbon is converted to CO_2, which is absorbed by Ascarite and weighed; any CO formed is converted to CO_2 by reaction with CuO. This analysis is considered to be precise to ±2 to 3%. The oxygen analysis is obtained by performing an inert-gas fusion (Leco instrument) and measuring the CO_2 formed by a gas chromatograph. The precision of this analysis is considered to be no better than 6 to 7%, and early analyses tended to verify this conclusion. Furthermore, on samples of low oxygen content (≤5%), errors were even larger, indicating insufficient amount of sample. An alternative analysis which is not limited by sample size and which is based on a fusion technique developed at Los Alamos yielded results no more precise than those obtained by the Leco technique. Hence, unless the oxygen content is too low, the Leco instrument (sample size limited to 100 mg) is preferred.

Material balances of 98 to 103% were originally obtained for some of the experiments listed in Table 6.4. We examined the results in some detail and determined the major problem areas to be sampling,

Table 6.4. Heat treatment of weak-acid (IRC-72) uranium-loaded resins

Furnace run No.[a]	Final temperature[b] (°C)	Tap density (g/cm³)	BET surface area (m²/g)	Composition (wt %)			Mole ratio		Predicted[c] (wt %)		Observed[d] (wt %)		
				U	O	C	U/O_x	U/C_y	UO_2	UC_2	UO_2		UC_2
Batch 38-IR													
A6541-59	1200(2)	3.1		70.0	7.6		1.6		99	1	100		
A6541-60	1300(2)	3.2		70.2	8.2	18.9	1.7	5.3	87	13	90		10
A6541-65	1400(1)	3.1		71.1	8.3	19.0	1.7	5.3	63	37	90		10
A6541-67	1400(1)	3.1		73.0	7.6		1.5		75	25	70		30
A6541-71	1400(2)	3.4		74.9	10.9	16.2	2.2	4.3		100	50	25	25
A6541-74	1400(3)	3.0	78	74.0	8.1	16.0	1.6	4.3		100	30	30	40
A6541-77	1400(3)	3.0	165	77.2	4.5	17.5	0.9	4.5		100	30	30	40
A6541-10	1600(2)	3.6	76	84.1						100	<5		>95
A6541-8	1600(1)/1800(1)	3.2	33	84.7						100	<5		>95
Batch 46-IR													
A6541-80	1400(1)	3.2	158	72.1	7.6	18.9	1.6	5.2	75	25	55	5	40
A6541-83	1400(2)	2.8		73.0	7.0	19.0	1.4	5.2	50	50	60	10	30
A6541-86	1400(3)	3.1	160	74.3	5.9	18.5	1.2	4.9	25	75	45	10	45
Batch 51-IR													
IE-31	1210(0.5)	3.7	106	73.4	10.0	16.4	2.0	4.4	100		100		
IE-34	1225(1)	3.7					2.3	4.3	100		100		
IE-32	1415(0.5)	3.7	121	74.1	9.4	16.0	1.9	4.3	91	9	95		5
IE-35	1400(1)	3.7	124	74.2	9.8	16.2	2.0	4.3	81	19	95		5
IE-39[e]	1400(1)	3.7	127	74.4	9.1	16.1	1.8	4.3	94	6	90		<5
IE-52	1400(2)	3.7	137	76.5	8.2	15.5	1.6	4.0	63	37	70		30
IE-53	1400(3)	3.8	130	75.3	9.6	15.3	1.9	4.0	44	56	75		25
IE-33	1620(0.5)	3.7	109	77.8	7.4	14.4	1.4	3.7	7	93	50		50
IE-36	1600(1)	3.9	111	81.2	4.2	14.5	0.8	3.6		100	50		50
IE-40	1600(1)	3.8	126	79.9	4.7	14.7	0.9	3.7		100	70		30
IR-42[e]	1600(2)	3.7	135	76.3	7.5	16.2	1.5	4.1	7	93	70		30
IE-50	1600(3)	5.4	25	89.2	0.15	10.6	0.03	2.4		100	<5	5	95
IE-51	1700(1)	5.7	22	89.7	0.10	10.2	0.02	2.3		100	<5	5	95
IE-38	1800(1)	5.2	31	89.0	1.39	10.7	0.2	2.4		100	<5	10	90
IE-54	1800(2)	5.1	27	89.5	<0.10	10.5	<0.02	2.3		100	15[f]		85

[a]Helium flow of 3 liters/min employed for the fluidizing gas for batches 38- and 46-IR; argon used for batch 51-IR. Starting materials were from three different batches: 38-IR was loaded to 42.8 wt % U; 46-IR was loaded to 42.9 wt % U; 51-IR was loaded to 44.4 wt % U.

[b]Temperature raised at rate of 200°C/hr to 600°C in all experiments, then raised directly (≤15 min) to the listed value, where it was kept for the noted times (hours in parentheses), except for run 5, where the temperature rose directly from room temperature to 1360°C within 1 hr.

[c]Calculated from CO pressure, heating time, temperature, and gas flow rate.

[d]Estimated from powder pattern x-ray analyses. Where three sets of figures are listed, the middle one is the estimated UC phase.

[e]Unusually large charge of material limited CO stripping.

[f]Sample contaminated during handling.

proper protection of the samples, and the oxygen analysis. The first two problem areas were resolved by better defining sampling and analytical procedures. The latter was resolved as indicated above. Subsequent tests, in which the above refinements were used, also shown in Table 6.4, yielded material balances of 100 ± 1%.

6.3.3 Effect of Heat Treatment on Composition

After carbonization, the microspheres are "heat treated" at elevated temperatures (1000 to 2000°C) to prepare the fuel kernels. Conversion of uranium dioxide to uranium carbide occurs readily above 1300°C by the reaction

$$UO_2 + 3.86C \rightleftharpoons UC_{1.86} + 2CO\,. \qquad (1)$$

The extent of the reaction is time and temperature dependent. Since CO is removed by the fluidizing gas stream, the reaction will proceed to completion unless the CO pressure is fixed in the fluidizing gas.

Lindemer[13] has suggested that the addition of some carbide to an oxide kernel will lower the rate of amoeba migration by reducing the rate of carbon transport as a result of fixing the CO pressure in equilibrium over the carbide phase. Approximately 1% carbide is required per 10% burnup of the fissile atom under irradiation according to the model.

We prepared various mixtures of UO_2 and UC_2 in excess carbon by varying both the heating temperature and the length of heating. This transformation of uranium oxide to carbide was studied by following the changes in composition analytically and by x-ray-diffraction powder pattern analysis. The results of these experiments are given in Table 6.5. The last column lists the calculated production of uranium carbide, based on the heating temperature, time of heating, and the

13. T. B. Lindemer, "Fuel Migration Studies," *GCR-TU Programs Annu. Progr. Rep. Sept. 30, 1971*, ORNL-4760, pp. 112–13.

Table 6.5. Effect of additives in fluidizing gas on heat treatment of weak-acid (IRC-72) uranium-loaded resins

Furnace run No.	Fluidizing gas plus additive[a] (atm)	Final temperature[b] (°C)	Tap density (g/cm³)	BET surface area (m²/g)	Analysis (wt %)			Mole ratio		Observed x-ray analysis (wt %)		
					U	O	C	U/O_y	U/C_z	UO_2		UC_2
				Batch 46-IR								
91	He/CO, 7×10^{-3}	1400(4.5)	2.90	150	69.9	10.9	19.6	2.2	5.3	100		
93	He/CO, 7×10^{-3}	1400(4.5)	3.13		69.9	11.2	19.5	2.3	5.3	100		
95	He/CO, 3×10^{-2}	1400(4.5)	3.24	158	70.0	11.3	19.4	2.3	5.3	100		
				Batch 51-IR								
58[c]	H_2	1400(1)	3.7	136	76.4	12.7	10.4	2.5	2.7	85		15
56[c]	H_2	1600(1)	4.4	24	89.6	0.12	10.1	0.02	2.3	15		85
55[d]	N_2	1600(1)	3.7	119	79.3	8.2	12.4	1.6	3.1			
57[d]	Ar, N_2	1600(1)	3.6	128	82.2	2.0	10.9	0.4	2.6	5		15
	0.5, 0.5					$4.6N_2$		1.0			80(UN)	
37[e]	Ar, C_2H_2	1800(1)	3.7	4.8	73.4	9.1	17.3	1.8	4.7	90		5–10
	0.98, 0.02	1550(0.25)										
49[e]	Ar, C_2H_2	1800(1)	5.0	1.2	87.7	0.8	12.2	0.1	2.8	<5		95
	0.98, 0.02	1500(0.2)									5(UC)	?
41[e]	Ar, C_2H_2	1800(2)	4.1	49	80.9	4.8	14.3	0.9	3.5			
	0.98, 0.02	1600(0.25)										

[a] Fluidizing gas flow of 3 liters/min employed.

[b] Temperature raised at rate of 200°C/hr to 600°C in all experiments, then raised directly (≤15 min) to the listed value, where it was kept for the noted time (hours in parentheses).

[c] Hydrogen used as fluidizing gas to accelerate process.

[d] Nitrogen used as fluidizing gas to initiate nitride formation.

[e] Acetylene added to fluidizing gas at 1550°C before heat treatment at 1800°C in run 37; in run 41, C_2H_2 added at 1600°C before heat treating at 1800°C; in run 49, C_2H_2 added at 1500°C *after* heat treating particles at 1800°C.

carbon monoxide pressure from reaction (1). In most cases, the agreement with the x-ray estimates is quite good. However, when longer heating times are employed, complete conversion of the oxide to the carbide at 1400°C is not accomplished, even though calculations indicate it should be. Sintering of the particles[14] at 1400°C may be responsible for incomplete conversion, since short heating times at 1600 and 1800°C do convert the oxide to the carbide completely, as indicated by our x-ray analyses.

6.3.4 Sealing of Surface Porosity in Kernels

Since the microspheres obtained after heat treatment to 1000°C are mildly reactive with air, experiments were directed toward sealing the surface of the particles by introducing small quantities of acetylene into the fluidizing gas. The results are shown in Table 6.5. The BET surface area was reduced from about 130 m^2/g to less than 5 m^2/g by this technique, and the expected change in fuel species from the oxide to the carbide which occurs during heat treatment was apparently stopped by sealing the surface. For example, in run 37, exposing the microspheres for 15 min to 0.02 atm of acetylene (in argon) at 1550°C, before heat treatment at 1800°C, resulted in only about 10% conversion of uranium oxide to uranium instead of the total conversion normally expected (see runs 10, 8, 51, and 38, Table 6.4). Similar results were obtained in experiment 41. However, when another portion of the same material was first heated to 1800°C for 1 hr and afterward sealed with acetylene at 1600°C, the uranium oxide phase was completely converted to uranium carbide, and the BET surface area was reduced still further, to about 1 m^2/g. The surface area of the microspheres apparently reaches a maximum value between 1400 and 1600°C (130 to 160 m^2/g) and drops markedly above 1600°C (i.e., to about 30 m^2/g), along with a concurrent increase in the density of the particles. This effect can be produced in a shorter time at 1600°C using hydrogen as the fluidizing gas (run 56). Particles heat treated above 1200°C showed no reaction with air in cursory preliminary tests.

14. T. B. Lindemer, *Nucl. Appl. Technol.* 9, 711 (1970).

6.3.5 Coating of Resin-Derived Kernels

Fuel particles from ion exchange resins are composed of the fuel phase uniformly distributed over a low-density carbon matrix. The density of the matrix and the void volume in the kernel vary significantly with heat treatment and resin type. The STRETCH code[15] and the TRISO code[16] are used to model behavior of the fuel particles during their reactor life and have been used to design coatings on resin-derived particles. The enclosed void volume in the kernel can be used to accommodate fuel swelling and gas release, and the apparent refractory behavior of the sulfide phases may allow us to operate at higher temperatures.

We prepared a series of coated particles for the irradiation experiment HRB-3 from strong-acid ion exchange resins. The kernels were fully loaded with partially enriched uranium and then partially converted to the carbide state. Since particles were judged to contain sufficient void volume in the kernel for the proposed exposure, the particles were coated with Triso coating with no buffer. The performance of these particles is discussed in Sect. 7.1. We experienced considerable difficulty with cracking of the SiC in metallographic preparation, but it behaved in a very satisfactory manner. Several other particles of this type were prepared for irradiation experiments. Fuel particles from weak-acid resins were used in irradiation experiments HRB-4 and HRB-5. In this case, we decided to include a 40-μm buffer in the particle design because the fuel density is much higher and the void volume lower. Again, the kernels were partially converted to the carbide. The coating operations were found to be entirely equivalent to those for other types of fissile particles, such as sol-gel oxides, except that the buffer coatings are much thinner. The thinner buffer greatly reduces the problems associated with bed volume increases during a coating run.

15. J. W. Prados and J. L. Scott, *Mathematical Model for Predicting Coated Particle Behavior*, ORNL-TM-1405 (March 1966).

16. J. L. Kaae, "A Mathematical Model for Calculating Stresses in a Pyrocarbon and Silicon Carbide Coated Fuel Particle," *J. Nucl. Mater.* 29, 249–66 (1969).

7. HTGR Fuel Irradiations and Postirradiation Evaluations

J. A. Conlin J. H. Coobs W. P. Eatherly F. J. Homan J. L. Scott

The HTGR irradiation test program at ORNL involves many capsule irradiations in test reactors and a series of pilot-scale irradiations in test elements in the Peach Bottom Reactor. The program has three main objectives: (1) to evaluate the performance of candidate fuels and to test performance models, (2) to proof test recycle fuels produced in prototype equipment, and (3) to provide irradiated fuel for head-end processing studies. Test conditions include fuel temperatures between 600 and 1500°C and fast-neutron fluences up to and exceeding the design maximum HTGR exposure of 8×10^{21} neutrons/cm^2 ($E > 0.18$ MeV). The experiments are designed to produce fuel burnup to about 12% FIMA in ThO_2 fertile fuels, about 25% FIMA in $(Th,U)O_2$ mixed fuels, and >50% FIMA in enriched UO_2 and UC_2 fissile-particle fuels. The test reactors used include the HFIR, the ORR, and the ETR, although no further testing in the ETR is planned due to the scheduled shutdown of the reactor in 1973. The experiments completed and reported and those in progress are listed and described in Table 7.1.

7.1 IRRADIATION TESTS IN THE HFIR REMOVABLE BERYLLIUM FACILITY

B. H. Montgomery J M Robbins
R. L. Hamner

One type of HFIR irradiation experiment consists of instrumented and gas-swept capsules that are operated in the HFIR removable beryllium (HRB) facility.[1] These capsules are of moderate size (1.3 in. diameter) and have provisions for specimen temperature control by gas mixing and monitoring of fission gas release by analysis of gas samples. The capsules accommodate fuel specimens in a graphite support sleeve that is geometrically representative of a single fuel channel of a large HTGR fuel element. Fuel loading, temperature, power density, and burnup rate are limited only by the capability of the fuel.

Previously, only one such facility was available using the RB-5 hole in the HFIR removable beryllium facility. During this report period we have opened up a second such facility using the RB-7 hole. This second facility, identical in all respects to the first, permits us to double the number of specimens irradiated in a given time period.

7.1.1 Capsule HRB-2

Examination of specimens and evaluation of the results from this capsule were completed. A report was issued that presents the results and conclusions from this experiment.[2]

7.1.2 Capsule HRB-3

The objectives and the capsule configuration for the HRB-3 experiment were reported previously.[3] Briefly,

1. H. C. McCurdy et al., "Instrumented Capsules for Fuel Test in HFIR," *GCR Program Semiannu. Progr. Rep. Sept. 30, 1969*, ORNL-4508, pp. 27–37.

2. J. H. Coobs et al., *Irradiation Performance in HFIR Experiment HRB-2 of HTGR Fuel Sticks Bonded with Reference and Advanced Matrix Materials*, ORNL-TM-3988 (January 1973).

3. W. P. Eatherly et al., "Design and Preparation of Irradiation Experiments," *GCR-TU Programs Annu. Progr. Rep. Sept. 30, 1971*, ORNL-4760, pp. 114–15.

Table 7.1. Description and status of HTGR irradiation experiments

Experiment	Specimen description	Maximum fast fluence (neutrons/cm^2)	Maximum particle temperature (°C)	Maximum burnup (% FIMA)		Irradiation schedule	
				Fissile particles	Fertile particles	Start	End
		x 10^{21}					
HRB-2	Various loose coated particles Experimental fuel rods bonded with various filler materials FSV production-type fuel rods	10	1200	30	15	12/70	11/71
HRB-3	Warm-molded fuel rods with resin-derived and ThO_2 particles Experimental fuel rods made by slug injection Experimental fuel rods prepared by GGA	9	~1500	28	15	1/72	10/72
HRB-4	Continuous-matrix fuel rods made by extrusion Experimental fuel rods made by slug injection Experimental fuel rods prepared by GGA	10	1250	30	15	10/72	6/73[a]
HRB-5	Continuous-matrix fuel rods made by extrusion Experimental fuel rods made by slug injection Experimental fuel rods prepared by GGA	5	1250	16	4.8	10/72	2/73[a]
HRB-6	Experimental fuel rods made by extrusion Experimental fuel rods prepared by GGA Experimental fuel rods made by slug injection Loose coated sol-gel and resin-derived particles	8	1250	23.8	9.7	2/73[a]	9/73[a]
HT-7	Various loose coated particles with inert kernels	9.6	1050			12/70	3/71
HT-8	Various loose Triso-coated particles from resin-derived kernels Intrusion-bonded rods with Triso-II coated inert kernels Loose Biso- and Triso-coated particles from GGA Experimental bonded rods from GGA	9.6	1050	19.4	9.7	5/71	8/71
HT-9	Various loose Triso-coated particles with inert kernels	5	1050			3/71	5/71
HT-10	Various loose Triso-coated particles with inert kernels, reirradiated from HT-9	14	1050			8/71	12/71
HT-11	Test canceled						
HT-12		4	1250		2.9	9/72	10/72
HT-13	Biso-coated sol-gel-derived ThO_2, coated at ORNL	9	~1550		9.7	10/72	1/73
HT-14	Biso-coated sol-gel-derived ThO_2, coated at GGA	13	~1550		17.3	12/72	4/73
HT-15		16	~1550		21	12/72	5/73
HT-16	Various carbon coatings on carbon substrates Carbon-coated Eu_2O_3	14	715			2/73[a]	7/73[a]
CI-28	Experimental fuel rods made by intrusion Various loose coated particles	1.5	1000	10		8/71	12/71
H-1	Bonded rods of main four RTE particle combinations	8	>1800	51	<1	6/71	5/72
H-2	Various loose coated particles				<1		
P-13N	Warm-molded fuel rods with resin-derived and ThO_2 particles	5	1500	>30		11/71	2/73
43-105	Various carbon coatings on $(Th_{0.97}{}^{235}U_{0.03})O_2$	6	1400		15	6/67	8/71
RTE-4	Large-scale tests of loose and bonded fuels; six fissile and three fertile particle types in ten combinations	1.5	1220	>25	<1	7/70	4/72
RTE-7		1.0	1220	15	<1	7/70	4/71

[a]Scheduled.

the capsule was designed to test 15 fuel rod specimens to exposures exceeding the design maximum fluence of 8×10^{21} neutrons/cm^2 ($E > 0.18$ MeV) at average fuel temperatures of about 1200°C. The specimens consisted of continuous-matrix fuel rods fabricated by molding, slug-injected fuel rods, and intrusion-bonded rods prepared by GGA. All specimens contained Triso-coated fissile and Biso-coated ThO_2 fertile particles.

Capsule HRB-3 design. The design of this capsule was similar to that of the second capsule of the series, HRB-2. The capsule, shown in Fig. 7.1, was a double-walled water-cooled stainless steel vessel 1.292 in. OD and 0.967 in. ID. The fuel specimens consisted of a series of 0.490-in.-diam bonded fuel rods having a total stack length of 15.3 in. and were supported in a one-piece sleeve made of Poco graphite, grade AXF-5Q. Design test conditions (1250°C peak fuel temperature and 700°C in the graphite wall at 5.5 kW/ft fission heat rate) were intended to match conditions typical of an HTGR.

Temperatures were monitored by nine sheathed 0.062-in.-diam thermocouples (eight Chromel P–Alumel and one W–3% Re vs W–25% Re) and one bare-wire W–3% Re vs W–25% Re central thermocouple. The stainless-steel-sheathed thermocouples were coated with a 0.005-in.-thick protective barrier of chemically vapor-deposited tungsten and were located in axial holes in the graphite sleeve adjacent to the fuel specimens (Fig. 7.2). The central thermocouple lead wires were threaded through a two-hole 0.062-in.-diam BeO insulator. The junction and lower 2 in. of the insulator were shielded from the fuel surface by three layers of 0.0025-in.-thick rhenium foil. The upper fuel specimens, 1A to 1F (see Fig. 7.2), had a 0.090-in. central hole for this thermocouple. Titanium and iron flux-monitor wires, enclosed in three platinum tubes, were located in the graphite sleeve in axial holes similar to those for the thermocouples. The graphite sleeve and the fuel specimen were continuously swept with a 3600-cm^3/hr high-purity helium-neon gas mixture at 1 to 2 atm. Gas samples of the sweep effluent were taken periodically for fission gas release determinations.

The fuel loadings were increased at the lower end of the capsule to compensate for the lower neutron flux and in the upper end for the loss of the volume created by the central thermocouple hole. Because of the high thermal flux in the HFIR-RB facility, the ^{235}U is consumed rapidly (50% in about 16 days at the reactor midplane). To provide for more continuing fission power, the fuel specimens were also loaded with ^{238}U, which converts to fissile material by neutron capture.

The capsule was designed to obtain reasonably uniform axial temperatures by tapering the graphite sleeve so as to increase the graphite-to-capsule-wall gas gap, thus varying the thermal resistance between the graphite sleeve and water-cooled capsule inversely with the calculated initial axial power. To compensate for overall power variations with time, the composition of the helium-neon sweep gas mixture which occupies the gap was varied to maintain the peak fuel temperature at the design level.

Preparation of test specimens. Four types of warm-molded continuous-matrix specimens (11 specimens) were required for the experiment. Two of the types were nominally 0.490 in. OD, 0.091 in. ID, and 0.75 in. long with two different volume loadings, 32.5 and 41.5 vol %. The other two types were similar except that they were prepared as solid cylinders. The coated particles used were Triso-coated UCS derived from strong-acid resin, Biso-coated sol-gel ThO_2, and Triso- and Biso-coated inert carbon particles derived from strong-acid resins. All were heat treated at 1800°C before incorporation in the specimens. The characteristics of these particles are given in Table 7.2. The matrix materials consisted of 53.5 wt % GLC 1074 graphite powder, 15 wt % Thermax, and 31.5 wt % Ashland grade 240 pitch. All components were slurry blended in a mixture of toluene and acetone. After evaporation of the volatiles, the mix was pressed in a steel die at 165°C and 100 psi. The specimens were then carbonized at 1000°C in a packed bed of graphite powder and heat treated at 1800°C. The matrix densities of all types were about the same, averaging 1.48 g/cm^3.

Three slug-injection bonded rods prepared for testing contained the same fissile and fertile particles as the molded rods. Two rods prepared by GGA were also irradiated. The whole column of specimens is described in Table 7.3.

Capsule HRB-3 operation. Capsule HRB-3 was inserted in the removable beryllium facility (RB-5) on January 6, 1972, and was irradiated for 11 HFIR cycles, or 253.75 days at 100 MW reactor power. The irradiation was completed and the capsule removed as scheduled on October 4, 1972. Capsule operation was stable throughout the irradiation, and all test parameters were within design limits. There was, as expected, an initial drop in power as the ^{235}U was consumed, followed by a gradual power buildup which varied with time, axial position, and fuel loading. This is shown graphically in Fig. 7.3, which presents the calculated fission power generated by two specimens near the reactor horizontal midplane.

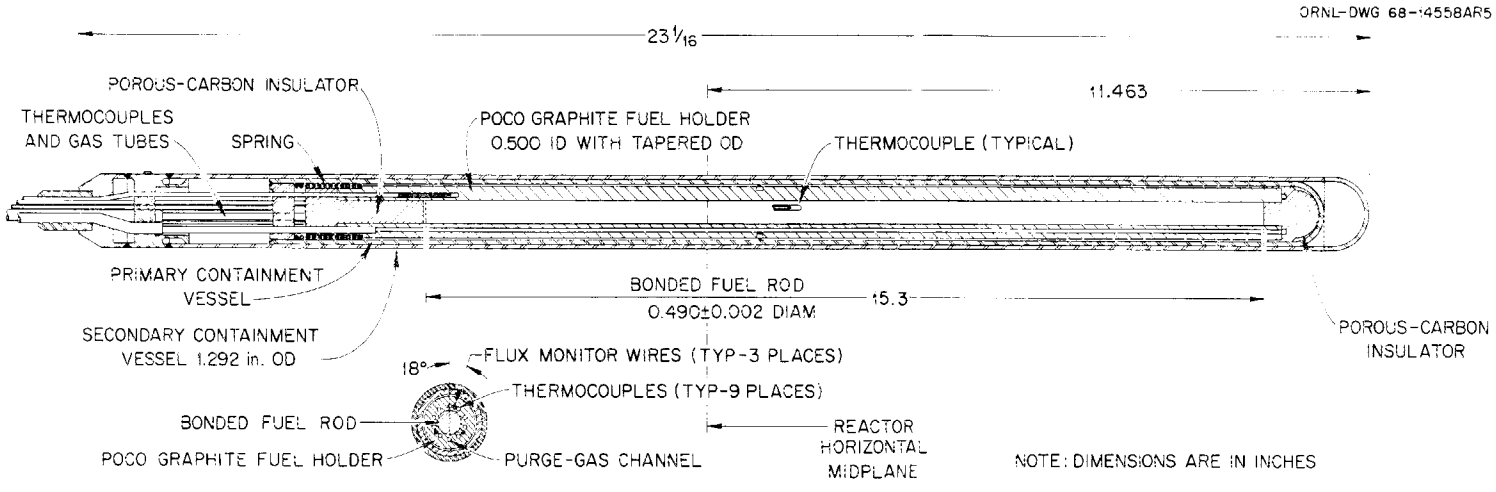

Fig. 7.1. HTGR instrumented capsule HRB-3 for irradiation in HFIR removable beryllium facility.

Table 7.2. Characterization of coated particles for HRB-3

Batch No.	OR 1627-28	OR-1562	OR 1596-99	OR 1577-78-80
Kernel				
Type material	UCS[a]	ThO_2[b]	Carbon[a]	Carbon[a]
Uranium content, wt %	17.0			
^{235}U enrichment, at. %	7.35			
Thorium content, wt %		51.6		
Diameter, μm	431[c] ± 32[d]	398 ± 17	437 ± 26	484 ± 33
Density, g/cm^3	2.73	9.9	1.3	
Buffer				
Thickness, μm	22 ± 3	55 ± 8		
Density, g/cm^3	1.8[c]	1.2[e]		
Inner carbon coating				
Thickness, μm				44 ± 7
Density, g/cm^3				1.0[e]
SiC				
Thickness, μm	23 ± 1		20 ± 1	
Density, g/cm^3	3.21 ± 0.0012		3.23 ± 0.006	
Outer carbon coating				
Thickness, μm	63 ± 8	76 ± 6	58 ± 8	75 ± 7
Density, g/cm^3	1.86 ± 0.0212	1.97 ± 0.007	1.93 ± 0.013	1.93 ± 0.004

[a]Strong-acid-resin derived.
[b]Sol-gel derived.
[c]Mean.
[d]Standard deviation.
[e]Calculated.

Table 7.3. Description of fuel rod specimens for testing in HRB-3

Position No.	Specimen No.	Fabrication technique	Supplier	Matrix density (g/cm^3)	Particle volume loading (%)	Dimensions (in.)	
						Length	Diameter[a]
1A	JH-206-3	Molded[b]	ORNL	1.49	32.7	0.750	0.488
1B	JH-214-3	Molded[b]	ORNL	1.47	41.6	0.753	0.489
1C	JH-214-1	Molded[b]	ORNL	1.48	32.5	0.750	0.489
1D	JH-206-4	Molded[b]	ORNL	1.46	41.6	0.751	0.489
1E	JH-210-4	Molded[b]	ORNL	1.47	32.5	0.747	0.490
1F	JH-214-2	Molded[b]	ORNL	1.47	41.6	0.751	0.489
2	16	Intrusion bonded	GGA		~61	1.001	0.487
3A	58 A71	Slug injection[c]	ORNL	0.60	59.8	1.977	0.493
3B	58 A73	Slug injection[c]	ORNL	0.60	59.4	1.991	0.493
3C	58 A75	Slug injection[c]	ORNL	0.61	59.6	1.985	0.492
4	19	Intrusion bonded	GGA		~61	0.999	0.487
5A	JH-199-1	Molded	ORNL	1.48	32.7	0.698	0.488
5B	JH-199-2	Molded	ORNL	1.47	41.6	0.702	0.489
6A	JH-199-3	Molded	ORNL	1.49	32.7	0.697	0.488
6B	JH-199-4	Molded	ORNL	1.47	41.6	0.701	0.489

[a]Specimens for positions 1A to 1F had 0.090-in.-diam central holes to accommodate thermocouple.
[b]All molded specimens have matrix consisting of 15% Thermax and 53.5% GLC 1074 graphite powder bonded with A240 pitch.
[c]Slug-injected bonded rods have matrix consisting of 28.5% Asbury 6353 natural flake graphite bonded with 15V pitch.

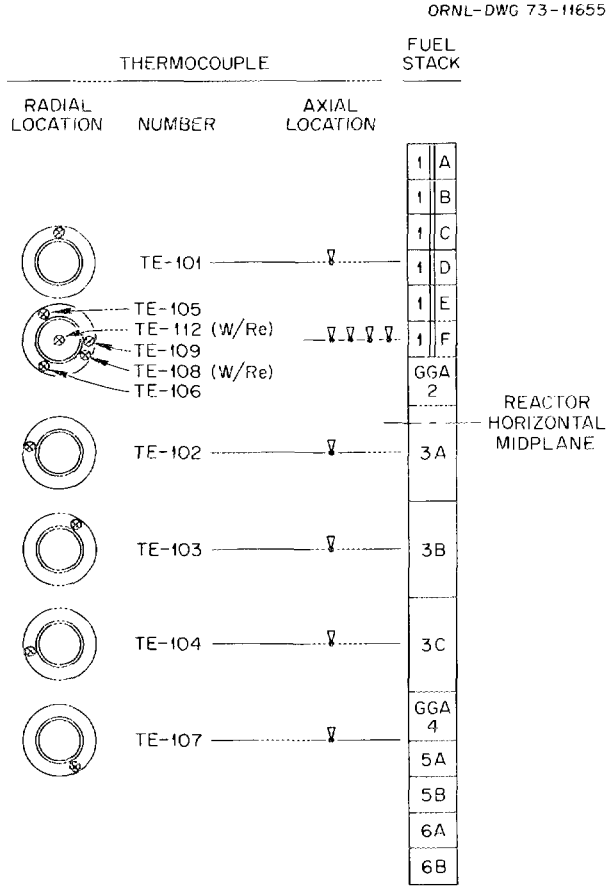

Fig. 7.2. HRB-3 fuel specimen and thermocouple locations.

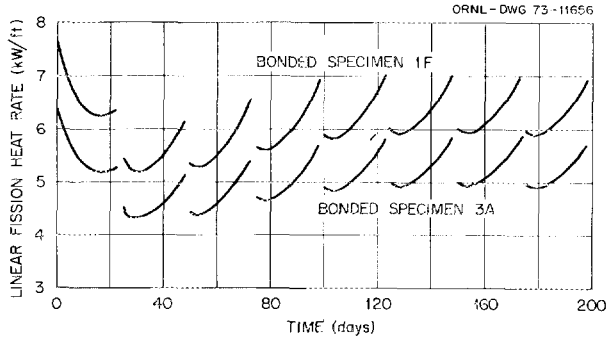

Fig. 7.3. Calculated linear fission heat rate vs time for two specimens in capsule HRB-3.

The calculated isotopic burnup and neutron fluence, along with fuel loadings for each sample, are shown in Table 7.4. These calculations were based on a peak (reactor horizontal midplane) fast flux of 5×10^{14} neutrons cm^{-2} sec^{-1} ($E > 0.18$ MeV) and a perturbed thermal flux of 1.18×10^{15} neutrons cm^{-2} sec^{-1} ($E > 0.41$ MeV).

The helium-neon sweep gas effluent was sampled periodically to measure fission gas release. The ratios of release rate to birth rate (R/B) of selected isotopes vs accumulated irradiation time are shown in Fig. 7.4. The birth rates used in this calculation take into account the depletion of ^{235}U and fissions of bred-in ^{233}U and ^{239}Pu. We first calculated the change in isotopic composition of the fuel for each specimen and then the fission product yield from each fissionable isotope. As may be seen in Fig. 7.4 the R/B ratios increased on day 59 due to an intentional increase in capsule temperatures. After day 79, it was necessary to change the gamma-ray spectrometer equipment due to the high radiation from the sweep gas samples. For an interim period between day 83 and day 106 the alternate system indicated R/B ratios a factor of 2 higher than those preceding. This is attributed to the use of different energy peaks for the counting of the sample activities for the two spectrometer systems.

Typical plots of the time-temperature history for eight of the thermocouples during one HFIR cycle of operation (HFIR fuel cycle 78, sixth cycle of irradiation for capsule HRB-3) are given in Figs. 7.5–7.10. (Two thermocouples, TE-104 and TE-110, failed.) Operating temperature was controlled by maintaining TE-107 at 875°C. The short low-temperature indication for all thermocouples at the beginning of each cycle was caused by capsule operation with a 100% helium sweep, which reduces the thermal resistance of the gap between the graphite sleeve and the capsule wall and results in the lower temperatures. The capsule was operated with 100% helium periodically to provide a relative measure of the power generation as a function of temperature without the complication of an uncertain gas conductivity.

Figure 7.11 presents a comparison of the calculated and the measured temperatures vs irradiation time in the plane of fuel rod 1F. All temperatures are for the seventh day of each reactor cycle and are for the case of 100% helium in the gas gap. Calculated temperatures are based on the local geometry (gas gaps between the fuel and graphite and the graphite and capsule wall were corrected for the estimated dimensional changes due to temperature and irradiation damage). The temperature calculations were based on the calculated heat generation as determined from the flux and calculated isotopic composition at that particular time. A constant fuel rod conductivity of 0.063 W cm^{-1} $(°C)^{-1}$ was assumed. The graphite temperatures, both calculated and measured, are in good agreement. The measured

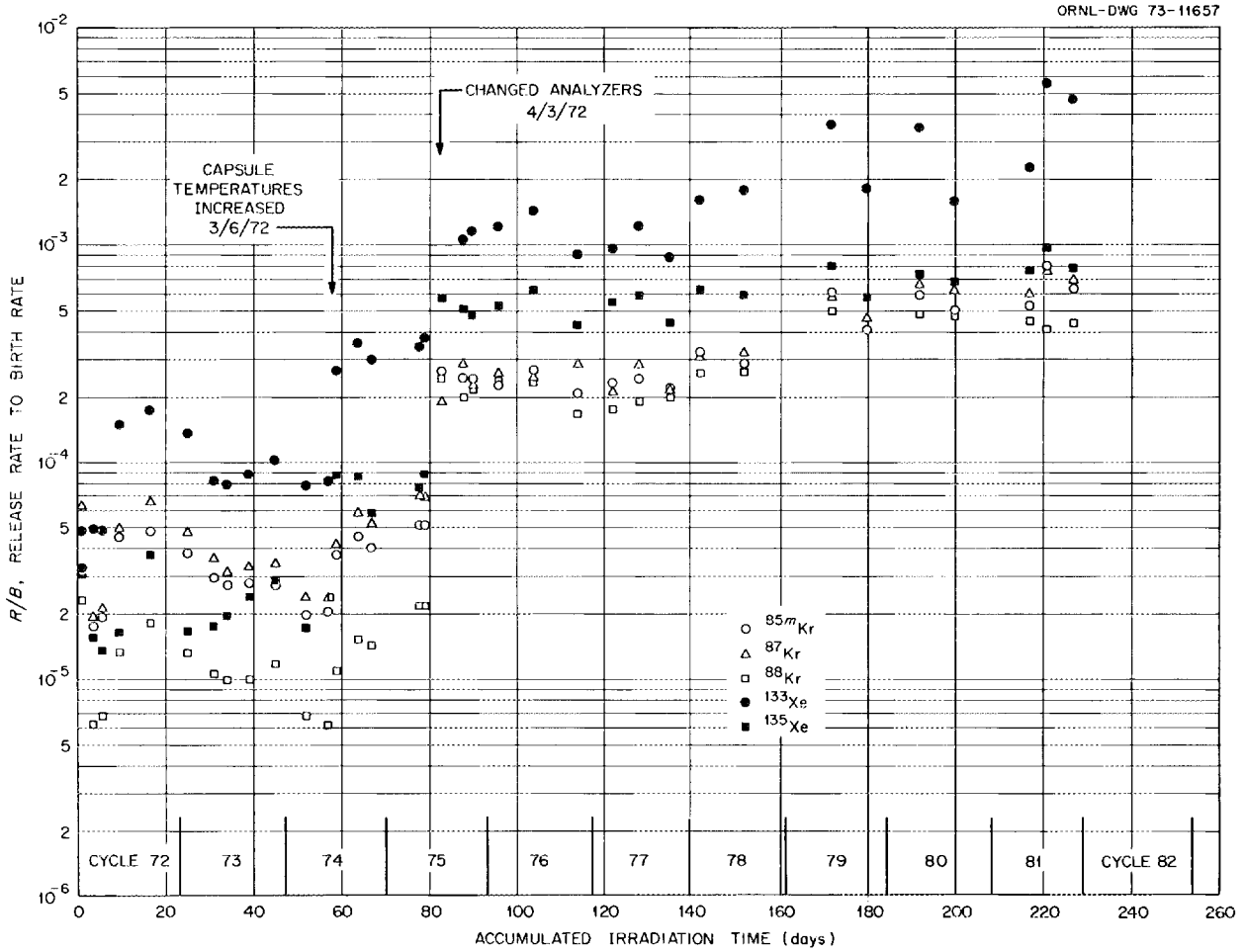

Fig. 7.4. Ratio of fission gas release rate to calculated birth rate (R/B) vs irradiation time for capsule HRB-3.

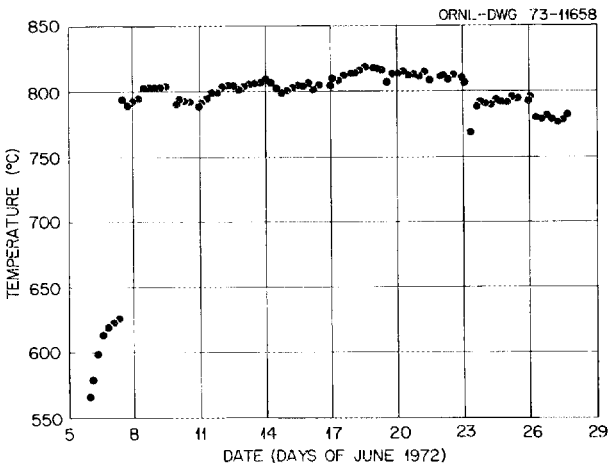

Fig. 7.5. Measured temperature at thermocouple 101 in capsule HRB-3 during HFIR cycle 78 (the sixth of an eleven-cycle irradiation)

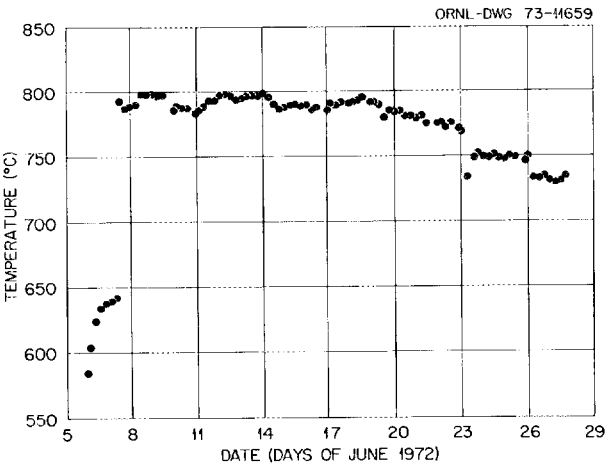

Fig. 7.6. Measured temperature at thermocouple 102 in capsule HRB-3 during HFIR cycle 78 (the sixth of an eleven-cycle irradiation).

Table 7.4. HRB-3 specimen loading, burnup, and fluence

Specimen No.	Length (in.)	Volume (cc)	Fuel loading (g/cc)			Burnup (%)			Fluence (neutrons/cm^2)	
			^{235}U	^{238}U	^{232}Th	^{235}U	^{238}U	^{232}Th	Fast ($E > 0.18$ Mev)	Thermal ($E < 0.414$ eV)
									$\times 10^{22}$	$\times 10^{22}$
1A	0.7495	2.2150	0.00646	0.08144	0.15833	84.0	18.0	8.8	0.80	1.49
1B	0.7527	2.2341	0.00640	0.08075	0.15693		20.5	10.0	0.87	1.69
1C	0.7499	2.2267	0.00642	0.08102	0.15749		21.9	11.1	0.93	1.86
1D	0.7512	2.2315	0.00641	0.08084	0.15720		23.0	12.2	0.98	2.03
1E	0.7468	2.2278	0.00642	0.08098	0.15737		24.5	13.0	1.03	2.19
1F	0.7508	2.2303	0.00641	0.08088	0.15724		25.4	13.8	1.07	2.35
2[a]	1.0010	3.0555	0.00517	0.06683	0.12993		26.5	14.7	1.10	2.48
3A	1.9772	6.1718	0.00522	0.06586	0.12824		26.5	15.0	1.10	2.60
3B	1.9910	6.2155	0.00519	0.06538	0.12726		24.3	13.9	1.03	2.52
3C	1.9850	6.1893	0.00522	0.06579	0.12764		20.2	11.8	0.89	2.21
4[a]	0.9990	3.0490	0.00518	0.06696	0.13019		16.3	9.8	0.75	1.86
5A	0.6976	2.1371	0.00533	0.06776	0.13158		13.5	8.2	0.66	1.63
5B	0.7021	2.1624	0.00527	0.06696	0.13009		11.5	7.1	0.58	1.45
6A	0.6971	2.1382	0.00645	0.08156	0.15845		9.5	5.9	0.50	1.25
6B	0.7009	2.1595	0.00639	0.08076	0.15684		7.5	4.7	0.43	1.06

[a]GGA specimens.

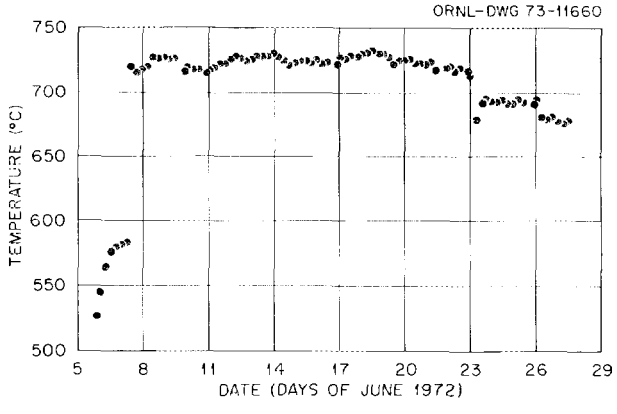

Fig. 7.7. Measured temperature at thermocouple 103 in capsule HRB-3 during HFIR cycle 78 (the sixth of an eleven-cycle irradiation).

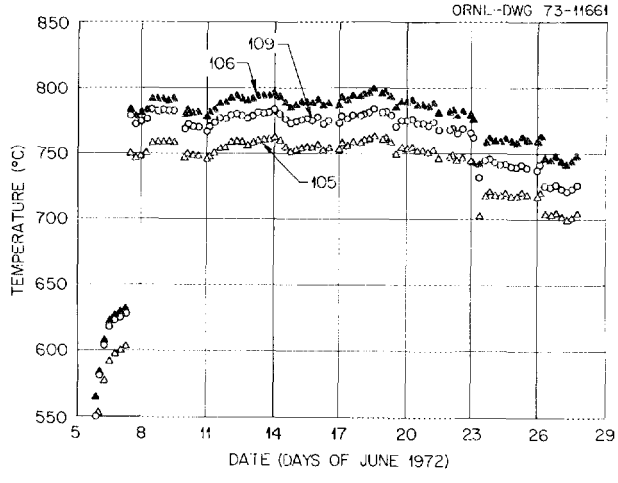

Fig. 7.8. Measured temperature at thermocouples 105, 106, and 109 in capsule HRB-3 during HFIR cycle 78 (the sixth of an eleven-cycle irradiation). Thermocouple 108 failed.

central temperature shows a continuous drop which is not reflected in the calculated values. No attempt was made to correct the data from the tungsten-rhenium central thermocouple for radiation-induced decalibration. We believe that this decalibration is primarily responsible for the disagreement. The initial calculated central temperature would be expected to agree with the central thermocouple. Since the initial calculated and measured graphite temperatures agree (indicating a fair knowledge of the heat generation), one is led to assume that the initial conductivity of the rod may be greater than the 0.063 W cm^{-1} (°C)$^{-1}$ assumed. However, one additional factor should be considered; the calculation assumes a uniform fuel-rod-to-graphite

annulus of 0.005 in. There is a calculated temperature difference between the rod surface and graphite of about 290°C. An eccentric annulus would affect this temperature difference and reduce the central fuel temperature somewhat.

Postirradiation examination and evaluation. The column of specimens was unloaded successfully through the lower end of the sleeve by tapping lightly on the end of the sleeve. All specimens were removed intact except the No. 2 fuel rod prepared by GGA. This rod crumbled badly and was recovered as several pieces and loose particles. The molded specimens were in excellent condition, as typified in Fig. 7.12 by the appearance of specimens 1E and 1F, which had the highest exposure. The surface cracking that was evident before irradiation did not become more severe, and there was no chipping or loss of material at the edges. The three slug-injected rods were also in good condition, although specimens 3A and 3B exhibited some chipping and loss of material due to greater shrinkage associated with the matrix cap.

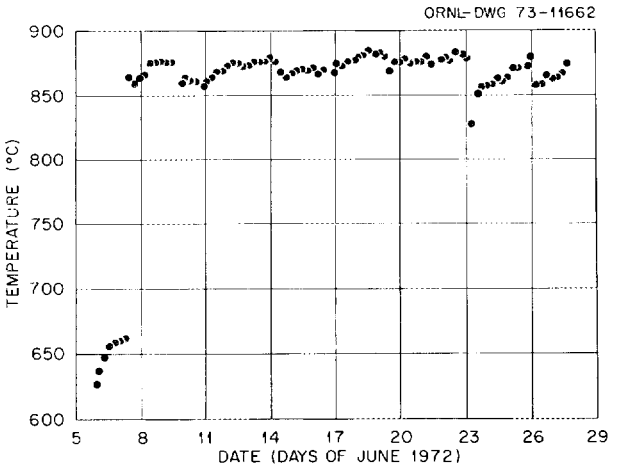

Fig. 7.9. Measured temperature at thermocouple 107 in capsule HRB-3 during HFIR cycle 78 (the sixth of an eleven-cycle irradiation).

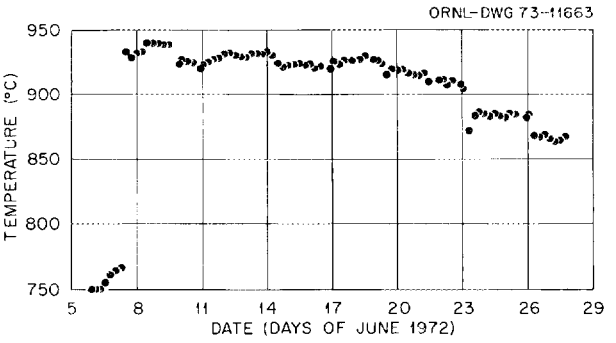

Fig. 7.10. Measured temperature at thermocouple 112 in capsule HRB-3 during HFIR cycle 78 (the sixth of an eleven-cycle irradiation).

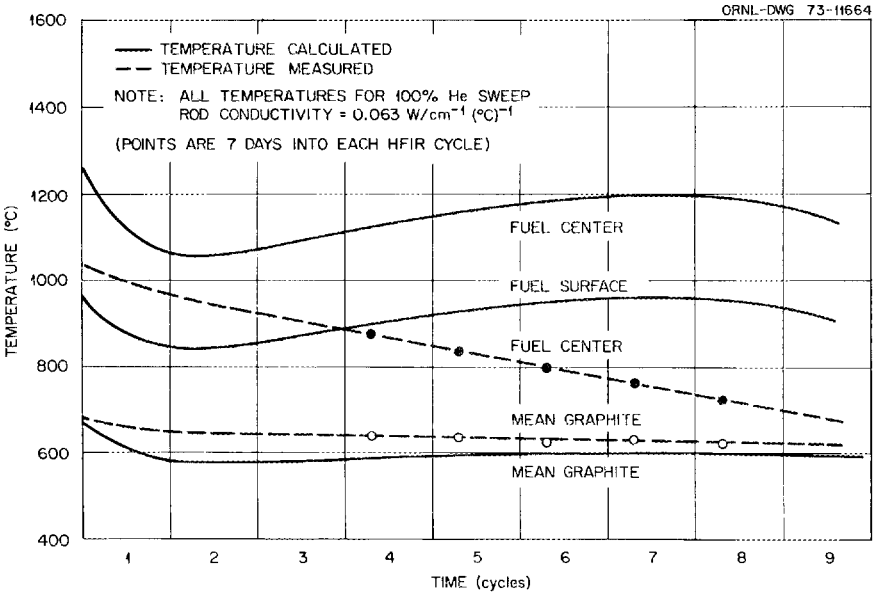

Fig. 7.11. Calculated and measured temperatures in capsule HRB-3 at the plane of specimen 1F.

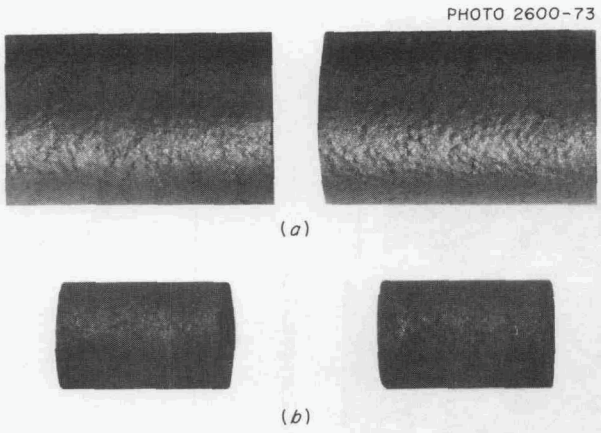

Fig. 7.12. Appearance of molded specimens 1E and 1F before (*a*) and after (*b*) irradiation in capsule HRB-3.

This effect is shown for specimen 3B in Fig. 7.13, which also illustrates that the remainder of the rod was in excellent condition.

Stereoscopic examination of all specimens confirmed these observations, indicating negligible loss of material from the edges of molded specimens. The weight change data presented in Table 7.5 also confirm this performance. During stereoscopic examination we observed a few broken coatings on particles at or near the surface of the molded and slug-injection bonded rods, but could not identify the type of particles that broke. Similar examination of the GGA specimens revealed a large fraction of failed coatings on Biso-coated ThO_2 fertile particles, especially in the No. 2 specimen that crumbled severely. After visual examination and measurement of the No. 4 specimen the two GGA samples (Nos. 2 and 4) were returned to Gulf General Atomic for further examination and final evaluation.

After completion of visual examination and weighing, all ORNL specimens were measured in several places (six diametral measurements on long rods and four measurements on 1-in. rods). The shrinkage data are compiled in Table 7.5, in which the three types of specimens are arranged in order of decreasing fluence. The shrinkage of the molded specimens was not isotropic, which would be expected because the filler materials in the matrix would exhibit some preferred orientation after the compacting operation. The changes observed in the five specimens with lower particle volume loadings were slightly greater but not significantly different from those containing 42 vol % coated particles. The dimensional behavior of these molded rods is controlled by the properties of the matrix, since the particle coatings are not in contact. Therefore, their shrinkage behavior is not readily

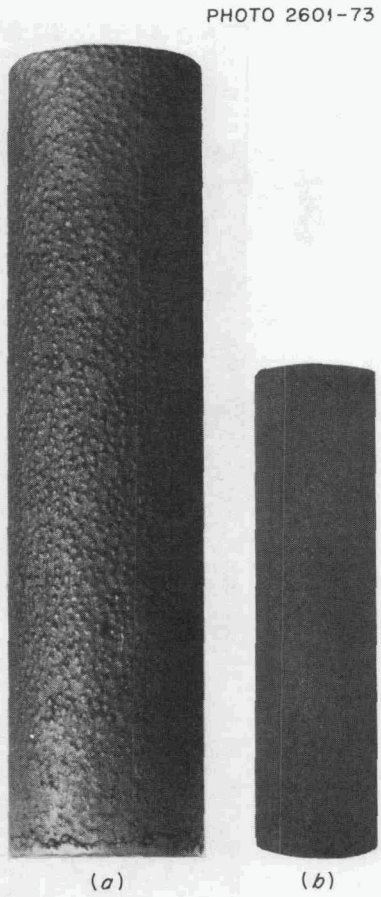

Fig. 7.13. Appearance of specimen 3B before (*a*) and after (*b*) irradiation in capsule HRB-3. Note that matrix cap crumbled and was lost.

comparable with that of other types of specimens. On the other hand, the shrinkage of the four intrusion-bonded specimens is nearly isotropic, as expected, and is about what would be expected for rods having a blend of Triso- and Biso-coated particles with high-density (about 2.0-g/cm^3) outer coatings. For the actual blend of Triso- and Biso-coated inert and fuel particles used in the series 3 specimens, and using shrinkage data observed in single-particle systems in previous experiments (see Sect. 7.5 of this report), one can calculate that the maximum linear shrinkage should be about 1.6% as compared with observed values of 1.8%.

Metallographic examination of molded specimens 1D and 1E has been completed. The dense matrix of these specimens showed some cracking before irradiation; there was little if any change in appearance of the matrix, and the specimens were quite strong. The micrograph in Fig. 7.14 shows the appearance of a

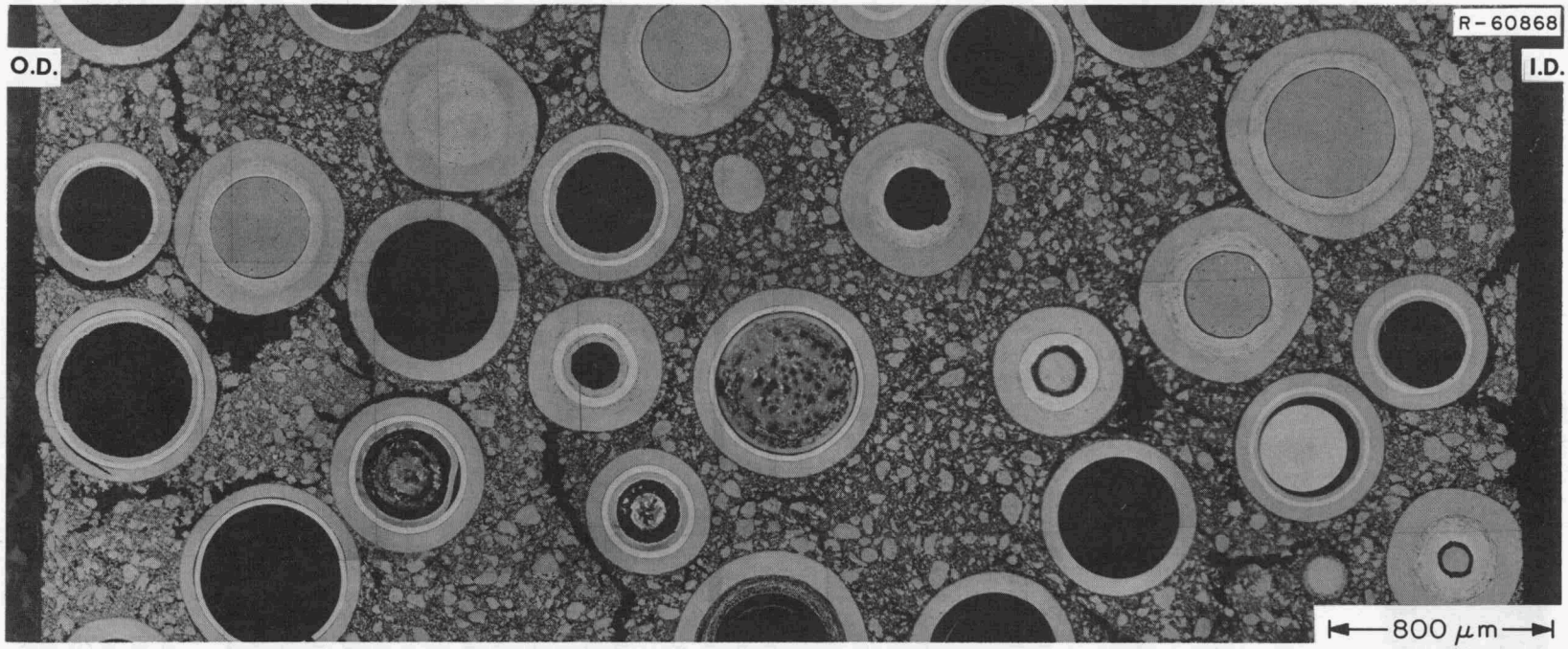

Fig. 7.14. Cross section of HRB-3 molded specimen 1D (42 vol % Triso strong-acid resin, Biso ThO_2, and inert particles).

Table 7.5. Dimensional and weight changes of fuel rod specimens in HRB-3 experiment

Specimen No.[a]	Calculated fast fluence [neutrons/cm^2 ($E > 0.18$ MeV)]	Particle volume loading (%)	Weight loss (%)	Dimensional shrinkage (%)	
				Diameter	Length
	$\times 10^{22}$				
1E	1.03	32.5	0.1	1.49	0.67
1C	0.93	32.5	0.2	1.64	0.72
1A	0.80	32.7	0.2	1.56	1.55
5A	0.66	32.7	0.0	1.78	1.03
6A	0.50	32.7	0.0	1.84	1.31
1F	1.07	41.6	0.1	1.47	0.69
1D	0.98	41.6	*b*	1.58	0.96
1B	0.87	41.6	0.2	1.45	1.13
5B	0.58	41.6	0.0	1.62	1.25
6B	0.43	41.6	0.3	1.64	1.27
3A	1.1	59.7	2.8	1.81	*c*
3B	1.03	59.4	3.3	1.83	3.05[d]
3C	0.89	59.6	0.56	1.75	1.47
4 (GGA)	0.75	~62	*e*	1.30	1.10

[a]Specimen series 1 consisted of molded rods with central thermocouple holes; series 5 and 6 were solid rods; and series 3 were 2-in.-long slug-injected rods.

[b]A portion of thermocouple protection sleeve adhered to specimen 1D.

[c]Specimen 3A was broken while measuring diameters.

[d]Specimen 3B crumbled somewhat at top end due to shrinkage associated with matrix cap.

[e]Not measured.

radial section across specimen 1D, illustrating the continuity of the matrix. The performance of the Biso-coated ThO_2 fertile particles was excellent, as illustrated by the appearance of several such particles in Fig. 7.14. No damaged coatings on ThO_2 particles were seen in examining the polished sections of these two specimens. The Triso-coated strong-acid resin (SAR) fissile particles also performed well, but exhibited a variety of kernel structures and some attack on the inner coatings of a few particles. In addition to the three fissile particles seen in Fig. 7.14, other typical structures are shown in Fig. 7.15. These structures may be due to some phase instability in the deoxidized resin particles. The observed coating attack was not highly detrimental to particle performance, but the mechanism for the phenomenon needs to be understood before the reliability of the system can be evaluated.

7.1.3 Capsules HRB-4 and HRB-5

The fourth and fifth capsules in the series of HFIR sweep-capsule experiments were similar in design to HRB-3 and had four main objectives as follows:

1. to test slug-injection bonded fuel rods prepared with different matrix materials and by different carbonization methods,
2. to test experimental fuel rods prepared by GGA,
3. to test extruded fuel rod specimens,
4. to measure central fuel temperatures and monitor changes in thermal conductivity of extruded rods.

The two capsules had similar fuel loadings and are scheduled for two irradiation exposures to cover the range of neutron fluence and burnup of interest. Central fuel rod temperatures in extruded specimens were measured with a tungsten-rhenium thermocouple in HRB-4 and with an ultrasonic thermometer in HRB-5.

Capsule design. The two capsules for this experiment contained 13 fuel rod specimens supported in a graphite sleeve, similar in many respects to previous capsules. The fuel rod loadings and their locations in the capsule are shown for HRB-4 in Table 7.6. Individual specimen

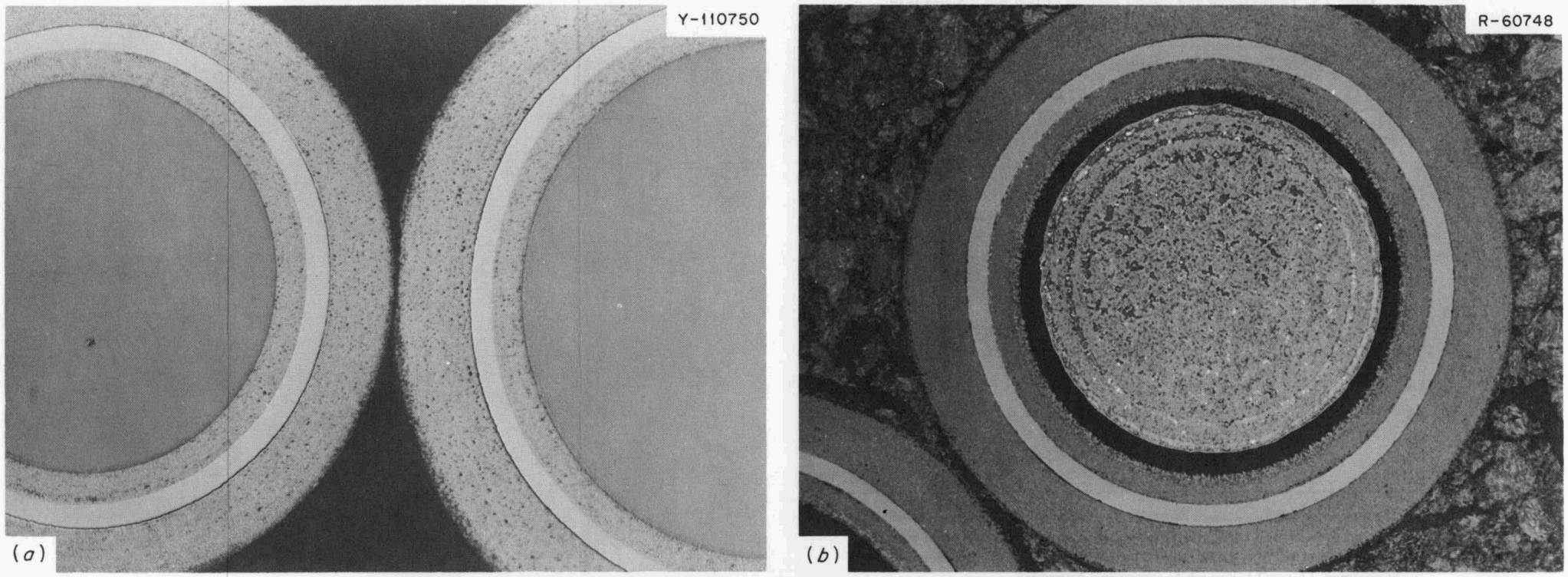

Fig. 7.15. Polished sections of resin-derived fissile particles (batch OR-1627) irradiated in capsule HRB-3. (*a*) Unirradiated; (*b,c*) irradiated at 1250°C to 28% burnup in specimen 1D. Note variability of structure and attack on inner coating. As polished. 200×.

Table 7.6. Capsule HRB-4 fuel specimen loading and location

	Length (in.)	Volume (cc)	Fuel loading (g/cc)			Reactor horizontal midplane to specimen center (in.)	Average fast flux [neutrons cm^{-2} sec^{-1} ($E > 0.18$ MeV)]
			^{235}U	^{238}U	^{232}Th		
							$\times 10^{14}$
1A	1.740	5.1772	0.0049	0.0770	0.1491	5.000	3.90
1B	1.743	5.2355	0.0050	0.0791	0.1533	3.250	4.50
1C	1.758	5.2624	0.0051	0.0795	0.1540	1.500	4.95
Reactor horizontal midplane							
2A	1.008	3.1321	0.0042	0.0660	0.1281	−0.125	5.00
2B	1.015	3.1609	0.0042	0.0654	0.1270	−1.125	4.98
2C	0.990	3.0743	0.0043	0.0673	0.1306	−2.125	4.83
3A	0.953	2.945	0.0043	0.0682	0.1321	−3.125	4.56
3B	0.953	2.945	0.0043	0.0682	0.1321	−4.125	4.24
3C	0.938	2.922	0.0044	0.0687	0.1331	−5.125	3.85
3D	0.956	2.978	0.0043	0.0675	0.1306	−6.125	3.43
4A	1.000	3.1113	0.0042	0.0665	0.1290	−7.125	2.99
4B	1.017	3.1791	0.0041	0.0651	0.1263	−8.125	2.50
4C	1.004	3.1228	0.0042	0.0662	0.1285	−9.125	1.97

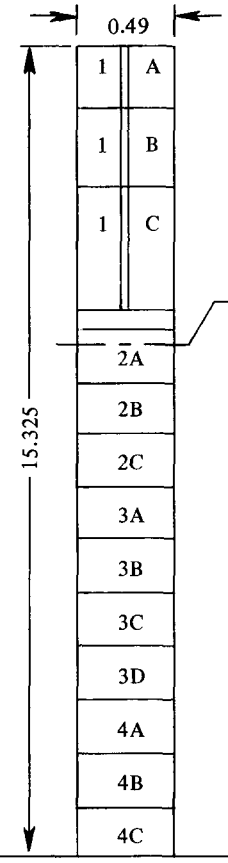

dimensions were slightly different in HRB-5, but the loadings and other data were identical. The radial and axial locations of thermocouples in the fuel and in the graphite sleeve are shown for HRB-4 in Fig. 7.16. The tungsten-rhenium central thermocouple was replaced by a 2-in.-long rhenium ultrasonic thermometer in HRB-5. The design gaps and loadings were calculated to produce an average heat rating of 5 kW/ft at the reactor horizontal midplane, which corresponds to a maximum fuel temperature of 1250°C and graphite sleeve temperatures ranging from 700 to 960°C.

Preparation of test specimens. All specimens contained the same Triso-coated fissile, Biso-coated fertile, and coated inert particles. The fissile particles were derived from weak-acid resins and were deoxidized before coating to convert the fuel to UC_2, and the fertile particles were ThO_2 microspheres prepared by the sol-gel method. Coatings specified for these particles were conservatively designed. The coated inert particles had kernels that were derived from strong-acid resins, heated to 3000°C before coating to eliminate sulfur. All coated-particle batches were heated to 1800°C before fabrication into fuel rods. The characteristics of these particles are given in Table 7.7.

A general description of the fuel rod specimens for the two capsules is presented in Table 7.8. In preparing the extrusions, the matrix materials and binder were slurry blended with the coated particles using acetone as diluent. After the acetone evaporated, the mix was extruded at room temperature at a pressure of 1000 psi

Table 7.7. Characterization of coated particles for HRB-4 and HRB-5

Batch No.	52A	OR-1856	OR-1833	OR-1815
Kernel				
Type material	UC_2[a]	ThO_2[b]	Carbon[c]	Carbon[c]
Uranium content, wt %	23.8			
^{235}U enrichment, at. %	5.99			
Thorium content, wt %		56.62		
Diameter, μm	366[d] ± 42[e]	488 ± 30	370[f]	370[f]
Density, g/cm^3	6.2	9.72	1.4	1.4
Buffer				
Thickness, μm	44.6 ± 6	88 ± 8	20[f]	30[f]
Density, g/cm^3	0.95[f]	0.95[f]	1.0[f]	1.0[f]
Inner carbon coating				
Thickness, μm	30.8 ± 4		20[f]	
Density, g/cm^3	1.94 ± 0.01		1.90 ± 0.06	
Sic				
Thickness, μm	31.8 ± 6.6		15 ± 2	
Density, g/cm^3	3.21 ± 0.006		3.21 ± 0.002	
Outer carbon coating				
Thickness, μm	28.3 ± 3.9	79 ± 7	30[f]	30[f]
Density, g/cm^3	1.89 ± 0.007	1.92 ± 0.023	1.98 ± 0.004	1.92 ± 0.022

[a]Weak-acid-resin derived.
[b]Sol-gel derived.
[c]Strong-acid-resin derived.
[d]Mean.
[e]Standard deviation.
[f]Standard deviation not determined.

Table 7.8. General description of specimens for HRB-4 and HRB-5

Specimen No.	Supplier	Nominal dimensions (in.)			Filler material[a]		Particle volume loading (%)	Fabrication technique	Carbonization mode
		OD	ID	Length	Amount (wt %)	Type[b]			
1A	ORNL	0.490	0.090	1.75	60	Robinson coke	32.5	Extrusion	In covered graphite tray
1B	ORNL	0.490	0.090	1.75	19	Thermax	32.5	Extrusion	
1C	ORNL	0.490	0.090	1.75			32.5	Extrusion	
2A	GGA	0.490		1.0	40	1089 graphite	55–58	Admix	In block (H-327)
2B	GGA	0.490		1.0	40	1089 graphite	55–58	Admix	In block (H-327)
2C	GGA	0.490		1.0	10 40	Thermax RC4 graphite	55–58	Admix	In block (H-327)
3A	ORNL	0.490		1.0	29.6	Asbury 6353	60–62	Slug injection	In packed alumina
3B	ORNL	0.490		1.0	38.7	RC4 graphite	60–62	Slug injection	In packed alumina
3C	ORNL	0.490		1.0	38.7	RC4 graphite	60–62	Slug injection	In block (H-327)
3D	ORNL	0.490		1.0	41.1	1089 graphite	60–62	Slug injection	In block (H-327)
4A	GGA	0.490		1.0	Same as 2A		55–58	Admix	In block (H-327)
4B	GGA	0.490		1.0	Same as 2B		55–58	Admix	In block (H-327)
4C	GGA	0.490		1.0	Same as 2C		55–58	Admix	In block (H-327)

[a]Binders used were Varcum for extruded rods and Ashland A240 pitch for all other rods.
[b]Filler materials designation and source are as follows:
Isotropic Robinson graphitized coke originally produced for AFML by Union Carbide Corp.
Thermax, carbon black, from R. T. Vanderbilt Company.
Isotropic type 1089 graphite flour from Great Lakes Carbon Company.
Isotropic type RC4 graphite flour from Airco-Speer Corp.
Anisotropic type Asbury natural flake graphite 6353 from Asbury Graphite, Inc.

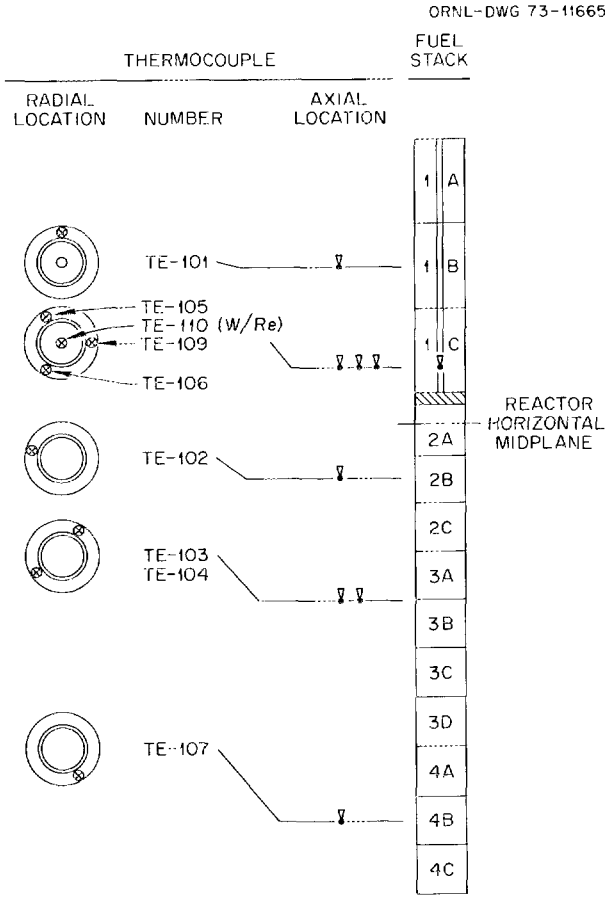

Fig. 7.16. Capsule HRB-4 fuel specimen and thermocouple locations.

into graphite trays, in which they remained throughout the curing cycle (16 hr at 90°C). After carbonizing at 1000°C on a 24-hr cycle, they were given a final treatment at 1800°C.

All specimens had a center hole for thermocouple placement and nominal particle volume loadings of 31%. The matrix density of the specimen for position 1A was somewhat lower than that for positions 1B and 1C (1.6 compared with 1.7 g/cm^3). The extrusions showed uniform fuel distribution according to radiography. Densities of all 17 specimens prepared from a given extrusion batch, measured as grams per inch of length, were $\leq$1% of the mean value, indicating further that a uniform distribution of fuel was achieved.

During fabrication of the slug-injection bonded fuel rods, special precautions were required to obtain a satisfactory blend of the four types of coated particles. A decade splitter was used to divide the particles required for a single fuel rod into ten equal portions, each containing all types of particles. These portions were then transferred to the mold with a probe to minimize free fall of the particles and to avoid segregation. Radiographs of fuel rods prepared in this manner showed quite uniform loadings. Some rods were carbonized and annealed at 1800°C to simulate in-block carbonization conditions, while others were carbonized in packed alumina. All the matrix mixtures were injected into the blended particle beds without difficulty. The particle packing, matrix density, and coke yield of the four types of fuel rods are given in Table 7.9.

Capsule operation. These two capsules were installed in the HFIR on October 6, 1972, and had accumulated 78.8 days of irradiation at 100 MW reactor power through December 31, 1972. Capsule HRB-4 was installed in the second, or new, facility (RB-7), and HRB-5 was inserted in the RB-5 facility. The ratios of fission gas release rate to birth rate as determined from gas samples taken periodically during the irradiation are given in Table 7.10.

Table 7.9. Summary of particle packing efficiency, matrix density, and in-situ coke yield of slug-injected fuel rods for the HRB-4 and HRB-5 irradiation tests

Specimen No.	Matrix filler[a]		Method of carbonization	Particle packing efficiency (%)	Matrix density (g/cm^3)	In-situ coke yield (%)
	Type	Amount (wt %)				
3A	Asbury 6353	29.6	Packed in Al_2O_3	61.0	0.563	19.6
3B	RC4	38.7	Packed in Al_2O_3	61.0	0.736	25.2
3C	RC4	38.7	In graphite tube	60.9	0.840	39.2
3D	GLC 1089	41.1	In graphite tube	60.5	0.845	37.7

[a]The binder for all matrices was Ashland A240 pitch.

Table 7.10. Fission gas release data on capsules HRB-4 and HRB-5

Sample No.	Date	Accumulated irradiation time (days)	*R/B* ratio				
			^{85m}Kr	^{87}Kr	^{88}Kr	^{133}Xe	^{135}Xe
			$\times 10^{-5}$	$\times 10^{-5}$	$\times 10^{-5}$	$\times 10^{-4}$	$\times 10^{-5}$
Capsule HRB-4							
2	10-17-72	9.2	1.42	0.670	0.541	0.320	0.111
3	10-18-72	10.2	1.50	0.558	0.563	0.355	0.134
4	10-23-72	15.1	2.35	1.25	0.786	0.520	2.46
5	10-31-72	22.1	7.36	3.46	4.18	2.55	7.12
6	11-16-72	35.9	17.3	7.14	4.80	5.27	20.8
7	11-27-72	45.5	11.2	6.38	7.77	6.60	10.8
8	12-1-72	49.7	15.8	8.95	12.4	8.69	15.7
9	12-7-72	55.7	16.2	8.65	11.1	8.57	15.9
10	12-19-72	66.9	9.51	5.21	7.10	5.08	8.69
Capsule HRB-5							
2	10-17-72	9.2	0.64	0.23	0.23	0.15	0.54
3	10-18-72	10.2	0.69	0.31	0.26	0.15	0.58
4	10-23-72	15.1	1.44	0.39	0.47	0.28	1.25
5	10-23-72	15.2	521	109	234	2710	30.4
6	10-31-72	22.1	19.3	8.0	11.4	7.5	18.6
7	11-16-72	35.8	35.4	18.3	27.7	9.0	40.6
8	11-27-72	45.8	8.93	5.2	6.1	5.3	5.67
9	12-1-72	49.7	21.1	10.7	17.6	14.2	18.2
10	12-7-72	55.7	14.3	6.5	10.2	8.8	11.1
11	12-19-72	67.2	7.2	3.5	4.8	4.2	1.24

7.1.4 Capsule HRB-6

The sixth capsule in the series of HTGR-HFIR irradiation experiments in the removable beryllium facility (RB-5) is to be inserted in March 1973. The capsule, designated HRB-6, will be instrumented and swept with inert gas mixtures in order to monitor the fuel performance. The experiment has five main objectives as follows:

1. to compare the irradiation behavior of Biso-coated 4:1 (Th,^{233}U)O_2 with Biso-coated 4:1 (Th,^{235}U)O_2 as loose particles and in bonded rods;
2. to supply samples of particles containing ^{233}U and ^{235}U for study of fission product retention within the coated particles and within a carbonaceous matrix;
3. to determine whether the differing fission product spectra from ^{233}U and ^{235}U affect the carbon transport and kernel migration within coated particles;
4. to further test fueled specimens prepared by extrusion, slug-injection, and intrusion bonding for dimensional stability when irradiated to full HTGR fluence;
5. to continue testing of ultrasonic thermometers as a means of measuring center-line temperature.

The experiment will contain loose samples of coated particles supported in a bonded rod holder and fuel rod specimens prepared by extrusion, slug injection, and hot intrusion. All fuel rods will be nominally 0.490 in. in diameter, and the extruded specimens and the intrusion-bonded rod designed to hold loose particles will have a center hole for placement of an ultrasonic thermometer. All specimens will contain the same fertile particles (Biso-coated ThO_2) and the same inert diluent particles (Biso-coated desulfurized carbon derived from strong-acid resin). Specimens prepared by Gulf General Atomic for the experiment will have a diluent "shim" particle, which consists of irregularly shaped graphite granules.

7.2 IRRADIATION TESTS IN THE HFIR TARGET FACILITY

B. H. Montgomery W. P. Eatherly
D. M. Hewette II J M Robbins
R. B. Fitts C. B. Pollock

A second type of HFIR capsule is the target or HT capsule, which is a small uninstrumented device consisting of an aluminum tube with an external configuration identical to that of a HFIR target rod. The design of typical target capsules has been described previously.[4] These capsules contain small specimens of coated-particle fuels and fuel-element materials in the form of loose particles, bonded fuel rods containing coated particles, blended coated-particle beds, pyrolytic carbon disk specimens, and experimental graphites. The specimens can be irradiated at temperatures up to 1250°C, depending on the heat flux, and to representative HTGR end-of-fuel-life fast-flux exposure in about three months. The test specimens are in general contained in a number of graphite specimen holders or magazines which occupy the central 20 in. of the capsule, corresponding to the active core length of the HFIR. The magazines are graphite cylinders positioned within the capsule by graphite and nickel supports. In addition to centering the magazine, the supports provide a thermal barrier at the magazine ends to minimize axial heat losses.

The test capsules have the advantage of low cost and short irradiation time to attain representative exposure, but they have certain limitations. Only small specimens with very small amounts of fissionable material can be accommodated. Since the capsules are uninstrumented, temperatures are not monitored during irradiation and can only be deduced by postirradiation analysis of melt wires and silicon carbide monitors. The capsules are sealed; no gas sweep is possible. During this period the 10th, 12th, 13th, 14th, and 15th capsules in the HT series were built and placed under irradiation, and reports describing the results from the 10th and several previous capsules were prepared.

7.2.1 Capsules HT-7 to HT-10

Examination and evaluation of this series of capsules were completed, and a report describing the results is in preparation. The abstract of this report is included below.[5]

A final topical report describes the testing of Triso-coated inert particles in capsules HT-7, -8, -9, and -10. The report describes the test vehicles, the operating conditions, and the various techniques used to characterize the particles before and after irradiation. The principal test variables were the densities of the LTI coatings (1.7 to 2.0 g/cm^3), the test temperatures (750 and 1050°C), and fast fluences (up to 14×10^{21} neutrons/cm^2). The results indicate that LTI coating density does not have a great effect on survival of Triso-coated particles under these operating conditions, as none of the loose particles failed in the test. The principal effect of LTI coating density was its influence on shrinkage of the outer coatings, which in turn influences the dimensional change of bonded rods made from the particles. The LTI coatings shrink because of densification under irradiation, and the shrinkage is inversely related to the starting density of the coatings. The greater shrinkage of low-density coatings produced matrix interactions and led to many coating fractures in bonded rods containing these particles. Coating densities increased with increasing fast-neutron fluence up to about 9×10^{21} neutrons/cm^2 and at higher fluences decreased in density.

7.2.2 Capsules HT-12 to HT-15

The fertile particle makes up 80% or more of the coated-particle volume in current fuel rod designs for HTGRs. The minimal requirements in these particles thus dominate the fuel rod fabrication requirements. We designed an experiment consisting of several capsules to perform stringent tests on such particles. Unlike many prior experiments, this set of HFIR target capsules was designed not to demonstrate the successful ability of coated particles to withstand reactor environments, but rather to induce predictable failures of the particles and thereby establish minimal design criteria.

For the purpose of the experiment we selected the fertile particle currently specified for initial and recycle fuel.[6] This particle has a 500-μm-diam ThO_2 kernel and a Biso coating consisting of an 85-μm-thick buffer layer and a 75-μm-thick outer isotropic carbon layer. The objective outlined was to develop information that would define the minimal requirements placed on the Biso coating in terms of thickness, thickness ratios, and physical properties. Variations on this reference design were selected for testing on the basis of performance predicted by the STRETCH code;[7] the creep coefficients and ultimate strength were presumed to be the significant variables.

4. B. H. Montgomery, "Target Irradiation Tests," *GCR-TU Programs Annu. Progr. Rep. Sept. 30, 1971*, ORNL-4760, pp. 134–36.

5. D. M. Hewette II et al., *Effects of Neutron Irradiation on Loose and Bonded Inert Particles Coated with Pyrolytic Carbon and Silicon Carbide*, ORNL-TM (in preparation).

6. *National HTGR Fuel Recycle Development Program Plan*, ORNL-4702, Rev. 1 (in preparation).

7. J. W. Prados and T. G. Godfrey, *STRETCH, a Computer Program for Predicting Coated Particle Irradiation Behavior, Modification IV, December 1967*, ORNL-TM-2127 (April 1968).

Experiment design. The experiment evolved around four capsules, each to contain two nominal temperature regimes. The samples, 50 to 75 coated particles, are supported in small graphite bottles with annular cavities for the particles. Several particle holders are in turn supported in a graphite tube which forms a magazine. Two magazines in each capsule were designed to develop a holder temperature of 1250°C and the other two a particle holder temperature of 900°C. The set of four capsules was designed to operate for two, four, six, and eight HFIR cycles to achieve a range of fast-neutron exposures from 2×10^{21} to 18×10^{21} neutrons/cm^2 ($E > 0.18$ MeV), or from 25 to about 200% of design HTGR maximum exposure. Burnup in the ThO_2 would range from 2 to about 20%.

A detailed heat transfer analysis using the HEATING III code[8] was made of one particle type to evaluate the temperature difference that could exist between the particle and the particle holder. The particle chosen had a 500-μm-diam ThO_2 kernel and an 820-μm overall diameter. The particle-to-holder contact diameter was varied from 0.00002 to 0.0002 in. (a factor of 100 in contact area). The particle was assumed to generate 0.87 W of heat (the maximum calculated for that type of particle in the experiment). The thermal conductivity of the graphite and pyrolytic carbon coating were assumed to be the same, 15 Btu hr^{-1} (°F)$^{-1}$ ft^{-1} [0.26 W cm^{-1} (°C)$^{-1}$]. The emissivity used for radiant heat transfer between the particle and graphite holder was 0.9, and the graphite holder temperature was fixed at 1200°C.

The results indicated a maximum particle coating temperature of 1556°C. The circumferential variation from a point adjacent to, but not at, the point of contact to the opposite side of the particle (point of highest coating temperature) was 70°C. The variation in peak coating temperature from a contact diameter of 0.00002 to 0.0002 in. was only 0.4°C. Photomicrographs indicate that unless severe Brinelling were to take place, a 0.0002-in. contact diameter is the maximum probable.

The results of the calculation were somewhat surprising. Most important, it demonstrated that the loose particles of this test series, where the heat generation per particle can be relatively large, can have a temperature considerably above that of the holder. This must be taken into account in evaluating the test results. Second, it showed that contact area is of little consequence and that the variation over the particle surface will be small for any reasonable coating conductivity.

Preparation of test samples. The ThO_2 kernels for the experiment were screened from a large batch of sol-gel microspheres so that the diameter distribution of separate batches had a standard deviation of ≤ 7 μm. We used both 400- and 500-μm-diam kernels in order to increase sample size, since geometric scaling factors on the coatings are quite certain. The STRETCH code was used to design the Biso coatings for the series, using nominal neutron flux and temperature values. The two most sensitive physical variables used in the code are the creep coefficient and the anisotropy. A creep coefficient of 10^{-27} psi^{-1} (neutrons/cm^2)$^{-1}$ was assumed for the calculation, and the effect of variations by a factor of 5 was studied. The Bacon anisotropy factor (BAF) was assumed to be 1.05, but values of 1.00 to 1.15 were also used in the calculations. Within these ranges the particles were designed to fail at the rate of two types per each two-cycle irradiation in the HFIR.

The batches were coated with carbon in a 1-in.-diam laboratory-scale coating furnace. The dense outer coatings were applied at very high rates (~20 μm/min as compared with about 5 μm/min in large coaters) using propylene to ensure that their structures were nearly isotropic. The properties of the nine batches are described in Table 7.11. The thickness distributions of the individual coated batches were carefully controlled to avoid any overlap of dimensions between batches.

In addition to the nine types of particles prepared by ORNL, seven additional types were prepared by GGA. The principal variable in the GGA particles was the

Table 7.11. Characteristics of Biso-coated ThO_2 particles for irradiation in capsules HT-12 to HT-15

Batch No.	Mean kernel diameter (μm)	Mean buffer layer thickness (μm)	Outer coating layer	
			Mean thickness (μm)	Density (g/cm^3)
OR-1837	402	1	24	2.02
OR-1830	402	1	38	2.01
OR-1846	402	20	21	1.99
OR-1826	402	21	31	2.01
OR-1840	402	25	50	2.01
OR-1749	402	33	36	1.92
OR-1838	402	32	64	1.96
OR-1850	508	45	48	1.99
OR-1849	508	79	75	1.99

8. W. D. Turner and M. Siman, *HEATING III: An IBM-360 Heat Conductor Program*, ORNL-TM-3208 (February 1971).

anisotropy. Thus, the final makeup of the experiment tests two fundamental variables, coating thickness and anisotropy. It should therefore be possible to empirically fix the pertinent physical parameters, at least in a grouped sense, from the observed times of particle failure.

Two preliminary experiments were performed. The first was a temperature cycling experiment in which particles were placed in the graphite canisters and the temperature was cycled ten times between room temperature and 1250°C in a furnace. The purpose was to ascertain whether temperature cycling would cause a ratchetting effect between the particles and the canister walls, causing mechanical breakage of the coatings. No breakage was found. The second experiment was a statistical analysis of the ability of various observers to determine particle diameters. The essential results of these experiments were that particle diameters and variances could be determined to within 1 μm, independent of the observer. Hence, particle design and changes in particle diameter due to radiation damage can be measured to an accuracy well within the design variables.

Capsule operation and preliminary results. These capsules were irradiated in the outer target positions of the HFIR. At the present time, only capsule HT-12 has been removed. It operated for 38.6 days at 100 MW reactor power and received a maximum fast-neutron fluence of 4.1×10^{21} neutrons/cm^2 ($E > 0.18$ MeV) and a maximum burnup of 2.9% FIMA in the fertile ThO_2 particles. Only the first sample listed in Table 7.11 failed, even though our calculations indicated that the first two would fail at the higher temperature and nominal exposure. However, this result is within the uncertainties of the model calculations and indicates that the experiment will accomplish most of the objectives.

After visual examination, the samples of GGA particles were returned to Gulf General Atomic for final examination and evaluation. Extensive failures were observed in some samples, which unequivocally demonstrates that the most sensitive parameter in particle coating design is the anisotropy. This further emphasizes the need for an accurate technique for optical determination of the anisotropy (see Sect. 6.1.5).

Preliminary results from capsules HT-13 through HT-15 should be available by June 1973. Dimensional change measurements will be made on all surviving particles, but activity levels are too high at the present time. Decay periods of 6 to 12 months will be required to obtain these dimensional measurements. Destructive testing, for example, internal gas pressures and anisotropy changes, will be performed subsequent to the dimensional measurements.

7.3 IRRADIATIONS IN ORR CORE FACILITIES

J. A. Conlin K. R. Thoms
R. B. Fitts

A sweep capsule irradiation designed to test a variety of loose coated particles to high burnup at low temperature was completed and examined. Results from the evaluation of this capsule, Cl-28, and its specimens are reported in Sect. 8.3 of this report.

We are also designing and preparing two high-flux facilities in the ORR core for joint ORNL-GGA irradiation testing. These facilities, which will occupy the C-3 and E-3 core positions, will be fully instrumented and will have temperature control capability by mixing of sweep gases. The ORR core loading will be adjusted to produce a fast-neutron flux in these facilities sufficiently high to give representative HTGR exposures of about 8×10^{21} neutrons/cm^2 in one year. One facility, C-3, will be occupied by a graphite irradiation capsule designed and fabricated by GGA. The second facility, E-3, will be occupied by a joint ORNL-GGA fueled experiment, which will be designed and constructed at ORNL. The capsule will have two independent cells, one of which will be filled with a GGA experiment and the other by ORNL fuels.

The first capsule, designated OF-1 (GGA designation P13Q), is divided into two cells, with the top cell, about 15 in. long, containing GGA fuel specimens and the bottom cell, about 8 in. long, containing ORNL fuel specimens. The cells are formed by brazing a nickel bulkhead in the primary containment tube at a point $3\frac{3}{8}$ in. below the reactor midplane. Each cell will have its own sweep-gas system, allowing independent temperature control and fission gas release measurements.

The upper cell, being designed and fabricated by GGA, will contain three graphite fuel bodies, each with seven axial holes -- three of 0.625 in. diameter for fuel rods and four of 0.500 in. diameter for additional samples. There will be 17 thermocouples and various dosimetry wires in this cell. The lower cell specimen was designed and fabricated by ORNL and will contain a graphite fuel body having five 0.494-in.-diam holes -- one central hole and four peripheral holes. Two of the peripheral holes will be used to test the in-block carbonization process, while the central hole and the other two peripheral holes will test packed-bed carbonized fuel rods. There will be 16 thermocouples

located to provide characterization of the thermal operating conditions in the cell and data on the thermal conductance of a reference slug-injected fuel rod.

The other capsule, designated OG-1, is being designed and built by GGA for irradiation in the ORR C-3 position. This capsule will contain ten graphite crucibles at temperatures ranging from 600 to 1400°C to be exposed to a peak fast fluence of 4×10^{21} neutrons/cm^2 ($E > 0.18$ Mev). The in-core section of this capsule is also divided into two cells. The upper cell will contain seven crucibles and the lower cell will contain three crucibles. The temperature of each cell will be controlled by an independent sweep gas system of helium, neon, argon, or mixtures of these gases.

Since gamma energy is the sole heat source for the OG-1 capsule and a considerable fraction of the total heat source for the OF-1 capsule, an attempt was made to determine the gamma heat profiles for both the E-3 and C-3 positions of the ORR with the core in the same configuration as it will be for irradiation of both of these capsules. The gamma heat measurements were made using an ion chamber which was inserted in each facility. First the ionization current was measured in the F-1 core position with the core in the geometry used during a previous irradiation experiment in the F-1 core position (high-burnup capsule 3). The core geometry was then rearranged to the geometry planned for these experiments, and the ionization current was measured in the C-3 and E-3 core positions. A thermal analysis of the operating temperatures of the high-burnup experiment provided an absolute value of 2.5 W/g for the gamma heat in graphite for the F-1 core position for the core geometry used in the high-burnup experiment. The gamma heat in the C-3 and E-2 positions was then determined by multiplying the F-1 gamma heat of 2.5 W/g by the rates of the ionization current in the C-3 or E-3 position to that of the F-1 position.

An axial traverse was made in each position with the reactor shut down to obtain background measurements and then the measurement repeated with the reactor at a nominal 300 kW. For the background measurements the nearest control rod was placed in its normal operating position, so that its influence on the background was representative of what it would be during the measurements at power. The measurements were made with the reactor operating long enough to obtain a heat balance and therefore a fairly accurate measurement of the reactor power. The measured background ionization currents were then subtracted from the measurements made at power and the results normalized to the peak value obtained in F-1, making adjustments for any differences in reactor power. The results of this experiment indicated that the peak gamma heating rate for both E-3 and C-3 will be on the order of 8 W/g in graphite.

Present plans call for OB-1 to be installed in the ORR during the June 17–22, 1973, shutdown. Capsule OF-1 will be installed in mid-July. Capsule OF-1 will be irradiated for one year and capsule OG-1 for six months.

7.4 IRRADIATION TESTS IN ETR CAPSULE FACILITIES

A. R. Olsen J. H. Coobs
R. A. Olstad R. B. Fitts

A set of two HTGR recycle fuel capsules, H-1 and H-2, has been irradiated in the ETR to the full design fast fluence of 8×10^{21} neutrons/cm^2 ($E > 0.18$ MeV). These capsules[9] incorporated hafnium-bearing neutron shields to reduce the thermal flux in the ETR test facility and to provide approximately equal thermal and fast flux exposures to the test samples. The design fluxes were verified by data from the ETR critical assembly mockup. These two capsules were the first of this type to be irradiated in the ETR.

In addition, we completed the irradiation and initial examination of capsule 43-105, the last of a group of five uninstrumented X-basket capsules designed for testing coated-particle fuels. The irradiation of two molded fuel-rod specimens prepared at ORNL was continued during the year in capsule P-13N in cooperation with GGA. No further ETR capsule experiments are planned since the reactor will not be available for such testing in the future.

7.4.1 ETR Capsules H-1 and H-2

A. R. Olsen R. B. Fitts

The ETR H-1 and H-2 recycle fuel test capsules were irradiated in the ETR between May 1971 and May 1972. The capsules were accidentally inverted during the last quarter of the irradiation period. The effect of this inversion on the operating conditions of the test samples was significant in about half of the samples and was small in the remaining samples.

A schematic of the H-capsule design is shown in Fig. 7.17. The capsules were surrounded by thermal-neutron shields made of Zr–40% Hf (top half) and 100% Hf

9. A. R. Olsen, "Capsule Tests," *GCR-TU Programs Semi-annu. Progr. Rep. Sept. 30, 1970,* ORNL-4637, pp. 110–11.

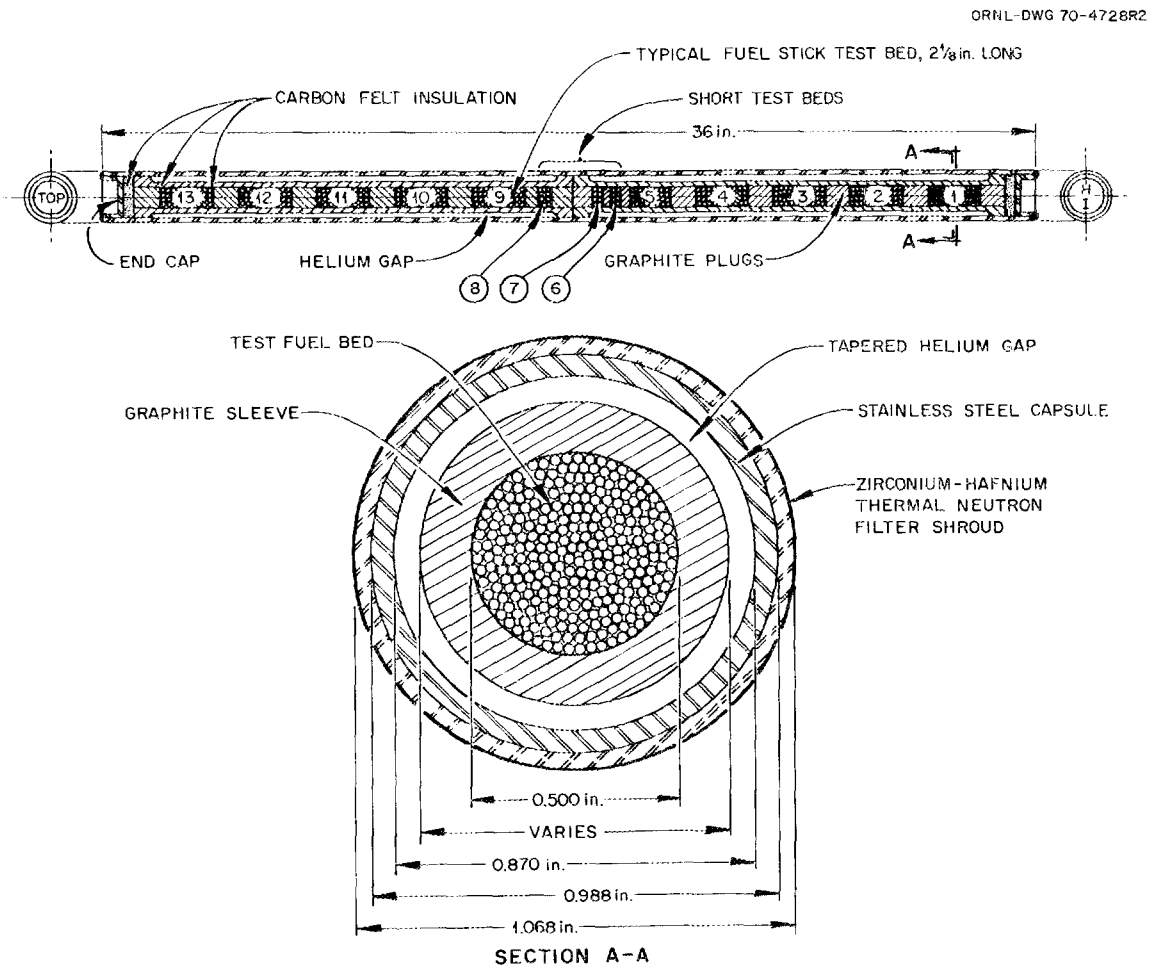

Fig. 7.17. Schematic of HTGR recycle irradiation capsule.

(bottom half). These shields were used to lower the thermal-neutron flux, regulating the fission heating and adjusting the ratio of thermal and fast flux in the test specimen. The fuel rod temperatures were further adjusted by providing a tapered gap between the graphite sleeve and the stainless steel capsule wall. The fuel regions are divided by graphite plugs into 13 test samples in each capsule. Ten of these in each capsule are approximately $2\frac{1}{8}$ in. long, and the three short rods are approximately $\frac{1}{2}$ in. long.

The fuel particle combinations in these capsules are given in Table 7.12. The *a*, *c*, *f*, and *g* combinations are the main ones used in the RTEs described previously.[10] The *R* combination is made with a Biso-coated uranium-loaded strong-acid resin particle and a coated ThO_2 Biso particle. The distribution of these samples in the two capsules and the planned irradiation temperatures are given in Table 7.13.

Table 7.12. Fuel particle combinations in HTGR recycle irradiation capsules

Combination	Kernel and coating type	
	Fissile particle	Fertile particle
a	4/1 $(Th/U)O_2$ Biso	ThO_2 Biso
c	2/1 $(Th/U)O_2$ Biso	ThO_2 Biso
f	UC_2 Triso	ThC_2 Biso
g	UO_2 Biso	ThO_2 Biso
R	Resin UOS Biso	ThO_2 Biso

10. R. B. Fitts, "Recycle Test Elements," *GCR-TU Programs Semiannu. Progr. Rep. Sept. 30, 1970*, ORNL-4637, pp. 111–13.

Table 7.13. Fuel loading in HTGR recycle irradiation capsules

Sample	Fuel combination	Nominal fuel bed center temperature (°C)	
		Capsule H-1	Capsule H-2
13	g[a]	1300	750
12	g	1300	750
11	c	1300	750
10	a	1300	750
9	f	1300	750
8[b]	R	1300	750
7[b]	R	1050	950
6[b]	a[a]	1050	950
5	f	1050	950
4	a	1050	950
3	c	1050	950
2	g	1050	950
1	f	1050	950

[a]Loose beds of particles; all others are pitch-bonded fuel sticks with Poco graphite filler.

[b]Short samples, ~0.5 in. long; all others are ~2⅛ in. long. Sample diameter is 0.5 in.

The postirradiation examination of the H-capsule is under way, and some initial results have been obtained. As mentioned above, the capsules were irradiated for approximately one-fourth of the time in an inverted position. Such a change in orientation would have a significant effect on the fission rates in the various fuel samples. The magnitude of this effect will be dependent on the fissile burnup at the time of the inversion, so actual peak operating temperatures must be defined by detailed history calculations which are under way. We do know that the rods in the upper sleeves, H-1-8 to H-1-13 and H-2-8 to H-2-13, operated above the respective design temperatures of 1300°C for H-1 and 750°C for H-2.

Dimensional data were obtained on the graphite sleeves which contained the samples. A detailed evaluation of these data cannot be made until the operating histories and fluence measurements are completed. However, the length changes and extent of bowing both decreased with decreasing design fluence and temperatures.

Since none of the fuel rods could be pushed out of the sleeves, it was necessary to saw two slits 180° apart the full length of each sleeve. The slits did not penetrate the full sleeve wall thickness. The remaining thin section was cracked by careful wedging to allow the two halves to separate and permit inspection and photography of the rods in place. The results of the preliminary visual examinations of the various fuel rods are given in Table 7.14. Some of the rods were sufficiently intact to obtain limited diameter measurements. These are included in the data in Table 7.15. From these data it is apparent that some of the rods were irradiated at very high temperatures. This is particularly true for those in the 1300°C design region, where the central portions appear to contain a powder rather than discrete coated particles.

The material from each rod has been recovered. A sample of each type of fuel rod has been provided for reprocessing studies, and additional samples will be available as needed. We have recovered the flux monitor capsules for further processing.

Metallographic examination has been completed on five of the fuel rod samples from these capsules. The results included below are typical of those to be expected from these capsules in that samples which were relatively unaffected by the capsule inversion yield data on the fuel performance during normal operation and those samples subjected to high temperatures at the end of the test yield information on fuel performance under off-normal conditions.

An example of the results on fuel that was not significantly affected by the inversion is shown in Fig. 7.18. This fuel rod operated at about 1000°C centerline temperature with a maximum thermal gradient of ~600°C to burnups of about 50% FIMA in the UO_2 fissile particles and ~3% in the ThO_2 fertile particles. These conditions are representative of average HTGR conditions, and the fuel performed quite well. A higher magnification view of the UO_2 fissile particle is shown in Fig. 7.19. An example of the accelerated burnup version (with a thorium:uranium ratio of 2:1) of the reference recycle fissile particle that survived to essentially full HTGR design exposure at near maximum conditions is shown in Fig. 7.20.

One of the fuel rod samples that operated under extreme conditions after the capsule was inverted is shown in Fig. 7.21. This fuel rod adhered to the graphite sleeve, part of which is visible on the left side of this cross section. The fuel particles on the side opposite the sleeve were near the center line of the fuel rod and were exposed to temperatures above 2000°C when the capsule was inverted. These particles failed and reacted with the fuel rod matrix. A higher magnification view of one of the ThO_2 Biso fertile particles, from near the center, which is in the process of failing by an apparent "amoeba" mechanism, is shown at higher magnification in Fig. 7.22. The transport and deposition of some material across the ThO_2 kernel, probably carbon, are evident in the

Table 7.14. Preliminary visual examination of fuel from capsules H-1 and H-2

Combination identification	Particle		Sample identification	Design operating temperature (°C)	Visual examination observations
	Fissile	Fertile			
a	$(4Th,U)O_2$ Biso	ThO_2 Biso	H-2-10	750	Rod intact with some transverse cracking; some fragmentation on removal; small diameter central core of reddish powder; rod diameter measured
			H-2-4	950	Rod intact; some minor surface sloughing; diameter measured
			H-2-6[b]	950	Loose particles; no apparent damage
			H-1-8[b]	1050	Loose particles; no apparent damage
			H-1-4	1050	Rod intact; some surface spalling; diameter measured
			H-1-10	1300	Rod intact with one transverse crack at holder break; some fragmentation on storage; reddish powder in center of rod; diameter measured
c	$(2Th,U)O_2$ Biso	ThO_2 Biso	H-2-11	750	Rod intact; some cracking of end toward capsule center; broke on removal; red powderish central core; diameter measured
			H-2-3	950	Rod broke into four large sections; very few loose particles
			H-1-3	1050	Large fragments on opening; completely debonded during removal
			H-1-11	1300	Rod broken in large fragments on opening; deteriorated severely on exposure to cell atmosphere
f	UC_2 Triso	ThC_2 Biso	H-2-9	750	Rod intact when sleeve opened; disintegrated to powder in cell atmosphere within 16 hr
			H-2-1	950	Rod broken into two large sections; very few loose particles; diameter measured
			H-2-5	950	Rod debonded; no evidence of broken particles
			H-1-1	1050	Rod intact; some end chipping during removal; diameter measured
			H-1-5	1050	Rod severely debonded; appeared to deteriorate more on exposure to cell atmosphere
			H-1-9	1300	Part of rod near center debonded with other end of rod fragmented; failed particles were apparent
g	UO_2 Biso	ThO_2 Biso	H-2-13[b]	750	Loose bed has partially sintered with a central core hole; most of bed still loose
			H-2-12	750	Rod fragmented into large pieces; some loose particles
			H-2-2	950	Rod intact; diameter measured
			H-1-2	1050	Rod fragmented and largely debonded in center; ends essentially intact; ends broke on removal
			H-1-12	1300	Rod intact with end near top broken off when holder broke; reddish powdered central core visible at break
			H-1-13[b]	1300	Loose particles recovered during capsule disassembly
R	UOS Biso	ThO_2 Biso	H-2-8	750	Rod intact with longitudinal crack; broke during removal along crack
			H-2-7	950	Rod completely debonded
			H-1-7	1050	Rod intact on opening; fragmented during removal
			H-I-8	1300	Completely debonded to loose particles; interior of sleeve also had a sootlike deposit

[a]Combinations of fissile and fertile particles are: a, $(4Th,U)O_2$ Biso with ThO_2 Biso; c, $(2Th,U)O_2$ Biso with ThO_2 Biso; f, UC_2 Triso with ThO_2 Biso; g, UO_2 Biso with ThO_2 Biso; and R, UOS Biso with ThO_2 Biso.

[b]Loose bed of particles.

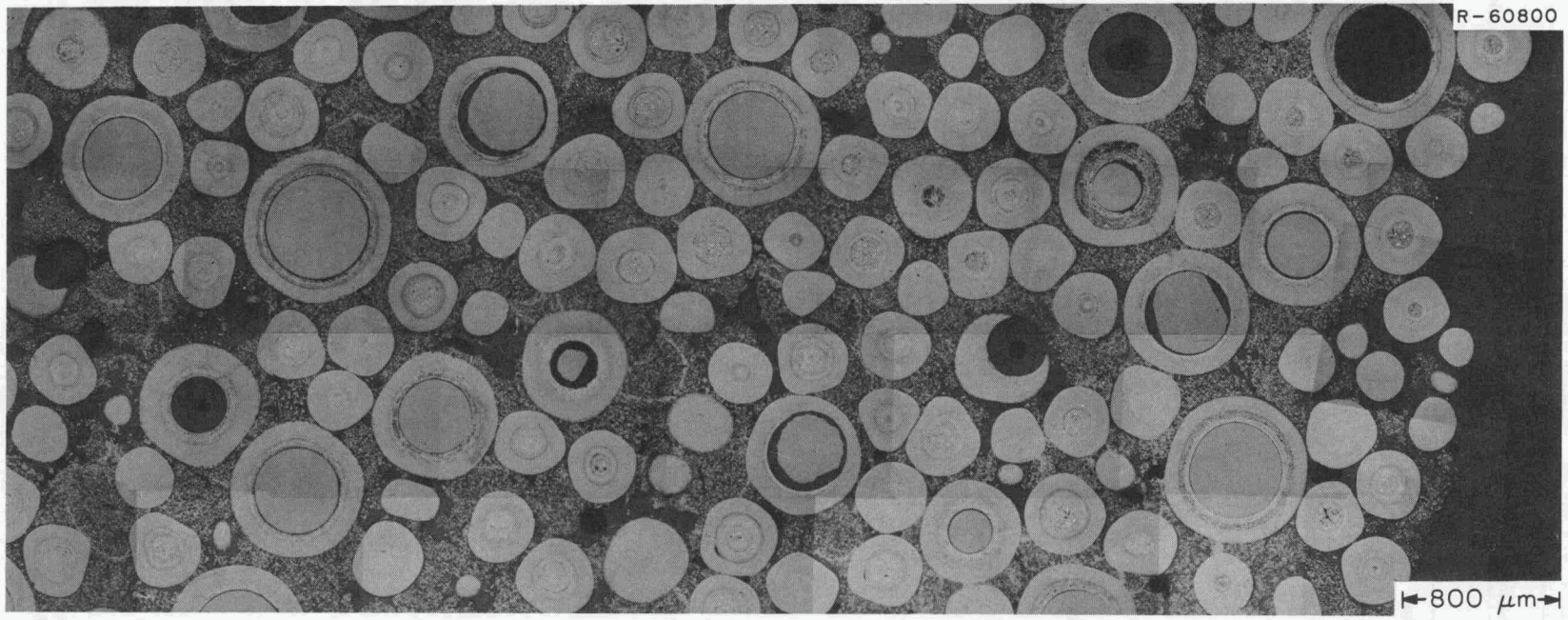

Fig. 7.18. Radial section of fuel rod H-1-2 containing Biso-coated UO_2 and Biso-coated ThO_2 particles.

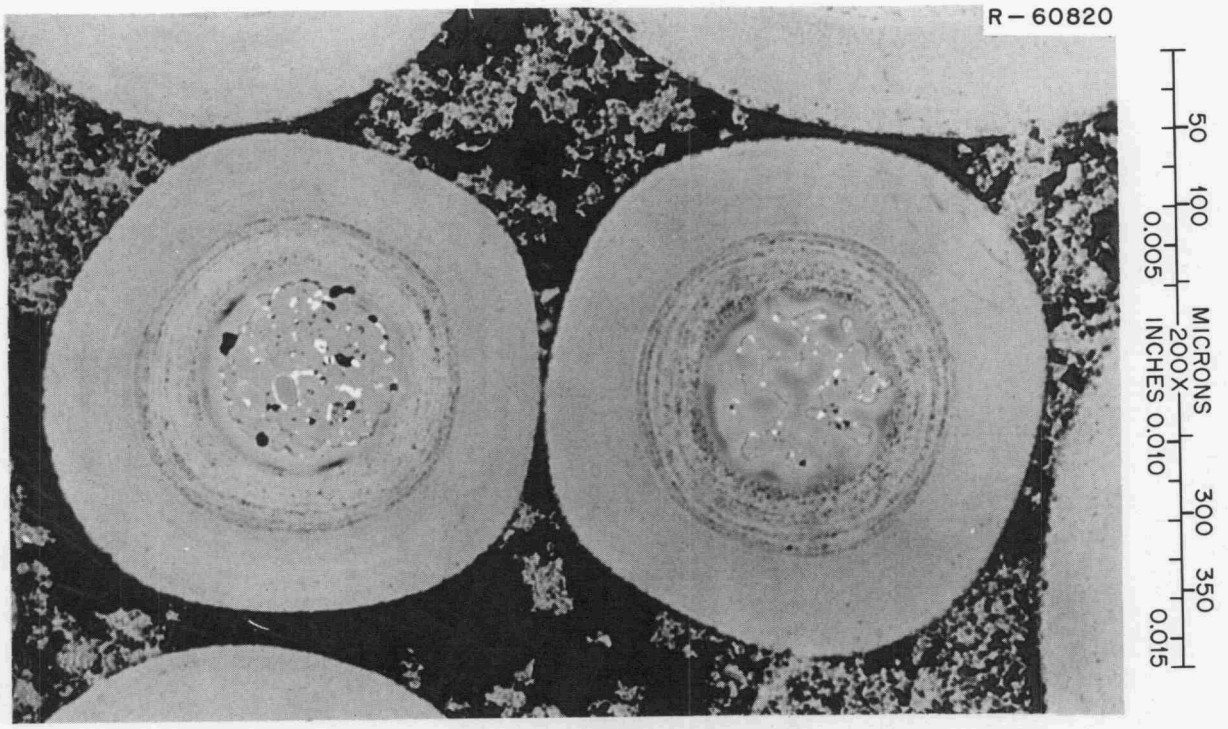

Fig. 7.19. Typical UO_2 Biso fissile particles from sample H-1-2 after irradiation at about 1000°C with a temperature gradient of about 600°C/cm to about 50% FIMA.

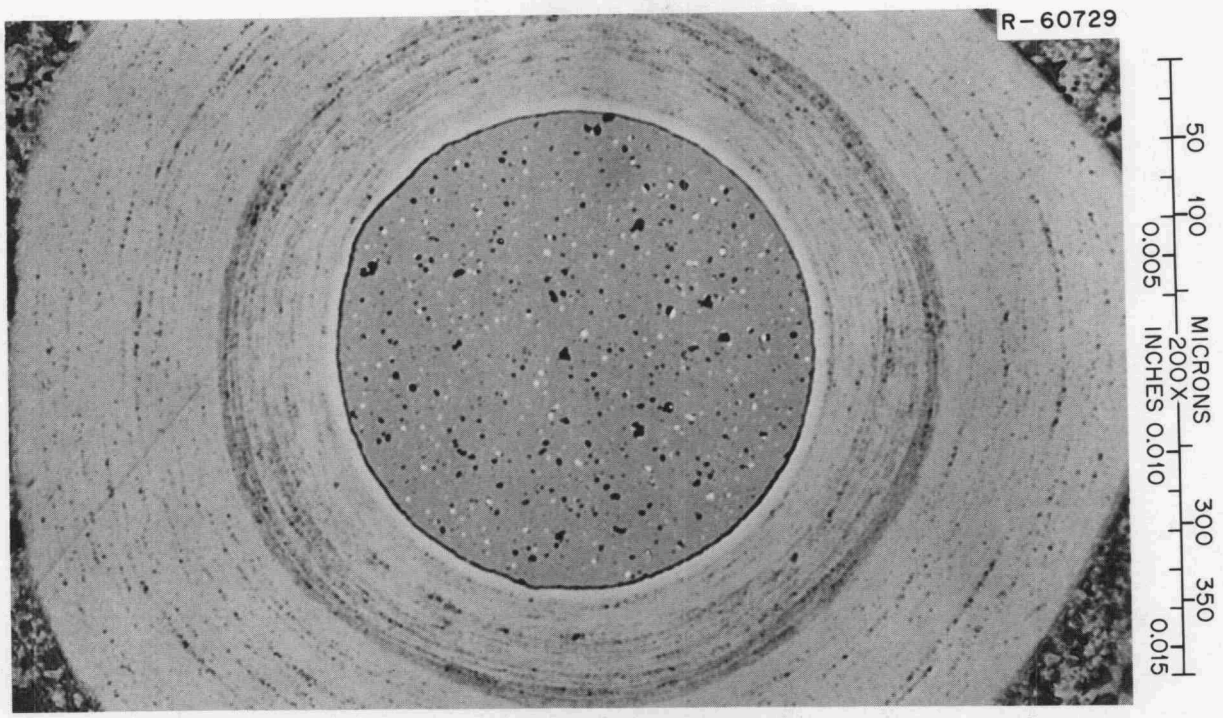

Fig. 7.20. Typical 2/1 $(Th/U)O_2$ Biso fissile particle from sample H-1-3 after irradiation at about 1300°C with a temperature gradient of about 600°C/cm to about 20% FIMA.

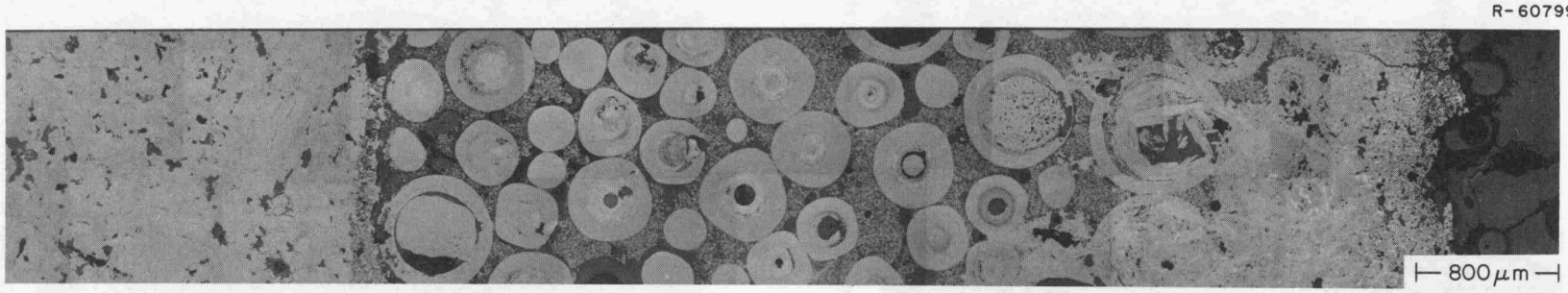

Fig. 7.21. Radial section of fuel rod H-1-12 containing Biso-coated UO_2 and Biso-coated ThO_2 particles. Note fuel migration and coring of sample from effects of extreme heat rating after capsule inversion.

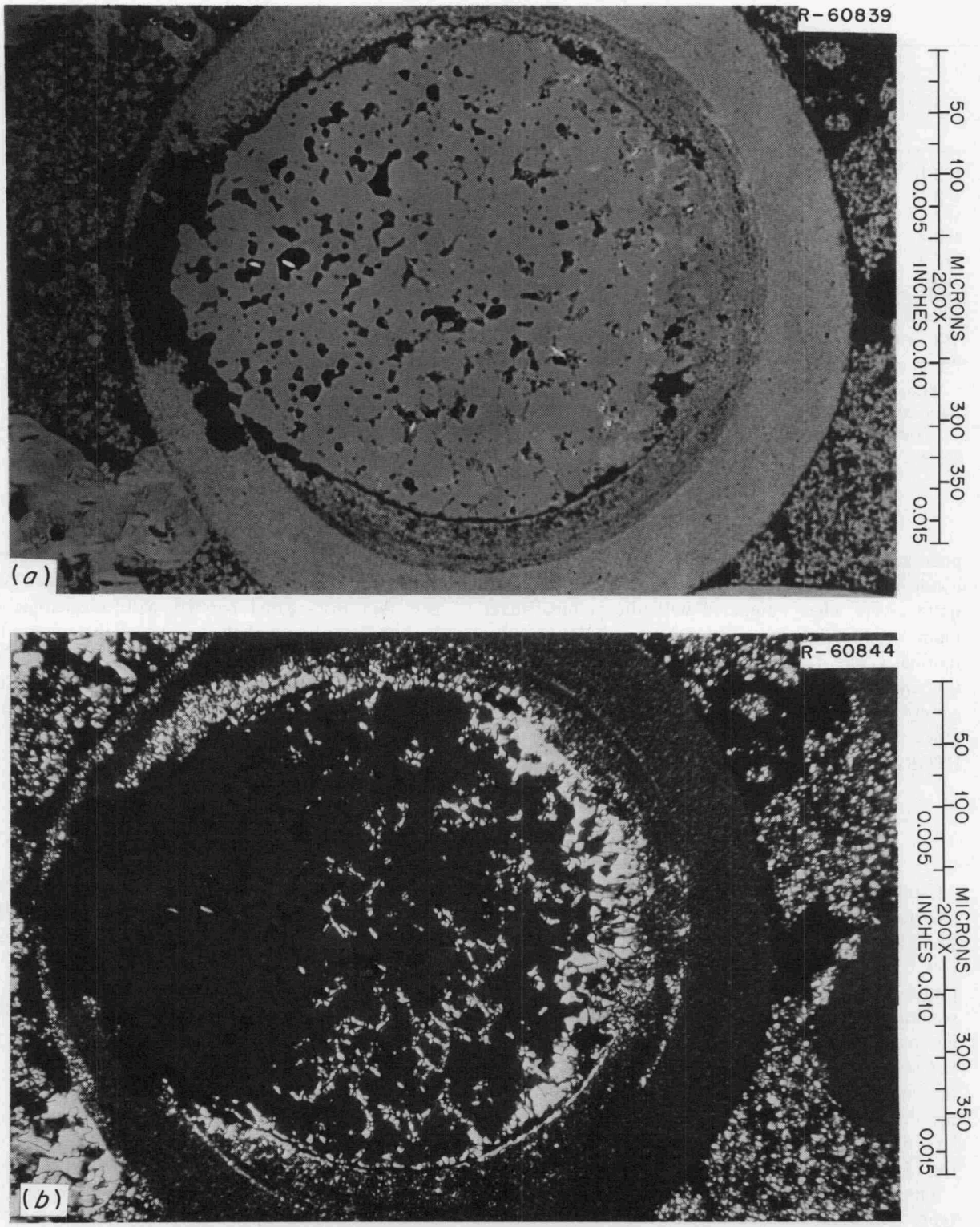

Fig. 7.22. ThO_2 Biso particles from sample H-1-12 after irradiation at about 1750°C with a thermal gradient of about 950°C/cm to about 3% FIMA. (*a*) As polished; (*b*) polarized light.

Table 7.15. Fuel rod diametral data for capsules H-1 and H-2

Rod No.	Design operating temperature (°C)	Combination[a]	Capsule diameter (in.)		Change in diameter (in.)	$\Delta D/D_0$ (%)
			Preirradiation	Postirradiation[b]		
H-2-10	750	a	0.4866	0.4485	0.0381	7.8
H-2-11	750	c	0.4871	0.4518	0.0353	7.2
H-2-1	950	f	0.4936	0.4769	0.0167	3.4
H-2-2	950	g	0.4899	0.4764	0.0135	2.8
H-2-3	950	c	0.4875	0.4731	0.0144	3.0
H-2-4	950	a	0.4871	0.4695	0.0176	3.6
H-1-1	1050	f	0.4930	0.4750	0.0180	3.7
H-1-4	1050	a	0.4889	0.4793	0.0096	2.0
H-1-10	1300	a	0.4869	0.4625	0.0244	5.0

[a]Combinations of fissile and fertile particles are: a, (4Th,U)O_2 Biso with ThO_2 Biso; c, (2Th,U)O_2 Biso with ThO_2 Biso; f, UC_2 Triso with ThO_2 Biso; g, UO_2 Biso with ThO_2 Biso; and R, UOS Biso with ThO_2 Biso.

[b]The diameter quoted is the maximum diameter obtained on any portion of the rod still intact after removal from the graphite sleeve.

polarized light photomicrograph of this particle. The conditions under which this transport occurred are quite severe when compared with the nominal maximum 1100-MW(e) design conditions of 1350°C with a thermal gradient of 650°C/cm; however, this information will be of value in assessing the mechanism of, and conditions required for, the operation of the amoeba effect in oxide kernel coated-particle fuels from HTGRs.

7.4.2 ETR Capsule X-Basket 5

A. R. Olsen J. H. Coobs

Capsule 43-105 (X-basket 5) is the last of a group of five uninstrumented capsules designed for irradiation in the ETR. This capsule was designed to investigate the effects of fast fluence on the performance of different pyrocarbon coatings and the effect of thorium on fuel swelling. All fuel kernels were 500-μm-diam sol-gel microspheres of ThO_2–3% UO_2 containing 93% enriched uranium. This composition was chosen so that the initial fission rate would be about equal to the maximum fission rate of ^{233}U generated from ^{232}Th later in the irradiation. The operating temperature of the fuel holders would thus be fairly constant.

Samples of the fuel were coated with ten different types of carbon coatings to study the combined effects of fast-neutron exposure and fuel burnup. These types included four Biso coatings with low-temperature isotropic (LTI) outer layers and varying ratios of buffer and outer coating, two batches with a thick LTI coating layer (no buffer), one batch with a high-temperature isotropic (HTI) outer layer on a 52-μm-thick buffer, and two Biso-coated batches with anisotropic outer layers. The types and thicknesses of the coating layers on the various batches are given in Table 7.16. Of the 11 batches listed, 1 contained poorly shaped kernels from a separate lot, and a final batch consisted of a heat-treated portion from one of the Biso-coated types listed above. Samples from these 11 batches were distributed in 30 sample containers as loose particles contained in an annulus. Containers 1 to 8 were designed to operate at 400°C, and the other 22 were designed for fuel temperatures of 1400°C.

The experiment was irradiated in a core position of the ETR from June 1967 to August 1971, with the exception of an 18-month period (June 1969 to December 1970) during which it was stored in the ETR pool. The effective full-power days of irradiation were 538 in a position with an advertised peak flux of 3.0×10^{14} neutrons cm^{-2} sec^{-1} (2200 m/sec). Thus, the peak thermal fluence was approximately 1.3×10^{22}. Analysis of the flux monitor tapes is in progress.

The experiment has been dismantled, and all components have been removed from their containers and placed in sample bottles. Some difficulties were encountered because of the dimensional changes in the graphite components. Dimensional data on these components have been obtained but have not yet been analyzed. There is evidence that the ATJ graphite has shrunk in the low-temperature regions and grown in the high-temperature regions.

Table 7.16. Visual failure analysis of loose particles from X-basket 5 (43-105)

Container No.	Coated particle[a] batch No.	Coatings[b]				Approximate number of failures (%)
		Inner		Outer		
		Type	Thickness (μm)	Type	Thickness (μm)	
1	OR-928	P	57	LTI	59	0
14						50
26						40
2	OR-933[c]	LTI	24	LTI	119	1.5
13						>80
25						>70
23	OR-932-R2			LTI	145	<1
3	OR-924-R3	P	40	LTL	100	100
17						100
27						>80
4	OR-931-R1	P	96	LTL	45	100
18						>80
28						100
5	OR-929-C[d]	P	52	HTI	51	0
19						100
29						100
6	OR-926	P	47	LTI	68	0
20						1
30						≪1
7	OR-925-R	P	47	LTI	72	0
9						<1
15						0
8	OR-923	P	22	LTI	63	1
10						35
16						50
24						60
11	OR-926-HT	P	47	LTI	68	<1
21						2.5
12	OR-930	P	81	LTI	67	4
22						2.5

[a]All particle kernels are $(Th_{0.97},U_{0.03})O_2$ sol-gel spheres of 480 μm diameter.

[b]Coating types are defined as follows: P, porous derived from C_2H_2 at 1050°C; LTI, low-temperature isotropic derived from C_3H_6 at 1250°C; LTL, low-temperature laminar derived from C_3H_6 at 1150°C (BAF approximately 2.1); HTI, high-temperature isotropic derived from CH_4 at 2000°C.

[c]Intermediate sealer layer 5 μm thick deposited at low rate from C_3H_6 at 1250°C.

[d]Intermediate LTI sealer layer 17 μm thick.

The results of the stereoscopic examination of all the coated particles from each of the 30 containers are summarized in the failure percentages given in Table 7.16. Particle batches OR-924-R3 and OR-931-R1 were both designed with anisotropic outer coatings that were expected to fail from fast-fluence damage. The high failure rate for OR-929-C (Biso-HTI) was not expected and will require additional examination and analysis before an explanation is available. The remaining particles should provide data to meet the objectives of this experiment.

One unsatisfactory feature of this capsule is the inclusion of melt wires in ThO_2 crucibles in the center post of some containers. The postirradiation examination shows melting or incipient melting of all these wires. However, we do not believe this is indicative of

the fuel bed temperatures because of the large amount of heat generated in the ThO_2 crucibles from gamma-ray absorption and fissioning of the ^{233}U formed in the crucible itself.

7.5 RECYCLE TEST ELEMENTS IN THE PEACH BOTTOM REACTOR

R. B. Fitts

A set of seven test fuel elements, known as recycle test elements (RTEs), is being irradiated in the Peach Bottom Reactor in a cooperative effort with Gulf General Atomic. These elements replace standard Peach Bottom fuel elements in the reactor. Each RTE contains six 15-in.-long graphite fuel bodies each of which has eight $\frac{1}{2}$-in.-diam holes to accommodate fuel samples; thus, 48 separate large fuel samples are irradiated in each RTE.

The irradiation of the first six recycle test elements[11] began in the Peach Bottom Reactor in July 1970, and the tests have progressed without incident since that time. In April 1971, the first of these elements to be removed from the reactor (RTE-7) was discharged, and an additional element (FTE-11, previously designated RTE-1) was inserted. One of the six elements remaining in the reactor (RTE-4) was discharged in June 1972, and the others will remain in the reactor until June 1973 or longer. The fuel loadings and design operating conditions for RTE-7 are shown in Table 7.17. During the 252 effective full-power days of operation, the peak fast-fluence exposure of $\sim 10^{21}$ neutrons/cm^2 ($E >$ 0.18 MeV) and the peak fuel burnup occurred in bodies 3 and 4. Details of the temperature distribution in this element were reported earlier.[12]

The main points of interest in postirradiation examination of the RTEs are:

1. the degree of success in separating the fuel from the graphite bodies,
2. the dimensional stability of the graphite and the fuel rods or beds,
3. the integrity and apparent stability of the coated particles,
4. the distribution of fission products within the fuel bodies.

Table 7.17. RTE-7 fuel loading

Body	Combination[a]				Operating temperature range (°C)
	W	X	Y	Z	
6	a	c	f	g	900–1050
5	a	c	f	g	980–1150
4	b	g	h	d	950–1230
3	b	d	g	i	925–1230
2	b	d	g	i	900–1130
1	b	d	g	i	590–880

[a]Particle combinations as given in *GCR-TU Programs Semiannu. Progr. Rep. Sept. 30, 1970,* ORNL-4637, Table 12.2. The capital letters represent quarter sections of the fuel bodies.

We found in RTE-7 that the fuel rods could all be easily removed from the bodies and all exhibited excellent surface appearance. Figure 7.23 shows typical end and side views of the fuel rods. The only apparent degradation was at the ends of rods, where a small amount of material was occasionally observed to be lost.

Measurements on the graphite bodies revealed essentially no change in their dimensions. Measurements on 114 of the 288 fuel rods in this test revealed significant isotropic changes in the fuel rod dimensions. The averaged changes from these fuels are presented in Table 7.18 along with pertinent fabrication data. Many of the fuel rods from RTE-7 are smaller than would have been expected from earlier test data (see Sect. 7.8). This may be due to the fact that the expected dimensional changes were based upon data taken at significantly higher fast-neutron doses ($>4 \times 10^{21}$) and incorrectly interpolated back to lower fluences. If this explanation is correct, the rate of diametral change early in the irradiation must be higher than previously expected. Alternatively, these greater dimensional changes may be a result of the difference in flux level and flux energy distribution between this and previous tests and therefore different rates of fast-neutron-induced carbon densification. The previous tests were accelerated tests conducted in environments not typical of the HTGR environment. Reasonable modification of the initial diameter change rate in the present relationship between diameter change and fast fluence will suffice to include the ORNL data from RTE-7 fuel rods containing Biso particles with data from earlier tests. However, the data from Triso-Triso (FSVR-type) fuels cannot be reconciled with the earlier data. Perhaps these fuel rods were below the specified diameter range as fabricated, but we have no indication from GGA that

11. W. D. Turner and M. Siman, *HEATING III: An IBM-360 Heat Conductor Program,* ORNL-TM-3208 (February 1971).
12. R. B. Fitts, "Recycle Test Elements," *GCR-TU Programs Annu. Progr. Rep. Sept. 30, 1971,* ORNL-4760, pp. 65–67.

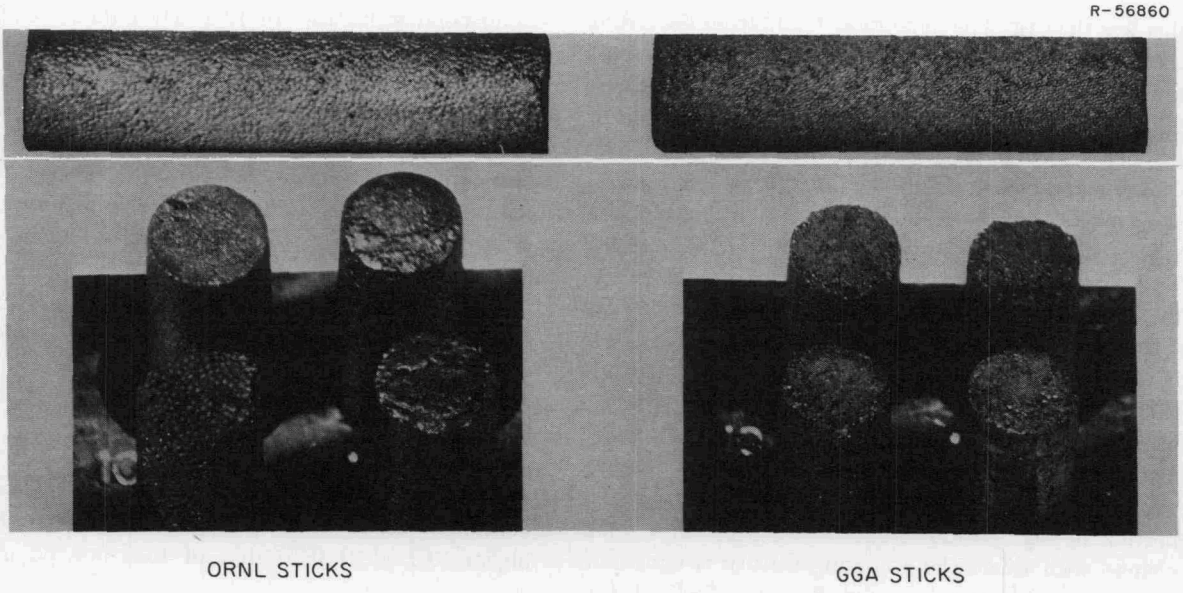

Fig. 7.23. Typical appearance of fuel rods from RTE-7 recycle test element.

Table 7.18. Fuel rod dimensional change summary for RTE-7 irradiation

Rod type	Fabrication data[a]				Irradiation conditions[b]		Average irradiation-induced diameter change[c] (%)
	Fuel hole	Fissile particle	Fertile particle	Average outer coating density (g/cm^3)	Temp. (°C)	Fast fluence ($neutrons/cm^2$)	
						$\times 10^{21}$	
a	7-5-1	$(4Th,U)O_2$ Biso	None	1.84	1100	0.97	−2.10
a	7-6-1	$(4Th,U)O_2$ Biso	None	1.84	1000	0.60	−1.29
a	7-6-2	$(4Th,U)O_2$ Biso	None	1.84	1000	0.60	−1.42
c	7-5-4	$(2Th,U)O_2$ Biso	ThO_2 Biso	1.88	1100	0.97	−2.09
c	7-6-3	$(2Th,U)O_2$ Biso	ThO_2 Biso	1.88	1000	0.60	−1.58
c	7-6-4	$(2Th,U)O_2$ Biso	ThO_2 Biso	1.88	1000	0.60	−1.61
g	7-3-5	UO_2 Biso	ThO_2 Biso	1.92	1200	1.26	−2.30
g	7-1-5	UO_2 Biso	ThO_2 Biso	1.92	800	0.85	−0.83
g	7-1-6	UO_2 Biso	ThO_2 Biso	1.92	800	0.85	−0.90
g	7-5-8	UO_2 Biso	ThO_2 Biso	1.84	1100	0.97	−2.05
g	7-6-7	UO_2 Biso	ThO_2 Biso	1.84	1000	0.60	−1.57
g	7-6-8	UO_2 Biso	ThO_2 Biso	1.84	1000	0.60	−1.42
d	7-3-4	$(2Th,U)O_2$ Biso	ThC_2 Biso	1.85	1200	1.26	−2.64
b[d]	7-3-1	UO_2 Biso	ThC_2 Biso	1.85	1200	1.26	−3.49[e]
f[d]	7-5-6	UC_2 Triso	ThC_2 Biso	1.77	1100	0.97	−2.69[e]
i[d]	7-3-8	UC_2 Triso	ThC_2 Triso	1.75	1200	1.26	−2.30[e]
j[d]	7-1-8	UC_2 Triso	ThC_2 Triso	1.75	800	0.85	−0.97[e]

[a]Oxide kernel particles made at ORNL; carbide kernel particles made at GGA.

[b]Estimated average value for six rods.

[c]Average of data from six fuel rods in a fuel hole.

[d]Made at GGA using natural flake graphite filler and carbonization in a split mold; all others made at ORNL using Poco graphite filler and packed-bed carbonization.

[e]No preirradiation data available; changes based on nominal specification diameter of 0.490 in.

this was the case. The dimensional data from the ORNL rods appear to be providing useful information on low-fluence dimensional changes and, combined with data from the remaining RTEs, should yield information on differences in dimensional changes associated with different rates of accumulating fast-neutron damage.

We have examined in some detail the shrinkage of two sets of RTE-7 fuel rods which contained UO_2 Biso plus ThO_2 Biso fuel particles. The two sets differed only in the outer coating density of the Biso-coated particles. Portions of each of these two groups of rods have been irradiated over the full range of temperatures and fluences obtained in RTE-7 and thus have provided a potential source of information on the combined effects of fluence and temperature at low fluence exposure levels. The data from these 36 fuel rods are plotted in Fig. 7.24. The general trend of dimensional change with fluence and coating density is consistent with that from earlier tests with Biso-type fuel rods (see Sect. 7.8). The most interesting point revealed by these data is the apparent effect of irradiation temperature on the diameter change for the fuels with average particle outer coating densities of 1.92. The data at 1200°C are significantly below the trend established by the approximately 800°C data. Unfortunately, the RTEs are not instrumented. Despite the fact that the variation of temperature and fluence in them should be uniform and thus provide reasonable confidence in these results, we shall have to look for and verify the temperature effect in other tests before placing too much emphasis on this result.

Metallographic examination has been completed on six of the fuel rods from this experiment. These rods, which contained a sample of all the fissile and fertile particles in RTE-7 except the UC_2 Biso material, are listed in Table 7.19.

Typical radial cross sections of fuel rods 7-3-6-3 and 7-3-2-3 are shown in Figs. 7.25 and 7.26.[13] The matrix density of the fuel rods bonded at ORNL was typically higher (0.7 g/cc) than that of rods bonded at GGA

13. Fuel rods are identified by a four-digit number specifying RTE No., body No., hole No., and rod position respectively.

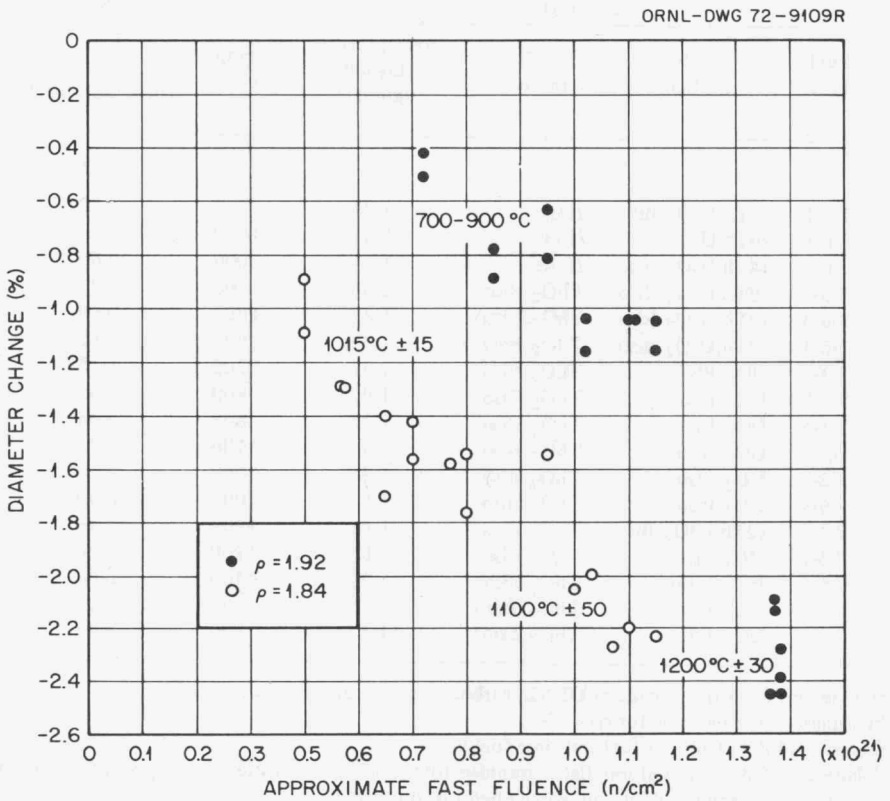

Fig. 7.24. Dimensional changes in (UO_2 Biso plus ThO_2 Biso) fuel rods from RTE-7 as a function of fast fluence.

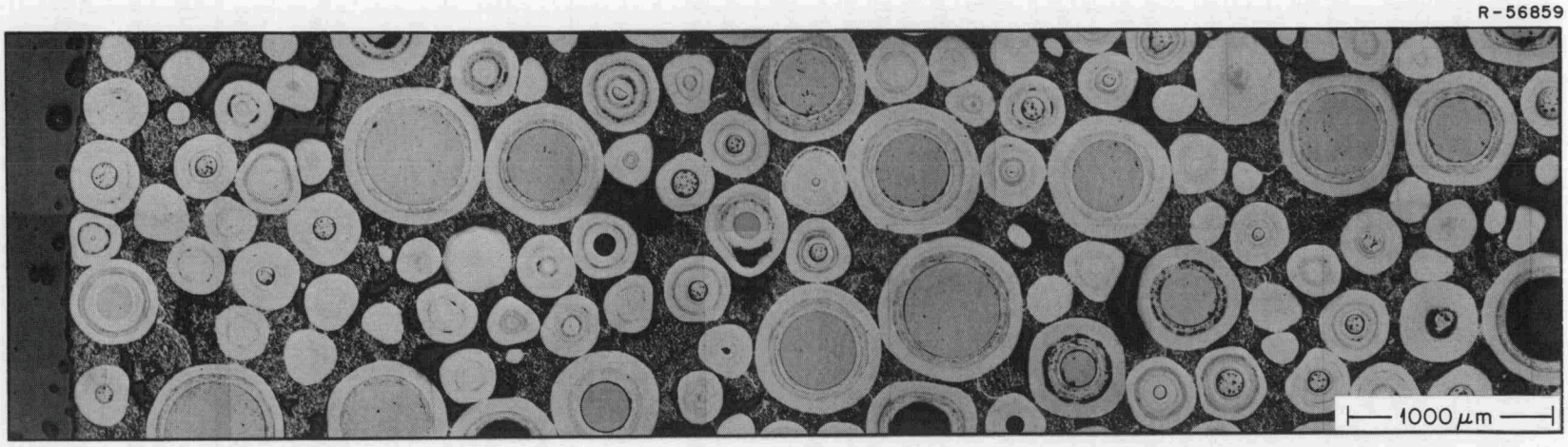

Fig. 7.25. Cross section of an ORNL bonded fuel rod from Peach Bottom recycle test element RTE-7. Fissile particles, Biso UO_2; fertile particles, Biso ThO_2.

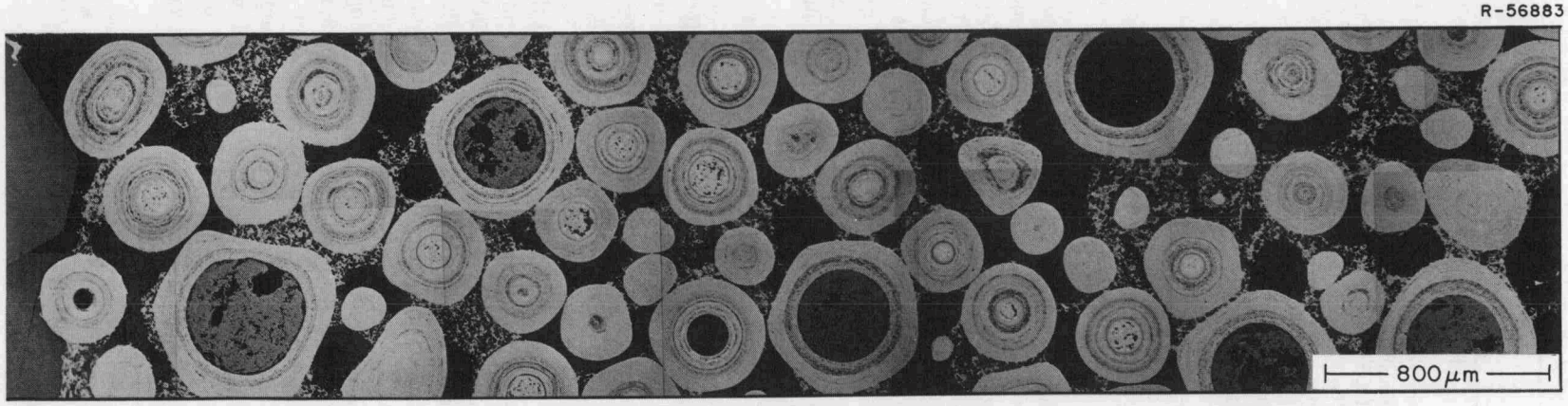

Fig. 7.26. Cross section of a GGA bonded fuel rod from Peach Bottom recycle test element RTE-7. Fissile particles, Biso UO_2; fertile particles, Biso ThC_2.

Table 7.19. Metallography samples from RTE-7

Fuel type	Fuel particles		Fuel rod No.	Design operating temperature (°C)
	Fissile	Fertile		
a	(Th, 20% U)O_2	None	7-5-2-5	1160
c	(Th, 33% U)O_2	ThO_2	7-5-3-5	1160
g	UO_2	ThO_2	7-3-6-3	1220
b	UO_2	ThC_2	7-3-2-3	1220
d[a]	(Th, 33% U)O_2	ThC_2	7-3-3-3	1220
f	UC_2(T)[b]	ThC_2	7-5-5-5	1160
i	UC_2(T)[b]	ThC(T)[b]	7-3-7-3	1220

[a]Not yet examined.
[b]Triso coated; others Biso coated.

(~0.5 g/cc) as illustrated in these two figures. The difference is primarily due to the type and amount of filler used in the rods. About 27 wt % natural flake graphite filler in 15V pitch (reference FSVR matrix) was used at GGA to form the matrix, while about 35 wt % of fine Poco graphite in 15V pitch was used at ORNL. Other than the difference in matrix morphology, the metallographic examination revealed no significant differences between the six types of fuel rods except, of course, particle types.

The fuel particles in RTE-7 all performed satisfactorily. Figure 7.27 shows typical photomicrographs of each type of particle examined. The only indication of potential difficulty with these particles was the presence of numerous cracks in the outer LTI layers of the Triso-coated particles in fuel rod 7-3-7-3 (Fig. 7.27*d*). There were no broken SiC layers visible in over 200 particles examined in this cross section, and the same UC_2 Triso fissile particles examined in fuel rod 7-5-5-5 contained no failed coatings. One of the fuel bodies from RTE-7, body 3, was examined by autoradiography and chemical analysis on the safety program[14] to determine the fission product activity remaining in the graphite after removal of the fuel. An autoradiograph of a thin section of the body, shown in Fig. 7.28, revealed a marked difference in the fission product activity around the individual holes. The activity around holes 7 and 8, which contained the Triso-coated fuel, was low, as would be expected. The other six holes, which all contained similar particles, showed significant variations in fission product activity. It is clear that there was a higher release of fission products from the fuel in holes 1 and 2 than from the others and that this difference was related to rod fabrication in some way. It is possible that particles were broken during rod fabrication, but no failed coatings were observed during metallographic examination of one of the fuel rods from this hole (Fig. 7.27*c*). It is known that these rods were less well bonded with matrix and were smaller than normal and thus operated at higher temperatures than the others. Chemical analysis of the body graphite showed that the ^{137}Cs content was markedly higher adjacent to holes 1 and 2 than elsewhere and that the ^{90}Sr content was markedly lower near holes 7 and 8.

The second recycle test element to be removed from the Peach Bottom Reactor is scheduled for postirradiation examination in early 1973. This element, RTE-4, received 384 equivalent full-power days of irradiation. The peak fast-fluence exposure was about 1.5×10^{21} neutrons/cm^2 ($E > 0.18$ MeV), and the average fuel burnup was about 3.5% FIMA. This element differed from RTE-7 in that each 15-in.-long fuel body contained a single fuel mixture. In addition, three of the six bodies contained loose beds of fuel particles mixed with graphite powder, and the fuel rods in two of the remaining three bodies were carbonized in place. The fuel loading and estimated operating temperatures for RTE-4 are described in Table 7.20. Fuel from each body will be examined for fuel performance. The body graphite and the filler powder from the loose particle

Table 7.20. RTE-4 fuel loading and design operating temperatures

Body	Estimated fuel temperature (°C)	Fuel type	Sample type	Coated particles	
				Fissile	Fertile
6	1065–1120	e	Loose[a]	UC_2 Biso	ThC_2 Biso
5[b]	1120–1230	d[b]	Rod[b]	2/1(Th/U)O_2 Biso	ThC_2 Biso
4	1230–1260	f	Rod	UC_2 Triso	ThC_2 Biso
3	1120–1230	a	Loose[a]	4/1(Th/U)O_2 Biso	ThC_2 Biso[c]
2	900–1120	f	Loose[a]	UC_2 Triso	ThC_2 Biso
1	570–900	e	Rod	UC_2 Biso	ThC_2 Biso

[a]Loose beds contain simultaneously loaded graphite powder as a bed stabilizer.
[b]Carbonized prior to loading; all other rods carbonized in the body.
[c]Loose bed of type "a" combination contained Biso ThC_2 in place of Biso ThO_2 fertile particles used in RTE-7 and other tests.

14. F. S. Dyer et al., "Postirradiation Examination of Special Peach Bottom Element RTE-7," *ORNL Nuclear Safety Research and Development Program Bimonthly Report for March–April 1972,* ORNL-TM-3831, p. 79.

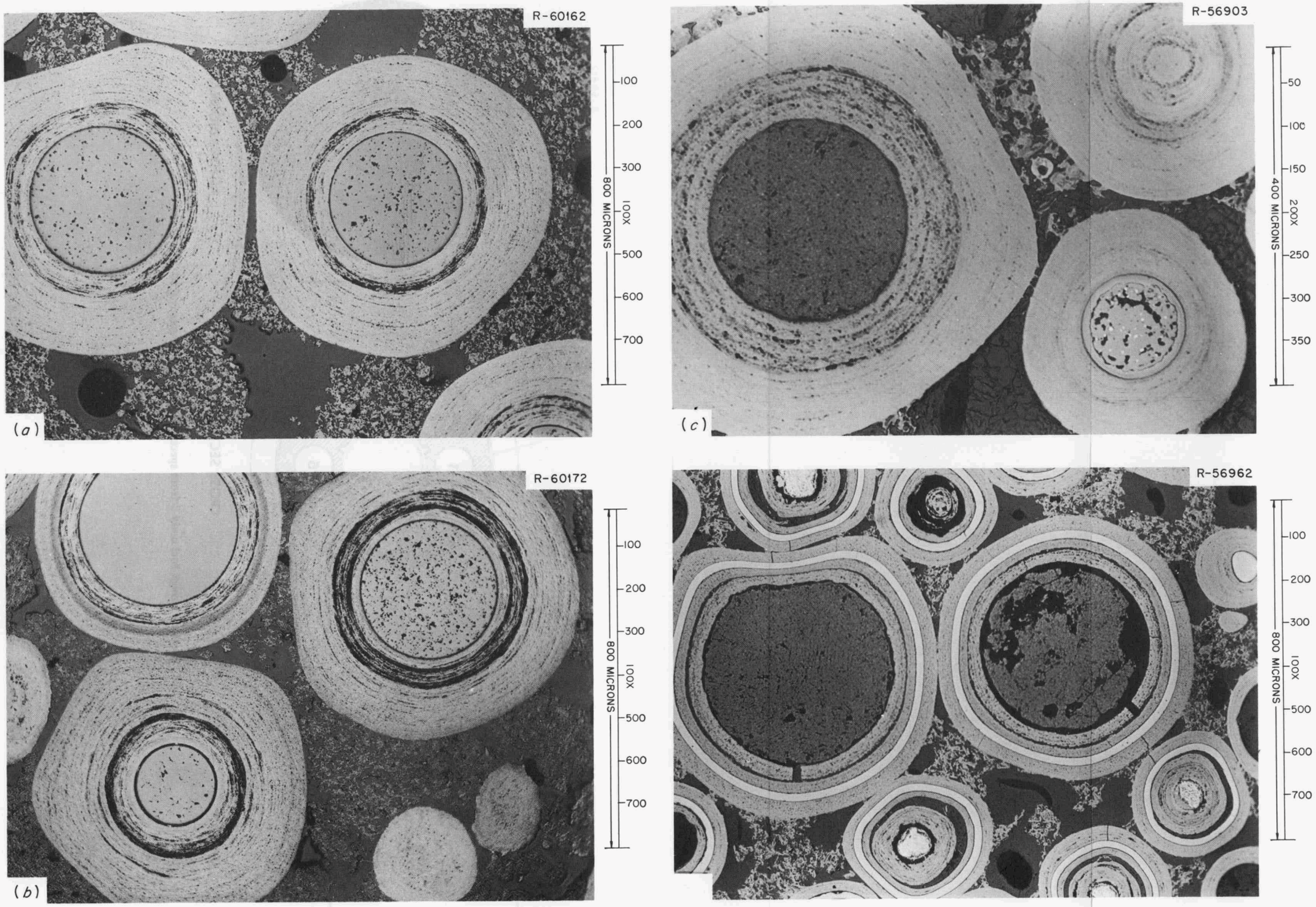

Fig. 7.27. Photomicrographs of coated particle fuels irradiated in recycle test element RTE-7. (*a*) (Th, 20% U)O_2 Biso particle from fuel rod 7-5-2-5. (*b*) (Th, 33% U)O_2 and ThO_2 Biso-coated particles from fuel rod 7-5-3-5 (ThO_2 particle shows no porosity in kernel). (*c*) UO_2 and ThC_2 Biso-coated particles from fuel rod 7-3-2-3. ThC_2 is the largest; particle on lower left is ThC_2 polished near top of kernel. (*d*) UC_2 and ThC_2 Triso-coated particles from fuel rod 7-3-7-3. ThC_2 is the largest; note cracks in outer LTI layer and intact SiC layers.

R-59412

HOLE NOS.	FUEL TYPES
1 - 2	BISO UO_2, BISO ThC_2
3 - 4	BISO $(Th,U)O_2$ (2:1), BISO ThC_2
5 - 6	BISO UO_2, BISO ThO_2
7 - 8	TRISO UC_2, TRISO ThC_2

LEGEND

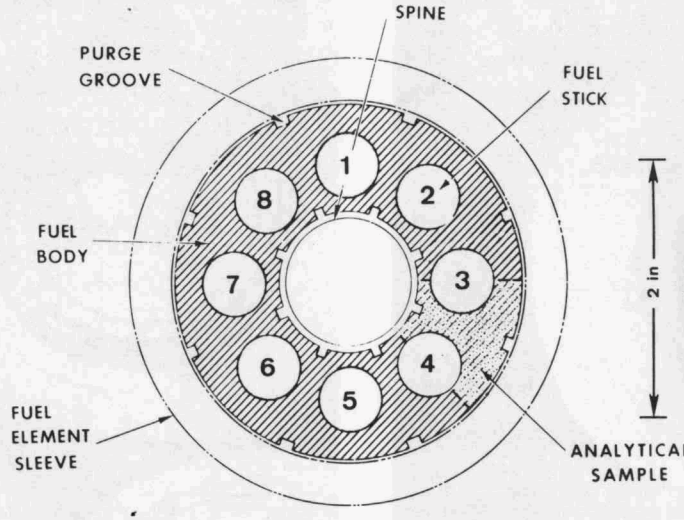

CROSS SECTION

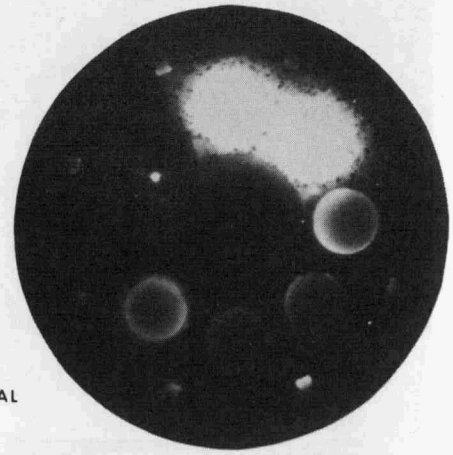

AUTORADIOGRAPH

Fig. 7.28. Section through fuel body 3 from special Peach Bottom element RTE-7.

beds will be analyzed for fission product content and distribution.

7.6 NUCLEAR ANALYSIS IN SUPPORT OF IRRADIATION EXPERIMENTS

H. T. Kerr

Irradiation experiments for the Gas-Cooled Reactor Program receive nuclear analytical support in two general areas. First, the design of irradiation experiments requires estimates of isotopic transmutation rates and neutron damage fluxes for the irradiation facilities of interest. This information is usually obtained from neutronic calculations and from previous experiments. The second area involves the design and postirradiation analysis of neutron activation dosimeters to obtain experimentally supported flux values within each irradiation experiment. For present purposes the GCR experiments can be categorized by irradiation facility:

1. HT capsules in the central target region of the HFIR,
2. HRB capsules in the removable beryllium region of the HFIR,
3. OF-1 and OG-1 capsules in the ORR,
4. H-1 and H-2 capsules in the ETR.

Information pertaining to the HT and HRB capsules is summarized below but is available in detail in ORNL-TM-4358.[15] Detailed discussions of the ORR and ETR capsules are given below since the information is not generally available.

Some important definitions must precede the following discussion. Two neutron damage fluxes are relevant to the HTGR program:

GGA damage flux ≡

$$\int_{0.18\ \mathrm{MeV}}^{\infty} \phi(\bar{r}, E)\, dE = \phi(E > 0.18\ \mathrm{MeV}),$$

Graphite damage flux =

$$\int_{0.050\ \mathrm{MeV}}^{\infty} \phi(\bar{r}, E)\, dE = \phi(E > 50\ \mathrm{keV}).$$

Isotopic transmutation rates are defined as

$$RR(\bar{r}) = \int_0^{\infty} \sigma(E)\, \phi(\bar{r}, E)\, dE,$$

where $RR(\bar{r})$ is the transmutation rate at position $\bar{r}$ per target atom, $\sigma(E)$ is the reaction cross section, and $\phi(\bar{r}, E)$ is the neutron flux at position $\bar{r}$ and energy E. It should be obvious that the difficulty in determining the values of these parameters depends on the availability of differential fluxes [i.e., $\phi(\bar{r}, E)$] within the irradiation specimen.

7.6.1 HT Capsules

Neutron fluxes and transmutation rates for the HT series were obtained from general neutronics calculations of the HFIR, from analysis of activation data in HT capsules, and from special dosimetry experiments in the HFIR target region. All data sources are described and recommended values for neutron fluxes in the target region given in ORNL-TM-4358.[15] The time dependence of damage fluxes in the HT capsules for three axial positions is shown in Fig. 7.29, and some

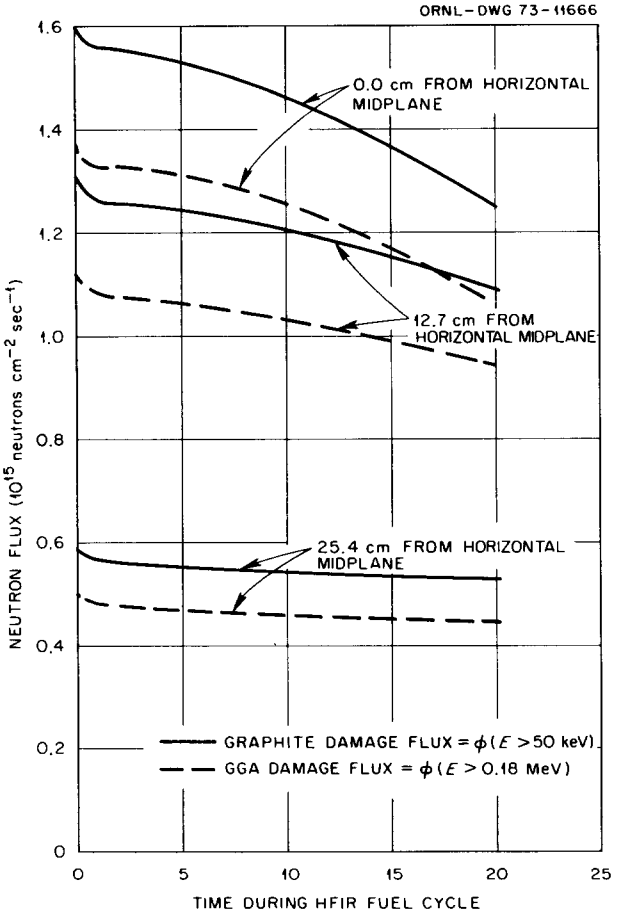

Fig. 7.29. Time-dependent neutron damage fluxes for three axial positions in the A-2 target facility of the HFIR.

15. H. T. Kerr, *Dosimetry and Neutron Fluxes in the HFIR*, ORNL-TM-4358 (in preparation).

Table 7.21. Unit reaction rates for the horizontal midplane of the HT facility in HFIR

Reactions per second per 10^9 atoms

	Capture	Fission
^{232}Th	16.7	0.07
^{233}Pa	216.0	0.88
^{233}U	130.0	1270.0
^{234}U	284.0	1.3
^{235}U	232.0	1270.0
^{238}U	32.0	0.28
^{239}Np	180.0	1.4
^{239}Pu	900.0	2070.0
^{240}Pu	2100.0	1.5
^{241}Pu	840.0	2610.0

important isotopic transmutation rates are shown in Table 7.21.

7.6.2 HRB Capsules

Neutron fluxes in the removable beryllium (RB) region of the HFIR have received considerable attention. Design of the HRB-1 and HRB-2 experiments was based on calculated fluxes reported in the HFIR design report ORNL-4621.[16] The calculated GGA damage flux in the RB facility had a steep radial gradient with a center-line value of 0.50×10^{15} neutrons cm^{-2} sec^{-1}. Therefore, irradiation of the HRB capsules for eight fuel cycles was required to reach a damage fluence of 8×10^{21} neutrons/cm^2. After irradiation of HRB-1 and HRB-2, a special capsule designated HRB-γ2 was designed for neutron dosimetry and gamma heating experiments. From the analysis of dosimeters in the HRB-γ2 experiment, the GGA damage flux was reported to be 0.36×10^{15} neutrons cm^{-2} sec^{-1}. This value represented a linear average of the fluxes derived from the individual monitors and as such ignored the strong radial gradient of the damage flux across the RB facility. An immediate consequence of this lower value was to extend the length of irradiation for the HRB capsules from 8 to 11 fuel cycles in order to achieve the damage fluence of 8×10^{21} neutrons/cm^2.

As additional data became available from other dosimetry experiments in the RB facility, higher damage fluxes were indicated than those derived from the HRB-γ2 experiment. Subsequently a reevaluation was made of the design and data for HRB-γ2, and a critical oversight was discovered: the orientation of the dosimeter holder within the capsule relative to the reactor center line was unknown. The effect of the unknown orientation on the value of the damage flux, shown in Fig. 7.30, prevents any conclusion with regard to fluxes in the HRB-γ2 experiment. Other experiments described in detail in ORNL-TM-4358 have resulted in damage fluxes only slightly lower than the calculated values.[15] The values now recommended for damage fluxes in the HRB capsules are shown in Figs. 7.31 and 7.32, and typical transmutation rates for HRB capsules are shown in Table 7.22.

Table 7.22. Unit reaction rates for the horizontal midplane of HRB capsules in the HFIR

Reactions per second per 10^9 atoms

	Capture	Fission
^{232}Th	11.8	0.02
^{233}Pa	106.0	0.27
^{233}U	52.8	501.0
^{234}U	124.0	0.42
^{235}U	93.0	482.0
^{238}U	18.3	0.07
^{239}Np	80.6	0.46
^{239}Pu	414.0	856.0
^{240}Pu	1026.0	0.52
^{241}Pu	338.0	1044.0

7.6.3 OF-1 and OG-1 Capsules

The OF-1 and OG-1 capsules are joint ORNL-GGA irradiation tests in the ORR. During the irradiation of these capsules, the ORR will be arranged in a special configuration to enhance the neutron flux levels in the C-3 and E-3 positions. Consequently, existing data on the neutron flux characteristics in the ORR were inadequate, and a program was initiated to determine the ORR fluxes in the special configuration. This program consisted of essentially four efforts:

1. A neutron dosimetry experiment was done by J. Swanks and F. Kam with the ORR in the special configuration. This experiment provided integral flux information, and the reported data points are shown in Figs. 7.33 and 7.34. The conventional 2200-m/sec thermal fluxes (ϕ_0) in Fig. 7.33 are difficult to use in predicting reaction rates for non-1/v reactions. They do, however, provide relative spatial mapping of the thermal-neutron flux. The high-energy fluxes [i.e., $\phi(E > 0.18$ MeV)] in Fig. 7.34 are integrals of spectra derived

16. R. D. Cheverton and T. M. Sims, *HFIR Core Nuclear Design*, ORNL-4621 (July 1971).

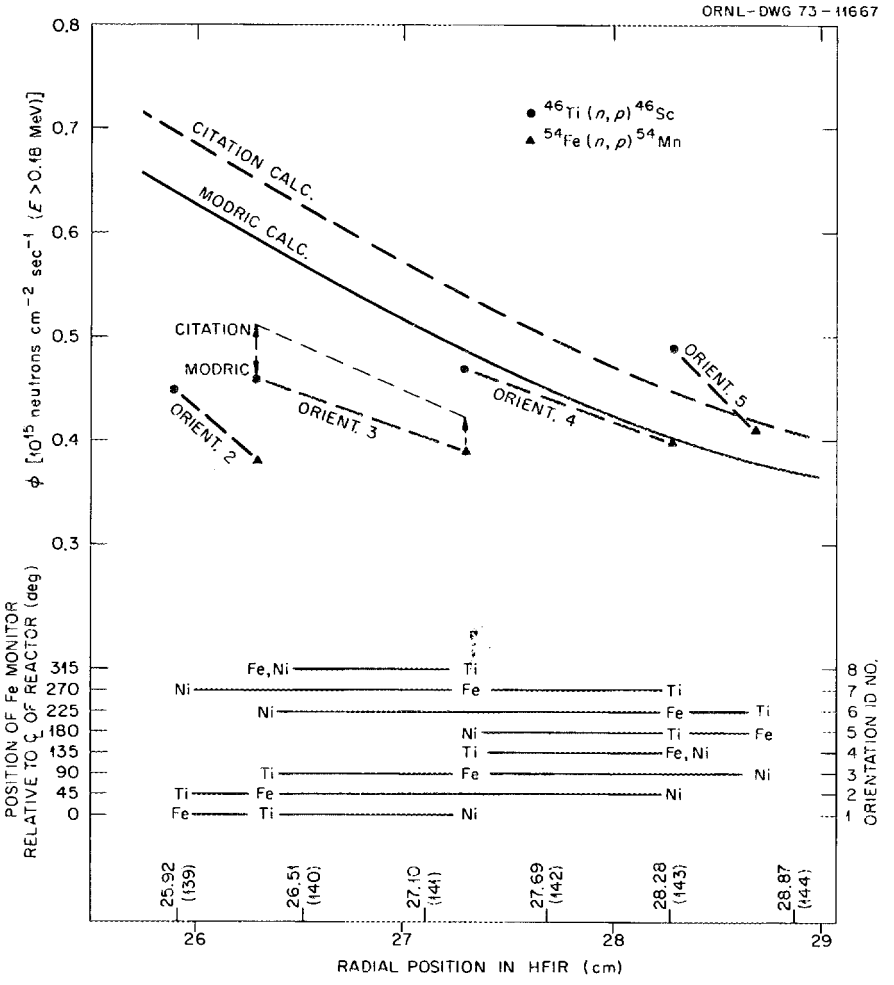

Fig. 7.30. Relationship between the damage fluxes derived from the HRB-γ2 experiment and the orientational uncertainty of the capsule.

by unfolding techniques from threshold-type monitor activations.

2. An analysis was made by H. Kerr to determine the sensitivity of the neutron characteristics within the irradiation specimen to the capsule design details. Calculations with the XSDRN code[17] indicated minor perturbations in the neutron flux level and energy spectra due to the stainless steel wall, the water gap, and the position of the three fuel rods in the fueled capsule.

3. An analytic effort was made by J. Swanks and M. Sims to calculate spatial and time-dependent neutron fluxes in the ORR special configuration using the CITATION code[18] with a three-dimensional multigroup model. Figure 7.33 shows the calculated thermal flux [i.e., $\phi(E < 0.55$ eV)] axial profiles in the C-3 and E-3 facilities of the ORR. Although the calculated thermal fluxes and the measured 2200-m/sec thermal fluxes in Fig. 7.33 are not directly comparable, the calculated profile is significantly flatter. Moreover, a comparison of the calculated and experimental thermal fluxes at other ORR positions shows significant differences that are apparently due to the computational model and will be resolved by further investigations.

17. N. M. Greene and C. W. Craven, Jr., *XSDRN: A Discrete Ordinates Spectral Averaging Code,* ORNL-TM-2500 (July 1969).

18. T. B. Fowler and D. R. Vondy, *Nuclear Reactor Core Analysis Code: CITATION,* ORNL-TM-2496 (July 1969).

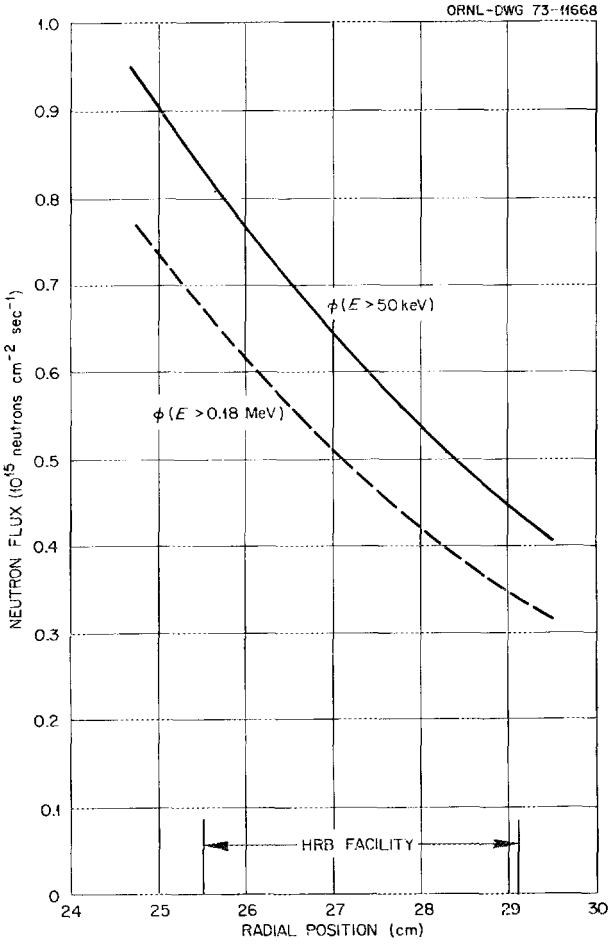

Fig. 7.31. Recommended damage fluxes of HMP of HFIR removable beryllium.

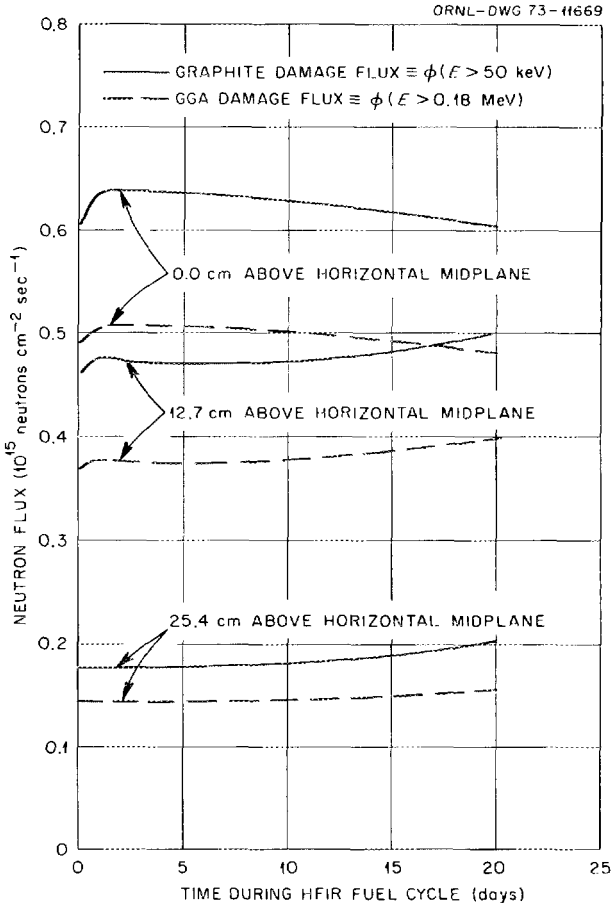

Fig. 7.32. Time-dependent neutron damage fluxes for three axial positions at a radial position of 27.1 cm in the removable beryllium region of the HFIR.

This effort will continue, and a final summary will be reported. The calculated and experimentally derived damage fluxes shown in Fig. 7.34 are in excellent agreement. Hopefully the calculated damage fluxes will be relatively unaffected by the modifications required to improve the thermal flux comparison in the CITATION model.

4. An experiment was done by K. Thoms to estimate the axial dependence of the gamma heating in the C-3 and E-3 positions for the ORR special configuration. An ionization chamber was extended into the experimental position with the reactor critical, and the instrument response was recorded at several positions during the axial traverse. The results are shown in Fig. 7.35. The axial distribution of the gamma response should correspond to the axial profile of the high-energy neutron flux because the principal source of both the gammas and the high-energy neutrons is fissions in adjacent fuel elements. A comparison of the profiles in Figs. 7.34 and 7.35 clearly shows the similarities between fast-neutron and gamma distributions. By properly interpreting the final results of these four efforts the neutron characteristics of the ORR special configuration can be established. Until the CITATION analyses described above are complete, the following data are recommended for use in designing the capsules.

Reaction rates. Unit reaction rates for all reactions should be taken from Table 7.23. For those reactions designated as predominantly thermal, the relative axial magnitudes should correspond to the axial profile of the experimental 2200-m/sec fluxes (i.e., the dashed curve in Fig. 7.33) for both the C-3 and E-3 facilities. For threshold reactions, the axial profiles in Fig. 7.34

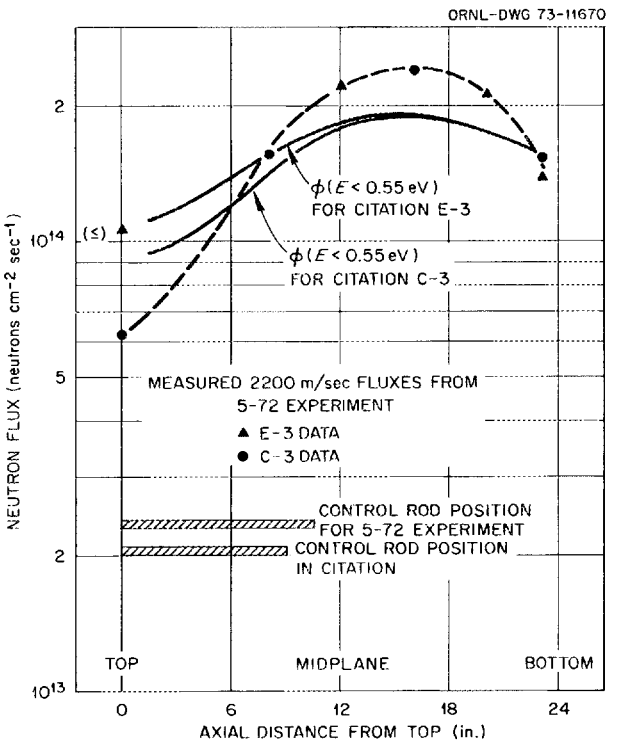

Fig. 7.33. Thermal flux vs axial position in the C-3 and E-3 facilities of ORR special configuration.

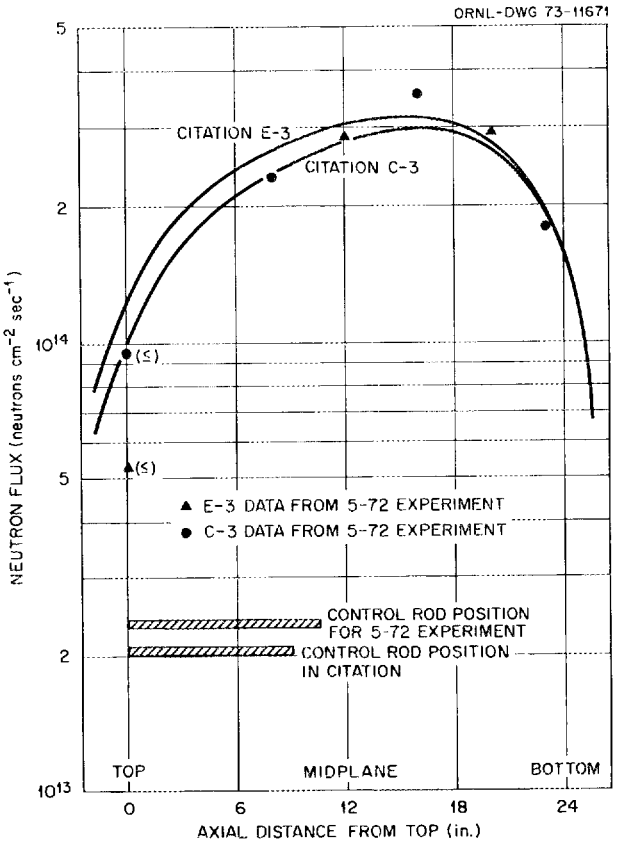

Fig. 7.34. Damage flux [ϕ(>0.18 MeV)] vs axial position in C-3 and E-3 facilities of ORR special configuration.

Table 7.23. Unit reaction rates for peak flux position[a] in GGA-ORNL capsules in the ORR

Reactions per second per 10^{10} atoms

Isotope	Fission	Capture
^{232}Th	0.138	17.2
^{233}Pa	1.75	204
^{233}U	699	80.5
^{234}U	2.65	225
^{235}U	618	130
^{236}U	1.15	65.3
^{237}Np	2.92	396
^{238}U	0.537	23.1
^{239}Pu	1334	712
^{240}Pu	2.95	2600
^{241}Pu	1500	470
^{242}Pu	2.73	33.7

[a]These reaction rates are preliminary and may be revised when the thermal flux discrepancies are resolved.

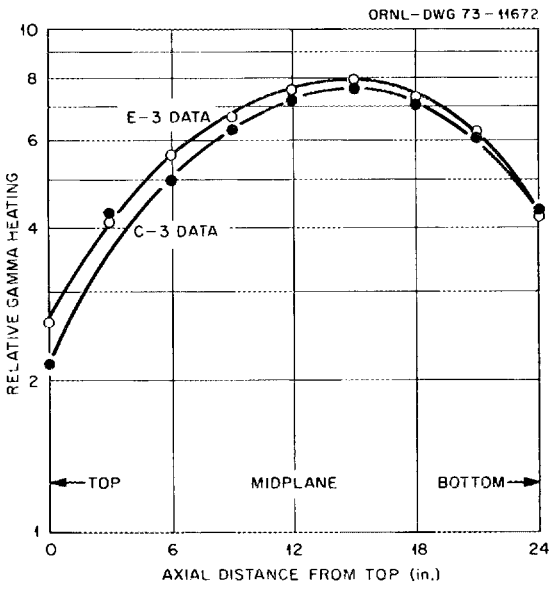

Fig. 7.35. Relative gamma heating vs axial position in the C-3 and E-3 facilities of the ORR special configuration.

should be used. Damage flux can be determined from Fig. 7.34.

Time dependence of the thermal flux. Although a detailed analysis is not yet available, a preliminary estimate showed the thermal flux becomes essentially symmetric toward the end of the cycle, with the same nominal peak values and slightly higher axially averaged values.

7.6.4 H-1 and H-2 Capsules

Two HTGR fuel irradiation experiments designated H-1 and H-2 were irradiated for 23,500 MWd in the SW and SE positions of the J-8 assembly of the ETR.[19] A neutron absorber shroud was designed for each capsule to increase the hardness of the neutron energy spectrum and to reduce axial flux asymmetries in the experimental fuel. Each shroud was a cylindrical annulus with a 40-mil wall thickness. The bottom end of the shroud was 100% Hf and the top end was 40% Hf–Zr alloy. In addition to the fuel, each capsule contained neutron dosimeter packages at five axial positions. Each package contained iron, nickel, titanium, and stainless steel flux monitors in stainless steel cans, designed to measure the high-energy damage flux and the thermal flux.

The analysis of the activation data was complicated by perturbations in the irradiation conditions. The ETR power level was very erratic during cycles 112 to 115. Normally the equivalent full-power history is used for dosimeter analysis because the neutron flux at an experimental position usually has nearly constant characteristics. In the ETR, however, frequent changes were made in the assemblies surrounding J-8 which altered the neutron characteristics. Also, the H-2 capsule was left out of the reactor for approximately 11 full-power days, and a long shutdown (~104 days) occurred between cycles 114 and 115. By far the most serious perturbation was a capsule handling error prior to cycle 115. While searching for the cause of power oscillations in the ETR, certain core pieces were being removed and replaced. When the H-1 and H-2 capsules were removed from their positions, they were accidentally replaced in an inverted position. This orientation placed the bottom part of the capsule with the strongly absorbing 100% Hf shroud in the top half of the core and the top end of the capsule with the mildly absorbing 40% Hf–Zr shroud in the bottom half. This inverted orientation of the shroud increased rather than suppressed the normal axial asymmetries of the ETR thermal flux. Consequently, the power generation in the top portion of the capsule (but bottom of reactor) exceeded design limits and caused excessive heating. In both capsules the dosimeter packages designated H-I-10/11 were not recovered and presumably melted. Also the dosimeters in the top and center positions of each capsule had been much hotter than those in the bottom positions, as evidenced by their physical appearance and mass changes.

The perturbations encountered in the H-1 and H-2 irradiations required modification of the standard procedures used for dosimeter analysis. The assumption was made that the neutron energy spectrum in the J-8 facility of ETR has the same characteristics as a similar position in the ORR (for which spectral data are available). Spectral perturbations associated with each shroud composition were calculated with the XSDRN code,[20] and reaction rates for materials within the capsules were determined. The greatly simplified power history in Fig. 7.36 was used with the assumption of axial flux symmetry about the horizontal midplane (HMP) for irradiation period A and strong axial asymmetry for irradiation period B. The preceding information and the neutron activation data were used to obtain average axial neutron flux profiles during the irradiation periods. A summary of both the low-energy neutron flux and the high-energy damage flux follows.

Two reactions were used to monitor the low-energy neutron flux at each axial position:

$$^{58}\mathrm{Fe}(n,\gamma)^{59}\mathrm{Fe} \quad (T_{1/2} = 45 \text{ days}),$$

$$^{59}\mathrm{Co}(n,\gamma)^{60}\mathrm{Co} \quad (T_{1/2} = 5.24 \text{ years}).$$

Since more than 90% of the short-lived ^{59}Fe existing at the end of irradiation, T_3, was produced during irradiation period B (see Fig. 7.36), the ^{58}Fe monitor data were used to obtain low-energy fluxes in period B directly. Then an estimate was made of the ^{60}Co

19. The ETR is a 175-MW reactor fueled with enriched uranium and moderated with water. The control rods are driven from the bottom of the core and are positioned in the upper part of the core during power operation. Consequently, the neutron flux axial distribution peaks toward the bottom of the core.

20. The XSDRN calculations were done by J. D. Jenkins and were one-dimensional transport theory calculations of the capsules using the boundary source option. These cases are similar to the ANISN calculations done by A. R. Olsen except the spectrum used for the boundary source in XSDRN is suitable for the ETR J-8 facility, whereas the boundary source spectrum in ANISN was for a water reflector region and is not suitable for the J-8 facility.

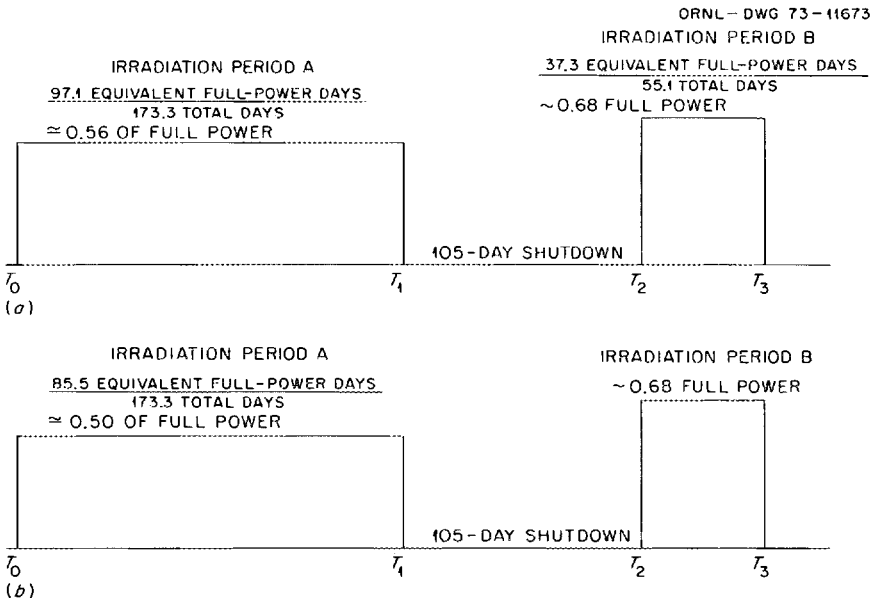

Fig. 7.36. Simplified power history for the ETR during cycles 112 to 115. During irradiation period A the capsules were correctly oriented; during period B, they were inverted. (*a*) Capsule H-1; (*b*) capsule H-2.

existing at T_3 which was produced during period B; the total ^{60}Co at T_3 was reduced by that amount, and the balance was assumed to result from irradiation during period A. The low-energy flux for period A was then derived from the remaining ^{60}Co. Figure 7.37 shows 2200-m/sec fluxes for the H-1 and H-2 capsules as well as "unperturbed" 2200-m/sec fluxes for the J-8 facility. As expected, the flux is more symmetric about the reactor midplane than the unperturbed flux during irradiation period A but is very asymmetric during irradiation period B. The high thermal flux in the top portion of the capsule during irradiation period B caused excessive power generation and resulted in severe damage to the experiments.

Three reactions were used to monitor the high-energy damage flux [i.e., $\phi(E > 0.18$ MeV)] at each axial position:

Reaction	Half-life, T	Threshold energy, E (MeV)
^{54}Fe$(n,p)^{54}$Mn	312 days	0.6
^{60}Ni$(n,p)^{60}$Co	5.24 years	2.0
^{46}Ti$(n,p)^{46}$Sc	83.8 days	1.8

The ^{54}Mn was counted in both iron and stainless steel monitors, and the specific activities at each monitor position agreed to within 5%. The dosimeter analysis for the high-energy fluxes was based on a two-part irradiation history and required consideration of the following factors.

1. Approximately 75% of the ^{46}Sc existing at the end of irradiation was produced during irradiation period B, so the ^{46}Sc data strongly reflected high-energy fluxes during period B.

2. The longer-lived ^{54}Mn and ^{60}Co were more strongly influenced by the high-energy fluxes during irradiation period A.

3. The titanium monitors, except those in the bottom capsule position, experienced significant mass changes by means of unspecified chemical reactions (presumably during irradiation period B). Since the mass increases were not systematic, there is some probability that the original monitor masses were not fully recovered and that uncertainties exist in the ^{46}Sc data. By utilizing activities from a given pair of flux monitors, a system of equations was derived which could be solved for the high-energy fluxes during periods A and B. This procedure was applied to the ^{60}Co-^{46}Sc pair and the ^{54}Mn-^{46}Sc pair at each axial position in both the H-1 and H-2 capsules, and the resulting fluxes are shown in Fig. 7.38. The fluxes derived from both monitor pairs are in good agreement at all positions except at the bottom of the capsules. When the fluxes from each monitor pair are time

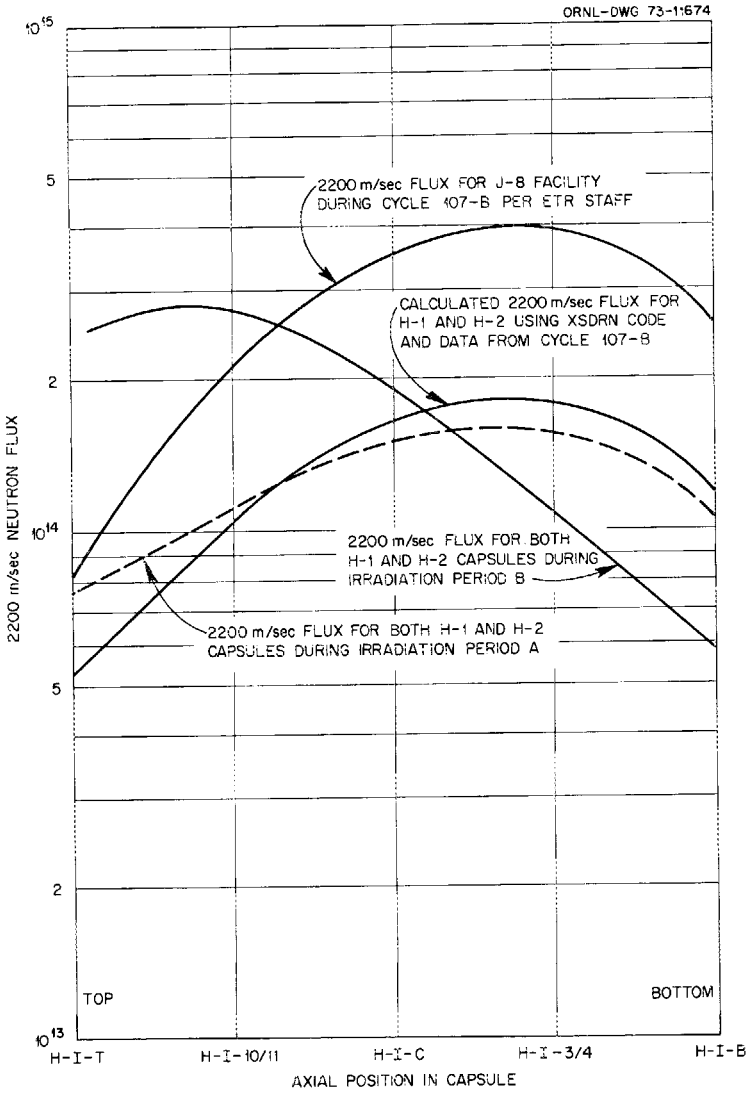

Fig. 7.37. Axial profiles for 2200-m/sec fluxes.

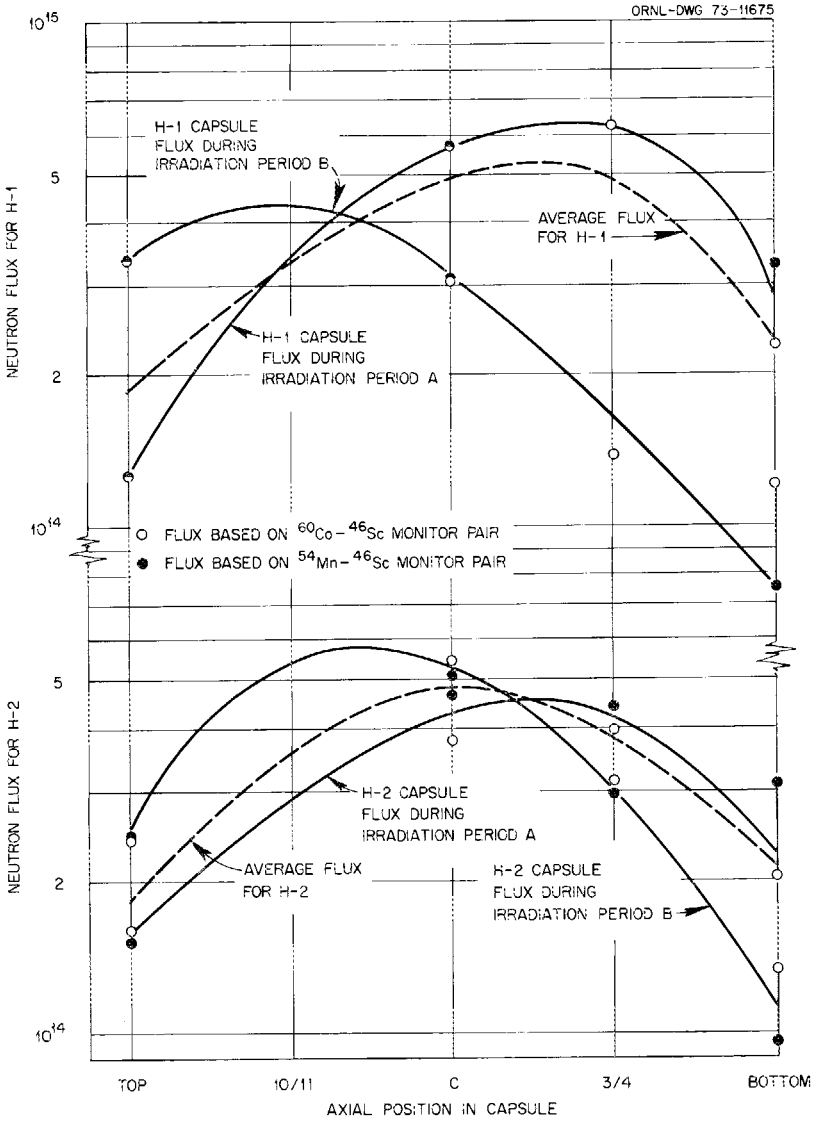

Fig. 7.38. Fast fluence (>0.18 MeV) axial profiles for H-1 and H-2 capsules.

averaged, the differences at the bottom positions are considerably reduced. The time-averaged high-energy fluxes for both capsules are also given in Fig. 7.38.

At each axial position, the neutron flux with energies above 1.0 MeV is about 53% of the damage flux [i.e., $\phi(E > 0.18$ MeV)] at the same axial position.

Finally, Table 7.24 gives reaction rates (per atom) for some heavy-metal isotopes normalized to the fluxes reported in Figs. 7.37 and 7.38.

Table 7.24. Reaction rate data for heavy-metal isotopes

Isotope	Reaction	Unit reaction rate (reactions/sec per 10^{10} atoms) at capsule axial position[a]				
		H-I-T	H-I-1/4	H-I-C	H-I-3/4	H-I-B
Irradiation period A						
^{232}Th	n,γ	11.2	17.5	24.2	27.6	16.8
^{233}Pa	n,γ	91.7	143	189	216	131
^{233}U	n,γ	36.4	56.7	71.2	81.4	49.5
	n,f	346	538	660	754	459
^{234}U	n,γ	82.9	129	140	160	97.3
^{235}U	n,γ	66.6	104	129	147	89.4
	n,f	327	509	610	697	424
Irradiation period B						
^{232}Th	n,γ	36.3	43.0	29.9	17.0	9.19
^{233}Pa	n,γ	296	351	234	133	71.9
^{233}U	n,γ	118	140	88.1	50.1	27.1
	n,f	1120	1330	817	465	251
^{234}U	n,γ	268	318	173	98.5	53.2
^{235}U	n,γ	215	255	160	91.1	49.2
	n,f	1050	1250	756	430	232

[a] T = top, C = center, B = bottom.

7.7 CHARACTERIZATION OF IRRADIATED PARTICLE COATINGS

E. L. Long, Jr. R. B. Fitts

We have compiled microhardness data on a set of coated particles in an effort to determine the correlation between radiation damage to pyrolytic carbon and changes in microhardness. Pyrolytic carbon has a somewhat unique property that prevents hardness determinations by the standard microindentation methods. Until a sufficient load is applied to the pyrolytic carbon to cause rupture, one is operating in the elastic range of the stress-strain relationship of the material, whereas in all metals the microindenter produces plastic flow when it first touches the surface. Therefore, to be able to measure the effect of the indenter, a thin plastic coating that records the penetration of the indenter is placed on the polished surface of the pyrolytic carbon. We cannot yet specify the effect of this plastic coating on the hardness numbers, particularly with the lighter indentation loads (10 to 25 g). To minimize the influence of the plastic film on the hardness data, we used the largest load possible. The load is limited by the thickness of the pyrolytic carbon because the indentation size is a function of the applied load.

We have examined particles from three lots of Triso-coated inert kernels that have been irradiated at a design temperature of 1050°C to three fluence levels: 4.7, 9.4, and 14.1 X 10^{21} neutrons/cm^2 ($E > 0.18$ MeV). The three batches of coated particles have outer coating densities of 1.68, 1.78, and 1.98 g/cm^3. Unfortunately, some of the outer coatings are rather thin (47 μm), which restricts us to relatively light loads of 50 g or less. However, we can report some apparent trends of the results so far. The hardnesses of the archive coatings are proportional to their initial density. Only the lowest density coatings, 1.68 and 1.78 g/cm^3, showed an increase in hardness at an irradiation exposure of 4.7 X 10^{21} neutrons/cm^3. At the next fluence level, 9.4 X 10^{21} neutrons/cm^3, the lowest density coatings showed a slight decrease in hardness, the medium-density coatings showed no further change, and the high-density coatings showed a 12% increase. At the highest fluence level in this series, 14.1 X 10^{21} neutrons/cm^3, all three coatings had decreased in hardness. The most significant change occurred in the high-density coatings, ~20%, as compared with the archive specimen. The other two coatings remained harder than their archive counterparts. The microhardness results discussed above are given in Table 7.25 and are plotted in Fig. 7.39.

The application of this technique to irradiated isotropic pyrolytic carbon shows potential as a direct means of measuring radiation damage. More effort will be required to modify the procedure to make it more amenable to the remote hot-cell operations required for highly radioactive fueled coated particles. Since the present series of coated particles contained inert kernels, we were able to make these hardness measurements in a cold laboratory. Also further effort should be expended to understand what causes the change in elastic hardness and to correlate these changes into more meaningful values, as has been done for numerous structural materials.

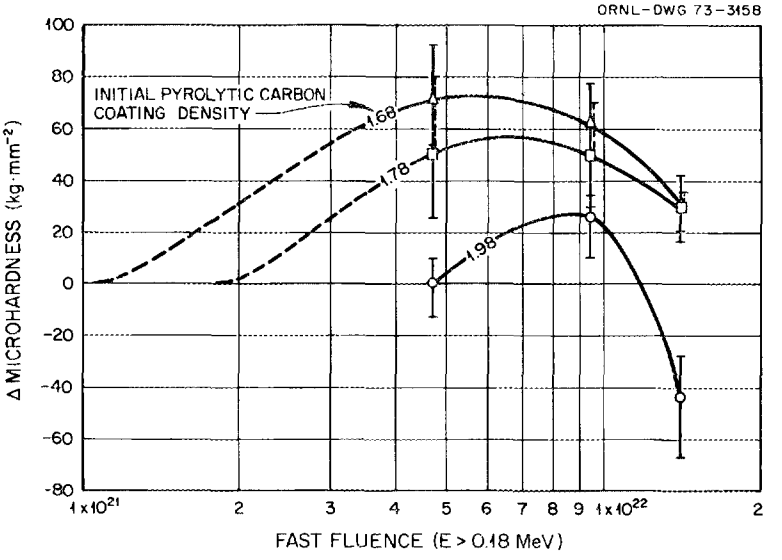

Fig. 7.39. Change in microhardness of irradiated particle coatings vs fast fluence (>0.18 MeV).

Table 7.25. Microhardness DPH-G[a] as a function of fluence and density

Density (g/cm^3)	Archive hardness	Hardness for fluence [10^{21} neutrons/cm^2 ($E > 0.18$ MeV)] of –		
		4.7	9.4	14.1
1.68	172[b]	261	288	213
1.78	192[c]	242	242	222
1.97	220[c]	221	246	176

[a]The "G" suffix is added to the customary DPH designation to indicate that the microhardness values are measurements of elastic hardness. Reported numbers are an average of at least eight determinations.

[b]Limited to a 100-g load because of coating thickness (~65 μm).

[c]Limited to a 50-g load because of thin coatings (≤50 μm).

7.8 SUMMARY OF FUEL ROD DIMENSIONAL CHANGES UNDER IRRADIATION

R. B. Fitts J. H. Coobs
R. A. Olstad

An understanding of the dimensional changes that occur in coated-particle-bearing fuel rods is important for the thermal and mechanical design of HTGR fuel elements and can also yield valuable information on the behavior of the coated particles themselves.

We have examined the diametral change data on 173 fuel rods irradiated by ORNL. These results are summarized in Figs. 7.40 and 7.41. The changes were obtained from pre- and postirradiation diameter and/or length measurements and include data on fuel rods operated between 700 and 1200°C. The bulk of the data was obtained on single fuel rods ½ to 2 in. long and 0.2 to 0.5 in. in diameter tested in the HFIR. The data given at and below 10^{21} neutrons/cm^2 fast fluence are from RTE-7, a large-scale test from the Peach Bottom Reactor. These data are average values derived from samples composed of from three to seven 2-in.-long, 0.5-in.-diam fuel rods.

The dimensional changes in an intrusion-bonded fuel rod, where the particles are in a close-packed configuration (~62% volume loading of particles), are thought to be controlled by the dimensional changes of the coatings.[21] This appears to be consistent with our observations in that the rods containing Triso-coated particles, with their more stable SiC layers, exhibit less dimensional change than those containing Biso-coated particles. In addition, the dimensional changes in both types of rods exhibit an inverse relationship to the density of the outer pyrolytic carbon coating. The particles with higher density as-fabricated outer coatings undergo less irradiation-induced densification and

21. S. Peterson (ed.), *Metals and Ceramics Div. Annu. Progr. Rep. June 1971*, ORNL-4770, pp. 145–46.

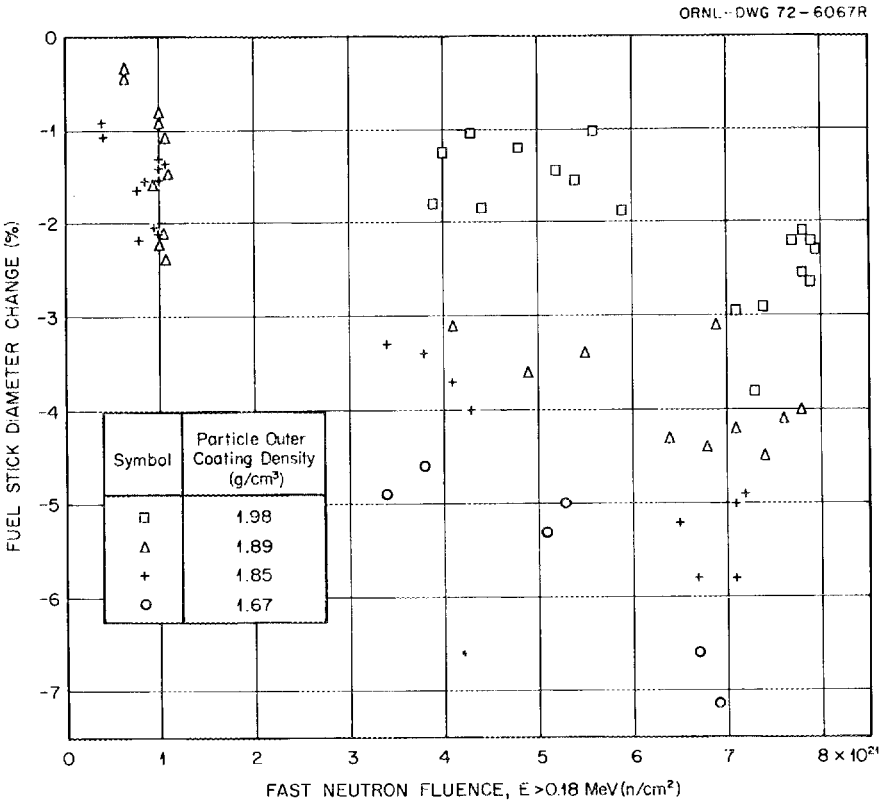

Fig. 7.40. Irradiation-induced dimensional changes in fuel rods containing Biso-coated particles (HT-4, HT-6, RTE-7, HRB-2).

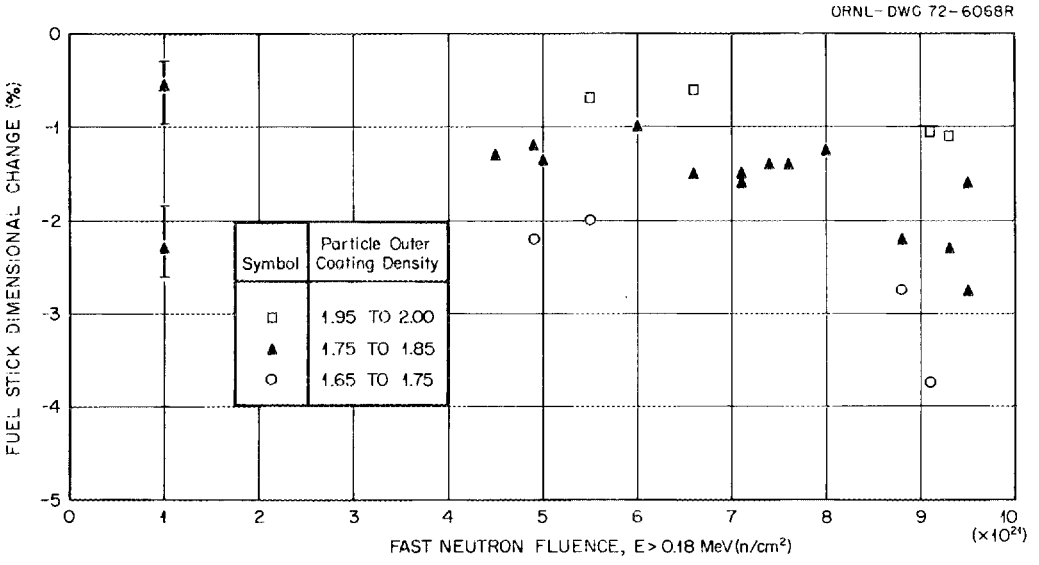

Fig. 7.41. Irradiation-induced dimensional changes in fuel rods containing Triso-coated particles (HT-8, RTE-7, HRB-2).

therefore result in lower fuel rod shrinkage under irradiation.

Portions of the data from fuel rods containing Biso-coated particles have been examined in detail. Part of the fuel in the large Peach Bottom Reactor element (RTE-7) contained similar UO_2 Biso and ThO_2 Biso fuel particles. These rods are described in more detail in Sect. 7.5, and the data from these rods are shown in Fig. 7.24. From these results it appears that at low fluence, the densification rates of the higher density coatings are different when irradiated at ~800°C than when irradiated at ~1200°C. The temperature spread over fuels with lower density coatings was not large enough to discern a temperature influence on their densification behavior. The influence of temperature is much less pronounced than the effects of fluence, but temperature does appear to be a significant variable. More data on this phenomenon will be obtained when subsequent, higher fluence exposure RTEs are examined.

The dimensional data from all these fuel rods will be examined by comparison with particle dimensional changes evaluated with coated particle performance computer codes such as STRETCH,[22] STRESS-II,[23] and TRISO.[24] In these codes the physical and mechanical properties of the coatings and the stress distributions, creep, and densification in the coatings are considered in detail.

As a preliminary look at the densification of the outer coatings on the Biso-coated particles in these fuel rods, we have performed a simple analysis of the density of the coatings at ~8×10^{21} neutrons/cm^2 fast fluence. This analysis was based on the assumption of isotropic densification of the coatings with no internal pressure stresses. Anisotropic densification causes a greater shrinkage of the coatings than isotropic densification does, but this effect is partially counterbalanced by the outward creep of the coatings caused by internal pressure. The results of this analysis, shown in Table 7.26, lead to a preliminary conclusion that the fuel rod dimensional changes at the maximum HTGR fluence can be predicted on the basis of the outer coatings densifying from their initial value to 2.15 g/cm^3 for initial densities above ~1.8 g/cm^3. The lower density coatings have only achieved a density of about 2.00 and appear to be still undergoing densification at this fluence, whereas the higher density coatings may have reached their maximum densities.

22. J. W. Prados and T. G. Godfrey, *STRETCH, a Computer Program for Predicting Coated Particle Irradiation Behavior, Modification IV, December 1967,* ORNL-TM-2127 (April 1968).

23. H. Walther and P. G. Novario, *Stress Analysis in Coated Particle Fuels, Part I: Theory and Examples; Part II: Computer Programme Stress I,* DP report 604 (August 1968) (Part II, July 1969).

24. J. L. Kaae, "A Mathematical Model for Calculating Stresses in a Four-Layer Carbon–Silicon Carbide-Coated Fuel Particle," *J. Nucl. Mater.* 32, 322 (1969).

Table 7.26. Evaluation of the density of particle coatings in ORNL fuel rods at 8×10^{21} neutrons/cm^2 fast-fluence exposure

Initial outer coating density (g/cm^3)	Range of measured fuel rod diameter change (%)		Calculated final outer coating density[a] (g/cm^3)		
	Maximum	Minimum	Maximum	Minimum	Average
1.98	3.35	2.00	2.18	2.10	2.14
1.89	4.70	4.00	2.16	2.12	2.14
1.85	6.20	5.15	2.19	2.14	2.16
1.67	7.50	5.15	2.05	1.93	2.00

[a]Based on assumption that coatings shrink isotropically and that densification is not affected by internal pressure.

8. HTGR Fuel Chemistry, Fuel Integrity, and Fission Product Behavior

H. J. de Nordwall

Coated particle integrity is determined by both mechanical and chemical factors. Current emphasis is placed upon the establishment of the mechanisms and rate-controlling factors that result in carbon transport within a coated oxide fuel particle held in a temperature gradient. This transport is observed to remove carbon from the hot side of the coating and transport it to the cold side and is a possible mechanism for coating failure. One goal of this work is to specify the kernel composition necessary to minimize carbon transport so that the coatings will not fail in service by this mechanism. A second goal is a first-principles mathematical description of carbon transport in coated oxide particles of the current reference designs.

The purpose of the studies of fission product behavior is to determine the cause and extent of fission product release from irradiated coated particle fuels, both at normal and abnormal reactor fuel temperatures. Knowledge of both the factors determining coated particle integrity and fission product transport is necessary for the analysis of fission product release from fuel elements and ultimately from the reactor, since changes in the fraction of fuel with failed coatings may affect fission product transport substantially. Transport of fission products at normal operating temperatures must be included in nuclear safety considerations, since the fission product release from a reactor at the time of an abnormal temperature fluctuation would depend upon the initial fission product distribution.

Several areas of investigation have been pursued during this reporting period. The theoretical analysis of carbon transport in oxide particles has been extended to the analysis of irradiation of particles coated only with pyrolytic carbon. The experimental program for measuring mass transport in a coated particle placed in a temperature gradient has been established. Specific oxide-base kernels containing UC_2 or $UN_{1.5}$ as a second constituent have been developed to mitigate the gas-phase transport of carbon resulting from the buildup of carbon monoxide pressure during nuclear fission. Calculations have been made to evaluate the possible retention of cesium, barium, and strontium by additions of refractory oxides to UO_2 kernels; the observation of the very large expansion of the coatings over UO_2 particles at $T > 2200°C$ has been explained.

The postirradiation high-temperature release of fission products from irradiation experiment Cl-28 has been determined; this experiment included coated particles containing several experimental kernel compositions. Similar studies were made for reference-type particles containing oxide or carbide kernels coated with propylene- or methane-derived pyrolytic carbon. Methods for the nondestructive recovery of coated particles from fuel rods were evaluated.

8.1 MASS TRANSPORT IN HTGR PARTICLES IN A TEMPERATURE GRADIENT

T. B. Lindemer

8.1.1 Gas-Phase Carbon Transport in Oxide Particles in a Temperature Gradient

The development and testing of mathematical analyses of gas-phase carbon-transporting processes in oxide particles are continuing in an effort to obtain a performance model having general applicability to the

design of oxide fuels. An analysis of available Dragon project data concerning the performance of UO_2-containing SiC-coated particles was presented in a previous report.[1] Subsequent work with the equations used to predict carbon transport revealed that the equations given in the previous report[1] are restricted to the case where the pressure of carbon monoxide (P_{CO}) in the particle at a given temperature is invariant with nuclear fission. Thus, although these equations appear to be correctly applied to the Dragon project particles, where P_{CO} is proposed to be fixed at one temperature by the SiC-SiO_2-C-CO equilibrium,[1] other equations need to be developed for particles coated only with pyrolytic carbon (Biso particles) and in which P_{CO} may vary during nuclear fission.

This variation is readily accommodated (in the previously reported equations[1]) by incorporating the terms involving P_{CO} (and P_{CO_2}) within the mean-value-theorem integral. This integral can be computed if the functional dependence of P_{CO} with nuclear fission is known. At the present time this dependence has not been adequately determined experimentally, and one needs to use estimates such as those published by Flowers and Horsley[2] for a specific fuel isotope. These estimates suggest a linear dependence of P_{CO} with nuclear fission. The resulting equation for carbon transport by the C-CO-CO_2 system in a Biso particle was used under the condition that the diffusion coefficient for gas in the porous buffer layer was about 0.01 to 0.02 of that in free space, as was suggested in our earlier analysis.[1] The calculated results predicted failure of Biso particles via thinning of the pyrocarbon coating under nearly all conditions of burnup, burnup rate, temperature, and temperature gradient normally prevalent in irradiation experiments. This predicted failure is clearly contrary to the generally observed survival of Biso-coated oxide particles during irradiation and suggests inadequacy of the model. This disagreement may be caused by errors in the assumptions leading to the derivation of the equations or incorrect values of the various quantities used in the equations. For example, the assumptions included the maintenance of local chemical equilibrium and no rate-limiting effects resulting from the chemical reactions involved in the mass-transporting cycles. On the other hand, if the assumptions are correct, then the predictions of the mathematical model would indicate, for example, a P_{CO} dependence upon nuclear fission of highly enriched $^{235}UO_2$ very much lower than that estimated by Flowers and Horsley,[2] or a lowering of the gas diffusion rate by a near-perfect closure or blockage of the gas diffusion paths within the low-density pyrocarbon buffer layer.

The effort that has been expended in the theoretical analysis of carbon transport and particle-failure mechanisms in oxide particles does indicate a critical dependence on P_{CO} resulting from the release of oxygen from the UO_2 during nuclear fission. This realization consequently leads to the design of chemical compositions of oxide kernels that will maintain a P_{CO} sufficiently low to prevent the operation of gas-phase carbon-transporting processes during service. Such compositions are discussed below.

8.1.2 Experimental Program for Measurement of Transport Phenomena

This work is primarily concerned with the measurement of carbon transport in oxide-fueled particles of reference design so that the first-principles analyses of this transport may be verified and improved. The measurement of transport in nonreference particles containing nitrogen- and sulfur-containing modifications of the oxide and carbide fuels is a secondary objective. Such measurements are expected to result in the better definition of transport mechanisms and to define those fuel compositions that may exhibit better resistance to fuel or carbon migration than that for the reference fuels. The kernel compositions given in Table 8.1 have been synthesized[3] and coated with propylene-derived pyrocarbon (Biso design). A carbon-resistance furnace that will establish a temperature gradient for these studies was delivered from Centorr Associates and installed at the end of this reporting period.

8.1.3 Thermodynamics of the UO_2-U_2N_3 Solid Solution

A limited thermodynamic study of the solid solution $UO_{2-x}N_{0.75x}$ is being performed. This work is directed primarily toward providing thermodynamic data for an understanding of possible mass

1. T. B. Lindemer, *GCR-TU Programs Annu. Progr. Rep. Sept. 30, 1971*, ORNL-4760, pp. 112–13.
2. R. H. Flowers and G. W. Horsley, *The Influence of Oxide Kernels on the Manufacture and Performance of Coated Particle Fuel*, AERE-R5949 (1968).
3. M. T. Morgan et al., *ORNL Nuclear Safety Research and Development Program Bimonthly Report for September–October 1972, Non-LMFBR Programs*, ORNL-TM-4030, pp. 41–44.

Table 8.1. Kernel compositions prepared for out-of-reactor tests in a temperature gradient

Kernel type	Objective
$UO_{2.000}$	Test of reference oxide
UC_2 (vacuum treated)	Test of reference carbide
UO_2 + ≤10% UC_2; carbide either as surface layer or uniform dispersion in oxide	Test of alternative oxide-base kernel having a P_{CO} overpressure much less than that for the reference oxide; determine migration behavior to 1800°C
$UO_{2-x}N_{0.75x}$, $0.1 \leq x \leq 0.6$	Same as above
$UC_{0.8}N_{0.2}$ + $UC_{\sim 1.8}N_{\sim 0.06}$	Test of alternative carbide-base kernel to determine migration behavior to 1800°C
$UC_{0.2}N_{0.8}$	Same as above
$U(C,S)_2$ + U(C,S)[a]	Same as above

[a]Prepared by C. B. Pollock of the Metals and Ceramics Division.

transport processes in coated kernels of substoichiometric compositions analogous to PuO_{2-y} when placed in a temperature gradient. A second objective is the synthesis of an oxide-base kernel composition having an (O + N)/U ratio substantially less than 2 and that is calculated to be capable of maintaining a P_{CO} substantially lower than that present in coated oxide fuels of present reference designs; such decreased values of P_{CO} are predicted to result in a significant decrease of the gas-phase transport of carbon. The oxynitride also appears to be much easier to synthesize than other oxide-base low-P_{CO} kernels such as UO_2-UC_2 or $(U,Ce)O_{2-x}$.

The abstract of a paper pertinent to this subject is reproduced below.[4]

The thermodynamic behavior of $UO_{2-x}N_{0.75x}$ has been investigated from 1250 to 1850°C by reacting UO_2 with carbon at controlled P_{N_2} and P_{CO}. Values of x resulting from this treatment were determined gravimetrically and fell in the range $0.02 \leq x \leq 0.50$. The range of gas pressures used was $1 \leq P_{CO} \leq 520$ torr and $18 \leq P_{N_2} \leq 600$ torr, with P_{CO} being held high enough to prevent the formation of $UC_{1-z}N_z$. The thermodynamic analysis was based on the reaction $[UO_2] + 2C + 0.75\ N_2 \rightarrow [UN_{1.5}] + 2CO$, where the brackets indicate solid solution in the oxynitride. Free energy functions from the literature and the experimental parameters were used to determine the ratio of the activity coefficients, $\gamma_{UN_{1.5}}/\gamma_{UO_2}$, with the standard states taken as pure UO_2 or $UN_{1.5}$. This ratio is dependent upon P_{CO} and P_{N_2} at a given temperature and generally decreases with increasing temperature from approximately 10^{-4} at 1250°C to 5×10^{-6} at 1850°C.

4. Abstract of paper presented at the Nuclear Division meeting of the American Ceramic Society, Cincinnati, Ohio, Apr. 29 to May 3, 1973.

8.2 CHEMICAL CHARACTERISTICS OF FUEL AND FISSION PRODUCTS

T. B. Lindemer M. T. Morgan

8.2.1 Evaluation of Oxide Additives for Retention of Cesium, Barium, and Strontium in Biso Particles

Thermochemical data that may be pertinent to the release of the fission products cesium, strontium, and barium from irradiated oxide-fueled Biso particles are being reviewed. The ultimate objective is to explain the results obtained by us and others in the field of fission product release from particles and to specify possible kernel additives that may form stable compounds with these three fission products, thus preventing their release from Biso-coated particles during service.

Several requirements apparently need to be imposed on the additive-fuel system. First, the additives should have a low nuclear cross section. Second, additive oxides should be stable at the oxygen potentials that exist in coated particles (e.g., they should not decompose to carbides). One must bear in mind that oxide compounds appearing in equilibrium diagrams published in the open literature are generally determined at atmospheric conditions of $P_{O_2} = 0.21$ atm and may be unstable at the conditions of $P_{O_2} = 10^{-20}$ to 10^{-12} atm expected to be present in oxide particles of the present designs. Third, oxides that are present as part of the fission product system were not considered, since irradiation experience indicates that they are ineffective in retaining cesium, strontium, or barium in the quantities present. Fourth, the additive should not

result in the formation of liquid phases at service temperatures because it appears that liquids will not retain fission products as effectively as solids and because nothing is known about possible deleterious effects of liquid phases in a coated particle.

The reviews accomplished to date permit the following observations. First, extensive investigations by German workers[5] reveal that Al_2O_3 may be effective in retaining strontium and barium at normal HTGR operating temperatures. Second, our thermodynamic calculations for the Cs_2O-Al_2O_3 system indicate that cesium probably will not be retained by the addition of Al_2O_3; however, in view of the probable errors in the thermodynamic quantities used in these calculations, it is possible that cesium could be retained, and an irradiation test is planned to evaluate the addition of Al_2O_3 to UO_2. Third, there is apparently no oxide additive that will retain fission products at temperatures higher than those at which the silicon carbide coating loses its retentive properties; thus, the incentive for using kernel additives instead of a silicon carbide layer for retention of fission products exists only at temperatures below 1500 to 1600°C.

8.2.2 Behavior of UO_2 Particles at $T \geqslant 2200$°C

A phenomenon that is relevant to the behavior of coated UO_2 particles at very high temperatures is the tendency for the particle to expand as a result of internal CO pressure. An intensive investigation of this at $2200 \leqslant T \leqslant 2600$°C was reported by Beutler, Hamner, and Prados[6] for as-coated particles. The phenomenon was obviously caused by the generation of carbon monoxide as a result of kernel-coating interaction.

We have calculated these pressures with the aid of thermodynamic data that was reported after the work of Beutler et al.[6] was performed. Consider that the particle contains a UO_2 kernel that is initially exactly stoichiometric. Heating of this particle to high temperatures while maintaining thermodynamic equilibrium in the UO_{2-x}-C-CO-CO_2 system can be shown to result in lowering of the O/U ratio of the kernel, with the consequent generation of a substantial pressure of CO (P_{CO_2} is insignificant). The pressure P_{CO} is obtained from the ideal gas law:

$$P_{CO} = \frac{xRT}{a\theta} , \tag{1}$$

where

x = substoichiometry in UO_{2-x},

R = 82.05 cm^3-atm/(mole °K),

T = temperature, °K,

a = ratio of the porosity or free volume in the kernel and the buffer pyrocarbon layer to the geometrical volume of the kernel,

θ = molar volume of UO_2, 24.6 cm^3/mole.

The pressure of CO is related to the pressure of oxygen, P_{O_2}, via the equilibrium

$$2C + O_2 \rightarrow 2CO ,$$

for which K_{eq}, where

$$K_{eq} = \frac{(P_{CO})^2}{P_{O_2}}, \tag{2}$$

can be evaluated from readily available thermodynamic data. The work of Pattoret et al.[7] related P_{O_2} at a given substoichiometry x at temperature by the general relation

$$P_{O_2} = 10^{(A - B/T)} . \tag{3}$$

Thus, one can demonstrate from the above equations that

$$a = \frac{xRT\, 10^{-0.5(A - B/T)}}{K_{eq}^{1/2}\, \theta} \tag{4}$$

for a given value of x. Once a is calculated, then P_{CO} is obtained from the first equation. The calculated results are shown in Fig. 8.1. These results are of course dependent on the x-P_{O_2} relationships, and there is some disagreement among various investigators on these relationships, especially for $x > 0.01$. Thus, the values

5. R. Förthman, M. Hamesch, and H. Nickel, *Investigations to Decrease the Release of Solid Fission Products from Coated Fuel Particles*, KFA report Jül-846-RW (May 1972).

6. H. Beutler, R. L. Hamner, and J. W. Prados, *GCR Program Semiannu. Progr. Rep. Sept. 30, 1966*, ORNL-4036, pp. 10–22.

7. A. Pattoret, J. Drowart, and S. Smoes, "Thermodynamic Studies by Mass Spectrometry on the U-O System," *Thermodynamics of Nuclear Materials, 1967*, pp. 613–36, IAEA, Vienna, 1968.

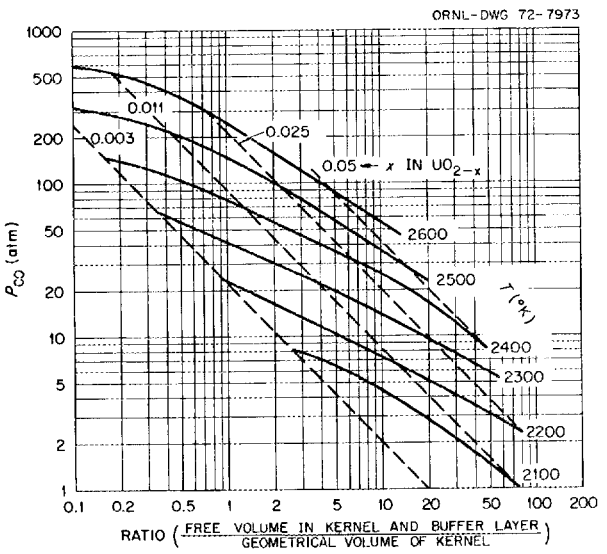

Fig. 8.1. Calculated carbon monoxide pressures in coated UO_{2-x} particles heated to indicated temperatures.

in Fig. 8.1 should be considered as only semiquantitatively correct.

There are several conclusions to be made here. The calculated pressures indicate that Beutler et al.[6] observed the results of CO pressures that were as high as ~500 atm in the expanded particles and possibly >1000 atm in the particles prior to expansion. Their results also show that the system reached equilibrium in <1 min. It should also be noted that the pressures shown in Fig. 8.1 are greater than that for the UO_2-"UC_2"-C-CO equilibrium; therefore, "UC_2" should not be present, and though one may postulate that the P_{CO} was generated as a result of the formation of "UC_2" from interaction of the kernel and the coating, this is incorrect. The observation that ThO_2 particles show much less coating expansion with identical heat treatments[6] is consistent with the thermodynamic observation that thoria does not exhibit as much substoichiometry as urania.

8.3 POSTIRRADIATION EVALUATION OF IRRADIATED FUELS

M. T. Morgan R. L. Towns
L. L. Fairchild

8.3.1 Postirradiation Analysis of the Cl-28 Experiment

The Cl-28 irradiation experiment was an instrumented and swept capsule designed to test bonded fuel rods and irradiate a variety of coated particles of conventional and advanced design for use in fission product release studies. The capsule contained samples from 21 batches of coated particles, each sample in a separate graphite tube. The sample tube and thermocouple positions are illustrated in Fig. 8.2.

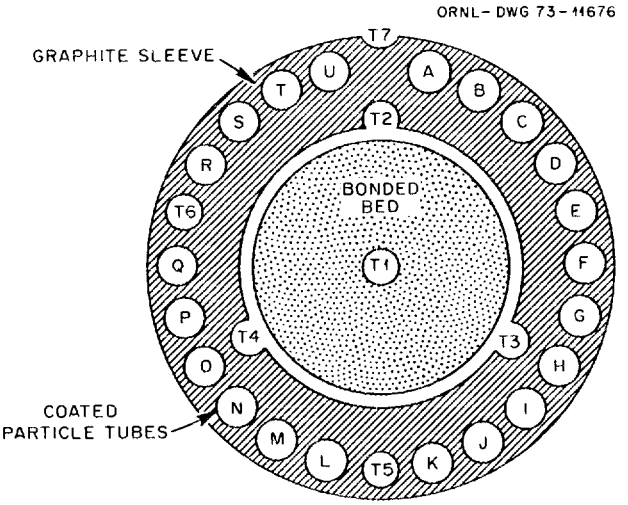

Fig. 8.2. Cross section of Cl-28 irradiation capsule.

Loading and operation of the experiment were described previously.[8] In summary, the experiment began to release fission gases during a first insertion in the ORR, so that full insertion could not be accomplished. When the activity was first noticed, the maximum temperature was 780°C and fuel tube temperatures were 650°C. Insertion was continued slowly during an 8-hr period until the maximum temperature reached 1000°C. The rare gas activity rose slightly during the first week of operation until it reached approximately three times the activity that was first recorded. This changed very little during the remainder of the irradiation, varying slightly as the temperature changed. Temperature data listed in Table 8.2 show irradiation durations at various temperatures as recorded by seven thermocouples. The burnup calculated from ^{235}U and ^{144}Ce analyses was 11% FIMA.

All coated particles were unloaded and inspected visually for cracks or other signs of failure. The fission product inventories of particles in individual tubes were

8. J. A. Conlin, "ORR Irradiations," *GCR-TU Programs Annu. Progr. Rep. Sept. 30, 1971,* ORNL-4760, pp. 136–37.

Table 8.2. Temperature distribution in CI-28 capsule during irradiation

Time at temp. (hr)	Temperature (°C) for thermocouples –						
	T1	T2	T3	T4	T5	T6	T7
200	684	565	670	533	498	512	445
555	714	591	700	559	524	538	466
250	743	615	728	584	547	558	487
243	775	648	761	613	578	591	510
246	814	679	799	644	612	624	539
41	832	695	812	662	625	640	546
56	855	718	838	685	648	660	567
~14	970	815	950	785	750	760	660
~39	1000	845	980	820	782	800	709
~3	1008	855	990	825	790	805	713
Max	~1015	865	1000	835	800	815	725

measured by radiochemical analyses, and the empty tubes were analyzed after removal of the particles. Where coating failures were observed or suspected the samples were leached with nitric acid. Results from these examinations are summarized in Table 8.3. The coating failures as determined by visual examination and by leaching are given as a percentage of the total number of coated particles in each tube. The fraction determined by leaching has been corrected to include failures determined visually, since only apparently intact particles were selected for leaching.

The fraction of ^{95}Zr in the graphite sample tubes is generally low except for tubes that contained visibly failed coated particles. In the latter case the ^{95}Zr was found in the tube where it was released, as shown in Fig. 8.3, where the ratio Zr_{ti}/Zr_{pi} is plotted vs tube position. The quantity Zr_{ti} is the ^{95}Zr activity in the empty tube, while Zr_{pi} is the total ^{95}Zr activity produced by particles in the same tube. The corresponding fraction of ^{137}Cs activity (Cs_{ti}/Cs_{pi}), also plotted in Fig. 8.3, is not related to the number of coated particle failures, but instead shows a periodic variation with position. This periodicity can be explained if we consider that the cesium contamination, unlike the zirconium, diffused throughout the capsule and is nearly the same for all positions (see Table 8.3) and that the Cs_{pi} is proportional to the fuel loading. The fuel loading varied periodically with position since large and small particles were alternated with tube position to distribute the load. The percentage of

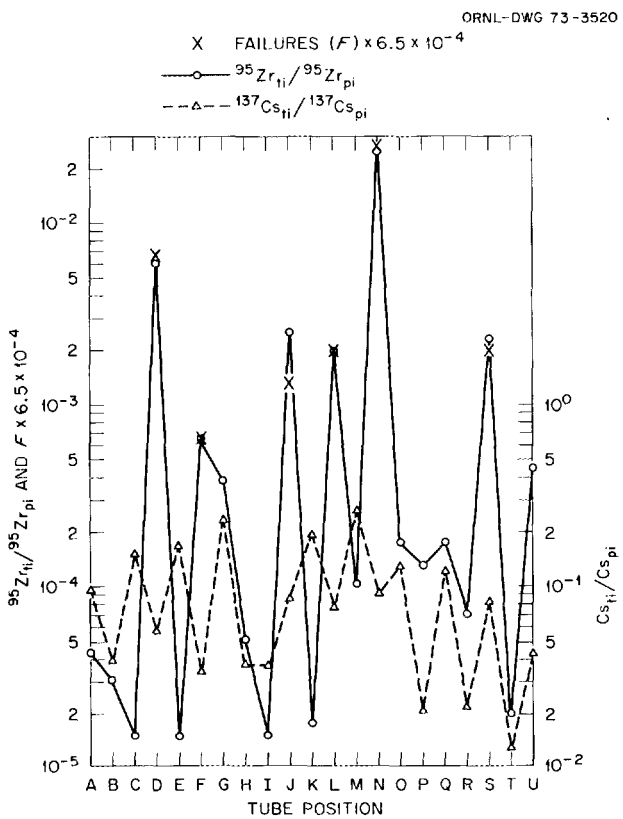

Fig. 8.3. Comparison of ^{95}Zr and ^{137}Cs contamination in graphite tubes from CI-28 with number of visible coated particle failures which occurred in the tubes as a function of tube position.

Table 8.3. Data from examination and analysis of loose coated fuel particles and tubes irradiated in capsule CI-28

Fuel tube	Coating type[a]	Fuel	Failed coatings (% of total)		Cesium remaining in coated particles (%)	Fraction in tubes (%)	
			Visual	Leached		Zr	Cs
A	HTI	UC_2	0		92	0.004	10
B	LTI	R-UOS[b]	0	100	72	0.003	4
C	Triso	UO_2	0		110	ND[c]	15
D	LTI	R-UCS[d]	25	70	87	0.60	6
E	Triso	UC_2	0		89	ND[c]	17
F	LTI	R-UC_2[e]	2	2	94	0.065	3
G	Production run		0		85	0.038	23
H	LTI	R-UC_2	0	0	99	0.005	4
I	Production run		0		100	ND[c]	4
J	Triso	R-UOS	5	14	95	0.25	9
K	LTI	UC_2	0		96	0.002	19
L	HTI	R-UOS	8	35	93	0.20	8
M	LTI	UO_2	0		99	0.010	25
N	LTI	R-UOS-Zr[f]	100	100		2.4	9
O	LTIA[g]	UC_2	0		102	0.017	12
P	HTI	R-UCS	0	10	94	0.013	2
Q	LTIA[g]	UO_2	0		113	0.017	12
R	LTIA[g]	R-UOS	0	10	95	0.007	2
S	Triso	R-UOS-Zr	8	17	91	0.23	8
T	HTI	UO_2	0		83	0.002	1
U	HTIA[g]	R-UOS	0	20	101	0.045	4

[a]HTI, high-temperature isotropic; LTI, low-temperature isotropic.
[b]Derived from strong-acid resin in as-carbonized condition.
[c]None detected.
[d]Strong-acid resin derived fuel, deoxidized at 1600°C.
[e]Weak-acid resin derived fuel, deoxidized at 1600°C.
[f]Strong-acid resin derived fuel containing 10% Zr, as carbonized.
[g]Heat treated at 1900°C after application of coating.

cesium remaining in the as-irradiated coated particles was based on a total cesium calculated from zirconium analyses for each batch. The analytical variation was at least ±10%, and the lowest fraction remaining was 72% in tube B with 100% of coating failures.

The source of the cesium contamination is probably both from the cracked coated particles and from the bonded rods. We calculated that if all the cesium found in the empty tubes came from cracked coated particles, this would amount to 24% of the total produced in those cracked particles. This would have been only a fraction of the total released since cesium was also dispersed throughout the graphite capsule. The bonded rods were at a higher temperature, and metallographic examination showed that many coated particles in the bonded rods had failed. Most of the failures occurred in the vicinity of the thermocouple hole, apparently due to mechanical interaction during assembly. A few isolated cracked coatings were found throughout the section taken of one bonded rod. Diffusion of cesium from intact coated particles would not be expected since pyrocarbon coatings are an effective barrier at the low temperature (800°C) which prevailed during this irradiation.

Subsequent annealing experiments on some particles also indicated high release of cesium from coated particles that were not broken but from which a significant fraction of fuel (25 to 90%) could be extracted by leaching. Furthermore, when the particles were cracked in a confined space, the noble gases were also found to have been released. Cracks were found in the coatings of two coated particles that were examined using a scanning electron microscope at 300X. To determine whether the coatings on particles from the three batches (tubes B, D, and N) that produced most

of the failures were defective before irradiation, unirradiated archive samples consisting of 20 coated particles from each batch were leached in 8 *M* nitric acid at 98°C for 2 hr; the leach solution contained less than 0.3% of the uranium in the particles, which was the limit of sensitivity of the analyses.

Examination of preirradiation radiographs of the loaded fuel tubes showed that the spacing was such that adjacent coated particles in some tubes might lock together under the force of gravity with the tube in a vertical position. Differential thermal expansion between the coated particles and the fuel tube could have produced the forces necessary to induce cracking of coatings or to expand any microcracks existing in some coated particles, producing the gross failures observed.

Results from the examination of particles and fuel tubes from this experiment lead to the following general conclusions.

1. The failures which caused fission gas release during irradiation were apparently due to fractured particles in the bonded rods which were damaged during assembly and to coated particle failures in the tubes due to differential thermal expansion between the coated particles and the tubes.
2. Cesium diffused throughout the graphite capsule at temperatures less than 800°C.
3. The ^{95}Zr contamination in the empty fuel tubes was directly proportional to the number of gross coating failures. The exact relationship obtained was not expected because zirconium does not diffuse easily (none came from coated particles with microcracks) and the principal means of zirconium transport is by fission recoil. Therefore the zirconium activity should be proportional to the amount of fuel exposed to the tube wall, which would vary with each cracked coated particle unless the coatings were separated completely from each particle.

8.3.2 Comparison of Fission Product Release from Various Types of Coated Fuel Particles

Fission product release from various types of coated fuel particles during postirradiation anneals is being measured to compare the coatings and to determine the effects of burnup, temperature, and coating characteristics on fission product diffusion. Approximate diffusion coefficients have been obtained from the relation:

$$D = \frac{L^2}{6t},$$

where L is coating thickness and t is the delay time required for the fission product to penetrate the coating.[9] This relation would be exact if we assume that the fission product concentration at the inner surface of the high-density isotropic pyrocarbon outer layer is constant during the anneals and that the fission product concentration at the outer surface of the outer layer is zero. While these conditions are only approximately true in our experiments, the relative values obtained are believed useful for comparison purposes and are believed to be close to the true diffusion coefficients. A study is being carried out to determine if more exact relations can be obtained from our data and to compare results obtained by different methods.

We measured the cesium release from additional samples of Biso-coated particles in annealing experiments during this reporting period. These data are plotted in Fig. 8.4 along with other data previously reported.[10] Data numbers in the figure correspond to

9. J. Crank, *Mathematics of Diffusion*, pp. 47–48, Clarendon, Oxford, 1965.

10. M. T. Morgan et al., "Fission Product Transport through Particle Coatings," *GCR-TU Programs Annu. Progr. Rep. Sept. 30, 1971*, ORNL-4760, pp. 140–43.

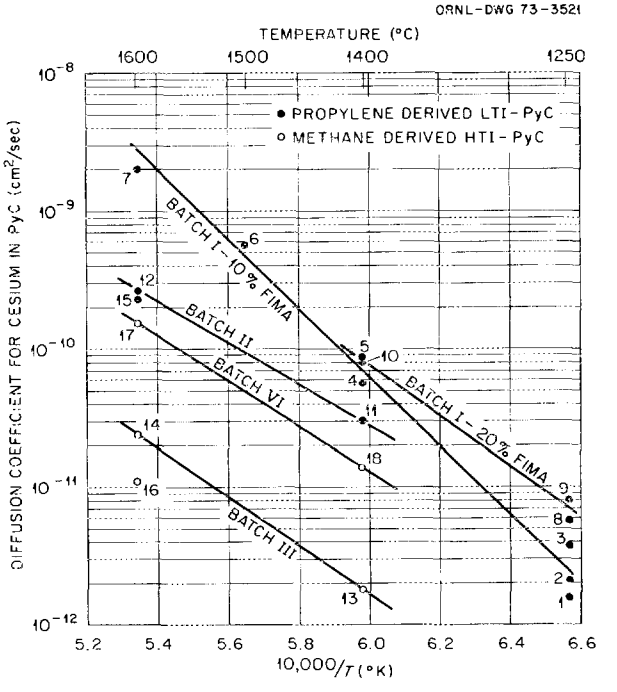

Fig. 8.4. Arrhenius plot for cesium diffusion in pyrocarbon from postirradiation anneals of coated particles.

data points listed in Table 8.4. The coating characteristics are given in Table 8.5 according to batch numbers. In contrast to the wide difference in cesium diffusion coefficients in LTI and HTI pyrocarbon obtained from previous work on coated particles from batches I, II, and III, the later data show closer agreement for some of the samples. Variations in preirradiation characteristics are not consistent with the diffusion coefficients obtained. Samples from batches I, II, III, and IV had comparable densities but yielded widely different diffusion coefficients. Samples from batches III and V were estimated to have slightly higher anisotropy factors and gave the lowest diffusion coefficients. Crystallite size was small for most of the LTI pyrocarbons except for batch IV, represented by data point 15, and was large in the HTI pyrocarbons. Batches VII and VIII are derived from propane and were omitted from Fig. 8.4.

In general, the pattern shows that some HTI pyrocarbons are much better than LTI pyrocarbons in retaining cesium, while others are about the same. The characteristics that influence the diffusion are not evident. More detailed postirradiation coating characterization is needed to enable irradiation effects on coating structure to be taken into account. Appropriate measurements are being planned. In addition to density, crystallite size, and anisotropy, another characteristic of pyrocarbon that may influence diffusion is the relative amount of amorphous and crystalline carbon in the structure. Methods developed in Germany at KFA are being studied for this determination.[11,12]

11. K. Koizlik et al., *Estimation of the Amorphous Fraction in Pyrolytic Carbon by Means of an Optical Method,* KFA report Jül-589-RW (April 1969).

12. L. Sutterlin et al., *Investigation of the Structure of Isotropic Pyrocarbon Layers on Coated Particles with Ultrasonic Energy,* KFA report Jül-798-RW (September 1971).

Table 8.4. Cesium diffusion coefficients in pyrocarbon coatings from postirradiation anneals of coated particles

Data point	Batch No.	Coating type	Annealing temp. (°C)	Burnup (% FIMA)	Average D (cm^2/sec)	Total particles tested[a]
1	I	LTI	1250	10	1.6×10^{-12}	1×10
2	I	LTI	1250	10	2.2×10^{-12}	2×80^b
3	I	LTI	1250	10	3.8×10^{-12}	1×10
4	I	LTI	1400	10	5.7×10^{-11}	4×1
5	I	LTI	1400	10	8.6×10^{-11}	7×1
6	I	LTI	1500	10	8.2×10^{-10}	8×1
7	I	LTI	1600	10	2.0×10^{-9}	7×1
8	I	LTI	1250	20	5.8×10^{-12}	2×80^b
9	I	LTI	1250	20	8.2×10^{-12}	1×8
10	I	LTI	1400	20	8.3×10^{-11}	4×1
11	II	LTI	1400	*c*	3.0×10^{-11}	4×1
12	II	LTI	1600	*c*	2.6×10^{-10}	2×1
13	III	HTI	1400	*c*	1.8×10^{-12}	4×1
14	III	HTI	1600	*c*	2.4×10^{-11}	2×1
15	IV	LTIA	1600	*c*	2.3×10^{-10}	2×1
16	V	HTI	1600	*c*	$\leq 1.1 \times 10^{-11}$	2×1
17	VI	HTI	1600	11	1.5×10^{-10}	2×1
18	VI	HTI	1400	11	1.4×10^{-11}	3×1
d	VII	LTI	1600	11	2.0×10^{-10}	2×1
d	VII	LTI	1400	11	1.3×10^{-11}	3×1
d	VIII	LTI	1600	11	2.0×10^{-10}	2×1

[a]Number of samples times number of coated particles per sample.

[b]Bonded rods containing about 80 coated particles in each.

[c]Irradiated in the HFIR to a fast fluence of 4×10^{21} neutrons/cm^2 in the HT-1 capsule and a burnup about 3% FIMA; all other irradiations were performed in the ORR with a low fast fluence.

[d]Omitted from Fig. 8.4.

Table 8.5. Preirradiation characteristics of pyrocarbon coatings of fuel particles used in cesium diffusion experiments

Batch	Coating type	Coating source gas	Density (g/cm^3)	BAF or OPTAF	Crystallite size (Å)	Fuel particle
I	LTI	Propylene	1.83	1.0[a]	35	UO_2
II	LTI	Propylene	1.99	1.0[b]	35	ThO_2
III	HTI	Methane	1.82	1.1[a]	112	ThO_2
IV	LTIA[c]	Propylene	2.04	1.0[a]	120	ThO_2
V	HTI	Methane	2.00	1.3[a]	120	ThO_2
VI	HTI	Methane	1.82	1.0[d]	116	UC_2
VII	LTI[e]	Propane	1.83	1.1[d]	27	UC_2
VIII	LTI[e]	Propane	1.85	1.0[d]		UO_2

[a]BAF estimated.
[b]BAF measured from disk samples.
[c]Preirradiation annealed at 1900°C.
[d]OPTAF.
[e]Propane yields an LTI pyrocarbon that is very similar to but not identical with propylene-derived coatings.

8.3.3 Disintegration of Fuel Rods and Associated Tests

The ability to debond coated particles in selected irradiated and unirradiated fuel rods would permit (1) determination of the fraction and number of broken coatings, (2) determination of fuel and fission product distribution in the coated particles and the matrix, and (3) performance of other tests on individual coated particles from the fuel rods. In order to determine the number of broken coatings, it is required that no coated particles be fractured in the disintegration process. Fractions of broken coated particles in a fuel rod may be less than 1 in 10^4.

To determine fuel and fission product distribution in a fuel rod, it is necessary to remove coated particles and the matrix in layers and to use a method which will not leach fuel or fission products from cracked coated particles or from layers of the fuel rod beneath the layer being removed. Therefore a dry method is preferred.

To perform tests on individual coated particles, intact particles from the fuel rod may be selected, and it is only necessary that the method of disintegration does not change the characteristics of the coatings.

We studied the following methods for the removal of particles from fuel rods:

1. air blasting with coke powder,
2. brushing with a stiff brush,
3. high-pressure water jet erosion,
4. electrolysis in nitric acid or cooking in fuming nitric acid,
5. ultrasonic field in liquid,
6. reaction in alkali metals,
7. oxidation in air at 600°C or oxidation in oxygen plasma,
8. freezing after impregnation with water or sudden warming after impregnation with liquid nitrogen.

A summary of the results is given in Table 8.6. Most of the tests were performed on intrusion-bonded fuel rods (60 vol % coated particles) that had been fired at 1800°C. Only the first four methods showed any promise. The use of an ultrasonic field on a fuel rod submerged either in alcohol or in nitric acid had no effect, and freezing after impregnation with water and sudden warming after impregnation with liquid nitrogen produced no change. Submersion in liquid alkali metals caused rapid disintegration of fuel rods, but it also excessively delaminated layers of particle coatings. Oxidation methods, with the exception of the electrolytic oxidation method first described by Bildstein,[13] also damaged the coatings before weakening the matrix sufficiently for removal of coated particles.

These preliminary tests were not sufficient in most cases to establish definitely that a method would or would not work, but they indicated methods which

13. H. Bildstein, unpublished work, Seibersdorf, Austria.

Table 8.6. Disintegration of coated-particle fuel rods

Method	Removal of coated particles	Removal in layers	Estimated damage to coated particles[a]		Leaching of fission product or fuel	Ease of operation
			Thinning	Cracking		
1	Slow	Uneven	Slight	None	No	Difficult
2	Slow	Uneven	Moderate	?	No	Difficult
3	Fast	Uneven	None	Slight to none	Possible	Fair
4	Slow	No	Slight	None	Yes	Easy

[a]Most of the fuel rods tested contained fractured particles as manufactured; therefore damage could only be estimated.

might accomplish our objectives with the least development. The method selected for immediate use for determining coating failures in a fuel rod is still the electrolytic disintegration in nitric acid. The possibility of alteration of the physical properties of the coating by this treatment must be explored further before the debonded coated particles can be used in annealing experiments. Water jet erosion seems to be the most practical way to remove the coated particles without causing alteration in coating properties, but this method needs further testing to ensure that coatings are not cracked in the process.

9. Reactions of HTGR Core Materials with Steam

A. P. Malinauskas H. J. de Nordwall

High-temperature gas-cooled nuclear reactors utilize graphite as a neutron moderator, as core structural material, and as a fuel cladding material. At elevated temperatures, however, graphite is readily oxidized, so an assessment of possible reactor operational abnormalities must include a consideration of the consequences of inadvertent introduction of oxidant into the helium coolant circuit. In the current-generation design the most likely oxidant is steam, and the most likely accident leading to its introduction into the coolant circuit is the rupture of a steam-generator tube.

Although extensive loss of core structural integrity is unlikely, highly localized attack of the graphite fuel containers is a possibility. This type of attack could weaken and ultimately breach the coolant channel wall, cause loss of fuel matrix, which in turn would result in a higher fuel temperature during subsequent operation, and cause oxidation and ultimate failure of pyrocarbon fuel coatings. The extent to which the various potential consequences actually occur depends in a complex manner on the carbon structures and the temperatures occurring in different parts of an element. This program seeks to resolve these dependencies in a manner that will minimize the amount of reevaluation necessary when material specifications are changed.

Another consequence of steam injection into the helium coolant stream would be the generation of potentially explosive quantities of hydrogen and carbon monoxide, since both gases comprise the main products of graphite corrosion by steam, in accordance with the reaction

$$C(s) + H_2O(g) = CO(g) + H_2(g) . \quad (1)$$

Unfortunately, laboratory-scale investigations of the kinetics associated with this reaction are complicated by their heterogeneous character, particularly in view of the real situation wherein much of the graphite surface available for potential reaction with steam is contained within the graphite body. Only under specialized conditions is reaction confined to the gross surface area (as opposed to total surface area as measured on a molecular scale). Moreover, since steam attack necessarily alters the surface on which reaction occurs, this effect must also be considered.

The complex geometrical system represented by a real fuel element consisting of pyrolytic-carbon-coated spheres in a carbonaceous matrix surrounded by a graphite wall is being examined in-pile so that the radial temperature gradients present during the early part of an accident may be reproduced and any unexpected radiolytic effects taken into account.

9.1 OUT-OF-PILE LABORATORY EXPERIMENTS

C. M. Blood A. P. Malinauskas

A series of determinations of the rate of attack of H-327 graphite by steam was completed during this report period. This series involved five graphite specimens in the form of hollow cylinders. Three of the cylinders were employed to investigate the effects of temperature on reaction rate, at constant steam input, over the temperature range 800 to 1000°C, whereas the remaining two specimens were used to study the effects of steam input at constant temperature and total pressure.

To guide a simultaneous attempt to unify the theoretical aspects associated with the phenomenon, measurements were also made of parameters which are

characteristic of the internal geometries of the specimens. These measurements included gas adsorption (BET) surface area determinations, gaseous permeability experiments, and measurements of binary mutual diffusion through the septa.

In addition to these investigations, an attempt was made to compare the corrosion characteristics of H-327 graphite with that of a bonded rod of coated fuel particles. These experiments yielded results in qualitative agreement with expected behavior, but were actually more useful as a demonstration of the significant inhibitory effect of the reaction products on the rate of corrosion. The inhibition, which was much greater than we had earlier anticipated, precluded any further analysis of the comparative results and suggested that greater attention be paid to this facet of the problem.

9.1.1 Rates of Reaction of H-327 Graphite

The experimental procedure followed throughout the course of this investigation essentially involved cycling the sample between surface area and gas transport measurements and rate of corrosion determinations. These latter measurements were performed by mounting a given cylindrical specimen on a quartz tube which was coaxially positioned within a larger quartz tube in a furnace and then passing a helium-steam mixture over the outer surface of the specimen for a predetermined period of time. The loss of graphite due to steam attack was determined gravimetrically.

The rate of flow of the gas mixture was about 1 liter (STP)/min; this value was chosen to ensure laminar flow conditions. In addition, the specimens (0.48 in. ID, 0.70 in. OD, and 2.0 in. long) were so mounted that the transition from quartz mount to graphite sample to quartz spacer involved no protuberances which could promote turbulence.

In Table 9.1 the specimens which were employed in this study are identified relative to initial sample weight and the experimental conditions of temperature and steam partial pressure which apply.

The development of surface area with graphite removal was sensibly reproducible from specimen to specimen, as illustrated by the data presented in Table 9.2, which is a tabulation of (interpolated) surface area values as a function of burnoff. Since the initial weights of the samples are quite similar, the results would not differ markedly had the comparison been made on the basis of absolute amount of graphite removed.

With the exception of the results at zero burnoff, the data listed in Table 9.2 can be described analytically within 15% accuracy by the function

$$S^2 = 122.4\,(100 g_R/g_o) - 3.35\,, \qquad (1)$$

in which S represents the surface area in square meters and the quantity $(100 g_R/g_o)$ is the percentage of original sample lost by corrosion (percent burnoff).

Another measure of internal geometry is the porosity-tortuosity factor ϵ/q, with which the free space gaseous diffusion coefficients must be modified so that the ordinary diffusion equations may be employed to describe diffusion through the porous media. Interpolated values of this parameter are listed as a function of burnoff in Table 9.3. These results can be described analytically within 30% accuracy by the equation

$$10^3(\epsilon/q) = 1.9\,(100 g_R/g_o) + 4.53\,. \qquad (2)$$

Although Eqs. (1) and (2) must be regarded as purely empirical representations of experimental data, the analytic forms do have some basis. The mathematical forms are in fact precisely the functional results which one develops by assuming the septa to be comprised of a bundle of identical parallel pores which are uniformly enlarged by steam attack. Unfortunately, this simple model leads to inconsistencies, as can be evidenced from the negative value of initial surface area squared which is predicted by Eq. (1). Nonetheless, the model does provide functional forms which can serve as useful approximations.

Values of apparent rates of reaction R_{app} are presented in Tables 9.4 and 9.5. Table 9.4 shows the

Table 9.1. Identification of H-327 specimens employed in the steam-graphite reaction studies

Sample code	2A	1A	1B	4D	4C
Initial weight, g	11.5203	11.5692	11.5619	11.6365	11.6764
Temperature, °C	800	900	1000	1000	1000
Steam pressure, atm	0.0950	0.0950	0.0950	0.0700	0.0450

Table 9.2. Comparative results of alterations in surface area of H-327 graphite samples due to corrosion by steam

Burnoff (%)	Surface area of sample (m^2)				
	2A	1A	1B	4D	4C
0.0	2.29	2.08	2.20	2.68	1.99
1.0	10.06	12.04	9.96	10.98	10.85
2.0	15.15	16.66	14.98	14.89	14.70
3.0	19.42	20.89	19.65	17.59	17.39
4.0	23.02	24.28	23.90	19.16	19.91
5.0	26.70	26.55	27.18	21.57	21.94

Table 9.3. Comparative values of ϵ/q for H-327 graphite specimens as a function of burnoff

Burnoff (%)	10^3 [porosity-tortuosity (ϵ/q) factor]				
	2A	1A	1B	4D	4C
0.0	4.19	3.96	4.03	4.42	5.16
1.0	7.28	6.25	6.06	6.35	6.85
2.0	10.15	8.89	7.52	7.71	8.33
3.0	12.64	9.58	8.61	9.55	10.01
4.0	14.20	13.39	9.47	11.27	11.80
5.0	14.61	18.25	10.48	12.87	13.57

Table 9.4. Effect of temperature on apparent rates of reaction of H-327 graphite due to exposure to 0.0950 atm partial pressure steam

Burnoff (%)	Apparent rate of reaction (mg/min)		
	2A, 800°C	1A, 900°C	1B, 1000°C
1.0	0.0318	0.208	1.68
2.0	0.0371	0.281	2.14
3.0	0.0327	0.337	2.22
4.0	0.0357	0.377	2.39
5.0	0.0390	0.411	2.58

Table 9.5. Effect of steam partial pressure on apparent rates of reaction of H-327 graphite at 1000°C

Burnoff (%)	Apparent rate of reaction (mg/min)		
	1B, 0.0950 atm	4D, 0.0700 atm	4C, 0.0450 atm
1.0	1.68	2.08	1.49
2.0	2.14	2.42	1.52
3.0	2.22	2.48	1.59
4.0	2.39	2.41	1.77
5.0	2.58	2.34	1.86

effect of temperature at constant steam partial pressure. Although the data clearly indicate the expected increase in R_{app} with burnoff, it makes little difference in determining an activation energy whether or not the data correspond to a given burnoff (over the range indicated in the table); that is, a value of about 55 ± 5 kcal/mole is obtained regardless of the actual data selected.

Table 9.5 represents an attempt to define the dependence of reaction rate on steam partial pressures at constant total pressure and temperature. Only the data corresponding to 5% burnoff display the qualitative behavior which had been anticipated. Nor have we yet established a cause for the apparently anomalous behavior at lower burnoff values. Part of the discrepancy is most likely due to a neglect of possible inhibition by the reaction products. That such effects can be significant has been aptly demonstrated by our studies of the relative rates of reaction of H-327 graphite and bonded coated-particle fuel rods.

9.1.2 Rates of Reaction of Bonded Rods

Since the primary purpose of this portion of the experimental program was to provide rate of reaction values of bonded rods relative to values for H-327 graphite, and since the bonded rods are in the form of solid cylinders, solid cylindrical specimens were employed. Also, the bonded rods were somewhat friable, so that it became necessary to provide a receptacle for the rod in order to use the gravimetric procedure. An alumina boat was employed for this purpose, and the bonded rod was positioned between two H-327 "control" specimens. While this arrangement did permit a direct comparison of the rates of reaction of the three specimens, it also promoted mixing of the gas stream within the reactor. As is pointed out later, this condition is believed to have caused one anomaly which was observed in the course of these experiments.

Four control specimens and two bonded rods were involved in the investigations. One of these bonded rods was similar to those employed in the complementary in-pile studies. This sample displayed unusual behavior during heating, and it was later established that the rod at no time during its fabrication was subjected to temperatures greater than 1000°C. This rod has been designated FS-4. The second fuel rod, FS-18, had been heat treated at 1800°C prior to our heat treatment studies. The control samples were all taken from adjacent positions of an H-327 graphite bar stock.

Results of heat treatments on two of the controls and the two fuel rods are given in Table 9.6. Like the

Table 9.6. Effects of 900°C heat treatment on specimen weight and surface area

Duration of heat treatment (hr)	FS-4		Control 1		Control 8		FS-18	
	Weight loss (mg)	Surface area (m^2)	Weight loss (mg)	Surface area (m^2)	Weight loss (mg)	Surface area (m^2)	Weight loss (mg)	Surface area (m^2)
0.0	0.0	0.23	0.0	0.38	0.0	0.43	0.0	0.24
2.67	25.8	39.28	1.0	0.65	1.1	0.64		
3.00	17.7	58.86	1.0	0.65	1.4	0.68		
3.0	13.3	62.47	1.1	0.74	1.2	0.62		
3.00	14.1	66.59	1.1	0.68	1.6	0.89		
27.08	26.4	102.14	6.3	0.92	6.6	0.80		
3.00			3.1	1.03	2.7	0.91	7.8	4.52
3.00			2.5	1.19	2.2	1.03	6.5	4.73
3.00			1.7	1.06	2.2	0.95	4.4	4.58
3.00			1.8	1.14	2.2	1.12	6.2	3.86
3.00			1.7	1.21	2.0	1.00	3.4	3.83
27.25	28.9	111.63	7.3	1.38	5.8	1.14		

reaction experiments, which these heat treatments preceded, the heating was performed with the fuel rod sandwiched between the control samples; in addition, the heat treatments were conducted under a flowing dry helium atmosphere. In view of the extremely large change in the surface area of fuel rod FS-4, which is obvious from the data tabulated, attempts to account for the in-pile behavior of the rod, when predicated on surface area considerations, are subject to very large uncertainties.

The steam corrosion studies which were performed are summarized in Table 9.7. The series A experiments indicate the expected qualitative dependence of apparent reaction rate on surface area. The series B

Table 9.7. Effects of steam exposure (about 0.08 atm partial pressure) on fuel compacts and H-327 graphite controls at 900°C

Specimen position	Influent		Central		Effluent	
	S (m^2)	R_{app} (mg/min)	S (m^2)	R_{app} (mg/min)	S (m^2)	R_{app} (mg/min)
Series A	Control 1		FS-18		Control 8	
	1.38		3.83		1.14	
	1.33	0.10	2.99	0.39	1.14	0.09
	1.27	0.19	2.52	0.53	1.20	0.11
	1.52	0.09	2.48	0.26	1.22	0.08
	1.64	0.10	2.79	0.31	1.52	0.10
Series B	Control 2		FS-4		Control 3	
	0.74		112		0.86	
	0.89	0.03	135	3.31	1.02	0.03
Series C	Control 1				Control 3	
	1.85	0.15			1.09	0.09
Series D	Control 2				Control 8	
	1.10	0.07			1.54	0.11
Series E	Control 1		FS-4		Control 8	
	1.79	0.04	122	2.30	1.54	0.04

experiment, on the other hand, indicated FS-4 to be significantly less reactive than FS-18 if surface area considerations were taken into account (although the apparent rate of reaction is obviously a factor of 10 greater). Similarly, control samples 2 and 3 appeared to be less reactive than 1 and 8. Series experiments C and D were then performed to determine the possible effect of rod FS-4 on the observations. In addition, FS-4 was also run with control samples 1 and 8 as an added check.

A plausible explanation of the observed behavior concerns the possibility of corrosion inhibition by the reaction products. Thus FS-4, which produces more H_2 and CO than FS-18, by about a factor of 10, influences the rates of reaction of the control samples. Similarly, its own rate of corrosion is also reduced, thus giving rise to the apparent discrepancy between FS-4 and FS-18 in terms of surface area considerations.

Surprisingly, however, no difference in reaction rate had been detected between the control located before FS-4 and that located behind the rod. One can thus only postulate the significant mixing of the gas stream which had been mentioned earlier.

9.1.3 Future Studies

Analyses of the reaction rate data which had been conducted prior to obtaining the results involving the bonded rods had assumed that the products formed in the reaction had negligible effect on the observed rate of corrosion. After the bonded rod experiments had been performed, however, it became apparent that this underlying assumption was suspect and could in fact account for other inconsistencies which were uncovered in the data analysis.

Attempts were therefore made to employ the rate data to elucidate the nature of the inhibition by the reaction products. Unfortunately, the data do not span a wide range of reaction products concentrations, so that, while the results can be employed to further demonstrate that such a dependence does exist, the associated scatter is too large to attempt quantitative evaluations. Hence, the experimental program has been redirected to obtain the desired information in a more straightforward fashion.

9.2 IN-PILE EXPERIMENTS

S. H. Freid

The four experiments in which a model HTGR fuel element was exposed to steam in a reactor have been evaluated. A summary of the experiments and the results obtained follows.

9.2.1 Experiment Description

A steam-helium mixture of predetermined composition was passed over a model fuel element that was heated by fission and exposed to reactor radiation. The gas leaving the capsule was analyzed for carbon oxides, hydrogen, and fission products to determine the rate and extent of reaction or to monitor the state of the fuel. The model fuel element shown in Fig. 9.1 consisted of a cylindrical H-327 graphite box containing a fuel rod. The ends of the box were protected from oxidation by alumina caps. Heat was generated by gamma heating and fission in UC_2 fuel particles coated with pyrocarbon and silicon carbide. Pyrocarbon-coated thoria particles were added as a diluent. The carbonaceous matrix was made from carbon black containing ^{14}C so that matrix oxidation could be distinguished from box oxidation.[1]

9.2.2 Gaseous Fission Product Release Measurement

During the first two experiments it was noted that admission of steam to the fuel specimen resulted in a rapid and significant increase in gaseous activity. This was followed by a smaller, but nevertheless pronounced, decrease in the rate of rare-gas emission when the steam supply was cut off. The effect was observed for all gaseous radionuclides measured. Since this observation could be important in assessing the consequences of certain accidents involving ingress of water, plans were made for more careful gas sampling in experiment SG-4. Figure 9.2 shows the result of analyses for ^{88}Kr ($t_{1/2}$ = 2.8 hr) as a function of time, average fuel temperature, and the presence or absence of steam. The rapid rise and fall of activity is immediately obvious. Release to birth rate (R/B) ratios for the krypton and xenon nuclides were measured before, during, and after the first exposure to steam in experiment SG-4. In general, the spread in values for each nuclide during constant operating conditions was quite small, and the data for both krypton and xenon tended to cluster about a single line of slope ($-\frac{1}{2}$) (see Fig. 9.3), which is the slope one would predict if a diffusional process were the rate-limiting step. However,

1. *Nuclear Safety Program Annu. Progr. Rep. December 31, 1970*, ORNL-4647, p. 97.

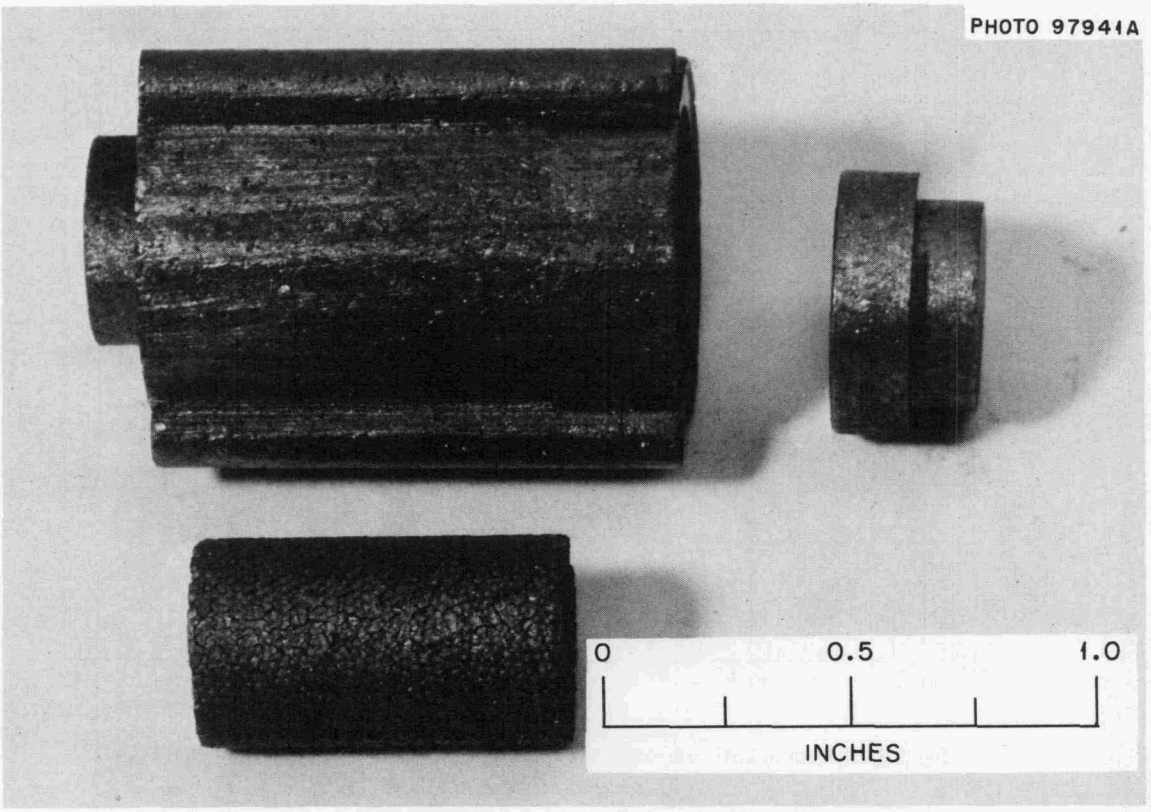

Fig. 9.1. Model HTGR fuel element used in HTGR fuel oxidation experiments.

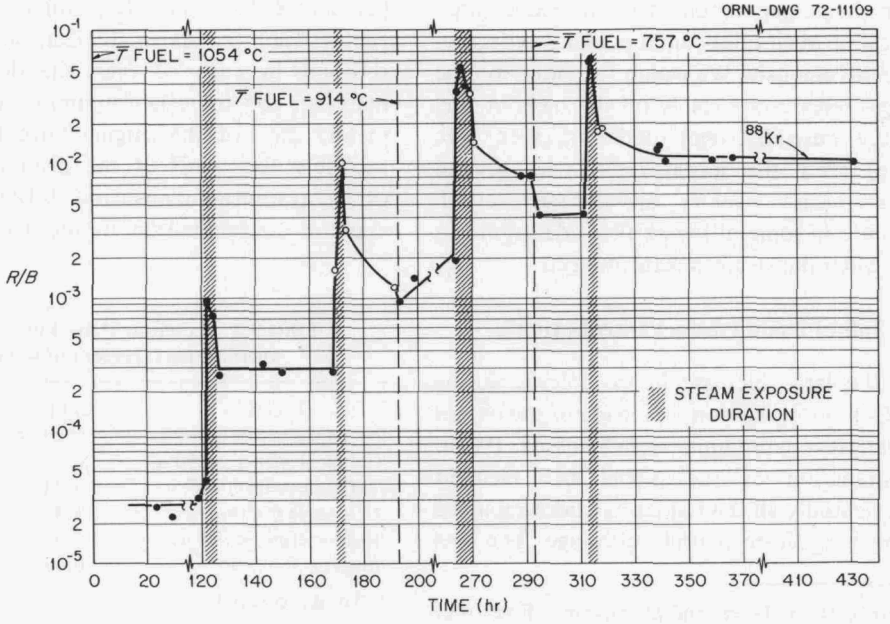

Fig. 9.2. ^{88}Kr release to birth ratio during in-pile experiment SG-4.

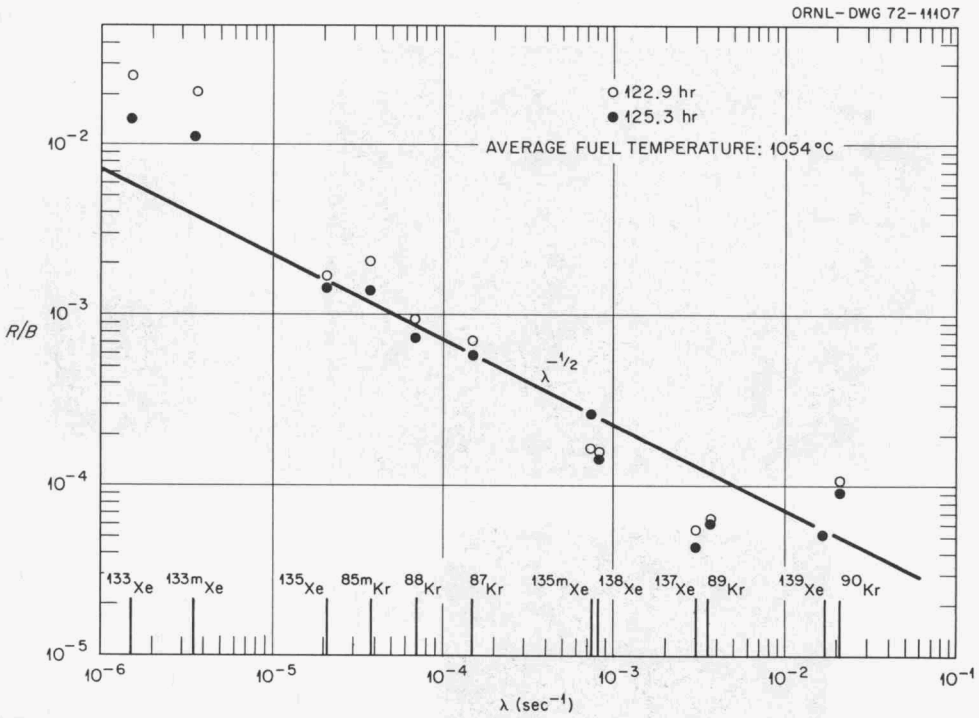

Fig. 9.3. Release to birth rate ratios during the first exposure to steam, experiment SG-4.

the fact that both krypton and xenon followed the same line indicates that the rate-limiting step was not diffusion of atoms through the fuel material, since one would expect the larger xenon atom to move more slowly.[2] Release to birth rates for all nuclides shifted to new values simultaneously. We cannot account for the rapid rise in gas release rate solely on the basis of fuel particle breakage caused by steam oxidation, since there was no trend, after the initial rapid rise, toward increasing gas release over a several-hour period. Mechanical failure in some of the particle coatings must have occurred when the steam was introduced.

9.2.3 Solid Fission Product Distribution

In view of the large increase in gas release during experiment SG-4, an evaluation was made of the extent to which other fission products were released. Postirradiation examination of the model fuel element showed that essentially all the binder had been removed and that there was severe particle breakage. The fuel residue was sieved, and the fractions were identified visually as (1) coarse material consisting of small chunks of the original fuel compact, (2) coated ThO_2 particles, (3) coated UC_2 particles, and (4) a fine (<177-μm) rubble. Table 9.8 shows the distribution of uranium and thorium in each of these fractions. The fine sieve material, 70% by weight uranium, accounts for approximately 26% of the original inventory. This rubble is probably the result of the disintegration of exposed UC_2 cores during conversion to UO_2 by steam. The 5% uranium contamination in the ThO_2 sieve fraction is

Table 9.8. Experiment SG-4 uranium and thorium distributions (percent of original loading)

Fraction	U/Th	Uranium	Thorium
Chunks (coarse, >850 μ)	0.5	14.6	12.4
ThO_2 sieve fraction[a]	0.04	5.1	51.6
UC_2 sieve fraction	9.3	67.9	3.2
Rubble (fine, <177 μ)	25.0	25.2	0.4
Initial U/Th ratio	0.43		
Total recovered		112.8	67.6

[a]Could not get all into solution.

2. R. M. Carroll, R. B. Perez, and O. Sisman, "Release of Fission Gas During Fissioning of UO_2," *J. Amer. Ceram. Soc.* **48**, 55 (1965).

Table 9.9. Experiment SG-4 fission product distribution

Location	Percent of calculated production						
	^{131}I	^{137}Cs	^{89}Sr	^{140}Ba	^{103}Ru	^{95}Zr	^{141}Ce
UC_2 sieve fraction	12.1	59.7	65.3	53.3	45.5	49.7	46.3
ThO_2 sieve fraction	4.3	7.8	10.2	17.5	4.7	5.8	5.6
Rubble sieve fraction (fine)	15.0	48.5	19.1	17.8	2.1	17.7	22.3
Graphite casing	0.3	1.9	0.5	0.3	0.4	0.3	0.3
Al_2O_3 caps and reaction chamber	0.5	0.2					
Stainless steel exit lines	9.4						
H_2SO_4 dryers	0.4						
Total recovered	42.0	118.1	95.1	88.6	52.7	73.2	74.5

due to UC_2 particles that were incompletely sieved out plus those uranium cores which were observed to penetrate into the coatings of intact ThO_2 particles.[3] The results of the analysis for the fine sieve fraction and the observation of many broken particles in the UC_2 sieve fraction indicate that under the severe conditions of this experiment, well in excess of 25% of the UC_2 particles were broken. Table 9.9 shows the distribution of ^{131}I, ^{137}Cs, ^{89}Sr, ^{140}Ba, ^{103}Ru, ^{95}Zr, and ^{141}Ce throughout the experimental facility. The large amount of cesium found is thought to be due to hot-cell contamination. The low ruthenium recovery may be an artifact of the analytical procedures employed or may be possibly due to the formation of a volatile compound. Iodine-131 was observed to have moved throughout the primary system under the conditions of this experiment. However, movement may only have occurred during the highest temperature part of the experiment.

9.2.4 Carbon Removal

The theoretical bases used in describing carbon removal from the model fuel element have been described previously. Analysis of carbon removal from a porous slab due to steam oxidation, whether controlled by in-pore diffusion or the rate of chemical reaction, ultimately involves the solution of a mass balance expression like the steady-state equation

$$nD'_{12}\frac{\partial^2 x_1}{\partial z^2} - \epsilon_t k x_1 = 0 , \qquad (1)$$

where k is defined by

$$-\partial n_1/\partial t = k x_1 , \qquad (2)$$

in which n_1 is the concentration of water (moles/cm^3), n is the total molar density (moles/cm^3), D'_{12} is the effective diffusion coefficient for the H_2O-He system in graphite, x_1 is the mole fraction of water, and ϵ_t is the total porosity of the graphite.[4]

In later work,[5] the rate constant k was redefined to permit differences in specific surface area to be considered and hence to reduce the dependence of k on graphite type. At the same time an idealized description of the development of new surface area with extent of reaction was formulated for a system in which reaction was not limited by diffusion. Changes in the product $\epsilon_t D'_{12}$ had not been adequate to explain observed changes in reaction rate with extent of reaction.[4]

For a proper description of the behavior of a fuel element, one must be able to describe the behavior of a body containing different graphites (e.g., the fuel matrix and the fuel element sleeve) at the same or at different temperatures. A simple two-zone model describing the reaction of graphite and fuel matrix was developed for this by Watson.[6]

In comparing the in-pile and laboratory experiments, a combination of these three approaches, to be described in detail in a forthcoming report, was used.

The basic equation was Eq. (1), now applied simultaneously to the fuel element sleeve and the fuel matrix, whose oxidation could be followed independently as a

3. S. H. Freid and H. J. de Nordwall, *ORNL Nuclear Safety Research and Development Program Bimonthly Rep. September–October 1971*, ORNL-TM-3623, pp. 74–76.

4. C. M. Blood et al., *Nuclear Safety Program Annu. Progr. Rep. Dec. 31, 1968*, ORNL-4374, p. 281.

5. A. P. Malinauskas, *Nuclear Safety Program Annu. Progr. Rep. Dec. 31, 1969*, ORNL-4511, pp. 85–89.

6. G. M. Watson and H. J. de Nordwall, ibid., pp. 89–91.

result of the ^{14}C doping. Fuel coating oxidation was assumed to be relatively slow.

The effective rate constant k used was that defined by

$$dn_{H_2O}/dt = nkx_1 \quad (3)$$

The reaction rate constant k and the gas transport and structural characteristics of the graphite as represented by D'_{12} and ϵ_t were expressed as functions of the extent of reaction, using laboratory measurements[7-9] of specific surface area and $\epsilon_t D'_{12}$. The steady-state condition was then replaced by a quasi-steady-state situation in which k and $\epsilon_t D'_{12}$ were allowed to change after discrete time intervals, during which steady state was assumed so that time-dependent properties could be handled without the labor of transient mathematical solutions.

Because of the empirical nature of the equations developed for k and $\epsilon_t D'_{12}$ as functions of burnoff, it would be unwise to apply the equations beyond the parameter ranges covered by experiment or to ascribe too much physical significance to the individual constants, though further laboratory work may permit more fundamental descriptions to be formulated. Five empirical constants were needed to describe the variation of k with temperature and extent of reaction. The maximum difference between observed and calculated carbon losses in the range 0 to 10% carbon loss was 30%. The temperature range covered by the data fitted was 800 to 1000°C; water mole fractions were between 0.04 and 0.1.

A laboratory experiment by Blood, Hebert, and Overholser,[10] in which a model fuel element similar to that used in the in-pile program had been oxidized in steam at 1000, 1100, and 1200°C, provided an opportunity to test the mathematical model for a composite system in the absence of radiation or fission products. Tables 9.10 and 9.11 give the results of a comparison of observed and calculated carbon losses at various times.

Table 9.10. Out-of-pile oxidation of fuel rod 10 at 1000°C and 0.1 mole fraction steam[a]

Time (min)	g_R(obs) (mg)	g_R(calc) (mg)	Δg_R (mg)	Agreement[b]
64.0	126.6	72.6	−54.0	0.57
127.5	238.3	173.6	−64.7	0.73
221.5	429.8	354.1	−75.7	0.82
285.5	558.8	499.4	−59.4	0.89
349.5	705.5	653.6	−51.9	0.93
413.5	872.9	820.6	−52.3	0.94
548.0	1206.2	1169.0	−37.2	0.97
613.0	1382.8	1321.3	−61.5	0.96
676.0	1559.9	1484.2	−75.7	0.95
750.0	1712.9	1662.2	−50.7	0.97
At 750 min, graphite container only				
740	1183.2	1120.9	−62.3	0.95
At 750 min, fuel compact only				
750	529.7	541.3	+11.6	1.02

[a]Reference 11.
[b]Agreement = predicted/observed.

Table 9.11. Out-of-pile oxidation of fuel rod 5 at 0.035 mole fraction steam[a]

Temperature (°C)	Time (min)	g_R(obs) (mg)	g_R(calc) (mg)	Δg_R (mg)	Agreement[b]
1000	122.5	110.8	93.2	−17.6	0.84
1100	216.5	521.8	299.5	−222.3	0.57
1000	338.5	684.9	440.5	−244.4	0.64
1200	432.5	1640.0	1154.5	−485.5	0.70

[a]Reference 11.
[b]Agreement = predicted/observed.

Considering that the graphite casing was not H-327, the agreement was quite good within the temperature range used in obtaining the empirical constants (i.e., at 1000°C) but poorer at higher (1100 and 1200°C) temperatures, where uncertainties in $\epsilon_t D'_{12}$ become more important. The result illustrates the consequences of using data for one graphite to describe the behavior of another.

Carbon losses occurring during the last two in-pile experiments are compared with calculated carbon losses in Figs. 9.4 and 9.5 and Tables 9.12 and 9.13. Results for experiments SG-1 and SG-2 are not shown here, because localized iron present in the fuel sleeve of

7. C. M. Blood and A. P. Malinauskas, *ORNL Nuclear Safety Research and Development Program Bimonthly Rep. March–April 1971*, ORNL-TM-3411, pp. 55–57.
8. C. M. Blood and A. P. Malinauskas, *ORNL Nuclear Safety Research and Development Program Bimonthly Rep. November–December 1971*, ORNL-TM-3670, pp. 73–76.
9. C. M. Blood and A. P. Malinauskas, *ORNL Nuclear Safety Research and Development Program Bimonthly Rep. March–April 1972*, ORNL-TM-3831, pp. 65–69.
10. C. M. Blood, G. M. Hebert, and L. G. Overholser, *Oxidation of Bonded Coated-Particle Fuel Compacts by Steam*, ORNL-4269 (July 1968).

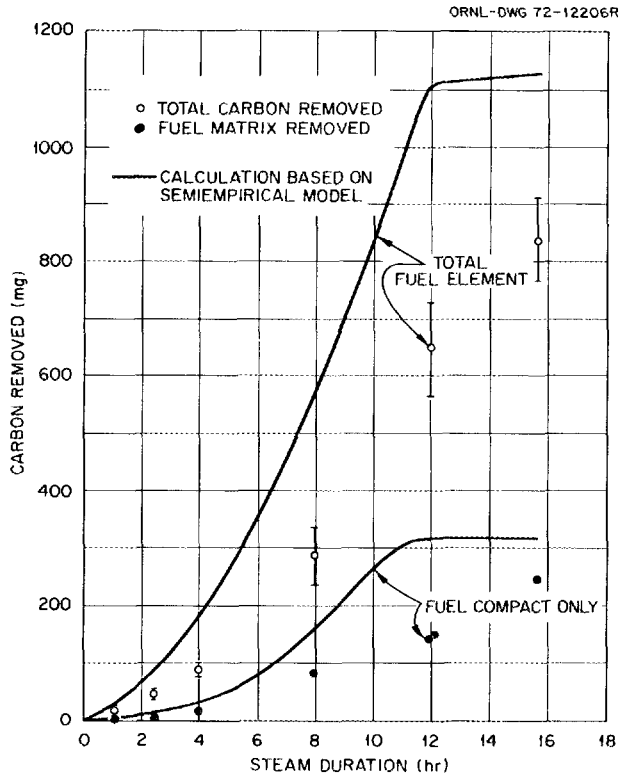

Fig. 9.4. Carbon removal from total fuel element and from fuel rod only during experiment SG-3.

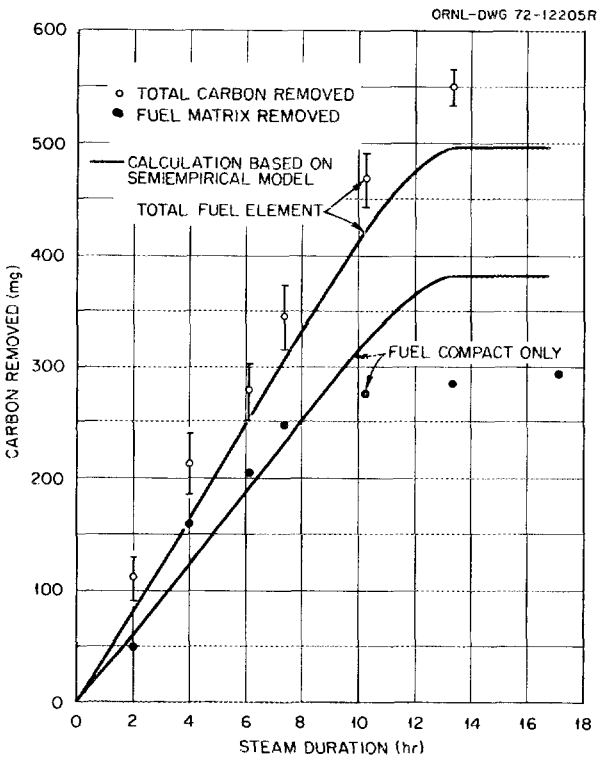

Fig. 9.5. Carbon removal from total fuel element and from fuel rod only during experiment SG-4.

Table 9.12. Steam-graphite experiment SG-3

Time (hr)	Mole fraction water	Calculated fuel center-line temp (°C)	Surface temp (°C)	Cumulative weight loss (mg)					
				Fuel rod			Whole element		
				Obs	Calc	Agreement[a]	Obs	Calc	Agreement[a]
1.1	0.03	1330	982	1	3.6	3.6	17	35	2.0
2.5	0.05	1330	982	4	12	3.0	44	72	1.6
4.0	0.09	1330	982	16	29	1.8	88	150	1.7
8.0	0.09	1330	982	83	162	2.0	288	575	2.0
12.0	0.09	1330	982	144	318	2.2	638[b]	1112	1.7
12.2	0.09	1060	800	150	318	2.1	663[b]	1112	1.7
15.7	0.09	1060	800	248	319	1.3	835[b]	1125	1.3

Postirradiation weight loss (mg)

	Obs	Calc	Agreement[a]
Casing	630(8)[c]	807	1.3
Fuel rod	206(63)	319	1.5
Total	836	1125	1.3

[a]Agreement = predicted/observed.
[b]Based upon a single estimate of CO – other values are mean of determinations made using infrared analyses and ascarite traps.
[c]Numbers in parentheses are percentage of initial weight of graphite and fuel matrix.

Table 9.13. Steam-graphite experiment SG-4

Time (hr)	Mole fraction water	Calculated fuel center-line temp (°C)	Surface temp (°C)	Cumulative weight loss (mg)					
				Fuel rod			Whole element		
				Obs	Calc	Agreement[a]	Obs	Calc	Agreement[a]
2.0	0.12	1380	820	48	60	1.3	111	80	0.72
4.0	0.12	1380	820	160	125	0.78	214	166	0.78
6.1	0.11	1380	820	211	192	0.91	279	254	0.91
7.4	0.11	1380	820	247	235	0.95	345	311	0.90
10.3	0.11	1190	730	275	324	1.2	468	424	0.91
13.3	0.07	1190	730	283	382	1.4	552	496	0.90
17.2	0.11	960	630	292	383	1.3	666	497	0.75

Postirradiation weight loss (mg)

	Obs	Calc	Agreement[a]
Casing	166(2)[b]	115	0.77
Fuel rod	497(126)	383	0.69
Total	663	498	0.65

[a]Agreement = predicted/observed.

[b]Numbers in parentheses are percentage of initial weight of graphite and fuel matrix; 126% indicates the same pyrocarbon oxidation occurred.

experiment SG-1 caused pitting[11] which invalidated the comparison; experiment SG-2 had to be abandoned due to a leak.

Carbon from the fuel compact matrix was identified by its ^{14}C tracer. All other gaseous carbon was assumed to originate from the graphite casing. In practice, a surprising amount of pyrocarbon corrosion occurred, and this CO, together with that produced by UC_2 oxidation and matrix degassing, would tend to enhance the apparent sleeve oxidation. The total carbon losses in experiments SG-3 and SG-4 as determined by weighing at the end of the experiment are also compared with predicted carbon losses in Tables 9.12 and 9.13.

The current mathematical representation of the carbon removal process describes the cumulative carbon weight loss in laboratory and in-pile experiments generally within ±50% of the calculated value. This error, which was not always the same sign, includes the measurement errors of the in-pile experiment. While this might be thought to be a considerable discrepancy, it should be viewed against the only estimate currently available of the precision of carbon oxidation calculations and the accuracy required in practical application.

A comparison of observed H-327 graphite oxidation with that predicted by the 1971 version of Gulf General Atomic's OXIDE code yielded the result that the computed carbon removal was about a factor of 10 higher than that determined in the laboratory.[11] The required precision for accident analysis is more difficult to specify, since it depends upon the probability of a particular class of steam accidents in which steam is exposed to the core at containment pressure with reduced cooling capability. The limiting consequence under such circumstances could be rapid reaction between the containment atmosphere, carbon monoxide, and hydrogen if certain composition limits were exceeded.

However, inspection of Tables 9.12 and 9.13 and Figs. 9.4 and 9.5 shows that carbon oxidation did not stop when the temperature was lowered in the later stages of the experiments. There are two possible reasons for this. The first is that the carbon being oxidized was fuel coating pyrocarbon or buffer, which would have been considerably hotter than the casing graphite even at the reduced power level. Oxidation of the fuel rod matrix would have further raised the temperature of the fuel in the casing above that calculated because of a lowering of the thermal conductivity of the rod matrix. Since coating carbon does not contain ^{14}C, this would not have been recognized as fuel body (or fuel rod) oxidation.

11. A. P. Malinauskas et al., *ORNL Nuclear Safety Research and Development Program Bimonthly Rep. July–August 1971*, ORNL-TM-3483, pp. 49–58.

The second explanation is that carbon oxidation was being catalyzed by the radiation field. Calculations of the rate of the radiolytic H_2O-C reaction indicated that the rate of energy deposition in the helium and water vapor was not large enough to account for the amount of reaction observed. However, one cannot exclude the possibility that decelerating fission fragments may produce much higher energy deposition in a system containing exposed ^{235}U.

10. Fission Product Behavior in HTGR Coolant Circuits

H. J. de Nordwall

This task is concerned with describing and explaining the distribution and adhesion of fission products in the coolant circuits of HTGRs. It includes the activities associated with the HTGR fission product surveillance program. The results of these studies will be used in the analysis of accidents involving depressurization and coolant composition change and in testing codes used to predict the inventory and distribution of fission products in the coolant circuit.

The activity level of noble gases (krypton and xenon) in the primary coolant circuit is generally established by the fuel particle release rate, the purification system removal rate, and their decay rates. Some of the noble-gas nuclides decay to radioactive metallic nuclides, which deposit on steel surfaces or on dust particles. Iodine differs from the noble gases in that it can also adsorb on graphite, steel, or dust surfaces. Metallic fission product nuclides, such as strontium and cesium, that enter the primary circuit will deposit on steel surfaces or dust particles. A small fraction of the gas-borne fission products will be carried by helium through any leaks in the primary containment boundary. The behavior of iodine and metallic fission products in the coolant circuit may be affected by their combination with coolant impurities. During accidents the pressure, velocity, and composition of the coolant can change significantly; for example, rupture of a steam generator may lead to a few percent of steam in the primary circuit.

Information is being sought on the adsorption and desorption behavior of iodine, the composition of coolant circuit surfaces, the morphology and composition of circulating particulate matter, the partial pressures of fission products in the primary circuit of the Peach Bottom HTGR, and the distribution of deposited fission products in the Peach Bottom HTGR.

The most important factor determining the concentration of condensable fission products in the coolant is the time-dependent source term, that is, their rate of release from the core. If a metal, such as strontium, is able to pass through the fuel sleeve in a time less than the fuel cycle irradiation time, a large increase in the concentration of that metal in the coolant can be expected. This breakthrough process is being monitored for the Peach Bottom HTGR by measuring fission product concentrations in the coolant and the fuel element sleeves at 300-day intervals. So far no evidence of cesium or strontium breakthrough has been seen.

10.1 IODINE ADSORPTION AND DESORPTION

M. F. Osborne

Thermochemical calculations have been made to determine the equilibrium partial pressures of the various species resulting from iodine reacting with iron, chromium, and nickel – the primary metallic components of the coolant circuit. Experimental studies of the adsorption-desorption characteristics of iodine on Fe_3O_4 have been conducted, both in vacuum and in a flowing helium-steam atmosphere. Measurements on other oxides and metals will follow. Work in both of these areas was begun during FY 1971 by E. Hoinkis, a visitor from the Hahn-Meitner Institute in Berlin.[1,2]

The adsorption of iodine (containing ^{131}I tracer) on finely divided Fe_3O_4 has been effected in the system

1. E. Hoinkis, *A Review of the Adsorption of Iodine on Metal and Its Behavior in Loops*, ORNL-TM-2916 (1970).

2. E. Hoinkis, "Temperature Programmed Desorption of Iodine from Fe_3O_4 Powder," *Trans. Amer. Nucl. Soc.* **14**(1), 70 (June 1971).

illustrated in Fig. 10.1. Iodine loadings on the powder have varied from ~0.01 to >0.5 monolayer, at powder temperatures of 200 to 450°C and iodine pressures of 10^{-11} to 10^{-7} atm. In short-term tests (approximately one day), powder samples were loaded to predetermined levels for desorption studies. Other experiments to determine the equilibrium loadings as a function of iodine pressure require several weeks. The results of one equilibrium experiment, at 300°C, are shown in Fig. 10.2. An apparent equilibrium loading of 0.09 monolayer was reached after some 40 hr at the initial iodine pressure of 10^{-10} atm. At the next pressure level (10^{-9} atm), apparent equilibrium was approached after some 120 hr. The failure of temperature control instrumentation during the 10^{-8}-atm pressure step prevented us from obtaining additional equilibrium data. Adsorption at 200°C and low iodine pressure was shown to be very slow; no equilibrium was attained after >100 hr at successive pressures of 10^{-11} and 10^{-10} atm. Further studies of equilibrium adsorption at 250 to 450°C are under way. Comparison of the adsorption coefficients obtained so far with data from the iodine-iron system[1] indicates that the capacity of an oxidized surface for adsorption of iodine is less than that of a metal surface.

The initial desorption studies were conducted in vacuum. The powder sample was heated at a linear rate from 50 to 550°C, at which temperature desorption was >95% complete. The maximum desorption rates occurred at 350 to 425°C, depending on loading and heating rate. These effects are illustrated in Figs. 10.3 and 10.4; the former compares heavy and light loadings, and the latter compares heating rates differing by a factor of 9. These studies showed that iodine atoms adsorb on Fe_3O_4 at sites of varying energy. With increasing coverage, a greater fraction of the iodine atoms are adsorbed on low-energy sites, resulting in a reduction in the temperature of maximum desorption rate, as shown in Fig. 10.3. Several isothermal tests were conducted, with typical results shown in Fig. 10.5. It is apparent from these curves that a modest temperature increase may result in a large increase in the amount of iodine in the coolant of an HTGR.

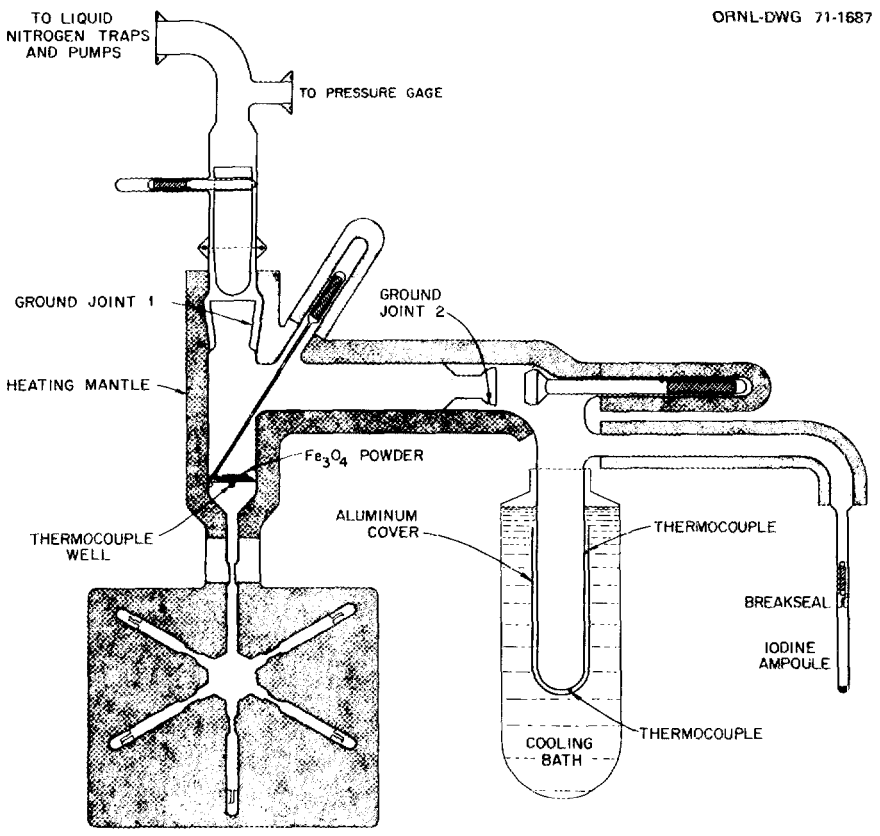

Fig. 10.1. Experimental apparatus for adsorbing iodine at low pressures on Fe_3O_4 powder.

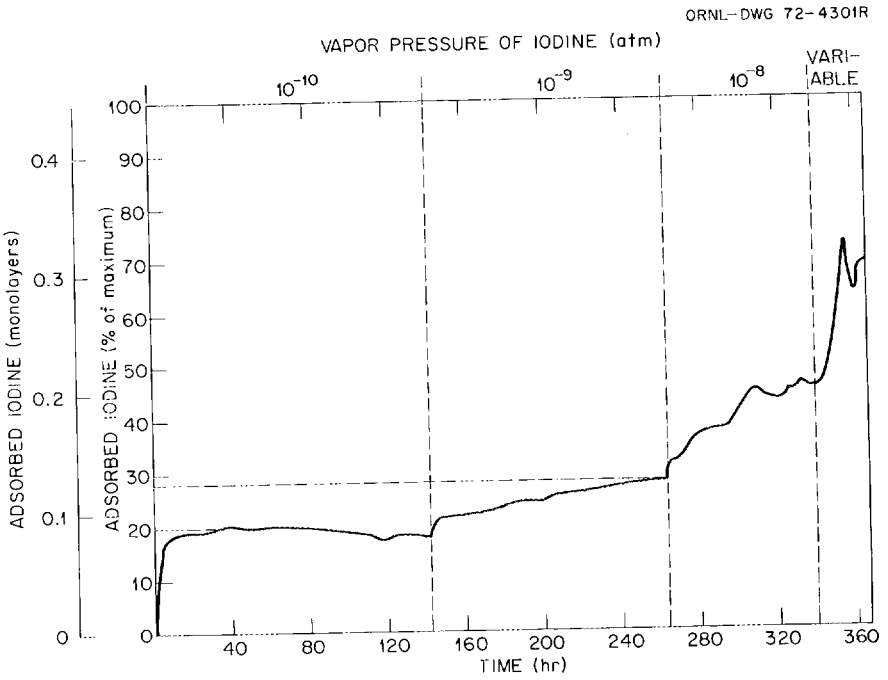

Fig. 10.2. Adsorption of iodine on Fe_3O_4 at 300°C as functions of time and iodine pressure.

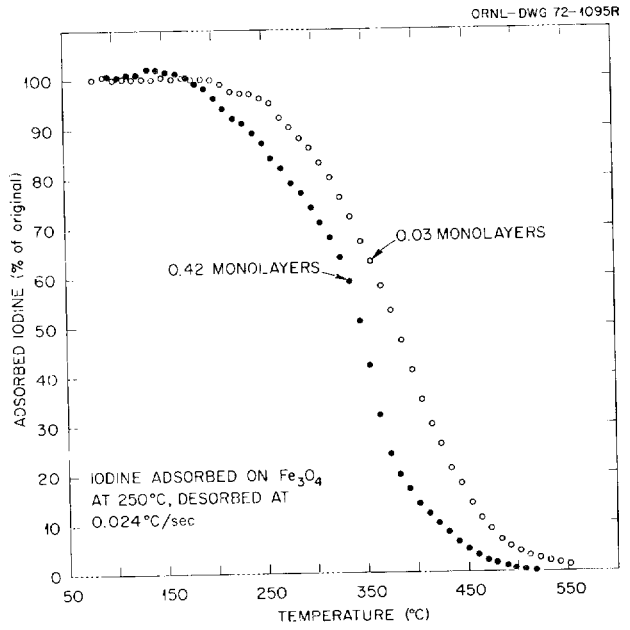

Fig. 10.3. Vacuum thermodesorption of iodine from Fe_3O_4 powder, showing the effect of iodine surface coverage on desorption temperature.

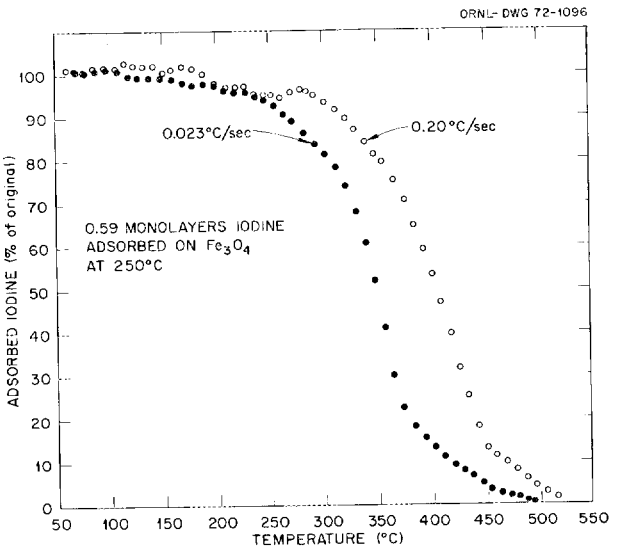

Fig. 10.4. Vacuum thermodesorption of iodine from Fe_3O_4 powder, showing the effect of heating rate on desorption temperature.

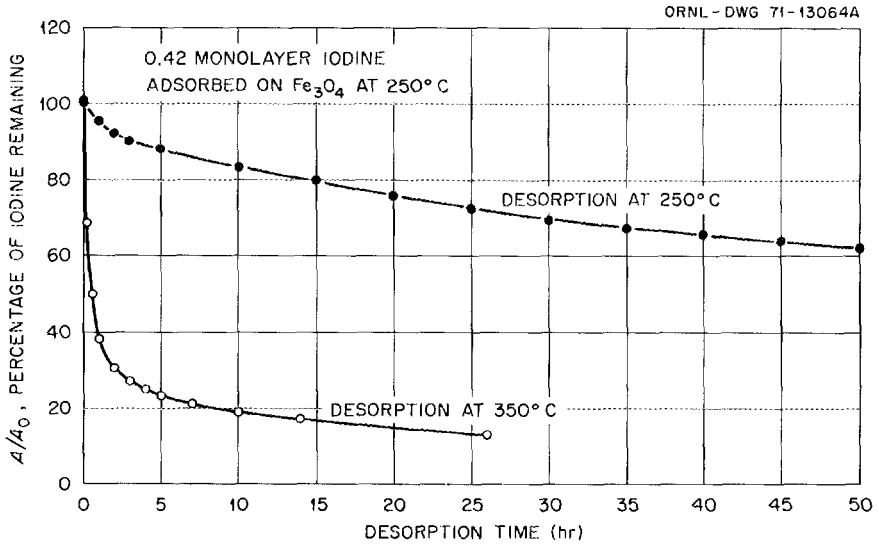

Fig. 10.5. Vacuum desorption of iodine from Fe_3O_4 powder heated isothermally.

Preliminary tests of iodine desorption into a flowing stream of dry helium or helium–3% steam have been conducted. Because of inconsistent results, the experimental apparatus and technique were revised, and the new system is in operation.

A previous study of the thermodynamics of the iron-iodine system[1] was extended to a similar evaluation of the chromium-iodine and nickel-iodine systems. The existing thermochemical data for the possible reactions were collected, and elementary equilibrium calculations of the partial pressures of iodine and the various metal iodides were performed. The primary reactions at 200 to 600°C are of the form

$$M(s) + 2I(g) \rightarrow MI_2(s) \rightarrow MI_2(g) \ .$$

Since most of the relevant experimental work has been conducted at temperatures above those of interest in the HTGR coolant, the expressions used in these calculations required extrapolation. Equilibrium constants determined by Cerný and Bartovská[3] were used to calculate the partial pressures in the Cr-I-CrI_2(s) system. The results are displayed in Figs. 10.6 and 10.7. In this temperature range the partial pressures of the chromium iodides in equilibrium with CrI_2(s) are several orders of magnitude lower than the corresponding partial pressures of the iron iodides in equilibrium with FeI_2(s). The solid curve in Fig. 10.7 represents the vapor pressure of CrI_2, and the dashed lines represent the partial pressures of CrI_2(g) in equilibrium with I(g) and Cr(s) at different temperatures. Similar data were obtained for CrI_3 and Cr_2I_4 at lower partial pressures.

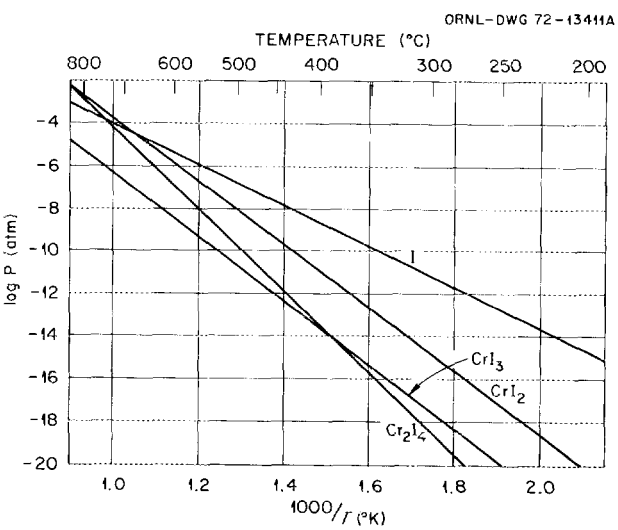

Fig. 10.6. Calculated partial pressures of iodine and the chromium iodides in equilibrium with solid CrI_2 and Cr as a function of temperature.

Since the thermochemical data are relatively sparse for the Cr-I and especially for the Ni-I systems,

3. C. Cerný and L. Bartovská, "The System Chromium-Iodine at Higher Temperatures," *Collect. Czech. Chem. Commun.* **31** (1966).

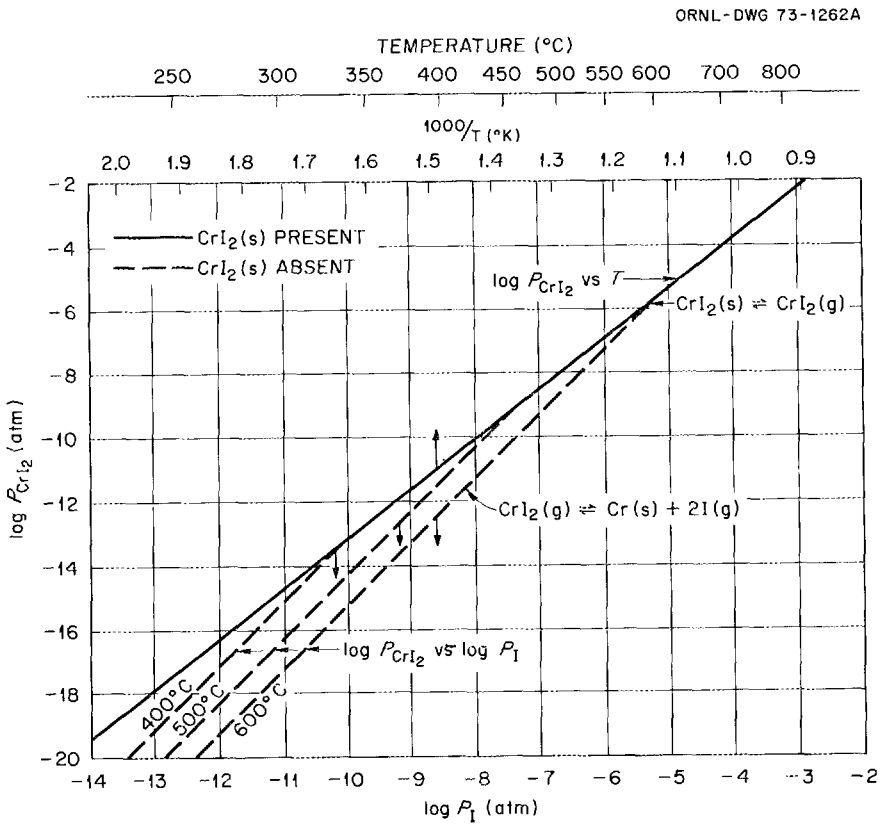

Fig. 10.7. Calculated partial pressures of $CrI_2(g)$ in equilibrium with $CrI_2(s)$ and Cr at various iodine pressures and temperatures.

independent estimates were compared wherever possible. The above calculated data were compared with data calculated from the free-energy functions at 500 to 1000°K reported by Brewer et al.;[4] good agreement was obtained for CrI_2, but the results for NiI_2 differed by at least one order of magnitude between 200 and 600°C.

10.2 FISSION PRODUCT BEHAVIOR IN THE COOLANT CIRCUIT OF THE PEACH BOTTOM HTGR

J. O. Kolb F. F. Dyer W. J. Martin

10.2.1 Deposited Activity in the Primary Circuit

Surface concentrations of fission products on the walls of the primary circuit ducts and the steam generator are measured by adaptations of remote gamma-ray spectroscopy methods used by Houtzeel and Dyer.[5] Gamma-ray spectra are taken by allowing gamma rays from a restricted portion of a duct to traverse a collimator slit in a shield surrounding a lithium-drifted germanium detector. If the surface activity being measured is uniformly deposited in a known geometrical configuration, the gamma spectrum can be reduced to quantitative surface concentrations. Surface concentrations on the large ducts of the Peach Bottom primary circuit were measured in May 1971 and again in May 1972. The points of measurements are shown in Figs. 10.8 and 10.9, and the derived surface concentrations of fission products, expressed in microcuries per square centimeter, are given in Tables 10.1 and 10.2. The reported surface concentrations represent

4. Leo Brewer, C. R. Somayajulu, and Elizabeth Brackett, "Thermodynamic Properties of Gaseous Metal Dihalides," *Chem. Rev.* 63, 111–21 (1963).

5. A. Houtzeel and F. F. Dyer, *A Study of Fission Products in the Molten-Salt Reactor Experiment by Gamma Spectrometry*, ORNL-TM-3151 (Aug. 16, 1972).

ORNL–DWG 73–1263

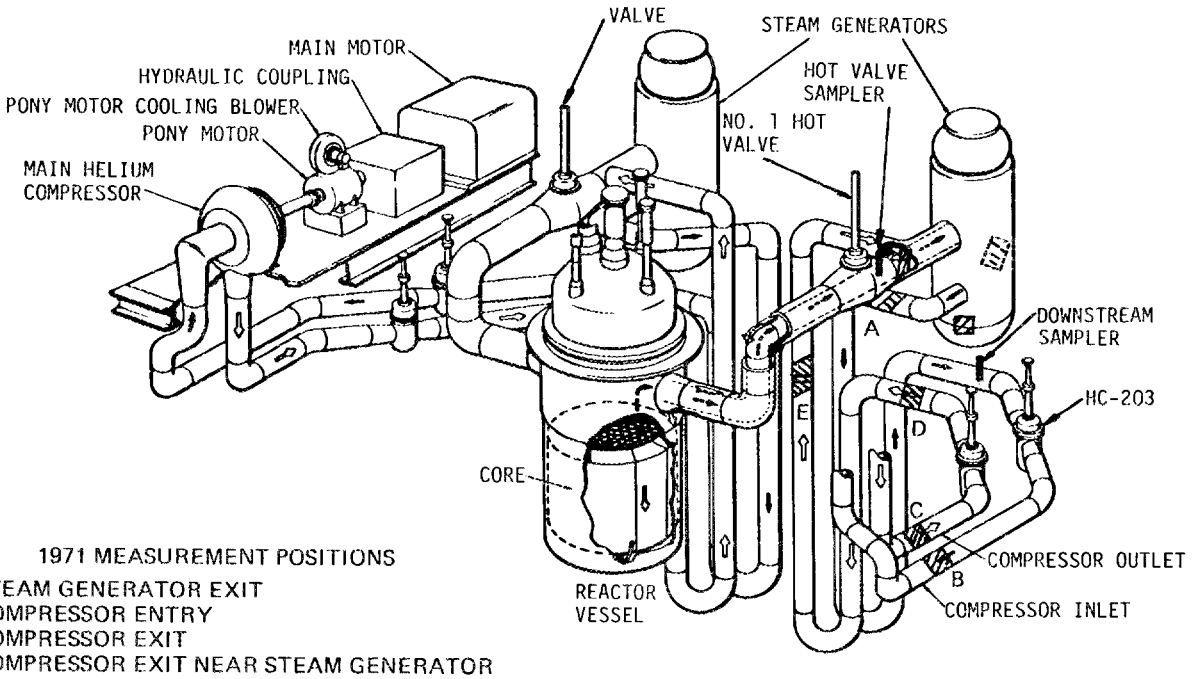

1971 MEASUREMENT POSITIONS

A STEAM GENERATOR EXIT
B COMPRESSOR ENTRY
C COMPRESSOR EXIT
D COMPRESSOR EXIT NEAR STEAM GENERATOR
E COMPRESSOR EXIT VERTICAL DUCT

Fig. 10.8. Positions of gamma-activity determinations in Peach Bottom HTGR No. 1 loop in May 1971.

ORNL–DWG 73–1264

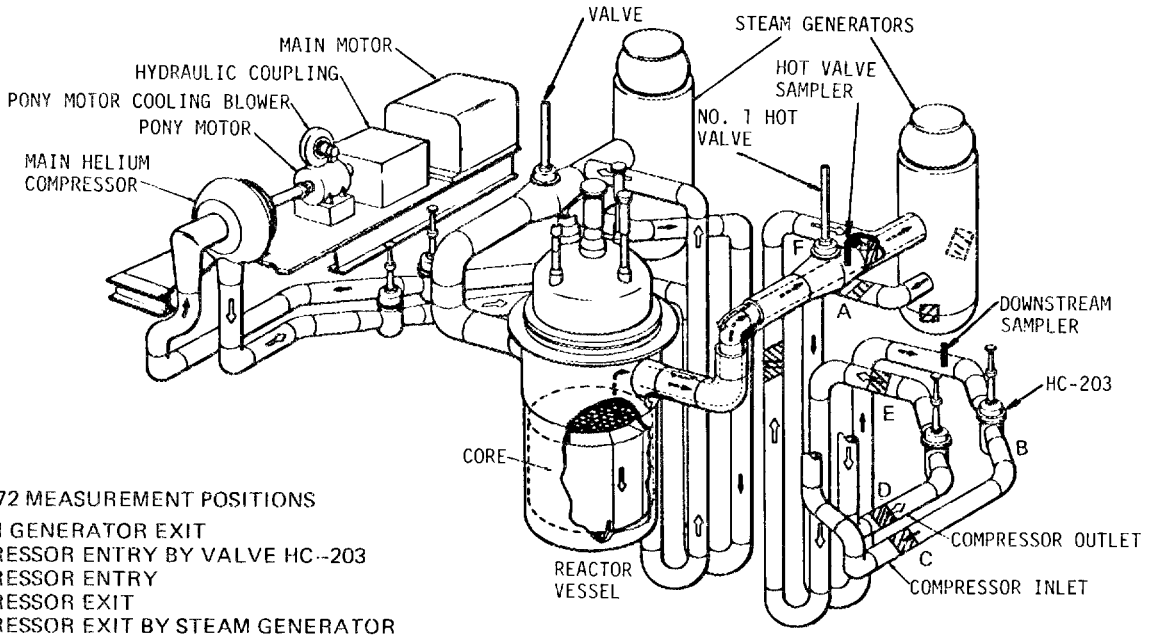

1972 MEASUREMENT POSITIONS

A STEAM GENERATOR EXIT
B COMPRESSOR ENTRY BY VALVE HC–203
C COMPRESSOR ENTRY
D COMPRESSOR EXIT
E COMPRESSOR EXIT BY STEAM GENERATOR
F COMPRESSOR RETURN BEFORE JOINING CONCENTRIC DUCT

Fig. 10.9. Positions of gamma-activity determinations in Peach Bottom HTGR No. 1 loop in May 1972.

Table 10.1. Summary of activities[a] (microcuries/cm^2) found on the Peach Bottom primary-circuit large ducts, 1971

Position	^{131}I	^{134}Cs	^{137}Cs	^{144}Ce	^{140}Ba	^{110m}Ag	^{95}Zr	^{59}Fe	^{60}Co	^{54}Mn	^{65}Zn	^{103}Ru	^{106}Ru	^{124}Sb	^{154}Eu	Ratio ^{137}Cs/^{134}Cs
Steam generator exit	8.5N3[b]	0.20	0.65	0.21	3.2N3	9.4N3	1.3N3[b]	6.6N3	6.2N3	3.1N3	1.1N2	2.0N3[b]	9.0N3[b]	6.0N4	4.6N4[b]	2.96
Compressor entry	1.9N2[b]	0.22	0.74	0.03	2.9N3	9.0N3	2.2N3[b]	1.9N3	8.2N4	2.6N3	1.0N2	4.6N3[b]	1.8N2[b]	3.0N4	7.1N4[b]	3.07
Compressor exit	1.3N2[b]	0.21	0.68	0.01	3.0N3	7.6N3	1.6N3[b]	9.5N4	3.9N4	2.1N3	1.0N2	3.0N3[b]	1.5N2[b]	3.4N4	4.6N4[b]	3.01
Compressor exit line near steam generator	8.5N3[b]	5.2N2	0.17	0.03	1.2N3	1.9N3	1.0N3[b]	4.5N3	3.0N3	1.2N3	2.2N3	2.0N3[b]	1.5N2[b]	3.3N4	4.2N4[b]	3.00
Compressor exit vertical duct	1.5N3[b]	4.6N2	0.14	0.04	1.9N3	2.5N2	2.3N3	7.8N3	9.6N3	1.4N3	1.8N3	3.9N4	4.9N3	3.5N4	4.6N4	2.81
															Mean	2.97

[a]N2, N3, etc., indicate value given × 10^{-2}, × 10^{-3}, etc.

[b]Represents upper limit; no peak found for this isotope.

Table 10.2. Summary of activities[a] (microcuries/cm^2) found on the Peach Bottom primary-circuit large ducts, 1972

Decay time for ^{131}I and ^{140}Ba too long to permit detection or warrant upper limit calculations

Position	^{134}Cs	^{137}Cs	^{144}Ce	^{110m}Ag	^{95}Zr	^{59}Fe	^{60}Co	^{54}Mn	^{65}Zn	^{103}Ru	^{106}Ru	^{124}Sb	^{154}Eu	Ratio ^{137}Cs/^{134}Cs
Steam generator exit	0.12	0.42	4.2N2	4.5N3		4.5N3	4.1N3	2.1N3	6.7N3					3.41
Compressor entry downstream of HC-203 valve	6.3N2	0.23	8.7N3	1.8N3	1.1N3[b]	1.0N3	7.4N4	1.0N3	3.0N3	4.9N3[b]	6.4N3[b]	1.5N4	1.1N4[b]	3.54
Compressor entry by cavity entry	6.6N2	0.24	6.0N3	2.5N3	6.4N4[b]	1.0N3	5.3N4	1.1N3	3.7N3	2.8N3[b]	3.6N3[b]	1.6N4	7.9N5[b]	3.43
Compressor exit by cavity entry	5.2N2	0.19	5.4N3	1.7N3	2.2N3[b]	1.0N3	3.3N4	5.8N3	1.8N3	8.5N3[b]	1.0N2[b]	1.7N4[b]	2.5N4[b]	3.44
Compressor exit line near steam generator	6.6N2	0.24	3.0N2	3.3N3	3.8N3[b]	1.0N2	1.1N2	2.3N3	3.9N3	1.2N2	1.2N2	7.6N4	7.1N4	3.52
Compressor return before joining concentric duct	3.7N2	0.14	1.7N2	1.1N3	1.9N3[b]	3.9N3	2.4N3	1.1N3	2.4N3	6.4N3[b]	4.6N3[b]	3.4N4[b]	3.3N4[b]	3.61
													Mean	3.49

[a]N2, N3, etc., indicate value given × 10^{-2}, × 10^{-3}, etc.

[b]Represents upper limit; no peak found for this isotope.

the activity present at the end of the prior reactor operating period, January 6, 1972, for the 1972 results and April 26, 1971, for the 1971 results.

Gamma spectra were also obtained on the concentric duct between the core and the steam generator. Since there is no a priori reason to expect the inner duct walls to have a surface deposit the same as that on the outer duct walls, the gamma spectrum cannot be unambiguously interpreted. However, on the basis of assumed ratios of surface concentrations on the hot inner duct and the cold outer duct, one may deduce that the concentric duct is not grossly more radioactive than the other ducts.

The internal surfaces of the steam generator are not amenable to analysis by this technique because of its thick steel walls, low surface activity, and geometrical complexity (along with the requirement that surfaces be uniformly radioactive).

The surface concentration results in Tables 10.1 and 10.2 show that most of the radionuclides appear to decrease along the sampled part of the coolant flow path, but only ^{137}Cs and ^{134}Cs drop appreciably (by a factor of about 4). Although concentrations of most of the radionuclides did not change significantly over the period between the two measurements, the surface concentrations of several radionuclides, notably ^{134}Cs, ^{137}Cs, and ^{144}Ce, dropped much more than can be accounted for by radioactive decay.

A second interesting feature is the ratio of ^{137}Cs to ^{134}Cs surface concentration. This ratio is nearly constant for all measured positions within each set of measurements, having a mean value of 3.49 in 1972 and 2.97 in 1971. When the 1972 ratio is corrected for radioactive decay to the 1971 reporting date, the corrected ratio is 2.81, a value close to the 1971 ratio. (The variation in these ratios was $<\pm 0.2$.) Although this ratio would not be a very sensitive indicator of changes that occur in addition to decay, it indicates that there are no gross replenishments of the cesium isotopes on the large ducts unless the newly deposited isotopes had a $^{137}Cs/^{134}Cs$ ratio close to 3.5, the value for "old" cesium.

This behavior can be explained by the relatively high level of fission product release and deposition from failed fuel during core I operation and subsequent net reentrainment of radionuclides into the coolant, which are in turn removed by the cleanup plant. All other radionuclides, except possibly ^{134}Cs and ^{137}Cs, have now reached steady state as determined by renewal from core II fuel release and removal by reentrainment and radioactive decay.

10.2.2 Sampling of the Coolant for Aerosols and Condensable Species

The No. 1 loop coolant is sampled at two locations; these are identified in Fig. 10.8. The hot valve, or upstream, sampler is located between the core and the steam generator in a thermowell adapted to sample the hot coolant from the core. The downstream sampler samples the coolant between the steam generator and the compressor. At both locations, a constant sample flow is drawn isokinetically through an inlet jet and then through diffusion tubes to identify condensable molecular species. The downstream sampler also contains silver membrane and fiber-glass absolute filters for dust collection. The hot-valve sampler flow passes through the sampler probe and then to a separate particle filter unit containing silver membrane and fiber-glass absolute filters. These sampler units are installed and removed during fuel-handling reactor shutdowns. During 1972, the first downstream sampler, unit 1, was removed and analyzed, and a hot-valve sampler particle filter, unit 1, was also analyzed.

Downstream sampler, unit 1. This sampler was operated for approximately 80 days at a 0.47-lb/hr flow rate between August 23 and December 14, 1971. The 894 lb of helium sampled passed through three 54-cm-long silver diffusion tubes, 0.156 in. in inside diameter, a 0.2-μ pore size silver membrane filter, and a fiber-glass backup filter.

The right side of Fig. 10.10 shows the silver membrane filter covered with black dust, and the left side shows the outlet ends of the silver diffusion tubes. A few specks of dust can be seen on the steel components.

Of the dust collected, 21 mg was on the silver membrane filter, 0.2 mg on the fiber-glass filter, and 2.6 mg was estimated to have been distributed between other components of the probe (tubes, inlet jet, etc.). Thus, a total of 23.8 mg of dust was collected in the 894 lb of helium, which corresponds to a dust concentration of 27 μg per pound of helium. The ^{235}U, ^{90}Sr, and gamma-emitting radionuclides on all the probe components have been measured, and the results, expressed as concentrations in the helium coolant corrected to January 6, 1972, are presented in Table 10.3.

The silver diffusion tubes were cut into 2-cm segments, and each segment was analyzed to obtain distribution profiles for the various long-lived fission products and neutron capture radionuclides. All radionuclides had essentially the same, nearly uniform, distribution along the diffusion tubes. This implies that they were either components of dust particles or, in the

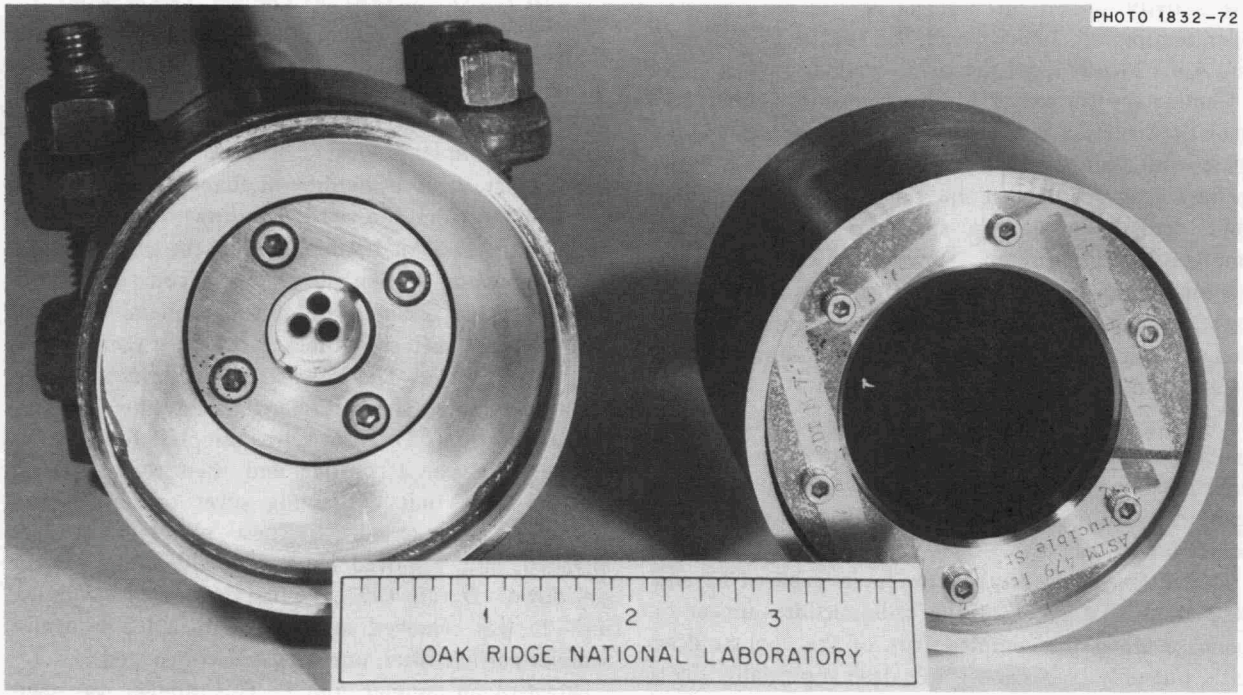

Fig. 10.10. Peach Bottom downstream coolant sampler (core II, period 2) after sawing open to expose filter element.

Table 10.3. Average concentrations of components collected in the Peach Bottom HTGR primary helium coolant sampler at downstream location[a]

Values in microcuries unless stated

Component	Concentration per pound of helium	Amount circulating in primary circuit[b]
Dust	26.6 μg	24,000 μg
^{235}U	7.9×10^{-11} μg	7.2×10^{-8} μg
^{54}Mn	2.7×10^{-4}	0.24
^{60}Co	3.8×10^{-4}	0.35
^{65}Zn	5.5×10^{-5}	0.05
^{110m}Ag	2.0×10^{-4}	0.18
^{134}Cs	7.0×10^{-4}	0.64
^{137}Cs	2.5×10^{-3}	2.27
^{90}Sr	1.4×10^{-4}	0.13

[a] Activities present on January 6, 1972.
[b] Assuming uniformity of concentration throughout circuit, which is suspect.

case of fission-gas daughters (e.g., ^{137}Cs), were deposited by parent decay in the tubes. Microscopic examination of the inside surfaces of the tube segments, using both optical and scanning electron microscopes, revealed a very large number of particles (many visible under a 20X lens). By directing a stream of air against these surfaces, it was possible to remove the particles that were visible under the 20X lens and thereby reduce the radionuclide levels by about 70%. Subsequent analysis of several tube segments thus treated indicated that the radionuclide distributions were still uniform. It was also observed that the ratios of the levels of such radionuclides as ^{137}Cs, ^{134}Cs, and ^{110m}Ag (radionuclides that may exist as molecular species in the HTGR) to radionuclides such as ^{54}Mn, ^{59}Fe, and ^{60}Co (radionuclides presumed to be dust components) were essentially unchanged after the larger particles were removed. Using a previously estimated value for the concentration of ^{137}Xe in the primary coolant,[6] it was estimated that perhaps one-half or more of the ^{137}Cs that remained on the tubes after the larger particles were blown off could be accounted for by ^{137}Xe decay. Thus no measure of the vapor pressure of ^{137}Cs, ^{134}Cs, or ^{110m}Ag could be obtained. However, upper limits for the vapor pressures of ^{137}Cs (based on ^{137}Cs levels after removal of large particles) and ^{90}Sr (based

6. *ORNL Nuclear Safety Research and Development Program Bimonthly Rep. January–February 1971,* ORNL-TM-3342, p. 55.

on total levels of ^{90}Sr on the tube segments) were calculated to be 5×10^{-16} and 4×10^{-21} atm respectively. Previous data from a Gulf General Atomic diffusion probe upstream of the steam generator indicated a ^{137}Cs vapor pressure of 6×10^{-15} atm.[7] Thus these results indicate that in passing through the steam generator the ^{137}Cs vapor pressure is reduced by at least a factor of 10.

Upstream particle filter, unit 1. This filter unit was operated between September 13 and November 24, 1972, and sampled 449 lb of helium at a flow rate of 0.26 lb/hr. The filter, a $1\frac{7}{8}$-in.-diam 0.2-μ pore size silver membrane filter, is shown in Fig. 10.11.

The amounts of gamma-emitting radionuclides and dust material on the filter have been determined as shown in Table 10.4. Values are given for ^{89}Sr and ^{90}Sr, but, since some of the particulate material was not dissolved in the radiochemical procedure, these results should be considered tentative. Since this filter is a few feet downstream from the hot-valve diffusion tube sampler, which could remove some dust from the sample flow, concentrations based on the weight of helium have not been presented. Based on the amount of dust on this filter, a dust concentration of 11 μg per pound of helium results, compared with 26.6 mg per

7. *ORNL Nuclear Safety Research and Development Program Bimonthly Rep. July–August 1971*, ORNL-TM-3554, p. 73.

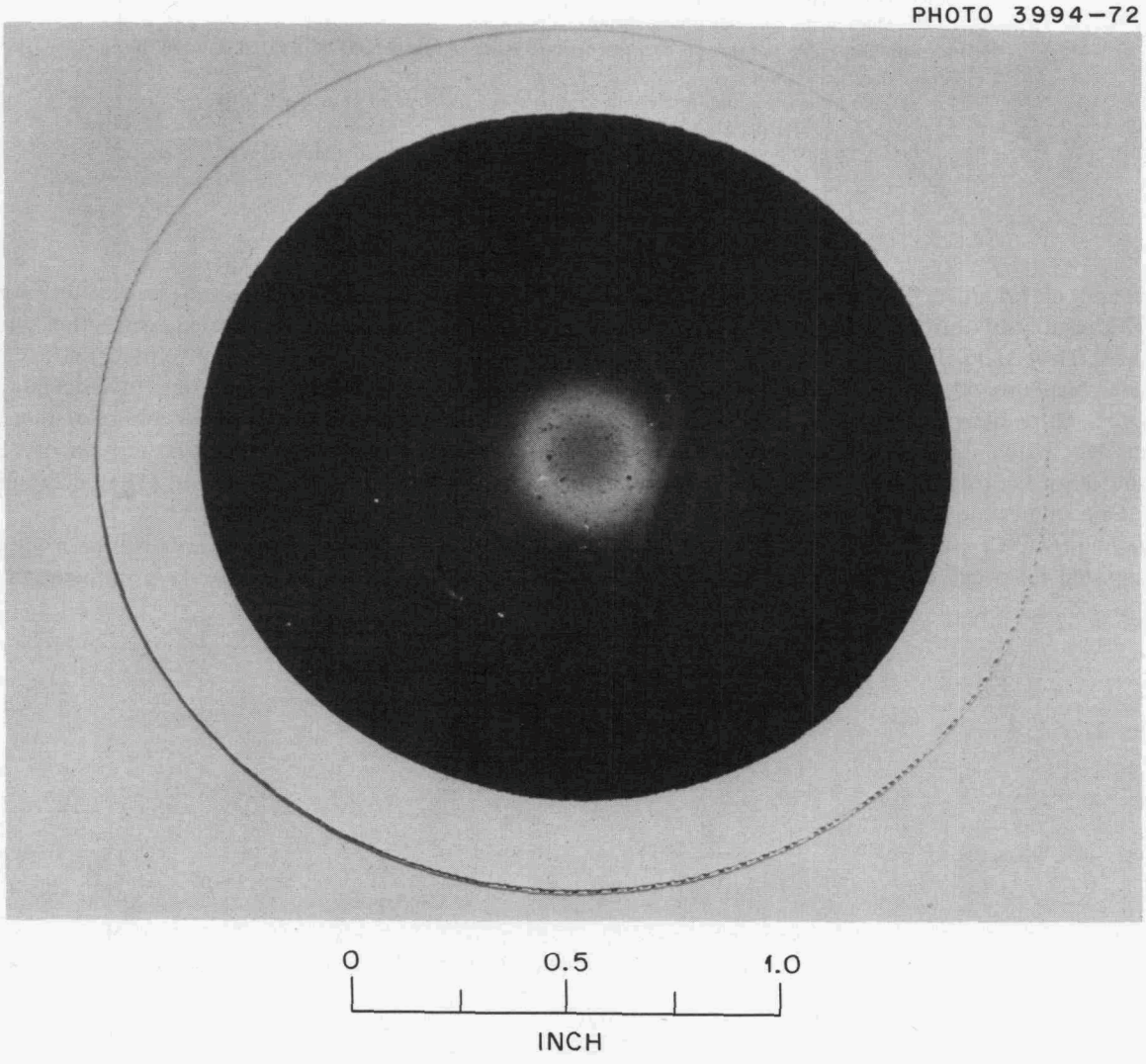

Fig. 10.11. Silver membrane filter covered with dust. Upstream sampler system, removed from reactor November 1972.

Table 10.4. Materials found on hot-valve sampling line filter[a] removed in November 1972

Species measured	Quantity found[b]	Species measured	Quantity found[b]
Dust	5 mg	^{106}Ru	1.1×10^{-2}[c]
^{235}U		^{110m}Ag	1.68×10^{-2}[c]
^{51}Cr	5.2×10^{-2}	^{131}I	1.8×10^{-3}[d]
^{54}Mn	2.91×10^{-2}	^{134}Cs	8.89×10^{-2}
^{59}Fe	0.125	^{137}Cs	0.359
^{60}Co	5.4×10^{-2}	^{140}Ba	7.5×10^{-3}
^{95}Zr	6.6×10^{-3}[e]	^{141}Ce	5.7×10^{-3}
^{89}Sr	7.3×10^{-3}	^{144}Ce	2.74×10^{-3}
^{90}Sr	6.0×10^{-3}	^{154}Eu	3.5×10^{-3}
^{103}Ru	3.5×10^{-3}	^{203}Hg	1.1×10^{-2}[f]

[a]Values given are for the total filter. Radionuclide results were corrected to reactor down date of Nov. 25, 1972.

[b]Values in microcuries unless stated.

[c]Radionuclide appears to be present, but values given should be treated as upper limits rather than firm results.

[d]Upper limit from high-resolution gamma spectroscopy; no photopeak found.

[e]Because of mutual photopeak interference this value is tentative.

[f]The 279-keV line in the gamma spectrum has been tentatively identified as ^{203}Hg.

pound of helium in the downstream sampler, unit 1. The results show that ^{140}Ba was also present on the dust. This is the first time that it has been detected unambiguously in the Peach Bottom surveillance program. More measurements and additional analysis are needed before unambiguous conclusions about the sources of the radionuclides found can be drawn.

One interesting feature of these results is that the ratio of ^{137}Cs to ^{134}Cs is 4.05. When this ratio is adjusted for decay of both radioisotopes to April 1971 (the time of the 1971 gamma scan of the large ducts), the value is 2.43. The adjusted ratio is thus significantly different from the ratio (2.97) found on the large ducts in April 1971. It is tempting to speculate that the current ratio partially reflects release of these nuclides from the core rather than the erosion of "old" dust from the primary circuit walls. (The uncertainty in the ^{137}Cs/^{134}Cs ratio is ±0.2.)

Further sets of measurements will be made after 600 and 900 effective full-power days of operation.

11. HTGR Safety Program Plan and Safety Analysis

H. J. de Nordwall

The HTGR Safety Program is in transition from demonstrating the feasibility of HTGR safety concepts to developing, validating, and documenting the technologies and analyses that will be used to assure safety for large HTGR plants. A significant expansion of program scope and effort is entailed. To ensure that this expansion takes place in an orderly manner, a plan for a National HTGR Safety Program is being prepared with the help of the Gulf General Atomic staff. In addition, improved means for representing the results of accident analyses are being sought, using a study of events that might follow an interruption of cooling as a trial case.

11.1 HTGR SAFETY PROGRAM PLAN

H. J. de Nordwall P. Rubel

A draft program plan is being prepared for submission to the AEC. The plan contains a brief description of the safety features of an HTGR and recommendations for additional work on tasks relating to accident analysis, fission product transport, safety instrumentation, materials, and containment technologies. Much of the emphasis in these areas is on improving descriptions of the long-term behavior of materials and systems that will actually be used in large HTGRs, though generic studies will not be abandoned.

Program guidance will be sought through parametric studies of various accident sequences, and the results of these analyses will be used to update the program plans.

11.2 SYSTEMS AND SAFETY ANALYSIS

P. Rubel

The immediate aim of systems and safety analyses is to describe potential HTGR accidents methodically, stage by stage, in order that the specific requirements for blocking accident progressions and/or mitigating their consequences may be deduced realistically. In the longer range, it is intended to establish a logical framework and an "importance perspective" in which to view all safety considerations objectively; this will aid in determining emphasis and priority of the Safety Program technical investigations.

The method of safety analyses proposed is as follows. Logical analyses will be performed and applied interactively. They will draw upon plant design data; systems response analyses; descriptions of fission product, component, and material behavior derived in other task areas; and other related experience. The analyses should cover all credible major accident-initiating conditions.

Three kinds of practical program guidance are expected to develop initially from these studies: (1) The events, conditions, and system responses critical to safety should come into clear relief via fault tree diagramming of potential accident sequences. (2) Significant value ranges for the parameters which determine component response prospects and fission product movement under contingency conditions will be defined by the plant transient analyses. (3) Component properties necessary to ensure the plant protective

functions will become apparent from the methodical reviews of plant contingency conditions. The probabilistic analyses address primarily the need for a broad safety perspective by examining the relative contributions of individual components or events to overall accident risk, that is, in terms associating probability with release or exposure magnitude.

11.2.1 Analysis of Core Auxiliary Cooling System for a Large Plant

Fault tree diagrams were executed to represent possible effects of component failures on core auxiliary cooling system functions in a large HTGR plant. The set includes "top" or main hierarchies of faults in major equipment and support subsystems and subsidiary trees for the subsystems.

While the present diagrams are generalized in content, they provide a logical reference for examining specific contingency effects on, first, the equipment and, ultimately, the system functions. A scheme for managing such detailed considerations was devised.

Preliminary work was done toward describing potential HTGR accidents by means of decision tree diagrams. In this format, initiating events are expanded through branching sequences of subsequent events toward alternative situation outcomes. The initial studies were concerned mainly with finding optimum starting points for the decision trees and focused on the coolant flow interruption problem to obtain practical guidance. It became apparent from the studies that the potential accidents could be described most effectively via two main sets of logic diagrams: (1) fault trees to develop the event sequences leading to a manageable number of "serious" plant contingencies and (2) decision trees that project each of these contingencies to their possible outcomes. Additional fault trees would be needed to summarize the prospects of certain individual events (decision modes) of the decision trees, mainly defined system failures.

11.2.2. Reliability Evaluation of the Fort St. Vrain Emergency Engine-Generator System

An analysis of the reliability of the Fort St. Vrain reactor plant emergency engine-generator system was conducted for the Safety Program by the UKAEA Systems Reliability Service (SRS). This work was intended to serve as a pilot study to cultivate the major data and experience resources represented by SRS, thus promoting the future analysis objectives of the program. Information describing the emergency power facility was furnished by Gulf General Atomic through ORNL.

Of immediate concern was the reliability of the unusual arrangement at Fort St. Vrain, whereby two full-capacity generators (1400 kW each) are driven by tandem half-capacity engines (900 hp). Since a failed engine is automatically disengaged by clutch actuation, the system can deliver adequate emergency power with any two engines out of service. However, the arrangement entails added complexity due to the controls which sense engine failure and initiate clutch operation, and the engine speed governors which also apportion load between engine pairs.

The analysis consisted mainly in execution and probabilistic evaluation of system fault trees. Detailed consideration was given by SRS to the more novel system feature, and engineering interpretations were derived from the system function logic. The study concluded that the Fort St. Vrain emergency power supply was equivalent in reliability to the more conventional arrangement of three independent single-engine single-generator units, each capable of supplying half of the total emergency load.

The SRS study is presented and reviewed in an ORNL report.[1] Included with the main analysis are comments by the SRS staff on UKAEA criteria for establishing reliability requirements and on a practical demonstration of system reliability.

---

1. P. Rubel, *Reliability Evaluation of the Fort St. Vrain Emergency Engine-Generator System,* ORNL-TM-3935 (December 1972).

12. Prestressed Concrete Pressure Vessel Development

G. D. Whitman

The program in support of the technology of prestressed concrete reactor pressure vessels (PCRVs) is now almost exclusively concerned with the thermal cylinder experiment. This project was conceived in the planning of the overall program with the goal of providing verification of analytical methods which can predict the time-dependent stress and strain behavior of a PCRV. In addition, data were to be obtained on the performance of the concept with special instrumentation under design and off-design thermal conditions.

The experimental phase of this project is essentially complete. The thermal cylinder was cast in February 1971, and since then it has been prestressed and subjected to a planned series of loadings without failure of the experiment or schedule slippage. Unfortunately, there has not been sufficient funding to maintain a satisfactory level of analytical methods development and study to parallel the experimental work. Preliminary results from computer analysis using materials properties from small specimens look very promising for a partial history of the experiment. More extensive analytical work is planned in the future to include the complete time history of the experiment.

One of the main features of the thermal cylinder model was a capability to overheat a region of the structure. This test was performed with no apparent distress to the system, since it continued to be leak tight, and no unusual behavior was observed. Plans are now being made to detention the model and examine the liner and portions of the concrete.

Two additional reports have been issued on the concrete creep investigations that were initiated at the beginning of the PCRV program. This work is concerned with creep recovery and the effects of curing history on creep behavior.

12.1 PCRV THERMAL CYLINDER TEST

J. P. Callahan R. S. Valachovic
G. C. Robinson

The thermal cylinder experiment was designed to provide test data for evaluating the capability of analytical methods to predict stress-strain behavior of relatively simple prestressed concrete structures subjected to well-defined loading and thermal histories. The thermal cylinder is approximately a one-sixth-scale model of the central barrel section of a cylindrical PCRV having a geometry similar to the Fort St. Vrain reactor. The model is 48 in. high, 18 in. thick, and 81 in. in outer diameter.

The test structure, shown schematically in Fig. 12.1, is described in detail in ref. 1, and the model assembly is described in ref. 2. Since the primary purpose of the thermal cylinder was to simulate the behavior of a

1. G. D. Whitman, J. P. Callahan, and J. M. Corum, *An Investigation of the Time-Dependent Behavior of Prestressed Concrete Pressure Vessels,* ORNL-TM-3246 (Dec. 10, 1970); also published in *Concrete for Nuclear Reactors,* vol. 3, Special Technical Publication SP-34, American Concrete Institute, pp. 823–46, 1972.

2. J. P. Callahan, J. M. Corum, and M. Richardson, "PCRV Thermal Cylinder Test," *GCR-TU Programs Annu. Progr. Rep. Sept. 30, 1971,* ORNL-4760, pp. 79–91.

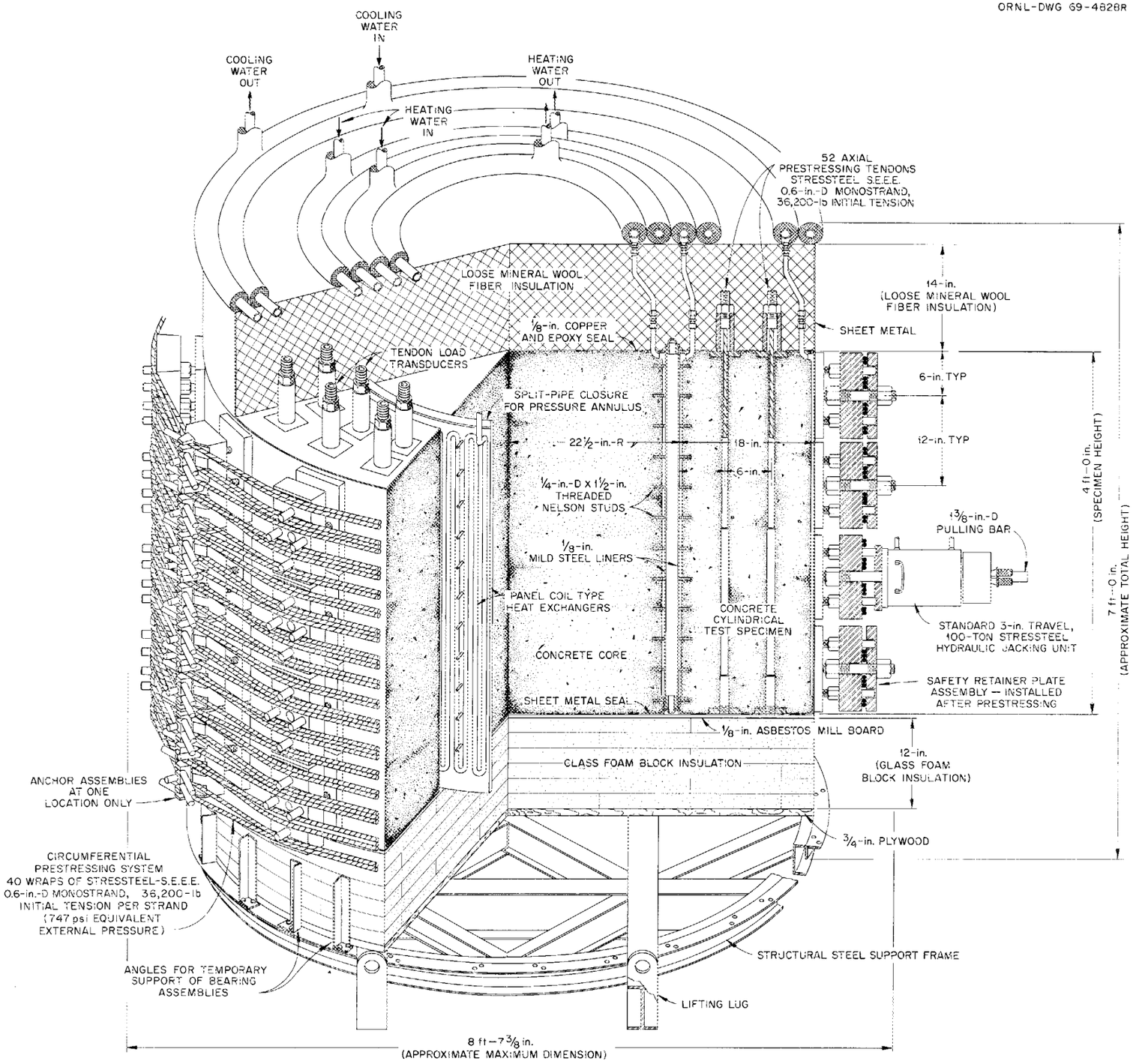

Fig. 12.1. Schematic representation of the thermal cylinder experiment.

massive prestressed concrete structure, all exposed surfaces were sealed to prevent moisture loss, and the ends of the model were insulated thermally to restrict heat flow to the radial direction.

The model is prestressed (in practice it was actually posttensioned) in both the axial and circumferential directions. The inner cavity of the cylinder contains a concrete core which provides the inner support for a relatively thin pressuring annulus as shown in Fig. 12.1. Since pressurization of the annulus induces a pure biaxial stress state in the core, the behavior of this region, as well as the outer test ring, provides basic information on the behavior of both the concrete and the instrumentation. The experiment was highly instrumented, and, in addition to providing experimental data on structural behavior, it also provided an opportunity to evaluate instrument performance under conditions simulating design and off-design conditions in a PCRV.

The temperature and loading history of the thermal cylinder is summarized in Fig. 12.2. In addition to prestressing, the testing conditions consisted of a 700-psi internal pressure loading and a thermal gradient imposed across the test section. During the initial testing period, which was intended to simulate normal PCRV operating conditions, temperatures of 150 and 75°F were maintained at inside and outside surfaces, respectively, of the test section. During a subsequent period, a narrow circumferential band on the inner surface of the test section was heated to 450°F for a period of 84 days. At the end of this period, the inside surface was cooled to 150°F and eventually cooled in a second step to 75°F. This second phase of the test simulates an off-design hot-spot condition in which the cooling and/or insulation is assumed to have failed in an operating nuclear reactor.

During the previous reporting period, the model and all ancillary systems were fabricated; the model was posttensioned, heated, and pressurized. Two separate events occurred during the present reporting period. Initially, the model remained prestressed, and the 700-psi pressure was maintained for a 194-day period simulating normal pressure vessel operation. The pressure was subsequently removed for 146 days, after which it was reapplied and maintained for the duration of the reporting period. The hot-spot test was conducted during this second pressurization period.

12.1.1 Instrumentation

Complete data sets were recorded during the course of each experimental event using the 155 gages listed in Table 12.1. The instrumentation consists of embedment gages cast directly in the concrete and more conventional types of resistance strain gages attached to the liner and prestressing tendons. Information is also provided in Table 12.1 on the operability of the gages before the hot-spot test and at the end of the experiment. No general statement can be made on overall gage performance, since there were 11 gage types or installations, each having a different level of development or calibration at the time of selection and each having been installed and checked under widely varying construction conditions. By and large the single-filament resistance gages performed well, and a major segment of data was obtained from these units. The performance of the vibrating-wire gages varied markedly by type, and this variation was due in part to mismatch in readout equipment. The evaluation of gage performance is continuing; the evaluations made to date are discussed below.

The embedment gages used in this experiment are described in ref. 2. The gages are positioned in quadrants designated *A, B, C,* and *D,* as shown in Fig. 12.3. The designation, location, and orientation of each gage are listed in Table 12.1. The first integer of the gage designation number indicates the radial location of the gage in the quadrant; the gages are numbered consecutively outward starting with the position nearest the pressuring annulus as shown in Fig. 12.3.

The vibrating-wire gages and wire-wound resistance gages were monitored using separate readout equipment. The remainder of the instrumentation, which also included 25 related thermocouples, was monitored with a computer-controlled data acquisition system.

The strain readings for the single-filament resistance gages and two types (A and B) of vibrating-wire gages are shown in Figs. 12.4, 12.5, and 12.6 respectively. Each figure contains strain-vs-time plots for axially, radially, and circumferentially oriented gages at position 1. The events represented include those occurring after prestressing through the period simulating normal pressure vessel operation. Each event is indicated at the top of the figures.

The results shown in Figs. 12.4 and 12.5 compare favorably with each other and with the analytical predictions for the various gage orientations and locations represented. Two of the gages, DEB-153 and CD9-101, ceased functioning at 240 days. Gage CD9-102 ceased functioning at 80 days but began working again at 210 days. The curve between these points was constructed on the basis of the behavior of the other two type A gages during the intervening period.

Table 12.1. Thermal cylinder instrumentation

Type of gage	Cylinder quadrant	Gage No.	Orientation	Status before hot-spot test	Final status
		Embedment strain gages			
Single-filament resistance	A	EB-131	Axial	Operative	Operative
	A	EB-231	Axial	Operative	Operative
	A	EB-351	Axial	Operative	Operative
	A	EB-132	Radial	Inoperative	Inoperative
	A	EB-232	Radial	Operative	Operative
	A	EB-352	Radial	Operative	Operative
	A	EB-133	Circumferential	Inoperative	Inoperative
	A	EB-233	Circumferential	Operative	Operative
	A	EB-353	Circumferential	Operative	Inoperative
	B	EB-151	Axial	Operative	Operative
	B	EB-251	Axial	Operative	Operative
	B	EB-351	Axial	Operative	Operative
	B	EB-152	Radial	Operative	Operative
	B	EB-252	Radial	Operative	Operative
	B	EB-153	Circumferential	Operative	Inoperative
	B	EB-253	Circumferential	Operative	Operative
	B	EB-353	Circumferential	Operative	Operative
	C	EB-151	Axial	Operative	Operative
	C	EB-241	Axial	Operative	Operative
	C	EB-341	Axial	Operative	Operative
	C	EB-152	Radial	Operative	Inoperative
	C	EB-242	Radial	Inoperative	Inoperative
	C	EB-342	Radial	Operative	Operative
	C	EB-153	Circumferential	Operative	Inoperative
	C	EB-243	Circumferential	Operative	Operative
	C	EB-343	Circumferential	Operative	Operative
	C-core	EB-141	Axial	Operative	Inoperative
	C-core	EB-251	Axial	Operative	Inoperative
	C-core	EB-341	Axial	Operative	Inoperative
	C-core	EB-342	Radial	Operative	Inoperative
	C-core	EB-143	Circumferential	Operative	Inoperative
	C-core	EB-253	Circumferential	Operative	Inoperative
	D	EB-151	Axial	Operative	Operative
	D	EB-251	Axial	Operative	Operative
	D	EB-341	Axial	Operative	Operative
	D	EB-152	Radial	Operative	Operative
	D	EB-252	Radial	Inoperative	Inoperative
	D	EB-342	Radial	Operative	Operative
	D	EB-153	Circumferential	Operative	Inoperative
	D	EB-253	Circumferential	Operative	Operative
	D	EB-343	Circumferential	Operative	Operative
	D-hot spot	HS-1-13-1	Axial	Inoperative	Inoperative
	D-hot spot	HS-2-10-1	Axial	Inoperative	Inoperative
	D-hot spot	HS-1-12-2	Radial	Operative	Operative
	D-hot spot	HS-2-11-2	Radial	Inoperative	Inoperative
	D-hot spot	HS-1-15-3	Circumferential	Operative	Operative
	D-hot spot	HS-2-11-3	Circumferential	Inoperative	Inoperative
Vibrating wire (type A)	B	D6-101	Axial	Inoperative	Inoperative
	B	D6-102	Radial	Inoperative	Inoperative
	B	D9-103	Circumferential	Inoperative	Inoperative
	C	D9-101	Axial	Inoperative	Inoperative
	C	D9-201	Axial	Operative	Operative
	C	D9-301	Axial	Inoperative[a]	Inoperative
	C	D9-401	Axial	Inoperative[a]	Inoperative
	C	D9-102	Radial	Inoperative	Inoperative

Table 12.1 (continued)

Type of gage	Cylinder quadrant	Gage No.	Orientation	Status before hot-spot test	Final status
	C	D6-202	Radial	Operative	Inoperative
	C	D6-302	Radial	Operative	Operative
	C	D6-402	Radial	Operative	Operative
	C	D9-103	Circumferential	Inoperative	Inoperative
	C	D9-203	Circumferential	Inoperative	Inoperative
	C	D9-303	Circumferential	Operative	Operative
	C	D9-403	Circumferential	Inoperative[a]	Inoperative
	D	D9-101	Axial	Inoperative	Inoperative
	D	D9-201	Axial	Inoperative	Inoperative
	D	D9-301	Axial	Operative	Operative
	D	D9-401	Axial	Inoperative[a]	Inoperative
	D	D6-102	Radial	Inoperative	Inoperative
	D	D6-202	Radial	Inoperative[a]	Inoperative
	D	D6-302	Radial	Inoperative	Inoperative
	D	D6-402	Radial	Inoperative[a]	Inoperative
	D	D9-103	Circumferential	Inoperative	Inoperative
	D	D9-203	Circumferential	Inoperative	Inoperative
	D	D9-303	Circumferential	Inoperative[a]	Inoperative
	D	D9-403	Circumferential	Operative	Operative
Vibrating wire (type B)	A	P-101	Axial	Operative	Inoperative
	A	P-201	Axial	Operative	Operative
	A	P-301	Axial	Operative	Operative
	A	P-102	Radial	Operative	Inoperative
	A	P-202	Radial	Operative	Operative
	A	P-302	Radial	Operative	Operative
	A	P-103	Circumferential	Inoperative	Inoperative
	A	P-203	Circumferential	Operative	Operative
	A	P-303	Circumferential	Operative	Operative
Vibrating wire (type C)	G	GGA-202	Radial	Inoperative	Inoperative
Wound-wire resistance	C	K-301	Axial	Operative	Operative
	C	K-302	Radial	Operative	Operative
	C	K-303	Circumferential	Inoperative[a]	Inoperative
	C-core	K-101	Axial	Operative	Operative
	C-core	K-102	Radial	Operative	Operative
	C-core	K-103	Circumferential	Operative	Operative
		Embedment stress cells			
Titanium resistance	C	T-141	Axial	Inoperative	Inoperative
	C	T-271	Axial	Operative	Operative
	C	T-3-15-1	Axial	Inoperative	Inoperative
	C	T-4-13-1	Axial	Inoperative[a]	Inoperative
	C	T-163	Circumferential	Operative	Operative
	C	T-253	Circumferential	Operative	Operative
	C	T-3-12-3	Circumferential	Operative	Operative
	C	T-4-11-3	Circumferential	Operative	Operative
Pressure diaphragm	A	PSC-111	Axial	Inoperative	Inoperative
	A	PSC-241	Axial	Inoperative	Inoperative
	A	PSC-341	Axial	Inoperative	Inoperative
	A	PSC-143	Circumferential	Inoperative	Inoperative
	A	PSC-253	Circumferential	Inoperative	Inoperative
	A	PSC-353	Circumferential	Inoperative	Inoperative
		Strain gages welded to B heat exchanger			
Weldable resistance	A	1	Axial	Operative	Operative
	A	2	Circumferential	Operative	Operative
	A	5	Axial	Operative	Operative

Table 12.1 (continued)

Type of gage	Cylinder quadrant	Gage No.	Orientation	Status before hot-spot test	Final status
	A	6	Circumferential	Inoperative	Inoperative
	B	1	Axial	Inoperative	Inoperative
	B	2	Circumferential	Inoperative	Operative
	B	5	Axial	Operative	Operative
	B	6	Circumferential	Inoperative	Inoperative
	C	1	Axial	Inoperative	Inoperative
	C	2	Circumferential	Inoperative	Operative
	C	5	Axial	Operative	Operative
	C	6	Circumferential	Operative	Operative
	D	1	Axial	Operative	Operative
	D	2	Circumferential	Operative	Operative
	D	5	Axial	Operative	Operative
	D	6	Circumferential	Operative	Operative
	D-hot spot	HS-1	Axial	Inoperative	Inoperative
	D-hot spot	HS-2	Circumferential	Inoperative	Inoperative
	D-hot spot	HS-5	Axial	Operative	Operative
	Strain gages bonded to axial prestressing tendons				
Bonded foil	A	CB-11A	Axial	Inoperative	Operative
	A	CB-12A	Axial	Inoperative	Operative
	B	CB-5A	Axial	Inoperative	Inoperative
	B	CB-6A	Axial	Inoperative	Operative
	C	CB-1A	Axial	Inoperative	Operative
	C	CB-2A	Axial	Operative	Operative
	C	CB-3A	Axial	Inoperative	Inoperative
	C	CB-4A	Axial	Operative	Operative
	D	CB-7A	Axial	Inoperative	Inoperative
	D	CB-8A	Axial	Operative	Operative
	D	CB-9A	Axial	Inoperative	Operative
	D	CB-10A	Axial	Operative	Operative
	Load cells on axial prestressing tendons				
Stress transducer	A	TR-11	Axial	Inoperative	Operative
	A	TR-12	Axial	Operative	Operative
	B	TR-5	Axial	Inoperative	Operative
	B	TR-6	Axial	Operative	Operative
	C	TR-1	Axial	Inoperative	Inoperative
	C	TR-2	Axial	Operative	Operative
	C	TR-3	Axial	Inoperative	Operative
	C	TR-4	Axial	Operative	Operative
	D	TR-7	Axial	Operative	Operative
	D	TR-8	Axial	Operative	Operative
	D	TR-9	Axial	Operative	Operative
	D	TR-10	Axial	Operative	Operative
	Strain gages bonded to circumferential prestressing tendons				
Bonded foil	B	CGA-1	Circumferential	Operative	Operative
	B	CGA-2	Circumferential	Operative	Operative
	B	CGB-1	Circumferential	Operative	Operative
	B	CGB-2	Circumferential	Operative	Operative
	B	CGC-1	Circumferential	Operative	Operative
	B	CGC-2	Circumferential	Operative	Operative
	B	CGD-1	Circumferential	Operative	Operative
	B	CGD-2	Circumferential	Operative	Operative

[a]Gages were inoperative at time of casting of cylinder.

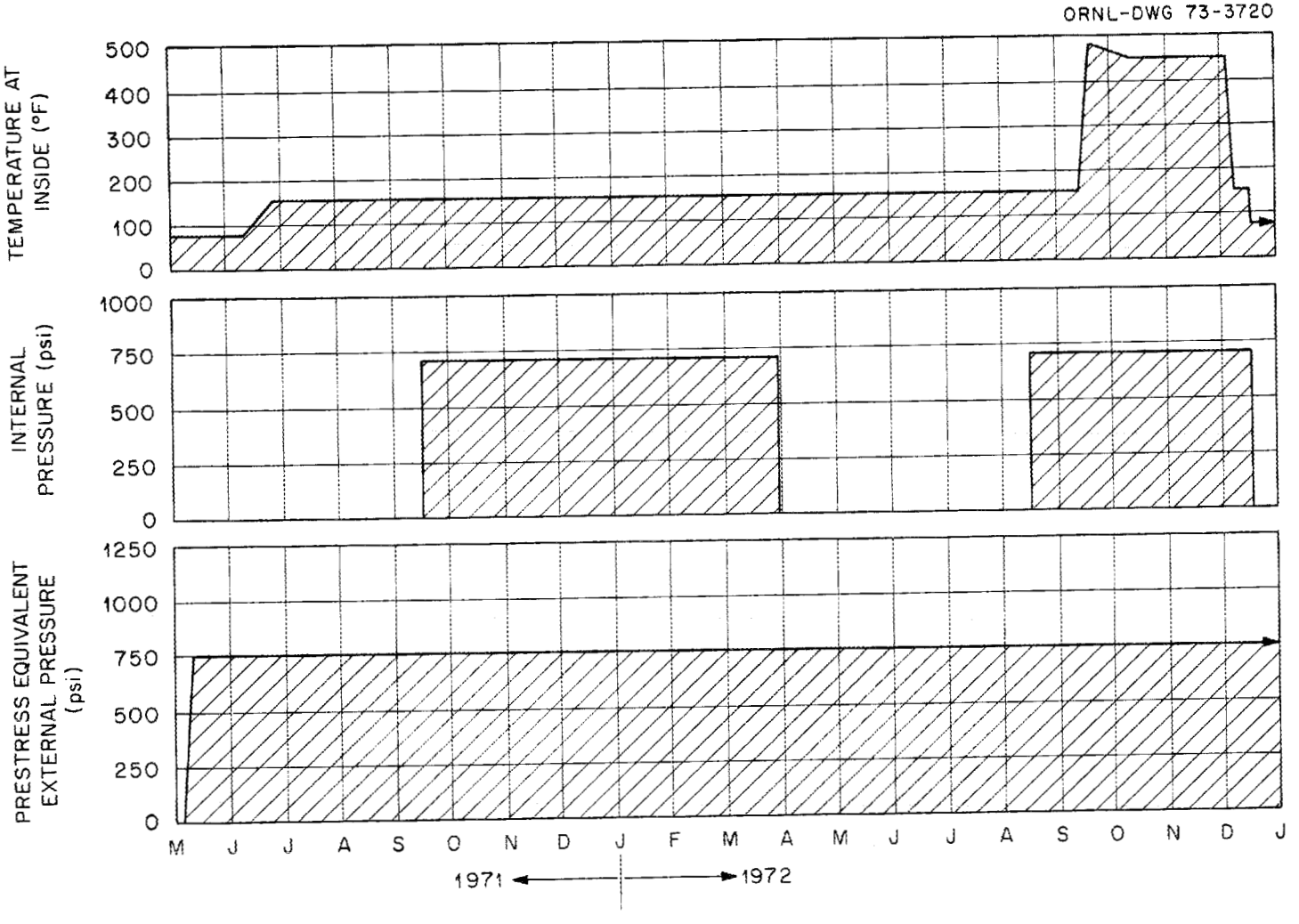

Fig. 12.2. Temperature and loading history of the thermal cylinder.

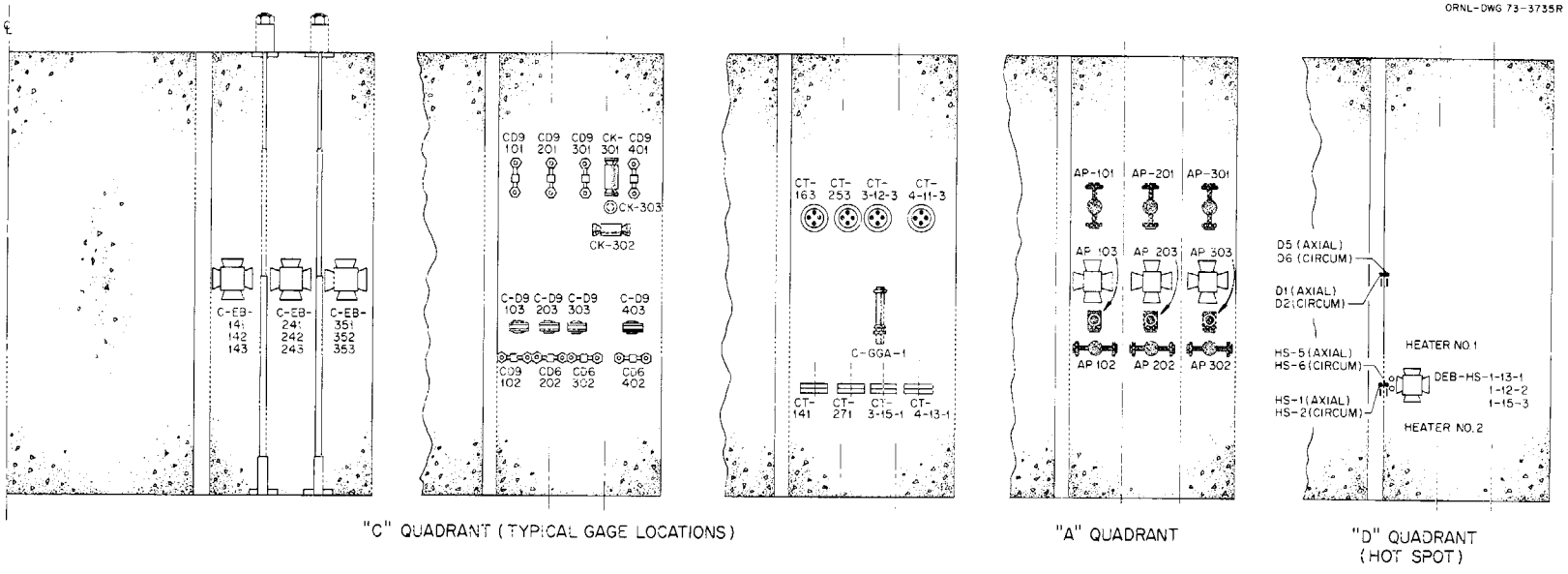

Fig. 12.3. Typical locations of each embedment gage type.

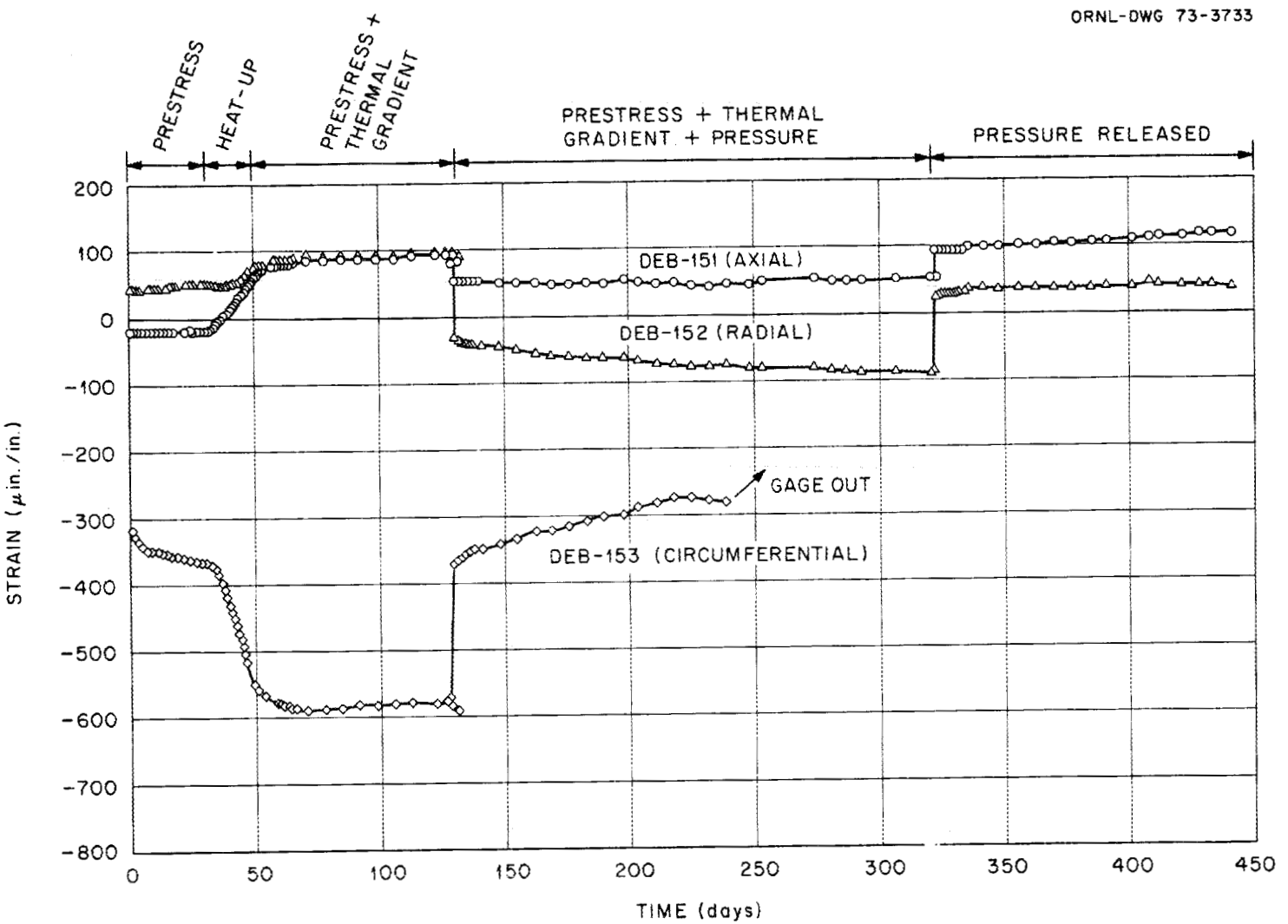

Fig. 12.4. Single-filament resistance gage strain data for DEB-151, 152, 153.

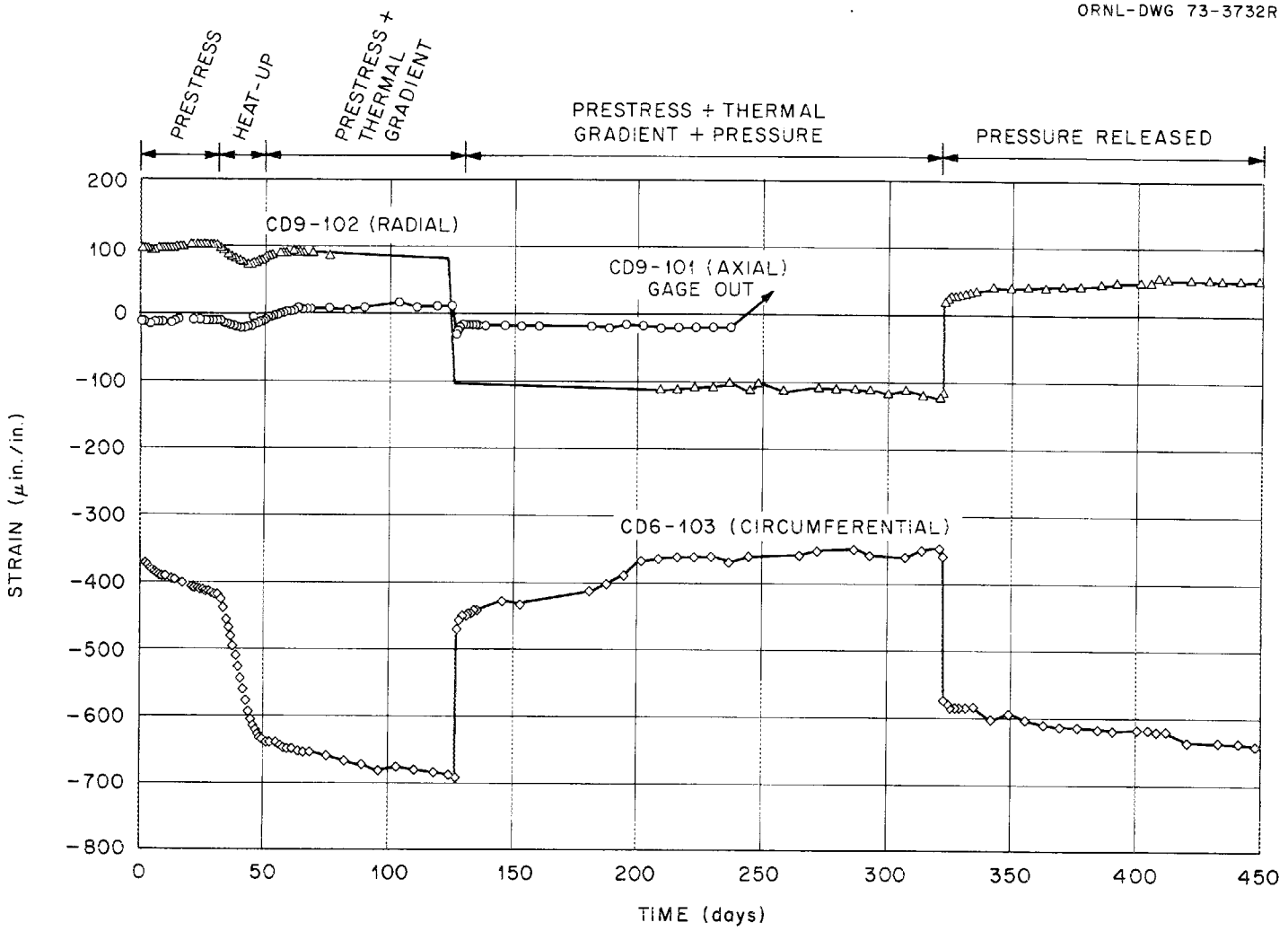

Fig. 12.5. Type A vibrating-wire gage strain data for CD9-101, CD9-102, and CD9-103.

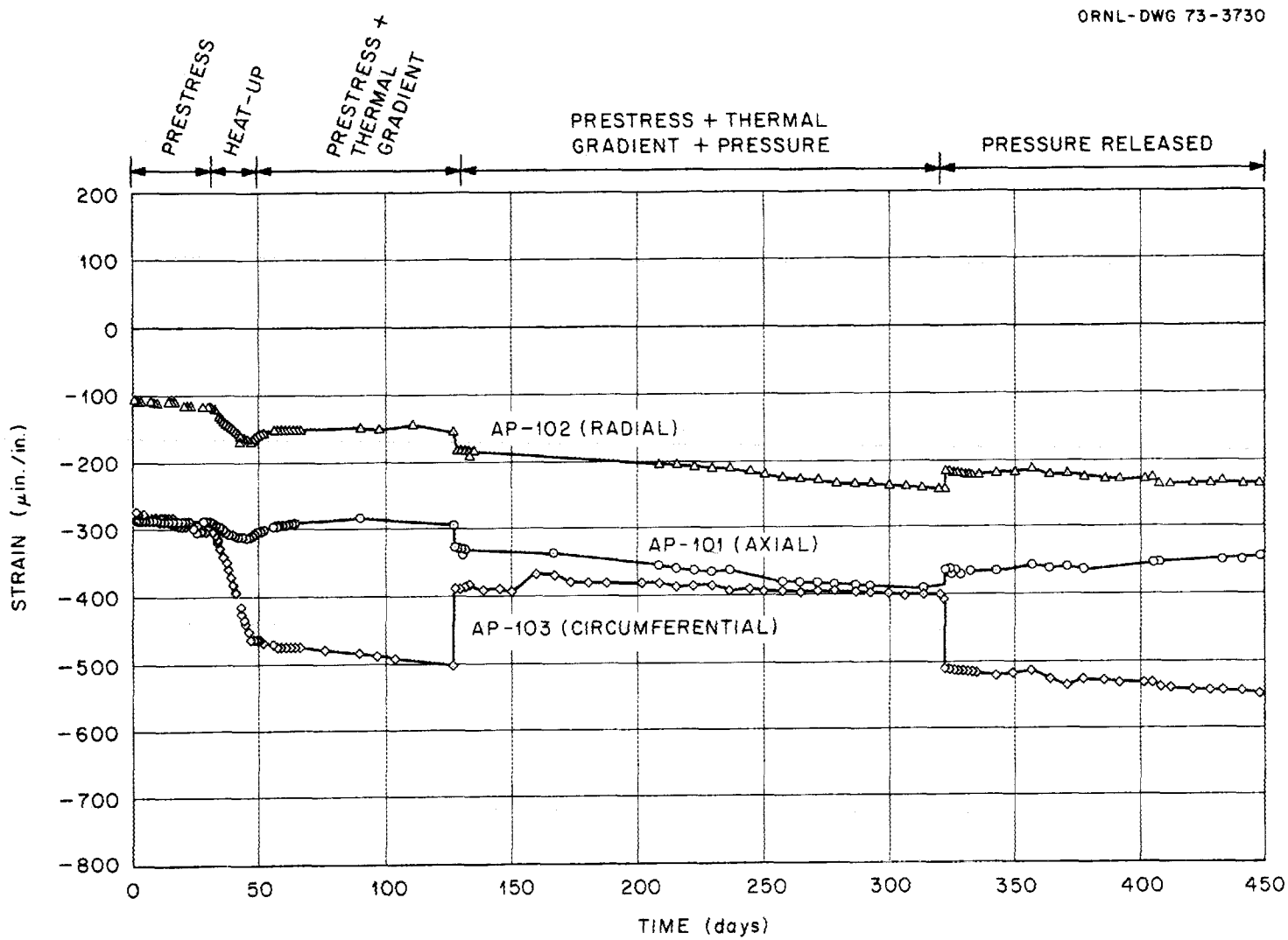

Fig. 12.6. Type B vibrating-wire gage strain data for AP-101, AP-102, and AP-103.

The results for axial and radial type B vibrating-wire gages (Fig. 12.6) do not agree with results of the two other gage types. On the other hand, the results for the circumferential gages generally agree for all three types.

The readout equipment used for all vibrating-wire gages was obtained from the type A gage manufacturer. The disagreement in readings seen for the type B gages was, in part, caused by problems encountered in monitoring other types of vibrating-wire gages with this equipment.

The remainder of the embedded instrumentation used in the model consisted of stress cells. The two basic types of cells employed (pressure diaphragm and titanium resistance) were described in the previous annual report.[2]

The first type consists of two parallel embedment strain gages, one of which has a thin pressuring diaphragm attached. The diaphragm pressure required to equalize the strains recorded by the attached gage and the separate parallel gage is assumed to be a direct measurement of the stress in the concrete. Six gages of this type were positioned in axial and circumferential pairs along the *A* quadrant of the model. The stresses produced by instantaneous loadings were measured with reasonable accuracy; however, a fairly sophisticated pressuring system was found to be required to measure relatively small time-dependent stress changes.

The second type of stress cell consists of a relatively thin partially hollow disk of titanium which encases an electrical resistance device for measuring deformation. Eight of these titanium-type cells were located along the *C* quadrant in four sets of axially and circumferentially oriented gages as shown in Fig. 12.3. The stresses recorded for the position 1 circumferential gage, for example, are shown in Fig. 12.7. As in the previous data curves, each experimental event is indicated at the top of the figure. As can be seen in the figure, the various applied loadings were sensed by this cell. The data appear reasonable up to 180 days, at which time there was a general relaxation of stress that is inconsistent with predicted behavior. A load change was properly sensed after this time, so that the cell was functioning. The data for the remainder of the cells did not show a consistent trend, and further study will be required before any conclusion can be reached.

Two companion specimens were cast using the same materials and procedures followed for the larger model. The 18- by 40-in. cylinders contained embedment gages of every type used in the thermal cylinder. These specimens were heated to 150°F coincident with thermal cylinder heatup and maintained at that temperature for the duration of the experiment.

Cylinder M-1 was subjected to a 3600-psi sustained uniaxial compression loading, and cylinder M-2 remained unstressed. The single-filament resistance gage readings for the two cylinders are shown in Fig. 12.8. The time scale is consistent with the three previous figures starting with thermal cylinder prestressing. Only one gage, the M-2 specimen axial gage, failed during the period of time shown in the figure. Based on the known properties of the concrete and the applied loading of the stressed cylinder, it can be concluded that these gages perform satisfactorily, and, based on the stable behavior of the gages in the unstressed specimen, little, if any, concrete shrinkage or swelling occurred, thus verifying the methods of sealing against moisture loss and the gage performance in simple states of stress.

The results for the wire-wound resistance-type strain gages are not included in the previous comparisons. Although these gages performed satisfactorily in the companion specimen tests, they failed to sense any strain changes resulting from pressurization of the thermal cylinder. The reasons for this anomalous behavior have not been determined.

In addition to concrete embedment instrumentation, the liner forming the inner surface of the test section (*B* heat exchanger) of the thermal cylinder was instrumented with the 16 weldable resistance strain gages listed in Table 12.1 and an equal number of companion compensating "dummy" gages. The gages were attached in axially and circumferentially oriented pairs to inner and outer surfaces of the liner at each of the four instrumented sections as shown in Fig. 12.3 and at the level of the Calrod hot-spot heaters. The strain readings for a representative set of these gages are shown in Figs. 12.9 and 12.10 for the annulus side and concrete side of the liner respectively. As in the previous strain vs time curves, the various events are indicated at the top of the figures. An inconsistent behavior is seen between the gages on opposite sides of the liner. This difference was consistent for the sets of gages attached at all four quadrants. The exceptionally large strains observed during heatup on the annulus side eventually diminish, and by 400 days the strains on opposite sides are essentially the same. Also, the strain changes produced by pressurization are consistent for gages on both sides of the liner.

Additional studies of the gages are being made to determine the cause of this behavior. The gages on the concrete side have integral leads in continuous stainless steel sheathing, while gages on the annulus side have soldered connections exposed in the annulus to the synthetic pressurization fluid. The change of the basic resistance of the gages on the annulus side that occurred

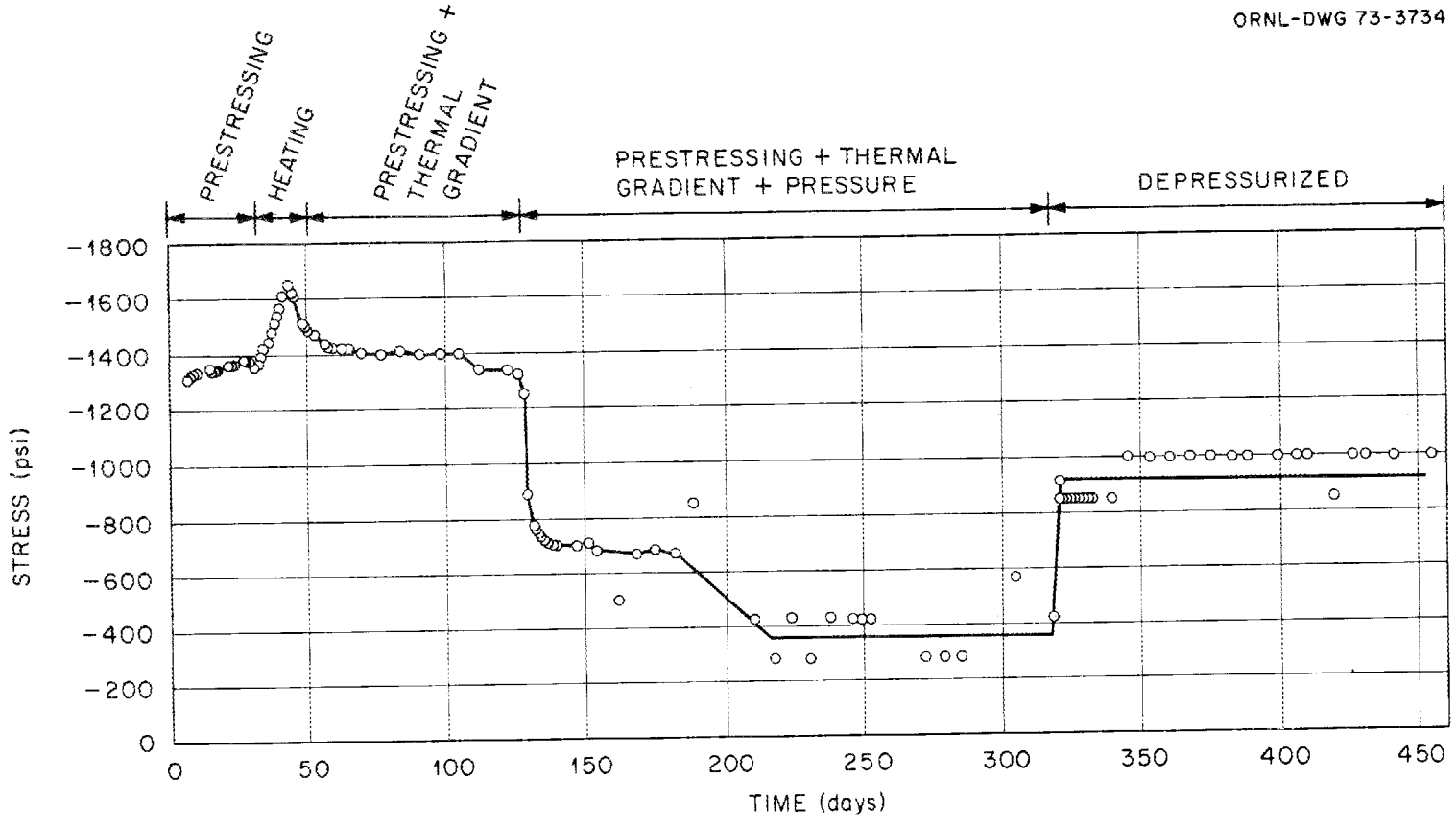

Fig. 12.7. Titanium gage stress data for CT-163.

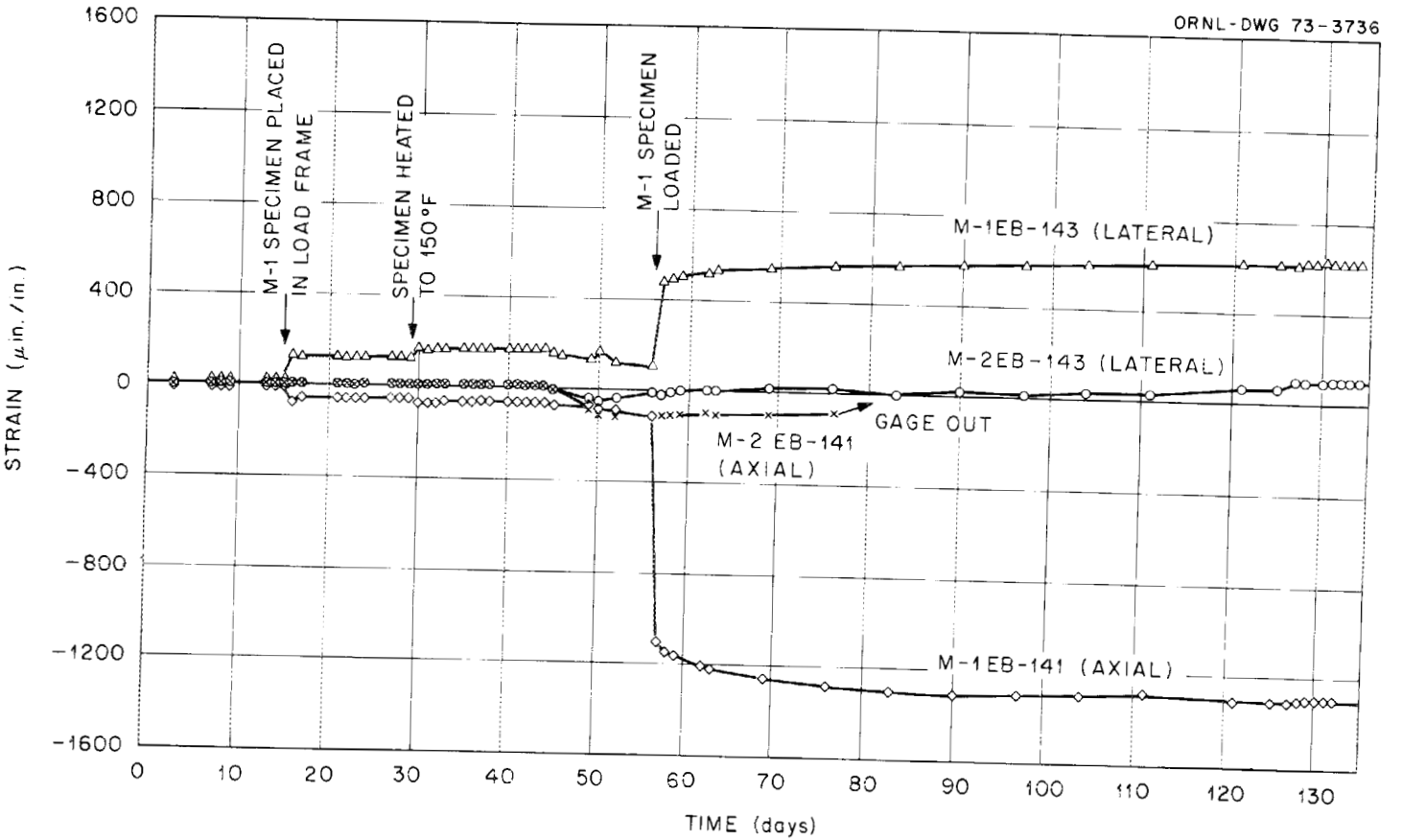

Fig. 12.8. Single-filament gage strain data for stressed M-1 and unstressed M-2, 18- by 40-in. concrete cylinders.

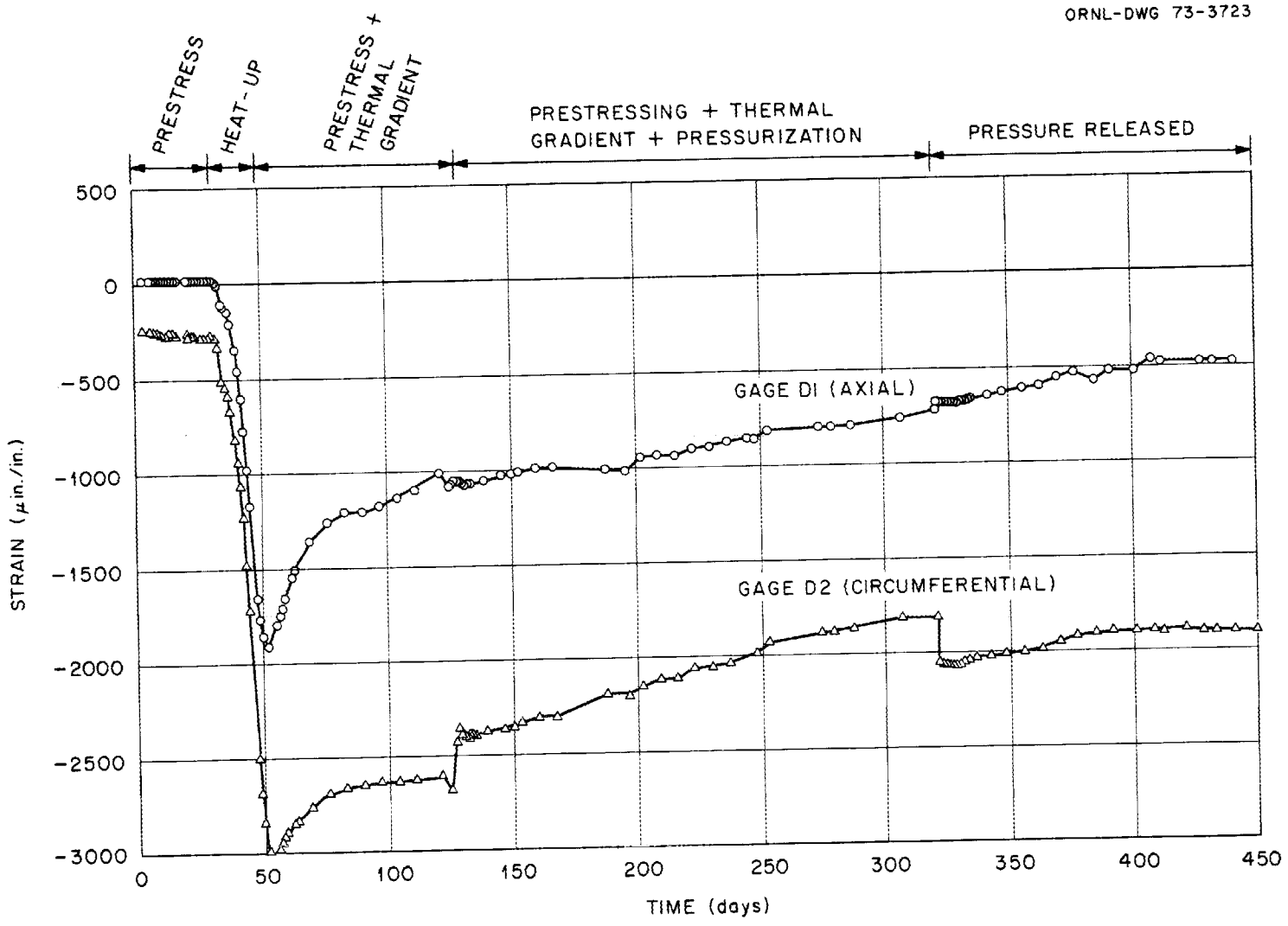

Fig. 12.9. Weldable gage strain data for annulus side of liner.

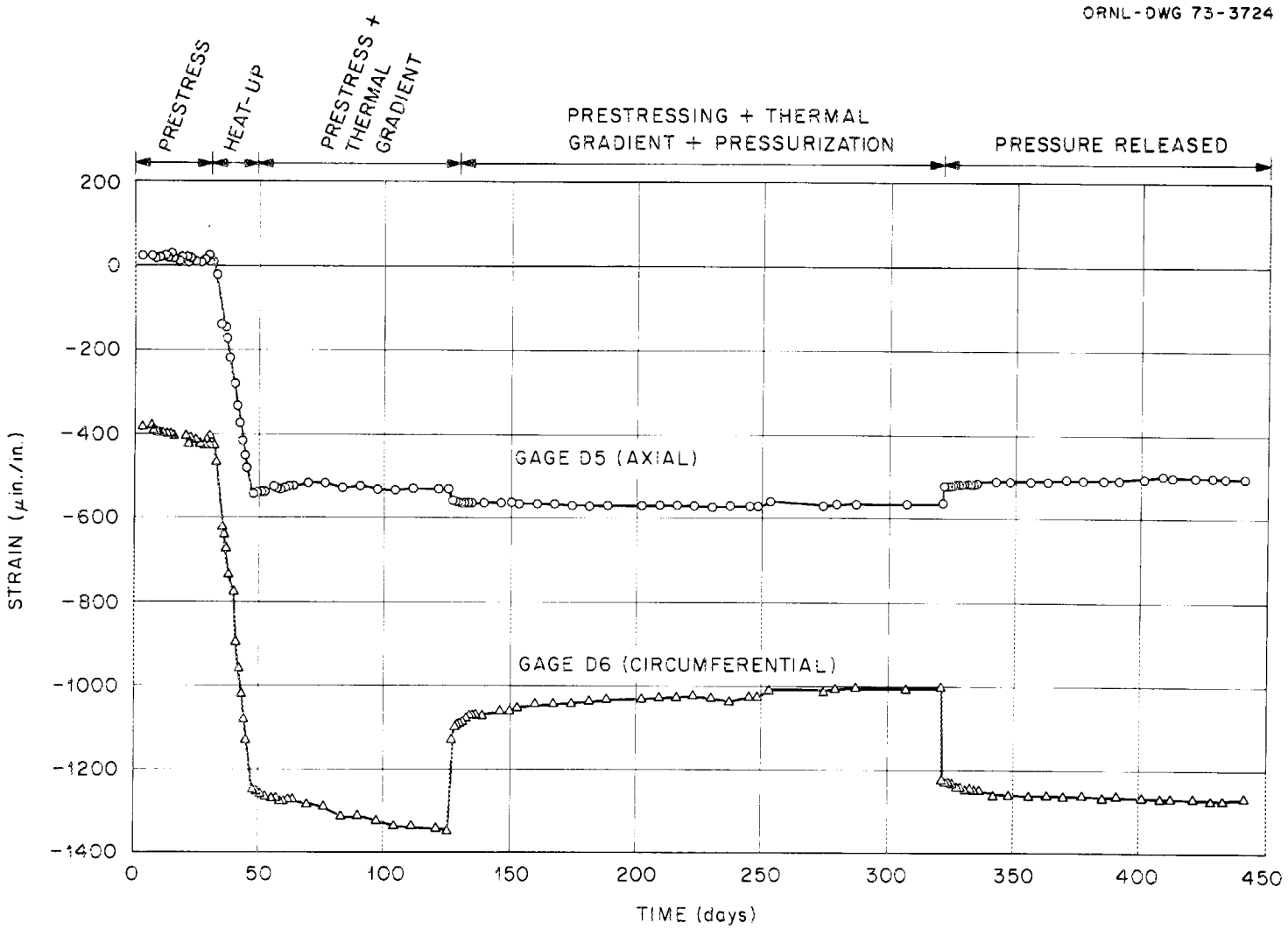

Fig. 12.16. Weldable gage strain data for concrete side of liner.

during the experiment may have been caused by exposure of the solder joints to the hydraulic fluid. Since the basic resistance of the gages on the concrete side remained constant, the strains recorded on this side are assumed to be correct.

Instrumentation used to monitor the prestressing consisted of 12 foil-type strain gages attached to individual strands of the axial tendons and 8 gages of the same type attached to the circumferential tendons in the positions shown in Fig. 12.11. In addition, load transducers of the type shown in Fig. 12.12 were attached to the ends of the 12 instrumented axial tendons shown in Fig. 12.11. The combination of strain gages and load transducers permits the detection of possible tendon relaxation. The strains recorded for circumferential and axial prestressing are shown in Figs. 12.13 and 12.14 respectively. Figure 12.15 is a plot of loads recorded on the transducers attached to the axial tendons. The initial prestressing load of −36,200 lb is indicated in the figure. The loadings are shown as negative, since the transducers are compressed by the tendons. Although considerable load relaxation was observed during heatup, the loads remained reasonably constant for the remainder of the design experiment.

12.1.2 Hot-Spot Test

Upon completing the study of PCRV stress-strain behavior under normal operating conditions, the 700-psi internal pressure was released, and the model remained unpressurized but with a 150 to 75°F temperature gradient across the test section for a period of 146 days. At the end of this period, the 700-psi pressure was reapplied and maintained for the duration of the hot-spot test. The inner water circulating system was shut down, and the two Calrod heaters located on the concrete side of the *B* heat exchanger were activated 21 days after repressurization. After an initial two-week adjustment period, the temperature stabilized at the specified value of 450°F on the heater sheath and was maintained near that level for the 84-day total duration of the test.

A heat transfer analysis of the experiment was performed for the hot-spot condition to evaluate the recorded temperatures obtained during this over-temperature condition. Internal and external boundary conditions and materials properties were varied to obtain the best fit of measured temperatures in the test specimen section. The material and heat transfer parameters which gave the best fit are listed in Table 12.2, and the recorded and predicted temperatures are shown in Fig. 12.16. The transport of heat by the synthetic fluid in the pressurizing annulus, refluxing of water-steam in the inactive circulating water heating coils, and the variation in properties of the concrete as a function of temperature made this analysis difficult. However, the agreement with experimental data is generally good.

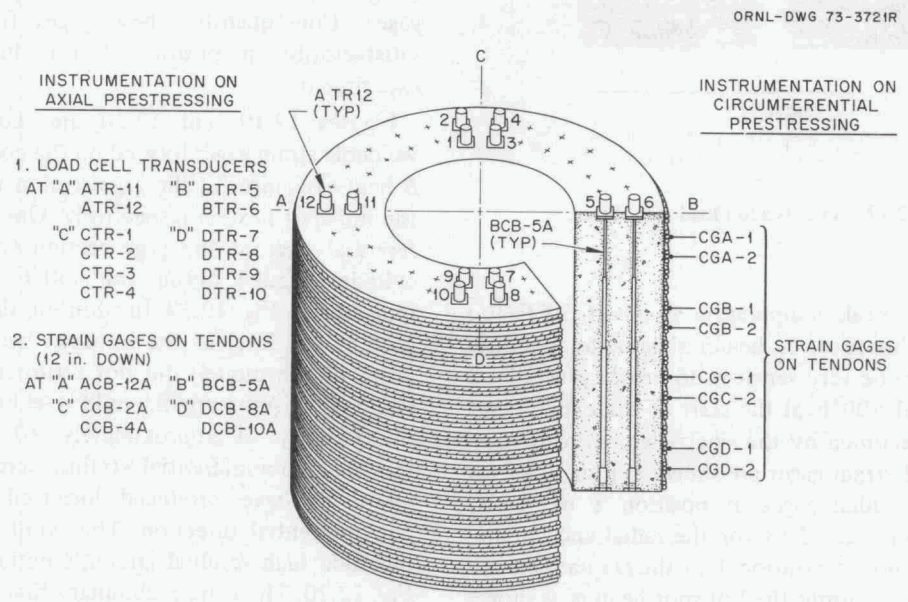

Fig. 12.11. Instrumentation on axial and circumferential prestressing.

PHOTO 78072

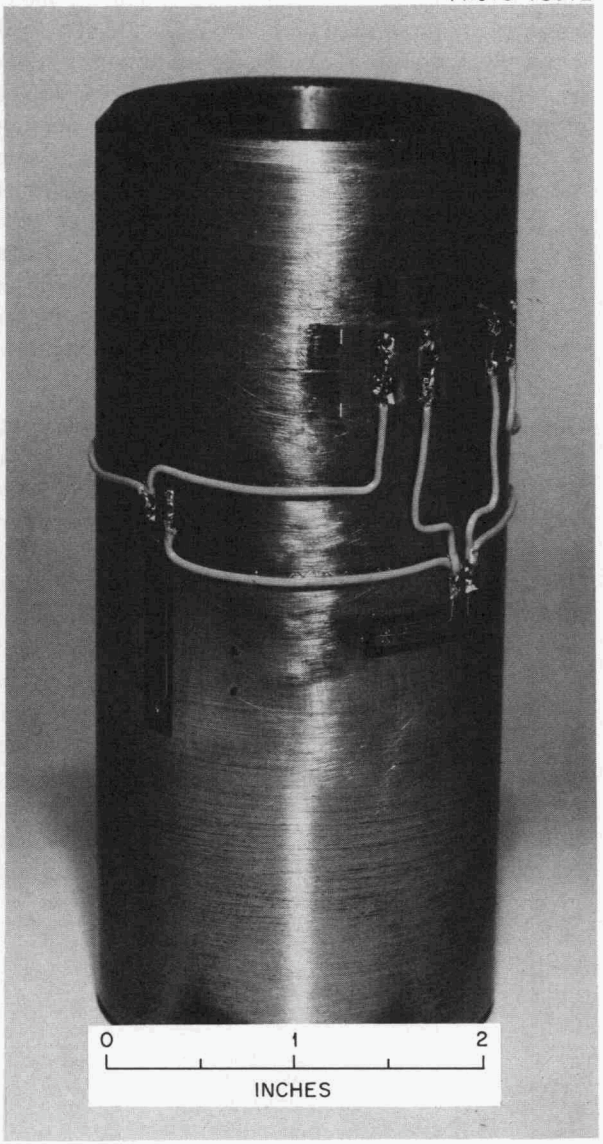

Fig. 12.12. Axial tendon load transducer.

The calculated peak temperature is about 50°F too high, but the hot-spot, or heater sheath, temperature was observed to be very sensitive to heater power level and approached 500°F at the start of the experiment.

The strains recorded by the single-element resistance-type embedded strain gages are shown in Fig. 12.17 for the axial and radial gages at position 1 of the *D* quadrant and in Fig. 12.18 for the radial and circumferential gages also at position 1 of the *D* quadrant but located directly opposite the hot-spot heaters as shown in Fig. 12.3. Both sets of curves include the strain-time history of the model since prestressing. The strains recorded for the hot-spot gages during the 450°F heating cycle are considerably higher than those for the set of gages located at mid-depth. The portion of the curve after the hot-spot heaters were turned off can be clearly seen in Fig. 12.18. The final point of the curve indicates readings taken after release of the internal pressure loading. In all cases except for the axial gage in the *D* quadrant, the final strain readings agreed reasonably well with the last readings taken before heatup. The 450°F temperature of the hot-spot test was considerably higher than the maximum allowable operating temperatures for the other types of embedment gages. Consequently, these gages failed to operate satisfactorily in position 1 for this phase of the experiment.

Table 12.2. Material and heat transfer parameters for hot-spot analysis

Electric heater power, 3100 W
Recorded sheath temperature, 450°F

	Concrete	Oil	Water
Density, lb/ft^3	150.0	88.3	60.0
Thermal conductivity, Btu hr^{-1} ft^{-1} (°F)$^{-1}$	1.65	0.068	0.4
Specific heat, Btu lb^{-1} (°F)$^{-1}$	0.2	0.28	1.0
Heat transfer coefficient, Btu hr^{-1} ft^{-1} (°F)$^{-1}$		[a]	2000

[a]Convection type, $h = 0.135(\Delta T)^{0.25}$, where h is coefficient (Btu hr^{-1} ft^{-2}) and ΔT is temperature difference between node bulk temperature and node surface temperature (°F).

Figures 12.19 and 12.20 are data plots for the weldable strain gages located on the concrete side of the *B* heat exchanger at the gage section and at the level of the hot-spot heaters respectively. One gage, the circumferential gage at the gage section (mid-depth of the cylinder), failed during the 450°F heating cycle as indicated in Fig. 12.19. In addition, the circumferential gage at the level of the hot-spot heaters (lower third point of the model) did not return to the preheating strain level. Assuming the mild steel liner has a modulus of elasticity of approximately 30 × 10^6 psi, the recorded circumferential strains were more than adequate to have produced localized yielding in the circumferential direction. This would account for the recorded high residual circumferential strain shown in Fig. 12.20. These are preliminary findings; the results of the hot-spot test are being studied further.

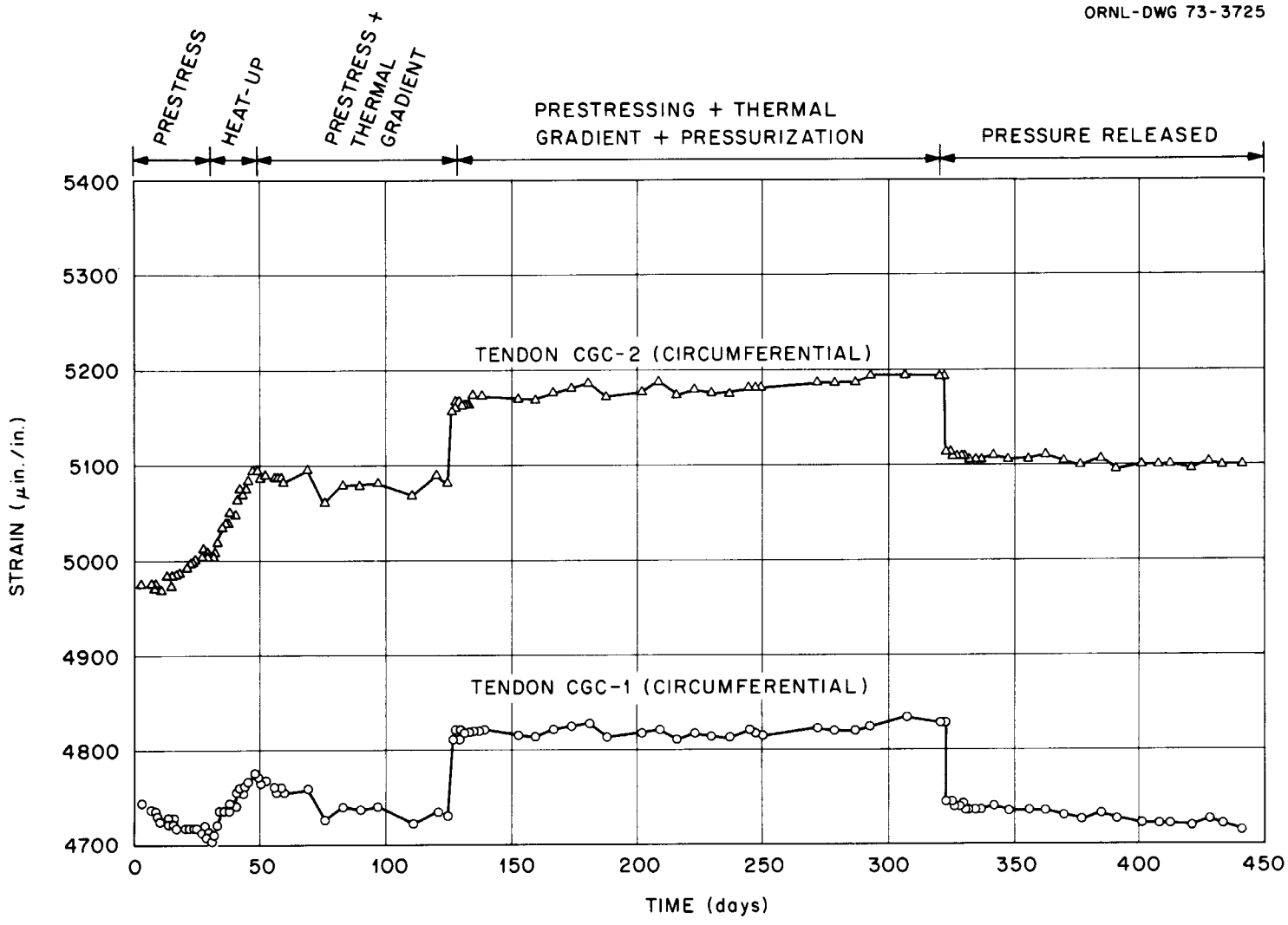

Fig. 12.13. Circumferential tendon bonded gage strain data.

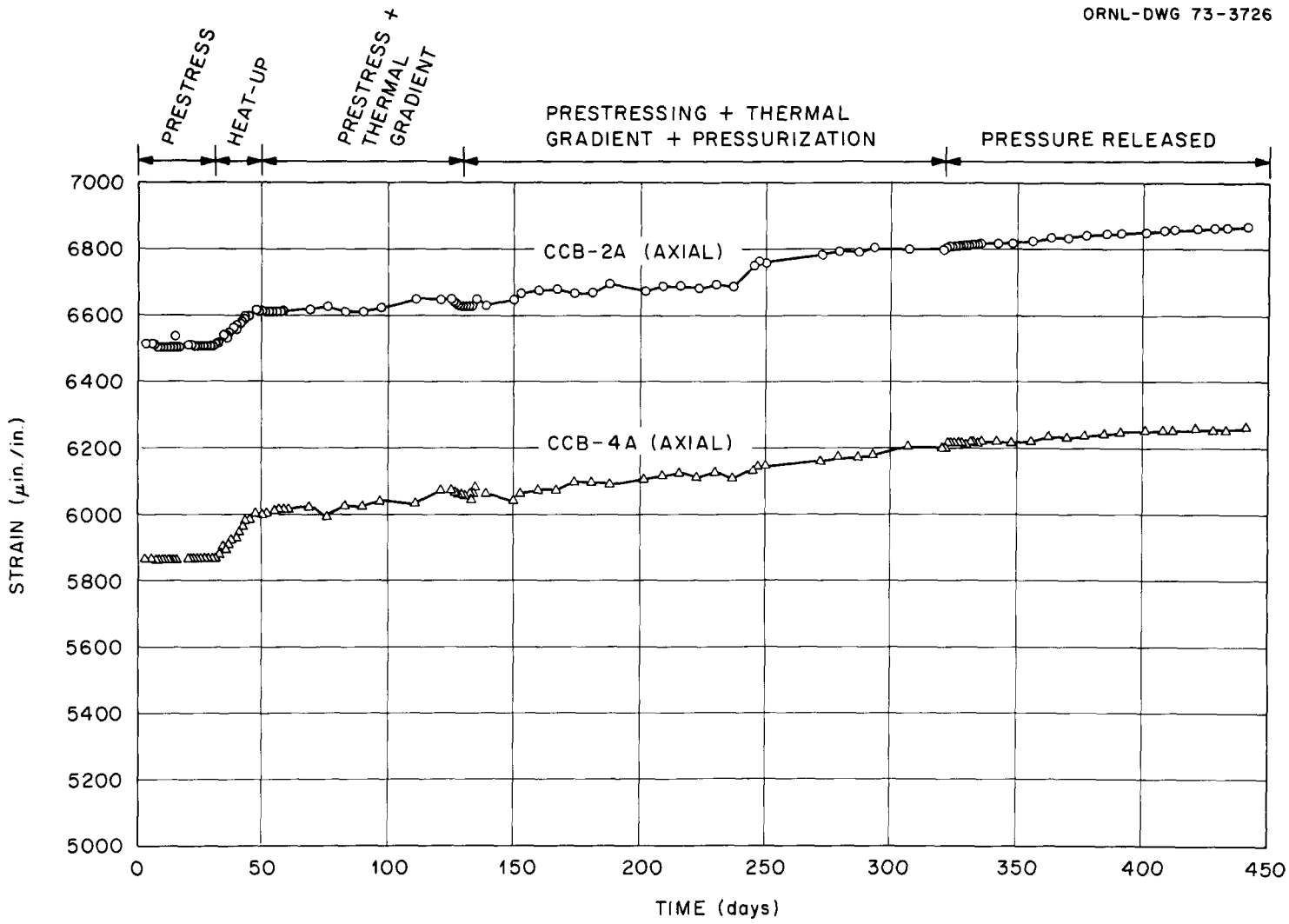

Fig. 12.14. Axial tendon bonded gage strain data.

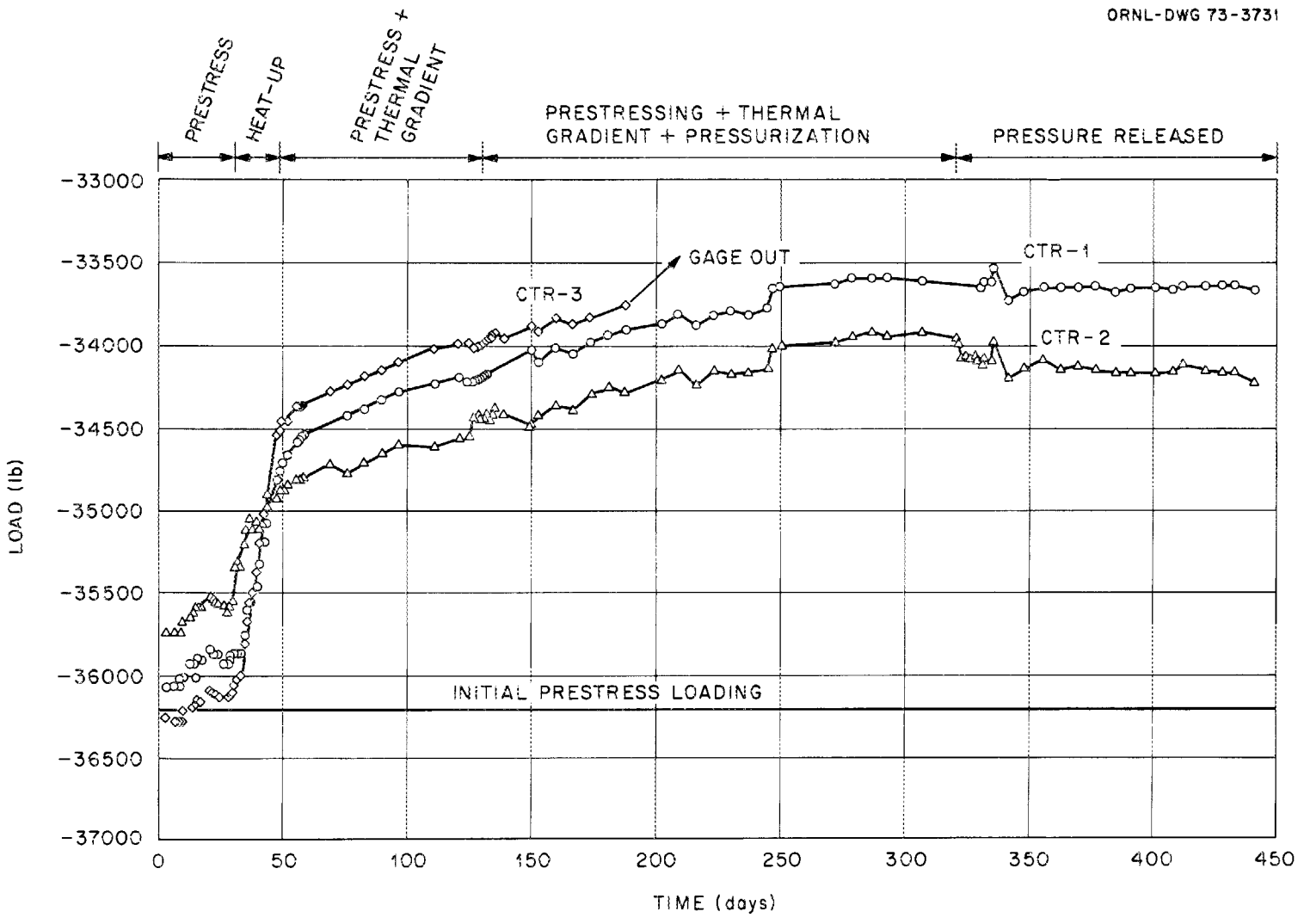

Fig. 12.15. Axial tendon transducers loading data.

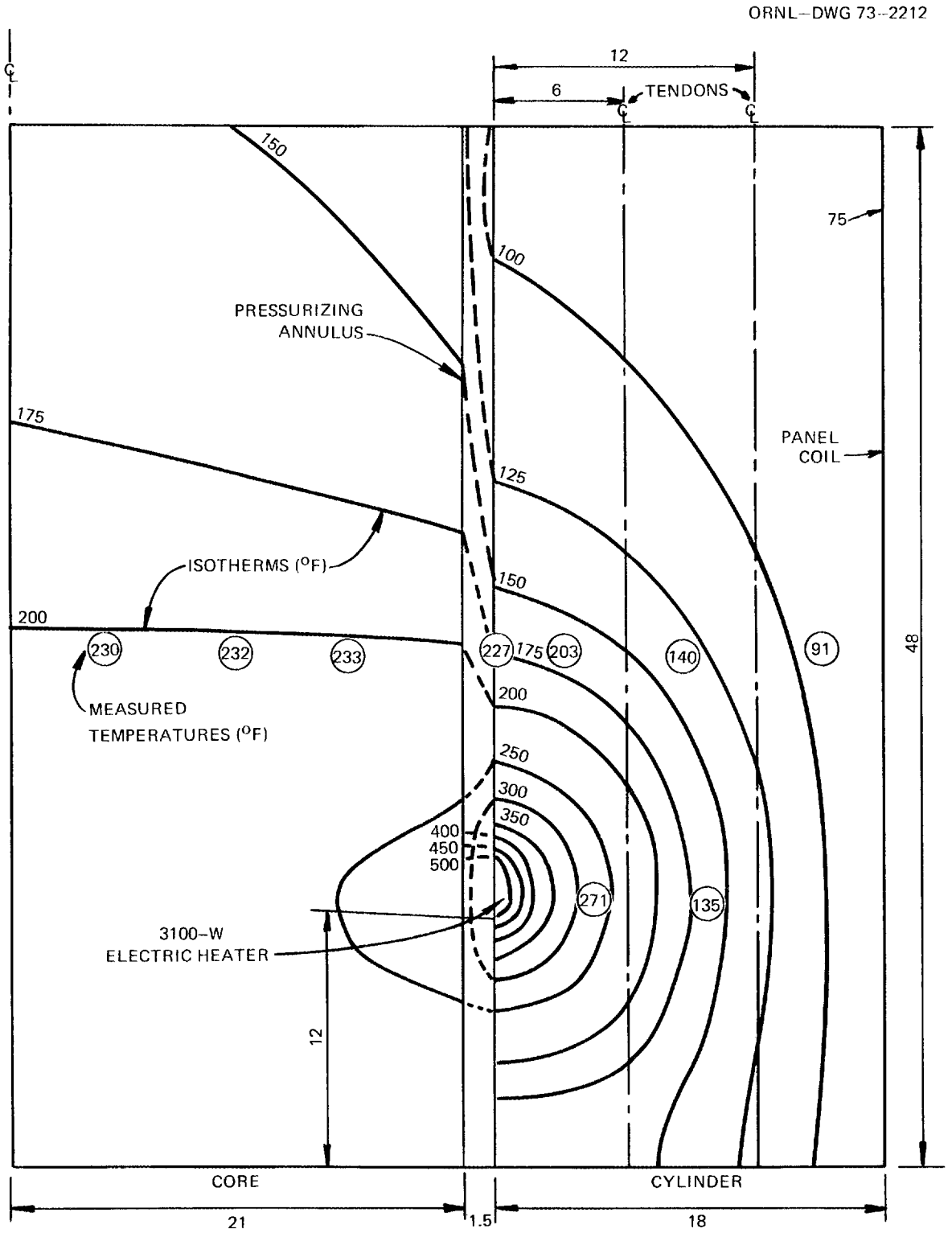

Fig. 12.16. Temperature profiles during thermal cylinder hot-spot test.

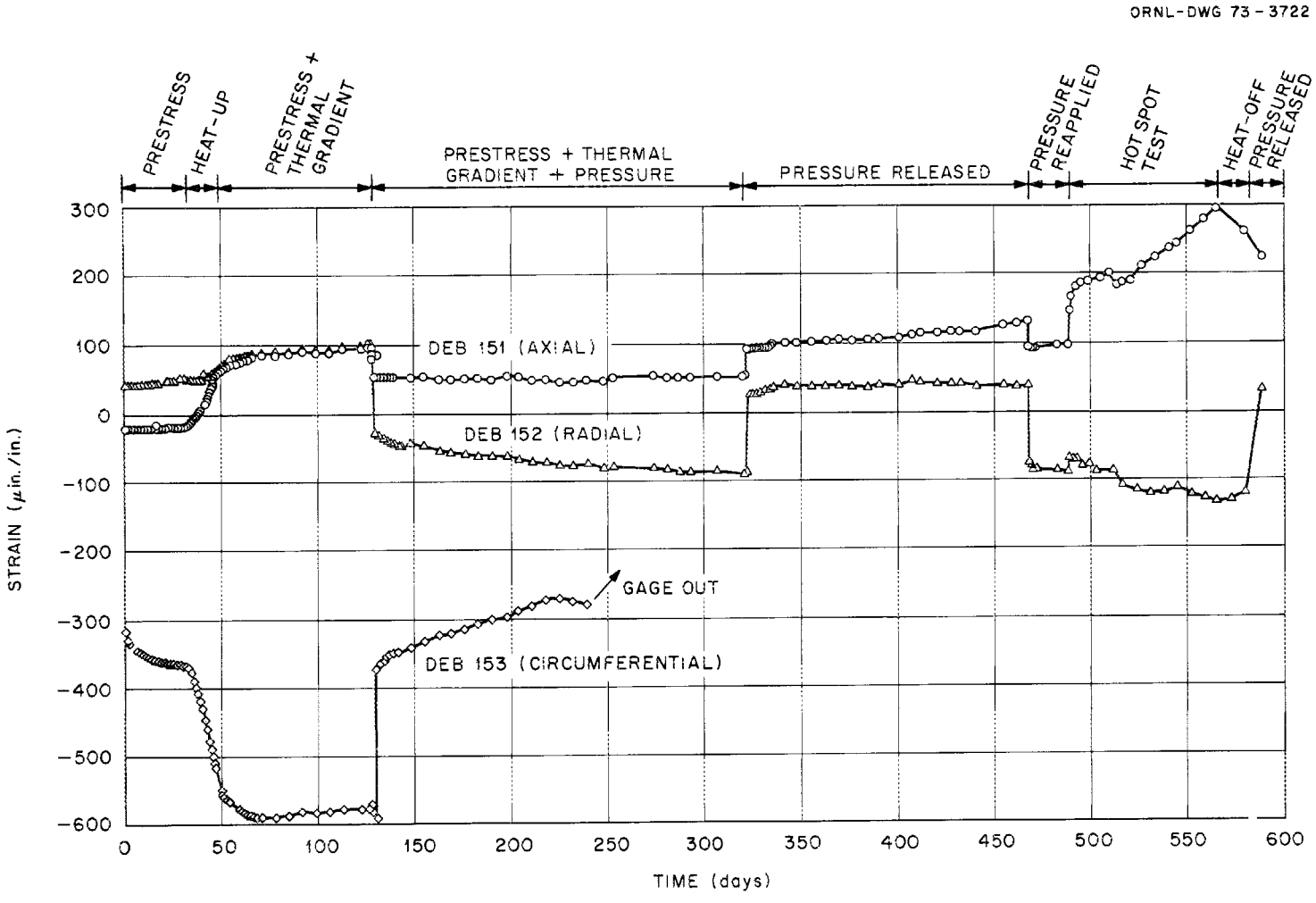

Fig. 12.17. Single-filament resistance gage strain data for DEB-151, -152, and -153 (including hot spot).

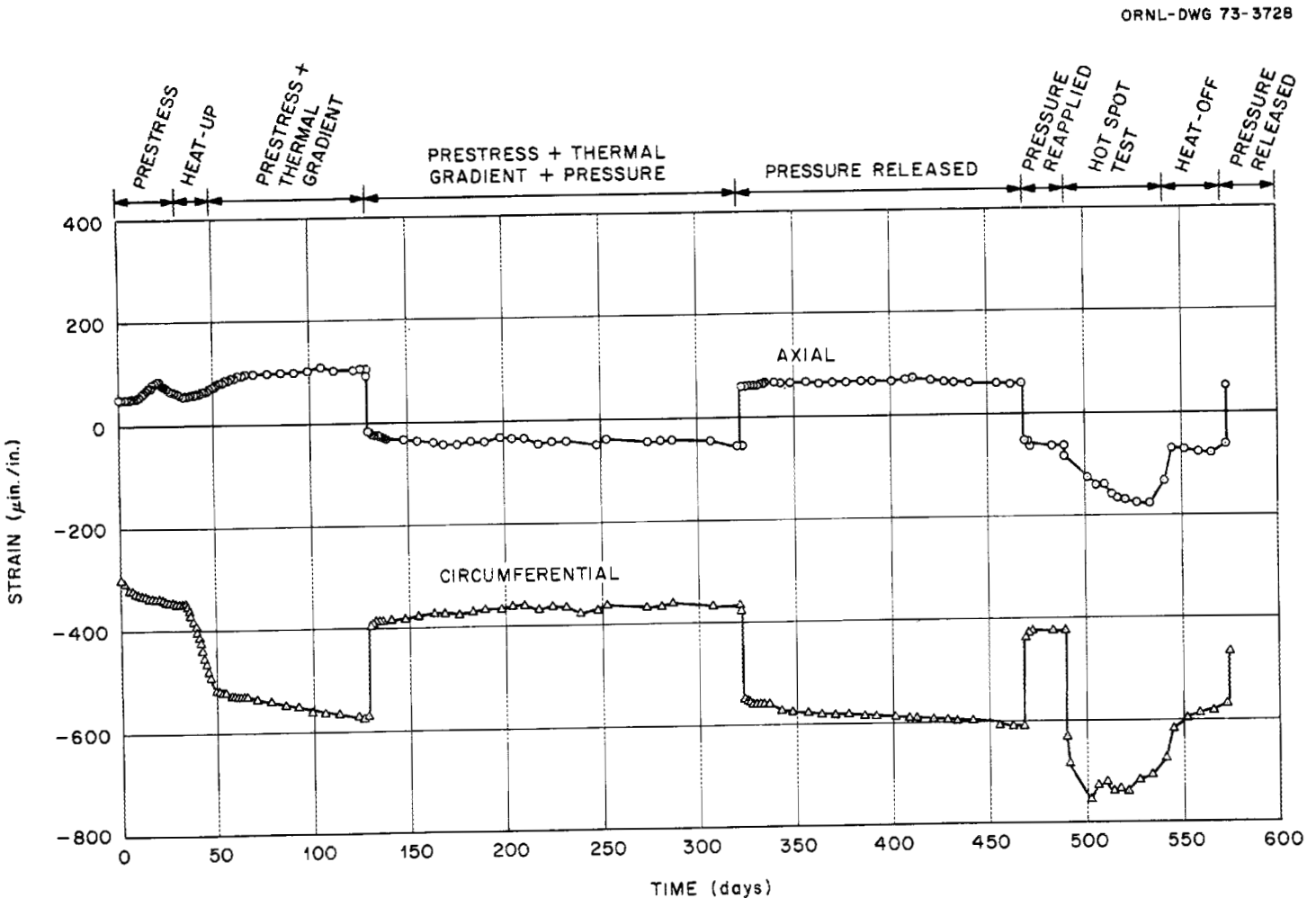

Fig. 12.18. Single-filament resistance gage strain data for DEBHS-122 and -133 (including hot spot).

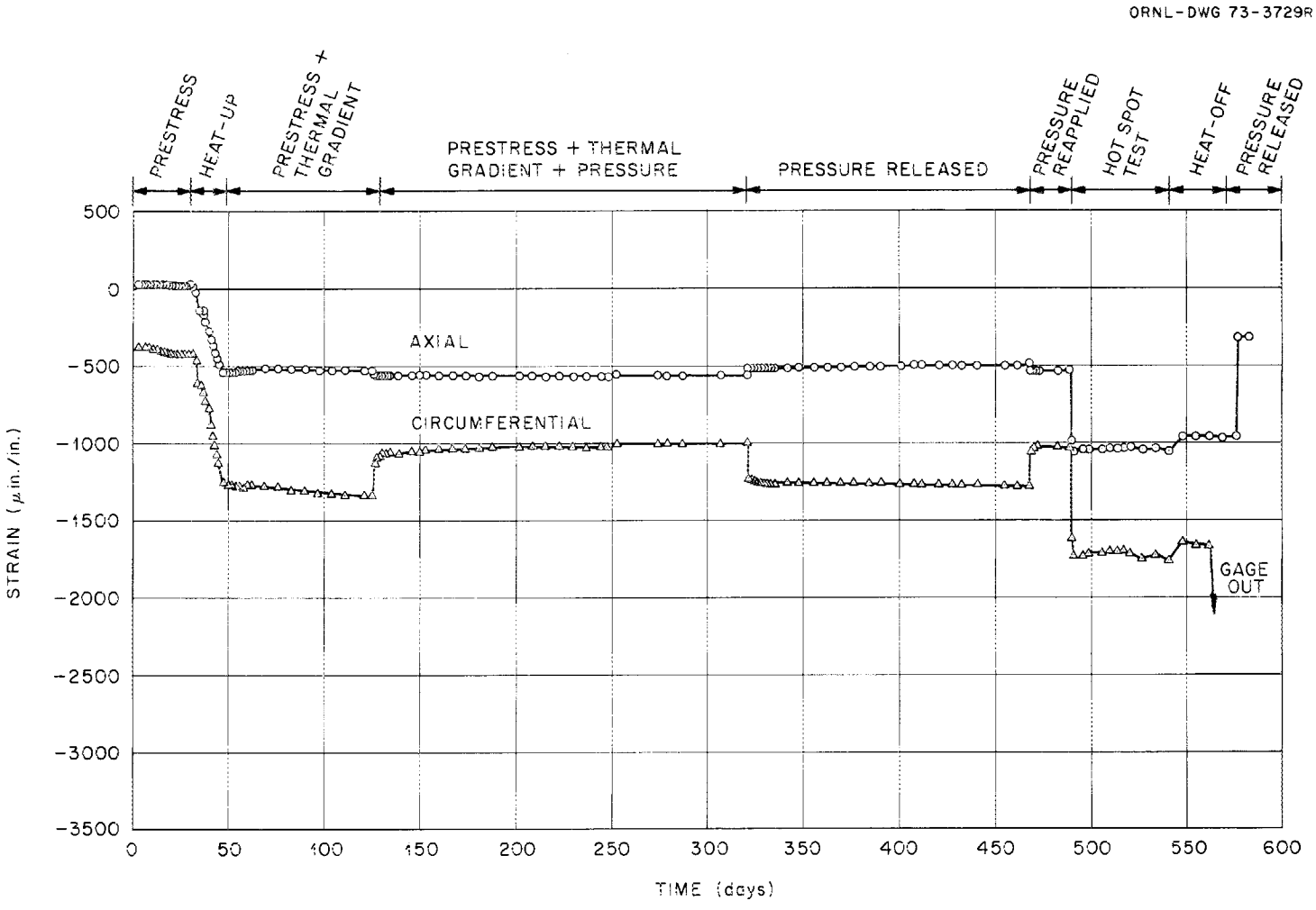

Fig. 12.19. Weldable gage strain data for concrete side of liner (including hot spot).

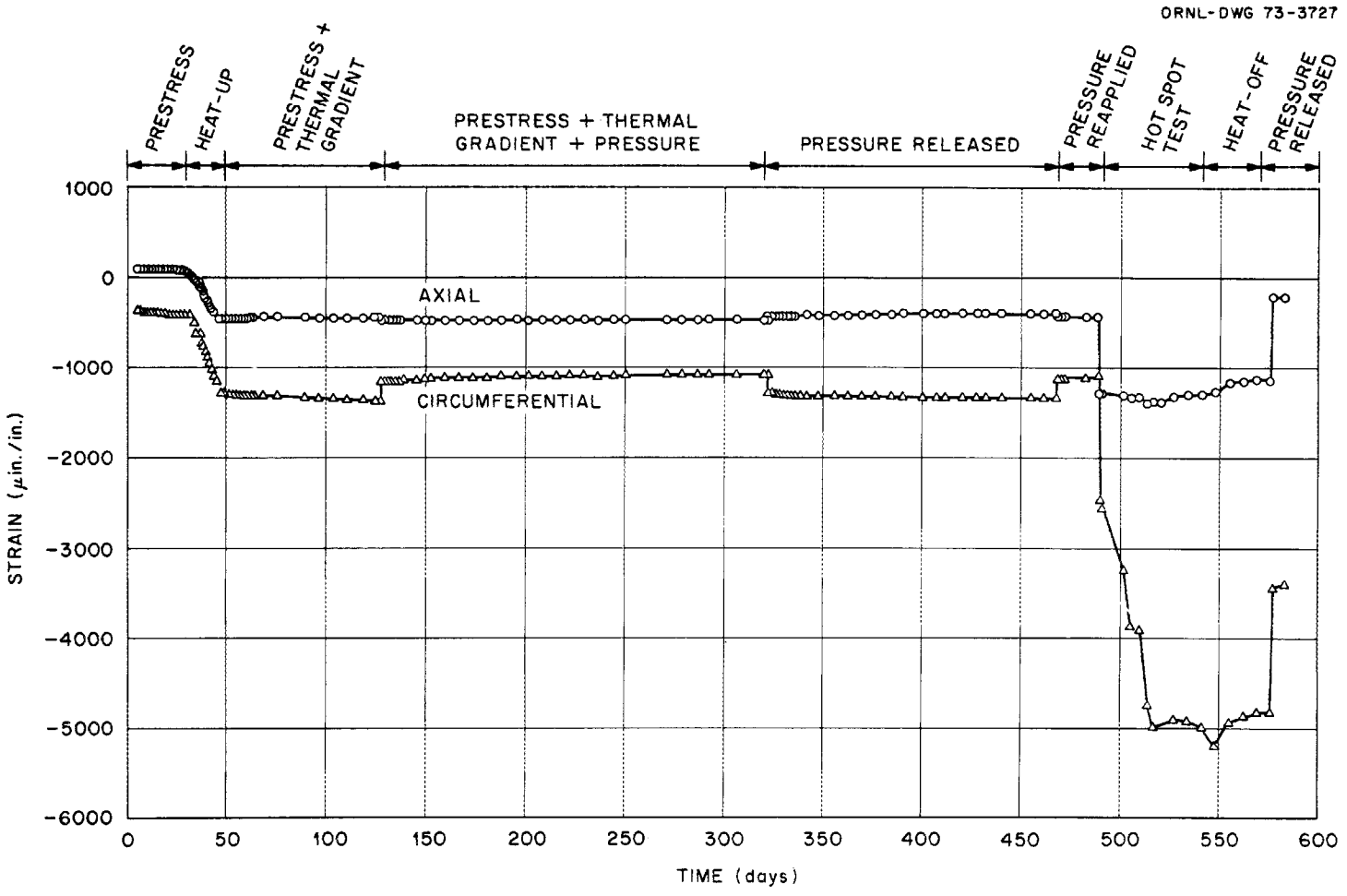

Fig. 12.20. Weldable gage strain data for concrete side of liner at hot spot.

12.1.3 Moisture Measurements

All moisture readings made using a Troxler probe-type neutron and gamma-ray backscattering instrument[2] have been reduced and evaluated. The average readings taken by lowering the moisture probe into sixteen 1-in.-OD thin-walled stainless tubes cast into the specimen along three radial lines have been reduced and evaluated. The average readings for each probe position are listed in Table 12.3. From left to right in the table the positions extend radially from the center of the core (designated as center) to the three positions located in the test annulus (designated as 3, 4, and 5). Position 3 is nearest the 150°F surface and the hot-spot heater, position 4 is in the center of the test section, and position 5 is located nearest to the 75°F surface, which is the outer surface of the section. In most cases each value listed in the table represents the average of nine 1-min readings or counts which are taken in sets of three at each of three levels in the cylinder.

Initially, little variation is seen in the readings for the various radial positions in the cylinder, which indicates that the moisture seal was effective and little migration of moisture had resulted from heating. The intensive heating during the hot-spot experiment resulted in excessively high counts at 614 days. Only those readings appearing to be relatively unaffected by the heating are shown in Table 12.3; however, the high reading shown for the center of the core was caused by heating of the moisture probe.

The 686-day readings which were taken shortly after hot-spot cooldown indicate a significant decrease in the core region moisture level. This region of the model had experienced relatively high temperatures over most of its volume. Since the copper-epoxy moisture seal used at the top of the model is not capable of preventing loss of moisture at temperatures above 150°F, which occurred during this phase of the experiment, moisture was apparently lost to the atmosphere. The moisture readings for the test section (annulus) did not change greatly at any time during the experiment, although there is an indication that some moisture migration may have occurred toward the cool outer surface as would be expected.

12.1.4 Comparisons of Experimental and Analytical Results

A preliminary time-dependent creep analysis was performed using the finite-element computer program SAFE-CRACK[3] which was developed by Gulf General Atomic, Inc. The creep analysis was used to predict the stress and strain behavior of the thermal cylinder starting with prestressing and including a total of 55 time steps which included the heating period and the initial 55 days of the first pressurization period. The analysis assumes linear viscoelastic behavior based on the superposition principle. It is a two-dimensional analysis capable of treating axisymmetric structures subjected to time-varying mechanical and thermal loadings. The analysis is also capable of considering time-

3. Y. R. Rashid, *Nonlinear Quasi-Static Analysis of Two-Dimensional Concrete Structures, Part I: Theory, and Part II: Computer Program Manual,* GA-9994, Gulf General Atomic (Mar. 23, 1970).

Table 12.3. Moisture content at various moisture tube positions in thermal cylinder

Days from casting	Moisture content (% by volume) at probe position –						Status of experiment
	Core			Annulus			
	Center	1	2	3 (hot)	4 (middle)	5 (cold)	
130		22.6	21.0	20.9	20.8	20.3	75–75°F
135	23.0	24.1	22.6	22.1	22.4	21.8	75–105°F
146	23.2	24.3	22.6	22.3	22.6	22.1	75–150°F
175	23.6	24.4	22.9	22.2	23.1	22.5	75–150°F
223	23.7	24.5	22.7	22.4	23.0	22.5	Before pressurization
236	23.7	23.7	22.3	21.9	22.5	22.2	After pressurization
318	23.4	23.6	23.2	22.3	22.8	22.4	
403	24.3	25.1	23.9	21.9	22.3	21.9	
425	24.3	25.1	23.9	21.9	22.2	21.7	After release of pressure
614	28.6				23.6	23.0	During hot-spot experiment, pressure on
686	15.7	18.4	15.5	22.2	23.5	23.5	After cooldown to 75–150°F
718	16.3	17.8	15.3	21.6	23.0	23.0	After complete cooldown to 75–75°F, after release of pressure

dependent cracking behavior of the structure. The concrete creep data developed at the University of Texas for the same basic concrete mixture were incorporated into the analysis.

The finite-element layout for the analysis is shown in Fig. 12.21. Both the cylinder and the core are included in the finite-element grid. The idealizations employed are membrane-type elements representing the steel liners (heat exchangers) and the sheet-metal bottom seals. The steel anchor plates for the axial tendons are represented by steel elements, and the circumferential prestress loading is simulated by an external pressure on the cylinder.

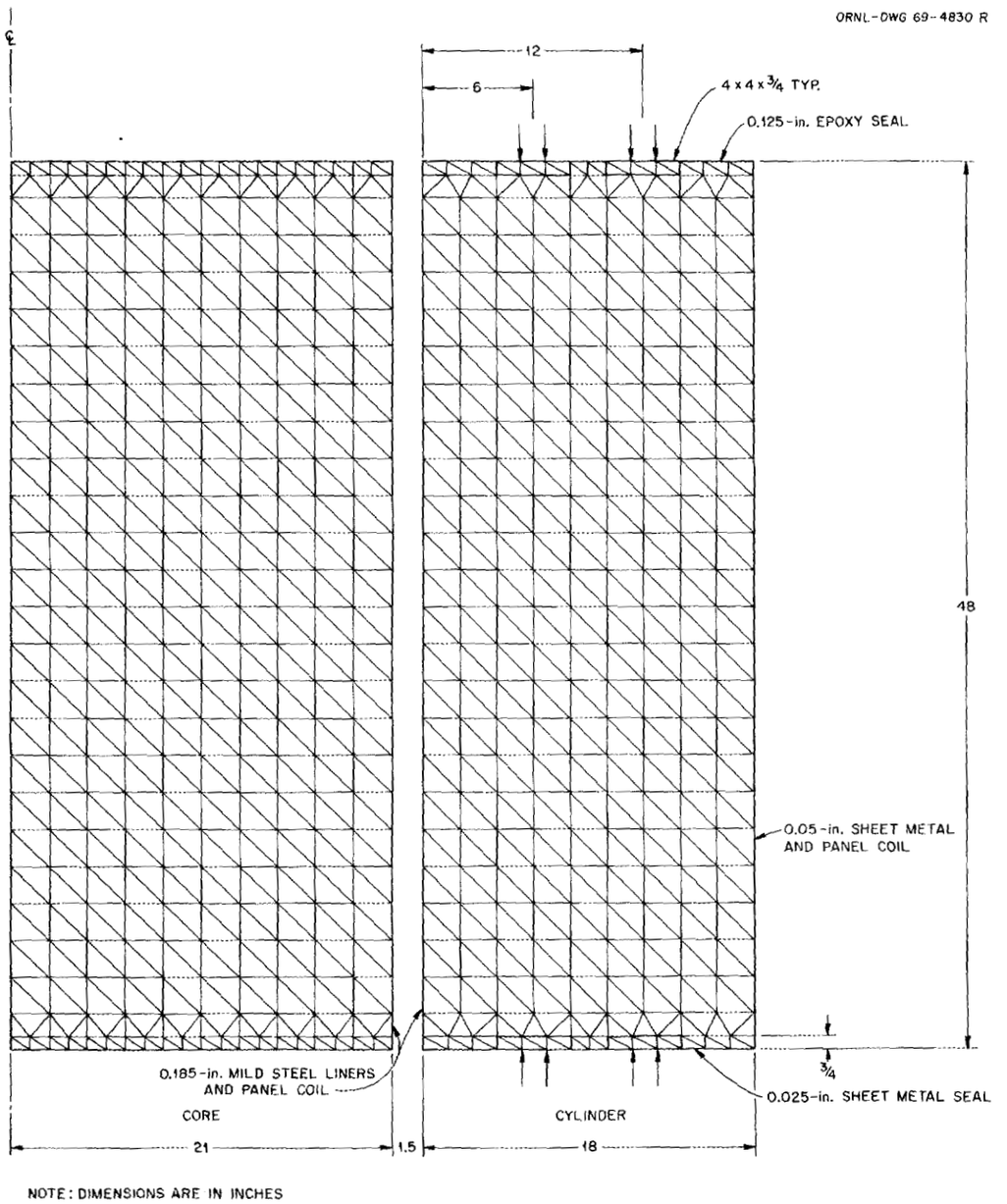

Fig. 12.21. Axisymmetric finite-element layouts for thermal cylinder test section and core.

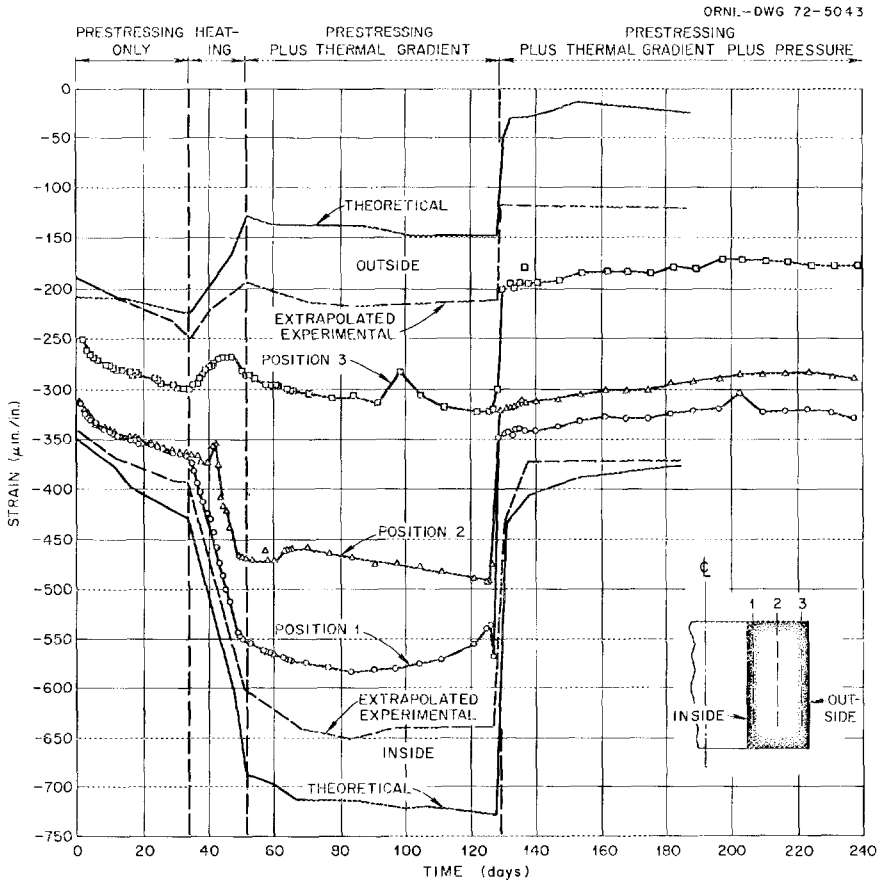

Fig. 12.22. Single-filament gage strain data for average circumferential strains.

The results for the average circumferential readings of the single-filament resistance gages at the three positions through the cross section are shown in Fig. 12.22. The extrapolated experimental results for the inner and outer surfaces are indicated by dashed lines, and the corresponding theoretical results are shown as solid lines. Considering the variables involved in testing a model as complex as the thermal cylinder, the results appear to be in reasonable agreement. A final analysis is being conducted using SAFE-CRACK which will include the entire loading history of the thermal cylinder model. Plans are also being made to disassemble the structure for detailed examination of the liner and concrete integrity.

12.2 CONCRETE TRIAXIAL CREEP STUDIES

Two additional reports[4,5] were issued by the University of Texas covering the results of studies on the creep recovery of concrete and the effect of curing on the creep behavior of concrete. This work was performed under Subcontract 3661 as a completion phase of the research conducted on PCRV concrete.[6]

The experimental investigation to evaluate creep recovery was conducted on plain concrete which had been under sustained load for one year. Creep recovery strains were observed to be affected by temperature, curing history, and stress conditions. Creep recovery

4. A Hijazi and T. W. Kennedy, *Creep Recovery of Concrete Subjected to Multiaxial Compressive Stresses and Elevated Temperatures,* Research Report 3661-1, Department of Civil Engineering, The University of Texas at Austin (March 1972).

5. T. W. Kennedy, *Long Term Creep Behavior of Concrete and the Effects of Curing,* Research Report 3661-2, Department of Civil Engineering, The University of Texas at Austin (June 1972).

6. G. D. Whitman, "Concrete Triaxial Creep Tests at the University of Texas," *GCR-TU Programs Annu. Progr. Rep. Sept. 30, 1971,* ORNL-4760, p. 95.

strains were larger at 150°F than at 75°F. Specimens that had been allowed to dry before sealing were seen to have greater creep recovery than specimens that were sealed on casting. The magnitude of creep recovery strain was also related to the magnitude of the previously sustained stress.

The creep recovery strains were small in comparison to the instantaneous recovery strains, in contrast to the fact that during the loading period the creep strains were large in comparison to the instantaneous strains and in some cases exceeded the magnitude of the instantaneous strains.

It was concluded that the principle of superposition of strains overestimates the actual creep recovery strains and thus should not be used unless a relatively large error can be tolerated.

The findings on the effect of curing time and history prior to loading on the instantaneous and long-term creep behavior of concrete were obtained on tests conducted at 75°F. The factors investigated were curing time (90, 183, and 365 days), curing history (as-cast and air-dried specimens), and uniaxial stress (660 and 2400 psi). Specimens cured for 90 days prior to loading were subjected to a sustained load for a period of one year, at which time the load was removed. The specimens cured for 183 and 365 days have not been unloaded and have been under load for 2.5 and 2 years respectively.

Creep strains were affected by both curing time prior to loading and curing history, whereas instantaneous strains were not.

Creep strains were larger for specimens subjected to shorter curing periods prior to loading. During the first year under load the creep strains in specimens cured for 183 and 365 days were approximately 85 and 68% of the creep strains in the specimens cured for 90 days.

Creep strains were larger for the air-dried specimens than for the as-cast specimens. The creep strain at any given time in the as-cast specimens was approximately 82% of that in the air-dried specimens at a stress level of 2400 psi. The creep behavior of the 183- and 365-day specimens indicates that the creep strains continue to increase at a decreasing rate with the magnitude of the strain approaching a constant value.

13. Exchange Programs

J. H. Coobs

There are currently two exchange programs in effect that concern high-temperature reactor development. The first and older of these is the USAEC/Dragon HTGR Exchange Agreement, which has been in effect since 1960, soon after the project was initiated. Under this agreement, information on the properties and performance of fuels and core materials are exchanged. The second is the USAEC/KFA Exchange Arrangement, which was negotiated and implemented during 1971 and which concerns information on fuel reprocessing as well as on fuel preparation and test results.

13.1 USAEC/DRAGON HTGR EXCHANGE AGREEMENT

Forty fuel compacts from the two Dragon fuel elements that contained ORNL fuel were received for evaluation. Four selected compacts from the shipment were crushed in the equipment used for hot cell head-end processing studies. This crushing test verified that the matrix separates from the particle coatings and few if any coatings are broken during crushing, which confirms the behavior observed in prior tests. Fragments from one compact that had moderate exposure (~15% FIMA and 2×10^{21} neutrons/cm^2 fast fluence) were examined by metallographic procedures. This examination showed that the particles gave excellent performance, as had been indicated by sweep gas analyses and measurements of activity in graphite fuel element sleeves. These mixed-oxide particles had sealed buffer and high-temperature isotropic outer coatings only. Small portions of the compacts will be deconsolidated in order to test the loose particles separately and remaining portions stored for possible use in future head-end processing studies.

Other activities under this agreement include the routine exchange of reports and visits of personnel. Two representatives from the Dragon Project attended the annual information meeting at ORNL in May 1972. During this visit current data on testing and performance of fuels and graphite were exchanged. The visitors showed particular interest in recent developments in resin-based fissile fuel kernels.

13.2 USAEC/KFA EXCHANGE ARRANGEMENT

In addition to the routine exchange of reports and occasional visits, an important exchange of personnel to work in fuel reprocessing development was implemented during this period. Since May 1972, a member of the staff of Kernforschunglage (KFA) has been working at ORNL on development of whole-block burning and other head-end recovery processes. About the same time, a staff member from ORNL joined the Institute of Chemical Technology at KFA and has been participating in the work on crushing and fluidized-bed burning of unirradiated and irradiated Arbeitsgemeinschaft Versuchs-Reaktor (AVR) fuel spheres. These assignments have stimulated the flow of information as well as being of direct benefit to the development programs.

14. GCFR Irradiation Experiments

J. A. Conlin

A series of fuel rod irradiation tests have been conducted at ORNL in support of fuel development for the gas-cooled fast reactor (GCFR). The GCFR is under development at Gulf General Atomic (GGA) with support from the U.S. Atomic Energy Commission (USAEC) and a number of electric utility companies. The fuels irradiation program for the GCFR consists of both thermal- and fast-flux testing in capsule and loop experiments. Thermal-flux tests are being performed at ORNL in a series of capsule tests in the Oak Ridge Research Reactor (ORR) poolside facility. These tests, supported by the USAEC, represent the combined efforts of GGA, ORNL, and ANL.

Two fuel rod concepts for the GCFR have been investigated in the ORNL thermal-flux tests: a sealed fuel rod design and a vented-and-pressure-equalized fuel rod design. Earlier tests of 20 fuel rods of the sealed type (ORR capsules P-1 through P-8) indicated this concept to be a feasible backup design; however, cladding temperatures and dimensions must be carefully specified and controlled to ensure that cladding ovality and subsequent failure by localized cladding collapse do not occur under the high coolant pressure (1250 psig) in the GCFR. The current irradiation tests, ORR capsules GB-9 and GB-10, were designed to permit evaluation of the vented fuel rod concept, which is the present reference fuel rod concept for the GCFR. The capsule GB-9 irradiation has been completed, and postirradiation examination of the fuel rod is nearing completion at ANL. Irradiation of the vented fuel rod in capsule GB-10 is in progress.

In the GCFR vented fuel element concept (Fig. 14.1), the top of each fuel rod is vented to an annular charcoal

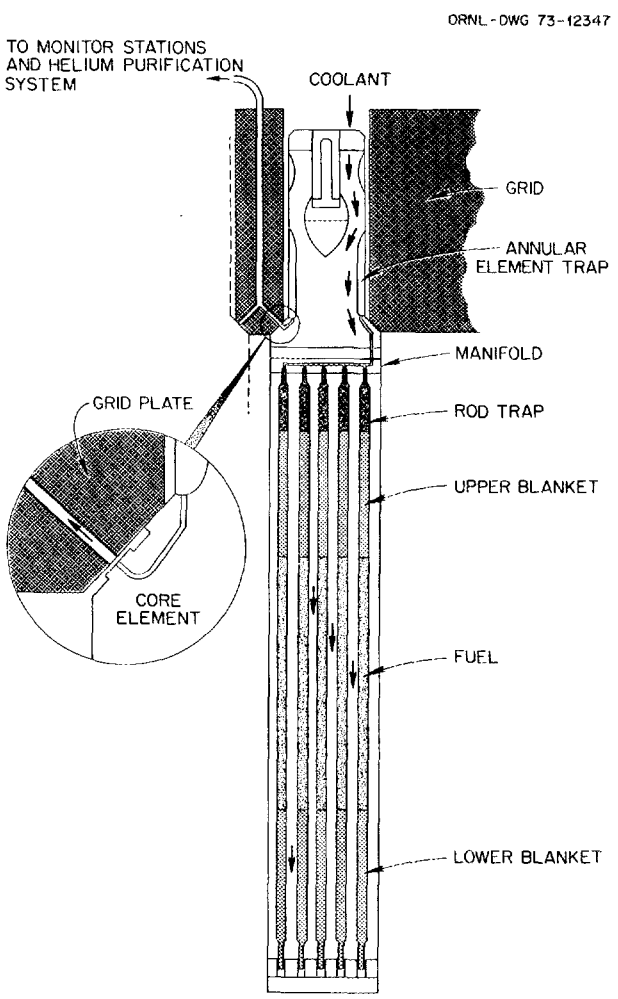

Fig. 14.1. GCFR vented fuel element.

trap and then through a fission-gas cleanup system to the inlet side of the main coolant circulators. The small pressure difference necessary for circulation of the helium coolant keeps the gas pressure inside the rods slightly below the 1250-psig coolant pressure outside the rods. The design and operation of this venting system, called the pressure-equalization system, have been described by Campana.[1] The individual stainless-steel-clad fuel rods have a fuel region of $(U,Pu)O_2$ pellets, an upper and lower blanket region of UO_2 pellets, and a 3-in.-long charcoal trap at the upper end of the rod. The rod traps, which operate at the inlet coolant temperature of about 300°C, form the first stage of the fission product trapping system. Their main purpose is to delay the release of volatile fission products (Br, I, Cs) should they escape in significant quantities through the upper blanket region. Large releases of the volatile fission products could impose undesirable heat loads on the remainder of the trapping system.

Capsules GB-9 and GB-10 were designed to provide the data needed for an initial evaluation of the overall performance of the GCFR vented-and-pressure-equalized fuel rod. The two capsules had the same basic design, and each contained a shortened prototype of the GCFR vented fuel rod. In order to simulate and study various aspects of the vented fuel rod concept in these tests, the interior of the fuel rod in each capsule was connected to a 1000-psig helium sweep system which was instrumented to provide continuous monitoring of fission product release from the rod. The sweep system was designed with many features analogous to the GCFR pressure-equalization system design.

The GB-9 and GB-10 capsules are unique in that they were designed to provide direct measurements of fission product release rates from an operating fast breeder reactor fuel rod. The fission product release data being obtained in these experiments are being used in important applications in both the GCFR and the Liquid-Metal Fast Breeder Reactor (LMFBR) development programs. This is possible because the GCFR and LMFBR fuel-rod materials and operating conditions are similar in many respects.

14.1 IRRADIATION OF GCFR-ORR CAPSULE GB-9

A. W. Longest J. A. Conlin
C. W. Cunningham K. R. Thoms
E. D. Clemmer

The irradiation of capsule GB-9, which began in April 1970, was terminated on November 18, 1971. The GB-9 fuel rod was operated at full power for 471 days under design conditions of 14.8 kW/ft peak heat-generation rate, 685 ± 15°C peak cladding outside temperature, and 300°C charcoal trap temperature. The estimated fuel burnup obtained was 54,000 MWd per metric ton of heavy metal, which was virtually equal to the original burnup goal of 55,000 MWd per metric ton; however, the burnup goal had been extended to 75,000 MWd/metric ton during the course of the irradiation. The experiment was terminated before reaching the revised burnup goal because of a break that occurred in the capsule secondary containment. The secondary gas line ($\frac{1}{8}$ in. OD, 0.020 in. wall), which exited from the bottom of the capsule secondary containment vessel, was broken while handling the capsule during a reactor shutdown. The capsule operation could not be continued because of the loss of secondary containment. The fuel rod was still intact, however, and most of the test objectives had already been realized. A rather extensive postirradiation examination of this first vented rod was initiated immediately.

The fuel rod in the GB-9 capsule (Fig. 14.2) was a shortened prototype of the GCFR vented-and-pressure-equalized fuel rod with a 10-in.-long fuel region of hollow $(U,Pu)O_2$ pellets, a 1.9-in.-long upper blanket region of depleted UO_2 pellets, and a full-length (3-in.-long) charcoal trap. Three gas line connections of the GB-9 rod to a 1000-psig helium sweep system permitted measurements of the fission product release from the rod under two sweep flow conditions: passage of the sweep across the top of the trap (normal case) and passage of the gas upward through the trap when the inlet flow was changed to a line terminating at the bottom of the charcoal trap region.

Most of the experimental results obtained during the GB-9 irradiation have been summarized and reported previously.[2-4] These results included information on steady-state fission-gas release vs fuel burnup, fission-gas release during slow pressure cycling, fission-gas release vs charcoal trap temperature, fission-gas release vs fuel rod power-temperature, decay heating in the charcoal

1. R. J. Campana, "Pressure Equalization System for Gas-Cooled Fast Breeder Reactor Fuel Elements," *Nucl. Technol.* **12**, 185 (October 1971).
2. A. W. Longest et al., "Irradiation of GCFR-ORR Capsule GB-9," *GCR-TU Programs Annu. Progr. Rep. Sept. 30, 1971*, ORNL-4760, pp. 149–63.
3. A. W. Longest et al., "Fission-Gas Release Measurements from Fast Breeder $(U,Pu)O_2$ Fuel," *Trans. Amer. Nucl. Soc.* **13**, 604 (1970).
4. A. W. Longest, R. B. Fitts, and J. A. Conlin, "Fission Gas Release Behavior in a Vented $(U,Pu)O_2$ GCFR Fuel Pin," *Trans. Amer. Nucl. Soc.* **15**, 197 (1972).

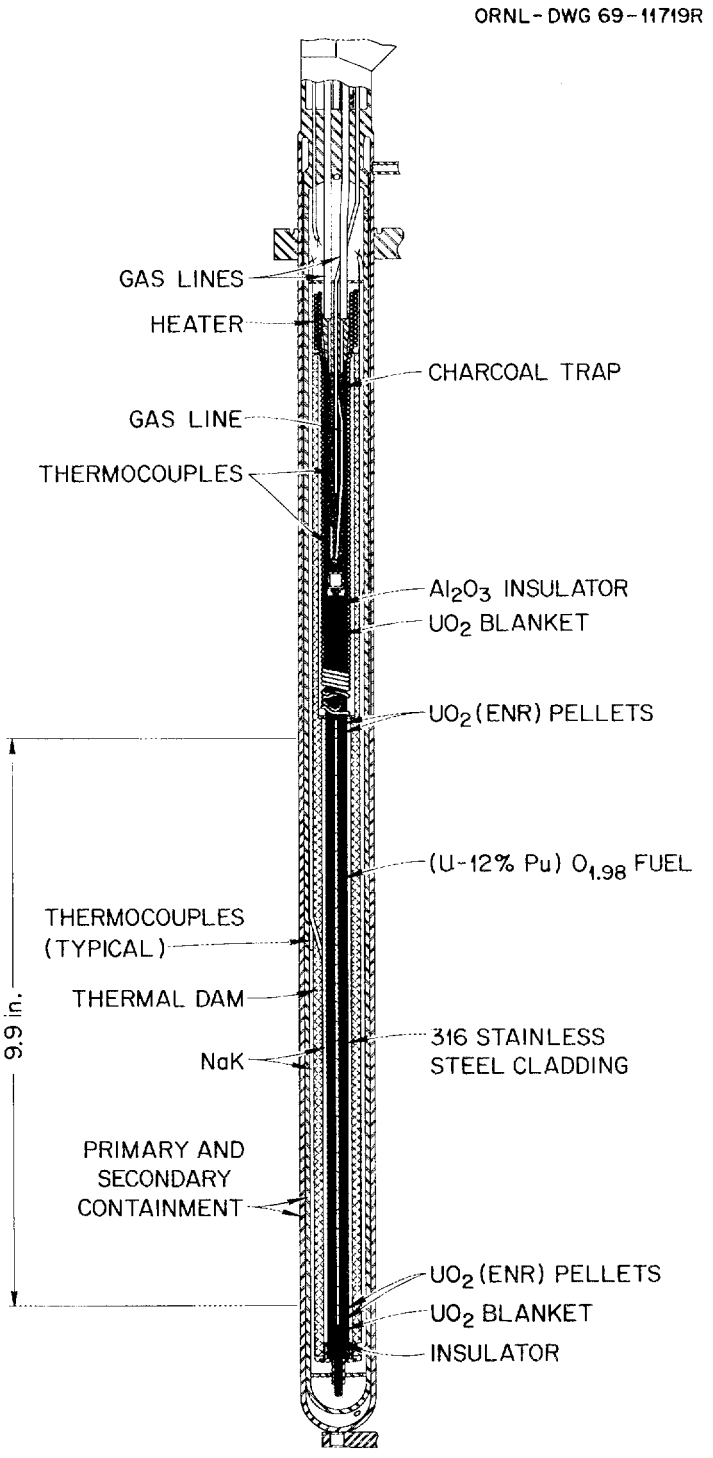

Fig. 14.2. GCFR-ORR capsule GB-9.

trap, iodine deposition in the charcoal trap, neutron radiography at fuel burnup levels of 20,000 and 44,000 MWd/metric ton, and fission-gas release vs sweep pressure. The special test to determine release vs sweep pressure was in progress at the 500-psig sweep pressure level at the time the irradiation was terminated. Therefore, we were unable to obtain information from this special test other than that previously reported.[2] A neutron radiograph was taken of the capsule on November 24, 1971, following termination of the test. This radiograph indicated the final condition of the fuel rod to be essentially the same as that reported on the basis of the radiographs taken at 44,000 MWd/metric ton burnup.[2]

A revision in the advertised operating power level of the GB-9 fuel rod is in order. More detailed calculations of the power and temperature asymmetries across the fuel rod indicate a fuel rod power of 14.8 kW/ft (average for a given cross section) for a corresponding "hot side" (or peak) cladding outer-surface temperature of 685°C instead of the 16 kW/ft reported previously.[2-4] This revision will be incorporated in a final report on the GB-9 experiment which we plan to issue in FY 74.

The GB-9 test has provided substantial information on the fission product release behavior to be expected from the GCFR vented fuel rod. The results have already been used in many aspects of the GCFR pressure-equalization system design. Under the "no-leak" conditions simulated by the GB-9 test, it was found that the fuel and blanket regions of the rod were quite effective in retaining the volatile fission products. During postirradiation examination of the GB-9 fuel rod, volatile fission products were found plated out at the blanket–fuel-pellet interfaces, where the temperatures drop sharply, instead of having been transported through the blanket region to the rod trap.[5] The absence of significant decay heat and iodine deposition in the rod trap during irradiation[2] was consistent with this postirradiation finding. Finally, the successful design and operation of the GB-9 capsule provided a sound basis for designing the more complex GB-10 experiment.

14.2 POSTIRRADIATION EXAMINATION OF GCFR-ORR CAPSULE GB-9

R. B. Fitts E. L. Long, Jr.

Postirradiation disassembly and examination of capsule GB-9 were implemented as quickly as possible after the irradiation was terminated. This was necessary to permit gamma-ray analysis for the location of various fission products before their loss through radioactive decay. The principal fission product activity of interest was ^{131}I, which has an eight-day half-life.

The GB-9 secondary containment had failed at a gas line which passed into the bottom of the capsule adjacent to a structural support member. This support piece was bent during capsule handling operations and was pushed onto the gas line, causing the line to fail in the heat-affected zone where it was welded to the capsule.

Figure 14.3 shows a view of the bottom end of the capsule and two views of the broken gas line where it was joined to the capsule. The side of the gas line was bent inward by the support piece just below the point of failure. The bottom of the capsule was hemispherical with the gas line welded into it. This weld is visible next to a cut which was made into the end of the capsule during postirradiation disassembly.

The GB-9 capsule was disassembled and the fuel pin recovered without difficulty. The gas lines entering the top of the fuel pin were sealed with an epoxy plug to prevent air from entering the fuel pin during handling and shipping. The appearance of the fuel pin was excellent, as shown in Fig. 14.4. The top view of the figure shows the fuel pin before removal of the spiral heater which maintained the UO_2 blanket and charcoal trap regions at the design temperature, and the lower view shows the fuel pin after removal of the heater. In both views the epoxy plug, capsule bulkhead, and instrumentation leads (cut off) are visible on the top of the fuel pin. Dimensional measurements on the fuel pin indicated less than 0.001 in. diametral change and about $\frac{1}{8}$ in. of bow along the fuel pin. This amount of bow is normal for a pin operated under the conditions of the GB-9 pin.

The gross gamma activity profile of the fuel pin revealed that the components of the pin were in their normal positions. The only unusual feature of the gross scan was the presence of five activity peaks along the fuel column portion of the pin. The source of these peaks could not be identified by spectral analysis of the gamma activity, and their origin will have to be sought during destructive examination of the fuel pin. Similar peaks were observed in one fuel pin from an earlier test in this series.[6] The peaks in that pin were associated

5. S. Langer et al., "Volatile Fission Product Migration and Plateout in GCFR Rod Irradiations," *Trans. Amer. Nucl. Soc.* 15, 850 (1972).

6. R. B. Fitts, E. L. Long, Jr., and D. R. Cuneo, "Postirradiation Examination of Capsule O4-P8," *GCR Program Semiannu. Progr. Rep. Mar. 31, 1970,* ORNL-4589, pp. 80–91.

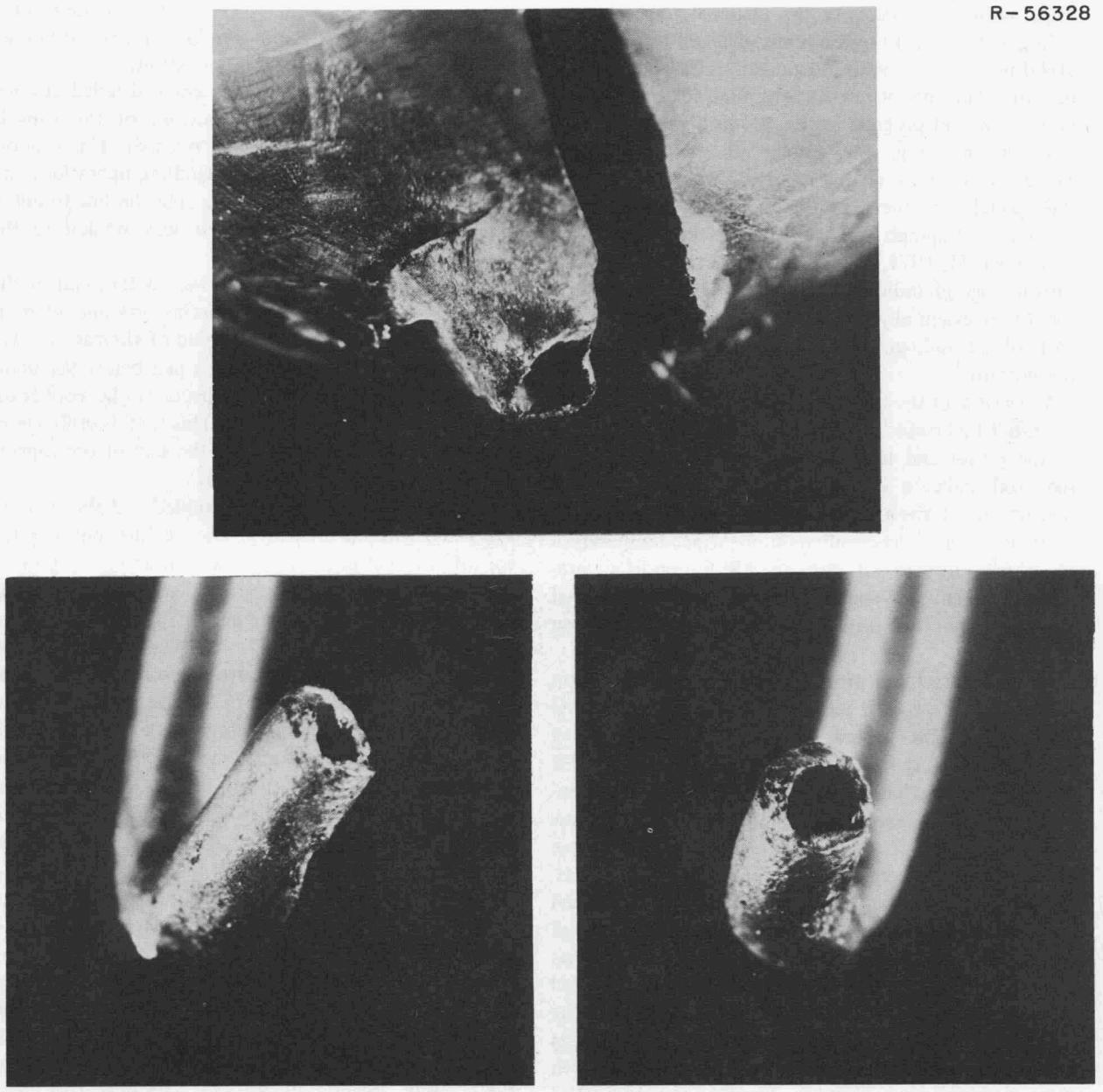

Fig. 14.3. Views of bottom of GB-9 capsule and broken gas line.

with a concentration of fission products, barium in particular, at the center of the fuel pellets. The NaI crystal used for gamma scans performed in the High-Radiation Level Examination Laboratory (HRLEL) at ORNL was not capable of resolving the ^{131}I gamma activity from the background of other fission products and activated components of the stainless steel cladding. This result was expected and was the main reason for sending the fuel pin to ANL for detailed postirradiation examination using a more sensitive Ge(Li) crystal gamma-ray detection system. The results from gamma scanning of the GB-9 fuel pin, including an initial iodine distribution scan made at ANL, are shown in Fig. 14.5. The results of the gamma spectrometry studies at ANL have been summarized by Langer et al.[5]

One sample of the GB-9 fuel pin was returned to ORNL from ANL for metallographic and microprobe

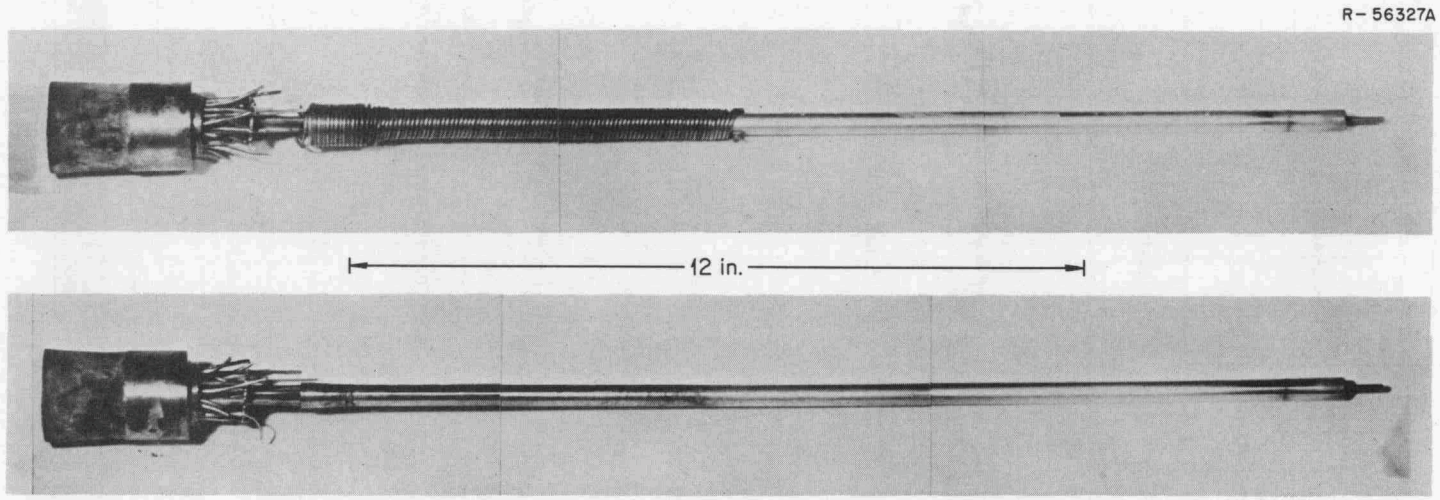

Fig. 14.4. Fuel pin from GCFR capsule GB-9 irradiated in the ORR to 54,000 MWd/metric ton.

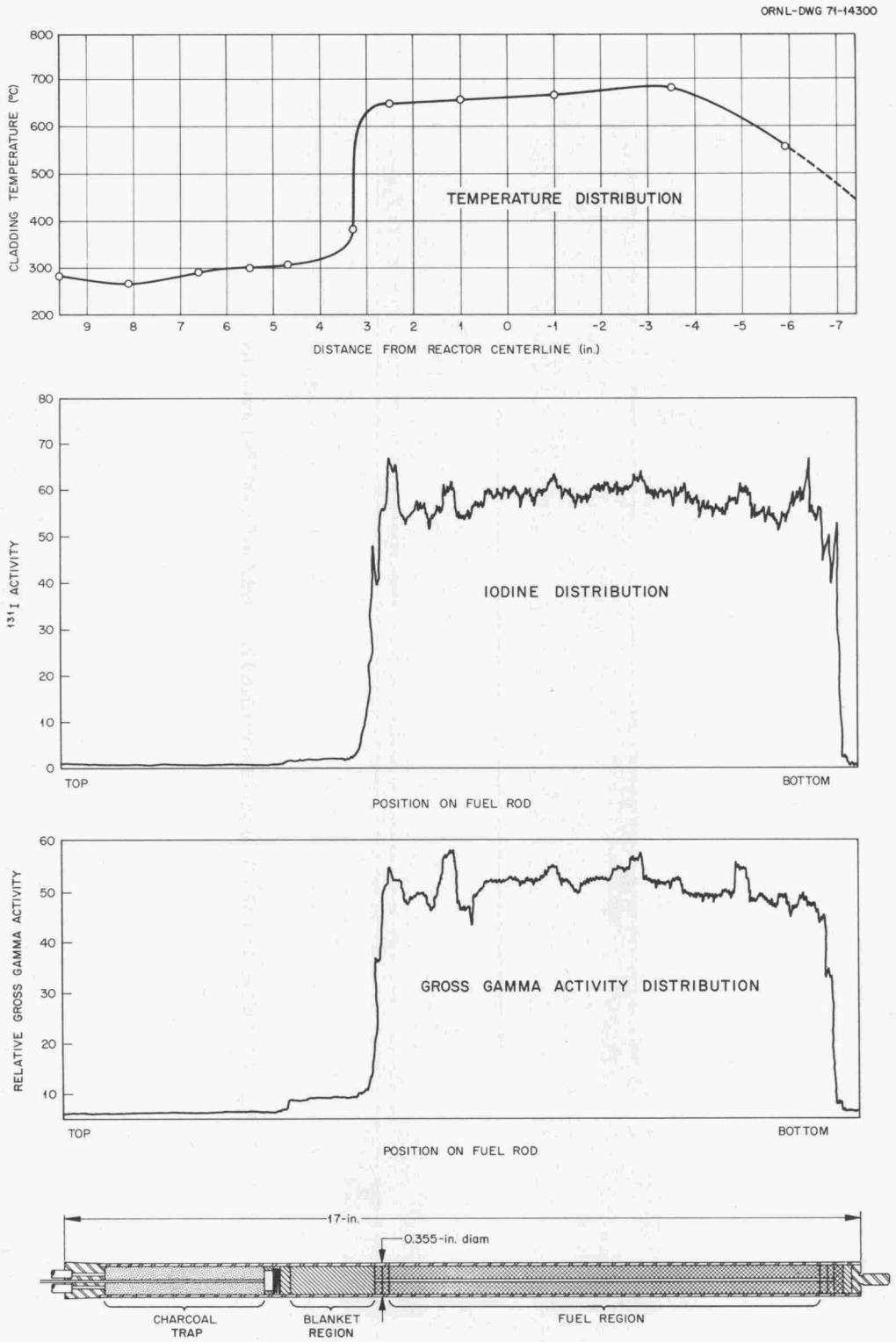

Fig. 14.5. Distribution of operating temperatures and postirradiation gamma activities along fuel pin GB-9.

analyses. This sample was taken from the fuel pin 4¾ in. above the bottom of the fuel column, near the region of maximum heat generation. This sample is being prepared and examined at ORNL for comparison with the earlier GCFR experiments examined here and to provide a comparison of the results obtained in an air-atmosphere hot cell (ORNL) with those obtained in an inert-atmosphere cell (ANL).

The only unusual microstructural feature noted in the preliminary metallographic examination of a transverse section from the GB-9 fuel pin was the presence of large amounts of metallic deposit at the fuel-cladding interface. After regrinding and repolishing the specimen, the metallic deposit was no longer present, indicating that the locations of these deposits are spotty and unpredictable.

The appearance of the transverse section after repolishing is shown in Fig. 14.6. Examination of this section revealed significant attack of the inner surface regions of the 0.065-cm (25-mil) thick type 316

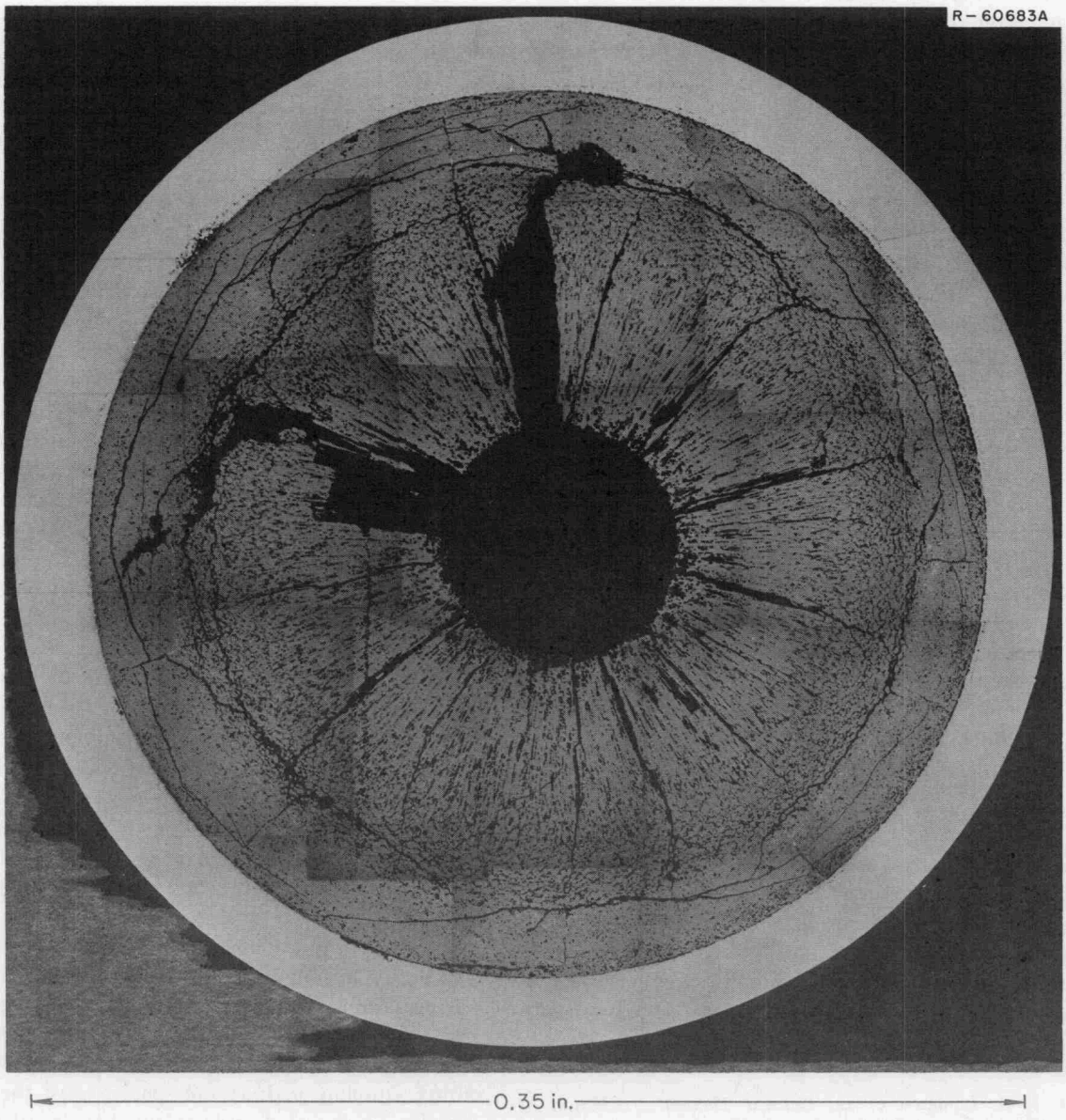

Fig. 14.6. Appearance of the transverse section from fuel pin GB-9. As polished.

stainless steel cladding. The attack varied in depth from about 1 to 4 mils. The attack of the cladding was intergranular, and in the regions of the most severe attack the grains were consumed and replaced by corrosion products (Fig. 14.7). The regions of the most severe attack occurred on the cooler side of the fuel rod. The cooler side was indicated by the movement of the central void in the fuel toward the hotter side of the fuel pin. Columnar grains began at the edge of the central void and continued to within ~0.115 cm (~45 mils) of the outer surface of the fuel. This observation compares favorably with a calculated temperature of ~1675°C. Varying degrees of restructuring in the form of equiaxed grain growth and porosity redistribution occurred in a 0.115-cm (45-mil) band in the peripheral region of the fuel. A concentration of metallic fission products was noted about 0.065 cm (25 mils) from the outer surface of the fuel.

We have been able to compare our metallographic results obtained by preparing a GB-9 specimen in air using aqueous polishing vehicles with those obtained by ANL on the adjacent GB-9 specimen in an inert atmosphere using nonaqueous polishing vehicles. There is no significant difference in the apparent structure of the specimens except that the specimen polished in the aqueous vehicle was somewhat superior in appearance, which is to be expected. It has been our experience that the use of nonaqueous vehicles results in exaggeration of porosity and relief between fuel and cladding by the time the fuel has been polished sufficiently to eliminate all artifacts introduced during the grinding process. We plan to perform an electron microprobe analysis on the ORNL specimen and compare our results with those of Argonne to determine if there are any significant differences in these analyses caused by the two methods of sample preparation.

14.3 DESIGN AND OPERATION OF GCFR-ORR CAPSULE GB-10

A. W. Longest J. A. Conlin

Capsule GB-10, a follow-up irradiation experiment to capsule GB-9, is presently under irradiation in the ORR poolside facility. The capsule was designed[7] further to evaluate the performance of the GCFR vented-and-pressure-equalized fuel rod. Using the experience gained from operation of capsule GB-9, capsule GB-10 was designed to provide the more detailed fission product release and transport information needed in both the GCFR and LMFBR development programs. Included for the first time is the capability for measuring the fission gases released directly from the mixed-oxide fuel during irradiation. In addition to studying the gaseous fission product release behavior, a major objective of capsule GB-10 is to obtain additional needed information on the release, transport, and trapping of the volatile fission products.

14.3.1 Description of Capsule

The GB-10 fuel rod (Fig. 14.8) is a shortened prototype of a GCFR vented-and-pressure-equalized fuel rod. It consists of a 9-in.-long $(U,Pu)O_2$ fuel column, a 2-in.-long upper blanket region of depleted UO_2 pellets, and a 1-in.-long charcoal trap above the blanket, all enclosed in 0.353-in.-OD, 0.305-in.-ID type 316 stainless steel cladding. The two UO_2 half pellets at each end of the mixed-oxide column were included to suppress power peaking at the end of the test fuel.

The GB-10 fuel rod is similar to the GB-9 rod but has a roughened outer surface and contains solid instead of hollow $(U,Pu)O_2$ fuel pellets. The fuel column smear density is 84% of theoretical compared with 85% in the GB-9 rod. The fuel stack height is slightly less than in the GB-9 rod, the upper blanket region of depleted UO_2 pellets is one pellet longer, and the charcoal trap is 1 in. long instead of 3 in. The charcoal trap was shortened to 1 in. in GB-10 to provide the same potential fission product loading as the rod trap in the reference GCFR rod; that is, the trap contains the same ratio of charcoal mass to power generated within the rod as the reference design.

Five sweep gas lines are built into the GB-10 rod. Four enter through brazed joints in the top end plug. Two of these lines terminate inside the top end plug, which has passages connecting the two lines to the top of the charcoal trap. A third line terminates at the bottom of the trap, and the fourth line terminates near the bottom of the upper blanket region. The fifth line enters through the bottom end plug and is welded to its top side.

The five sweep gas lines are connected to a 1000-psig high-purity helium sweep gas system by means of the valving arrangement shown in Fig. 14.9. The normal sweep flow mode is with passage of the continuously flowing gas in and out of the top end plug. However, during sampling periods and special tests, the capsule can also be operated under a number of other sweep flow modes, including passage of the sweep through the

7. J. R. Lindgren et al., *Planned Thermal Irradiation of Manifolded-Vented $(U,Pu)O_2$-Fueled Rod in ORR Capsule GB-10*, GA-A12123 (1972).

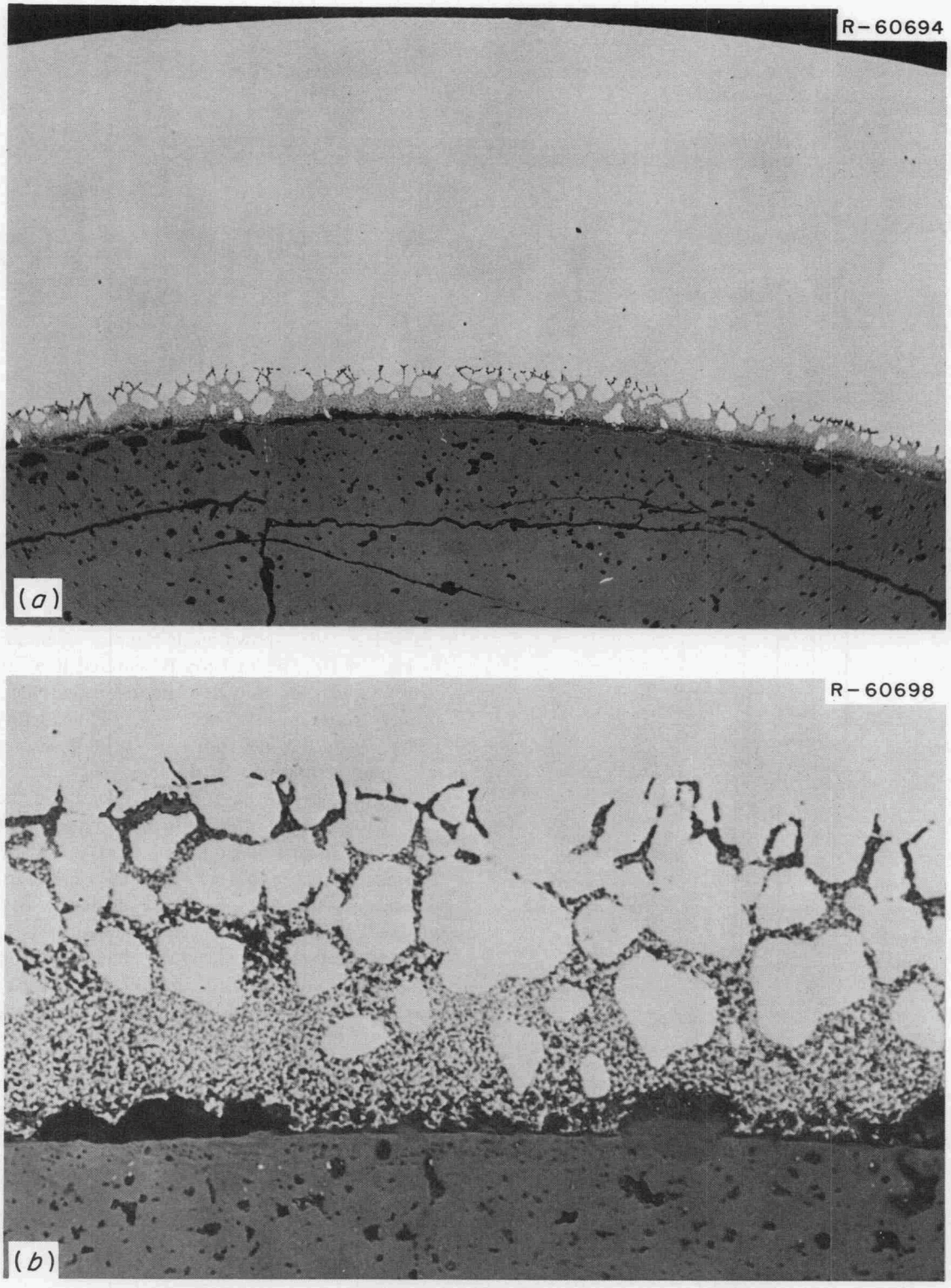

Fig. 14.7. Appearance of typical fuel-cladding interfaces from mixed-oxide fuel pin GB-9. As polished. (*a*) 100×; (*b*) 500×.

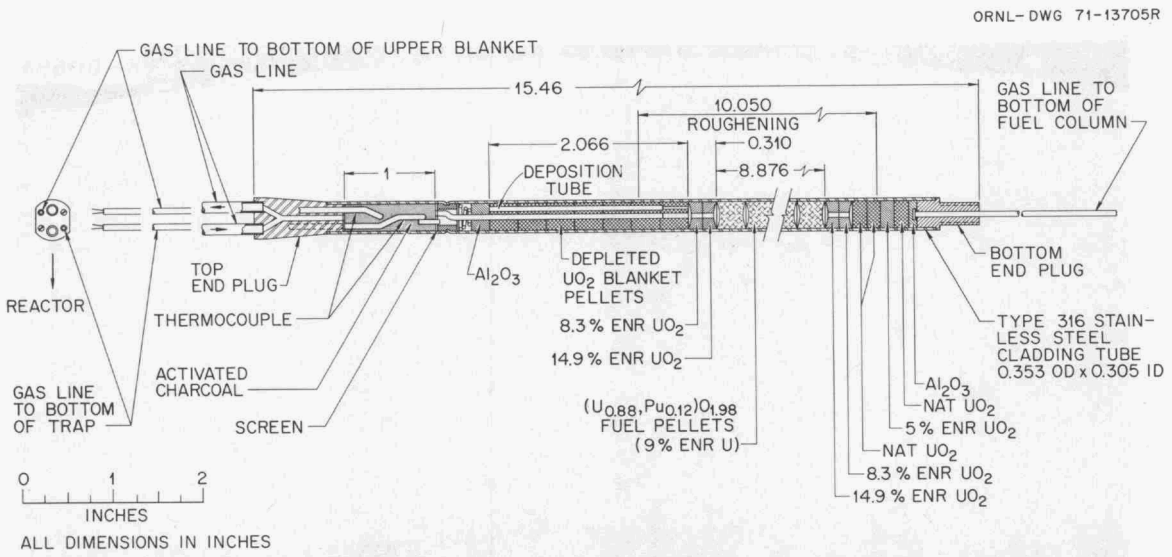

Fig. 14.8. Fuel rod specimen for irradiation in GCFR-ORR capsule GB-10.

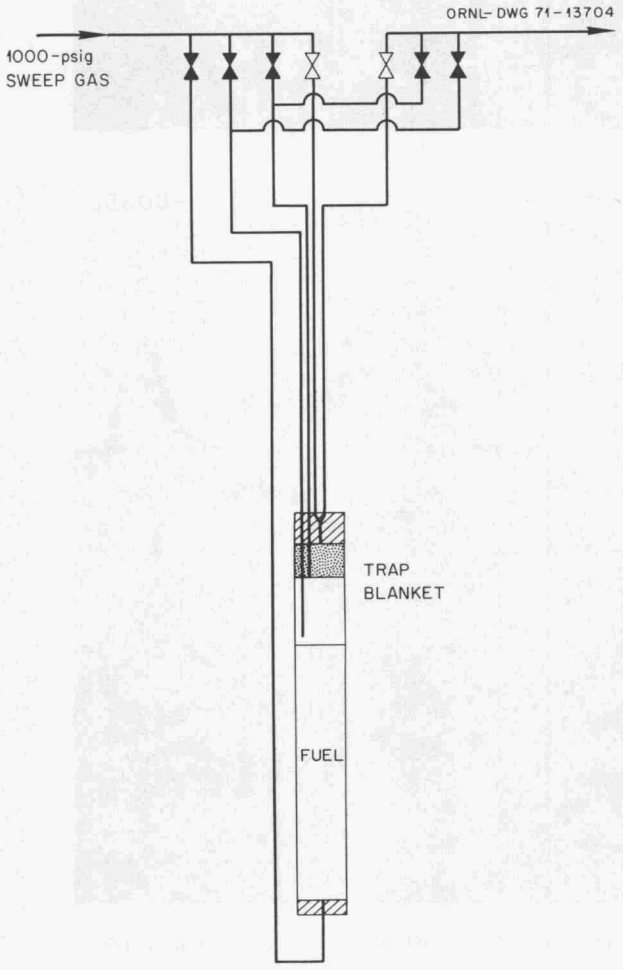

Fig. 14.9. Sweep lines for GCFR-ORR capsule GB-10.

fuel region. The latter sweep flow mode simulates the fission product release behavior of a GCFR fuel rod with a cladding leak in the fuel zone.

The test rod is shown inside the instrumented capsule in Fig. 14.10. The fuel rod is centered in a Zircaloy-2 sleeve, which in turn is centered inside the capsule primary containment. The capsule is filled with NaK to a level above the fuel rod, and a helium gas pressure of 975 psig is normally maintained over the NaK. An electrical heater formed into a coil around the upper end of the Zircaloy-2 sleeve is used to maintain the trap and upper blanket region of the rod at 300°C. Eleven thermocouples are located inside the capsule at various points along the rod, and two are located on the outside of the capsule secondary containment. The thermocouples used to monitor the fuel region cladding temperature enter through the Zircaloy-2 sleeve and are staked into place with their junctions near the inside surface of the sleeve.

The sweep and cladding external gas systems for capsule GB-10 are shown in Fig. 14.11. Flow through the sweep system (150 to 1300 cm^3/min STP) is regulated by adjusting the downstream flow resistance with a needle valve. An automatic pressure control valve adjusts the inlet sweep flow and maintains the sweep pressure 25 ± 0.1 psi above the pressure in the normally static gas system external to the cladding.

Fission-gas release from the rod is monitored by taking gas samples periodically and analyzing the samples by gamma-ray spectrometry. The effluent

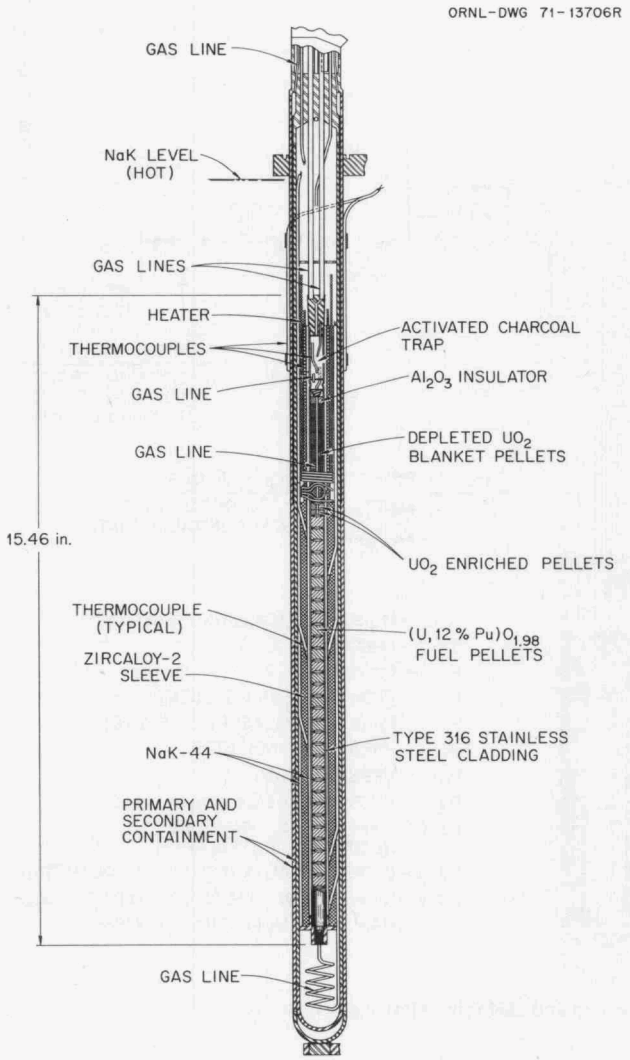

Fig. 14.10. GCFR-ORR capsule GB-10.

sweep line activity is monitored continuously by two ionization chambers (see Fig. 14.11).

The planned steady-state full-power operating conditions for capsule GB-10 are summarized in Table 14.1. In addition to measuring the fission-gas release under steady-state conditions, special tests are planned to determine release behavior as a function of operating temperatures and sweep pressure. Other special tests will be performed during shutdown periods to obtain information on fission product decay heating of the charcoal trap and deposition of released iodine in the three main regions of the rod (trap, blanket, and fuel).

A photograph of the fuel rod assembly taken before the primary and secondary containment vessels were

Table 14.1. GCFR-ORR capsule GB-10 planned operating conditions

Steady-state design conditions	
Cladding outer surface temperature, °C	
Fuel region, peak	685 ± 15
Mid region of upper blanket region	~350
Charcoal trap	300
Fuel region heat-generation rate, kW/ft	
Peak	14.8
Average	14.0
Thermal-neutron flux (equivalent 2200 m/sec), neutrons cm^{-2} sec^{-1}	$\sim 1.4 \times 10^{13}$
Cladding pressure, psig	
External	975
Internal	1000
Planned exposure	
Irradiation duration at power, days	~660
Burnup of $(U,Pu)O_2$, MWd/metric ton	~75,000
Fast-neutron exposure ($E > 0.18$ MeV), neutrons/cm^2	$\sim 7 \times 10^{19}$

installed is shown in Fig. 14.12. Closeup views of the lower and upper ends of the assembly are shown in Figs. 14.13 and 14.14 respectively.

Preirradiation neutron radiographs were taken of the capsule on July 28, 1972, at 0, 45, and 90° orientations. These radiographs will be used for comparison with later neutron radiographs to be taken several times during the irradiation period.

14.3.2 Calculated Temperature Profile

Calculated axial temperature profiles through capsule GB-10 are shown in Fig. 14.15 for radii corresponding to the inner and outer surfaces of the fuel rod cladding. In the region of the charcoal trap, the cladding temperature can be varied over the range 200 to 400°C by adjusting the output of the capsule heater. By adjusting the capsule position in the facility, the peak cladding outer surface temperature (as estimated from the readings of the thermocouples monitoring the fuel region) can be maintained within a ±15°C range of the desired operating point.

The cladding temperature profile is reasonably typical of that of a GCFR rod except at the lower end. Temperatures below the 5%-enriched UO_2 pellet are not typical. The downward flow of hot coolant gas in the GCFR will keep the lower blanket and bottom end of the GCFR rod at a higher temperature than that of

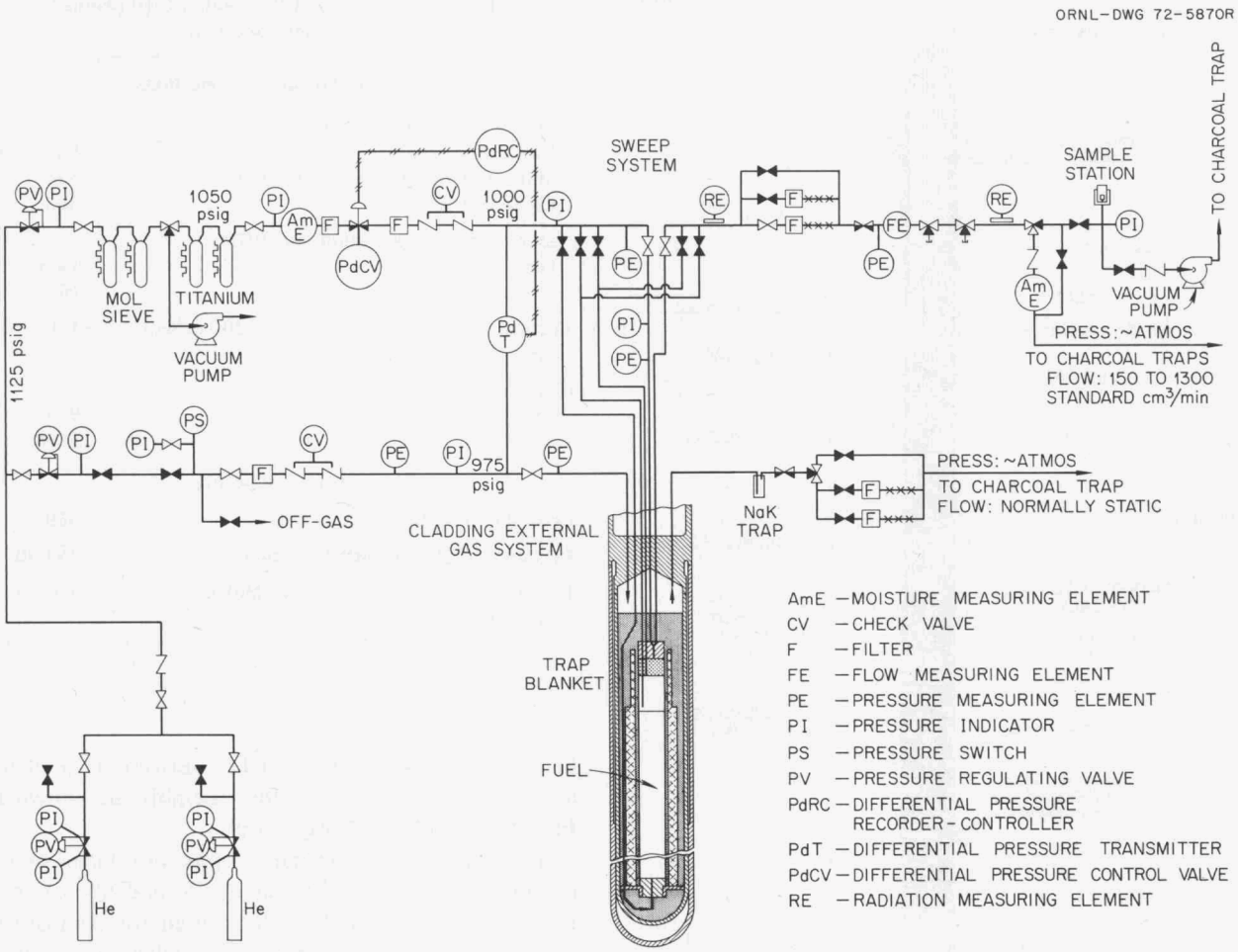

Fig. 14.11. GCFR-ORR capsule GB-10 sweep and cladding external gas systems.

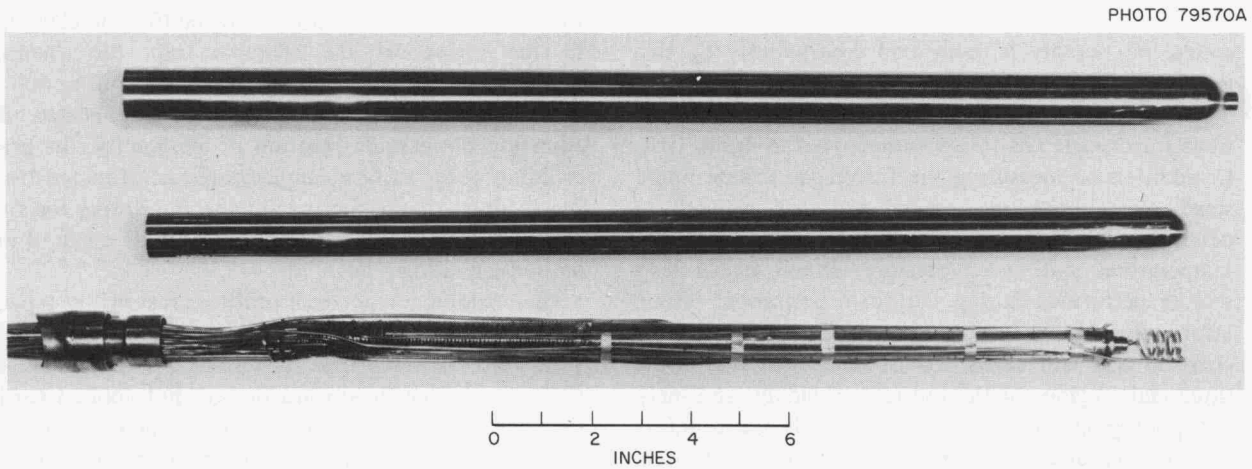

Fig. 14.12. Capsule GB-10 fuel rod assembly.

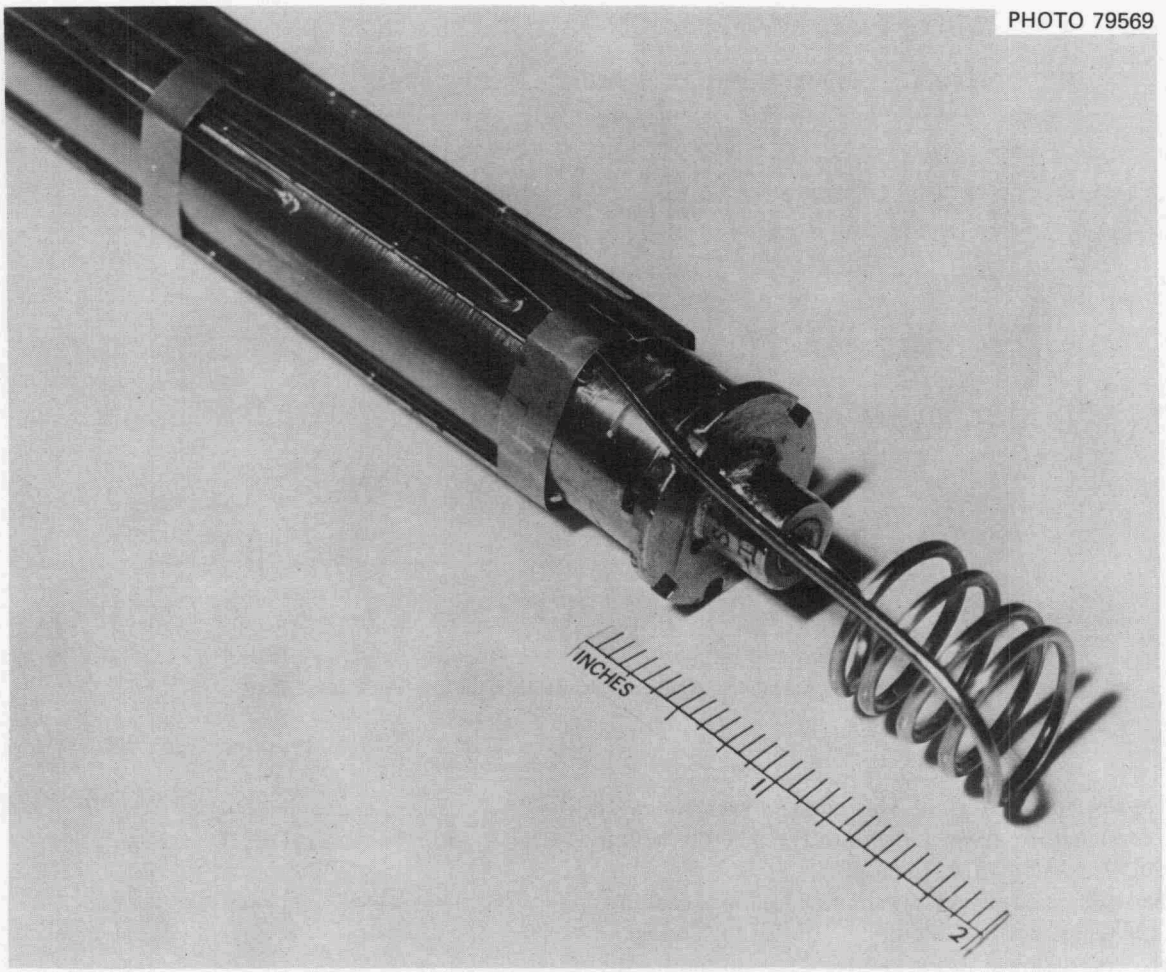

Fig. 14.13. Lower end of capsule GB-10 fuel rod assembly.

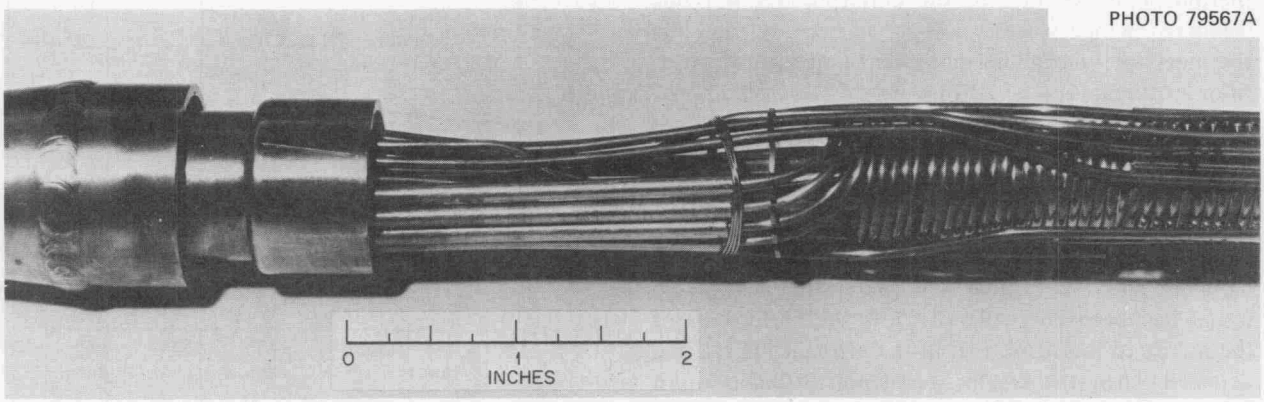

Fig. 14.14. Upper end of capsule GB-10 fuel rod assembly.

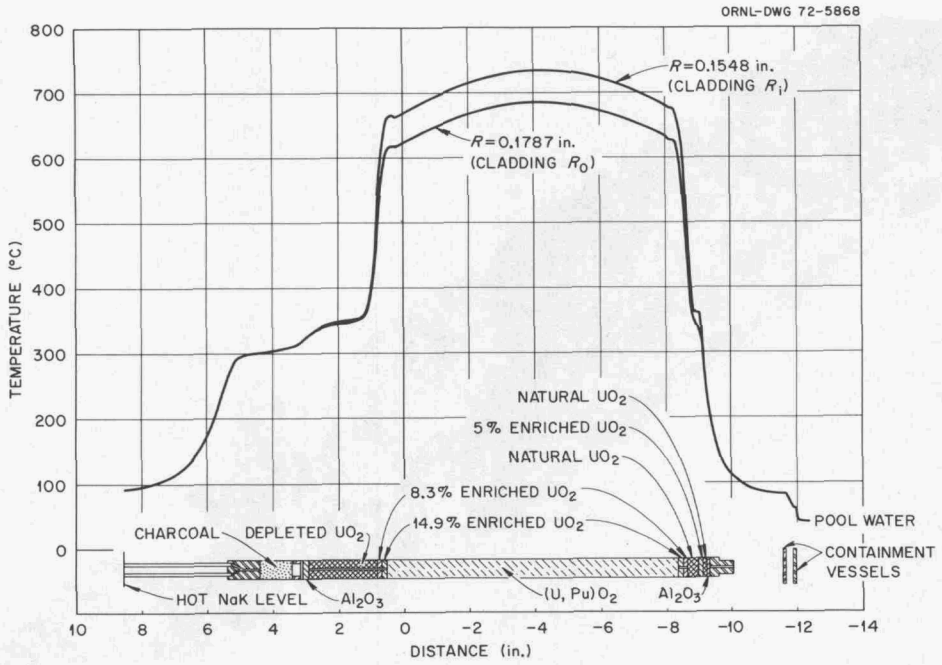

Fig. 14.15. Calculated axial temperature distributions for capsule GB-10.

the upper blanket region. This cooler lower region is not expected to have a significant effect on fission product transport within the rod.

The calculated angular variation of the cladding surface temperature at the middle of the fueled region of the rod is shown in Fig. 14.16. Also plotted in this figure is the angular temperature distribution at the approximate radial location of the thermocouples monitoring the fuel region cladding temperatures. Detailed calculations of the radial and angular distributions of power and temperature are required to relate the thermocouple readings to the corresponding hot side cladding temperatures.[7] The uncertainty in the thermocouple-to-cladding hot side temperature corrections is estimated to be ±20°C.

14.3.3 Startup of Experiment

We had planned to start the irradiation on August 8, 1972, after the sweep system had been purged free of moisture and the capsule and gas system instrumentation had been checked out. However, an increase of the indicated moisture level in the effluent helium was detected when the system was depressurized prior to the August 8 reactor refueling shutdown. It was found that the indicated moisture level increased from ~3 to ~30–200 ppm when the system was depressurized

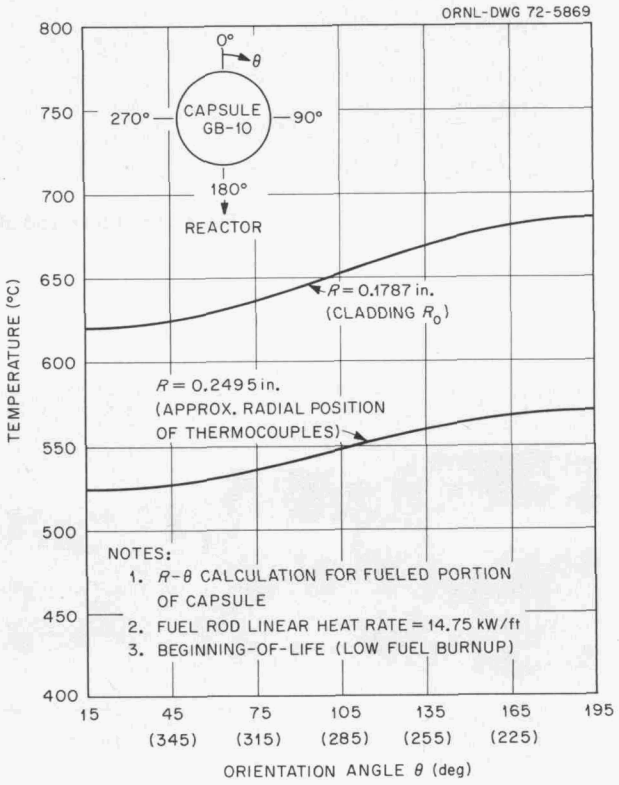

Fig. 14.16. Calculated angular temperature distributions for capsule GB-10.

from 1000 to ~20 psig, with the increase starting abruptly after the sweep system pressure reached ~200 to 300 psig. This behavior was similar to that which would be expected if moisture were present in a side leg of the main piping. Thus, we decided to postpone the startup until the moisture indication could be reduced or the behavior satisfactorily explained.

Repeated depressurizations did not prove to be an effective method for removing the moisture. Therefore during a reactor refueling shutdown on August 22, 1972, a valve was installed in the GB-10 effluent sweep line downstream of the gas-sampling station to permit evacuation of the sweep system. Three evacuations of the sweep system were conducted with the effluent passing over the downstream moisture probe in each case. During the first evacuation, the moisture indication increased from a dew point of ~−71 to ~−19°C, which indicated that moisture was present in one section of the piping. After a second evacuation during which heat was applied to part of the system, the sweep system was then pressurized to 1000 psig and purged overnight under a constant pressure at a slow sweep flow rate; the next day the system was depressurized from 1000 psig to a vacuum. There was no increase of the indicated moisture level during the depressurization and only a small increase as the system was evacuated.

The capsule irradiation was started on August 29, 1972, by slowly inserting the capsule first in 25°C, then in 50°C, and finally in 100°C steps until a fuel rod power of 12 kW/ft was reached (565°C peak cladding outer surface temperature). The sweep was passed through the fuel region during the startup. There was only a slight increase (from ~0.9 to 1.2 ppm) in the indicated moisture level of the effluent helium during heatup of the fuel. The indicated moisture levels at the start of the irradiation were ~0.035 ppm upstream of the capsule (at 1000 psig pressure) and ~0.90 ppm downstream of the capsule (at ~10.5 psig).

The effluent sweep line activity increased to an indicated 800 mR/hr during the initial capsule startup. The indicated line activity responded to each temperature increase and became increasingly sensitive to temperature as the fuel rod power of 12 kW/ft was approached. Following each temperature increase, the line activity increased and leveled off in a smooth manner. Soon after reaching 12 kW/ft, the sweep flow was valved across the top of the fuel rod, which is the normal flow mode during nonsampling periods. Under this sweep flow mode the steady-state line activity was ~20 mR/hr at a sweep flow rate of ~200 cm^3 STP/min.

While flowing 1000 psig helium through the fuel region during the initial startup, we observed variations of the pressure differential across the fuel rod and ~70 ft of the 0.027-in.-ID inlet sweep line. Pressure-drop calculations indicate that the ~70 ft of inlet sweep line accounts for about 4 to 5 psi of the total measured pressure differential for the conditions of 1000 psig pressure and ~1000 cm^3 STP/min flow rate. In addition, operation under the various flow modes has shown that the upper blanket and charcoal trap sections of the rod offer negligible resistance to flow compared with the path through the fuel region. The pressure differential, which is at present limited in accuracy, was initially ~65 psi at the startup sweep flow rate of ~1000 cm^3 STP/min and remained constant during the early part of the capsule heatup. The differential then behaved as follows: (1) decreased from ~65 to ~25 psi as a fuel rod power of ~9 kW/ft was approached and remained constant at ~25 psi during a 1-hr hold at ~9 kW/ft, (2) fluctuated between ~25 and ~70 psi for a period of 30 min while the fuel rod power was increased from 9 to 12 kW/ft and for another 30 min after reaching 12 kW/ft, and (3) stabilized at 25 psi. Subsequent intermittent measurements of the pressure differential show a gradual decrease to ~10 psi or slightly less during the first few weeks of irradiation with no further detectable change.

The operation of GB-10 will be continued at the reduced fuel rod power level of 12 kW/ft (565°C peak cladding outer surface temperature) until the fission-gas release rates become constant with time or fuel burnup reaches about 25,000 MWd/metric ton, whichever comes first. Subsequent operation will include an intermediate power level of 13.5 kW/ft (630°C peak cladding outer surface temperature) and finally the full-power level of 14.8 kW/ft (685°C peak cladding outer surface temperature) for the remainder of the 2¾-year irradiation to a fuel burnup of 75,000 MWd per metric ton of heavy metal. This plan for the irradiation was agreed upon by persons representing GCFR and LMFBR interests in the experiment and is designed to best meet the needs of both programs.

The first set of sweep gas samples were taken on August 31, 1972, after the fuel rod had operated at 12 kW/ft for ~40 hr. Samples were taken under five different sweep flow modes, including passage of the gas through the fuel region and out of the line that terminates at the bottom of the upper blanket region (see Fig. 14.9). With GB-10 we can obtain measurements under ten different sweep flow modes; however, we routinely use only four or five of the more important flow modes, as indicated in the following section.

14.3.4 Steady-State Release Rates at Low Burnup

The results of gas release measurements made under steady-state conditions during the period from startup to the end of November 1972 are shown for four of the GB-10 sweep flow modes in Figs. 14.17–14.20. In calculating the fractional release values (R/B) plotted in these figures, the birth rate B of each isotope was assumed to be at its equilibrium value corresponding to the total fuel rod power at the time of sampling in all

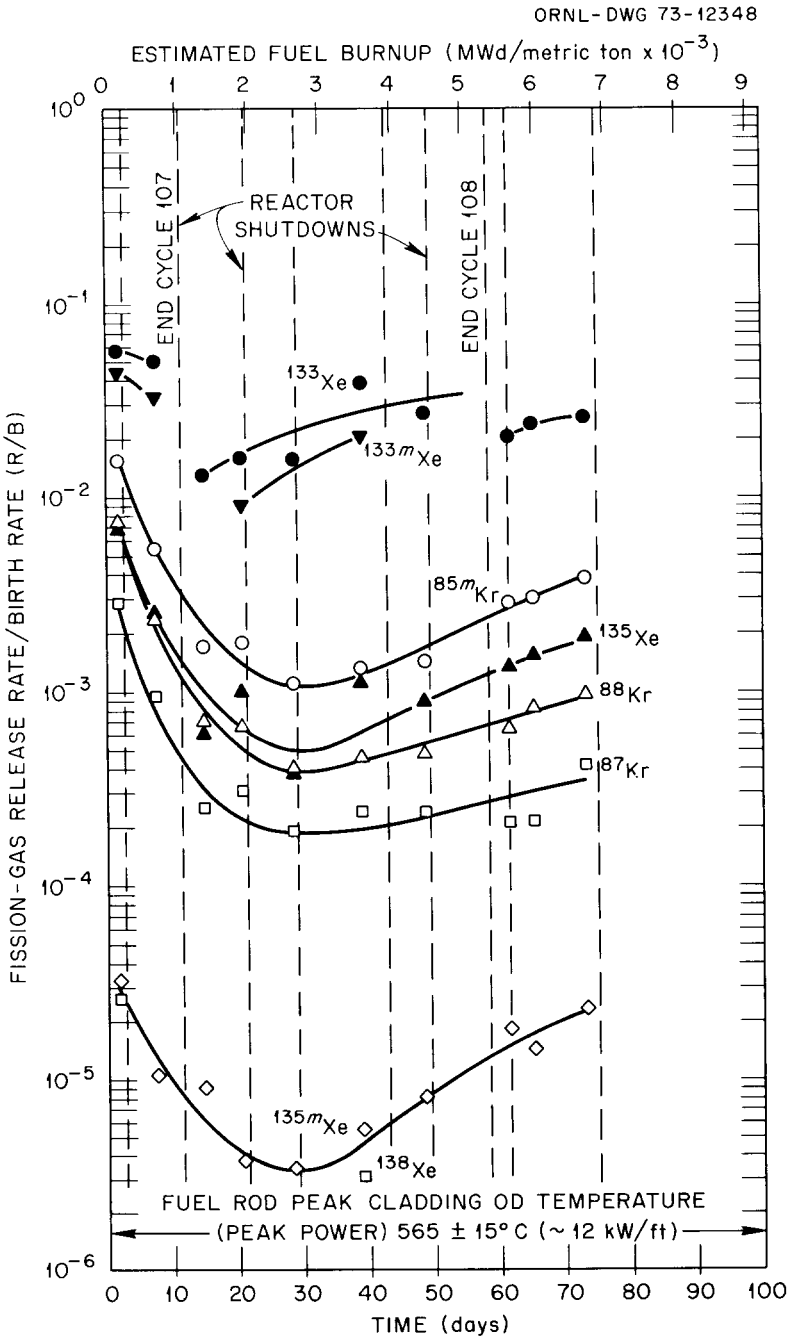

Fig. 14.17. Steady-state fission-gas release from GB-10 fuel rod vs time for sweep flow mode TT-TT.

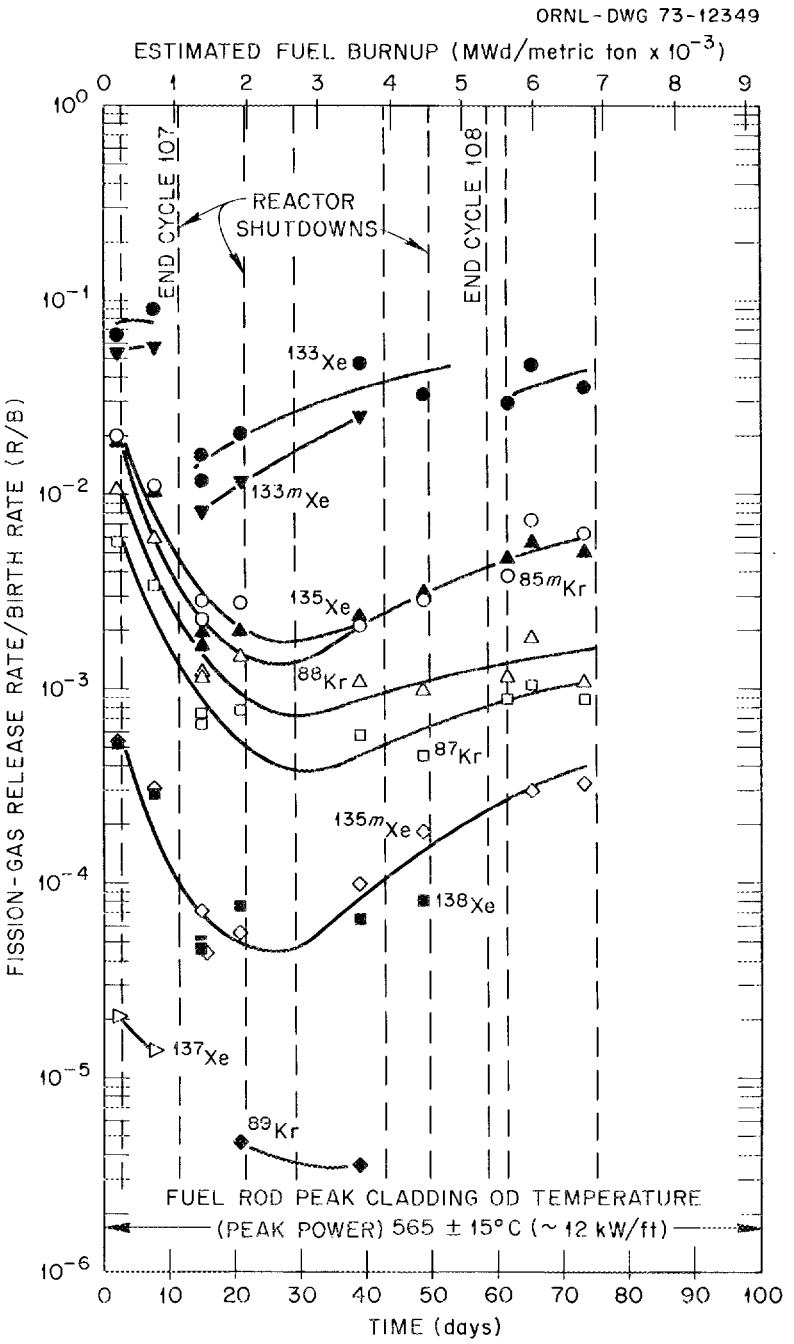

Fig. 14.18. Steady-state fission-gas release from GB-10 fuel rod vs time for sweep flow mode TT-BT.

cases. The various GB-10 sweep flow modes are abbreviated in these figures as follows:

TT-TT, TT-BT, etc., denote sweep flow mode; that is, the first set of two letters denotes the inlet line being used and the second set the effluent line being used;

TT denotes a line to top of fuel rod trap (actually to top end plug);

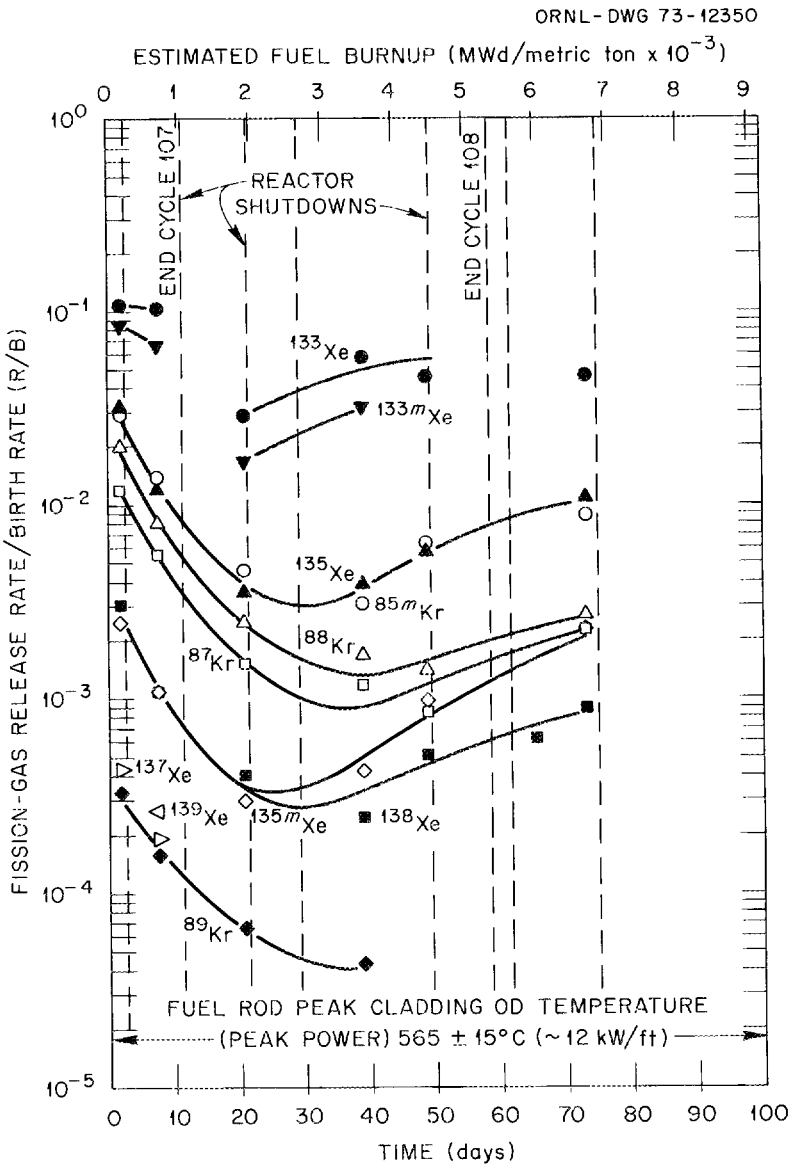

Fig. 14.19. Steady-state fission-gas release from GB-10 fuel rod vs time for sweep flow mode TT-BB.

BT denotes the line terminating at the bottom of the trap;

BB denotes the line terminating near the bottom of the upper blanket region;

BF denotes the line to the bottom of the fuel rod.

In taking the gas samples under the steady-state operating conditions, the normal sampling order is to start at the top of the rod (TT-TT sweep flow mode) and work downward so that the inventory of fission products below the sweeping point in each case is not disturbed. Corrections are made for decay of the fission gases during their travel to the sampling point. Sweep gas travel times (measured on October 9–10, 1972) from the fuel rod to the sampling point range from 40 to 55 sec for the various sweep flow modes under the normal sampling flow rate (~1200 cm^3 STP/min) and sweep-system pressures.

Figures 14.17–14.20 show an interesting trend in the fission-gas release from the mixed-oxide fuel. During the first month of irradiation, the relatively high initial fission-gas release rates decreased by a factor of about

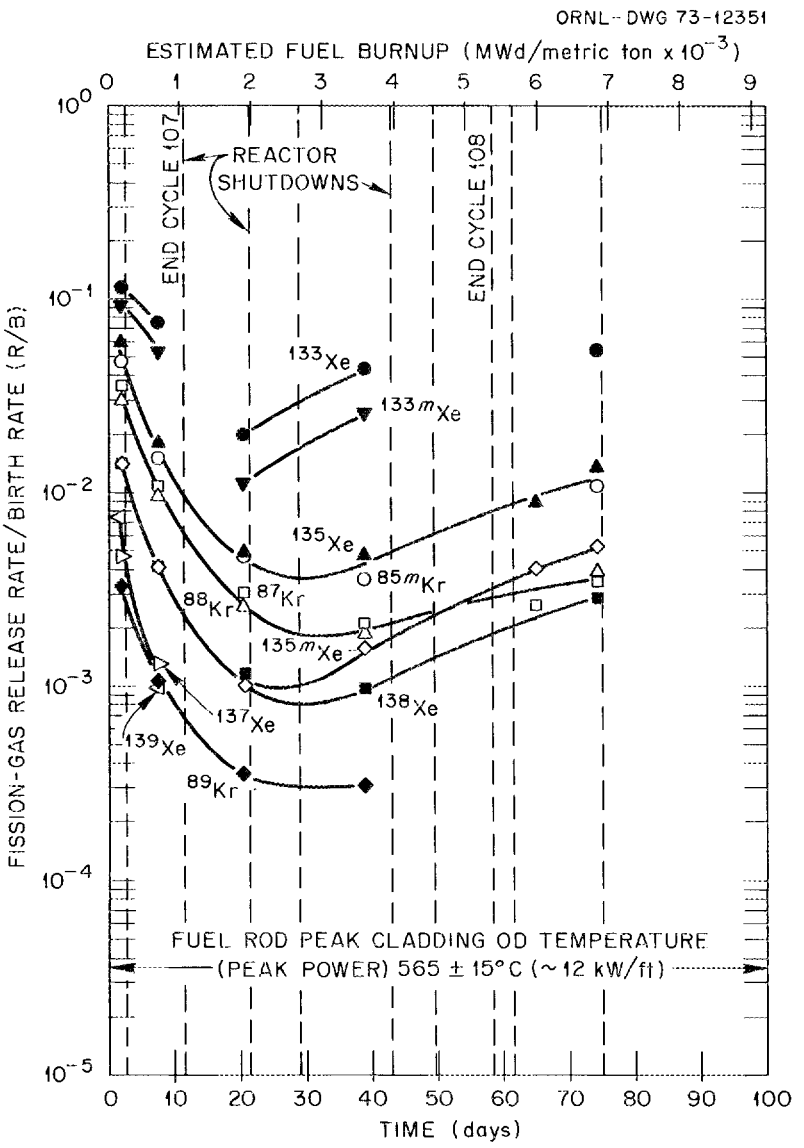

Fig. 14.20. Steady-state fission-gas release from GB-10 fuel rod vs time for sweep flow mode BF-BB.

10. The release rates leveled off and then started an increasing trend which continued to the end of November. Release rate calculations for several more-recent sets of samples are incomplete at this time; however, the effluent sweep-line activity monitors have indicated a leveling-off trend in the activity release rate in December. In general, the effluent sweep-line activity data show good consistency with the gas sample data.

The steady-state release data obtained early in the irradiation of capsule GB-9 were reviewed and compared with the GB-10 release data. In the case of capsule GB-9, the first set of gas samples were taken after three days at full power of ~14.8 kW/ft. Subsequent samples indicated a rise in fission-gas release rates which continued until the release rates leveled off at ~10,000 to 15,000 MWd/metric ton burnup. The data from the effluent sweep-line activity monitors, however, showed that at the beginning of the irradiation the initial activity release rate decreased by almost a factor of 2 the first two days at full power. The line activity then leveled off and started the long-term increasing trend. Thus, this transient period appears to be much longer and more pronounced at the lower power level of GB-10 (12 kW/ft vs 14.8 kW/ft). The difference in

the initial condition of the fuel is probably a big factor in the early release behavior (~87% dense solid pellets in GB-10 vs ~91% dense hollow pellets in GB-9 with about the same fuel-column smear density as GB-10). The reasons for the early release behavior in the two experiments are not known but are believed to be associated with changes in the fuel and fuel temperature distribution resulting from fuel restructuring, formation of a central hole, and changes in the pellet-to-cladding gap. The observed release behavior in the two experiments offers an opportunity for checking and possibly refining theoretical release models currently in use.

14.3.5 Transient Conditions and Special Tests

In addition to the fission-gas release measurements obtained to date under the steady-state operating conditions, the activity release from the GB-10 rod has been monitored during two rapid cool-off periods (reactor scrams) and two heatup periods with the sweep passing through the fuel region. The first shutdown test was conducted on September 1, 1972, after the fuel rod had been at power for 3 days, and the second test was conducted on September 28, 1972, after the fuel rod had been at power for 22 days. The release behavior was the same during both shutdowns. In each case, there was a small, short-duration spike of ~20 to 30% increase in the effluent sweep line activity upon shutdown followed by rapid decay of the line activity to a background level. The amount of activity released during the spikes or bursts was insignificant (short duration) compared with the activity released during steady-state operation. During the startup periods, the indicated line activity responded to each temperature increase and leveled off in a smooth manner. The release behavior was similar to that during the initial capsule startup in that there were no obvious burst-type releases of activity upon heatup of the mixed oxide fuel.

We plan to conduct special tests as the irradiation progresses. These special tests will be designed to determine release dependence on the sweep pressure and to obtain information on iodine transport and plate-out in the three main regions of the rod and possibly on some of the sweep lines.

We have some evidence suggesting that iodine can be transported a significant distance through the small-diameter sweep lines if the sweep-gas flow rate through the fuel column and sweep lines is fast enough. While taking a set of gas samples on November 29, 1972, an instability in the sweep-gas flow rate occurred which allowed the gas leaving the rod to pass through the effluent line at a somewhat faster rate than normal. At the time this occurred, the sweep gas was being passed through the fuel column and out of the line that terminates near the bottom of the upper blanket region (sweep flow mode BF-BB). Following the sampling period, the sweep flow mode was returned, as is our normal practice, to the condition where the sweep passes across the top of the fuel rod trap (TT-TT). However, the effluent-line activity at the first downstream radiation monitor did not decay back to its normally low level in 2 to 3 hr as is usual. Instead of indicating the presence of only short-lived deposited activity on the line, the radiation monitor indicated longer-lived activity, which decayed in a manner that suggested iodine isotopes may have been transported through the ~70 ft of 0.027-in.-ID line at pool water temperature to the monitor. It may be possible to obtain additional information on iodine transport in special tests by increasing the flow rate and/or operating at lower sweep pressures.

We later determined that the flow instability that occurred during the BF-BB sampling on November 29, 1972, was caused by a flow restriction (or partial plugging) in a section of the bottom of the blanket (BB) effluent line located in the poolside facility valve box. After this section of line first became restricted on November 29, the restriction twice disappeared but returned shortly thereafter in each case. Each time the restriction disappeared it allowed gas from the rod to pass through the lines at a faster rate than normal until the pressure behind the restriction built back to normal. Since November 29, a similar partial restriction developed each time the BF-BB flow mode was used but with no recurrence of the line becoming temporarily unrestricted while under the BF-BB flow condition or of the apparent deposition of long-lived activity on the lines at the monitor in the valve box. When the sweep flow mode is changed to BF-BB, the flow rate drops off about 25% in 2 hr. Thus the restriction is not considered to be a serious problem at this time. There has been no evidence of a tendency for the lines to plug under any of the other GB-10 sweep flow modes. In fact, after one week of operation under the TT-TT sweep flow mode prior to a sampling period, the BB effluent line is again unrestricted, and the partial restriction only redevelops when the BF-BB flow mode is used.

On December 23, 1972, the ORR reactor power increased to ~120% (~36 MW) of nominal full power (30 MW). Abnormal operation of the servo-control system caused one of the shim rods to withdraw slowly

until an automatic reverse in power at the 120% of full power level took place. A manual scram was initiated by the operator. This abnormal occurrence was described in Incident Report No. ORNL-72-73. The GB-10 fuel rod received the same percentage increase in power (from ~12 to ~14.4 kW/ft). The duration of the power increase was very short, and we believe the actual time at increased power was much too short to have any effect on the GB-10 fuel structure (thermocouple temperatures spiked only about 25°C out of about 430°C).

14.3.6 Decay Heating in Charcoal Trap

Based on the early operation of the GB-10 fuel rod at the reduced power of 12 kW/ft, it appears that the release of volatile fission products and the resultant heat load on the GCFR trapping system will be much lower than expected under the "leaking rod" condition. We have observed no significant decay heating in the rod trap during or following operation under the BF-TT sweep flow mode. So far there has been no evidence suggesting the rod trap is needed either for reducing heat loads on the GCFR trapping system or for protecting the manifold passages against plate-out constriction or plugging. If this continues to be the case throughout operation of GB-10 at the higher power levels, the rod traps may be eliminated from the GCFR design.[8]

---

8. R. J. Campana et al., "The Effect of Irradiation Results on the GCFR Pressure Equalization System (Venting) Design," *Trans. Amer. Nucl. Soc.* **16**, 109 (1973).

15. GCFR Steam Generator Modeling Studies

O. W. Burke R. S. Stone

This work was initiated July 1, 1972. The purpose of the present task is to develop a hybrid computer model of the steam generator for a gas-cooled fast reactor (GCFR) and to use this model to simulate various system transients as well as steady-state operations. The simulation model will ultimately be used to evaluate the thermal transients in the steam generator and the design of the proposed control system. Transient results can be used as a basis for system modifications in the event that redesign is indicated. The results will also be helpful in evaluating the design of the rest of the system. The results obtained from this simulation model will be compared with those obtained from the Gulf General Atomic digital model.

A hybrid computer model of a once-through steam generator, operating in the supercritical range, previously developed by the author on another project,[1] is being modified so that it can be used to simulate the GCFR subcritical steam generator. The bulk of the modifications is associated with the addition of the two-phase relationships for the two-phase section of the GCFR steam generator.

The ORNL hybrid computer being used in this task consists of a solid-state analog computer interfaced to a digital computer. The analog computer is a state-of-the-art all-solid-state computer with a ±100-V reference. This equipment has the high-frequency response capability and the high-speed mode switching capability required of a modern hybrid computer. The size of the analog computer is indicated by the following list of equipment:

Equipment	Number of units
Summer-integrator	60
Summer	96
Reference digital-to-analog converter	8
Multiplying digital-to-analog converter	12
Digital coefficient unit	48
Servo-set potentiometer	68
Hand-set potentiometer	12
Quarter-square multiplier	16
Analog-to-logic comparator	24
Analog-to-digital converter with 32 multiplexer channels	1

The analog computer also has a large complement of patchable logic, including gates, flip-flops, counters, etc.

The digital computer is a modern 36-bit word computer with 32,000 words of fast memory (~1.45 μsec cycle time). It accepts either assembly language or FORTRAN IV programs. Communication with the analog computer is through FORTRAN callable subroutines.

The computer model of the steam generator was developed from a set of coupled nonlinear partial differential equations derived from the laws of conservation of mass, momentum, and energy pertaining to the counterflowing primary and secondary fluids. The equations, written in one space dimension x (the direction of water flow) and time t are the following. Conservation of mass (water):

$$\frac{\partial \rho}{\partial t} + \frac{\partial}{\partial x}(\rho v) = 0. \qquad (1)$$

1. O. W. Burke, *Hybrid Computer Simulation of the MSBR*, ORNL-TM-3767 (May 5, 1972).

Conservation of momentum (water):

$$\frac{\partial(\rho v)}{\partial t} + \frac{\partial(\rho v^2)}{\partial x} = -\frac{k\,\partial p}{\partial x} - cv^2. \tag{2}$$

Conservation of energy (water):

$$\frac{\partial(\rho h)}{\partial t} + \frac{\partial(\rho h v)}{\partial x} = k_1 H(\theta - T). \tag{3}$$

Conservation of energy (salt):

$$\frac{\partial \theta}{\partial t} + V_s \frac{\partial \theta}{\partial x} = \frac{Hk_2}{\rho_s c_p}(T - \theta). \tag{4}$$

The equations of state for water:

$$T = T(p, h);$$

$$\rho = \rho(p, h).$$

The variables used in the above equations are defined as follows:

T = water temperature, °F,

ρ = water density, lb/ft^3,

v = water velocity, fps,

p = water pressure, psi,

c = coefficient of friction,

k = constant used to make units consistent,

h = specific enthalpy of water, Btu/lb,

H = heat transfer coefficient, salt to water, Btu sec^{-1} ft^{-2} (°F)$^{-1}$,

k_1 = ratio of the surface area of a tube to the water volume in the tube, ft^{-1},

k_2 = ratio of the surface area of a tube to the salt volume adjacent to the tube, ft^{-1},

ρ_s = salt density (assumed constant), lb/ft^3,

c_p = specific heat of salt at constant pressure, Btu lb^{-1} (°F)$^{-1}$ (assumed constant),

θ = salt temperature, °F,

V_s = salt velocity, fps.

The partial differential equations were differenced in time, so that the resulting model is a continuous-space, discrete-time model. An iterative process is used to obtain a solution at each point in time.

The first part of the investigation was spent in improving the existing model. This preliminary task was performed at this particular time so that the effects of the changes could be more easily checked out, since we knew what results to expect, based on previous runs.

In the existing model, the single-phase supercritical steam properties are stored as tables in the digital computer. Since the GCFR steam generator operates in the subcooled, boiling, and superheated regions, new water-steam relationships had to be developed. In the subcooled region, the water properties are treated as if they are independent of pressure and are a function of enthalpy only. The water temperature, density, viscosity, thermal conductivity, and Prandtl number are generated on the analog computer diode function generators. The outputs from these devices are continuous in space. In the boiling or mixed-phase region, the water-steam properties are also generated on the analog computer. The saturation temperature, the densities of saturated liquid and saturated vapor, and the enthalpies of saturated liquid and saturated vapor, as functions of water-steam pressure, are generated on diode function generators. Function generators are also used to generate the saturated liquid and saturated vapor values for the viscosity, the thermal conductivity, and the Prandtl number as functions of the saturation temperature. The steam quality in the two-phase region is generated on the analog computer using these property values.

Circuitry was developed on the analog computer to detect the points in space where the fluid reaches saturated conditions and where the quality reaches a value of 1.00. This circuitry generates logic signals that are used in the digital program to branch to the calculations appropriate to the indicated water-steam region.

The task of altering the digital computer program to represent the water-steam two-phase relationships is in progress. The steam generator model of the economizer, boiler, and superheater should be operational by the end of June 1973.

GAS-COOLED REACTOR PROGRAMS

NOVEMBER 1, 1973

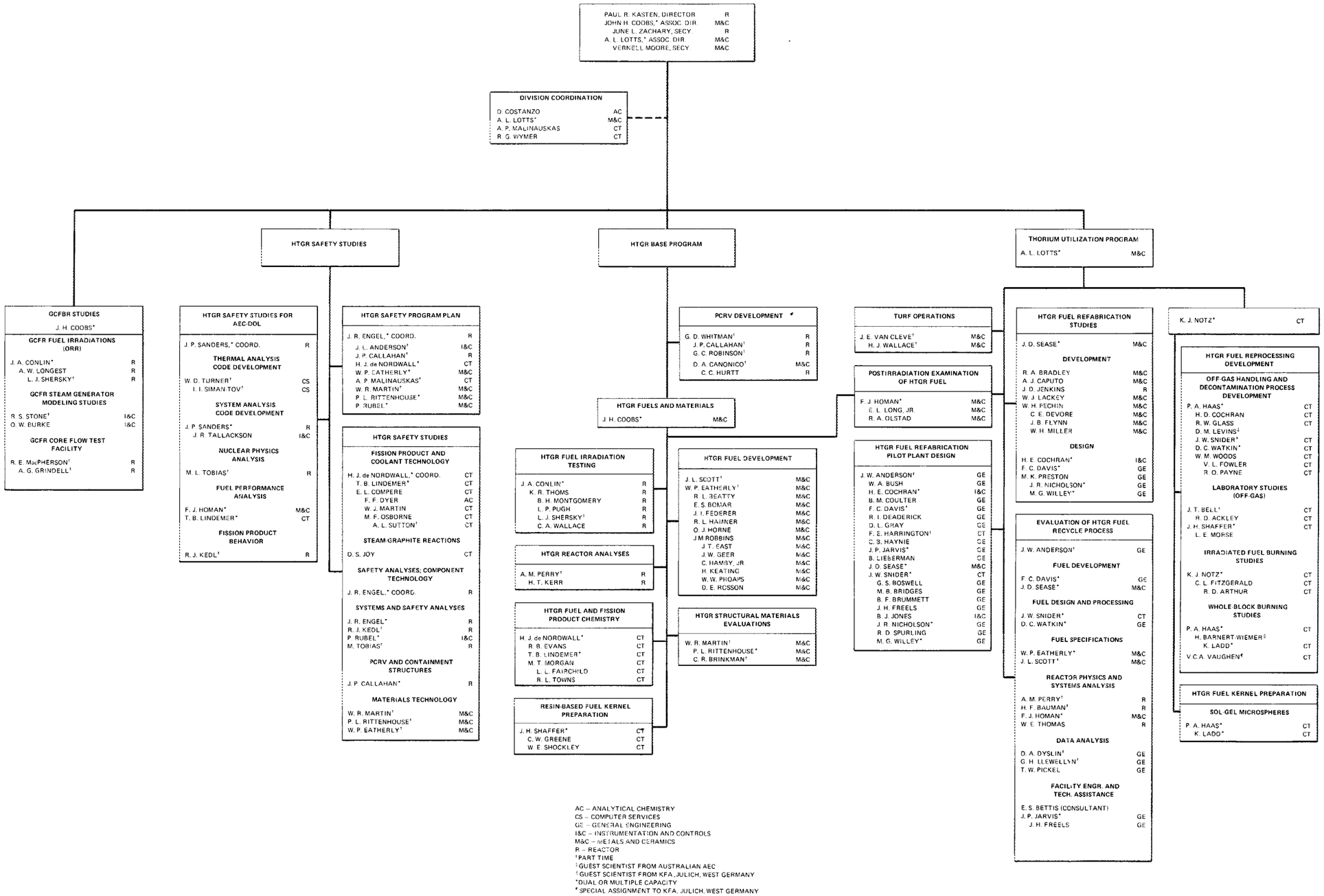

AC – ANALYTICAL CHEMISTRY
CS – COMPUTER SERVICES
GE – GENERAL ENGINEERING
I&C – INSTRUMENTATION AND CONTROLS
M&C – METALS AND CERAMICS
R – REACTOR
†PART TIME
‡GUEST SCIENTIST FROM AUSTRALIAN AEC
§GUEST SCIENTIST FROM KFA, JULICH, WEST GERMANY
*DUAL OR MULTIPLE CAPACITY
¶SPECIAL ASSIGNMENT TO KFA, JULICH, WEST GERMANY

ORNL-4911
UC-77 — Gas Cooled Reactor Technology

INTERNAL DISTRIBUTION

1. R. D. Ackley
2. G. M. Adamson
3. H. I. Adler
4. J. L. Anderson
5. J. W. Anderson
6. J. A. Auxier
7. H. F. Bauman
8. S. E. Beall
9. R. L. Beatty
10. M. Bender
11. L. L. Bennett
12. C. E. Bettis
13. E. S. Bettis (Consultant)
14. R. E. Blanco
15. E. G. Bohlmann
16. E. S. Bomar
17. W. D. Bond
18. C. J. Borkowski
19. R. A. Bradley
20. R. B. Briggs
21. R. E. Brooksbank
22. K. B. Brown
23. F. R. Bruce
24. R. H. Bryan
25. O. W. Burke
26. W. A. Bush
27. J. P. Callahan
28. A. J. Caputo
29. H. P. Carter
30. J. M. Chandler
31. H. D. Cochran
32. H. E. Cochran
33. E. L. Compere
34. J. A. Conlin
35–39. J. H. Coobs
40. W. H. Cook
41. D. Costanzo
42. W. B. Cottrell
43. J. A. Cox
44. B. M. Coulter
45. F. L. Culler
46. J. E. Cunningham
47. F. C. Davis
48. R. I. Deaderick
49. H. J. de Nordwall
50. F. F. Dyer
51. D. A. Dyslin
52. W. P. Eatherly
53. J. R. Engel
54. R. B. Evans III
55. J. I. Federer
56. D. E. Ferguson
57. B. C. Finney
58. C. L. Fitzgerald
59. J. L. Fowler
60. A. P. Fraas
61. R. W. Glass
62. D. L. Gray
63. R. J. Gray
64. B. L. Greenstreet
65. W. R. Grimes
66. A. G. Grindell
67. P. A. Haas
68. R. L. Hamner
69. W. O. Harms
70. F. E. Harrington
71. C. B. Haynie
72. R. F. Hibbs (UCC)
73. M. R. Hill
74. R. M. Hill, Jr.
75. H. W. Hoffman
76. F. J. Homan
77. O. J. Horne
78. J. P. Jarvis
79. J. D. Jenkins
80–229. P. R. Kasten
230. R. J. Kedl
231. H. T. Kerr
232. E. M. King
233. W. J. Lackey
234. B. Leiberman
235. D. M. Levins
236. T. B. Lindemer
237. R. S. Livingston
238. G. H. Llewellyn
239. M. H. Lloyd
240. E. L. Long, Jr.
241. A. W. Longest
242–247. A. L. Lotts
248. R. S. Lowrie
249. R. E. MacPherson
250. A. P. Malinauskas

251. W. J. Martin
252. W. R. Martin
253. H. C. McCurdy
254. W. T. McDuffee
255. H. F. McDuffie
256. D. L. McElroy
257. L. E. McNeese
258. B. H. Montgomery
259. M. T. Morgan
260. L. E. Morse
261. F. H. Neill
262. J. P. Nichols
263. K. J. Notz
264. L. C. Oakes
265. R. A. Olstad
266. M. F. Osborne
267. P. Patriarca
268–269. R. B. Parker
270. W. H. Pechin
271. A. M. Perry
272. T. W. Pickel
273. H. Postma
274. M. K. Preston
275. M. E. Ramsey
276. P. L. Rittenhouse
277. J. M. Robbins
278. M. W. Rosenthal
279. P. Rubel
280. J. P. Sanders
281. J. L. Scott
282. J. D. Sease
283. J. H. Shaffer
284. M. R. Sheldon
285. R. L. Shepard
286. S. Siegel
287. G. M. Slaughter
288. J. W. Snider
289. I. Spiewak
290. R. S. Stone
291. D. A. Sundberg
292. J. R. Tallackson
293. E. H. Taylor
294. W. E. Thomas
295. K. R. Thoms
296. M. Tobias
297. D. B. Trauger
298. W. E. Unger
299. J. E. Van Cleve
300. V. C. A. Vaughen
301. D. C. Watkin
302. A. M. Weinberg
303. J. R. Weir
304. J. C. White
305. G. D. Whitman
306. M. K. Wilkinson
307. W. M. Woods
308. R. G. Wymer
309. Gale Young
310. ORNL Patent Office
311–312. MIT Practice School Library
313. Y-12 Document Reference Section
314–316. Central Research Library
317–322. Laboratory Records Department
323. Laboratory Records, RC

EXTERNAL DISTRIBUTION

324. Research and Technical Support Division, AEC, ORO
325. Patent Office, AEC, ORO
326–484. Given distribution as shown in TID-4500 under Gas Cooled Reactor Technology category (25 copies -- NTIS)

☆U.S. GOVERNMENT PRINTING OFFICE: 1973-747-302/125